BIOADHESION

EDITED BY: Stanislav N. Gorb and Ken Nakano
PUBLISHED IN: Frontiers in Mechanical Engineering

frontiers Research Topics

ISSN 1664-8714
ISBN 978-2-88971-420-9
DOI 10.3389/978-2-88971-420-9

About Frontiers

Frontiers is more than just an open-access publisher of scholarly articles: it is a pioneering approach to the world of academia, radically improving the way scholarly research is managed. The grand vision of Frontiers is a world where all people have an equal opportunity to seek, share and generate knowledge. Frontiers provides immediate and permanent online open access to all its publications, but this alone is not enough to realize our grand goals.

Frontiers Journal Series

The Frontiers Journal Series is a multi-tier and interdisciplinary set of open-access, online journals, promising a paradigm shift from the current review, selection and dissemination processes in academic publishing. All Frontiers journals are driven by researchers for researchers; therefore, they constitute a service to the scholarly community. At the same time, the Frontiers Journal Series operates on a revolutionary invention, the tiered publishing system, initially addressing specific communities of scholars, and gradually climbing up to broader public understanding, thus serving the interests of the lay society, too.

Dedication to Quality

Each Frontiers article is a landmark of the highest quality, thanks to genuinely collaborative interactions between authors and review editors, who include some of the world's best academicians. Research must be certified by peers before entering a stream of knowledge that may eventually reach the public - and shape society; therefore, Frontiers only applies the most rigorous and unbiased reviews.
Frontiers revolutionizes research publishing by freely delivering the most outstanding research, evaluated with no bias from both the academic and social point of view. By applying the most advanced information technologies, Frontiers is catapulting scholarly publishing into a new generation.

What are Frontiers Research Topics?

Frontiers Research Topics are very popular trademarks of the Frontiers Journals Series: they are collections of at least ten articles, all centered on a particular subject. With their unique mix of varied contributions from Original Research to Review Articles, Frontiers Research Topics unify the most influential researchers, the latest key findings and historical advances in a hot research area! Find out more on how to host your own Frontiers Research Topic or contribute to one as an author by contacting the Frontiers Editorial Office: frontiersin.org/about/contact

BIOADHESION

Topic Editors:
Stanislav N. Gorb, University of Kiel, Germany
Ken Nakano, Yokohama National University, Japan

Image: jo Crebbin/Shutterstock.com

Citation: Gorb, S. N., Nakano, K., eds. (2021). Bioadhesion. Lausanne: Frontiers Media SA. doi: 10.3389/978-2-88971-420-9

Table of Contents

frontiers in Mechanical Engineering

EDITORIAL
published: 11 August 2021
doi: 10.3389/fmech.2021.740496

Editorial: Bioadhesion

Stanislav N. Gorb[1*†] *and Ken Nakano*[2*†]

[1]*Department of Functional Morphology and Biomechanics, Kiel University, Kiel, Germany,* [2]*Faculty of Environment and Information Sciences, Yokohama National University, Yokohama, Japan*

Keywords: biological surfaces, bioinspired materials, biomimetic systems, attachment, detachment

Editorial on the Research Topic

Bioadhesion

Materials and systems preventing the separation of two surfaces may be defined as adhesives. There are a variety of natural adhesive devices based on entirely mechanical principles, while others additionally rely on the chemistry of polymers and colloids. Adhesive organs are functional systems, the purpose of which is either temporary or permanent attachment of an organism to the substrate surface, to another organism, or temporary interconnection of body parts within an organism. Their design varies enormously and is subject to different functional loads. There is no doubt that many functional solutions have evolved independently in different lineages of organisms. Many species of animals and plants are supplied with diverse adhesive surfaces, the morphology of which depends on the species biology, and the particular function in which the adhesive device is involved.

There are numerous publications on cell adhesion phenomena, but much fewer references are devoted to the non-specific adhesion of living organisms. Because of the structural, mechanical, and chemical complexity of biological surfaces related to adhesion, exact working mechanisms have been clarified only for some systems. In this Research Topic (RT) "Bioadhesion", we aimed at collecting articles dealing with biological surfaces and systems specialized for adhesion enhancement. These contributions discuss adhesive function of biological surfaces and their relationship with the structure, contact mechanics and chemistry of surfaces. Because of the diversity of functions in adhesion-related biological surfaces, biology could provide interesting inspirations for a broad range of topics in physics, chemistry, and engineering.

In the following, we briefly introduce the 13 articles comprising this RT. They can be broadly divided into four categories: 1) bacterial adhesion, 2) plant adhesion, 3) animal adhesion, and 4) biomimetic adhesion.

BACTERIAL ADHESION

This collection of articles begins with a Mini Review article on bacterial adhesion entitled "*Modeling Bacterial Adhesion to Unconditioned Abiotic Surfaces*" presented by Spengler et al. As a first step toward biofilm formation, understanding bacterial adhesion is of fundamental interests in many applications. The authors presented the approaches of understanding bacterial adhesion on the whole-cell level in the framework of colloidal science and contact mechanics. Then, they discussed the prospects and limitations of the models and describe the efforts made outside the frameworks in describing bacterial adhesion mediated by cell surface macromolecules.

PLANT ADHESION

Two Original Research articles on plant adhesion are contained in this collection. The first article is "*Root Hair Adhesion in Posidonia oceanica (L.) Delile Seedlings: A Numerical Modelling Approach*"

OPEN ACCESS

Edited and reviewed by:
Valentin L. Popov, Technical University of Berlin, Germany

***Correspondence:**
Stanislav N. Gorb
sgorb@zoologie.uni-kiel.de
Ken Nakano
nakano@ynu.ac.jp

†These authors have contributed equally to this work and share first authorship

Specialty section:
This article was submitted to Tribology, a section of the journal Frontiers in Mechanical Engineering

Received: *13 July 2021*
Accepted: *26 July 2021*
Published: *11 August 2021*

Citation:
Gorb SN and Nakano K (2021) Editorial: Bioadhesion. Front. Mech. Eng 7:740496. doi: 10.3389/fmech.2021.740496

presented by Zenone et al. In the marine environment, the seagrass *Posidonia oceanica* attaches firmly to solid substrates *via* adhesive root hairs, forming micro-pad structures at their tips. The authors used novel morphological and ultrastructural data to develop a numerical model to study the dynamics of root hair adhesion during contact formation on rough solid substrates.

The second article on plant adhesion is "*Push and Pull: Biomechanics of the Pollination Apparatus of Oncidium spp.*" presented by Thielen et al. In orchid pollination process, a mechanical barrier ensuring that only suitable pollinators can access the flowers and remove the pollen is the vital selective trait. The authors described the functional morphology of the pollination apparatus in two orchid species, *Oncidium wentworthianum* and *O. otogaya*, by experimentally studying adhesive events in the pollination process.

ANIMAL ADHESION

Six Original Research articles on animal adhesion are contained in this collection. The first article is "*Setal Field Transects, Evolutionary Transitions and Gecko–Anole Convergence Provide Insights Into the Fundamentals of Form and Function of the Digital Adhesive System of Lizards*" presented by Russell and Garner. During the last two decades many investigations examining the gecko adhesive system have been carried out, where most of the research has been focused on few species. The authors of this broad comparative study examined in detail setal transects of adhesive pads, evolutionary transitions from non-adhesive to adhesive digits, and the convergent evolution of adhesive apparatuses in geckos' and anoles.

The second article on animal adhesion is "*Adhesion Behaviors of Abalone Under the Action of Water Flow*" presented by Zhang et al. The abalone is well known for its non-permanent adhesive system, detailed information of which might be beneficial to such areas as underwater robotics, high precision sensors, and intelligent devices. The authors conducted experiments, to observe the posture response of an abalone under various water flow conditions. They also performed numerical simulations to display the stress field, reasonably explaining the results of experimental observations.

The third article on animal adhesion is "*Adhesive Behavior of Propolis on Different Substrates*" presented by Saccardi et al. Propolis is a sticky substance used by bees to seal gaps in their hive and protect the colony against pathogens. The authors performed 1) adhesion tests with propolis on various substrates, 2) differential scanning calorimetry analysis, and 3) compression tests. The obtained data are interpreted from a biomechanical point of view, and the significance of the obtained results for bee biology was discussed.

The fourth article on animal adhesion is "*Adhesive Droplets of Glowworm Snares (Keroplatidae: Arachnocampa spp.) Are a Complex Mix of Organic Compounds*" presented by Wolff et al. Glowworms are an iconic part of the fauna of Australia and New Zealand that combine the construction of a sticky snare with a bioluminescent lure. The authors studied the chemical composition of the water-soluble fraction of adhesive droplets from the snares of three glowworm species using nuclear magnetic resonance and mass spectrometry. The obtained results contribute to our understanding of the unique prey capture strategy of glowworms.

The fifth article on animal adhesion is "*Perspective for a New Bioinspired Permanent Adhesive for dry Conditions - Insights in the Glue Producing Japanese art of Defence System of the Oita Salamander Hynobius dunni*" presented by Von Byern et al. The defense secretion system in amphibians is expected to provide potential for novel fast-curing secretion able to adhere to various surfaces under dry conditions. With the microanatomical and histochemical characterization of the endemic Japanese Oita salamander *Hynobius dunni*, the authors discussed the nature of the chemical composition of glue-producing glands and its divergence to the other well-characterized species *Plethodon shermani*.

The sixth and final article on animal adhesion is "*Adhesion of Individual Attachment Setae of the Spider Cupiennius salei to Substrates With Different Roughness and Surface Energy*" presented by Poerschke et al. Dynamic adhesion is known to be a key ability of spiders to climb up smooth surfaces. The authors examined the adhesion of single setae of the spider *Cupiennius salei* and studied the pretarsus morphology and the fine structure of individual setae. They showed that the adhesion force on the smooth hydrophobic polytetrafluoroethylene was 30% of that on a smooth hydrophilic glass substrate. The main finding of this article is that both the structure and adhesive performance of individual setae very strongly differ depending on the setal position on the pretarsus.

BIOMIMETIC ADHESION

Four articles on biomimetic adhesion are contained in this collection: two Review articles are followed by two Original Research articles. The first article is "*Applications of Bioinspired Reversible Dry and Wet Adhesives: A Review*" presented by Kang et al. Bioinspired adhesives that emulate the unique dry and wet adhesion mechanisms of living systems have been actively explored over the past two decades. This review summarizes recent efforts to apply synthetic dry and wet adhesives, mainly focusing on grippers, robots, and wearable sensors.

The second article on biomimetic adhesion is "*Mechanics of Crater-Enabled Soft Dry Adhesives: A Review*" presented by Wang et al. Recently, cratered surfaces emerged as a different tool for dry adhesion, as they exhibit many advantageous properties, such as tunable pressure-sensitive adhesion, high underwater adhesive strength, and good reusability. This review summarizes the authors' recent work (combining experimental, modeling, and computational components) on the mechanical characterization of cratered surfaces.

The third article on biomimetic adhesion is "*On the Nanomechanical and Viscoelastic Properties of Coatings Made of Recombinant Sea Star Adhesive Proteins*" presented by Lefevre et al. To attach to surfaces in the sea, sea stars produce proteinaceous adhesive secretions. Some recombinant proteins adsorb seawater and form coatings on different surfaces. The authors used atomic force microscopy to characterize the nanomechanical properties of

these coatings with an emphasis on functional characteristics, such as adhesive properties and modulus of elasticity.

The fourth and final article on biomimetic adhesion is "*Multi-Technique Investigation of a Biomimetic Insect Tarsal Adhesive Fluid*" presented by Fowler et al. The authors combined sum frequency generation with multiple bulk characterization techniques to examine a biomimetic adhesive fluid inspired by the tarsal fluid of insects. They showed that the adhesive mechanism of insect tarsal fluid relies upon contributions from surface-specific properties optimizing traction force and bulk properties promoting rapid surface wetting and maintaining pull-off force for fast detachment.

At the end of this Editorial, the editors would like to express their sincere thanks to all authors for their valuable contributions to this article collection on biological and bioinspired adhesion. It successfully demonstrates how diverse and expansive this field currently is. The editors also strongly hope that the readers will find different perspectives and deep insights in this collection to inspire their future studies on bioadhesion.

AUTHOR CONTRIBUTIONS

All authors listed have made a substantial, direct, and intellectual contribution to the work and approved it for publication.

Conflict of Interest: The authors declare that the research was conducted in the absence of any commercial or financial relationships that could be construed as a potential conflict of interest.

Publisher's Note: All claims expressed in this article are solely those of the authors and do not necessarily represent those of their affiliated organizations, or those of the publisher, the editors and the reviewers. Any product that may be evaluated in this article, or claim that may be made by its manufacturer, is not guaranteed or endorsed by the publisher.

frontiers in Mechanical Engineering

ORIGINAL RESEARCH
published: 19 November 2020
doi: 10.3389/fmech.2020.590894

Root Hair Adhesion in *Posidonia oceanica* (L.) Delile Seedlings: A Numerical Modelling Approach

Arturo Zenone[1,2]*, *Alexander E. Filippov*[1,3], *Alexander Kovalev*[1], *Fabio Badalamenti*[2] and *Stanislav N. Gorb*[1]

[1]Department of Functional Morphology and Biomechanics, Zoological Institute, Kiel University, Kiel, Germany, [2]Institute for the Anthropic impacts and Sustainability in marine environment, CNR, Palermo, Italy, [3]Donetsk Institute of Physics and Engineering, Academy of Sciences of Ukraine, Donetsk, Ukraine

Animals and plants use adhesion to move, to anchor to a substrate, or to disperse seeds and fruits. Some plants developed a root pad as a common strategy to adhere to consolidated substrates. In the marine environment, the seagrass *Posidonia oceanica* attaches firmly to consolidated substrates via adhesive root hairs, forming a pad structure. We used novel morphological and ultrastructural data to develop a numerical model to study the dynamics of root hair adhesion during contact formation on rough consolidated substrates for this species. Morphological analysis, conducted using Scanning Electron Microscope, highlighted the role of root hair branching in pad formation. Transmission Electron Microscope microscopy allowed us to identify a glue-like substance at the pad/substrate interface. The numerical model highlighted the role played by the cell wall's elasticity in pad formation and its importance in guaranteeing a firm adhesion. Furthermore, the effectiveness of these mechanisms was assessed at different simulated roughness levels. Increasing knowledge on the adhesion mechanism of seagrass to consolidated substrates could be pivotal in developing advanced seedling-based restoration protocols. The findings of this study could contribute to restoration activities planned to contrast seagrass regression. Transplanting initiatives using seedlings can now better address the search for suitable and low-impact ways to fix germinated plants to the substrate.

Keywords: ***P. oceanica,*** **root hair, adhesion, branching, transplanting initiatives**

OPEN ACCESS

Edited by:
Alessandro Ruggiero, University of Salerno, Italy

Reviewed by:
Abhishek Srivastava, Western Digital, United States
Yoshitaka Nakanishi, Kumamoto University, Japan

***Correspondence:**
Arturo Zenone
arturozeno@gmail.com

Specialty section:
This article was submitted to Tribology, a section of the journal Frontiers in Mechanical Engineering

Received: *03 August 2020*
Accepted: *18 September 2020*
Published: *19 November 2020*

Citation:
Zenone A, Filippov AE, Kovalev A, Badalamenti F and Gorb SN (2020) Root Hair Adhesion in Posidonia oceanica *(L.) Delile Seedlings: A Numerical Modelling Approach. Front. Mech. Eng. 6:590894. doi: 10.3389/fmech.2020.590894*

INTRODUCTION

Living organisms employ a great variety of attachment structures, such as hooks, suction cups, sticky pads, and glue-like substances (Scherge and Gorb, 2001), to give them the capability to climb (e.g., English Ivy), walk on smooth surfaces (e.g., geckos), be transported (e.g., zoochory), or be strongly fixed to consolidated substrates (e.g., mussels and barnacles). Plants use adhesion mainly to disperse fruits and seeds, but some species form adhesive structures to anchor to the substrate. These pad-like structures often consist of multi-layered multicellular formations that can originate from tendrils, modified leaves, or roots (Groot et al., 2003; Melzer et al., 2010; Steinbrecher et al., 2010; Steinbrecher et al., 2011; Melzer et al., 2012; Seidelmann et al., 2012; Bohn et al., 2015; Yang and Deng, 2017). The pad attachment occurs via mechanical interlocking which consists in replicating the surface of a given substrate, filling up the surface profile, and eventually becoming stiff by thickening the cell walls. Adhesion can act with or without the support of a glue. This mechanism has been shown to

produce a firm attachment on a variety of surfaces in different plant species (Scherge and Gorb, 2001).

Seagrasses have thrived in the oceans for tens of millions of years (Larkum et al., 2018), but it is only in recent decades that they have begun to experience a severe regression due to human activities along coastal areas (Waycott et al., 2009; Telesca et al., 2015). Therefore, several attempts are underway to restore damaged meadows and to improve their ecological resilience (Unsworth et al., 2015). Seagrasses natural recovery usually occurs trough vegetative proliferation. In a species that lacks floating rhizomes, the recolonization of strongly damaged meadows may occur via sexual propagules. In this case, the success of seedling settlement and recruitment represents a bottleneck in the seagrass sexual reproduction strategy as its failure could impair the connectivity and genetic variability of these important habitat-forming species (Jahnke et al., 2016).

Most seagrass species have been reported to grow on soft bottoms (Green and Short, 2003; Balestri et al., 2015), but a few of them (i.e., *Phyllospadix spp.*, *Posidonia oceanica*) possess specific morphological adaptations that enable them to colonize and grow on hard bottoms (Barnabas, 1994; Badalamenti et al., 2015). These species show a variety of morphological features, such as rudimental anchorage apparatuses or more sophisticated structures (e.g., adhesive root hairs) to adhere to consolidated substrates (Barnabas, 1994; Green and Short, 2003; Badalamenti et al., 2015).

The combination of knowledge on the specific morphology of the seagrass root system with the characteristics of the habitats in which each species settles and recruits is a prerequisite for developing projects aimed at advancing restoration protocols. In recent years, many transplanting projects have been planned to restore damaged meadows, and the use of sexual propagules could be pivotal in achieving restoration goals. In this context, an increase in the current knowledge on the mechanisms of root adhesion, which provide the plantlet with a strong anchorage and persistence against drag forces on the sea floor, is of fundamental importance (Badalamenti et al., 2015).

In the Mediterranean Sea, seedlings of the endemic seagrass *Posidonia oceanica* (L.) Delile successfully colonize hard bottoms and their settlement occurs preferentially on consolidated and firm substrates via adhesive root hairs (Badalamenti et al., 2015). Such a strategy represents a mechanism for early settlement on vegetated and unvegetated rocky shores, which favors plantlet persistence on consolidated substrates compared to unconsolidated ones (Alagna et al., 2015; Badalamenti et al., 2015). Root hairs appear soon after germination at the hypocotyl and both at the principal and adventitious roots. When not in contact with the substrate, root hair tips remain long and straight, but they quickly begin to branch after contact formation (Alagna et al., 2015; Badalamenti et al., 2015; Zenone et al., 2020). *P. oceanica* may thrive in habitats characterized by high hydrodynamism (Montefalcone et al., 2016) hence its anchorage system has to be highly efficient, especially in the early life stages, when seeds reach the recruitment sites and settlement occurs.

Posidonia oceanica roots form a pad starting from the branching of a single cell, the root hair, which determines the anchoring via mechanical interlocking (Zenone et al., 2020). Root hairs adapt themselves to the characteristics of the substrate on which the attachment process occurs. The pad morphology depends on the substrate micro-roughness and optimal adhesion is achieved at a micro-roughness of 3–52 μm (asperities diameter), while the maximum adhesion force occurs at a micro-roughness of 12 μm, a value similar to the average diameter of the root hair (Zenone et al., 2020).

In recent years, numerical models have been elaborated to integrate a variety of important biological and physical processes involving plant growth (Godin and Sinoquet, 2005; Dupuy et al., 2010). This approach is useful to address biological questions, as models may show hidden properties and behaviors that can be validated with experimental observations. In the present paper, we report on a numerical model that is inspired by the morphological characteristics of the *P. oceanica* root hairs to investigate the dynamics of *P. oceanica* root hair adhesion during contact formation on rough consolidated substrates.

The model was constructed to answer the following questions: 1) Does the root hair growth change vary the cell's elastic properties when substrate micro-roughness is kept constant? 2) Does the contact formation change, varying the levels of substrate roughness, when the cell's elastic properties are kept constant? and 3) Can attachment properties of the root hair be explained exclusively by mechanical interlocking? In this work, we hypothesize that: 1) root hair softness plays a fundamental role in the adhesion process; 2) the substrate micro-roughness at to the scale of the root hair diameter improves proper contact area formation and additionally contributes to the mechanical interlocking; and 3) a glue-like substance may be additionally involved in the adhesion mechanism, as hypothesized by Zenone et al. (2020).

MATERIALS AND METHODS

Posidonia oceanica seeds were collected along the Sicilian coast (NW Sicily) between May and June 2017 and left growing (**Figure 1A**) for 6 months on 3 cm × 3 cm tiles of epoxy resin replicas (Spurr, 1969) of sand paper (12 μm asperities size, Starcke Ersta Abrasives, Germany). Resin replicas were created using a two-step molding method (Gorb, 2007).

Different microscopy techniques were used to investigate the root hairs morphology and their principal characteristics. All the morphological features were measured on images from a set of 30 seedling samples (see **Table 1** for details) by means of ImageJ software (Schneider et al., 2012).

Mean curvature and mean pad radius were calculated according to **Eqs. 10–14** (see below for details) using Matlab (ver. R2019b, The Math Works, Inc., (2018) United States). For this, a batch of homogeneously distributed points ($N \geq 100$) were selected along the pad perimeter. The coordinates of the points were used for calculation of the mean pad radius and the mean curvature.

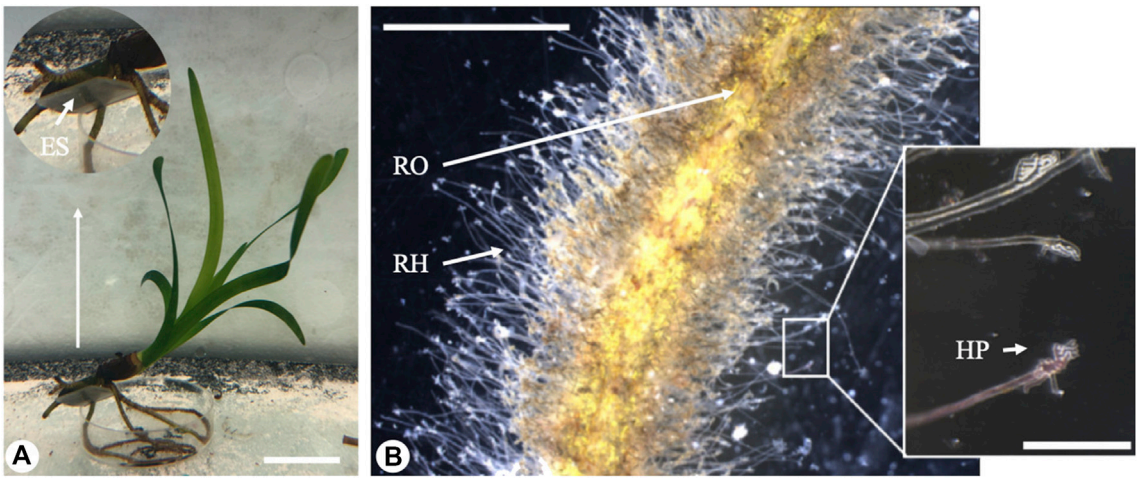

FIGURE 1 | The figure shows: **(A)** a *Posidonia oceanica* seedling grown experimentally in the aquarium and the detail of the roots grown in contact with the experimental tile (ES) (scale bar - 20 mm). **(B)** a root (RO) anchored through root hairs (RH) to the experimental tile surface (scale bar - 2 mm) with the detail of root hair pads (HP) adhering to the substrate (scale bar - 200 μm).

TABLE 1 | Measurements and estimations from the biological root hairs used as model parameters.

Parameter	*N*	Mean	SD	unit
Life time of a RH	—	7,000[a]	—	min
Hardening time	—	40[a]	—	min
RH width	10	12.31	1.94	μm
RH branch width	10	6.11	0.74	μm
RH apical cell wall	5	0.86	0.14	μm
RH basal cell wall	5	1.5	0.24	μm
Dx pad	10	76.81	12.17	μm
Dy pad	10	81.71	25.8	μm
Pad radius	10	28.95	4.06	μm
Curvature	3	0.13	0.03	μm^{-1}
Substrate particle size	10	12.75	2.42	μm
K (Elastic constant)		225[a]	—	N/m

[a]*Estimation.*

Root Hair Tips Morphology (Scanning Electron Microscope)

Root hair morphology was analyzed using a Scanning Electron Microscope (SEM, Hitachi TM3000; Hitachi High-Technologies, Corp., Tokyo, Japan). Portions of resin tiles with root hairs adhered on their surfaces were dehydrated in hexamethyldisilane (HMDS/1,1,1,3,3,3-Hexamethyldisilazan, Carl Roth GmbH & Co. KG, Karlsruhe, Germany). For HMDS drying, tiles were cut into pieces of 1 mm^3, fixed in a solution of 2.5% Glutardialdehyde and 2% Formaldehyde in 0.1 M cacodylate buffer overnight, and washed two times in 0.1 M cacodylate buffer, each for 20 min. They were then stained in a solution of 1% OsO4 in a 0.1 M cacodylate buffer for 1 h, then washed two times again in the 0.1 M cacodylate buffer for 20 min. Samples were then dehydrated by a graded series of ethanol (30 and 50%, 15 min each) and transferred to a 70% ethanol solution. Samples were then air-dried in a desiccator overnight. Finally, samples were mounted on SEM aluminum stubs, coated with gold palladium (10 nm thickness; Leica Bal-TEC SCD500, Leica Microsystems GmbH, Wetzlar, Germany), and immediately visualized in the SEM.

Root Hair Ultrastructure (Cryo-Scanning Electron Microscope and Transmission Electron Microscope)

Fresh portions of roots were visualized at high resolution using a cryo-SEM Hitachi S-4800 (Hitachi High-Technologies Corp., Tokyo, Japan) equipped with a Gatan ALTO2500 cryo-preparation system (Gatan, Inc., Abingdon, United Kingdom). Fresh root portions were fixed to the holder and immediately placed in the cryo-chamber (−140°C). The frozen samples were sputter-coated with gold–palladium (layer thickness 10–20 nm) and transferred to the SEM.

The root hair tips at the interface with the substrate were examined using a Transmission Electron Microscope (TEM) (Tecnai Spirit BioTWIN; FEI Company, Eindhoven, Netherlands). Samples were cut into small pieces of about 1 mm^3, fixed in 2.5% glutardialdehyde and 1% OsO4, dehydrated by a graded alcohol series to 100%, and gradually transferred to Spurr resin which was then cured at 70°C for 12 h. Resin blocs were trimmed and cut into semithin (1–3 μm) and ultrathin (50–60 nm) sections with a Leica EM UC7 ultramicrotome (Leica Microsystems GmbH; Wetzlar, Germany). Ultrathin sections were post-stained with gadolinium (III) acetate tetrahydrate and lead citrate and examined in TEM.

Numerical Modelling

In order to understand interactions between individual root hairs and rigid substrates of different roughness levels, we developed a

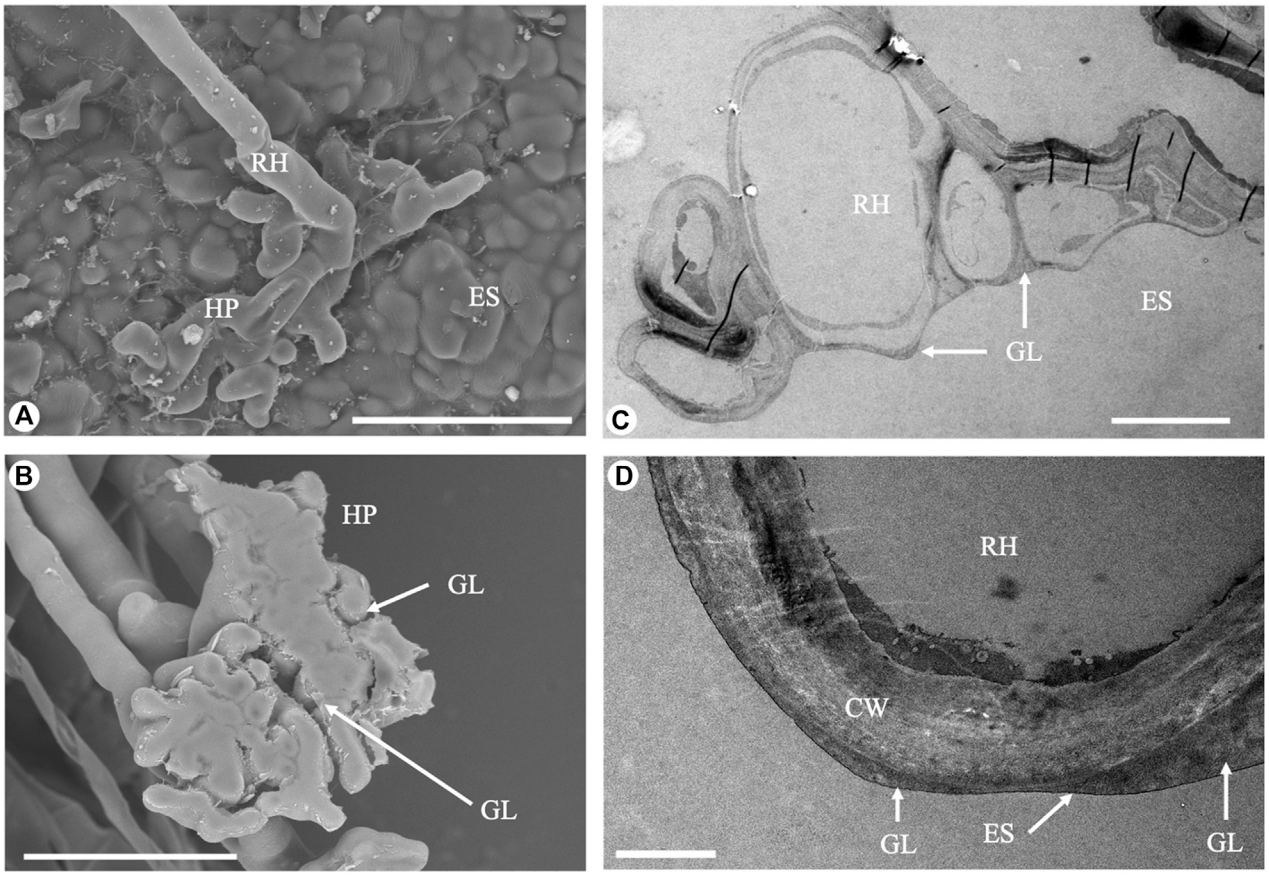

FIGURE 2 | Electron microscopy images of the root hairs. **(A)** Branched root hair adhering to a rough surface (Scanning Electron Microscope, scale bar - 50 μm). **(B)** Detached root hair pad: a glue-like substance is visible at the base (Scanning Electron Microscope, scale bar - 50 μm). **(C)** Cross-section of a root hair adhering to a rough surface (Transmission Electron Microscope, scale bar - 10 μm). **(D)** Details of the interface between the root hair and the experimental substrate: a thin glue-like substance layer fills the small interstices (Transmission Electron Microscope, scale bar - 1 μm). RH, root hair; HP, root hair pad; CW, cell wall; ES, experimental substrate; GL: glue-like substance.

simplified two-dimensional numerical model aimed at solving the complex original 3-dimensional problem. We substituted the root hair material by its boundary with an effective "stiffness" reminiscent of the surface tension.

This approach is based on an assumption that young root hair tips, being thin-walled bladders with a fluid inside, might behave similarly to a fluid-like system in contact with a solid substrate. Further, we defined the boundary conditions as a movable and growing "elastic chain." It allows us to naturally describe a multi-valued function of the boundary and its evolution over time. The rigidity of the chain corresponds to the surface tension of real material and allows simulating the system under consideration.

The model includes the following elements. The boundary of the root hair is modelled by an elastic fiber whose elasticity varies along its length, depends on time, and can change from initially soft to much stiffer or almost rigid (but still with some degree of flexibility). The fiber is constructed as an array of nodes connected by the segments $\vec{r}_j = \{x_j, y_j\}$. Longitudinal $\vec{F}^{\parallel}_{jj'}$ and transversal $\vec{F}^{\perp}_j$ stiffness of each segment is simulated by the following interactions between the segments:

$$\vec{F}^{\parallel}_{jj'} = K^{\parallel}\left(\vec{r}_j - \vec{r}_{j'}\right)\left[1 - \left(\vec{r}_j - \vec{r}_{j'}\right)^2 / dr^2\right], \quad (1)$$

and

$$\vec{F}^{\perp}_j = K^{\perp}\left(2\vec{r}_j - \vec{r}_{j+1} - \vec{r}_{j-1}\right). \quad (2)$$

The coordinates at the beginning and end of the segment represent the two nearest neighbors j; $j' = j \pm 1$ and $j = 1, \ldots, N_s$. Here, N_s is the total number of segments which varies with time according to the rules which will be described below. We estimated the *P. oceanica* root hair elastic constant $K^{\perp}_j$ as 225 N/m (**Table 1**).

The longitudinal force, $\vec{F}^{\parallel}_{jj'}$ is described by a two-valley potential which tends to keep the distance between the nodes $\vec{r}_j$ and $\vec{r}_{j\pm1}$ close to the equilibrium length of the segment dr. The transversal elastic force, $\vec{F}^{\perp}_j$, holds $\vec{r}_j$ close to the position between its nearest neighbours $(\vec{r}_{j+1} + \vec{r}_{j-1})/2$, and therefore tends to keep the angle between the neighbouring segments close to 180°.

It is important to note that the "chain" simulates a boundary of the root hair pad, so its beginning and its end must be connected. It means

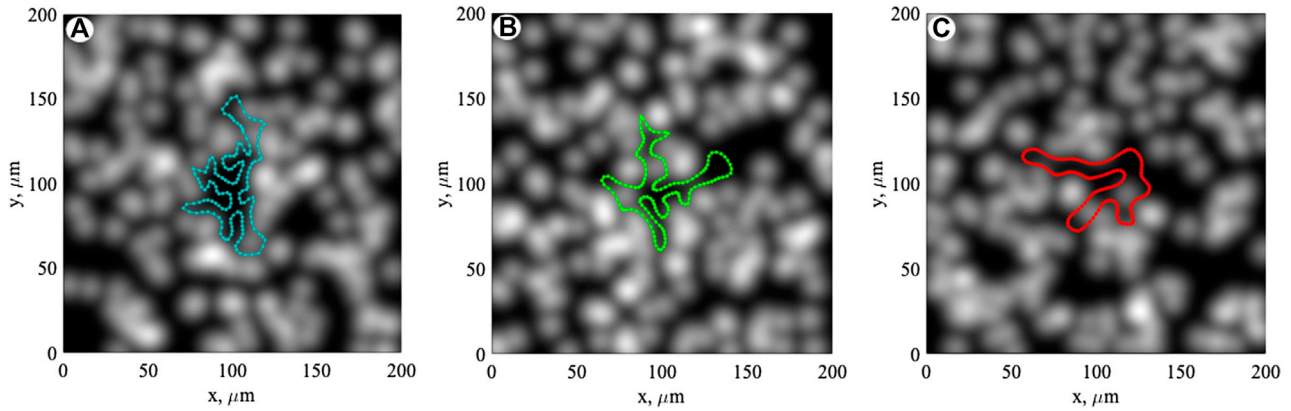

FIGURE 3 | Typical configurations of the boundary for three different elastic constants, $K_{01}^{\perp}$, $K_{02}^{\perp}$, and $K_{03}^{\perp}$, are shown in the subplots **(A)**, **(B)**, and **(C)**, respectively. Different colors corresponding to these three cases (blue, green, and red, respectively) are maintained in the subsequent plots. The substrate structure is shown by gray scale map, where white and black correspond to the highest and lowest asperities height, respectively.

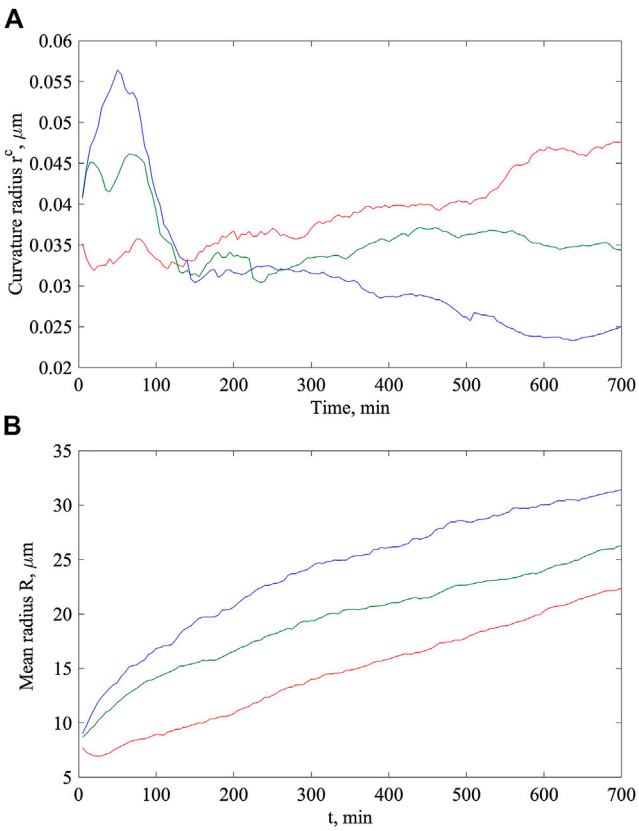

FIGURE 4 | Time dependencies of the curvature radius **(A)** and mean radius of the root hair **(B)** calculated for the same initial elastic constants: $K_{01}^{\perp}$, $K_{02}^{\perp}$, and $K_{03}^{\perp}$ as above. The meaning of the colors is the same as in **Figure 2**.

that the last element of the array $\vec{r}_{N_s} = \{x_{N_s}, y_{N_s}\}$ must be initially placed at a distance from the first one $\vec{r}_1 = \{x_1, y_1\}$ equal to the segment length ***dr*** and it must elastically interact with it, according to the same interactions given by **Eqs. 1** and **2**, as all other segments.

A further demand from the model is that the root should grow with time. To reproduce root hair elastic properties, the length of each segment must be kept more or less fixed. So, an increase of root hair length will be simulated by changing the number of the

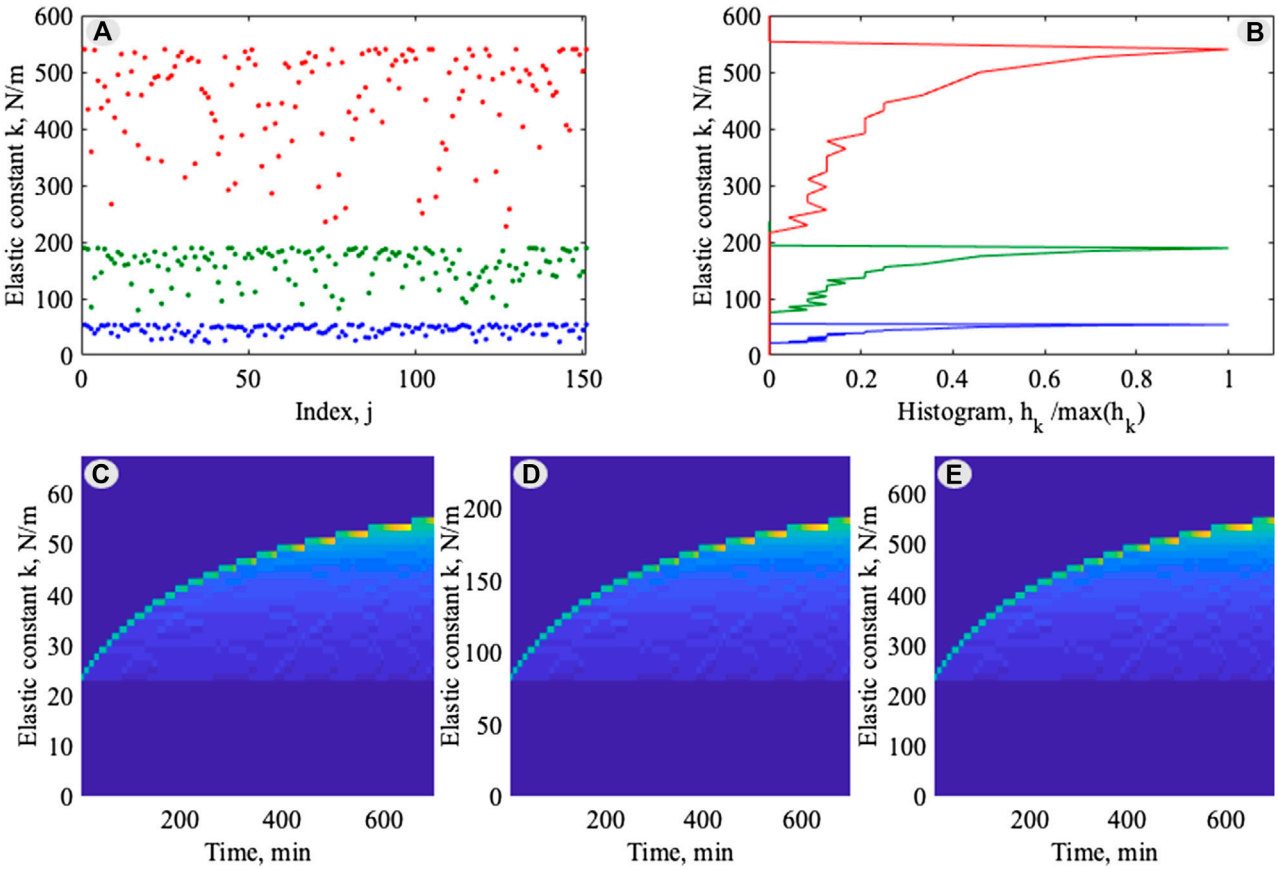

FIGURE 5 | Statistically universal evolution of the individual time-dependent elastic constants: **(A)** instant configuration of the values $K_j^{\perp} = K_j^{\perp}(\tau_j)$ plotted versus index j; **(B)** histograms of the current distributions shown in the previous subplot; **(C–E)** color-maps of the time-dependent histograms for the values $K_{01}^{\perp}$, $K_{02}^{\perp}$, and $K_{03}^{\perp}$, respectively. Deep blue and deep red colors correspond to the minimal and maximal values, respectively.

segments N_s. In other words, the size of the nodes array increases with time. Moreover, according to the experimental observation, the elasticity of each segment starting from its appearance changes with the time too. In other words, both elastic coefficients $K_{jj}^{\parallel}$ and $K_j^{\perp}$ are time-dependent. The resulting distribution of the elasticity along the root at every particular moment should reflect the gradients of the elasticity between softer newly generated segments and harder ones in the older parts of the boundary. In this case, we considered a sort of aging of the root hair in the model, intended as a hardening with a characteristic time of about 40 min (**Table 1**).

Counting on the particular nature of the system, we will insert a new node $\vec{r}_k = \{x_k, y_k\}$ between two already existing nodes $\vec{r}_k$ and $\vec{r}_{k+1}$ after time interval Δt. We will do this randomly along the whole chain. If we suppose that the boundary grows isotropically (i.e., branching occurs at different portions of the root hair pad), the random number j should be uniformly distributed in interval $j = [1: N_s]$. However, the boundary of real root has preferable centers of growth independently on the substrate asperities. To simulate this, we defined some segments, where insertion of the new segments occurs with a higher probability. To be definite, we defined five symmetrically placed orientations (in originally isotropic boundary), where new segments can be inserted with 10% higher probability than into other ones.

The ratio between Δt and discrete time steps dt of the calculation, $\Delta t/dr$ regulates the rate of the root growth. From a mathematical point of view, the only limitation is $\Delta t/dr \gg 1$, but biologically the rate must also be adjusted to the total time of the process (real time of root growth: 7,000 min, **Table 1**).

In general, root hairs are very soft at the growing tip. However, their hardiness increases along the shaft (Grierson et al., 2014). In the model, the elastic constant $K_k^{\perp}$ of each newly created segment is very small and increases with time. Mathematically, it means that every segment has its life counter τ_j which starts from $\tau_j = 0$, when the segment is "just born," and increases synchronously with common time steps: $\tau_j(t + dt) = \tau_j(t) + dt$. In other words, each value of $K_j^{\perp}$ starts from $min(K_j^{\perp}) = K_k^{\perp}$ at $\tau_j = 0$ and goes asymptotically at $\tau_j \to \infty$ to the maximal rigidity $max(K_j^{\perp}) = \lambda K_k^{\perp}$, where coefficient $\lambda > 1$. For a real system, the coefficient λ can be very large, but for the transparency of final plots of the simulation results, we used $\lambda = 3$. Of course, resulting structures in all the numerical experiments are defined by a competition between the

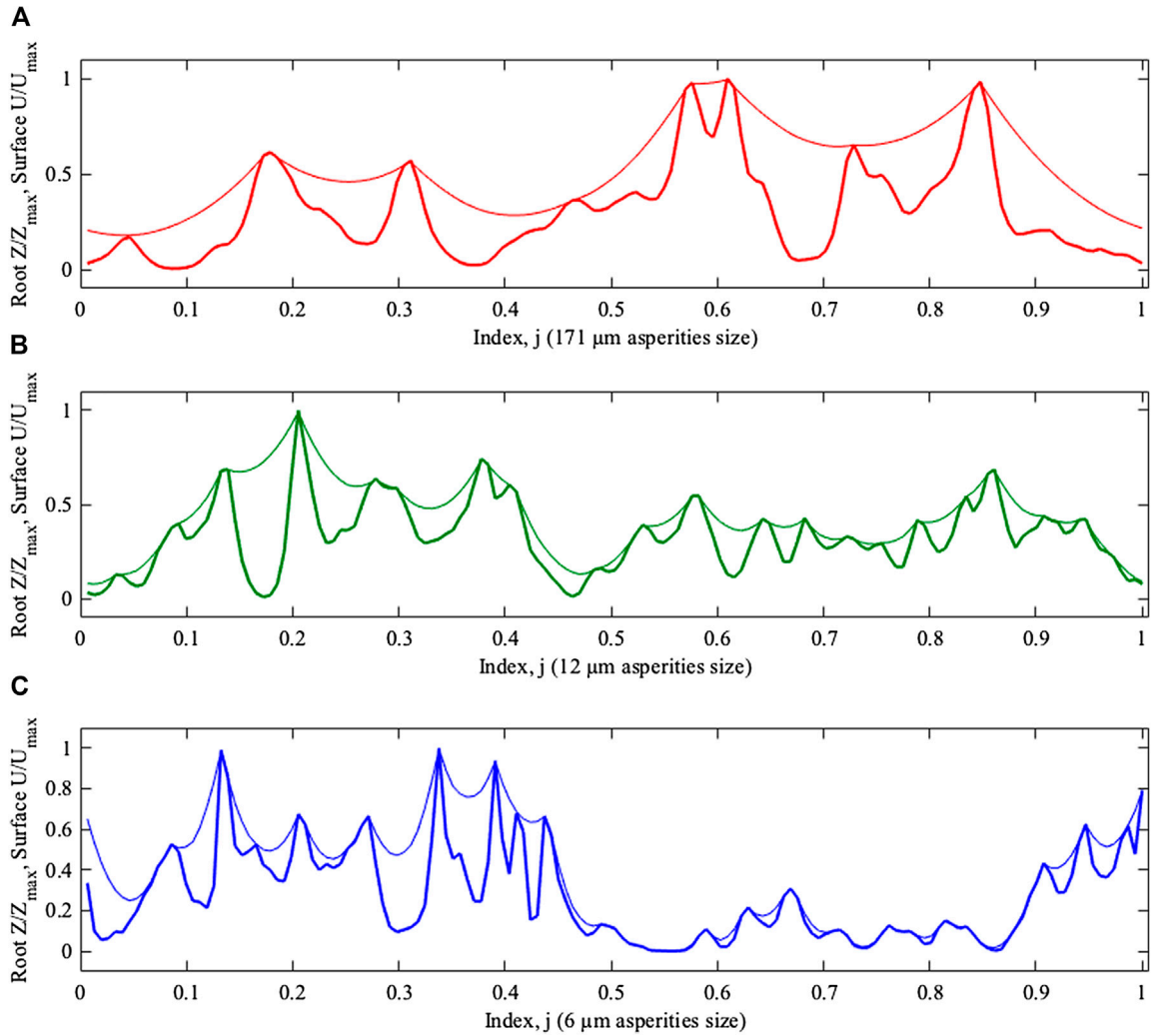

FIGURE 6 | Equilibrium z-positions of the elastic boundaries plotted along closed curve as the functions of the index j of nodes normalized to the number N_c (thin lines). The subplots **(A–C)** correspond to the three different roughness levels (red - 171 μm, green - 12 μm, blue - 6 μm asperities size, respectively). Random realizations of the rigid surfaces are plotted by the bold lines.

anisotropic creation of new segments, the hardening of the segments with the time, and the interaction of the growing boundary with the surface asperities.

The contact surface can be modelled in different ways depending on the particular problem. A widely accepted approach is based on the supposition of scale-invariant fractal distribution of the surface heights. In this case, one can construct the surface using Fourier transform with a large number of corresponding waves. Depending on the number of waves and on both limits, the surface will be, more or less, close to the real fractal one and include or not include irregularities with small sizes (Filippov and Popov, 2007).

Like many other natural surfaces, here, the surface was physically created by a set of deposited particles (spheres with radius R, 12.75 ± 2.42 μm, **Table 1**). A natural way to produce such a surface mathematically is to apply the depositing of spheres procedure. In the purely numerical approach, different roughness of the surfaces can be achieved by depositing mathematically defined spheres with radius R on an originally flat surface. In this case, one takes an array of spheres with a radius close to R and puts them successively on randomly chosen positions $\{x_n, y_n\}$, with $n = 1, 2 \ldots, N$. Total number N of the spheres should be chosen to cover the surface with a density close to the incrementally used one. Each sphere is added virtually to the corresponding segment of the surface: $\delta z_n(x; x_n; y; y_n) = \sqrt{\left|R^2 - (x - x_n)^2 - (y - y_n)^2\right|}$. Due to the random deposition, the spheres can fall either on top of already existing coverage or onto the flat base surface. As a result of such a deposition, the total surface gradually accumulates all the spheres $z(x, y) = \sum_{n=1}^{N} \delta z_n(x; x_n; y; y_n)$ which are, generally speaking, placed on top of each other. It essentially complicates the procedure, which should be repeated many times during the numerical simulations.

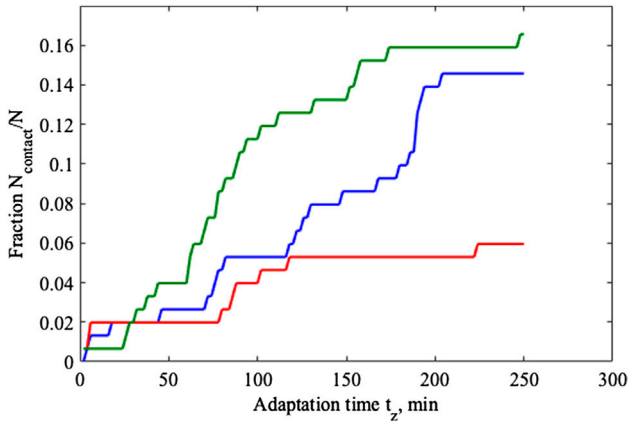

FIGURE 7 | Relaxation of the fractions in contact $F_r = F_r(t_z)$ to the equilibrium values for three different roughness (see **Figure 6** for details). Meaning of the colors is the same as above.

One can simplify the procedure when considering that, for our aim, the specific form of the deposed particles is not very important. In such a case, one can treat the random deposition procedure as an abstract way to construct the desired surface. One of the simplest ways to do this is to model the rough surface $Z(x, y)$ by a random deposition of Gaussians:

$$Z(x,y) = \sum_n G_n(x,y,\{x_n,y_n\}) = \sum_n a_n\left[-\left((x-x_n)^2+(y-y_n)^2\right)/w_n^2\right] \tag{3}$$

The advantage of this approach is its mathematical transparency, since the simple manipulation of the position, amplitude, and width of the Gaussian functions will suffice to generate the desired kind of surface irregularity. In particular, the typical distance between the hills and valleys of the randomly generated surface $Z(x, y) = \sum_n G_n$ can be regulated by the number of Gaussian curves. An additional convenience of this method is the fact that the amplitude of the asperities is not controlled during accumulation of the sum $\sum_n G_n$. Instead, the amplitude of the roughness after accumulation is regulated by the normalization:

$$Z(x,y) \to A\left(Z(x,y) - min(Z)\right)/\left(max(Z) - min(Z)\right), \tag{4}$$

where the desired amplitude A can be chosen from the limit of completely flat surface $A = 0$ to values comparable with the characteristic heights of the system under consideration. This approach has been implemented into the model here.

Two basic mechanisms only will be involved in our minimalistic model: mechanical (potential) interaction with the surface and energy dissipation. These mechanisms restrict the scale of the objects which we include into the model from working in dimensionless units. The irregularities, which one can incorporate into the model, have to correspond to the size of the typical curvature, which can be described by the chain formed by the discrete segments. In this context, the surfaces with irregularities much smaller or larger than the size of the discrete segments must be treated as almost flat. That is why we will use the segment length approximately 10 times shorter than the numerically generated surface irregularities. Formal model, based on this assumption, can well explain the results of experimental studies on real surface profiles, depending on the effective "surface tension" determined by the "chain" stiffness.

In contrast to our previous studies (Filippov and Popov, 2007; Gorb and Filippov, 2014) , where the elastic curve of the connected segments represented the real fiber of an attachment pad contacting with a surface by the adhesive force of its terminal segments, now the "chain" has a meaning of the soft boundary separating internal material of the root from the external space. So, its extension, caused by the insert of the additional segments, does not mean the simple elongation of the "fiber" but rather the addition of the 2-dimentional internal area of a root hair cell enveloped by the cell wall. Further, we will return to the question and show how to implement it into the model.

In any case, expanding the boundary mechanically interacts with the relief, repulsing from its bulges and attracting to the valleys. This interaction is described by the force caused by continual potential:

$$\vec{F}_j^{potential} = -\partial Z(x,y)/\partial \vec{r}. \tag{5}$$

Here, the derivatives are supposed to be calculated for each node at its discrete position: $x = x_j$, $y = y_j$. However, the "continuous" surface is defined on the mesh. Technically, operation **Eq. 5** means that we find a cell of the mesh closest to the position $x = x_j$, $y = y_j$ and calculate the derivative **Eq. 5** for this cell.

Moving different segments according to the potential interactions, in principle, can result in their overlapping, what is unphysical for the boundary, containing practically incompressible material inside, with its own internal pressure. The repulsion between nodes, which could avoid overlapping between

segments, should be incorporated into the of interactions. For isotropic roots, the easiest way to simulate internal pressure is to use repulsion of all the nodes from the common center. However, the form of the root boundary is very complex. It expands to the plenty of random potential valleys and produces many "local centers," the positions of which are impossible to predict. It is preferable to use a mutual short-range repulsion between all the nodes of the chain:

$$\vec{F}_j^{pressure} = G\sum_{j'}\left(\vec{r}_j - \vec{r}_{j'}\right)\left[-\frac{\left(\vec{r}_{j-}\vec{r}_{j'}\right)^2}{R_G^2}\right] \quad (6)$$

This interaction should be weak and short-range, just enough to prevent the segments from overlapping. For isotropic roots, it automatically reduces to the repulsion from the common center, but for many protrusions, it causes several independent repulsions from the local centers.

Counting on the microscopic nature of the problem, we will use the so-called "over-damped" equations of motion without inertial terms. Accumulating all the forces of the problem, one can now write the equation of motion as follows:

$$\partial\vec{r}_j/\partial t = \sum_{j'}\vec{F}_{jj'}^{\parallel} + \vec{F}_j^{\perp} + \vec{F}_j^{potential} + \vec{F}_j^{pressure}. \quad (7)$$

Here, index j runs from 1 to current number N_s of the segments $j = [1: N_s]$. A formal solution of these equations must be accompanied by the creation of new nodes in random $\vec{r}_k$, according to the above-described digital procedure, and to the aging of the already existing ones, which leads to an increase of their rigidity $K_j^{\perp} = K_j^{\perp}(\tau_j)$.

One can determine a mean rigidity of the root boundary from the beginning of its growth to the current time moment. To do this, one has to integrate each elastic constant $K_j^{\perp}(\tau_j)$ over time starting from the moment of the appearance of particular segments. It gives an array of the time average elasticity of all the segments:

$$\overline{K}_j^{\perp} = \frac{1}{\tau_j}\int_0^{\tau_j} d\tau_j' K_j^{\perp}\left(\tau_j'\right). \quad (8)$$

Now, the mean rigidity of the root can be found as the statistical average over the ensemble of the segments:

$$<\overline{K}_j^{\perp}> = \frac{1}{N_c}\sum_{j=1}^{N_c} K_j^{\perp} \quad (9)$$

However, both these averaging **Eqs. 8** and **9** are linear operations. Their results are proportional to the starting elastic constant $K_j^{\perp}(\tau_j = 0)$. The fluctuations of the initial elastic constant are small, and one can ignore the difference between $K_j^{\perp}(\tau_j = 0)$ values of different segments and of $K_j^{\perp}(\tau_j = 0) = K_0^{\perp} \approx const$. Therefore, one can characterize different variants of the system by the sole value of $K^{\perp}$.

RESULTS

Root Hair Tip Morphology (Scanning Electron Microscope)

Posidonia oceanica seedlings produced root hairs with a total length ranging between 200 and 1,000 μm and a mean width of 12.31 ± 1.94 μm (mean ± SD, **Table 1**). The portion of root hairs in contact with the substrate always showed a strongly branched and dactyliform pad-shaped structure (insert of **Figures 1B** and **2A**). These branches were very thin (6.11 ± 0.74 μm), with a width equal on average to about half that of the root hair shank. The mean pad radius was 28.95 ± 4.06 μm.

The contour curvature of the root hair pads attached to the substrate (resin tiles replica of a polishing paper with 12 μm particle size) was 0.1317 ± 0.0317 μm^{-1} (**Table 1**, mean ± SD).

A thin layer of a solidified substance was discovered in SEM images of the root hair pad base and of the resin tile where some of the root hairs had been detached (**Figure 2B**). Such an observation was confirmed by TEM analysis (**Figures 2C,D**).

Root Hair Ultrastructure (Cryo-Scanning Electron Microscope and Transmission Electron Microscope)

The average cell wall thickness, measured along the shaft in fractured root hairs using Cryo-SEM, was 1.50 ± 0.24 μm. In the apical region, the cell wall thickness was lower, at 0.86 ± 0.14 μm. Cross sections of root hairs adhering to the substrate were visualized in TEM, and results confirmed the presence of a glue-like substance filling the empty spaces at the root hair/substrate interface. The observed substance created a layer of different thickness in all samples tested (**Figures 2C,D**). The layer was thin when the root hair was in close contact with the substrate, and thicker when interstices or small gaps were present and the root hair could not penetrate into the gaps between the asperities. Moreover, TEM images allowed an estimating of the actual portion of root hair in real contact with the substrate.

Numerical Simulation

In order to model the behavior of the system with different elasticity levels, we used three representative values of the initial elastic constant: small $K_{01}^{\perp} = 21.7\,N/m$, medium $K_{02}^{\perp} = 76\,N/m$, and large $K_{03}^{\perp} = 217\,N/m$. These values are comparable with the experimental expectations, but the differences between them are one order of magnitude. The numerical modelling approach permitted us to study the possible behavior of the system, even if the values are not observed in real plants.

Typical configurations of the boundary for these three elastic constants - $K_{01}^{\perp}$, $K_{02}^{\perp}$, and $K_{03}^{\perp}$ - are shown in **Figure 3**. It is important to note that each new repetition of the numerical run produces new particular realizations of the surface and resulting structures. Numerous generations of these structures confirm a general qualitative difference between the systems with different surface tensions (corresponds to $K_0^{\perp}$), which is already seen from

Figure 3: The curvature of the boundary increases with an increasing value of $K_0^{\perp}$.

A typical dynamic scenario of the expansion of the root boundary on the substrate is reproduced also in **Supplementary Movie S1**. It is directly seen how the boundary dynamically reacts on the surface structure, repulsing from the asperities and filling the valleys between them.

The visual difference between the smoothness of the boundaries plotted in the subplots **(A–C)** must be characterized quantitatively. For this goal one can calculate the curvature of each curve. Local curvature in arbitrary points $\chi(l) = (x(l), y(l))$ of parametrically defined curves is defined by the radius R^c of the circle touching the curve in this point. An analytical formula for the curvature can be written as follows:

$$Curv(l) = \left| \frac{x'y'' - y'x''}{(x'^2 + y'^2)^{\frac{3}{2}}} \right|, \tag{10}$$

where derivatives are calculated along the curve: $x' = \frac{\partial x}{\partial l}$, $x'' = \frac{\partial^2 x}{\partial^2 l}$, so on. Formally, the combination $(x'y'' - y'x'')/(x'^2 + y'^2)^{\frac{3}{2}}$ in **Eq. 10** can give both positive and negative values of the curvature. For our goal, we need its absolute value. The curvature was calculated as discrete array $Curv_j$.

The curvature varies with time, because the root starts to grow from a smooth circular boundary and develops into a more and more complex structure. We have performed this calculation for all three cases: $K_{01}^{\perp}$, $K_{02}^{\perp}$, and $K_{03}^{\perp}$. As a time-dependent integral characteristic, the mean value of the curvature could be:

$$Curv(t) = \frac{1}{N_s} \sum_{j=1}^{N_s} = Curv_j(t) \tag{11}$$

It is convenient for us to represent the value of the curvature radius as $R^c(t) = 1/Curv(t)$. The resulting curvature radiuses for all three cases, $K_{01}^{\perp}$, $K_{02}^{\perp}$, and $K_{03}^{\perp}$, are shown in subplot **(A)** of **Figure 4** by the blue, green, and red curves, which correspond to the colours used in the subplots **(A–C)** in **Figure 3**, respectively. Another important characteristic is the space to which the root hair expands in the current moment. It can be estimated from the mean radius R^{Area} of the boundary calculated starting from the "center of mass" (x^c, y^c) of all its segments, where:

$$x^c = \frac{1}{N_s} \sum_{j=1}^{N_s} x_j, y^c = \frac{1}{N_s} \sum_{j=1}^{N_s} y_j. \tag{12}$$

Individual components of this radius can be calculated as follows:

$$R_j^{Area} = \sqrt{\left(x_j - x^c\right)^2 + \left(y_j - y^c\right)^2} \tag{13}$$

And its mean value is equal to:

$$R^{Area} = < R_j^{Area} > = \frac{1}{N_s} \sum_{j=1}^{N_s} R_j^{Area} \tag{14}$$

For the expanding root hair, this radius also depends on time $R^{Area} = R^{Area}(t)$. But its increase has a meaning other than the time dependence of curvature $Curv(t)$. The curvature increases because the boundary of the root becomes more complex, but the radius $R^{Area}(t)$ increases simply because the area covered by the root is expanding.

The mean radius (R^{Area}) of the hair root increases linearly with time for the three modelled typologies of the hair stiffness; this is shown in the subplot **(B)** of **Figure 4**. Soft root hairs show the steepest slope, followed by root hairs with intermediate stiffness and then by hard root hairs. The soft and intermediate soft root hairs show a similar trend, with a rapid growth at the beginning of the development and a more constant growth in the sequent phases. At large times, the softest root hair reaches the largest pad size due to greater elasticity. The simulated root hair with intermediate stiffness reaches values similar to the one measured in the real root hair pad observed at SEM.

As we already discussed, the elastic constants evolve independently for different segments of the boundary depending on the individual time elapsed from the moment of their appearance $K_j^{\perp} = K_j^{\perp}(\tau_j)$. Moreover, the number of the segments $N^s = N^s(t)$ increases with time and the array of the individual times τ_j becomes longer as well. It makes the visualization of the time evolution of all individual values $K_j^{\perp} = K_j^{\perp}(\tau_j)$ in one static plot difficult.

However, one can use the following approach. First of all, we plot, as a set of dots, all the values $K_j^{\perp} = K_j^{\perp}(\tau_j)$ vs. index j. Each new member of the array appears with an arbitrary index inside the array, but it automatically finds its own place in the plot expanding the array. As a result, we get a cloud of points independently filling the range from the minimal value $K^{\perp}$ to the maximal value $\lambda K_k^{\perp}$. An instant plot of this configuration is shown by colored dots for all three variants in subplot **(A)** of **Figure 5**. One can see that the positions of the points are not sorted along the index j. Obviously, they are different for different realizations. There is a well pronounced compaction of the points near $\lambda K_k^{\perp}$, where all the points concentrate at the final stage of their motion for each of the three cases: $K_{01}^{\perp}$, $K_{02}^{\perp}$, and $K_{03}^{\perp}$. This process in dynamics is reproduced in **Supplementary Movie S2**.

To provide a statistical description of the points distribution, one can calculate the histogram of this distribution along the vertical axis. The number of segments $N^s = N^s(t)$ increases with time and the histogram becomes smooth enough to find out the regularity of the process. Histograms for all three cases are plotted in subplot **(B)** of **Figure 5**. Perfect correlation between the direct observation of the compaction of the points near final stiffness and calculated maximum of each histogram is obvious. The only difference between the cases is the final value $\lambda K_k^{\perp}$, which is proportional to the initial one ($K^{\perp}$).

What is more important here, is that all three curves have generally the same structure, which confirms the universality of the process independently on the $K^{\perp}$. One can expect that this universality takes place for the whole time interval from $t = 0$ to current $t = 700$ min. Having an array of the histograms of $K^{\perp}(t)$ for every time moment t, one can collect them into a two-dimensional array and plot them together as a color-map. This

procedure has been performed by us for all three cases and corresponding maps are presented in the subplots **(C–E)** of **Figure 5**. Zero value of the probability is represented here by a deep blue color, while maximum value is represented by deep red. In fact, these maps show in static form (despite the changeable length of the array!) the complete process of evolution of all the values $K_j^{\perp}(t)$ together. As expected, for all the cases, universality is obvious. The only difference is in the starting value $K^{\perp}$.

However, an important question remains for the validation of the model. As we stressed from the very beginning, the original problem is a complex 3-dimensional problem, and the present study is just an attempt to model it using a 2-dimensional approach. However, we still can advance the model for such a compromised approach. Let us stop the expansion of the root at some (final or intermediate) stage. Its boundary, at this moment, has a certain shape determined by a competition of all the forces involved in the problem. In particular, it is a competition between the repulsion from the surface asperities $Z(x, y) = \sum G_n$ and the bending stiffness. As a result, the height $Z(x_j, y_j)$, corresponding to the different nodes $\vec{r}_j = (x_j, y_j)$, is different.

However, the ability of the boundary to bend in Z-direction is also limited. One can suppose that transversal elastic constant in this direction is practically the same as it is for the horizontal plane: $K^z \approx K^{\perp}$. It causes vertical elastic force:

$$\vec{F}_j^{z\perp} = K^z\left(2z - z_{j+1} - z_{j-1}\right) \tag{15}$$

In Z-direction, the hair root boundary chain also tends to find a compromise between this force and interaction with the rigid surface in the same manner as it was done in (x, y)-plane. We can calculate this compromise using the relaxation approach. For definiteness, we apply constant vertical attraction force $\vec{f}_j^z = \vec{f}^z = const < 0$ and exponential repulsion from the surface $\vec{F}_j^z = A^{(-(z_j - Z)/a_z}$. Now, by considering all the vertical forces, one can solve the relaxation equation:

$$\partial z_j/\partial t_z = \vec{f}_j^z + \vec{F}_j^{z\perp} + \vec{F}_j^z \tag{16}$$

and find an equilibrium configuration. Here, adaptation time t_z runs from $t_z = 0$ and stops when the derivative $\partial z_j/\partial t_z$ becomes negligibly small $\partial z_j/\partial t_z \to 0$.

We have solved this equation for three different roughness levels (6, 12, and 171 μm asperities size) using the average $K^{\perp}$ constant corresponding to the real situation. The results are plotted using three different colors for these cases: red, green, and blue corresponding to high, medium, and low roughness, respectively (**Figure 6**). As expected, the result is different for different roughness levels. Because the boundary is a closed curve, one cannot plot corresponding functions along any of the horizontal coordinates (x, y). The only possibility is to plot them along the index of the nodes: $j = 1, \ldots, N_s$. Counting that, the number of the segments N_s varies with the time and the evolution of the root, since the process can be stopped at any arbitrary moment. It is convenient to normalize the horizontal axis in the plots of **Figure 6** to this number j/N_s and plot in the interval $[0, 1]$. The substrate surface in all the subplots is shown by the bold line.

In principle, the difference between the cases with different roughness levels is seen directly from **Figure 6**. However, it is necessary to extract this information quantitatively; it is also essential that this extraction should be done for any adaptation time t_z moment, but not for the only fixed one, which was used in **Figure 6** to illustrate the final results of the solution of the relaxation equation. We decided to use the fraction of the segments in contact with the substrate as a measure of the root hair boundary configuration difference. In fact, it means that we have to formalize a procedure of finding a fraction of the segments in contact, solve **Eq. 16** at every step of t_z, and calculate the fractions using this formalized procedure.

Natural formalization is to apply the following condition: if distance between the boundary and surface is less than the threshold $(z_j - Z) < \Delta z^{tresh}$, the segment is in contact. In the opposite case, it is not. We can consider the Δz^{tresh} as the thickness of the solidified substance. Formally, this condition can be written in the form:

$$Cond_j^z = \begin{cases} 1, & if\ \left(z_j - Z\right) < \Delta z^{tresh} \\ 0, & if\ \left(z_j - Z\right) \geq \Delta z^{tresh} \end{cases} \tag{17}$$

Using this condition, the fraction of segments in contact can be easily calculated as the following sum:

$$Fr = \sum_{j=1}^{N_s} Cond_j^z \tag{18}$$

This procedure is quite efficient and it allows for performing the calculation of the fraction depending on time $Fr = Fr(t_z)$. The results for the three different roughness levels (6, 12, and 171 μm asperity size) used for the simulations are presented in **Figure 7**. Root hairs, due to their specific elasticity and their morphological characteristics, cannot establish good contact with surfaces with too high or too low roughness levels. Optimal contact was produced by the root hair on the average simulated roughness.

DISCUSSION

Root hairs originate from trichoblasts by a highly polarized growth process that occurs at the apex of the cell, referred to as tip growth, and the concomitant repression of proximal growth along the shank (Hirano et al., 2018). Cytoarchitecture of the root hair is highly polar-organized during growth but it disappears in mature cells, when growth usually ceases (Ryan et al., 2001; Ketelaar et al., 2002; Emons and Ketelaar, 2009; Balcerowicz et al., 2015). The root hair's cell wall is a complex network of polysaccharides. The major components are cellulose microfibrils, the polysaccharides matrix made up of hemicelluloses and pectins, and various cell wall proteins (Somssich et al., 2016). A primary cell wall, which is a

thin layer that continually expands outwards, is deposited at the root hair tip, while a strong multi-layered secondary cell wall develops inside the primary cell wall, 20–30 μm from the tip, and continues along the shank (Dumais et al., 2004). Once tip growth ends, hair tips also become covered by a secondary cell wall (Galway et al., 1999).

Cellulose microfibrils are randomly distributed in the primary cell wall of root hairs, while in the nonexpanding tubular portion they present an oriented distribution (Galway, 2006). Hemicelluloses and pectins serve as cementing material and any change in their chemical nature influences the plasticity and elasticity of the cell wall. Both the microfibrils arrangement and the chemical properties of polysaccharides in the cell wall create an anisotropic gradient along the cell, which is a matter of considerable importance in the root hair adhesion process.

Our analysis of the morphology and ultrastructure of *P. oceanica* seedlings showed a unique pad formation process characterized by the root hair tip branching behavior and by the presence of a solidifying (filler) substance at the substrate/pad interface. These two features, reported here for the first time, together with the presented numerical model simulations allow for better understanding of the adhesion mechanism of *P. oceanica* described in previous works (Alagna et al., 2015; Badalamenti et al., 2015; Tomasello et al., 2018; Zenone et al., 2020). The numerical model simulated the contact formation of the *P. oceanica* seedling root hair on hard rough substrates, clarifying what role the physical properties of the root hairs play in pad formation and in the facilitation of the attachment process.

In contrast with most terrestrial plants, where root hairs increase the root surface area to enhance mineral and water absorption, in *P. oceanica*, and possibly also in other seagrass species, the main role played by root hairs is to provide anchorage to seedlings. However, similar anchorage systems have been described in some terrestrial climbing plants [eg, *Ficus pumila* (Groot et al., 2003), *Parthenocissus tricuspidata* (Scherge and Gorb, 2001; Steinbrecher et al., 2010; Steinbrecher et al., 2011), *Hedera helix* (Melzer et al., 2010, Melzer et al., 2012), *Amphilophium crucigerum* (Seidelmann et al., 2012), *Passiflora discophora* (Bohn et al., 2015), and *Syngonium podophyllum* (Yang and Deng, 2017)]. To the best of our knowledge, no similar detailed studies exist for most seagrass species, even though the morphology and ultrastructure of root hair have been described for some of them (Cooper and McRoy, 1988; Roberts, 1993; Tomasello et al., 2018).

The terrestrial species *P. tricuspidata, P. discophora,* and *A. crucigerum*, build a multi-layered and multicellular pad at the base of tendrils to increase the contact area and produce a firm adhesion to climb on a given surface. Other terrestrial species (e.g., *S. podophyllum*, *H. helix*, and *F. pumila*) climb by means of clusters of adventitious roots which are covered by root hairs that emerge from internodes of the plant stem and form an adhesive pad according to a multistep process (Groot et al., 2003; Melzer et al., 2010; Melzer et al., 2012; Yang and Deng, 2017). In both cases, the pad formed is a complex structure and its adhesion occurs at different spatial scales and in different moments. For these species, root/root hair adhesion occurs according to different steps. Generally, the first step starts with one of the plant adhesive structures that grows towards the substrate. In the second step, the adhesive structure establishes contact with the substrate. In this phase, adhesion is very weak. In the third step, adhesion become stronger as a consequence of mechanical interlocking, and the presence of a glue-like substance may facilitate adhesion strength in some species. The fourth and last step is the hardening of the glue, a fundamental process for bonding and strengthening the attachment. In *F. pumila*, *S. podophyllum*, and *H. helix*, root hairs adhere to the substrate by mechanical interlocking, swelling, or flattening the root hair tip to increase the contact area.

In *P. oceanica*, the pad structure is produced by the root hair tip branching. According to our results, root hair branching increases the real contact area about 50 times compared to the contact area of a single tubular root hair. The branching of *P. oceanica* root hairs is a pivotal mechanism for pad formation, and supports the hypothesis that adhesive root hairs may represent an adaptive trait to life in marine rocky habitats characterized by strong turbulent water movements (Badalamenti et al., 2015; Montefalcone et al., 2016). Interestingly, in terrestrial plants, root hair branching is reported to happen only under stress conditions (Yang et al., 2011; Bobrownyzky, 2015) or in mutant phenotypes (Engstrom et al., 2011).

The role played by the pad in anchoring the root hair is most likely improved by the presence of a filler substance at the interface between the pad base and the substrate. The "glue" thickness observed at the root hair/substrate interface in TEM in this study was not homogeneous. It was thinner where the root hair pad was in close contact with the substrate, and thicker where the contact was looser due to the presence of gaps or interstices. The glue can be seen as a form filler whose role is related to the improvement of root hair adhesion to the substrate by the enhancement of the gap closure at the micro-scale. On rough substrates, root hairs grow between the asperities or inside gaps and small crevices. Under these conditions, root hairs were observed filling up the empty spaces either by the branches, by the compliancy of the cell wall, or by the glue. Such a strategy improves the plant surface-replicating mechanisms. Without the glue presence, attachment would solely be based on mechanical interlocking (between the root hair pad and substrate). It can be hypothesized that the glue may facilitate the first adhesion of the root hair to the substrate and to some extent may reduce the friction of the root hair tip during growth (until the glue is solidified). A low friction environment at the root hair tip region could represent an advantage for the plant to penetrate small interstices and to follow the topography of the substrate, which we clearly see in model simulations.

The elasticity of the root hair tip has strongly affected the effectiveness of formation of the pad in our model simulations performed on a constant micro-roughness (i.e., asperities diameter of 12 μm). When the root hair tip is too soft (low value of the initial elastic constant $\boldsymbol{K}$) it produces a large and complex pad (i.e., characterized by several branches) but, due to its softness, strong mechanical interlocking can be inefficient. On the contrary, a root hair tip that is too hard (high value of the initial elastic constant) improves mechanical interlocking but, due to its high stiffness, it produces a small and simple pad,

ultimately reducing the area in contact with the substrate. The curvature radius ($\boldsymbol{R^c}$, i.e., the inverse of curvature) of the root hair pad increases with increasing elastic constant $\boldsymbol{K_0^{\perp}}$. Our model showed how root hair radius increases with time, reaching the greatest pad apparent contact surface at lowest stiffness and the smallest at highest stiffness.

In the model, the medium-level elasticity (initial constant elasticity, $\boldsymbol{K_{02}^{\perp}}$ corresponding to the estimated root hair natural elasticity) proved to be optimal for developing a pad capable of increasing the amount of surface in contact with the substrate and maximizing the mechanical interlocking at the roughness provided. Substrate roughness is a key factor affecting root hair adhesion strength. No general rules define the relation between the roughness and the adhesion strength, as it is highly dependent on the observed system (Budhe et al., 2015). Zenone et al. (2020) reported that the highest adhesion strength in *P. oceanica* was achieved by seedling root hairs grown at a roughness of 12 μm (asperities diameter), a value roughly corresponding to the root hair diameter. Roughness lower than 3 μm and greater than 52 μm negatively affected the adhesion strength. No adhesion was recorded on a smooth glass replica (supposed no roughness), highlighting the important role played by substrate roughness in the adhesion process of *P. oceanica* root hairs.

Compared to a smooth substrate, roughness allows root hairs to grow between the interstices, offering paths of minimum growth resistance and inducing an increase in the curvature of the pad which, in turn, contributes to generating a stronger adhesion to the substrate. In the model simulation performed under the estimated natural elasticity constant ($\boldsymbol{K_{02}^{\perp}}$), the highest adhesion (i.e., the number of simulated root hair segments in contact with the substrate surface) was reached at the intermediate surface micro-roughness level. At this roughness, the fraction of segments in contact with the substrate surface was higher than that observed at lower and higher roughness levels. This high real contact surface is very likely responsible for a stronger adhesion and corroborates the results reported in Zenone et al. (2020). At the high roughness level, the low number of contact segments recorded by the model may limit the mechanical interlocking and, consequently, the adhesion strength. Under this condition, curvature does not cause adhesion enhancement.

The shape and size of the simulated root hair pads properly reflected the real system, shedding light on the role played by pads in the attachment process of *P. oceanica* seedlings' root hairs to the substrate. Root hair specific elasticity and pad formation seem to be the best combination to produce the optimal contact to a substrate with a roughness level at the scale of the root hair diameter (i.e., 12 μm). It is important to highlight that $\Delta \boldsymbol{z^{tresh}}$ introduced in the model corresponds to the layer of the filler substance reported in this work. It is very likely that, during the course of evolution, *P. oceanica* has found a perfect fit between the size of the root hair, the elasticity gradient of the cell wall, the secretion of a glue, and, presumably, the natural roughness of the substrates, to determine through the pad formation a strong anchorage to consolidated substrates and to allow seedlings to colonize and grow in very high energy environments.

Several restoration attempts have been made in the Mediterranean Sea to contrast the general regression caused by human impact on *P. oceanica* meadows, such as transplanting plugs, sods, or bare-root rhizomes collected from donor plants (Meinesz et al., 1993; Molenaar and Meinesz, 1995; Piazzi et al., 1998; Carannante, 2011; Calvo et al., 2014; Alagna et al., 2019a). These initiatives have raised concerns in relation to their environmental sustainability (Balestri et al., 2019) and also because their large-scale application has rarely achieved high success rates (van Katwijk et al., 2016). To reduce the environmental impact on donor meadows, an approach known as "nursery seagrass" has been proposed which involves the propagation of plants from seeds reared in aquaculture facilities (Balestri and Lardicci, 2012; Balestri and Lardicci, 2014; Balestri et al., 2015). Research has recently focused on finding a suitable and low-impact way to fix germinated plants to the substrate (Alagna et al., 2019b). The adhesion mechanism of *P. oceanica* seedlings and the model we described here may give a boost to the use of particular consolidated substrates with specific roughness levels for new restoration initiatives. Identifying the right substrate where the seedlings adhere before transplantation could represent an effective approach to avoid the limits highlighted by other experiences (Alagna et al., 2019a). The model developed in this study could be useful in identifying the best characteristics of natural substrates, where the seedlings adhere and obtain a first stable anchorage before releasing them at sea.

DATA AVAILABILITY STATEMENT

The original contributions presented in the study are included in the article/**Supplementary Material**, further inquiries can be directed to the corresponding author.

AUTHOR CONTRIBUTIONS

AZ, SG, and FB conceived and designed the research. AZ conducted the experiments and analysis. AF and AK developed the model. SG contributed analytical tools. AZ and AK analyzed data. AZ and AF wrote the manuscript. SG, FB, and AK revised the manuscript. All authors read and approved the final manuscript.

FUNDING

This paper has been partially supported by the project Marine Hazard, PON03PE_00203_1, Italian Ministry of Education, University and Research (MIUR). We acknowledge financial support by DFG within the funding program Open Access Publizieren.

ACKNOWLEDGMENTS

The Authors would like to thank Esther Appel for her collaboration in laboratory work at the Functional

Morphology and Biomechanics lab in Kiel and Giuseppe Di Stefano for the technical support at IAS-CNR lab in Castellammare del Golfo. This study was developed during a short-term scientific mission granted to AZ by Cost Action ENBA (CA15216).

SUPPLEMENTARY MATERIAL

The Supplementary Material for this article can be found online at: https://www.frontiersin.org/articles/10.3389/fmech.2020.590894/full#supplementary-material

REFERENCES

Alagna, A., Vega Fernández, T., D'Anna, D., Magliola, C., Mazzola, S., and Badalamenti, F. (2015). Assessing *Posidonia oceanica* seedling substrate preference: an experimental determination of seedling anchorage success in rocky vs. sandy substrates. *PLoS One* 10, e0125321. doi:10.1371/journal.pone.0125321

Alagna, A., D'Anna, G., Musco, L., Vega Fernández, T., Gresta, M., Pierozzi, N., et al. (2019a). Taking advantage of seagrass recovery potential to develop novel and effective meadow rehabilitation methods. *Mar. Pollut. Bull.* 149, 110578. doi:10.1016/j.marpolbul.2019.110578

Alagna, A., Zenone, A., and Badalamenti, F. (2019b). The perfect microsite: how to maximize *Posidonia oceanica* seedling settlement success for restoration purposes using ecological knowledge. *Mar. Environ. Res.* 161, 104846. doi:10.1016/j.marenvres.2019.104846

Badalamenti, F., Alagna, A., and Fici, S. (2015). Evidences of adaptive traits to rocky substrates undermine paradigm of habitat preference of the Mediterranean seagrass *Posidonia oceanica*. *Sci. Rep.* 5, 8804. doi:10.1038/srep08804

Balcerowicz, D., Schoenaers, S., and Vissenberg, K. (2015). Cell fate determination and the switch from diffuse growth to planar polarity in Arabidopsis root epidermal cells. *Front. Plant Sci.* 6, 1163. doi:10.3389/fpls.2015.01163

Balestri, E., De Battisti, D., Vallerini, F., and Lardicci, C. (2015). First evidence of root morphological and architectural variations in young *Posidonia oceanica* plants colonizing different substrate typologies. *Estuar. Coast Shelf Sci.* 154, 205–213. doi:10.1016/j.ecss.2015.01.002

Balestri, E., and Lardicci, C. (2012). Nursery-propagated plants from seed: a tool to improve the effectiveness and sustainability of seagrass restoration. *J. Appl. Ecol.* 49, 1426–1435. doi:10.1111/j.1365-2664.2012.02197.x

Balestri, E., and Lardicci, C. (2014). Effects of sediment fertilization and burial on *Cymodocea nodosa* transplants: implications for seagrass restoration under a changing climate. *Restor. Ecol.* 22, 240–247. doi:10.1111/rec.12052

Balestri, E., Vallerini, F., Seggiani, M., Cinelli, P., Menicagli, V., Vannini, C., et al. (2019). Use of bio-containers from seagrass wrack with nursery planting to improve the eco-sustainability of coastal habitat restoration. *J. Environ. Manage.* 251, 109604. doi:10.1016/j.jenvman.2019.109604

Barnabas, A. D. (1994). Anatomical, histochemical and ultrastructural features of the seagrass *Phyllospadix scouleri* hook. *Aq. Bot.* 49, 167–182. doi:10.1016/0304-3770(94)90036-1

Bobrownyzky, J. (2016). Production of branched root hairs under progressive drought stress in *Arabidopsis thaliana*. *Cytol. For. Genet.* 50, 324–329. doi:10.3103/S0095452716050030

Bohn, H. F., Gunther, F., Fink, S., and Speck, T. (2015). A passionate free climber: structural development and functional morphology of the adhesive tendrils in *Passiflora discophora*. *Int. J. Plant. Sci.* 176, 294–305. doi:10.1086/680231

Budhe, S., Ghumatkar, A., Birajdar, N., and Banea, M. D. (2015). Effect of surface roughness using different adherend materials on the adhesive bond strength. *Appl. Adhes. Sci.* 3, 20. doi:10.1186/s40563-015-0050-4

Calvo, S., Scannavino, A., Luzzu, F., Di Maida, G., Pirrotta, M., Orestano, C., et al. (2014). "Tecnica di reimpianto mediante supporto biodegradabile," in *Conservazione e gestione della naturalità negli ecosistemi marino-costieri. Il trapianto delle praterie di* Posidonia oceanica. Editors T. Bacci, B. La Porta, C. Maggi, O. Nonnis, D. Paganelli, S. F. Rende, and M. Polifrone (Roma, Italy: ISPRA), 47–51. Manuali e Linee Guida no. 106/2014.

Carannante, F. (2011). *Monitoraggio a lungo termine di trapianti di* Posidonia oceanica *su vasta scala*. PhD Thesis. Viterbo (Italy): University of Tuscia.

Cooper, L. W., and McRoy, C. P. (1988). Anatomical adaptations to rocky substrate sand surf exposure by the seagrass genus *Phyllospadix*. *Aquat. Bot.* 32, 365–381. doi:10.1016/0304-3770(88)90108-8

Dumais, J., Long, S. R., and Shaw, S. L. (2004). The mechanics of surface expansion anisotropy in *Medicago truncatula* root hairs. *Plant. Physiol.* 136, 3266–3275. doi:10.1104/pp.104.043752

Dupuy, L., Gregory, P. J., and Bengough, A. G. (2010). Root growth models: towards a new generation of continuous approaches. *J. Exp. Bot.* 61, 2131–2143. doi:10.1093/jxb/erp389

Emons, A. M. C., and Ketelaar, T. (2009). "Intracellular organization: a prerequisite for root hair elongation and cell wall deposition," in *Roots hairs*. Editors A. M. C. Emons and T. Ketelaar (Berlin, Germany: Springer), 27–44. Plant Cell Monographs.

Engstrom, E., Andersen, C., Gumulak-Smith, J., Hu, J., Orlova, E., Sozzani, R., et al. (2011). *Arabidopsis* homologs of the *Petunia* HAIRY MERISTEM gene are required for maintenance of shoot and root indeterminacy. *Plant Physiol.* 155, 735–750. doi:10.1104/pp.110.168757

Filippov, A. E., and Popov, V. (2007). Flexible tissue with fibres interacting with an adhesive surface. *J. Phys. Condens. Matter* 19, 096012. doi:10.1088/0953-8984/19/9/096012

Galway, M. E. (2006) Root hair cell walls: filling in the framework. *Can. J. Bot.* 84, 613–621. doi:10.1139/B06-006

Galway, M. E., Lane, D. C., and Schiefelbein, J. W. (1999). Defective control of growth rate and cell diameter in tip-growing root hairs of the rhd4 mutant of *Arabidopsis thaliana*. *Can. J. Bot.* 77, 494–507. doi:10.1139/cjb-77-4-494

Godin, C., and Sinoquet, H (2005). Functional–structural plant modelling. *New Phytol.* 166, 705–708. doi:10.1111/j.1469-8137.2005.01445.x

Gorb, S. N. (2007). Visualization of native surfaces by two-step molding. *Micros. Today.* 15, 44–46.

Gorb, S. N., and Filippov, A. E. (2014). Fibrillar adhesion with no clusterisation: functional significance of material gradient along adhesive setae of insects. *Beilstein J. Nanotechnol.* 5, 837–845. doi:10.3762/bjnano.5.95

Green, E. P., and Short, F. T. (2003) *World atlas of seagrasses. Prepared by the UNEP world conservation monitoring centre*. Berkeley, CA: University of California Press.

Grierson, C., Nielsen, E., Ketelaarc, T., and Schiefelbe, J. (2014). Root hairs. *Arabidopsis Book* 12, e0172. doi:10.1199/tab.0172

Groot, E. P., Sweeney, E. J., and Rost, T. L. (2003). Development of the adhesive pad on climbing fig (*Ficus pumila*) stems from clusters of adventitious roots. *Plant Soil* 248, 85–96. doi:10.1023/A:1022342025447

Hirano, T., Konno, H., Takeda, S., Dolan, L., Kato, M., Aoyama, T., et al. (2018). PtdIns(3,5)P2 mediates root hair shank hardening in Arabidopsis. *Nat. Plants* 4, 888–897. doi:10.1038/s41477-018-0277-8

Jahnke, M., Christensen, A., Micu, D., Milchakova, N., Sezgin, M., Todorova, V., et al. (2016). Patterns and mechanisms of dispersal in a keystone seagrass species. *Mar. Environ. Res.* 117, 54–62. doi:10.1016/j.marenvres.2016.04.004

Ketelaar, T., Faivre-Moskalenko, C., Esseling, J. J., and de Ruijter, N.C. A., Grierson, C. S., Dogterom, M., , et al. (2002). Positioning of nuclei in *Arabidopsis* root hairs: an actin-regulated process of tip growth, *Plant Cell*, 14, 2941–2955. doi:10.1105/tpc.005892

Larkum, A. W. D., Waycott, M., and Conran, J. G. (2018). "Evolution and biogeography of seagrasses," in *Seagrasses of Australia*. Editors A. Larkum, G. Kendrick, and P Ralph (Cham, Switzerland: Springer). doi:10.1007/978-3-319-71354-0_1

The MathWorks, Inc. (2018). *MATLAB 9.7.0.1190202 (R2019b)*. Natick, MA: The MathWorks, Inc.

Meinesz, A., Caye, G., Loques, F., and Molenaar, H. (1993). Polymorphism and development of *Posidonia oceanica* transplanted from different parts of the mediterranean into the national park of port-cros. *Bot. Mar.* 36, 209–216. doi:10.1515/botm.1993.36.3.209

Melzer, B., Seidel, R., Steinbrecher, T., and Speck, T. (2012). Structure, attachment properties, and ecological importance of the attachment system of English ivy (*Hedera helix*). *J. Exp. Bot.* 63, 191–201. doi:10.1093/jxb/err260

Melzer, B., Steinbrecher, T., Seidel, R., Kraft, O., Schwaiger, R., and Speck, T. (2010). The attachment strategy of English ivy: a complex mechanism acting on several hierarchical levels. *J. R. Soc. Interface* 7, 1383–1389. doi:10.1098/rsif.2010.0140

Molenaar, H., and Meinesz, A. (1995). Vegetative reproduction in *Posidonia oceanica*: survival and development of transplanted cuttings according to different spacings, arrangements and substratum. *Bot. Mar.* 38, 313–322. doi:10.1515/botm.1995.38.1-6.313

Montefalcone, M., Vacchi, M., Carbone, C., Cabella, R., Schiaffino, C. F., Elter, F. M., et al. (2016). Seagrass on the rocks: *Posidonia oceanica* settled on shallow-water hard substrata withstands wave stress beyond predictions. *Estuar. Coast. Shelf S* 180, 114–122. doi:10.1016/j.ecss.2016.06.024

Piazzi, L., Balestri, E., Magri, M., and Cinelli, F. (1998). Experimental transplanting of *Posidonia oceanica* (L.) delile into a disturbed habitat in the Mediterranean Sea. *Bot. Mar.* 41, 593–602. doi:10.1515/botm.1998.41.1-6.593

Roberts, D. G. (1993). Root hair structure and development in the seagrass *Halophila ovalis* (R. Br.) Hook. f. *Aust. J. Mar. Freshwater Res.* 44, 85–100. doi:10.1071/MF9930085

Ryan, E., Steer, M., and Dolan, L. (2001). Cell biology and genetics of root hair formation in *Arabidopsis thaliana*. *Protoplasma* 215, 140–149. doi:10.1007/BF01280310

Scherge, M., and Gorb, S. N. (2001). *Biological micro-and nanotribology: nature's solutions*, New York, NY: Springer-verlag.

Schneider, C. A., Rasband, W. S., and Eliceiri, K. W. (2012). NIH Image to ImageJ: 25 years of image analysis. *Nat. Methods* 9, 671–675. doi:10.1038/nmeth.2089

Seidelmann, K., Melzer, B., and Speck, T. (2012). The complex leaves of the monkey's comb (*Amphilophium crucigerum*, Bignoniaceae): a climbing strategy without glue. *Am. J. Bot.* 99, 1737–1744. doi:10.3732/ajb.1200288

Somssich, M., Khan, G. A., and Persson, S. (2016). Cell wall heterogeneity in root development of *Arabidopsis*. *Front. Plant Sci.* 7, 1242. doi:10.3389/fpls.2016.01242

Spurr, R. A. (1969). A low-viscosity epoxy resin embedding medium for electron microscopy. *J. Ultra Mol. Struct. R.* 26, 31–43. doi:10.1016/s0022-5320(69)90033-1

Steinbrecher, T., Beuchle, G., Melzer, B., Speck, T., Kraft, O., and Schwaiger, R. (2011). Structural development and morphology of the attachment system of *Parthenocissus tricuspidata*. *Int. J. Plant Sci.* 172, 1120–1129. doi:10.1086/662129

Steinbrecher, T., Danninger, E., Harder, D., Speck, T., Kraft, O., and Schwaiger, R. (2010). Quantifying the attachment strength of climbing plants: a new approach. *Acta Biomater.* 6, 1497–1504. doi:10.1016/j.actbio.2009.10.003

Telesca, L., Belluscio, A., Criscoli, A., Ardizzone, G., Apostolaki, E. T., Fraschetti, S., et al. (2015). Seagrass meadows (*Posidonia oceanica*) distribution and trajectories of change. *Sci. Rep.* 5, 12505. doi:10.1038/srep12505

Tomasello, A., Perrone, R., Colombo, P., Pirrotta, M., and Calvo, S. (2018). Root hair anatomy and morphology in *Posidonia oceanica* (L.) Delile and substratum typology: first observations of a spiral form. *Aquat. Bot.* 145, 45–48. doi:10.1016/j.aquabot.2017.12.001

Unsworth, R. K. F., Collier, C. J., Waycott, M., Mckenzie, L. J., and Cullen-Unsworth, L. C. (2015). A framework for the resilience of seagrass ecosystems. *Mar. Pollut. Bull.* 100, 34–46. doi:10.1016/j.marpolbul.2015.08.016

van Katwijk, M. M., Thorhaug, A., Marbà, N., Orth, R. J., Duarte, C. M., Kendrick, G. A., et al. (2016). Global analysis of seagrass restoration: the importance of large-scale planting. *J. Appl. Ecol.* 53, 567–578. doi:10.1111/1365-2664.12562

Waycott, M., Duarte, C. M., Carruthers, T. J. B., Orth, R. J., Dennison, W. C., Olyarnik, S., et al. (2009). Accelerating loss of seagrasses across the globe threatens coastal ecosystems. *Proc. Natl. Acad. Sci. U. S. A* 106, 12377–12381. doi:10.1073/pnas.0905620106

Yang, N., Zhu, C., Gan, L., Ng, D., and Xia, K. (2011). Ammonium-stimulated root hair branching is enhanced by methyl jasmonate and suppressed by ethylene in *Arabidopsis thaliana*. *J. Plant Biol.* 54, 92–100. doi:10.1007/s12374-011-9147-x

Yang, X., and Deng, W. (2017). Morphological and structural characterization of the attachment system in aerial roots of *Syngonium podophyllum*. *Planta* 245, 507–521. doi:10.1007/s00425-016-2621-4

Zenone, A., Alagna, A., D'Anna, G., Kovalev, A., Kreitschitz, A., Badalamenti, F., et al. (2020). Biological adhesion in seagrasses: the role of substrate roughness in *Posidonia oceanica* (L.) Delile seedling anchorage via adhesive root hairs. *Mar. Environ. Res.* 160, 105012. doi:10.1016/j.marenvres.2020.105012

Conflict of Interest: The authors declare that the research was conducted in the absence of any commercial or financial relationships that could be construed as a potential conflict of interest.

frontiers in Mechanical Engineering

REVIEW
published: 21 December 2020
doi: 10.3389/fmech.2020.601510

Mechanics of Crater-Enabled Soft Dry Adhesives: A Review

Liu Wang[1], *Kyoung-Ho Ha*[2], *Gregory J. Rodin*[1], *Kenneth M. Liechti*[1] *and Nanshu Lu*[1,2,3]*

[1]Center for Mechanics of Solids, Structures and Materials, Department of Aerospace Engineering and Engineering Mechanics, The University of Texas, Austin, TX, United States, [2]Departement of Mechanical Engineering, The University of Texas, Austin, TX, United States, [3]Department of Biomedical Engineering, Texas Materials Institute, The University of Texas, Austin, TX, United States

Dry adhesion is governed by physical rather than chemical interactions. Those may include van der Waals and electrostatic forces, friction, and suction. Soft dry adhesives, which can be repeatedly attached to and detached from surfaces, can be useful for many exciting applications including reversible tapes, robotic footpads and grippers, and bio-integrated electronics. So far, the most studied Soft dry adhesives are gecko-inspired micro-pillar arrays, but they suffer from limited reusability and weak adhesion underwater. Recently cratered surfaces emerged as an alternative to micro-pillar arrays, as they exhibit many advantageous properties, such as tunable pressure-sensitive adhesion, high underwater adhesive strength, and good reusability. This review summarizes recent work of the authors on mechanical characterization of cratered surfaces, which combines experimental, modeling, and computational components. Using fundamental relationships describing air or liquid inside the crater, we examine the effects of material properties, crater shapes, air vs. liquid ambient environments, and surface patterns. We also identify some unresolved issues and limitations of the current approach, and provide an outlook for future research directions.

Keywords: dry adhesive, suction, crater, micro-pillar, adhesive strength, underwater adhesion

OPEN ACCESS

Edited by:
Stanislav N. Gorb,
University of Kiel, Germany

Reviewed by:
Hyun-Joon Kim,
Kyungpook National University, South Korea
Árpád Czifra,
Óbuda University, Hungary

***Correspondence:**
Nanshu Lu
nanshulu@utexas.edu

Specialty section:
This article was submitted to Tribology, a section of the journal Frontiers in Mechanical Engineering

Received: *01 September 2020*
Accepted: *27 October 2020*
Published: *21 December 2020*

Citation:
Wang L, Ha K-H, Rodin GJ, Liechti KM and Lu N (2020) Mechanics of Crater-Enabled Soft Dry Adhesives: A Review. Front. Mech. Eng. 6:601510. doi: 10.3389/fmech.2020.601510

INTRODUCTION

Soft adhesives are conformable and deformable binding agents between two surfaces. Engineered soft adhesives have become part of our daily life, *e.g.,* medical bandages for wound healing, stretchable brace tapes for joint protection, and double-sided tapes for paper sticking. Soft adhesives are usually categorized as either soft wet adhesives (SWAs) or soft dry adhesives (SDAs). SWAs bond surfaces together through either chemical reactions or mechanical loading (Czech et al., 2013; Cho et al., 2019; Yuk et al., 2019; Chen et al., 2020a). For example, a well-known class of SWAs is pressure-sensitive adhesives (PSAs) which consist of a viscoelastic bonding agent that can instantaneously form a bond to the adherend under applied pressure (Creton, 2003; Czech and Kowalczyk, 2011). Acrylics, polyether, silicones, polyesters, and polyurethanes are commonly used bonding agent for PSAs (Singh et al., 2011; Cilurzo et al., 2012). Due to their viscous nature, PSAs can flow to conform to rough surfaces upon compression, and the inherent tackiness and low surface energy of the adhesive materials facilitate strong bonding onto a variety of substrates (Singh et al., 2014). However, with the rapid development of bioelectronics and the increasing demand for seamless integration between humans and machines, conventional SWAs are facing some challenges. First, despite their relatively strong bonding capability, the tacky binding agent can be easily contaminated with impurities (e.g., dust, sebum, etc.), limiting both the ability to reposition and reuse. Second, the binding agent may

contain chemicals harmful to humans, resulting in irritation (Kawahara and Tojo, 2007), contact dermatitis (Christoffers et al., 2014), and even injury or damage (Matsumura et al., 2013; Hwang et al., 2018). In contrast, SDAs bond by employing physical interactions such as electrostatic attraction, van der Waals (vdW) forces, suction, or friction (Eisenhaure and Kim, 2017). In general, SDAs require relatively smooth surfaces to enable such physical interactions, e.g., no air leakage or intimate contact for vdW interaction, thus they were not used as widely as SWAs. But in the last two decades, SDAs have garnered tremendous attention with great promise in the fields of healthcare, soft robotics, and human-machine interface (Brodoceanu et al., 2016; Li et al., 2016; Xiaosong et al., 2019; Chen et al., 2020b). Of particular interest are SDAs that are capable of repeated attachment and detachment, whose usefulness has been demonstrated in many exciting applications such as breathable skin patches (Kwak et al., 2011), robotic footpads or grippers (Gorb et al., 2007), and reusable bio-integrated electronics (Hwang et al., 2018).

PILLAR- AND CRATER-ENABLED SOFT DRY ADHESIVES

So far, the most widely studied SDAs are surfaces with arrays of micro-pillars. The inspiration came from terrestrial species including lizards and geckos whose toe pads are covered by intricate fibrils that enable strong attachment as well as easy release (Autumn et al., 2000; Autumn et al., 2002; Arzt et al., 2003; Gao and Yao, 2004; Hansen and Autumn, 2005; Yao and Gao, 2006). Autumn et al. (2000) first discovered the hierarchical *lamellae* and *setae* structures of gecko toe pads by scanning electron microscopy (SEM). There, each seta branches into hundreds of 200 nm thin *spatula*, capable of conforming to curvilinear and rough surfaces. The normal adhesive strength of those toe pads was measured at of 100 kPa (Autumn et al., 2000), which is comparable to that of a 3M Scotch™ tape (200 kPa). The strong adhesion of the gecko toe pads was solely attributed to vdW forces between the nanoscale spatula and the target surface, rather than chemical bonding (Autumn et al., 2002). Aside from the remarkable attachment performance, the fibrillary system also exhibits superior reversibility and self-cleaning capability (Hansen and Autumn, 2005).

Figures 1A–E showcase several representative synthetic micro-scale surface features resembling gecko fibrils. The simplest design is micro-pillars with flat tips (Del Campo and Arzt, 2007; Del Campo et al., 2007a; Del Campo et al., 2007b) (**Figure 1A**). More advanced designs involve micro-pillars with hierarchy (Greiner et al., 2009; Wang et al., 2014) (**Figure 1B**). Spatula tips (Del Campo and Arzt, 2007; Del Campo et al., 2007a) (**Figure 1C**) have been designed to more closely mimic the gecko's toe pads. Emulating the design principle of the tilting setae on gecko's toe pads, slanted structures have been widely exploited to generate directional adhesion (**Figure 1D**) (Autumn et al., 2006a; Murphy et al., 2009; Moon et al., 2010; Afferrante and Carbone, 2012; Jin et al., 2014; Wang et al., 2014; Wang et al., 2015; Seo et al., 2016; Wang, 2018). This represents a breakthrough in developing reversible adhesives that truly resemble their natural prototypes. Among all the tip geometries, the mushroom-like shape (**Figure 1E**) stands out as it exhibits large adhesive strength by reducing the stress concentration at the pillar-substrate interfaces (Del Campo et al., 2007a; Carbone et al., 2011; Carbone and Pierro, 2012; Bae et al., 2013; Wang et al., 2014; Marvi et al., 2015; Kim et al., 2016). The vibrant research on micro-pillar-based SDAs has been summaried by many excellent review articles, with various focuses on the adhesion mechanisms, design principles, fabrication methods, and performance characterizations (Pattantyus-Abraham et al., 2013; Zhou et al., 2013; Sahay et al., 2015; Eisenhaure and Kim, 2017; Xiaosong et al., 2019). **Figures 1F–L** display examples of another type of SDAs, suction- or crater-based adhesives, which is the focus of this paper and will be discussed in detail later.

Despite extensive research in the last two decades, as far as applications are concerned, micro-pillar-enabled SDAs are facing some major barriers. First, according to "contact splitting" theory (Arzt et al., 2003; Chan et al., 2007; Kamperman et al., 2010), the adhesion can be enhanced by splitting up the contact with the adherend into finer subcontacts, enabled by extremely tiny fibrils. However, scaling-down the pillar size faces fundamental physical limitations and dramatically increases manufacturing difficulties and costs. Those challenges have been recognized in both electron beam lithography (Pease, 1981; Vieu et al., 2000) and nano-embossing (Becker and Heim, 2000; Kim et al., 2007). Furthermore, slender pillars are prone to buckling and collapsing, resulting in undesirable entanglements and/or mats (see **Figure 2A**). In fact, buckling may even lead to rupture and detachment (Chan et al., 2007; Del Campo and Arzt, 2007; Greiner et al., 2007; Kim et al., 2007; Kim et al., 2016; Eisenhaure and Kim, 2017). All of these degradation mechanisms may significantly impair the adhesive strength, leading to limited robustness and reusability. On a different note, it has been widely reported that micro-pillars may lose their van der Waals adhesion on wet surfaces or in aquatic environments (Buhl et al., 2009; Pesika et al., 2009; Baik et al., 2017; Cadirov et al., 2017; Ma et al., 2018). A typical adhesion test shown in **Figure 2B** unveils that humidity dramatically decreases the adhesion of micro-pillar arrays (Cadirov et al., 2017). This is consistent with another experimental observation that micro-pillar arrays almost completely lose adhesion with moisture or underwater (see the green bars in **Figure 2C**) (Baik et al., 2017). **Figure 2D**, taken from the same paper (Baik et al., 2017), highlights the adhesion of cratered surfaces, which will be discussed later.

According to Bartlett *et al.* (Bartlett et al., 2012; Bartlett and Crosby, 2014), the adhesive force of micro-pillars can be scaled as $F_{ad} \sim \sqrt{A/C}$ where A is the actual contact area and C is the system compliance in the loading direction. Based on this scaling law, aside from enlarging effective contact area A, the adhesive force may also be enhanced by decreasing the system compliance C. An easy way to minimize the compliance C is by utilizing stiff materials. Here, we summarize existing data from the literature in an Ashby plot (**Figure 3**, numbers are listed in **Table 1** and **Table 2**) where the experimentally measured

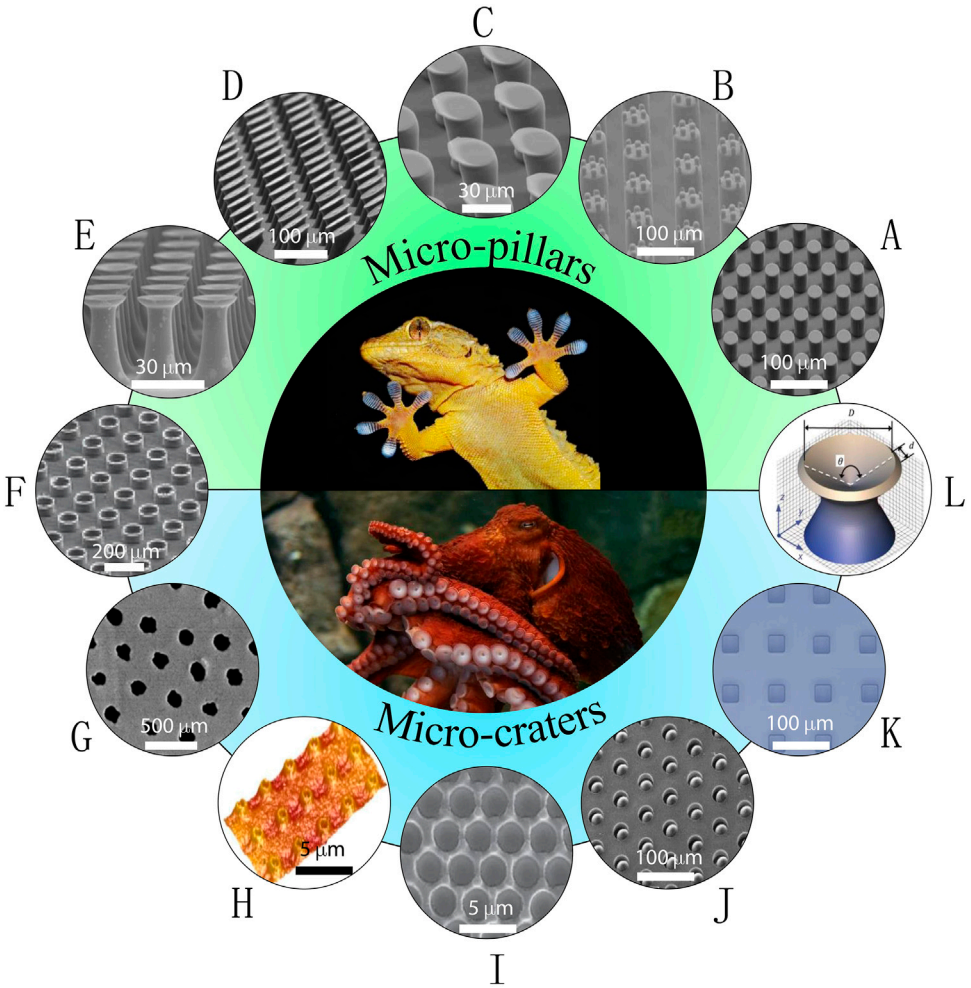

FIGURE 1 | Examples of nature-inspired soft dry adhesives (SDAs). **(A–E)** Gecko-inspired synthetic micro-pillars with various tip geometries: **(A)** flat tip (reprinted with permission from ref (Del Campo et al., 2007b)); **(B)** hierarchical tip (reprinted with permission from ref (Greiner et al., 2009)); **(C)** spatular tip (reprinted with permission from ref (Del Campo and Arzt, 2007)); **(D)** slanted tip (reprinted with permission from ref (Murphy et al., 2009)); **(E)** mushroom-like tip (reprinted with permission from ref (Wang et al., 2014)). **(F)** A combinational structure – micro-pillars with concave tip (reprinted with permission from ref (Baik et al., 2018)). **(G–K)** Octopus-inspired synthetic micro-suckers or craters: **(G)** nano-craters on UV resin surfaces (reprinted with permission from ref (Chang et al., 2014)); **(H)** reversible adhesive skin patch with micro-craters on multilayer PDMS (reprinted with permission from ref (Choi et al., 2016)); **(I)** micro-craters on PDMS surface (reprinted with permission from ref (Akerboom et al., 2015)); **(J)** micro-craters with interior protuberances (reprinted with permission from ref (Baik et al., 2017)); (K) square-patterned micro-craters on PDMS surface (reprinted with permission from ref (Nanni et al., 2015)). **(L)** Another combinational structure – pillar with funnel-shaped tip (reprinted with permission from ref (Fischer et al., 2017)).

normal adhesive strength is plotted versus material Young's modulus (Geim et al., 2003; Sitti and Fearing, 2003; Kim and Sitti, 2006; Del Campo et al., 2007b; Lee et al., 2008; Lu et al., 2008; Cheung and Sitti, 2009; Davies et al., 2009; Murphy et al., 2009; Parness et al., 2009; Sameoto and Menon, 2009; Kwak et al., 2011; Bae et al., 2013; Tsai and Chang, 2013; Jin et al., 2014; Fischer et al., 2016; Kim et al., 2016; Drotlef et al., 2017; Hu et al., 2017). In this plot, the purple zone represents pillar-based adhesives in dry environments, the orange zone highlights crater-based adhesives under normal ambient conditions, and the green zone indicates crater-based adhesives under high humidity, wet or underwater environments. In particular, setae (material: β-keratin with $E \sim 1$–2 GPa) on gecko toe pads can produce ~100 kPa adhesive strength (Autumn et al., 2000; Autumn et al., 2006b; Huber et al., 2008) as highlighted by the gecko icon in the plot. To achieve adhesion on par with gecko toe pads, stiff materials are usually employed such as polythiophene nanotubes ($E \sim$ GPa) (Lu et al., 2008) and carbon nanotubes ($E \sim$ TPa) (Zhao et al., 2006). But reducing the compliance C would also inherently compromise the softness of the adhesive and their conformability to curvilinear surfaces, especially when the surface is deformable (e.g., human skin), (Qiao et al., 2015; Wang and Lu, 2016; Wang et al., 2017a), which limits their applications. However, when micro-pillars are fabricated out of soft materials ($E < 3$ MPa), their adhesive performance is significantly compromised as shown in **Figure 3**, resulting in two distinctive purple zones.

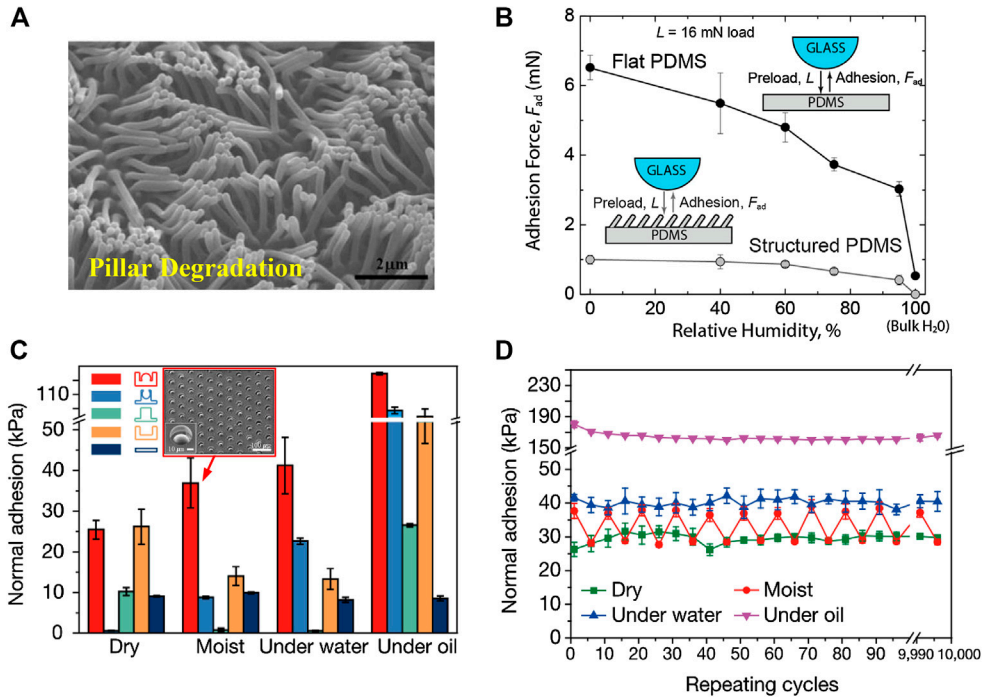

FIGURE 2 | Limitations of pillared surfaces and advantages of cratered surfaces as SDAs. **(A)** A scanning electron microscopy (SEM) image of pillar condensation. (reprinted with permission from ref (Kim et al., 2007)). **(B)** Adhesion force of micro-pillars as a function of relative humidity (reprinted with permission from ref (Cadirov et al., 2017)). **(C)** Adhesive strengths of various pillared and cratered structures where red: protuberance-shaped crater; blue: perforated cylinders; green: cylindrical pillar; brown: cylindrical hole; black: flat surface (reprinted with permission from ref (Baik et al., 2017)). **(D)** Repeatable adhesion of the crater-enabled SDAs after more than 10000 cycles of attachment and detachment (reprinted with permission from ref (Baik et al., 2017)).

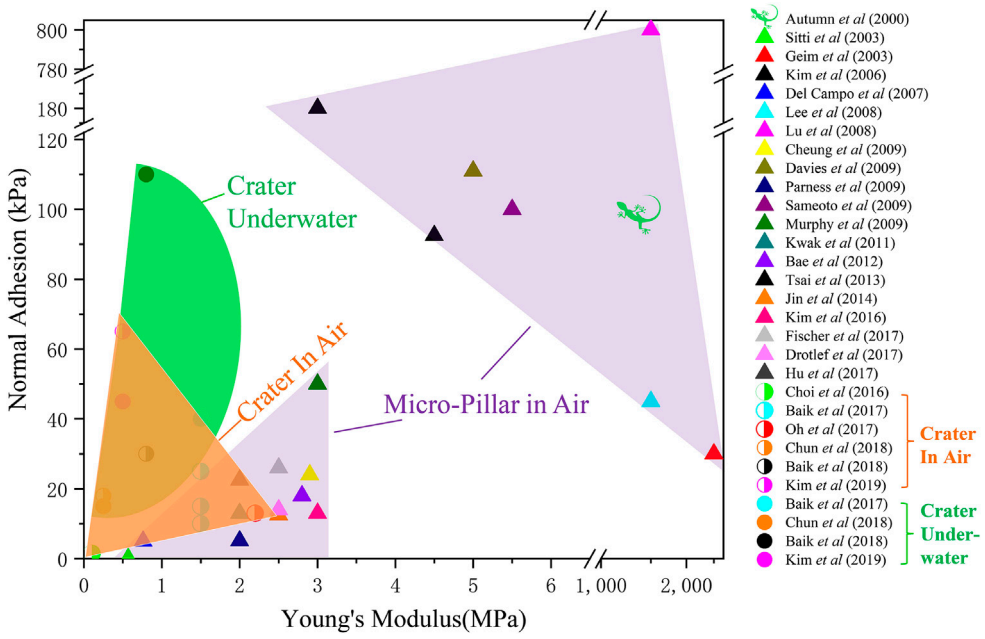

FIGURE 3 | An Ashby plot of normal adhesive strength vs. material Young's modulus for both pillar-enabled and crater-enabled SDAs. Purple regimes enclose data of pillared surfaces in air. The orange regime denotes craters in air and the green regime represents craters underwater.

TABLE 1 | Micro-pillar-enabled Soft dry adhesives.

Material	Modulus (MPa)	Normal adhesion (kPa)	Tip diameter (μm)	Pillar length (μm)	Tip shape	Reference
Polythiophene nanotube	1,500	800	0.2	12	Nanohair	(Lu et al., 2008)
Polyurethane	3	180	4.5	20	Mushroom	(Kim and Sitti, 2006)
Sylgard 184	1–10	111–219	40	100	Mushroom	(Davies et al., 2009)
MWCNT	10E5	117	0.02–0.03	5–10	Fiber	(Zhao et al., 2006)
Sylgard 184	1–10	100–180	10	20	Mushroom	(Sameoto and Menon, 2009)
Gecko (β –keratin)	1,500	100	—	—	Hierarchical	(Autumn et al., 2000)
Sylgard 184	0.76	5	10	30	Mushroom	(Del Campo et al., 2007b)
Graded PDMS	5	92.5	2	2	Round	(Tsai and Chang, 2013)
Polyurethane	2.9	24	50	100	Mushroom	(Cheung and Sitti, 2009)
Polyurethane	3	50	35	100	Tilted	(Murphy et al., 2009)
Polyimide	2,500	30	0.2–4	0.15–2	Fiber	(Geim et al., 2003)
PDMS	2–3	22.5	20	55	Mushroom	(Hu et al., 2017)
PDMS	2	13	5	5–20	Mushroom	(Kwak et al., 2011)
PDMS	1.5–3.5	13	5	30	Mushroom	(Kim et al., 2016)
PDMS	2–3	12.5	13	80	Tilted	(Jin et al., 2014)
PDMS	2–3	10.5	—	100	Wedge	(Tao et al., 2017)
PDMS	2.8–8.2	7.5–18	5	20	Mushroom	(Bae et al., 2013)
PDMS	2–3	7.5–14	60–95	120	Mushroom	(Drotlef et al., 2017)
Silicones	1.75–2.63	5.1	50	200	Wedge	(Parness et al., 2009)
Silicone rubber	0.57	0.028	0.2	60	Fiber	(Sitti and Fearing, 2003)

TABLE 2 | Crater-Enabled Soft dry adhesives.

Material	Modulus (MPa)	Shape	Ambient condition	Diameter (μm)	Normal adhesion (kPa)	Reference
s-PUA	1.5	Protuberance	In air	30	15	(Baik et al., 2017)
				100	26	
				300	25	
			Underwater	30	25	
				100	42	
				300	15	
PDMS	0.8	Concave	In air	30	20	(Baik et al., 2018)
				100	30	
				1,000	8	
			Underwater	30	32	
				100	115	
				1,000	55	
	2.2	Concave with rim	In air	5	13	(Oh et al., 2018)
	0.5	Protuberance	In air	30	60	(Kim et al., 2019)
			Underwater		45	
	0.2		In air	30	18	(Chun et al., 2018)
			Underwater		13	
PDMS	0.105	Concave	In air	1	1.5	(Choi et al., 2016)

Another class of reusable SDAs emerged as arrays of micro-craters (i.e., dimples or depressions engineered on polymer surfaces). In fact, utilizing suction for attachment has been widely observed in nature. The arms of aquatic cephalopods such as squid and octopus are equipped with hundreds of suckers for anchoring and object manipulation (Smith, 1991; Kier and Smith, 2002; Von Byern and Klepal, 2006; Tramacere et al., 2013; Tramacere et al., 2014b). The pressure drop inside the sucker, termed negative pressure, can reach 300 kPa for octopus and 800 kPa for decapod (Smith, 1991; Smith, 1996). Cephalopod suckers have been emulated on aquatic robots using active pumps (Wang et al., 2017c; Shintake et al., 2018) as well as passive adhesive tapes (Choi et al., 2016; Baik et al., 2017). Passive cratered surfaces have demonstrated remarkable adhesion capabilities in recent years. Just to name a few, in 2014, Chang *et al.* (Chang et al., 2014) created an array of submicron-sized craters on UV resin (**Figure 1G**) and measured adhesive shear strengths as high as 750 kPa on silicon wafers (Chang et al., 2014). In 2015, Choi *et al.* fabricated an array of 1 μm-diameter craters on the surface of a multilayer polydimethylsiloxane (PDMS) (**Figure 1H**) and the measured adhesive strength exceeded that of the same PDMS with either flat or pillared surface (Choi et al., 2016). Also in 2015, Akerboom *et al.* fabricated close-packed nano-dimples on 10:1 (base-to-curing agent ratio) PDMS (**Figure 1I**) and found a larger pull-off force in comparison to flat PDMS surfaces (Akerboom et al., 2015). In

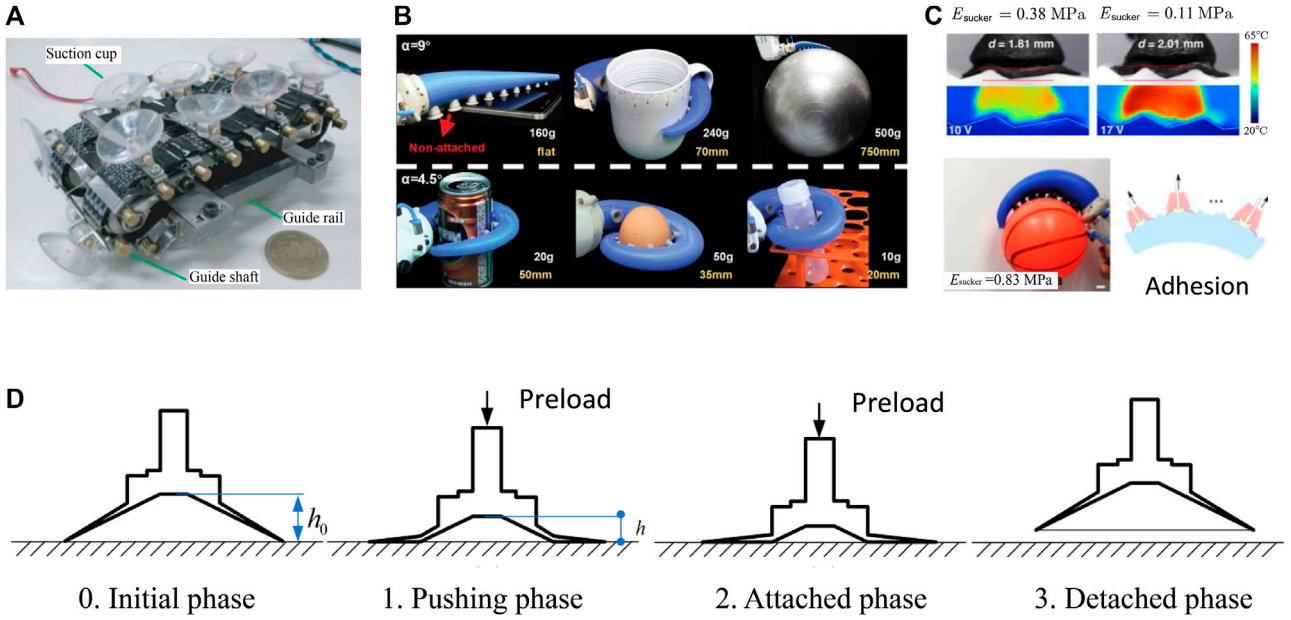

FIGURE 4 | Suction cup example applications and models. **(A)** Wall-climbing robots with suction cups as attaching components (reprinted with permission from ref (Yoshida and Ma, 2010)). **(B)** A suction-cup-based tapered soft actuator capable of gripping objects of various shapes (reprinted with permission from ref (Xie et al., 2020)). **(C)** An organohydrogel-based soft gripper with electrically programmable stiffness for achieving conformable contact with rough surfaces. [reprinted with permission from ref (Zhuo et al., 2020)]. **(D)** Schematics of a pressing-detaching process of a suction cup [reprinted with permission from ref (Ge et al., 2015)].

2017, Baik *et al.* fabricated dome-shaped protuberances within micro-craters (**Figure 1J**), whose adhesive strength was found to be 2-3 times higher than micro-pillars in dry condition (Baik et al., 2017). Similarly, enhanced adhesion has been reported by Nanni *et al.* who engineered PDMS with square-shaped craters (**Figure 1K**) (Nanni et al., 2015).

Beyond simple pillars or craters, researchers have combined the pillar effects with the suction mechanism. It has been experimentally confirmed that suction contributed 20% towards the total adhesive force in mushroom-like micro-pillars (Varenberg and Gorb, 2008; Tinnemann et al., 2019). The authors argued that vacuum may be generated between the thin mushroom-like tip and the surface during the detachment. In fact, micro-pillar stalks terminated with concave dome tip (Baik et al., 2018) (**Figure 1F**) or funnel-shaped tip (Fischer et al., 2017) (**Figure 1L**) have been realized and adhesive strength has been elevated to an ultrahigh value of 5.6 MPa (Fischer et al., 2017), which is gigantic compared with kPa-range adhesive strengths for simple pillars (e.g., **Figures 1A–E**) or simple craters (**Figures 1G–K**).

Although both are SDAs, crater-enabled adhesives have the following advantages relative to pillar-enabled adhesives: ease of fabrication, pressure-sensitive adhesion, excellent wet adhesion, superior scratch resistance and reusability, and high material compliance. Generally, cratered surfaces are engineered by molding a soft elastomer on a negative template with domes. Such a fabrication method is generally easier than the process to produce hierarchical (Del Campo and Arzt, 2007; Greiner et al., 2009) or composite micro-pillars (Bae et al., 2013; Drotlef et al., 2019). Distinct from the micro-pillars whose adhesive strength is usually fixed once fabricated (Murphy et al., 2009; Mengüç et al., 2012; Chary et al., 2013), the adhesion of cratered surfaces depends on the preload (Akerboom et al., 2015; Baik et al., 2019b). It is also worth noting that crater arrays, similar to octopus suckers, show a conspicuously enhanced adhesive strength underwater or on wet surfaces (see the red bar in **Figure 2C** and the green domain in **Figure 3**). Also, without delicate protruding structures, cratered surfaces are more scratch resistant and reusable. For example, Baik *et al.* (Baik et al., 2017) demonstrated that the adhesive force of craters remained almost unchanged after 10,000 cycles of attachment and detachment (**Figure 2D**). Last but not least, as presented in **Figure 3**, crater-enabled SDAs are capable of producing higher adhesion while maintaining the desirable levels of material softness. Such high softness endows them with exceptional deformability as well as conformability on deformable, rough surfaces including bio-tissues (Choi et al., 2016). These advantages of crater-based adhesives have enabled many exciting applications including wall-climbing robots (Aksak et al., 2008; Sahay et al., 2015), object manipulation (Chang et al., 2014) such as wafer handling (Lee et al., 2016), and bio-integrated medical devices (Chun et al., 2018; Hwang et al., 2018; Oh et al., 2018; Baik et al., 2019a; Baik et al., 2019b; Kim et al., 2019; Iwasaki et al., 2020).

Let us point out that harnessing suction for attachment is ubiquitous. Thin-walled suction cups are widely used in everyday suction hooks and climbing robot pads (**Figure 4A**) (Yoshida and Ma, 2010; Manabe et al., 2012) due to their strong attachment and quick release. By assembling suction cups onto a tapered

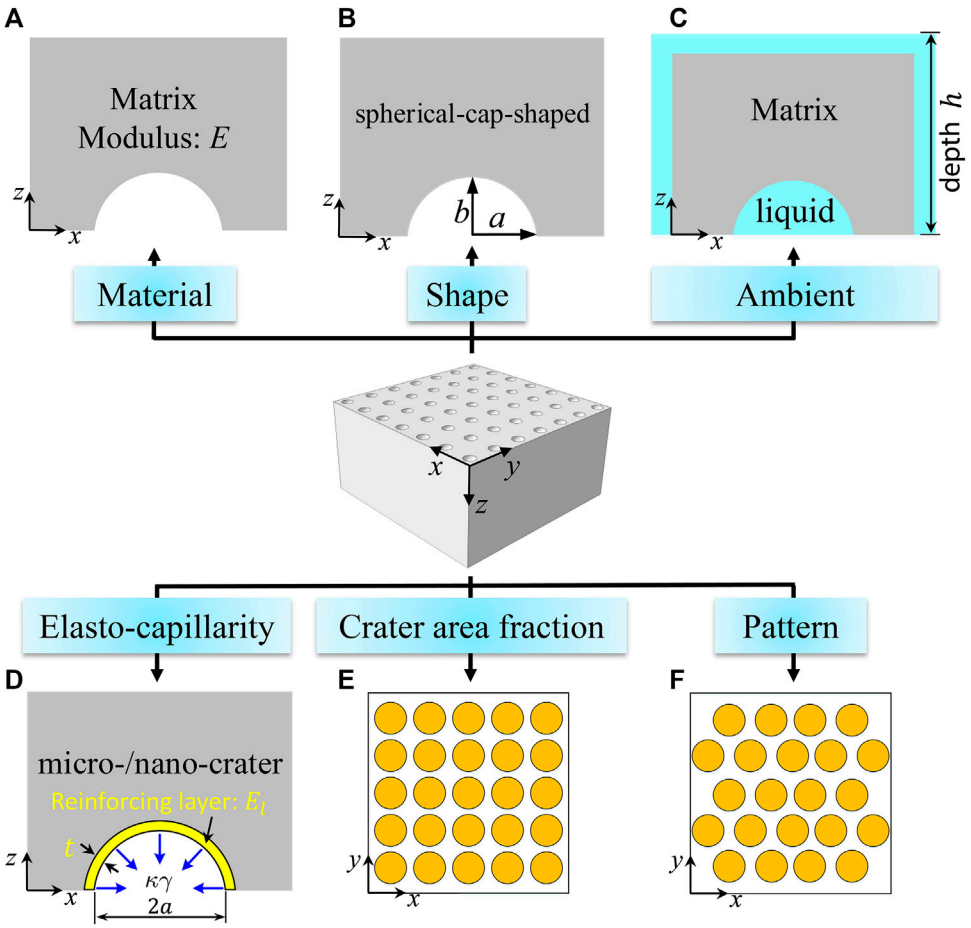

FIGURE 5 | Six factors that affect the suction effects of crater arrays discussed in this review article: **(A)** matrix modulus; **(B)** crater shape, **(C)** ambient environment; **(D)** elasto-capillarity at small length scale; **(E)** crater area fraction; **(F)** the pattern of a crater array.

elastomeric arm, Xie *et al.* recently demonstrated a soft actuator that was capable of grasping objects of various shapes (**Figure 4B**) (Xie et al., 2020). The same group also provided a feasible solution for preventing air leakage when gripping rough surfaces by programming the compliance of the sucker. The sucker was made of electrically responsive organohydrogel, which softened under high voltage, giving rise to conformable contact with rough surfaces (**Figure 4C**) (Zhuo et al., 2020). Theoretical analysis and experimental measurements have been carried out to understand both the attachment and detachment behaviors of suction cups. For instance, by actively pumping out the air through a connected tube, Liu et al., (2006) has reported the relationship between the negative pressure inside the cup and the active area, i.e. the area not in contact between the cup and the substrate. The suction force can be readily obtained through negative pressure multiplied by the active area. Different from air-pumping, Ge *et al.* proposed a pushing-detaching framework for characterizing the suction force of a commonly used passive suction cup (**Figure 4D**) (Ge et al., 2015). The process is illustrated in **Figure 4D**. In the beginning, the cup is resting on the substrate surface. Then a preload is applied to deform the suction cup such that air inside the cup is squeezed out and the suction cup successfully attaches to the substrate. To detach it, a pulling force is applied until it reaches the pull-off force. Based on this process, the suction force of the cup has been modeled and experimentally validated. However, such analysis is only applicable to thin-walled suction cups rather than craters which are dimples on the surface surrounded by the polymer matrix.

Despite a significant body of experimental evidence that suction is a significant adhesion mechanism for cratered surfaces, until recently, theoretical understanding and consequently model-guided design procedures were lacking. Our recent series of papers were a attempt intended to remedy this situation. We have developed an integrated computational-experimental-modeling approach for the quantitative characterization and understanding of the suction behaviors for various cratered surfaces under both dry and wet conditions. In the next section, we summarize our results by focusing on four factors controlling suction of isolated craters (**Figure. 5**): Young's modulus of the polymer matrix (**Figure 5A**) (Qiao et al., 2017), crater shape (**Figure 5B**) (Qiao et al., 2017;

Wang et al., 2019), air/underwater ambient environment (**Figure 5C**) (Wang et al., 2017b; Qiao et al., 2018), and elasto-capillary effect on micro/nano-craters (**Figure 5D**) (Wang et al., 2017b). In **Section IV**, we will discuss cratered surfaces and address the importance of the crater areal fraction as defined by the ratio between the projected area of crater and the base plane area of specimen (**Figure 5E**) (Wang et al., 2019) and patterns (**Figure 5F**) (Wang et al., 2019) of cratered arrays.

ISOLATED CRATERS

This section summarizes our results for isolated craters. The term isolated means that the crater dimensions are much smaller than all other specimen dimensions, and therefore the specimen can be regarded as a semi-infinite solid, where the only relevant dimensions are those of the crater.

Isolated Craters in Air

We begin this section by considering isolated craters in air as a precursor to considering the presence of liquids on the performance of isolated craters.

Modeling Framework

Following the earlier work on thin-walled suction cups (Ge et al., 2015), a loading-unloading process is established for calculating the suction force of an isolated crater, as illustrated by **Figures 6A–C**. Initially, the air inside the crater is characterized by the ambient pressure, p_0, volume V_0, and number of molecules N_0 (**Figure 6A**). The suction effect is realized in the following two steps:

(1) The specimen is subjected to a remote compressive stress σ, which squeezes air out of the crater. We refer to σ as the preload, and denote the state at the end of this step by the triplet (p_1, V_1, N_1) (Stage 1, **Figure 6B**).
(2) The specimen is unloaded in such a manner that air does not return to the crater and the crater springs back. This action results in a pressure drop inside the crater which produces the suction force. At the end of this step, the air in the crater is characterized by the triplet $(p_2,\ V_2,\ N_2)$ (Stage 2, **Figure 6C**). Accordingly, the pressure drop is

$$-\Delta p = p_1 - p_2$$

and the suction force

$$F = -\Delta p A_2 \tag{1}$$

where A_2 is the projected area of the crater at Stage 2.

Key assumptions adopted in this framework are:

a. The air flows freely out of the crater upon loading (Step 1), so that $p_1 = p_0$.
b. No air exchange takes place upon unloading (Step 2), so that $N_2 = N_1$.
c. The entire process is isothermal and air is an ideal gas, so that $p_1 V_1 = p_2 V_2$.

Assumptions (a) and (b) are consistent with the abovementioned models of thin-walled suction cups (Liu et al., 2006; Ge et al., 2015). However, in our experiment, to be discussed later, Assumption (a) is hard to achieve without a vent hole drilled in the substrate. Therefore, future research is required to realize Assumption (a) without any vent hole. Furthermore, secure sealing after loading should be validated to justify Assumption (b). With these three assumptions, the pressure drop can be related to the crater volumes as

$$-\Delta p = \left(1 - \frac{V_1}{V_2}\right) p_0 \tag{2}$$

Therefore, the suction force becomes

$$F = \left(1 - \frac{V_1}{V_2}\right) p_0 A_2 \tag{3}$$

If the ambient pressure is equal to the atmospheric pressure p_a, we can define the suction-induced effective adhesive strength as

$$\sigma_{eff} = \frac{F}{A_0} = \left(1 - \frac{V_1}{V_2}\right) \frac{A_2}{A_0} p_a. \tag{4}$$

According to this equation, obtaining a large value of σ_{eff} requires both small V_1 after loading, and large A_2 and V_2 after unloading. The maximum possible σ_{eff} is atmospheric pressure, i.e., p_0, which can be achieved when the crater is fully closed after loading, i.e., $V_1 = 0$, and recovers to $A_2 = A_0$ after unloading.

Simulation and Experimental Setups

Axisymmetric finite element models (FEM) for isolated craters were built to simulate the suction force using commercial software, ABAQUS 6.13 (**Figure 6**). The built-in function *FLUID CAVITY was implemented to model the ideal gas behavior inside the craters. The specimen/substrate interface was assumed to be frictionless, and the substrate was assumed to be rigid. The material behavior of 30:1 PDMS was characterized as an incompressible neo-Hookean model with Young's modulus E = 141.9 kPa according to our measurements (Qiao et al., 2017). Experimentally, PDMS with base-to-curing-agent mass ratio equal to 30:1 was cured at 70°C for 12 h to mold specimens with and without craters (see inset in **Figure 6E**). A small vent hole with diameter of 0.8 mm was drilled in the rigid plate and roughly aligned with the center of the crater. Oil lubricant was applied at the specimen/plate interface. Loading and unloading tests were carried out with the vent hole open during loading and closed during unloading and the pull-off force was measured. A representative experimental loading-unloading curve is given in **Figure 6E**. The suction force can be readily calculated by subtracting the adhesive force over the contact zone (which is very small and independent of preload) from the measured pull-off force at the pull-off point (Qiao et al., 2017).

Results

Spherical-cap-shaped (SCS) craters with various aspect ratios were studied both numerically and experimentally. The schematic of a SCS crater is shown in **Figure 5B** where the

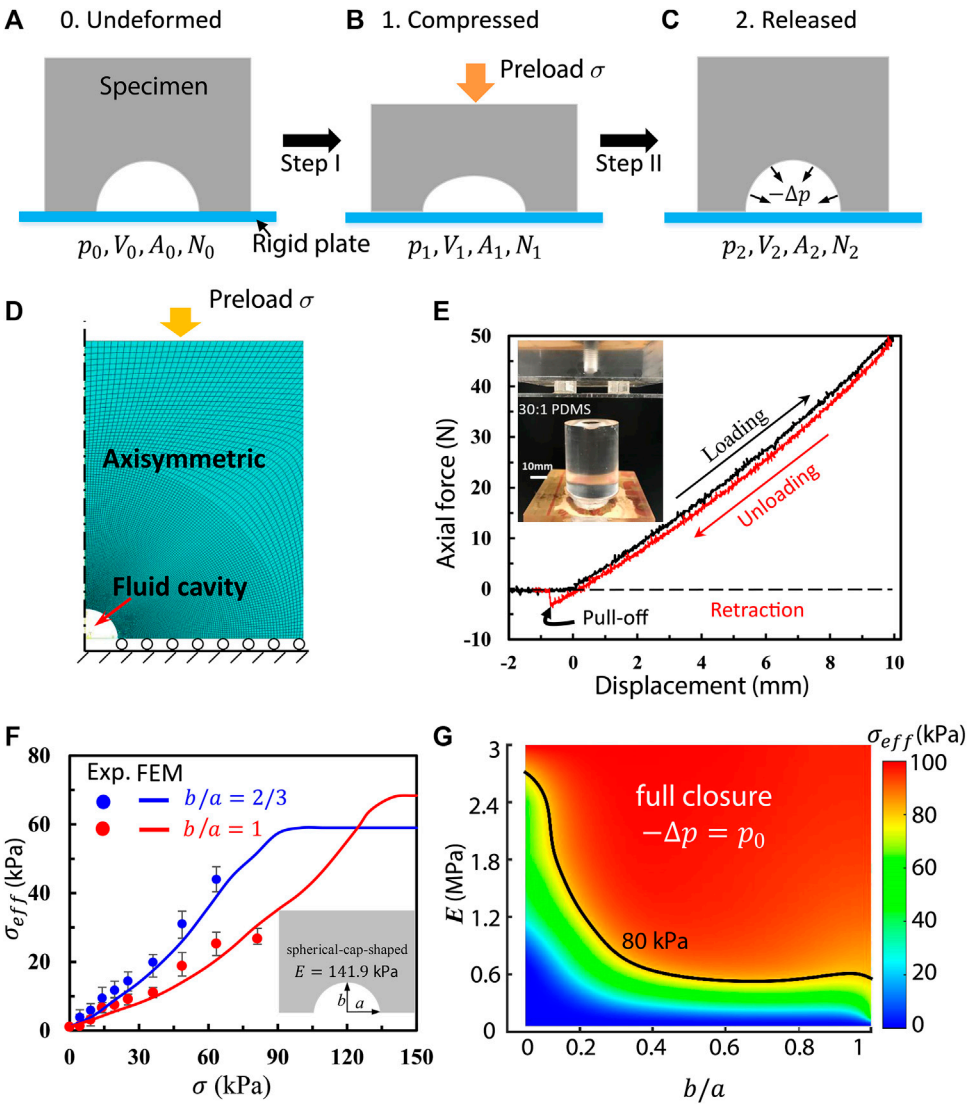

FIGURE 6 | The model of a macroscopic, isolated crater in air. **(A–C)** Schematics of the loading-unloading process that generates suction. **(D)** An axisymmetric finite element model (FEM) for simulating isolated craters. **(E)** A representative loading-unloading-retraction curve for a cratered specimen. The inset shows the experimental setup. **(F)** Effective adhesive strength as a function of the preload for spherical-cap-shaped (SCS) craters with aspect ratios b/a = 2/3 and 1. **(G)** A contour plot for effective adhesive strength σ_{eff} as a function of the matrix Young's modulus E and crater aspect ratio b/a. [reprinted with permission from (Qiao et al., 2017)]

base radius and height of the craters are labeled as a and b, repectively. **Figure 6F** plots the effective adhesive strength σ_{eff} as a function of preload for two aspect ratios, $b/a = 1$ (blue) and $b/a = 2/3$ (red). Experimental results are plotted as markers and FEM results as solid curves. The following conclusions can be drawn from **Figure 6F**. First, suction-enabled adhesion intrinsically depends on preload, and generally higher suction force can be achieved by increasing the preload. Second, when the preload is large enough to fully close the crater at Stage 1, further compression will not enhance the suction anymore as shown by the plateau of the two curves. Third, under small preloads, shallower craters generate higher suction forces than deeper ones.

It is also worth noting that experimental and FEM results agree well. Therefore, such a simulation approach can be confidently used for characterizing other cratered specimens, e.g., of different Young's moduli and crater shapes. A contour plot for the effective adhesive strength as a function of material Young's modulus E and aspect ratio b/a is given in **Figure 6G**. Results presented in **Figure 6G** are evaluated at full closure, i.e., $-\Delta p = p_0$ is attained for all scenarios. It is clear that deeper craters with stiffer matrices are capable of producing larger suction provided full closure at Stage 1. Note that it is an opposite conclusion compared with what we discussed in **Figure 6F** – shallower crater generates higher suction provided the same preload. This can be understood as follows: it is easier for shallower craters to

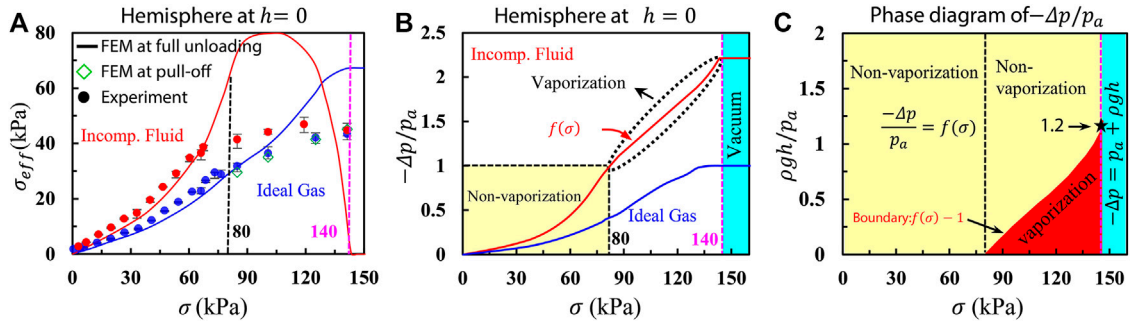

FIGURE 7 | Experimental and modeling results for craters underwater. **(A)** Effective adhesive strength σ_{eff} as a function of preload σ for craters in air (blue) and underwater (red). Curves are FEM results at the unloading point. Solid markers are experimental results and open diamond markers are FEM results at the pull-off point. **(B)** Pressure drop as a function of preload σ. For craters filled with liquid, when internal pressure approaches zero, rapid vaporization can happen at room temperature, which violates the incompressible fluid assumption. **(C)** Phase diagram of pressure drop as a function of liquid depth h and preload σ. [reprinted with permission from (Qiao et al., 2018)]

reach full closure when the preload is small, i.e., a smaller V_1, thus achieve a higher suction force according to **Eq. 4**. However, when the preload is large enough to fully close craters, i.e., $V_1 = 0$, deeper craters will spring back more with a larger projected area, i.e., a large A_2, giving rise to a higher suction force.The black curve in **Figure 6G** represents an iso-strength curve of σ_{eff} = 80 kPa. Note that crater shape is limited to a spherical cap in **Figure 6G** and is varied by choosing different aspect ratios. Other shapes such as spheroidal (Qiao et al., 2017) and cylindrical (Wang et al., 2019) craters have also been investigated but are not discussed in this review.

Macroscopic, Isolated Craters Underwater

Similar to suction cups on aquatic cephalopods (Tramacere et al., 2014a; Tramacere et al., 2014b), craters underwater also exhibit much larger adhesive strength than those in air (see **Figure 3**). This is addressed by considering a cratered specimen resting on a fixed rigid platform, both submerged in liquid at depth h (**Figure 5C**). The ambient pressure is now

$$p_0 = \rho g h + p_a \tag{5}$$

where ρ is the liquid density and g is the gravitational constant. Assume that the suction force is still generated through a loading-unloading process as illustrated in **Figure 6A** but in an aquatic environment. Similar to air-filled craters, the pressure inside the crater at States 0 and 1 are assumed to be the same, i.e., $p_1 = p_0$ and the number of liquid molecules remains unchanged during State 2, i.e., $N_1 = N_2$. However, rather than adopting the ideal gas relationship $p_1 V_1 = p_2 V_2$, the liquid inside the crater is assumed to be incompressible, so that $V_1 = V_2$. Both FEM and experiments were conducted to quantify the underwater suction under various preloads (Qiao et al., 2018).

Zero Liquid Depth

We begin the discussion by first forming an understanding when $h = 0$, $p_0 = p_a$. Results for a hemispherical crater in air (blue) and underwater (red) at $h = 0$ are displayed in **Figure 7A**. It is obvious that craters of both fillings experience an increase in suction with growing preload, whereas the liquid-filled craters exhibit a faster increase due to the stronger constraint on the polymer matrix under volume conservation, i.e., $V_1 = V_2$, compared with the ideal gas relation, $p_1 V_1 = p_2 V_2$. Also, for both cases, FEM results (solid curves) are in excellent agreement with experiment (circular markers) when the preload is smaller than 80 kPa, while the two responses start to deviate as the preload further increases. For the crater in air, such a discrepancy can be successfully resolved by adding an experimentally extracted retraction strain in FEM (green open diamond markers in **Figure 7A**) because the strain at pull-off is discernibly higher than the strain at full unloading when the specimen is subjected to large preload. For the crater underwater, however, the discrepancy could come from vaporization of the liquid inside the crater when the internal pressure is extremely low or close to zero.

Figure 7B plots the normalized pressure drop obtained by FEM as a function of preload for both air-filled and liquid-filled hemispherical craters. The blue curve clearly shows that the pressure drop of the air-filled crater gradually increases with growing preload and eventually reaches a plateau of $-\Delta p = p_\alpha$ when fully closed, i.e., vacuum, at σ_f =140 kPa as highlighted by the vertical dashed magenta line. However, the crater underwater undergoes a faster pressure drop than those in air such that it reaches vacuum (i.e. $-\Delta p = p_\alpha$) prior to the full closure. The intersection of the horizontal dashed black line of $-\Delta p = p_\alpha$ and the curve of $-\Delta p/p_\alpha(\sigma)$ determines a critical preload of σ_v^0=80 kPa. The critical preload suggests a threshold above which the liquid in the crater will vaporize. In the simplest pictureIn other words, when $\sigma < \sigma_v^0$, the liquid inside the crater remains as an incompressible fluid, while when $\sigma \geq \sigma_v^0$, it should rapidly vaporize even in at room temperature. This liquid-to-gas phase transition violates the assumption of an incompressible fluid. Hence the FEM results beyond this point are no longer meaningful. It is also worth pointing out that when the craters are fully closed at σ_f =140 kPa, the craters in air or water behave essentially the same as $-\Delta p = p_\alpha$ is realized for both craters if h=0. This explains the fully overlapped experimental results at $\sigma = \sigma_f$ as highlighted by the vertical magenta dashed line in Figure 7A.

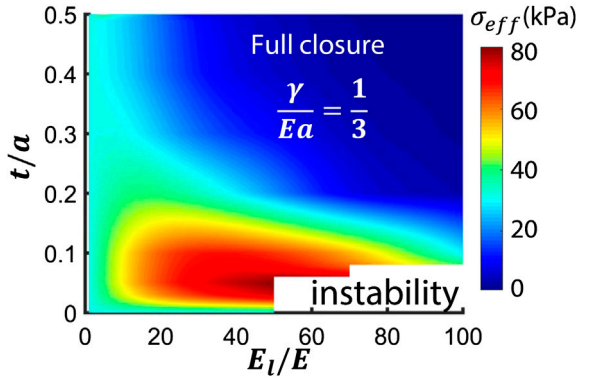

FIGURE 8 | A contour plot of effective adhesive strength σ_{eff} as a function of normalized thickness and Young' modulus of the reinforcing layer. Results are obtained under full closure with an elasto-capillary number $\gamma/(Ea)$ = 1/3. [reprinted with permission from (Wang et al., 2017b)].

Finite Liquid Depth

It is interesting to realize that the red curve in **Figure 7B** should be applicable to any $h > 0$ as long as both the polymer matrix and the liquid inside the crater are incompressible. This is because the hydrostatic pressure term ρgh in **Eq. 5** has no effect on the deformation of the incompressible matrix. Different h's only dictate the critical preload for vaporization, σ_v, beyond which the FEM results are invalid. This can be understood by looking at the "phase diagram" in **Figure 7C** where the horizontal axis is the preload σ and the vertical axis is the normalized liquid depth $\rho gh/p_a$. The yellow regimes are non-vaporization zones in which the pressure drop is h-independent. The red regime is where vaporization is expected to occur. The cyan regime represents complete vacuum. Right before vaporization occurs, the pressure drop simply equals the ambient pressure i.e., $-\Delta p = p_a + \rho gh$. Thus, when $\sigma < \sigma_v^0$, no vaporization would take place for any h as p_2 is still positive after unloading. When $\sigma_v^0 \le \sigma < \sigma_f$, we can introduce a function to represent the red curve in **Figure 7B**, say $-\Delta p/p_a(\sigma) = f(\sigma)$ for $0 < \sigma < \sigma_f$. Then σ_v can be obtained by solving $f(\sigma_v) = 1 + \rho gh/p_a$ for a given liquid depth h. If $\rho gh/p_a \ge f(\sigma) - 1$, the liquid still remains incompressible fluid; otherwise, the liquid vaporizes. When $\sigma \ge \sigma_f$, the hemispherical crater attains full closure with complete vacuum, leading to $-\Delta p = p_a + \rho gh$. Therefore, when the crater is fully closed, craters in deeper water will produce a higher suction force.

In summary, craters underwater, on the one hand, are capable of producing higher suction force than those in air due to the volume constraints; on the other hand, vaporization may take place, which undermines the suction.

Isolated Craters in Air With Surface Tension

Up to this point, we neglected polymer surface tension, which may become important for small craters on a soft matrix. The significance of surface tension can be realized by examining molded polymer surfaces. A commonly adopted fabrication method for cratered surfaces is molding polymers out of a negative template, which are usually created using either micromachining (Choi et al., 2016) or colloidal lithography (Chang et al., 2014; Akerboom et al., 2015). Such methods work well for relatively stiff polymers such as UV resin ($E \sim$ GPa) (Chang et al., 2014) or even 10:1 PDMS ($E \sim$ MPa) (Akerboom et al., 2015). However, molding microscale craters on soft polymer sheet, e.g. 40:1 PDMS ($E \sim 100$ kPa) (Choi et al., 2016), resulted in much smaller crater size compared with the domes on the template after demolding. This can be attributed to the so-called elasto-capillarity effects in which the polymer surface tension is a driving force for diminishing the sizes of craters when the crater length scale is comparable to the elasto-capillary length defined as $L_e = \gamma/E$ where γ is the surface tension of the polymer (Roman and Bico, 2010; Liu and Feng, 2012; Bico et al., 2018). To attain the desired crater shape, adding a stiffer reinforcing layer inside the crater has proven to be effective. The schematic of a reinforced crater is depicted in **Figure 5D**. The thickness and Young's modulus of the reinforcing layer are denoted as t and E_l, respectively. The effect of surface tension is equivalently interpreted as a normal traction $t_n = \kappa\gamma$ on the inner surface of the crater (shown by blue arrows), where κ is the sum of the two principal curvatures. To quantitatively characterize the effects of surface tension and reinforcing shell on the suction force generated by those craters, a demolding step was added prior to loading and unloading (Wang et al., 2017b). Therefore, the entire process of suction generation becomes demolding, loading, and unloading steps.

We investigated the surface tension effect by considering isolated hemi-spherical craters with reinforcements parameterized by their thickness and Young's modulus. A contour plot for the effective adhesive strength σ_{eff} as a function of normalized thickness t/a and modulus E_l/E is presented in **Figure 8**. It clearly suggests that there is an optimal combined range of t/a and E_l/E to generate large suction. When the reinforcing shell is too thin or too soft, it is simply too weak to resist the surface tension effect. When the reinforcing shell is too thick or too stiff, it preserves the crater shape after demolding, but it also prevents the crater from deformation during loading. As a result, a large V_1 leads to small σ_{eff} according to **Eq. 4**. The effect of strong and weak reinforcing shells is best visualized by the supplementary videos of (Wang et al., 2017b). Therefore, the optimal choice of t/a and E_l/E for large σ_{eff} lies in the domain $E_l/E \in (20, 50)$ and $t/a \in (0.025, 0.15)$ as shown by the red regime in **Figure 8**.

In fact, adding a reinforcing layer may even enhance the suction force for craters with negligible surface tension effects. This is because a thin reinforcing layer can assist the crater to spring back upon unloading, while leaving the overall structural stiffness almost unchanged (Qiao et al., 2017). Surprisingly, a reinforced SCS crater with aspect ratio $b/a = 0.85$ shows a maximum $\sigma_{eff} = 1.2p_a$, which is higher than the atmospheric pressure because $A_2 > A_0$ is achieved due to wrinkling instabilities on the crater inner surface. Such a wrinkling instability is because of the stiffness mismatch between the reinforcing layer and the polymer matrix when being compressed. Although the wrinkled surface may enlarge the projected area of the crater after unloading, it is not easy to control, thus it is not within the

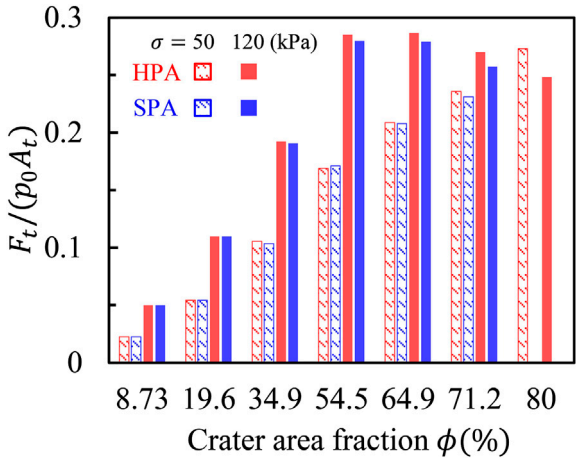

FIGURE 9 | Normalized total suction force $F_t/(p_0A_t)$ as a function of crater area fraction ϕ for crater arrays with fixed crater shape (SCS with b/a = 2/3) and matrix Young's modulus E = 141.9 kPa. Red represents hexagonal pattern arrays (HPA) and blue for square-patterned arrays (SPA). Shaded bars are for small preload case (σ = 50 kPa) and solid bars are for large preload case (σ = 120 kPa). [reprinted with permission from (Wang et al., 2019)]

scope of the current analysis. A detailed discussion can be found in Qiao et al., (2017).

CRATER ARRAYS IN AIR

Isolated craters discussed in the previous section represent cratered surfaces with very small crater areal fraction, i.e., $\phi \to 0$, such that the interaction between craters is negligible. When craters are closely packed, the behavior of each crater may be affected by its neighboring craters. Actually, experimental evidence has shown that the crater areal fraction is another crucial geometric parameter that governs the adhesive strength. For example, Nanni *et al.* measured the adhesion of elastomeric surfaces structured with micro-dimples of different areal fractions (**Figure 1K**) (Nanni et al., 2015). They observed that the adhesive strength exhibits a non-monotonic dependence on the crater areal fraction. In addition to the areal fraction, different patterns of crater arrays have been reported such as hexagonal (**Figures 1I,J**) and square (**Figure 1K**). In this section, we briefly discuss our recent progress in simulating the suction effects in hexagonal-patterned arrays (HPA) and square-patterned arrays (SPA) with various ϕ's.

Consider two polymer sheets with the same total base plane area of A_t. Then the crater area fraction is defined as $\phi = A_0/A_t$. One is engineered with SPA (**Figure 5E**) and the other with HPA (**Figure 5F**). Different from simulations for isolated craters where axisymmetric models were used, simulations for crater arrays demand three-dimensional models and periodic boundary conditions. The suction force is still generated via the loading-unloading process as illustrated in **Figure 6A**. The normalized total suction force of the polymer sheet ($F_t/(p_0A_t)$) is obtained and plotted as a function of ϕ in **Figure 9**, where red represents HPA and blue SPA. Shaded bars correspond to a relatively small preload of 50 kPa and solid ones for a large preload of 120 kPa. Note that results presented in **Figure 9** are for SCS crater arrays with crater aspect ratio of b/a = 2/3 and matrix Young's modulus of E = 141.9 kPa. The aspect ratio b/a = 2/3 is intentionally selected since the initial volume of a cylinder-shaped crater with b/a = 2/3 is identical to that of a SCS crater with aspect ratio b/a = 1. **Figure 9** clearly shows that under a small preload of 50 kPa (shaded bars), the total suction force increases with growing ϕ. The reason is twofold. First, crater arrays with large ϕ tend to have lower structural stiffness, leading to a larger deformation under the same preload, i.e., small V_1 produces large F according to **Eq. 3**. Second, large ϕ means more craters are contributing to F_t. However, under a large preload, e.g. 120 kPa, the total suction force exhibits a non-monotonic dependence on ϕ and the maximum is achieved when $\phi \in$ (54.5%, 64.9%). This is because, when σ = 120 kPa, craters are fully closed after loading and craters with large ϕ may not recover after unloading due to low structural stiffness. Therefore, one can conclude that the interaction between craters may impair the overall adhesive strength of the polymer sheet under large preload. This non-monotonic trend is essentially similar to the experimental observation reported by Nanni et al., (2015). It is also worth noting that the difference between SPA and HPA is not significant for the same ϕ according to **Figure 9**.

SUMMARY AND OUTLOOKS

Progress in the development of reversible SDAs has been rapid. So far, micro-pillared surfaces have been regarded as the primary option. In this review, we focus on cratered surfaces as an alternative, with the emphasis on our recent mechanistic understandings of suction effects of craters arrays. Through theoretical analysis, numerical simulation, and experimental measurements, the effect of polymer matrix stiffness, crater shape, air/water ambient environments, elasto-capillarity, crater area fraction, and pattern of crater arrays are systematically studied.

However, there is a major limitation in the present modeling framework, related to the simplified loading-unloading process for realizing suction effects as illustrated by **Figures 6A–C**. First, the substrate is assumed to be rigid and the crater/substrate interface is assumed to be frictionless. Deformable substrates (e.g., skin) and interfacial friction may prevent the venting of air/liquid during loading, and thus diminish the suction effects. Second, effective venting during loading and tight sealing during unloading and beyond, play crucial roles in strong and sustained adhesion, which should be a future direction for the design of cratered surfaces. Moreover, existing models cannot explain the experimental findings that even with exactly the same crater shape, areal fraction, and pattern, crater arrays may still exhibit different adhesive strength when the size of the crater varies (Baik et al., 2017). This size effect (not pertaining to elasto-capilarity) remains unresolved. In addition to passive cratered

surfaces, reversible suction-based adhesion can also be enabled by active materials in response to external stimuli, such as temperature (Lee et al., 2016) or magnetic field (Yu et al., 2018; Linghu et al., 2019), which have not been systematically modeled.

Another potential direction for future work is to employ cohesive zone modeling in the analysis of the performance of cratered surfaces. This would allow for the intrinsic interactions (normal and shear) between contacting surfaces to be accounted for. In addition, such an approach would allow the strength and adhesion energy of different configurations to be compared, rather than relying solely on strength comparisons, which is the current practice. There may be performance regimes that are strength controlled and others that are dominated by energy considerations. This could result in the development of a richer parameter space for exploring the performance of cratered surfaces.

In summary, cratered surfaces represent a new class of SDAs with strong adhesion, remarkable reusability, and superior biocompatibility. After about 6 years of studies, research into the performance of cratered SDAs are still in its infancy. Preliminiary understandings summarized in this review were achieved under many simplifications and assumptions. The mechanics and realization of practically useful cratered SDAs are still elusive with wide open oppurtunities. Our understanding of the underlying mechanisms, exploration of optimal design, and employment of active materials require the collective wisdom of both mechanical engineers and material scientists.

AUTHOR CONTRIBUTIONS

LW, K-HH, GR, KL, and NL participated fully to the data acquisition, analysis, and paper writing. All authors contributed to the article and approved the submitted version.

FUNDING

All authors acknowledge the support from the National Science Foundation (NSF) Division of Civil, Mechanical and Manufacturing Innovation (CMMI) award (Grant No. 1663551). LW acknowledges the Warren A. and Alice L. Meyer endowed graduate fellowship awarded by the Cockrell School of Engineering at the University of Texas at Austin. K-HH acknowledges the Philip C. and Linda L. Lewis Foundation Graduate Fellowship in Mechanical Engineering at the University of Texas at Austin.

REFERENCES

Afferrante, L., and Carbone, G. (2012). Biomimetic surfaces with controlled direction-dependent adhesion. *J. R. Soc. Interface.* 9, 3359–3365. doi:10.1098/rsif.2012.0452

Akerboom, S., Appel, J., Labonte, D., Federle, W., Sprakel, J., and Kamperman, M. (2015). Enhanced adhesion of bioinspired nanopatterned elastomers via colloidal surface assembly. *J. R. Soc. Interface.* 12, 20141061. doi:10.1098/rsif.2014.1061

Aksak, B., Murphy, M. P., and Sitti, M. (2008). "Gecko inspired micro-fibrillar adhesives for wall climbing robots on micro/nanoscale rough surfaces", in 2008 IEEE International Conference on Robotics and automation, Pasadena, CA, May 19–23 (IEEE), 3058–3063.

Arzt, E., Gorb, S., and Spolenak, R. (2003). From micro to nano contacts in biological attachment devices. *Proc. Natl. Acad. Sci. Unit. States Am.* 100, 10603–10606. doi:10.1073/pnas.1534701100

Autumn, K., Liang, Y. A., Hsieh, S. T., Zesch, W., Chan, W. P., Kenny, T. W., et al. (2000). Adhesive force of a single gecko foot-hair. *Nature* 405, 681–685. doi:10.1038/35015073

Autumn, K., Dittmore, A., Santos, D., Spenko, M., and Cutkosky, M. (2006a). Frictional adhesion: a new angle on gecko attachment. *J. Exp. Biol.* 209, 3569–3579. doi:10.1242/jeb.02486

Autumn, K., Majidi, C., Groff, R., Dittmore, A., and Fearing, R. (2006b). Effective elastic modulus of isolated gecko setal arrays. *J. Exp. Biol.* 209, 3558–3568. doi:10.1242/jeb.02469

Autumn, K., Sitti, M., Liang, Y. A., Peattie, A. M., Hansen, W. R., Sponberg, S., et al. (2002). Evidence for van der Waals adhesion in gecko setae. *Proc. Natl. Acad. Sci. Unit. States Am.* 99, 12252–12256. doi:10.1073/pnas.192252799

Bae, W. G., Kim, D., Kwak, M. K., Ha, L., Kang, S. M., and Suh, K. Y. (2013). Enhanced skin adhesive patch with modulus-tunable composite micropillars. *Advanced healthcare materials* 2, 109–113. doi:10.1002/adhm.201200098

Baik, S., Kim, D. W., Park, Y., Lee, T.-J., Ho Bhang, S., and Pang, C. (2017). A wet-tolerant adhesive patch inspired by protuberances in suction cups of octopi. *Nature* 546, 396–400. doi:10.1038/nature22382

Baik, S., Kim, J., Lee, H. J., Lee, T. H., and Pang, C. (2018). Highly adaptable and biocompatible Octopus-like adhesive patches with meniscus-controlled unfoldable 3D microtips for underwater surface and hairy skin. *Adv. Sci.* 5, 1800100. doi:10.1002/advs.201800100

Baik, S., Lee, H. J., Kim, D. W., Kim, J. W., Lee, Y., and Pang, C. (2019a). Bioinspired adhesive architectures: from skin patch to integrated bioelectronics. *Adv. Mater.* 31, 1803309. doi:10.1002/adma.201803309

Baik, S., Lee, H. J., Kim, D. W., Min, H., and Pang, C. (2019b). Capillarity-enhanced organ-attachable adhesive with highly drainable wrinkled octopus-inspired architectures. *ACS Appl. Mater. Interfaces.* 11, 25674–25681. doi:10.1021/acsami.9b05511

Bartlett, M. D., Croll, A. B., King, D. R., Paret, B. M., Irschick, D. J., and Crosby, A. J. (2012). Looking beyond fibrillar features to scale gecko-like adhesion. *Adv. Mater.* 24, 1078–1083. doi:10.1002/adma.201104191

Bartlett, M. D., and Crosby, A. J. (2014). High capacity, easy release adhesives from renewable materials. *Adv. Mater.* 26, 3405–3409. doi:10.1002/adma.201305593

Becker, H., and Heim, U. (2000). Hot embossing as a method for the fabrication of polymer high aspect ratio structures. *Sensor Actuator Phys.* 83, 130–135. doi:10.1016/s0924-4247(00)00296-x

Bico, J., Reyssat, É., and Roman, B. (2018). Elastocapillarity: when surface tension deforms elastic solids. *Ann. review.* 50, 629–659. doi:10.1146/annurev-fluid-122316-050130

Brodoceanu, D., Bauer, C. T., Kroner, E., Arzt, E., and Kraus, T. (2016). Hierarchical bioinspired adhesive surfaces—a review. *Bioinspiration Biomimetics* 11, 051001. doi:10.1088/1748-3190/11/5/051001

Buhl, S., Greiner, C., Campo, A. d., and Arzt, E. (2009). Humidity influence on the adhesion of biomimetic fibrillar surfaces. *Ijmr* 100, 1119–1126. doi:10.3139/146.110146

Cadirov, N., Booth, J. A., Turner, K. L., and Israelachvili, J. N. (2017). Influence of humidity on grip and release adhesion mechanisms for gecko-inspired microfibrillar surfaces. *ACS Appl. Mater. Interfaces.* 9, 14497–14505. doi:10.1021/acsami.7b01624

Carbone, G., Pierro, E., and Gorb, S. N. (2011). Origin of the superior adhesive performance of mushroom-shaped microstructured surfaces. *Soft Matter* 7, 5545–5552. doi:10.1039/c0sm01482f

Carbone, G., and Pierro, E. (2012). Sticky bio-inspired micropillars: finding the best shape. *Small* 8, 1449–1454. doi:10.1002/smll.201102021

Chan, E. P., Greiner, C., Arzt, E., and Crosby, A. J. (2007). Designing model systems for enhanced adhesion. *MRS Bull.* 32, 496–503. doi:10.1557/mrs2007.84

Chang, W.-Y., Wu, Y., and Chung, Y.-C. (2014). Facile fabrication of ordered nanostructures from protruding nanoballs to recessional nanosuckers via solvent treatment on covered nanosphere assembled monolayers. *Nano Lett.* 14, 1546–1550. doi:10.1021/nl4048042

Chary, S., Tamelier, J., and Turner, K. (2013). A microfabricated gecko-inspired controllable and reusable dry adhesive. *Smart Mater. Struct.* 22, 025013. doi:10.1088/0964-1726/22/2/025013

Chen, X., Yuk, H., Wu, J., Nabzdyk, C. S., and Zhao, X. (2020a). Instant tough bioadhesive with triggerable benign detachment. *Proc. Natl. Acad. Sci. U.S.A.* 117, 15497–15503. doi:10.1073/pnas.2006389117

Chen, Y., Meng, J., Gu, Z., Wan, X., Jiang, L., and Wang, S. (2020b). Bioinspired multiscale wet adhesive surfaces: structures and controlled adhesion. *Adv. Funct. Mater.* 30, 1905287. doi:10.1002/adfm.201905287

Cheung, E., and Sitti, M. (2009). Adhesion of biologically inspired polymer microfibers on soft surfaces. *Langmuir* 25, 6613–6616. doi:10.1021/la900997p

Cho, H., Wu, G., Christopher Jolly, J., Fortoul, N., He, Z., Gao, Y., et al. (2019). Intrinsically reversible superglues via shape adaptation inspired by snail epiphragm. *Proc. Natl. Acad. Sci. U.S.A.* 116, 13774–13779. doi:10.1073/pnas.1818534116

Choi, M. K., Park, O. K., Choi, C., Qiao, S., Ghaffari, R., Kim, J., et al. (2016). Cephalopod-inspired miniaturized suction cups for smart medical skin. *Adv. Healthcare Mater.* 5, 80–87. doi:10.1002/adhm.201500285

Christoffers, W. A., Coenraads, P.-J., and Schuttelaar, M.-L. (2014). Bullous allergic reaction caused by colophonium in medical adhesives. *Contact Dermatitis* 70, 256–257. doi:10.1111/cod.12170

Chun, S., Kim, D. W., Baik, S., Lee, H. J., Lee, J. H., Bhang, S. H., et al. (2018). Conductive and stretchable adhesive electronics with miniaturized octopus-like suckers against dry/wet skin for biosignal monitoring. *Adv. Funct. Mater.* 28, 1805224. doi:10.1002/adfm.201805224

Cilurzo, F., Gennari, C. G. M., and Minghetti, P. (2012). Adhesive properties: a critical issue in transdermal patch development. *Expet Opin. Drug Deliv.* 9, 33–45. doi:10.1517/17425247.2012.637107

Creton, C. (2003). Pressure-sensitive adhesives: an introductory course. *MRS Bull.* 28, 434–439. doi:10.1557/mrs2003.124

Czech, Z., and Kowalczyk, A. (2011). "Pressure-sensitive adhesives for medical applications," in *Wide spectra of quality control*. Shanghai, China: InTech.

Czech, Z., Wilpiszewska, K., Tyliszczak, B., Jiang, X., Bai, Y., and Shao, L. (2013). Biodegradable self-adhesive tapes with starch carrier. *Int. J. Adhesion Adhes.* 44, 195–199. doi:10.1016/j.ijadhadh.2013.03.002

Davies, J., Haq, S., Hawke, T., and Sargent, J. P. (2009). A practical approach to the development of a synthetic Gecko tape. *Int. J. Adhesion Adhes.* 29, 380–390. doi:10.1016/j.ijadhadh.2008.07.009

Del Campo, A., and Arzt, E. (2007). Design parameters and current fabrication approaches for developing bioinspired dry adhesives. *Macromol. Biosci.* 7, 118–127. doi:10.1002/mabi.200600214

Del Campo, A., Greiner, C., Álvarez, I., and Arzt, E. (2007a). Patterned surfaces with pillars with controlled 3 D tip geometry mimicking bioattachment devices. *Adv. Mater.* 19, 1973–1977. doi:10.1002/adma.200602476

Del Campo, A., Greiner, C., and Arzt, E. (2007b). Contact shape controls adhesion of bioinspired fibrillar surfaces. *Langmuir* 23, 10235–10243. doi:10.1021/la7010502

Drotlef, D.-M., Amjadi, M., Yunusa, M., and Sitti, M. (2017). Bioinspired composite microfibers for skin adhesion and signal amplification of wearable sensors. *Adv. Mater.* 29, 1701353. doi:10.1002/adma.201701353

Drotlef, D. M., Dayan, C. B., and Sitti, M. (2019). Bio-inspired composite microfibers for strong and reversible adhesion on smooth surfaces. *Integr. Comp. Biol.* 59, 227–235. doi:10.1093/icb/icz009

Eisenhaure, J., and Kim, S. (2017). A review of the state of dry adhesives: biomimetic structures and the alternative designs they inspire. *Micromachines* 8, 125. doi:10.3390/mi8040125

Fischer, S. C. L., Arzt, E., and Hensel, R. (2016). Composite pillars with a tunable interface for adhesion to rough substrates. *ACS Appl. Mater. Interfaces.* 9, 1036–1044. doi:10.1021/acsami.6b11642

Fischer, S. C. L., Groß, K., Torrents Abad, O., Becker, M. M., Park, E., Hensel, R., et al. (2017). Funnel-shaped microstructures for strong reversible adhesion. *Adv. Mater. Interfaces.* 4, 1700292. doi:10.1002/admi.201700292

Gao, H., and Yao, H. (2004). Shape insensitive optimal adhesion of nanoscale fibrillar structures. *Proc. Natl. Acad. Sci. Unit. States Am.* 101, 7851–7856. doi:10.1073/pnas.0400757101

Ge, D., Matsuno, T., Sun, Y., Ren, C., Tang, Y., and Ma, S. (2015). Quantitative study on the attachment and detachment of a passive suction cup. *Vacuum* 116, 13–20. doi:10.1016/j.vacuum.2015.02.013

Geim, A. K., Dubonos, S. V., Grigorieva, I. V., Novoselov, K. S., Zhukov, A. A., and Shapoval, S. Y. (2003). Microfabricated adhesive mimicking gecko foot-hair. *Nature Mater* 2, 461–463. doi:10.1038/nmat917

Gorb, S. N., Sinha, M., Peressadko, A., Daltorio, K. A., and Quinn, R. D. (2007). Insects did it first: a micropatterned adhesive tape for robotic applications. *Bioinspir. Biomim.* 2, S117–S125. doi:10.1088/1748-3182/2/4/s01

Greiner, C., Arzt, E., and Del Campo, A. (2009). Hierarchical gecko-like adhesives. *Adv. Mater.* 21, 479–482. doi:10.1002/adma.200801548

Greiner, C., del Campo, A., and Arzt, E. (2007). Adhesion of bioinspired micropatterned surfaces: effects of pillar radius, aspect ratio, and preload. *Langmuir* 23, 3495–3502. doi:10.1021/la0633987

Hansen, W. R., and Autumn, K. (2005). Evidence for self-cleaning in gecko setae. *Proc. Natl. Acad. Sci. Unit. States Am.* 102, 385–389. doi:10.1073/pnas.0408304102

Hu, H., Tian, H., Shao, J., Li, X., Wang, Y., Wang, Y., et al. (2017). Discretely supported dry adhesive film inspired by biological bending behavior for enhanced performance on a rough surface. *ACS Appl. Mater. Interfaces.* 9, 7752–7760. doi:10.1021/acsami.6b14951

Huber, G., Orso, S., Spolenak, R., Wegst, U. G. K., Enders, S., Gorb, S. N., et al. (2008). Mechanical properties of a single gecko seta. *Ijmr* 99, 1113–1118. doi:10.3139/146.101750

Hwang, I., Kim, H. N., Seong, M., Lee, S. H., Kang, M., Yi, H., et al. (2018). Multifunctional smart skin adhesive patches for advanced health care. *Adv. healthc. mater.* 7, e1800275. doi:10.1002/adhm.201800275

Iwasaki, H., Lefevre, F., Damian, D. D., Iwase, E., and Miyashita, S. (2020). Autonomous and reversible adhesion using elastomeric suction cups for in-vivo medical treatments. *IEEE Robotics and Automation Letters* 5, 2015–2022. doi:10.1109/LRA.2020.2970633

Jin, K., Cremaldi, J. C., Erickson, J. S., Tian, Y., Israelachvili, J. N., and Pesika, N. S. (2014). Biomimetic bidirectional switchable adhesive inspired by the gecko. *Adv. Funct. Mater.* 24, 574–579. doi:10.1002/adfm.201301960

Kamperman, M., Kroner, E., Del Campo, A., Mcmeeking, R. M., and Arzt, E. (2010). Functional adhesive surfaces with "gecko" effect: the concept of contact splitting. *Adv. Eng. Mater.* 12, 335–348. doi:10.1002/adem.201000104

Kawahara, K., and Tojo, K. (2007). Skin irritation in transdermal drug delivery systems: a strategy for its reduction. *Pharm. Res. (N. Y.)* 24, 399. doi:10.1007/s11095-006-9165-4

Kier, W. M., and Smith, A. M. (2002). The structure and adhesive mechanism of octopus suckers. *Integr. Comp. Biol.* 42, 1146–1153. doi:10.1093/icb/42.6.1146

Kim, D. S., Lee, H. S., Lee, J., Kim, S., Lee, K.-H., Moon, W., et al. (2007). Replication of high-aspect-ratio nanopillar array for biomimetic gecko foot-hair prototype by UV nano embossing with anodic aluminum oxide mold, *Microsyst. Technol.* 13, 601–606. doi:10.1007/s00542-006-0220-1

Kim, D. W., Baik, S., Min, H., Chun, S., Lee, H. J., Kim, K. H., et al. (2019). Highly permeable skin patch with conductive hierarchical architectures inspired by Amphibians and octopi for omnidirectionally enhanced wet adhesion. *Adv. Funct. Mater.* 29, 1807614. doi:10.1002/adfm.201807614

Kim, S., and Sitti, M. (2006). Biologically inspired polymer microfibers with spatulate tips as repeatable fibrillar adhesives. *Appl. Phys. Lett.* 89, 261911. doi:10.1063/1.2424442

Kim, T., Park, J., Sohn, J., Cho, D., and Jeon, S. (2016). Bioinspired, highly stretchable, and conductive dry adhesives based on 1D-2D hybrid carbon nanocomposites for all-in-one ECG electrodes. *ACS Nano.* 10, 4770–4778. doi:10.1021/acsnano.6b01355

Kwak, M. K., Jeong, H.-E., and Suh, K. Y. (2011). Rational design and enhanced biocompatibility of a dry adhesive medical skin patch. *Adv. Mater.* 23, 3949–3953. doi:10.1002/adma.201101694

Lee, H., Um, D.-S., Lee, Y., Lim, S., Kim, H.-j., and Ko, H. (2016). Octopus-inspired smart adhesive pads for transfer printing of semiconducting nanomembranes. *Adv. Mater.* 28, 7457–7465. doi:10.1002/adma.201601407

Lee, J., Fearing, R. S., and Komvopoulos, K. (2008). Directional adhesion of gecko-inspired angled microfiber arrays. *Appl. Phys. Lett.* 93, 191910. doi:10.1063/1.3006334

Li, Y., Krahn, J., and Menon, C. (2016). Bioinspired dry adhesive materials and their application in robotics: a review. *J Bionic Eng.* 13, 181–199. doi:10.1016/s1672-6529(16)60293-7

Linghu, C., Wang, C., Cen, N., Wu, J., Lai, Z., and Song, J. (2019). Rapidly tunable and highly reversible bio-inspired dry adhesion for transfer printing in air and a vacuum. *Soft Matter* 15, 30–37. doi:10.1039/c8sm01996g

Liu, J.-L., and Feng, X.-Q. (2012). On elastocapillarity: a review. *Acta Mech. Sin.* 28, 928–940. doi:10.1007/s10409-012-0131-6

Liu, J., Tanaka, K., Bao, L. M., and Yamaura, I. (2006). Analytical modelling of suction cups used for window-cleaning robots. *Vacuum* 80, 593–598. doi:10.1016/j.vacuum.2005.10.002

Lu, G., Hong, W., Tong, L., Bai, H., Wei, Y., and Shi, G. (2008). Drying enhanced adhesion of polythiophene nanotubule arrays on smooth surfaces. *ACS Nano.* 2,2342–2348. doi:10.1021/nn800443m

Ma, Y., Ma, S., Wu, Y., Pei, X., Gorb, S. N., Wang, Z., et al. (2018). Remote control over underwater dynamic attachment/detachment and locomotion, *Adv. Mater.* 30, 1801595. doi:10.1002/adma.201801595

Manabe, R., Suzumori, K., and Wakimoto, S. (2012). "A functional adhesive robot skin with integrated micro rubber suction cups", in 2012 IEEE international conference on Robotics and automation (ICRA), Saint Paul, MN, May 14–18 (IEEE), 904–909. doi:10.1109/ICRA.2012.6224687

Marvi, H., Song, S., and Sitti, M. (2015). Experimental investigation of optimal adhesion of mushroomlike elastomer microfibrillar adhesives. *Langmuir* 31, 10119–10124. doi:10.1021/acs.langmuir.5b02415

Matsumura, H., Ahmatjan, N., Ida, Y., Imai, R., and Wanatabe, K. (2013). A model for quantitative evaluation of skin damage at adhesive wound dressing removal. *Int. Wound J.* 10, 291–294. doi:10.1111/j.1742-481x.2012.00975.x

Mengüç, Y., Yang, S. Y., Kim, S., Rogers, J. A., and Sitti, M. (2012). Gecko-inspired controllable adhesive structures applied to micromanipulation. *Adv. Funct. Mater.* 22, 1246–1254. doi:10.1002/adfm.201101783

Moon, M.-W., Cha, T.-G., Lee, K.-R., Vaziri, A., and Kim, H.-Y. (2010). Tilted Janus polymer pillars. *Soft Matter* 6, 3924–3929. doi:10.1039/c0sm00126k

Murphy, M. P., Aksak, B., and Sitti, M. (2009). Gecko-inspired directional and controllable adhesion. *Small* 5, 170–175. doi:10.1002/smll.200801161

Nanni, G., Fragouli, D., Ceseracciu, L., and Athanassiou, A. (2015). Adhesion of elastomeric surfaces structured with micro-dimples. *Appl. Surf. Sci.* 326, 145–150. doi:10.1016/j.apsusc.2014.11.108

Oh, J. H., Hong, S. Y., Park, H., Jin, S. W., Jeong, Y. R., Oh, S. Y., et al. (2018). Fabrication of high-sensitivity skin-attachable temperature sensors with bioinspired microstructured adhesive. *ACS Appl. Mater. Interfaces.* 10, 7263–7270. doi:10.1021/acsami.7b17727

Parness, A., Soto, D., Esparza, N., Gravish, N., Wilkinson, M., Autumn, K., et al. (2009). A microfabricated wedge-shaped adhesive array displaying gecko-like dynamic adhesion, directionality and long lifetime. *J. R. Soc. Interface.* 6, 1223–1232. doi:10.1098/rsif.2009.0048

Pattantyus-Abraham, A., Krahn, J., and Menon, C. (2013). Recent advances in nanostructured biomimetic dry adhesives. *Frontiers in Bioengineering and Biotechnology* 1, 22. doi:10.3389/fbioe.2013.00022

Pease, R. F. W. (1981). Electron beam lithography. *Contemp. Phys.* 22, 265–290. doi:10.1080/00107518108231531

Pesika, N. S., Zeng, H., Kristiansen, K., Zhao, B., Tian, Y., Autumn, K., et al. (2009). Gecko adhesion pad: a smart surface? *J. Phys. Condens. Matter.* 21, 464132. doi:10.1088/0953-8984/21/46/464132

Qiao, S., Gratadour, J.-B., Wang, L., and Lu, N. (2015). Conformability of a thin elastic membrane laminated on a rigid substrate with corrugated surface. *IEEE Trans. Compon., Packag. Manufact. Technol.* 5, 1237–1243. doi:10.1109/tcpmt.2015.2453319

Qiao, S., Wang, L., Ha, K.-H., and Lu, N. (2018). Suction effects of craters under water. *Soft Matter* 14, 8509–8520. doi:10.1039/c8sm01601a

Qiao, S., Wang, L., Jeong, H., Rodin, G. J., and Lu, N. (2017). Suction effects in cratered surfaces. *J. R. Soc. Interface.* 14, 20170377. doi:10.1098/rsif.2017.0377

Roman, B., and Bico, J. (2010). Elasto-capillarity: deforming an elastic structure with a liquid droplet. *J. Phys. Condens. Matter.* 22, 493110. doi:10.1088/0953-8984/22/49/493101

Sahay, R., Low, H. Y., Baji, A., Shaohui, F., and Wood, K. L. (2015). A state-of-the-art review and analysis on the design of dry adhesion materials for applications such as climbing micro-robots. *RSC Adv.* 5, 50821–50832. doi:10.1039/C5RA06770G

Sameoto, D., and Menon, C. (2009). A low-cost, high-yield fabrication method for producing optimized biomimetic dry adhesives. *J. Micromech. Microeng.* 19, 115002. doi:10.1088/0960-1317/19/11/115002

Seo, J., Eisenhaure, J., and Kim, S. (2016). Micro-wedge array surface of a shape memory polymer as a reversible dry adhesive. *Extreme Mechanics Letters* 9, 207–214. doi:10.1016/j.eml.2016.07.007

Shintake, J., Cacucciolo, V., Floreano, D., and Shea, H. J. a. M. (2018). Soft robotic grippers. *Adv Mater.* 30, 1707035. doi:10.1002/adma.201707035

Singh, A. K., Mehra, D. S., Niyogi, U. K., Sabharwal, S., and Khandal, R. K. (2011). Polyurethane based pressure sensitive adhesives (PSAs) using electron beam irradiation for medical application. *J. Polym. Mater.* 28, 525–542.

Singh, A. K., Mehra, D. S., Niyogi, U. K., Sabharwal, S., and Singh, G. (2014). Breathability studies of electron beam curable polyurethane pressure sensitive adhesive for bio-medical application. *Radiat. Phys. Chem.* 103, 75–83. doi:10.1016/j.radphyschem.2014.05.015

Sitti, M., and Fearing, R. S. (2003). Synthetic gecko foot-hair micro/nano-structures as dry adhesives. *J. Adhes. Sci. Technol.* 17, 1055–1073. doi:10.1163/156856103322113788

Smith, A. (1996). Cephalopod sucker design and the physical limits to negative pressure. *J. Exp. Biol.* 199, 949–958.

Smith, A. M. (1991). Negative pressure generated by octopus suckers: a study of the tensile strength of water in nature. *J. Exp. Biol.* 157, 257–271.

Tao, D., Gao, X., Lu, H., Liu, Z., Li, Y., Tong, H., et al. (2017). Controllable anisotropic dry adhesion in vacuum: gecko inspired wedged surface fabricated with ultraprecision diamond cutting. *Adv. Funct. Mater.* 27, 1606576. doi:10.1002/adfm.201606576

Tinnemann, V., Hernández, L., Fischer, S. C., Arzt, E., Bennewitz, R., and Hensel, R. (2019). In Situ observation reveals local detachment mechanisms and suction effects in micropatterned adhesives. *Adv. Funct. Mater.* 29, 1807713. doi:10.1002/adfm.201807713

Tramacere, F., Beccai, L., Kuba, M., Gozzi, A., Bifone, A., and Mazzolai, B. (2013). The morphology and adhesion mechanism of Octopus vulgaris suckers. *PLoS One.* 8, e65074. doi:10.1371/journal.pone.0065074

Tramacere, F., Appel, E., Mazzolai, B., and Gorb, S. N. (2014a). Hairy suckers: the surface microstructure and its possible functional significance in the Octopus vulgaris sucker. *Beilstein J. Nanotechnol.* 5, 561–565. doi:10.3762/bjnano.5.66

Tramacere, F., Kovalev, A., Kleinteich, T., Gorb, S. N., and Mazzolai, B. (2014b). Structure and mechanical properties of Octopus vulgaris suckers. *J. R. Soc. Interface.* 11, 20130816. doi:10.1098/rsif.2013.0816

Tsai, C.-Y., and Chang, C.-C. (2013). Auto-adhesive transdermal drug delivery patches using beetle inspired micropillar structures. *J. Mater. Chem. B* 1, 5963–5970. doi:10.1039/c3tb20735h

Varenberg, M., and Gorb, S. (2008). A beetle-inspired solution for underwater adhesion. *J. R. Soc. Interface.* 5, 383–385. doi:10.1098/rsif.2007.1171

Vieu, C., Carcenac, F., Pépin, A., Chen, Y., Mejias, M., Lebib, A., et al. (2000). Electron beam lithography: resolution limits and applications. *Appl. Surf. Sci.* 164, 111–117. doi:10.1016/s0169-4332(00)00352-4

Von Byern, J., and Klepal, W. (2006). Adhesive mechanisms in cephalopods: a review. *Biofouling* 22, 329–338. doi:10.1080/08927010600967840

Wang, L., Ha, K.-H., Qiao, S., and Lu, N. (2019). Suction effects of crater arrays. *Extreme Mechanics Letters* 30, 100496. doi:10.1016/j.eml.2019.100496

Wang, L., and Lu, N. (2016). Conformability of a thin elastic membrane laminated on a soft substrate with slightly wavy surface. *J. Appl. Mech.* 83, 041007. doi:10.1115/1.4032466

Wang, L., Qiao, S., Ameri, S. K., Jeong, H., and Lu, N. (2017a). A thin elastic membrane conformed to a soft and rough substrate subjected to stretching/compression. *J. Appl. Mech.* 84,111003. doi:10.1115/1.4037740

Wang, L., Qiao, S., and Lu, N. (2017b). Effects of surface tension on the suction forces generated by miniature craters. *Extreme Mechanics Letters* 15, 130–138. doi:10.1016/j.eml.2017.07.004

Wang, Y., Yang, X., Chen, Y., Wainwright, D. K., Kenaley, C. P., Gong, Z., et al. (2017c). A biorobotic adhesive disc for underwater hitchhiking inspired by the remora suckerfish. *Science Robotics* 2, eaan8072. doi:10.1126/scirobotics.aan8072

Wang, Y., Hu, H., Shao, J., and Ding, Y. (2014). Fabrication of well-defined mushroom-shaped structures for biomimetic dry adhesive by conventional photolithography and molding. *ACS Appl. Mater. Interfaces.* 6, 2213–2218. doi:10.1021/am4052393

Wang, Y., Li, X., Tian, H., Hu, H., Tian, Y., Shao, J., et al. (2015). Rectangle-capped and tilted micropillar array for enhanced anisotropic anti-shearing in biomimetic adhesion. *J. R. Soc. Interface.* 12, 20150090. doi:10.1098/rsif.2015.0090

Wang, Z. (2018). Slanted functional gradient micropillars for optimal bioinspired dry adhesion. *ACS Nano.* 12, 1273–1284. doi:10.1021/acsnano.7b07493

Xiaosong, L., Dashuai, T., Hongyu, L., Pengpeng, B., Zheyu, L., Liran, M., et al. (2019). Recent developments in gecko-inspired dry adhesive surfaces from fabrication to application. *Surf. Topogr. Metrol. Prop.* 7 (2), 23001.

Xie, Z., Domel, A. G., An, N., Green, C., Gong, Z., Wang, T., et al. (2020). Octopus arm-inspired tapered soft actuators with suckers for improved grasping. *Soft Robot.* 7, 639–648. doi:10.1089/soro.2019.0082

Yao, H., and Gao, H. (2006). Mechanics of robust and releasable adhesion in biology: bottom-up designed hierarchical structures of gecko. *J. Mech. Phys. Solid.* 54, 1120–1146. doi:10.1016/j.jmps.2006.01.002

Yoshida, Y., and Ma, S. (2010). "Design of a wall-climbing robot with passive suction cups," in 2010 IEEE international Conference on Robotics and biomimetics, Tianjin, China, December 14–18 (IEEE), 1513–1518. doi:10.1109/ROBIO.2010.5723554

Yu, Q., Chen, F., Zhou, H., Yu, X., Cheng, H., and Wu, H. (2018). Design and analysis of magnetic-assisted transfer printing. *J. Appl. Mech.* 85, 101009. doi:10.1115/1.4040599

Yuk, H., Varela, C. E., Nabzdyk, C. S., Mao, X., Padera, R. F., Roche, E. T., et al. (2019). Dry double-sided tape for adhesion of wet tissues and devices. *Nature* 575, 169–174. doi:10.1038/s41586-019-1710-5

Zhao, Y., Tong, T., Delzeit, L., Kashani, A., Meyyappan, M., and Majumdar, A. (2006). Interfacial energy and strength of multiwalled-carbon-nanotube-based dry adhesive. *J. Vac. Sci. Technol. B* 24, 331–335. doi:10.1116/1.2163891

Zhou, M., Pesika, N., Zeng, H., Tian, Y., and Israelachvili, J. (2013). Recent advances in gecko adhesion and friction mechanisms and development of gecko-inspired dry adhesive surfaces. *Friction* 1, 114–129. doi:10.1007/s40544-013-0011-5

Zhuo, S., Zhao, Z., Xie, Z., Hao, Y., Xu, Y., Zhao, T., et al. (2020). Complex multiphase organohydrogels with programmable mechanics toward adaptive soft-matter machines. *Science Advances* 6, eaax1464. doi:10.1126/sciadv.aax1464

Conflict of Interest: The authors declare that the research was conducted in the absence of any commercial or financial relationships that could be construed as a potential conflict of interest.

frontiers in Mechanical Engineering

ORIGINAL RESEARCH
published: 27 January 2021
doi: 10.3389/fmech.2020.635694

"Push and Pull": Biomechanics of the Pollination Apparatus of *Oncidium* spp.

Marc Thielen[1*†], *Dagmar Voigt*[2†], *Friederike Gallenmüller*[1†], *Thomas Speck*[1,3†] *and Stanislav Gorb*[4†]

[1]*Plant Biomechanics Group Freiburg, Faculty of Biology, University of Freiburg, Freiburg im Breisgau, Germany,* [2]*Institute for Botany, Faculty of Biology, Technical University of Dresden, Dresden, Germany,* [3]*Cluster of Excellence LivMatS @ FIT Freiburg Center for Interactive Materials and Bioinspired Technologies, University of Freiburg, Freiburg im Breisgau, Germany,* [4]*Functional Morphology and Biomechanics, Zoological Institute, Kiel University, Kiel, Germany*

OPEN ACCESS

Edited by:
Yu Tian,
Tsinghua University, China

Reviewed by:
Antonio Papangelo,
Politecnico di Bari, Italy
Feodor M. Borodich,
Cardiff University, United Kingdom

***Correspondence:**
Marc Thielen
marc.thielen@biologie.uni-freiburg.de

†ORCID:
Marc Thielen
orcid.org/0000-0002-7773-6724
Dagmar Voigt
orcid.org/0000-0003-2772-8504
Friederike Gallenmüller
orcid.org/0000-0001-9891-094X
Thomas Speck
orcid.org/0000-0002-2245-2636
Stanislav Gorb
orcid.org/0000-0001-9712-7953

Specialty section:
This article was submitted to Tribology, a section of the journal Frontiers in Mechanical Engineering

Received: *30 November 2020*
Accepted: *22 December 2020*
Published: *27 January 2021*

Citation:
Thielen M, Voigt D, Gallenmüller F, Speck T and Gorb S (2021) "Push and Pull": Biomechanics of the Pollination Apparatus of Oncidium *spp.. Front. Mech. Eng 6:635694. doi: 10.3389/fmech.2020.635694*

Comprising ca. 28,000, species the Orchidaceae constitute one of the most species-rich plant families. Orchids differ from other monocotyledons i.a., in the formation of so-called pollinaria, which are entities consisting of pollen grains aggregated into compact pollinia and accessory structures, a viscidium and mostly also a pollinium stalk. The viscidium releases an adhesive material that attaches the pollinarium to a pollinator. Pollinaria are part of a complex pollination apparatus that enables the orchids to colonize niches in which only a few individuals of the respective pollinator occur infrequently. Because the aggregated pollen grains are removed from the flower at once, the development of a mechanical barrier ensuring that only suitable pollinators are able to access the flowers and more importantly to remove the pollen are important selective traits. In this paper we describe the functional morphology of the pollination apparatus in two orchid species, *Oncidium wentworthianum* and *O. otogaya*, by experimentally mimicking the pollination process. Furthermore, we analyzed the mechanical resistance of this apparatus by means of force measurements and showed that it most probably constitutes a hierarchical two-stage barrier. The first stage consists of the presence of the anther cap that not only protects the pollinia, but also serves to prevent premature removal of young and unripe pollinaria from the flower. As soon as the pollinaria are ripe, the anther cap sheds and the second stage of the mechanical barrier takes effect, a severable bond between pollinarium and rostellum. This bond can be overcome by a potential pollinator, applying a load of at least 10.8 mN (*O. otogaya*) or 12.6 mN (*O. wentworthianum*), respectively, on the viscidium which at the same time disengages the pollinarium from its anchorage. The adhesive material produced by the viscidium creates sufficient adhesive contact between pollinarium and pollinator. Potential pollinators, such as *Centris* spp. or *Trigona* spp. bees, should be well able to exert such forces by pushing their head/forebody into the orchid flowers. Thus, whether a pollinator is able to detach the pollinarium depends on both how forcefully it can push and how strongly it can pull the orchid pollination apparatus.

Keywords: adhesion, biomechanics, *Oncidium*, orchid, pollinarium, pollination, viscidium

INTRODUCTION

Many people are passionate about the splendor of orchid flowers without probably being aware of their functional-morphological peculiarities. Also Darwin was fascinated by these plants (Yam et al., 2009) and dedicated a whole book exclusively to the pollination of orchids by insects (Darwin, 1890). The complex pollination mechanism, which we describe below, was undoubtedly one of the factors responsible for the enormous radiation of the Orchidaceae family (Johnson and Edwards, 2000), resulting in more than 28,000 species currently known (Christenhusz and Byng, 2016). They are organized into the five subfamilies Apostasioideae, Vanilloideae, Cypripedioideae, Orchidoideae, and Epidendroideae (Chase et al., 2015; Givnish et al., 2015): the latter two being the most derived and species-rich subfamilies, and accounting for 98% of all orchids species (Singer and Cocucci, 1997).

Most orchids are characterized by the fact that style and staminal filaments are fused into a column, also called gynostemium, and that part of the stigma, the rostellum, is sterile and involved into pollen transfer. Another key development in orchids is the pollinium, which is a cohesive mass of agglomerated pollen grains that is removed as a unit during the pollination process (Pacini and Hesse, 2002; Harder and Johnson, 2008). In many orchids several pollinia are attached via a caudicle (derived from the anther) and/or a stalk-like stipe (derived from the column), to a sticky pad formed by the rostellum (Dressler, 1993; Stern, 2014). This pad is referred to as viscidium, syn. retinaculum (Schick, 1989), and becomes attached to the pollinator through its adhesive material. The entirety of pollinia, caudicle/stipe, and viscidium is called a pollinarium and is the main part of a complex and sophisticated pollination apparatus that made it possible for the orchids also to colonize niches in which only a few individuals of the respective pollinator occur and thus pollinator visits are infrequent (Johnson and Edwards, 2000). The viscidium thereby sticks to the departing pollinator and the entire pollinarium is removed from the flower and transferred to the stigmatic surface of a conspecific flower. The avoidance of self-pollination is a fascinating topic on its own, which we do not elaborate on here [for more details we refer to, e.g., Borba and Semir (1999) and Johnson and Edwards (2000)]. The fact that all pollen grains are removed at once, however, renders pollination into an "all-or-nothing" process, hence, demonstrating the importance that pollinaria can only be removed by suitable pollinators (Wagenitz, 1981; Jersáková et al., 2006). Filtering for efficient pollinators by the morphological evolutionary adaptation of flowers to prevent a loss of the whole gamet production is particularly pronounced in Epidendroideae, but also widespread among other orchid families (Tremblay, 1992; Pansarin et al., 2017). Filtering is realized by 1) attracting suitable pollinators by either visual or olfactory stimuli (Faegri and Pijl, 1979) and/or 2) morphological traits or mechanical barriers of the flower that only allow legitimate pollinators to access the pollen or a reward of whatever kind (Brantjes, 1981; Dressler, 1981; Claßen-Bockhoff et al., 2004; Reith et al., 2006; Córdoba and Cocucci, 2011). Vice versa, coevolutionary processes lead to morphological, physiological, and behavioral pollinator specialization (Darwin, 1890; Johnson and Anderson, 2010).

Here, we analyze the flower's mechanical barriers in two *Oncidium* Sw. species belonging to the subtribe Oncidiinae (Orchidaceae), which represents the most highly derived orchids of the New World (Dressler, 1993; Mosquera-Mosquera et al., 2019). Flowers of Oncidiinae (**Figure 1**) characteristically have large lips featuring so-called calli. The latter resemble tumors from which the name of the type genus, *Oncidium*, derives (from the greek word "onkos" = swelling or tumor) (Castro and Singer, 2019). The callus attracts oil gathering bees either by offering true reward produced in epidermal elaiophores or by deceit (Pemberton, 2008). A thickened structure of the column situated below the stigmatic surface, the so-called *tabula infrastigmatica*, serves female oil-collecting bees as a grip. They can grasp it with their mandibles to free their anterior legs for oil collection (Dressler, 1981; Davies et al., 2014). During this maneuver they come into contact with the viscidium, overcome the mechanical barrier, and establish a sufficiently large contact area with the viscidium that causes the pollinarium to stay attached to the insect and to be removed from the flower when it departs. According to Schick (1989) the adhesive may consist of two phases: a hydrophilic derivative of the cell walls and a lipophilic part, originating from the protoplasm and heterogeneous in nature itself.

The detailed pollination process of *Oncidium* orchids, however, is still largely unknown and also pollinators are rather generically reported. Castro and Singer (2019) summarized that Oncidiinae are mostly pollinated by oil- or perfume-collecting bees. Pollinators of *Oncidium* spp. are reported to be mainly fairly large apid bees (*Hymenoptera*, *Apidae*) belonging to the genera of *Centris* Fabricius, *Trigona* Jurine, *Tetrapedia* Klug, and *Epicharis* Klug (Dressler, 1993; Parra-Tabla et al., 2000; Singer, 2003; Carmona-Díaz and García-Franco, 2008; Castro and Singer, 2019; Ferreira et al., 2019).

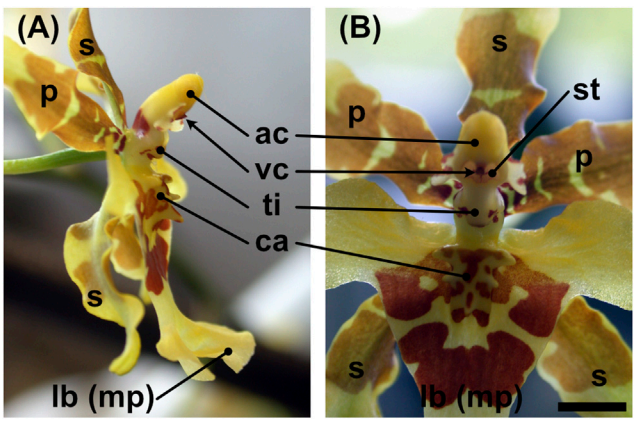

FIGURE 1 | Flower of *Oncidium wentworthianum* in **(A)** lateral view and **(B)** frontal view. ac = anther cap, ca = callus, lb (mp) = labellum (modified petal), *p* = petal, s = sepal, st = (fertile part of the) stigma, ti = *tabula infrastigmatica*, vc = viscidium. Scale bar: ca. 4 mm.

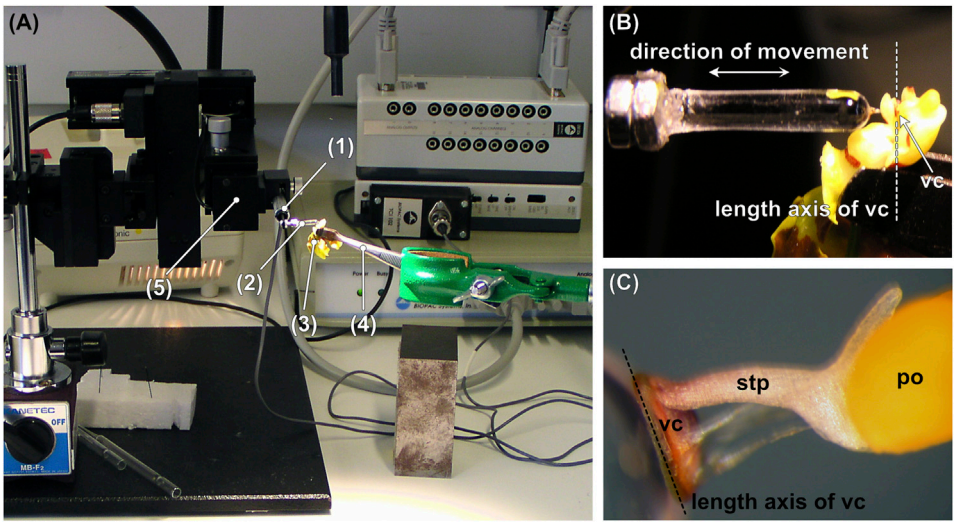

FIGURE 2 | (A) Test setup consisting of a pollinator-mimicking glass rod, which is mounted on a force transducer coupled to a motorized micromanipulator. **(B)** Detail of **(A)** showing the glass rod that is approached and retracted perpendicular to the length axis of the viscidium. **(C)** Pollinarium attached to the tip of the glass rod. po = pollinium, stp = stipe, vc = viscidium. 1) Force transducer, 2) glass rod, 3) flower, 4) tweezers, 5) motorized micromanipulator.

MATERIALS AND METHODS

Plant Material

Experiments were performed with *Oncidium wentworthianum* Bateman ex Lindl. and *O. otogaya*, both provided by the Zoological-Botanical Garden "Wilhelma," Stuttgart, Germany. Plants of both species were grown in a mixture of orchid soil and tree bark. From *O. otogaya*, only an offshoot was available whose roots were wrapped in filter paper towels during the time of the study (approx. 2 weeks) and moistened with tap water each day. *O. wentworthianum* remained in the flowerpot during the time of measurement; the root ball was dipped in tap water every 2 days for about 1 min. Both orchids were kept in a glass cabinet during the experimental period to assure an elevated relative humidity.

Light Microscopy

A Leica MZ 125 stereomicroscope (Leica Microsystems, Wetzlar, Germany) was used for sample preparation and to get an *in situ* impression of flower details. Images were taken using a Nikon Coolpix E995 digital camera adapted to the stereomicroscope with a C-Mount adapter and a MDC 2 relay lens MXA 29005 (Nikon Corporation, Tokyo, Japan).

Cryo-Scanning Electron Microscopy (cryo-SEM)

A Hitachi S-4800 (Hitachi High-Technologies Corp., Tokyo, Japan) cryo-SEM equipped with a Gatan ALTO 2500 cryopreparation system (Gatan, Inc., Abingdon, United Kingdom) was used for imaging the flower surface details. Therefore, the viscidium of a fresh flower was partly removed manually using the head of a pin and mounted on metal holders with Tissue-Tek® O.C.T.™ Compound (Sakura Finetek Europe B. V., Zoeterwoude, The Netherlands). The samples on holders were frozen on a cryostage at 140°C, sputter-coated with gold-palladium (6 nm) in the cryopreparation chamber, and examined in the SEM at −120°C and an accelerating voltage of 1 kV.

Force Measurements

To measure the forces necessary to remove pollinaria from *Oncidium* spp. flowers the natural process was mimicked using a custom-build lab setup (**Figure 2A**). Living, turgescent individual *Oncidium* flowers were held with flat-ended tweezers that were mounted on an adjustable stand by a clamp (**Figures 2A,B**). Flowers, which for morphological reasons could not be grasped with the tweezers without being damaged, were mounted on a piece of stiff Styrofoam using double-sided adhesive tape. Manageability of the flower and accessibility of the viscidium were ensured by trimming the petals and the column wings (staminodia) with a razor blade. Thereby care was taken not to damage the viscidium, rostellum, or anther cap and to keep the flowers turgescent during the measurements (10 min)

The pollinator was mimicked by a round-tipped glass rod (diameter = 2.87 mm, length = 14.69 mm) produced by heating and melting the end of a glass rod, which gave a perfectly round tip due to the surface tension of the molten glass (**Figure 2C**). The glass rod was attached to a Fort 10 force transducer (10 g capacity, World Precision Instruments, Inc., Sarasota, FL, United States) and moved (i.e., approached and retracted) perpendicular to the longitudinal axis of the viscidium at a continuous speed of 190 µm s^{-1} using a motorized micromanipulator DC3001R combined with a MS314 controller (World Precision Instruments, Inc., Sarasota, FL, United States). Data were recorded using AcqKnowledge 3.7.0 software (Biopac Systems Ltd., Goleta, CA, United States) at a sample rate of 500 s^{-1}. After

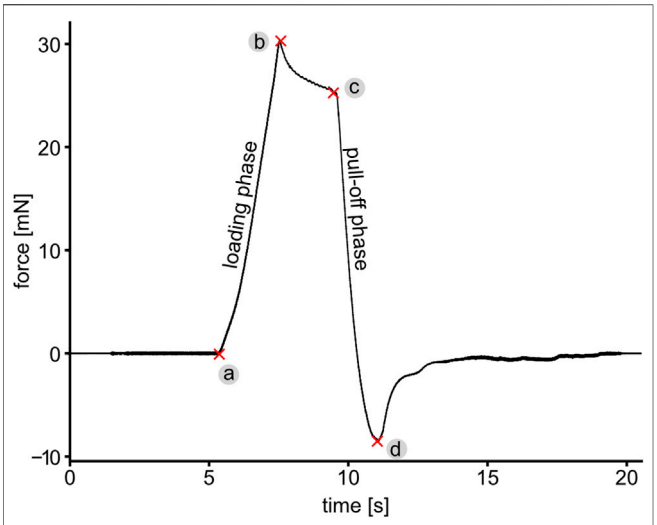

FIGURE 3 | A representative force-time curve showing different phases of the force measurement, while pushing and pulling the pollinarium with a glass rod. (a) Contact formation, (a–b) loading phase, (b–c) time in contact showing viscoelastic relaxation similar to pressure sensitive adhesives and (c–d and further until the end of curve) pull-off phase. The maximum pushing and pulling force are denoted as points (b) and (d), respectively. The maximum pulling force is hereinafter referred to as the pull-off force, which characterizes either the detachment force of the viscidium from the glass rod (in the case the pollinarium cannot be removed from the flower) or the force required to pull the whole pollinarium out of the flower.

making contact with the viscidium, the tip of the glass rod was moved forward for between 0.22 and 11.94 s, preloading the sticky viscidium material at forces between 0.045 and 74.087 mN. After keeping the glass rod in contact with the viscidium/flower for several seconds (min. = 1.01 s, max = 6.15 s), the glass rod was pulled off from the flower, either with the pollinarium sticking to it or not.

To determine to what extent the anther cap affects the force required to extract the pollinarium, the anther cap was removed vertically upwards in about half of the flowers shortly before starting the experiment, by using pointed tweezers (in some flowers the anther cap had already fallen off by itself). From 29 *O. otogaya* flowers, 16 were tested without anther cap. From *O. wentworthianum* 18 out of 29 were tested without anther cap.

The force measurements were conducted at 23.7 ± 1.69°C temperature and 47.3 ± 9.98% relative humidity. After each measurement, the adhesive residues left by the viscidium on the glass rod were wiped off with acetone-soaked filter paper.

Data Evaluation

The parameters gained from the raw data (i.e., force-time curves) (**Figure 3** and **Supplementary Material**) using the AcqKnowledge 3.7.0 software (Biopac Systems Ltd., Goleta, CA, United States) were 1) load, 2) duration of load, 3) relaxation time, and 4) pull-off force. Data analysis and statistical evaluation were performed using the software R version 3.2.3 (R Core Team, 2015). The relationship between load and pull-off force was checked using the Spearman rank order correlation test, because tests for normality (Shapiro-Wilk test) revealed nonnormal distribution of the data.

Estimation of Adhesive Strength of the Viscidium

The adhesive strength was calculated as the ratio of the maximum pulling force over the contact area. The contact area A_c was estimated from the distance d traveled by the glass rod during the loading phase (i.e., loading duration * loading velocity) and the radius r of the glass rod under the assumption that A_c corresponds to the lateral area of a spherical dome:

$$A_c = 2\pi rd.$$

Adhesive strength was only estimated for trials that did not lead to removal of the pollinarium from the flower. It should be noted that the forward movement of the glass rod led not only to deformation of the adhesive material but probably also to deformations of the underlying flower structures. Estimations of the contact area and consequently of the adhesive strength are thus to be interpreted with care and should be considered as first-order approximations.

RESULTS

Morphology of the Pollination Apparatus

The viscidium of *Oncidium* spp. is ellipsoidal, about 1 mm high, 0.4 mm wide, and 0.1 mm thick. It sits in a pouch-shaped structure, formed by the rostellum that is narrowing toward the column (**Figure 4A**). The stipe is attached to the upper edge of the cushion-shaped viscidium. In case of the presence of an anther cap, it is almost completely covered by this. The anther cap is attached to the flower via a thin band of tissue on either side (**Figure 4A**) and features a lip-like thickened structure where it touches the stipe (**Figure 4B**). When the anther cap is removed, the two pollinia and the stipe, which connects the pollinia to the viscidium, become visible (**Figure 4C**). After manipulation of the pollinarium with a pinhead, in order to (partly) release it from the rostellum/flower, the viscidium is shown to protrude into the rostellar pouch with a 0.2 mm thick half-lobed structure at its backside (**Figure 4D**). It appears that the cushion-like viscidium completely consists of a translucent adhesive material that is overlaid only by a very thin membrane (**Figure 4E**). Apparently, this adhesive dries and hardens very quickly as can be seen in **Figure 4F** by a more than 2 mm long, obviously quite stiff (no drooping caused by gravity) and erect filament of adhesive that remained stuck to the tip of the glass rod after touching and pulling-off from the viscidium and thereby damaging the thin adhesive coverage, but not removing the pollinarium from the flower (**Figure 4F**). Only the bottom and side parts of the viscidium seem to be connected to the rim of the rostellar pouch by the same (or a similar) sticky material that covers the viscidium, as can be seen from the hardened remnants of the substance pointing toward the pollinia in **Figure 2C**. Except at the upper end of the pouch, the viscidium seems to

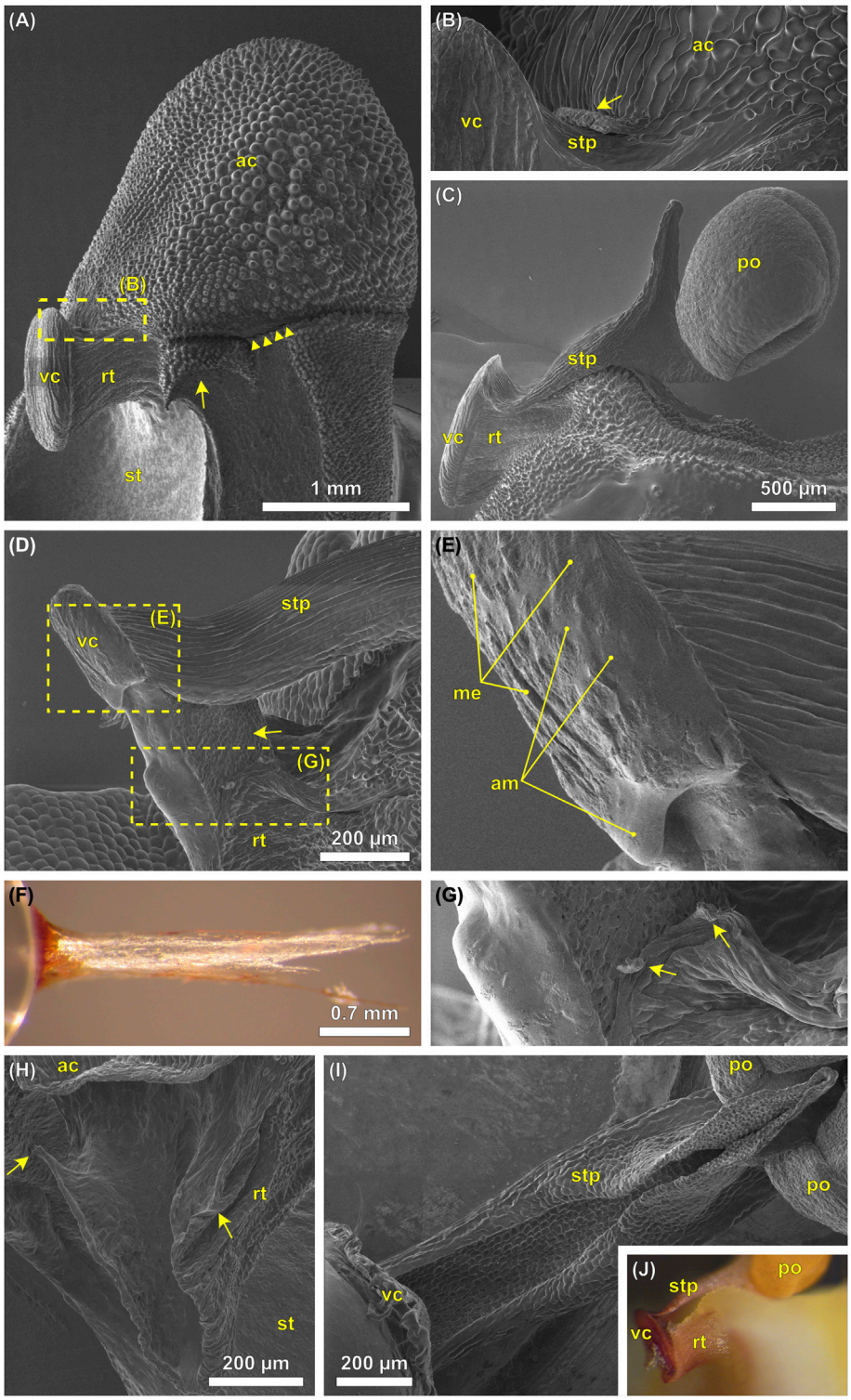

FIGURE 4 | (A–E,G–I) Cryo-SEM images and **(F,J)** digital photographs of the pollination apparatus of *Oncidium wentworthianum*. **(A)** A flower with unreleased pollinarium and still attached anther cap. The column wings (staminodia) have been trimmed using a razor blade (arrow) to allow for a lateral perspective. The connective tissue between anther cap and flower is ruptured, probably during sample preparation (arrowheads). **(B)** Detail of image **(A)** showing the lip (arrow) of the anther cap that touches the stipe. **(C)** Lateral view of the pollinarium, which still sits in the rostellar pouch. The anther cap has been removed. The stipe is slightly bent upwards what might have been caused by removal of the anther cap and/or by the freezing process during cryo-SEM. **(D)** A pollinarium that was manipulated with a pinhead. The viscidium is partly released from its original position revealing the scutellum at its backside (arrow). The rostellar pouch thereby was deformed. The adhesive substance of

(*Continued*)

FIGURE 4 | the viscidium was partly damaged/removed. **(E)** Detail of image **(D)** showing the upper part of the viscidium with the adhesive material (am). This substance is covered by a (in this case partly torn) membrane (me). **(F)** Rod-shaped remnants of the adhesive material sticking to the tip of the glass rod. **(G)** Detail of image **(D)** showing the upper part of the rostellar pouch with protruding tissue "bridges" (arrows) probably having been connected to the viscidium. **(H)** Empty rostellar pouch with its upper edges which probably have the strongest connection to the viscidium. Note that in this case the pollinarium was manually removed from the flower without first removing the anther cap. **(I)** Artificially released pollinarium seen from below. The viscidium is attached to a pinhead (bottom left). It is not clear whether the stipe has formed into a semitubular shape due to its removal from the flower and a following change of shape due to mechanical stress or if it represents the *in situ* state. **(J)** Pollinarium that is partly detached from the flower upon manipulation. Viscidium and stipe have been pushed deeper into the rostellar pouch and upwards. ac, anther cap; am, adhesive material; me, membrane; po, pollinium; rt, rostellum; st, stigma; stp, stipe; vc, viscidium.

have been attached to the rostellum via tiny and distinct tissue connections (**Figures 4G,H**). At least in the "released" state, the stipe can be described as a semitubular structure with its opening facing the opening of the rostellar pouch (**Figure 4I**).

Forces Required to Overcome an Initial Pollinium Attachment to the Plant

By applying load to the viscidium, while mimicking a pollinator visit, the viscidium is pushed deeper into the pocket formed by the rostellum, and at the same time, it is forced upwards. This upward movement causes the stipe to detach from the rostellum (**Figure 4J**). Once the viscidium was properly attached to the glass rod, and the pollinarium has been removed from the flower; it could not be removed from the glass rod except by scratching it off. Attempts to do so by pulling always resulted in tearing apart the stipe.

From all 29 *O. otogaya* flowers tested, the pollinarium could be successfully removed in only 8 cases. These were solely flowers, which did not have an anther cap. Among the *O. wentworthianum* flowers the pollinarium could be removed in 11 out of 29 trials with only one successful removal from a flower with the anther cap still attached (**Table 1**).

There was significant evidence ($p < 0.05$) suggesting a negative linear correlation between pull-off force and load, only for trials in which the pollinarium was not removed from the flower. This is true for both *O. otogaya* and *O. wentworthianum* (**Table 1**; **Figure 5**). The absolute pull-off forces, necessary to remove the pollinaria from the flowers, were comparatively low and ranged between 2.95 and 8.29 mN for *O. otogaya* and between 3.46 and 12.19 mN (3.46 and 7.46 mN, if only flowers without anther cap were considered) for *O. wentworthianum*.

For flowers without anther cap, the minimal load needed to start a successful removal process of the pollinarium was 8.99 mN in *O. otogaya* and 11.66 mN in *O. wentworthianum*. After applying loads higher than 10.82 mN (*O. otogaya*) and 12.58 mN (*O. wentworthianum*), respectively, the pollinarium could always be removed in flowers without anther cap (**Figures 6A,B**).

Adhesive Strength of the Viscidium

The adhesive strength of the viscidia was calculated from the estimated contact area and the maximum pull-off force. For obvious reasons this could only be done for trials in which the pollinarium itself remained attached to the flower. For *O. otogaya* the mean adhesive strength is 5.62 ± 4.01 kPa (max. 15.38 kPa), and 4.07 ± 2.08 kPa (max. 8.96 kPa) for *O. wentworthianum*.

DISCUSSION

The experiments mimicking the first stage of the pollination process of *Oncidium* flowers, i.e., the removal of the pollinarium from the flower, reveal that a successful pollinarium removal depends on whether the anther cap is present or not. As anther caps in *Oncidium* sp. seem to be shed with an increasing flower age, which is for example reported for *Oncidium sphacelatum* (Pemberton, 2008), their presence or absence is an indirect indicator of pollen "ripeness." This is related to the developmental stage of any other flower structure contributing to a fully functional pollination apparatus. When mature, the backside of the viscidium, referred to as scutellum, consists of dead cells with thickened walls, and while still in contact with the rostellum in its central part, the peripheral tissue already separates from the rostellum as observed by Schick (1989) in *O. hastatum*, except for the tissue strands seen in **Figure 4G** at the upper edge of the rostellar pouch. Concurrently the stipe differentiates from the rostellum tissue by insertion of a separation layer and mechanical stresses progressively build up in the stipe due to thickening of the cell walls (Schick, 1989).

Due to narrowing of the rostellar pouch, pushing back of the viscidium automatically leads to its upward movement, which leads to rupturing of the connection between viscidium and rostellum and between rostellum and stipe (**Figures 4G,H,J**, **7B**). Furthermore, the rostellar pouch is also widened during this process, additionally helping to release the stipe from the rostellum. The semitubular shape of the stipe is probably induced by previously build-up stresses that are released, when the connection between rostellum and stipe breaks, and increases its *ex situ* bending stiffness, ensuring precise positioning of the pollinia in relation to the viscidium (Schick, 1989) and thereby also an exact deposit on the stigma in the next visited flower. The probability of self-pollination is drastically reduced because the stipe of the pollinarium attached to the pollinator reconfigures over a time period of several minutes or hours, which eventually brings the pollinia into a position that allows them to come into contact with the stigma (Johnsson and Edwards, 2000). The mature pollination apparatus finds itself in a rather delicate mechanical state of equilibrium. In compliance with the development of mechanical stresses reported by Schick (1989), our cryo-SEM analysis suggests that the mature stipe is prestressed transversely to its longitudinal axis (**Figure 4I**), which in combination with the deformation caused by a pollinator pushing against the viscidium causes the stipe to curl and to consequently detach and lift off from the rostellum. When the anther cap is still present its lip blocks

TABLE 1 | Correlation analysis between load and pull-off force (Spearman's rank correlation) in flowers with and without anther cap and removed/nonremoved pollinarium.

Plant species	Flower with anther cap	Removal of pollinarium from flower	*p*-value	ρ	*n*	R^2
Oncidium otogaya	Yes	No	<0.001	−0.90	13	0.99
	Yes	Yes	NA	NA	0	NA
	No	No	<0.01	−0.88	8	0.65
	No	Yes	>0.05	−0.52	8	0.27
Oncidium wentworthianum	Yes	No	<0.05	−0.78	10	0.35
	Yes	Yes	NA	NA	1	NA
	No	No	<0.05	−0.74	8	0.40
	No	Yes	> 0.05	−0.41	10	0.11

Correlation coefficient ρ at a significance level of 0.05. p, probability value; n, sample size; R^2, coefficient of determination.

this relaxation and the back and upward movement caused by a pollinator and thus forestalls a premature release of the pollinium (**Figures 4B**, **7A**).

A load slightly higher than 10 mN, that is required to successfully remove the pollinarium from the flowers of the two *Oncidium* species, serves 1) for the establishment of a sufficient contact between the adhesive of the viscidium and the glass rod (or the pollinator) and 2) for the release of the mechanical anchoring of the pollinarium. The linear correlation between the load and pull-off force indicates a dependence of the viscidium's adhesive force on the load, which let us hypothesize a pressure sensitive property of the adhesive. This is also supported by the viscoelastic relaxation under load (**Figure 3**), which is typical for pressure sensitive adhesives (Feldstein, 2009). Calculations of the adhesive strength yielded values that are considerably lower than those of artificial pressure sensitive adhesives, like for example styrenic block copolymers (~200–800 kPa) (Pandey et al., 2020) or comparable biological pressure sensitive adhesives. Trichome secretions of the flypaper trap of the protocarnivorous plant *Roridula gorgonias* for example have a median adhesive strength between 17.5 and 156.2 kPa, depending on trichome length and corresponding functional adaptation (Voigt et al., 2009). The values determined here, however, are based on *in vivo* experiments; i.e., the viscidium was attached to the rostellum and not to an uncompliant, stiff support. It is thus likely that the established contact area is overestimated which in turn entails an underestimation of the adhesive strength. In any case, a

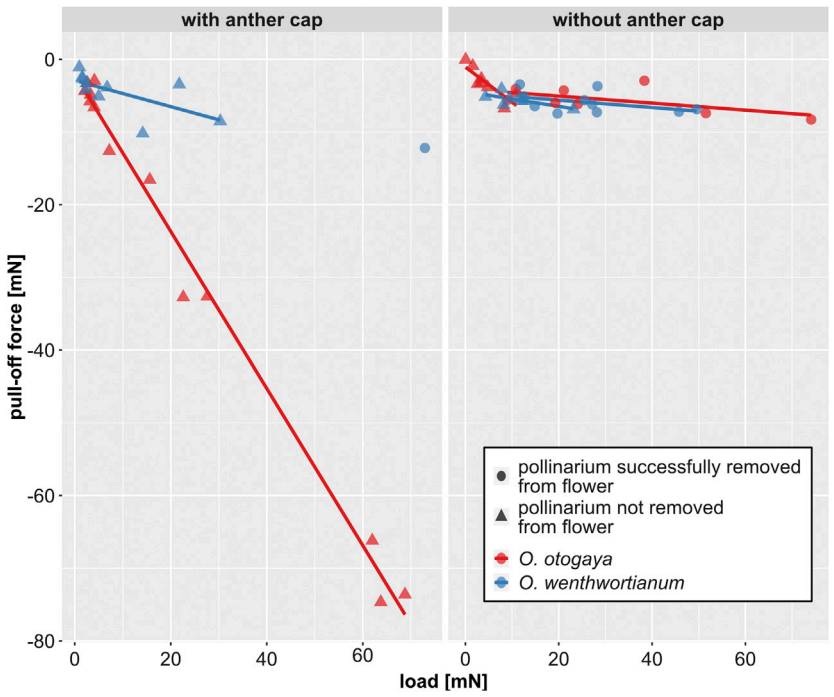

FIGURE 5 | Pull-off force vs. load, measured in *Oncidium otogaya* and *O. wentworthianum* flowers with (left) and without anther cap (right) and grouped by species (color of the symbol) and success of pollinarium removal (shape of the symbol). Statistical details for the linear regression lines are displayed in **Table 1**.

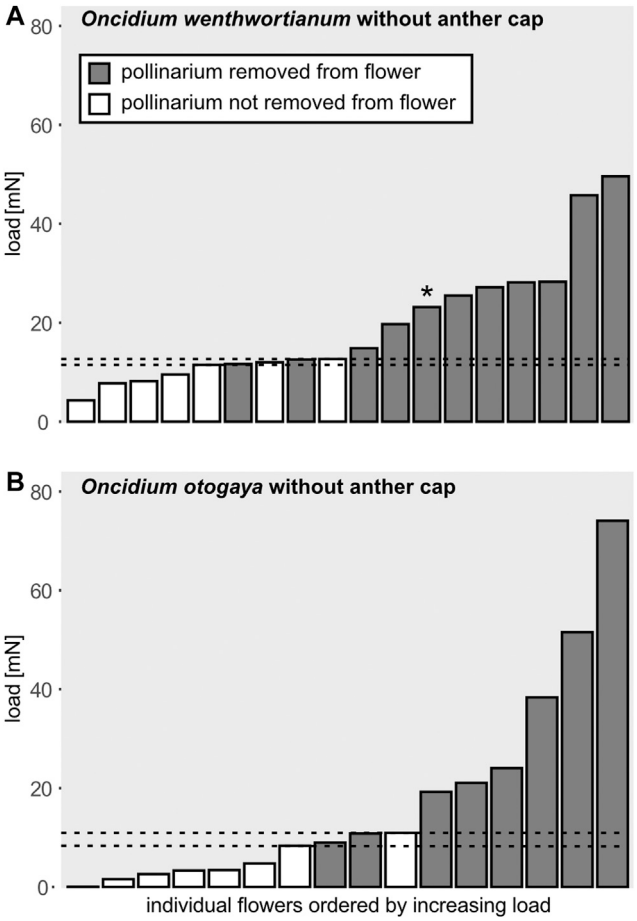

FIGURE 6 | Applied load and related success of removal of the pollinarium in **(A)** *Oncidium wentworthianum* and **(B)** *O. otogaya* for flowers without anther cap. The gray bars show the applied load that leads to successful pull-off of the pollinarium from the flower. The white bars correspond to the load that was not sufficient to separate the pollinarium from the flower. The dotted lines indicate the threshold of the load sufficient to overcome the initial attachment of the pollinarium to the flower. When the applied load was higher than the upper threshold, the pollinarium could be removed from the flower in all attempts. When the applied load was lower than the lower threshold, the pollinarium could be removed from the flower in no attempt. (*This pollinarium was successfully and completely separated; however, after a short distance of pull-off it got stuck and detached from the glass rod. The pollinarium was thus rated as successfully removed from the flower.)

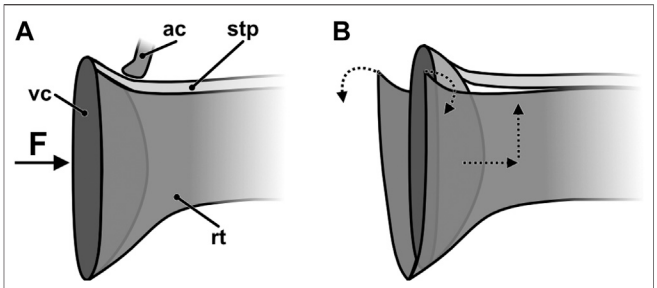

FIGURE 7 | Schematic drawing of the viscidium sitting in the rostellar pouch **(A)** before and **(B)** after applying a sufficient force, e.g., by a pollinator. The dotted arrows indicate direction of movement and of deformation. ac, anther cap (only the lip is shown); F, load; rt, rostellum; stp, stipe; vs, viscidium.

correlation between load and pull-off force is beneficial to the plant in that insects that fail to remove the pollinarium, either because the anther cap is still present or because they are not strong enough to overcome the mechanical barrier, can at least free themselves and do not remain stuck to the flower and block it against suitable pollinators. The pull-off forces required to fully withdraw the pollinarium from the flower are rather low (7.46 and 8.29 mN), as compared to the loading forces required to detach the pollinarium, and are needed to overcome the connection between scutellum and rostellum, as well as the friction between pollinarium and the flower structure.

Potential pollinators of *Oncidium* spp. have been reported to be fairly large apid bees, which, deducing from their size [*Centris* Fabricius: 9–19 mm, *Trigona* Jurine: 4–9 mm, *Tetrapedia* Klug: 8–13 mm, and *Epicharis* Klug: 15–25 mm (Michener, 2000)], probably are able to easily produce forces well above 10 mN. Information on forces insects in general and bees in particular are able to apply by pushing is scarce. The forces measured by Reith et al. (2006) for *Bombus terrestris* L. (Hymenoptera, Apidae, size: 12–19 mm) are 24.6 ± 14.8 mN (max. 59 mN) for workers and 46.8 ± 25.5 mN (max. 90 mN) for queens. For *Apis mellifera* L., a mean value of 14 ± 7.4 mN (max. 29 mN) was measured, which is approximately half the force measured by Córdoba and Cocucci (2011) for *A. mellifera* (26.26 ± 3.89 mN). For different *Bombus* species the latter authors measured forces of well over 200 mN. It should however be noted that Reith et al. (2006) and Córdoba and Cocucci (2011) used different experimental setups to assess the insects pushing forces. Whereas in the approach of Córdoba and Cocucci (2011) the force insects exert for opening a trap door in a kind of escape reaction was recorded, in the approach of Reith et al. (2006) the pushing forces invested by insects to get access to a food source in an artificial flower were measured. As the pollinaria are dislodged by the bee rather accidentally (at least from the bee's point of view) while collecting oil from the elaiophores (Singer, 2003; Pansarin et al., 2017), it seems evident that they will not push on the viscidium with their full strength. Also Córdoba and Cocucci (2011) reported that pollinators are able to exert a lot higher maximum force than actually needed to operate the flower's mechanism. While only female *Centris* bees collect oil, there are reports of male *Centris* bees that may be involved in the pollination process of *Oncidium* as well. When the flowers of *Oncidium* move or "dance" in the wind (hence their name "dancing ladies"), they may be mistakenly perceived by male *Centris* bees as enemies and tempt them to attack in a behavior known as pseudoantagonism (Dressler, 1993; Castro and Singer, 2019). While attachment of the pollinia would be in principle possible also to male *Centris* bees, regarding the remarkably quick-setting properties of the glue of the viscidium (Dressler, 1961) (**Figure 4F**), Castro and Singer (2019) doubt the existence of such an attachment mechanism of rapidly striking a flower while attempting to

attack an enemy as extremely unlikely. The impossibility of adhesion generation by fast movement may be explained by the viscoelastic property of the viscidium material. The fast contact formation will not generate large contact and sufficient pull-off force, because at short relaxation times it is hardly possible. Only the slow motion or large contact times will potentially generate large contact area and strong pull-off force. It may be hypothesized that viscoelastic properties of the viscidium material might represent a safety mechanism preventing occasional detachment of the pollinium due to short fast contacts caused for example by wing actions.

Besides the force that the pollinator is able to generate "accidentally," its body dimension is also an important factor. The bee or more general the pollinator must be big and forceful enough to hit the viscidium, when sitting on the labellum. Further aspects, potentially essential for a comprehensive understanding of the pollinator-flower-interactions, concern properties of the surface structures (e.g., papillae or cuticular folds, cell shapes, and dimensions), the nature and position of the attachment of the viscidium to the insect integument, the chemical and physical properties of the adhesive substance, and the process of detachment deposition of the pollinia on the stigma. These could be addressed in future studies to further enhance the understanding of the form-structure-function relationships in the pollination apparatus of *Oncidium* species and their coevolution with *Centris* bees.

CONCLUSION

In the studied *Oncidium* species, the complex pollination apparatus constitutes a two-stage barrier preventing risk of erroneous removal of pollinium from the flower. At the first stage, the presence of an anther cap efficiently prevents visiting pollinators from removing the pollinaria before these reach maturity. At the second stage, a mechanical barrier formed by a severable interconnection between the pollinaria and another part of the flower, the rostellum, ensures that only legitimate pollinators, able to push and then pull the pollination apparatus strongly enough, are able to remove the pollinaria which can be hypothesized as effect of coevolution between plants and their pollinators.

DATA AVAILABILITY STATEMENT

Summarized raw data are included in the articel **Supplementary Material**, further inquiries can be directed to the corresponding author.

AUTHOR CONTRIBUTIONS

SG and TS initiated the research. SG, DV, and FG designed and supervised the study. Data collection, data assessment, and statistical analyses were carried out by MT. Data evaluation and discussion of results were a joint effort by all authors. MT contributed to the first draft of the manuscript. All authors improved further versions of the manuscript and gave final approval for publication.

FUNDING

This project was financed by institutional budgets. Partial support was provided by the European Network of Bioadhesion Expertise: Fundamental Knowledge to Inspire Advanced Bonding Technologies (COST Action CA15216"ENBA"). The article processing charge was funded by the Baden-Württemberg Ministry of Science, Research and Art and the University of Freiburg in the funding program Open Access Publishing.

ACKNOWLEDGMENTS

The authors want to thank F. Lô-Kockel† and B. Schäfer from the Zoological-Botanical Garden "Wilhelma" in Stuttgart, Germany, for kindly providing the orchids analyzed in this project. Also, the help of Jan Schuppert (Max Planck Institute for Metals Research, Stuttgart) with cryo-SEM imaging is acknowledged.

SUPPLEMENTARY MATERIAL

The Supplementary Material for this article can be found online at: https://www.frontiersin.org/articles/10.3389/fmech.2020.635694/full#supplementary-material.

REFERENCES

Borba, E. L., and Semir, J. (1999). Temporal variation in pollinarium size after its removal in species of Bulbophyllum: a different mechanism preventing self-pollination in Orchidaceae. *Plant Systemat. Evol.* 217, 197–204. doi:10.1007/BF00984365

Brantjes, N. B. M. (1981). Floral mechanics in phlomis (lamiaceae). *Ann. Bot.* 47, 279–282. doi:10.1093/oxfordjournals.aob.a086018

Cameron, L. D., and Johnson, S. D. (2008). Function and evolution of aggregated pollen in angiosperms. *Int. J. Plant Sci.* 169, 59–78. doi:10.1086/523364

Carmona-Díaz, G., and García-Franco, J. G. (2008). Reproductive success in the Mexican rewardless Oncidium cosymbephorum (Orchidaceae) facilitated by the oil-rewarding Malpighia glabra (Malpighiaceae). *Plant Ecol.* 203, 253–261. doi:10.1007/s11258-008-9543-6

Castro, J. B., and Singer, R. B. (2019). A literature review of the pollination strategies and breeding systems in Oncidiinae orchids. *Acta Bot. Bras.* 33, 618–643. doi:10.1590/0102-33062019abb0111

Chase, M. W., Cameron, K. M., Freudenstein, J. V., Pridgeon, A. M., Salazar, G., Berg, C., et al. (2015). An updated classification of Orchidaceae. *Bot. J. Linn. Soc.* 177, 151–174. doi:10.1111/boj.12234

Christenhusz, M. J. M., and Byng, J. W. (2016). The number of known plants species in the world and its annual increase. *Phytotaxa*. 261, 201. doi:10.11646/doi.org/phytotaxa.261.3.1

Claßen-Bockhoff, R., Speck, T., Tweraser, E., Wester, P., Thimm, S., and Reith, R. (2004). The staminal lever mechanism in Salvia L. (Lamiaceae): a key innovation for adaptive radiation?. *Org. Divers. Evol.* 4, 189–205. doi:10.1016/j.ode.2004.01.004

Córdoba, S. A., and Cocucci, A. A. (2011). Flower power: its association with bee power and floral functional morphology in papilionate legumes. *Ann. Bot.* 108, 919–931. doi:10.1093/aob/mcr196

Darwin, C. (1890). *The various contrivances by which orchids are fertilised by insects*. London, UK: John Murray. doi:10.5962/bhl.title.37883

Davies, K. L., Stpiczyńska, M., and Rawski, M. (2014). Comparative anatomy of floral elaiophores in vitekorchis romowicz & szlach., cyrtochilum kunth and a florally dimorphic species of Oncidium Sw. (Orchidaceae: Oncidiinae). *Ann. Bot*. 113, 1155–1173. doi:10.1093/aob/mcu045

Dressler, R. L. (1961). The structure of the orchid flower. *Missouri Bot. Gard. Bull*. 49, 60–69.

Dressler, R. L. (1981). *The orchids: natural history and classification*. Cambridge, MA: Harvard University Press.

Dressler, R. L. (1993). *Phylogeny and classification of the orchid family*. Cambridge, UK: Cambridge University Press.

Faegri, K., and Pijl, L. v. d. (1979). *The principles of pollination ecology*. 3rd Edn. Oxford, UK: Pergamon Press.

Feldstein, M. M. (2009). Contribution of relaxation processes to adhesive-joint strength of viscoelastic polymers. *Polym. Sci*. 51, 1341–1354. doi:10.1134/S0965545X09110194

Ferreira, N. P., Chiavelli, L. U. R., Savaris, C. R., Oliveira, S. M., Lucca, D. L., Milaneze-Gutierre, et al. (2019). Chemical study of the flowers of the orchid Oncidium baueri Lindley and their visiting bees Trigona spinipes Fabricius. *Biochem. Systemat. Ecol*. 86, 103918. doi:10.1016/jdoi.org/.bse.2019.103918

Givnish, T. J., Spalink, D., Ames, M., Lyon, S. P., Hunter, S. J., Zuluaga, A., et al. (2015). Orchid phylogenomics and multiple drivers of their extraordinary diversification. *Proc. Biol. Sci*. 282, 20151553. doi:10.1098/rspb.2015.1553

Jersáková, J., Johnson, S. D., and Kindlmann, P. (2006). Mechanisms and evolution of deceptive pollination in orchids. *Biol. Rev*. 81, 219–235. doi:10.1017/S1464793105006986

Johnson, S. D., and Anderson, B. (2010). Coevolution between food-rewarding flowers and their pollinators. *Evo. Edu. Outreach*. 3, 32–39. doi:10.1007/s12052-009-0192-6

Johnson, S. D., and Edwards, T. J. (2000). The structure and function of orchid pollinaria. *Plant Systemat. Evol*. 222, 243–269. doi:10.1007/BF00984105

Michener, C. D. (2000). *The bees of the world*. Baltimore, MD: The Johns Hopkins University Press.

Mosquera-Mosquera, H. R., Valencia-Barrera, R. M., and Acedo, C. (2019). Variation and evolutionary transformation of some characters of the pollinarium and pistil in Epidendroideae (Orchidaceae). *Plant Systemat. Evol*. 305, 353–374. doi:10.1007/s00606-019-01575-5

Pacini, E., and Hesse, M. (2002). Types of pollen dispersal units in orchids, and their consequences for germination and fertilization. *Ann. Bot*. 89, 653–664. doi:10.1093/aob/mcf138

Pandey, V., Fleury, A., Villey, R., Creton, C., and Ciccotti, M. (2020). Linking peel and tack performances of pressure sensitive adhesives. *Soft Matter*. 16, 3267–3275. doi:10.1039/C9SM02172H

Pansarin, E. R., Alves-Dos-Santos, I., and Pansarin, L. M. (2017). Comparative reproductive biology and pollinator specificity among sympatric Gomesa (Orchidaceae: Oncidiinae). *Plant Biol*. 19, 147–155. doi:10.1111/plb.12525

Parra-Tabla, V., Vargas, C. F., Magaña-Rueda, S., and Navarro, J. (2000). Female and male pollination success of Oncidium ascendens Lindey (Orchidaceae) in two contrasting habitat patches: forest vs agricultural field. *Biol. Conserv*. 94, 335–340. doi:10.1016/S0006-3207(99)00187-1

Pemberton, R. W. (2008). Pollination of the ornamental orchid Oncidium sphacelatum by the naturalized oil-collecting bee (Centris nitida) in Florida. *Selbyana*. 29, 87–91.

R Core Team (2015). *R: a language and environment for statistical computing*. Vienna, Austria: R Foundation for Statistical Computing.

Reith, M., Claßen-Bockhoff, R., and Speck, T. (2006). "Biomechanics in Salvia flowers: the role of lever and flower tube in specialization on pollinators," in *Ecology and Biomechanics - a mechanical approach to the ecology of animals and plants*. Editors A. Herrel, T. Speck, and N. P. Rowe (Boca Raton, FL: CRC Press), 123–146.

Schick, B. (1989). "I: dactylorhiza majalis (Rchb.) Hunt & Summerh., Disa uniflora Bergius und Oncidium hastatum Lindl," in *Zur Anatomie und Biotechnik des Bestäubungsapparates der Orchideen.Botanische Jahrbücher für Systematik, Pflanzengeschichte und Pflanzengeographie*. Editors J. Grau, B. Hiepko, and P. Leins (Stuttgart, Germany: Schweizerbart'sche Verlagsbuchhandlung (Nägele u. Obermiller), 215–262.

Singer, R. B. (2003). Orchid pollination: recent developments from Brazil. *Lankesteriana*. 7, 111–114.

Singer, R. B., and Cocucci, A. A. (1997). Eye attached Hemipollinaria in the hawkmoth and settling moth pollination of Habenaria (Orchidaceae): a study on functional morphology in 5 species from subtropical South America. *Bot. Acta*. 110, 328–337. doi:10.1111/j.1438-8677.1997.tb00648.x

Stern, W. L. (2014). *Anatomy of the monocotyledons, Vol. X: Orchidaceae*. Oxford, UK: Oxford University Press.

Tremblay, R. L. (1992). Trends in the pollination ecology of the Orchidaceae: evolution and systematics. *Can. J. Bot*. 70, 642–650.doi:10.1139/b92-083

Voigt, D., Gorb, E., and Gorb, S. (2009). Hierarchical organisation of the trap in the protocarnivorous plant Roridula gorgonias (Roridulaceae). *J. Exp. Biol*. 212 (19), 3184–3191. doi:10.1242/jeb.034280

Wagenitz, G. (1981). Orchideen und Compositen, Vergleich zweier Familien und Evolutionsstrategien. *Ber. Deutsch. Bot. Ges*. 94, 229–247.

Yam, T. W., Arditti, J., and Cameron, K. M. (2009). "The orchids have been a splendid sport"--an alternative look at Charles Darwin's contribution to orchid biology. *Am. J. Bot*. 96, 2128–2154. doi:10.3732/ajb.0900122

Conflict of Interest: The authors declare that the research was conducted in the absence of any commercial or financial relationships that could be construed as a potential conflict of interest.

frontiers in Mechanical Engineering

ORIGINAL RESEARCH
published: 27 January 2021
doi: 10.3389/fmech.2020.621741

Setal Field Transects, Evolutionary Transitions and Gecko–Anole Convergence Provide Insights Into the Fundamentals of Form and Function of the Digital Adhesive System of Lizards

Anthony P. Russell[1]* *and Austin M. Garner*[2]

[1]*Department of Biological Sciences, University of Calgary, Calgary, AB, Canada,* [2]*Integrated Bioscience Program, Department of Biology, The University of Akron, Akron, OH, United States*

Recent years have witnessed a multitude of studies focusing on gekkotan adhesion. Intense interest in this phenomenon was triggered by the discovery of the manner and magnitude of the forces generated by the hair-like filaments (setae) on the toe pads and inspired the development of the next generation of smart, reversible synthetic adhesives. Most studies pursuing these goals have concentrated on the generalized form and properties of gekkotan setae outlined in those key early studies, resulting in the fabrication of synthetic filaments of uniform dimensions. Although there are over 1,800 species of extant geckos, and hundreds of species of anoles (a separate lizard lineage that has convergently evolved adhesive toe pads), most investigations have used relatively few species as the source of basic information, the Tokay gecko (*Gekko gecko*) being the most prominent among these. Such exemplar taxa generally exhibit structurally intricate setae and morphologically complex configurations of the adhesive apparatus. Setal structure taken to be characteristic of these taxa is generally reported by singular statements of maximal length, diameter, density and branching pattern. Contemporaneous work focusing on the configuration of setae at locations across the toe pads and upon the evolutionary origin of adhesively competent digits in anoles and specific lineages of geckos, however, has revealed extensive variation of setal structure within individuals, information about how setae may have arisen from non-adhesive filamentous precursors, and how newly adhesively competent digits have been integrated into pre-existing patterns of locomotor mechanics and kinematics. Such observations provide insights into what is minimally necessary for adhesively competent digits to function and reveal the simplest configuration of components that make this possible. We contend that information gleaned from such studies will assist those seeking to employ the principles of fibrillar-based adhesion, as exemplified by lizards, for bio-inspired applications.

Keywords: *Anolis*, biomimetics, convergent evolution, fibrillar adhesion, Gekkota, synthetic adhesives

OPEN ACCESS

Edited by:
Stanislav N. Gorb,
University of Kiel, Germany

Reviewed by:
Luciano Afferrante,
Politecnico di Bari, Italy
Yoshitaka Nakanishi,
Kumamoto University, Japan

***Correspondence:**
Anthony P. Russell
arussell@ucalgary.ca

Specialty section:
This article was submitted to Tribology, a section of the journal Frontiers in Mechanical Engineering

Received: *26 October 2020*
Accepted: *15 December 2020*
Published: *27 January 2021*

Citation:
Russell AP and Garner AM (2021) Setal Field Transects, Evolutionary Transitions and Gecko–Anole Convergence Provide Insights Into the Fundamentals of Form and Function of the Digital Adhesive System of Lizards. Front. Mech. Eng 6:621741. doi: 10.3389/fmech.2020.621741

INTRODUCTION

Recent years have witnessed a deluge of studies focusing on gekkotan adhesion, a remarkable phenomenon whereby geckos can attach to, and move on, smooth, low friction surfaces using series of expanded scales (scansors or lamellae) that possess arrays of hair-like fibers (setae) carrying multiple flattened, triangular-shaped tips (spatulae) (Ruibal and Ernst, 1965; Autumn et al., 2000; Autumn et al., 2002). Intense interest in this was triggered by the discovery of the manner and magnitude of the forces generated by a single seta of the Tokay gecko (*Gekko gecko*) (Autumn et al., 2000). These revelations served as inspiration for the development of the next generation of smart, reversible synthetic adhesives. The structure and dimensions of the setae examined by Autumn et al. (2000) have become the exemplar for gecko filaments. Attempts to simulate their attributes through fabrication of synthetic fibrils have been guided by these findings.

It is sobering to realize, however, that there are over 1,800 species of extant geckos (Uetz et al., 2020), as well as hundreds of species of anoles (a separate group of lizards that has convergently evolved adhesive toe pads–see below; Poe et al., 2017). Relatively few species, however, have been employed as the source of basic information about setal structure, and those that have generally exhibit structurally intricate setae and morphologically complex configurations of the entire adhesive apparatus (Garner et al., 2020; Russell et al., 2019; Russell and Gamble, 2019). The setal structure taken to be characteristic of these taxa is usually represented by a singular statement of seemingly important dimensions: length, diameter, density and branching pattern. Collectively these oft-repeated properties have led to setal arrays being conceptualized as organized assemblages of fibrils of essentially identical configuration (Garner and Russell, in review).

Work focusing on the form of setae at locations across toe pads, and on the evolutionary origin of adhesively-competent digits in specific lineages of geckos has, however, shed light on (1) the variation of setal structure within individuals (Russell et al., 2007; Johnson and Russell, 2009; Webster et al., 2009; Russell and Johnson, 2014); (2) the manner in which setae may have arisen from non-adhesive filamentous precursors (Russell et al., 2015; Higham et al., 2017); and (3) the way digits exhibiting the first stages of adhesive competence (in that they can support the animal during static clinging and locomotion on vertical, low friction substrata) have been integrated into pre-existing patterns of locomotor mechanics and kinematics (Russell et al., 2015; Higham et al., 2017). More recently, similarly-focused investigation of the structure of setae and the configuration of the adhesive apparatus of anoline lizards have provided insights into which structural and functional attributes are shared with geckos (Garner et al., 2020), thereby enhancing our understanding of which features appear to be of fundamental mechanical importance for the operation of a digit-based adhesive system. We contend that information gleaned from such studies can be of assistance to those seeking to adapt the principles of fibrillar-based adhesion of lizards for technological applications by revealing what is minimally necessary and sufficient for adhesively competent digits to function. Recognition of such attributes should help to simplify the pathway to the development of effective synthetic setae and mechanical mechanisms to operate them (as assessed against the performance of the actual structures being mimicked). As Niewiarowski et al. (2016) note, "no synthetic mimic can yet perform as well as a gecko".

TRANSECTS OF SETAL FIELDS

Large numbers of publications dealing with the attributes of the adhesive setae of geckos provide information about their dimensions and morphology (**Table 1**). Parameters such as setal length, diameter, density, and spatular width and length have been documented. There is, however, considerable inconsistency in such reports (**Table 1**), this perhaps being attributable to the actual variation expressed between setae, both within and between species (see below). Generalizations about the numbers of terminal branches (hundreds to thousands) that setae bear also abound. Collectively these reports provide little in the way of insight into which of these features are particularly important, or why they should be so. Comparative observations between species (**Table 2**) intimate that there are species-specific differences in setal structure (Peattie, 2007), with even closely-related species seemingly exhibiting quite different dimensional properties (**Table 2**—see the data for the three species of *Gekko*). Questions arise, therefore, as to what this enormous variation might mean and what aspects of it, if any, might be critical for the development of artificial simulacra.

The sources cited in **Tables 1** and **2** (apart from Ruibal and Ernst, 1965) do not mention the location on the toe pad from which the exemplar setae were sampled (scansors closer to or farther from the toe tip) and give little or no information about whether setal features vary predictably along the toe pads. Transects along the entire length of toe pads, however, reveal that variation of setal length, basal diameter and stalk density is extensive within individuals of a given species (**Figures 1**–**4**), and that this variation is regularized and predictable both along the length of the entire toe pad, as well as locally along the length of each scansor (Russell et al., 2007; Johnson and Russell, 2009; Webster et al., 2009; Russell and Johnson, 2014). There are similarities in the patterns evident in the transect data of the setal fields of *Chondrodactylus bibronii* (**Figure 1**) and *Gekko gecko* (**Figures 2**–**4**), with the lengths of the setae decreasing from distal to proximal along the length of each scansor and along the length of the toe pad as a whole, and with the setal stalk diameters (and thus the aspect ratio of the setae) changing in a regularized fashion (**Figures 1** and **2**). There are also notable differences between *C. bibronii* and *G. gecko* with regard to setal and stalk diameters, with the setae of the former increasing in diameter from distal to proximal on each scansor (**Figure 1**) and those of the latter doing the opposite.

The extent of the variance of setal form and stalk density within a single species becomes more poignant when compared to the single seta statements for other species. Variation in setal length, basal diameter and stalk density of *Chondrodactylus bibronii* (**Figure 1**) when compared to those parameters reported by Peattie (2007) for eight other species of gecko

TABLE 1 | Data reported for setal dimensions for geckos in general and for Gekko gecko, indicating the variability in the values. For *Gekko gecko*, which has been used extensively in research focusing on gecko adhesion, the values reported span large ranges but generally are not accompanied by information as to where on the toe pad the measurements were taken from. Apart from a few early investigations, most of the values reported are taken from papers published between 2005 and 2016.

Setal length (μm)	Setal basal diameter (μm)	Setal density (mm^{-2})	Spatula width (μm)	Spatula length (μm)
Geckos				
20–100[28]	1–2[28]		0.2[8,24,31]	0.5[6,7]
30–120[10,30]	1–5[23]		0.2–0.3[6,7,18]	
30–130[6,7,11,16]	5–10[6,7]		0.2–0.5[11,13]	
80–120[12]	20[24]			
100[23]				
110[29]				
Gekko gecko				
30–130[1,20,25]	1–2[2]	5300[27]	0.1[27]	0.2[3,4]
80–100[26]	2.5[18]	14000[6]	0.1–0.2[25]	0.3[9]
90[22]	3–5[19]		0.2[4,5,9,15,17,19,21]	
110[3,4,15]	4.2[3,9,15]		0.2–0.5[1,20]	
120[9]	5[4]			
	5–10[25]			
	10[22]			

The sources of the data are indicated by superscript numbers in the table and refer to the following publications: [1]Alexander (2006); [2]Alibardi and Toni (2005); [3]Autumn and Gravish (2008); [4]Autumn and Hansen (2006); [5]Autumn et al. (2006); [6]Bhushan (2007); [7]Bhushan and Sayer (2007); [8]Kellar and Bogue (2008); [9]Chen et al. (2008); [10]Dalla Valle et al. (2007); [11]Del Campo and Arzt (2007); [12]Dellit (1934); [13]Filippov and Popov (2006); [14]Gao et al. (2005); [15]Gravish et al. (2008); [16]Hallahan et al. (2008); [17]Hansen and Autumn (2005); [18]Hiller (1968); [19]Huber et al. (2005); [20]Hui et al. (2007); [21]Lee et al. (2007); [22]Maderson (1964); [23]Niewiarowski et al. (2016); [24]Northen et al. (2008); [25]Pugno and Lepore (2008); [26]Rizzo et al. (2006); [27]Sun et al. (2005); [28]Toni et al. (2007); [29]Yao and Gao (2006); [30]Yu et al. (2006); [31]Xu et al. (2015).

TABLE 2 | Data ranges furnished by (1) Ruibal and Ernst (1965), (2) Schleich and Kästle (1986) and (3) Bauer (1998) for setal dimensions of individual species of geckos.

Species	Family	Setal length (μm)	Setal basal diameter (μm)	Setal density (mm^2)	Source
Amalosia lesueurii	Diplodactylidae	17+	1.5–3+	150,000	(2)
Bavayia cyclura	Diplodactylidae	32*+	1.3+	429,000	(3)
Bavayia sauvagii	Diplodactylidae	31*+	1.5+	335,000	(3)
Correlophus sarasinorum	Diplodactylidae	36*+	1.3+	134,000	(3)
Dactylocnemis pacificus	Diplodactylidae	17.5–20+	1.5+	200,000	(2)
Dactylocnemis pacificus	Diplodactylidae	17+	1.5+	280,000	(3)
Eurydactylodes vieillardi	Diplodactylidae	19+		363,000	(3)
Naultinus elegans	Diplodactylidae	15+	0.8	621,000	(3)
Naultinus rudis	Diplodactylidae	21+	0.8	490,000	(3)
Pseudothecadactylus lindneri	Diplodactylidae	37*+	1.2+	142,000	(3)
Rhacodactylus auriculatus	Diplodactylidae	38*+		172,000	(3)
Toropuku stephensi	Diplodactylidae	17+	0.8	458,000	(3)
Woodworthia maculata	Diplodactylidae	13+	0.6	342,000	(3)
Chondrodactylus bibronii	Gekkonidae	96*+	3.5*+	16,000*	(2)
Hemidactylus bouvieri	Gekkonidae	10–50+	1.5–2.5+	110,000	(2)
Gekko gecko	Gekkonidae	75–108+ 30–130+	3–4.5*+2,2–4.7*	14,400*	(2)
Gekko kuhli	Gekkonidae	24–91+			(2)
Gekko vittatus	Gekkonidae	37–78*+	3.5*+	25,600*	(2)
Tarentola caboverdiana	Phyllodactlidae	27–68+	4–4.5*	26,000*	(2)
Thecadactylus rapicauda	Phyllodactylidae	50–60*+	1.8+	6,000	(2)
Aristelliger praesignis	Sphaerodactylidae	46–57*+	1.3+		(1)
Sphaerodactylus cinereus	Sphaerodactylidae	10–65			(1)

Values that fall entirely within the ranges of setal dimensions reported for Chondrodactylus bibronii *in* ***Figure 1*** *are denoted by an asterisk (*), and those that fall entirely within the ranges of setal dimensions reported for* Gekko gecko *in* ***Figure 2*** *are denoted by a plus sign (+).*

(encompassing representatives of three families, each of which has independently evolved adhesive toe pads–Russell and Gamble, 2019), reveals that the majority of the variation reportedly encompassed by these eight species (Peattie, 2007) is subsumed within the range of variation displayed by *C. bibronii*. The same is true (even more so) for the setal length and setal stalk diameter variation shown by *Gekko gecko* (**Figure 2**). Further evidence of this overlap of setal dimensions between *C. bibronii*, *G. gecko* and other species of gecko is evident from the data compiled by Ruibal and Ernst (1965) and Schleich and Kästle (1986), as presented in **Table 2**.

Although the clinging performance of whole animals (Irschick et al., 1996) has been correlated with toe pad area, it is evident from transect surveys of the toe pads that setae in different

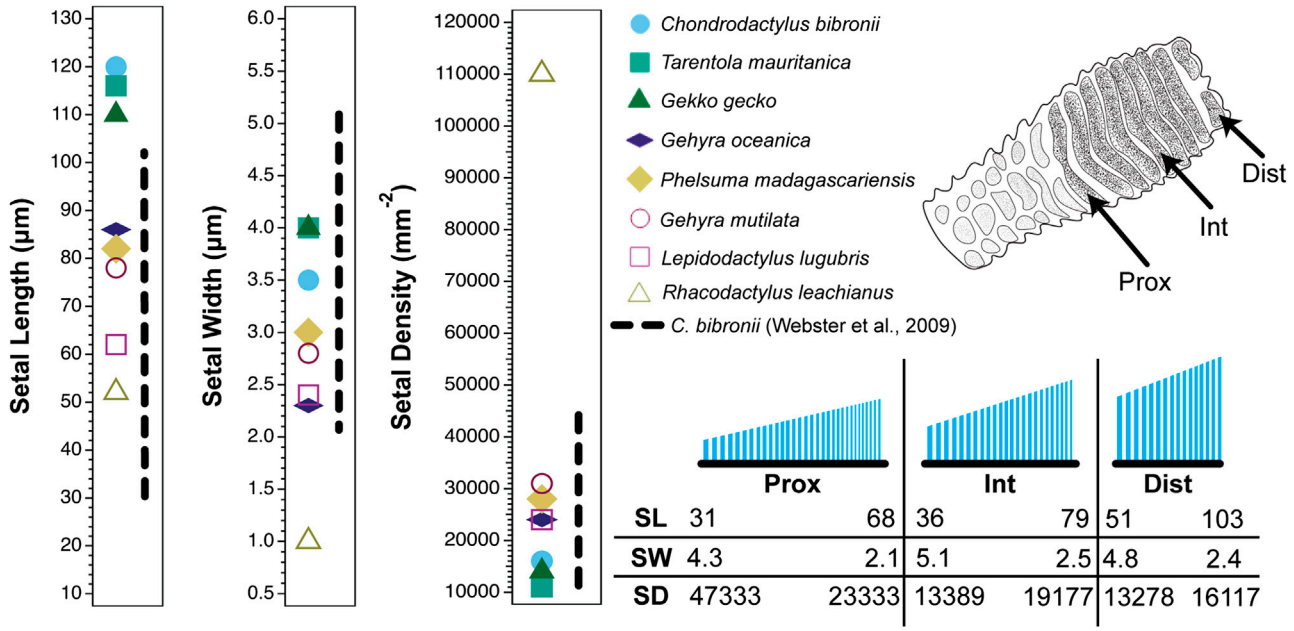

FIGURE 1 | Setal dimensions (length, width, and density) recorded for digit IV, left pes of the gekkonid gecko *Chondrodactylus bibronii* showing variation in relation to location on the toe pad. Data are presented for a proximal (prox), intermediate (int) and distal (dist) scansor (see inset of the ventral view of the digit in the upper right corner of the figure). The different symbols on each graph at the left indicate singular values reported for setal length, width and density for eight gecko species by Peattie (2007) (see legend). The vertical dashed line to the right of the symbols for each graph represents the range of values expressed by *Chondrodactylus bibronii* as measured by Webster et al. (2009). The lower right inset is a schematic of the setae on the proximal, intermediate and distal scansors. Below this schematic are values of particular setal lengths (SL; µm), widths (SW; µm) and densities (SD; mm^{-2}) that correspond to proximal and distal stations along the proximodistal length of each scansor (distal to the right).

locations differ in aspect ratio (and therefore bending stiffness) (**Figures 1** and **2**) and the number of spatulate tips that the setae carry (**Figure 4**) (Russell et al., 2007). For *Gekko gecko*, the most proximal fibrils recognizable as true setae (with spatulate tips) are carried on scansor/lamella numbers 14 and 15 (**Figure 4H,I**). These bear relatively few tips (**Figure 4H,I**) (certainly not the hundreds to thousands typically stated to characterize the setae of this species). They are relatively short and range down to less than 25 µm at the proximal ends of these plates (**Figure 3E**). Bending stiffness and the number of adhesive contacts likely directly influence adhesive force production, thus we find it probable that setae from various regions of the toe pad differentially contribute to total adhesive force capacity. In addition to variability in dimensions, fibrillar outgrowths on the subdigital surface of gecko vary considerably in form. The 16th subdigital plate (**Figure 4J**) of *Gekko gecko* bears filaments that are short, bifid at their distal tips and lack spatulae. Such forms may very well be capable of generating considerable van der Waals interactions, but whether such interactions are capable of supporting whole animal attachment and locomotion is not known.

Beyond the setae themselves, the data summarized in **Figure 4** for the Tokay gecko indicate that there are major differences in the surface area of the individual scansors/lamellae that make up the toe pad, with this increasing from distal to proximal. If all setae are idealized as identical structures along the length of the toe pads, this would suggest that those scansors with the greatest surface area contribute a proportionally greater amount of the total adhesive force available to the digit. Average setal tip width and average setal tip area gradually decrease from distal to proximal along the length of the toe pad, however, as does total setal tip area. Together with changes of setal density and setal stalk diameter along the length of the toe pad (**Figures 1** and **2**), the variation of setal structure along the digital transect is bewilderingly complex. What this means for the potential generation of adhesive force at any station within the toe pad is unknown. It is evident, however, that bringing setae into close enough contact with the locomotor substratum to enable them to generate van der Waals and frictional adhesive attachment will be restricted to certain patches on any given footfall (Russell and Johnson, 2007; Russell and Johnson, 2014) rather than the entirety of the toe pad creating such engagement. It is possible that there is compensatory tradeoff along the length of the toe pad with regard to setal dimensions and configuration such that each localized area has the same potential for adhesive force generation (Russell et al., 2007), but we know nothing about the relative force generation attributes of these different setal configurations.

Such patterns of variation have consequences for the way in which we conceive and design simulacra of setae. Our understanding of the adhesive capacity of individual setae is

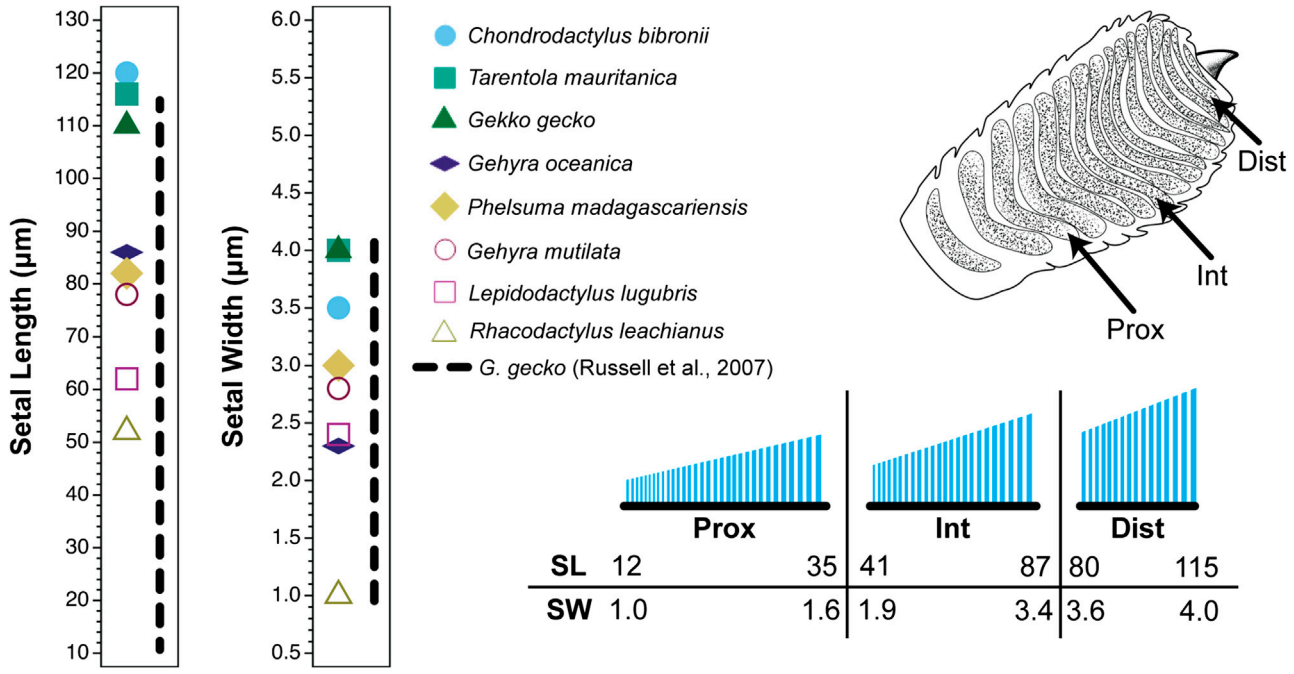

FIGURE 2 | Setal dimensions recorded for digit IV, right manus of the gekkonid gecko *Gekko gecko* showing variation in relation to location on the toe pad. Data are presented for a proximal (prox), intermediate (int) and distal (dist) scansor (see inset of the ventral view of the digit in the upper right corner of the figure). The different symbols on each graph at the left indicate singular values reported for setal length and width for eight gecko species by Peattie (2007) (see legend). The vertical dashed line to the right of the symbols for each graph represents the range of values expressed by *Gekko gecko* as measured by Russell et al. (2007). The lower right inset is a schematic of the setae on the proximal, intermediate and distal scansors. Below this schematic are values of particular setal lengths (SL; μm) and widths (SW; μm) that correspond to proximal and distal stations along the proximodistal length of each scansor (distal to the right).

based upon a single set of observations of filaments taken from an undisclosed part of a digit (Autumn et al., 2000). These observations have neither been repeated for setae with other configurations in the same species, nor for those from other species. There is still much to learn about the mechanical properties of gecko setae and it is unlikely that the single available set of observations (Autumn et al., 2000) suffices to explain the properties of all observed configurations. The current perception of the total clinging ability of a single digit of the Tokay gecko (*Gekko gecko*), as extrapolated from multiplying the adhesive force of a single (idealized) seta (Autumn et al., 2000) by the stated number of setae carried on such a digit (Sun et al., 2005; Autumn et al., 2006; Tian et al., 2006; Hui et al., 2007) is likely a considerable overestimate. Whole animal observations of clinging force per digit result in performance values lower by an order of magnitude or more (Irschick et al., 1996; Autumn et al., 2000, 2002; Autumn and Peattie, 2002). The discrepancy between these two approaches may reside, to some extent in the variability of the number of spatulate tips per seta along the length of the toe pad (**Figure 4**), differences in setal density at different stations on the toe pad (**Figures 1–3**), and the number of setae actually making contact with the surface (which may be reduced based on the surface roughness of the substratum).

There is still much to learn about how individual setae perform and how that performance relates to their structural properties. It is likely that much of this can be achieved through modeling, but the variation must be assessed and appreciated before it can be incorporated into such models. Much of the variation seen (at least within a single species) likely relates to the functioning of the entire setal field and the way in which it is applied to and released from the substratum. It is the entire setal field upon which the animal relies to ensure that, upon each footfall, sufficient contact is made to ensure effective attachment. A deeper understanding of the local regional variation in structure of the setae and their patterning into fields is required for more effective (and purpose-specific) fields of artificial biomimetic fibrils to be developed (Russell et al., 2019). Finding ways of simplifying such surveys of variation is paramount and we here turn to taxa that exhibit, within their ranks, evolutionary transitions from non-adhesively to adhesively competent digits. Such transitions offer the promise of determining what is minimally necessary and sufficient for a functional digital adhesive system to become incorporated into the pre-existing locomotor mechanics of lizards.

EVOLUTIONARY TRANSITIONS

The gekkotan adhesive system has been both gained and lost on multiple occasions (Gamble et al., 2012; Gamble, 2019). Although geckos are widely known for their possession of adhesive toe pads, somewhere in the region of 40% of the 1800+ living species lack them. Peattie (2008) opined that the discovery of "an extant

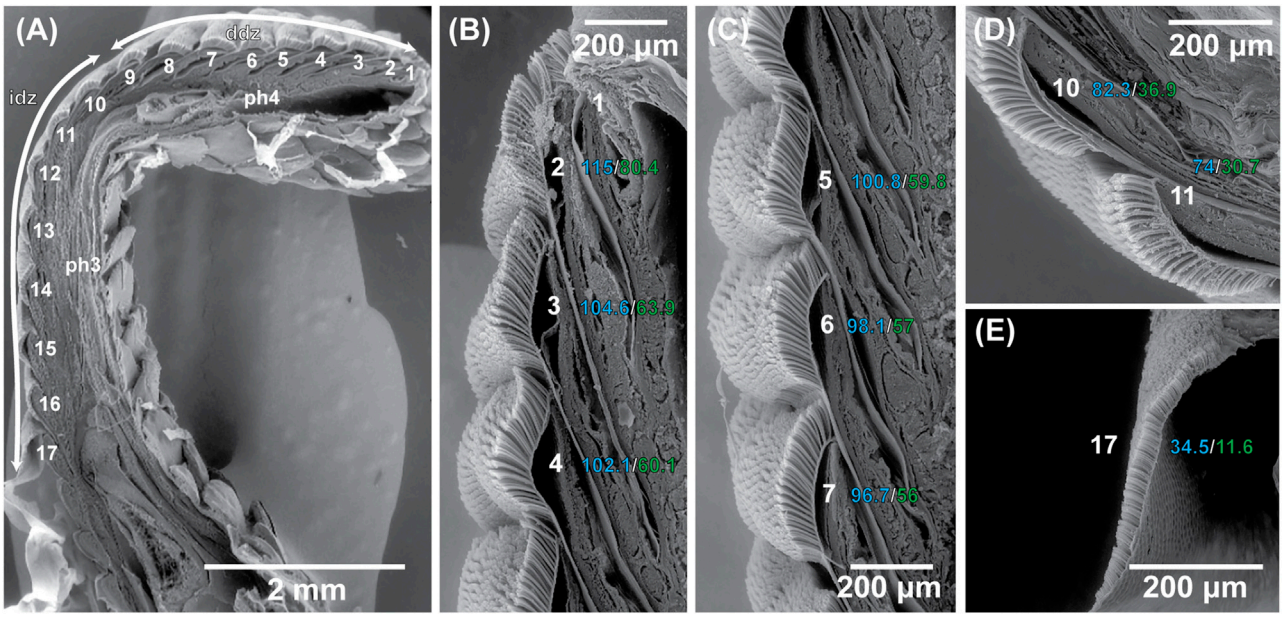

FIGURE 3 | Scanning electron microscopic visualization of the sagittally-sectioned fourth digit of the right manus of the Tokay gecko, *Gekko gecko*. **(A)** Visualization of the entire toe pad showing the location and relative dimensions of the scansors and lamellae (numbered sequentially 1–17 from distal to proximal). The distal region of the digit (ddz) carries a series of scansors (1–9) that lie beneath the fourth phalanx (ph4). The intermediate region of the digit (idz) carries a series of scansors and lamellae (10–17) that lie beneath phalanx 3 (ph3), the transition from scansor to lamella occurring between plates 13 and 14. Lamellae are distinguished from scansors by not being served by branches of the lateral digital tendon system. Panels **(B)–(E)** depict enlargements of the individual scansors and lamellae, showing the relative lengths of the plates and the configuration of the fields of setae carried on their outer surfaces. On each plate the lengths of the filaments decrease from a maximum at the distal end to a minimum at the proximal end, and from distal to proximal along the toe pad the lengths of the filaments decrease, although there is overlap of the span of lengths between adjacent plates. For plates 1–7, 10–11, and 17 maximum filament length (in µm) is indicated in blue and minimum filament length (in µm) in green. Data from Russell et al. (2007).

intermediate" would greatly enhance our understanding of how the gekkotan adhesive system arose. Russell and Gamble (2019) identified a number of candidate taxa for exhibiting such a transition, but only the genus *Gonatodes* has been studied in detail in this regard (Russell et al., 2015; Higham et al., 2017).

Examination of the setal fields of *Gekko* (see above), reveals that the simplest of its spatulated setae are relatively short and subdivided into few terminal branches (**Figure 4H**). We do not know how effective these are in contributing to the total adhesive effectiveness of that species. We do know, however, that the relatively short, sparsely-branched setae of *Gontodes humeralis* (Russell et al., 2015) are sufficiently developed and numerous to permit support of its own body mass at rest and during steady vertical locomotion on a low-friction substratum (Higham et al., 2017). Equivalent locomotor capabilities are not present in any of its close relatives (Higham et al., 2017). Thus, *Gonatodes* provides the opportunity, using appropriate phylogenetic comparison and the establishment of evolutionary polarity (Russell et al., 2015), to establish what might be the minimal set of modifications for the emergence of a functioning digital adhesive system that is effective at the whole organism level.

Trends in digit evolution within the genus *Gonatodes* are depicted in **Figure 5**, which shows the pertinent digital features of three exemplar species. *Gonatodes ocellatus* has digits that are elongate and slender with a marked inflection, beneath which reside enlarged friction plates (**Figure 5A–C**). *Gonatodes vittatus* (**Figure 5F–H**) has relatively shorter digits with a less marked inflection, fewer ventral scales, and a flatter proximal portion. *Gonatodes humeralis* (**Figures 5L–N**) lacks a marked digital inflection and bears noticeably enlarged scales at the base of the digits. Full details of the morphological features of the digits of these three species are provided by Russell et al. (2015). The salient points of the transition to adhesive competence constitute a correlated suite of small shifts leading to the rather dramatic functional outcome of whole animal adhesive competency (Higham et al., 2017).

In the shift from strongly inflected digits, in which friction plates at the midpoint of the digit (Padian and Olsen, 1984; Russell and Bauer, 1990; Peattie, 2008) enhance traction (**Figures 5A–C and 6A–D**), to the adhesively-competent digits of *G. humeralis* (**Figures 5L–N** and **6E,F**), the digits become relatively shorter (in relation to overall body size; **Figure 5A,C,F,H,L,N**). This shift is associated with a change in the relative proportions of the proximal and distal regions of the digits (**Figure 5B,G,M**) and a greater discrepancy in size between the scales on the underside of the digits in their proximal and distal regions (**Figures 5B,G,M** and **6A,C,E**). Those of the proximal zone become relatively larger (both longer and wider), markedly fewer in number and exhibit greater overlap between successive scales (**Figure 5B**, **5G**, and **5M**). The relative

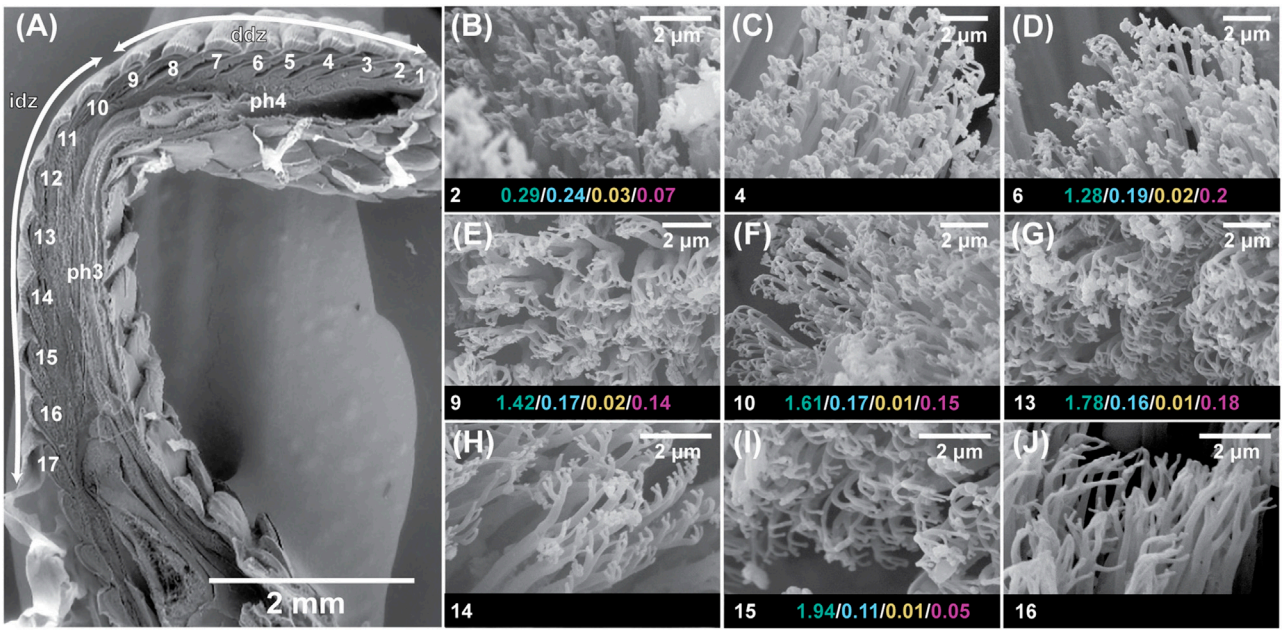

FIGURE 4 | Scanning electron microscopic visualization of the sagittally-sectioned fourth digit of the right manus of the Tokay gecko, *Gekko gecko*. Panel **(A)** is identical to panel **(A)** in **Figure 3**. Panels **(B)–(J)** depict enlargements of the filaments carried on each plate. For scansors/lamellae 2, 6, 9, 10, 13, and 15 the following data are provided: scansor/lamella surface area (mm^2) in green/average setal tip width (µm) in blue/average setal tip area ($µm^2$) in yellow/total setal tip area per scansor/lamella (mm^2) in purple. Data from Russell et al. (2007).

enlargement of the subdigital scales is particularly evident for the friction plates (Padian and Olsen, 1984; Russell and Bauer, 1990) (**Figures 5B,G,M** and **6C,E**) that lie beneath the digital inflection (labeled "inf" on **Figures 5C,5H** and **6C**). In *G. humeralis* (**Figure 5M**), this enlargement is accompanied by a flattening of the proximal part of the digit such that all of the scales on the underside of the proximal region (**Figure 5M**) are co-planar and contact the substratum as a continuous strip. The inflection of the digit thus shifts from a "v"-like configuration when viewed in profile (**Figure 5D,I**) to a step (**Figure 5N,O** and **6E**).

Within the digits, the changes in digital proportions and configuration are accompanied by changes in the arrangement of the phalanges. The basalmost phalanx (**Figures 5D,I,O** and **6C,E**) increases in relative length whereas the penultimate phalanx (**Figures 5D,L,O** and **6C,E**) becomes relatively shorter. The intermediate phalanges (**Figures 5D,L,O** and **6C,E**) retain their relative proportions but become reoriented such that the proximal one becomes linearly aligned with the proximalmost phalanx (**Figures 5D,L,O** and **6E**) and the distal one becomes more vertically-oriented, resulting in the "v"-like configuration of these two phalanges (**Figures 5D** and **6C**) transforming into a step (**Figures 5O** and **6E**). This transition is associated with a proximal extension of the friction plate area (**Figures 5D,L,O** and **6E**) to become more extensive beneath the proximal part of the digit, resulting in the formation of an incipient toe pad (**Figures 5M,N** and **6E**).

In all three exemplar species (**Figure 5**), the epidermal filaments on the underside of the toes are longest on the friction plates. In *G. ocellatus*, they are tapered spinules, the longest being about 3.2 µm in length (**Figure 5E**). In *G. vittatus*, the longest of these filaments are about 4.0–6.0 µm in length, with bifid tips, the split occurring at a point about two thirds of their height from the base (**Figure 5K**), appearing much like the filaments on the proximal lamellae of the digits of *Gekko gecko* (**Figure 4J**). This bifurcation is thought to be associated with friction enhancement (Lange, 1931; Ruibal and Ernst, 1965; Schleich and Kästle, 1979; Peattie, 2008; Müller and Hildenhagen, 2009; Spinner et al., 2013; Russell et al., 2015). In *Gonatodes humeralis*, the lengths, diameters, spacing and form of the subdigital spinules are similar to those of *G. ocellatus* and *G. vittatus* for the scales on the underside of the distal region of the digit (Russell et al., 2015). On the incipient toe pads, however, the distally-situated epidermal outgrowths range from 10.0 to 15.0 µm in length, their density is relatively low and the spacing relatively great (Russell et al., 2015). These are true setae that are divided terminally and carry spatulate tips of about 0.12 µm wide (**Figure 5P,Q**). Such setae are similar in form to those on the most proximal scansors of *Gekko gecko* (**Figures 3E** and **4H**). Unlike the latter, however, the setae on each plate are shorter distally than they are more proximally (13.0 vs 15.1µm), a pattern also observed in *Anolis* (see below; Garner et al., 2020). The branched, spatula-bearing setae occur only at the

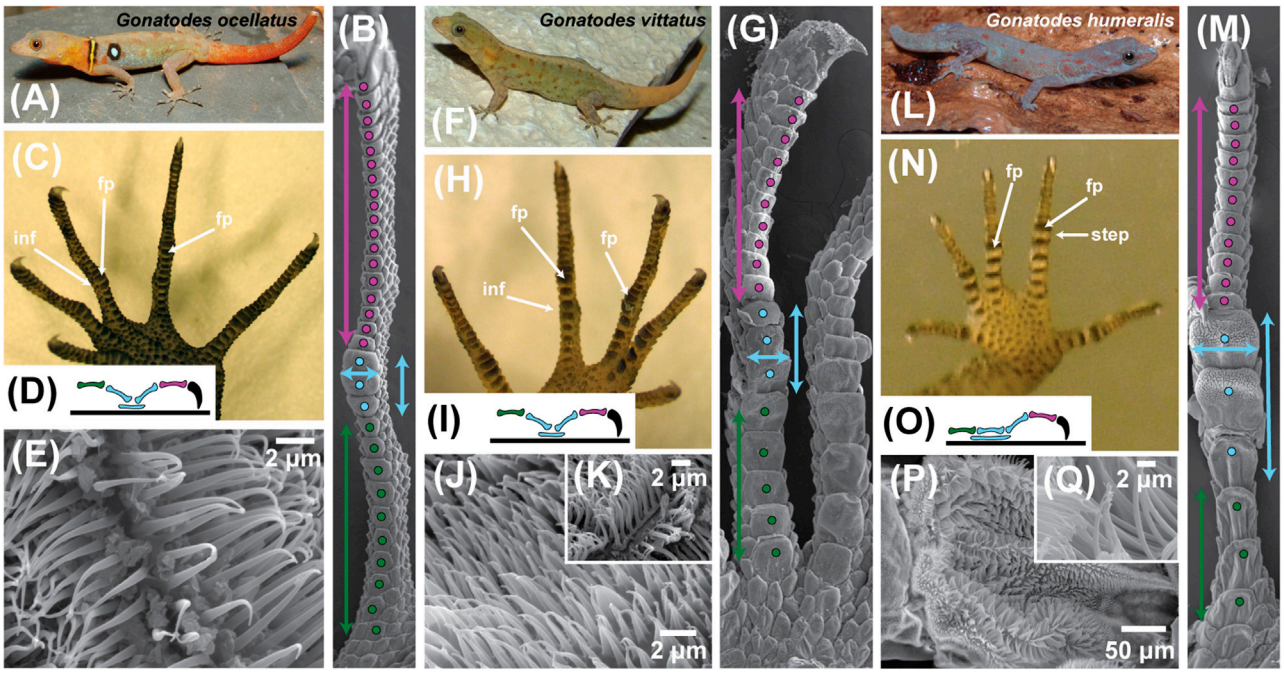

FIGURE 5 | Trends in digit form within the sphaerodactylid gekkotan genus *Gonatodes*. This genus is regarded as lacking subdigital toe pads but exhibits digital adhesive competence in one of its species. Shifts in form and proportion in association with the acquisition of whole animal adhesive competence are illustrated using three exemplar species **(A)** *Gonatodes ocellatus*, **(F)** *G. vittatus* and **(L)** *G. humeralis*. For each species a set of illustrations [panels **(A)–(E)** for *G. ocellatus*; **(G)–(K)** for *G. vittatus* and **(M)–(Q)** for *G. humeralis*) is used to illustrate the trends to whole animal adhesive competence in *G. humeralis*. Panels **(B)**, **(G)** and **(M)** depict scanning electron micrographs of the ventral aspect of digit IV of the left pes (hind foot) of the three species, with features of interest indicated by color-coded symbols. Panels **(C), (H)** and **(N)** represent the ventral view of the left pes of the three species and panels **(D)**, **(I)** and **(O)** depict a schematic of the lateral view of the skeleton of digit IV of the pes of each species, with the phalanges color coded to match the coding in panels **(B)**, **(G)** and **(M)**. Panels **(E)**, **(J)** and **(K)**, and **(P)** and **(Q)** are scanning electron micrographs of the filamentous outgrowths of the epidermis beneath the mid-digit inflection point of digit IV of the pes. Coding conventions are as follows: purple dots–scales beneath the distal region of the digit; purple double-headed vertical arrows–proximodistal extent of the distal region of the digit; purple phalanx–penultimate phalanx; blue dots–scales comprising the friction plate region of the digit; blue double-headed vertical arrows–length of the friction plate region; blue double-headed horizontal arrows–width of the friction plate region; blue phalanges–intermediate phalanges; blue ellipsoid–extent of the friction plate region below the intermediate phalanges; green dots–scales beneath the basal region of the digit; green double-headed vertical arrows–proximodistal extent of the basal region of the digit; green phalanx–basal phalanx; curved, black claw–ungual phalanx and claw. The blue and green dotted regions combined constitute the proximal region of the digit. Abbreviations: fp–friction plates; inf–digital inflection; step–step-like transition between the proximal and distal digital regions in *G. humeralis*.

distal end of the incipient toe pad plates (**Figure 5M**) and give way to spinules more proximally. Transition from simple tapered spinules (there is a mixture of unbranched and branched spinules far proximally on such scales) to setae is thus evident within the confines of a single scale.

Although Peattie (2008) suggested that "true adhesive pads require complex morphological elaborations within the toe" to enable operation of an adhesive system, *Gonatodes humeralis* demonstrates that this is not so, there being no modifications of the digital musculotendinous, circulatory and skeletal systems that are generally considered to be necessary (Peattie, 2008) for the operation of a functional adhesive system in geckos. In terms of their anatomy, the seta-bearing scales of *G. humeralis* are not scansors (Russell, 2002), but instead are more akin to the basal lamellae found in many geckos. The latter bear elaborate epidermal outgrowths, but are not associated with a lateral digital tendon network (see below). The lamellae of the Tokay gecko (*Gekko gecko*) carry epidermal outgrowths that range in length from 1.2 µm at their proximal end to over 12.0 µm distally (Russell et al., 2007: fig. 5), the latter being multiply branched and carrying spatulate tips. Thus, Tokay geckos also possess setae that are carried on highly modified scales (lamellae–**Figure 3A,E**) that lack the characteristics of scansors. Such scales bear a strong structural resemblance to the seta-bearing scales of *G. humeralis* and serve to support the idea of a transition from friction-enhancing to adhesion-promoting structures prior to the widening of the digits and the acquisition of features that provide the capability for actively controlling the adhesive process via distoproximal digital hyperextension (Russell and Bels, 2001).

When climbing vertical, low friction substrata (Higham et al., 2017), *Gonatodes humeralis* employs limb and digit kinematics that are essentially unchanged from those of lizards in general (Brinkman, 1980; Russell and Bauer, 2008) (**Figure 6A,B**). The digits are placed onto the substratum and withdrawn from contact with it such that the distal ends of the digits are the last regions to be withdrawn from it. In *Gekko gecko*, the opposite occurs, enabled by the specialized musculature of the digits that

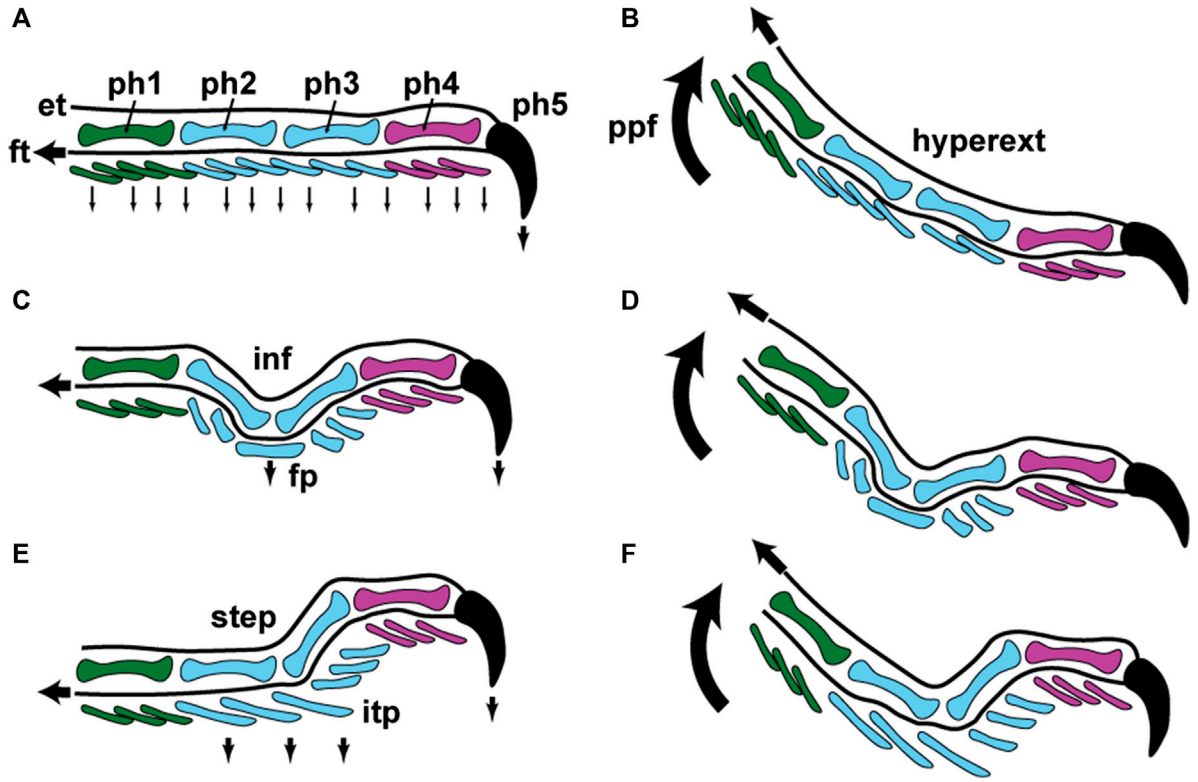

FIGURE 6 | Schematic representations of lizard digit kinematics during locomotion and inferences about how incipient toe pads became incorporated into this pattern. Color conventions for the phalanges (ph1–ph5) and ventral scales of the digit are identical to those in **Figure 5**, panels **(B), (D)**; **(G), (I)**; and **(M), (O)**. **(A)** and **(B)** fourth digit of hind foot in lateral view when applied to the substratum **(A)** and when being raised from contact with it **(B)**. In panel **(A)** the digit is applied to the substratum with the first four phalanges (ph1–ph4) aligned with each other and the fifth (ph5) and its surrounding claw sheath being driven into the substratum via contraction of the flexor muscles of the digit through the flexor tendons (ft–proximally-pointing black arrow). The digit thus operates as a directional device along its long axis, the phalanges behaving as a series of compression struts with the reaction forces driving the ventral surface of the digit (series of small, ventrally-pointing black arrows) into contact with the substratum. In panel **(B)** the foot is peeled from the substratum by the heel being raised from the surface via pedal plantar flexion (ppf–curved, upwardly-pointing arrow). Scales are lifted away from the substratum in a proximal to distal sequence and the claw finally being released from contact through contraction of the digital extensor muscles operating through the extensor tendon (et–proximally-pointing black arrow). The digit is bowed as a result of this, becoming hyperextended (hyperext). Panels **(C)** and **(D)** depict the same situation for a digit with a mid-digital inflection (inf—as encountered in many climbing lizards and as seen in *Gonatodes ocellatus* and *G. vittatus* (**Figure 5**, panels **C, D**; **and H, I**). Because of the inflection only the claw (ph5) and the friction plates (fp) make contact with the surface. The friction plates are driven into contact with the substratum (black, ventrally-directed arrow beneath the friction plates) through tension placed on the flexor tendon (ft) In *Gonatodes* the ventral surface of the friction plates is clad in elongated filaments that may be bifid at their tips to enhance frictional contact (as in *G. vittatus*–**Figure 5**, panel **K**). Release of the digit **(D)** occurs via hyperextension, as depicted in panel **B**. Panels **(E)** and **(F)** show application and release for a gecko with incipient toe pads, such as *Gonatodes humeralis* (**Figure 5**, panels **M, N**). The inflection of the digit is modified into a step (step: **Figure 5**, panel **O**) and the friction plates are transformed into an incipient toe pad (itp) (**Figure 5**, panels **M, N**), the plates of which bear a free distal margin on which spatulate-tipped setae (**Figure 5**, panel **Q**) are carried. Digital mechanics relation to attachment and detachment of the incipient toe pad are essentially unchanged from the patterns depicted in panels **A–D**.

allows their distal ends to be raised from the substratum while their proximal ends remain in contact (Russell, 2002), a process known as hyperextension. When the digits of *Gekko gecko* make contact with the substratum, they do so with their proximal ends first. The distal parts, carrying the toe pads, are unfurled after this. *Gonatodes humeralis*, however, like lizards in general (**Figure 6A–D**), removes its digits from the locomotor surface by raising its heel first and rising onto the tips of the digits, thereby removing the ventral surface of the digits from contact with the substratum in a proximal to distal sequence (Higham et al., 2017). This results in hyperextension of the digits (as it does in lizards in general), and thus hyperextension is involved with removal of the incipient toe pads from adhesive contact with the substratum (**Figure 6E and F**). This breaking of adhesive contact is accommodated within a pre-existing pattern of digit kinematics (**Figure 6**). Adhesive competence of the digits of *G. humeralis* has been subsumed into an essentially unchanged pattern of digit mechanics. Geckos with incipient toe pads provide insights into the most basic aspects of digit configuration and kinematics compatible with the deployment of an effective adhesive system that can assist locomotion (**Figure 6**).

Gonatodes humeralis, unlike other species of *Gonatodes*, can scale smooth, low friction vertically-oriented substrata (Higham et al., 2017). Although the adhesive forces generated are rather

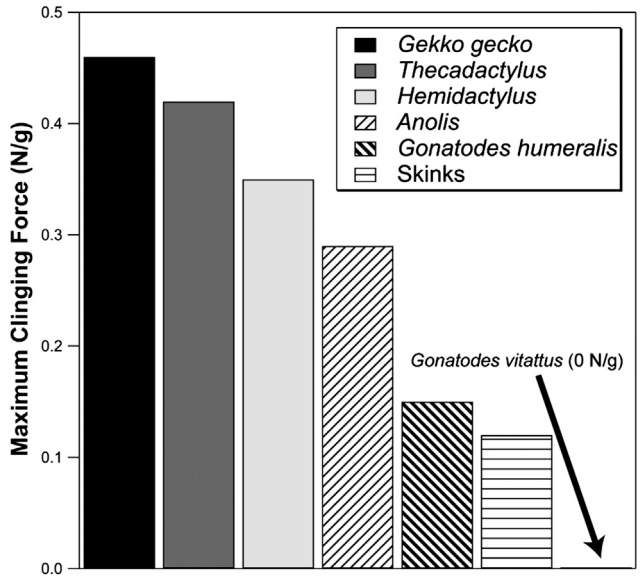

FIGURE 7 | Comparison of the maximum adhesive clinging abilities of lizards (recorded as Newtons per gram of body mass). Skinks exhibit very modest output. Anoles exert, at their greatest output, more adhesive force than skinks. Geckos maximally exert adhesive forces well above that of the best-performing anoles (although lesser-performing geckos overlap with the better-performing anoles). *Gekko gecko* represents the greatest adhesive output yet measured for geckos. In comparison, *Gonatodes vittatus* generates no adhesive attachment forces whereas *G. humeralis* performs as well as many anole species and approaches the lower end of the adhesive performance spectrum of geckos with toe pads. Data from Higham et al. (2017) and Irschick et al. (1996).

low by gecko standards, they are comparable to those generated by anoles (**Figure 7**). Given that the setae of *G. humeralis* are similar in form to the simplest setae of *Gekko gecko* (**Figure 4H**), it can be inferred that the latter are also capable of generating adhesive interactions.

To this point, we have established the following. (I) That the setae of geckos with structurally complex toe pads, such as *Gekko gecko* and *Chondrodactylus bibronii*, exhibit clinal variation in setal dimensions and form along the length of the digit, with the setae located proximally on the toe pad being relatively short and only modestly branched. (II) That similarly built setae are present on the incipient toe pads of geckos such as *Gonatodes humeralis*, which exhibits little in the way of the "complex morphological adaptations" thought to be required for the operation of an adhesive system (Peattie, 2008). The adhesive capabilities of *G. humeralis* suggest that the simpler setae occurring more proximally on the digits of *Gekko gecko* (**Figure 4H,I**) are also adhesively effective. These observations demonstrate that an operational adhesive system is possible in the absence of either complexly branched setae bearing "100–1,000. . .spatulae" (Autumn and Hansen, 2006) and complex anatomical modifications promoting attachment and detachment. We now ask (III) whether such basic levels of organization are evident in toe pads of other taxa, turning our attention to the dactyloid iguanian genus *Anolis* to explore this possibility.

GECKO–ANOLE CONVERGENCE

The evolutionary phenomenon of convergence (the independent acquisition of form and function–Kuhn et al., 2020) potentially provides evidence for determining the most fundamental attributes of complex adaptations (*sensu* Frazzetta, 1975). Independent but structurally similar "solutions" to challenges imposed by the environment provide insights into the evolutionary responses possible. The adhesive toe pads of geckos and anoles are regarded as convergent adaptations (Russell and Garner, in review), their adhesive toe pads having arisen completely independently. This provides the opportunity to examine which attributes are repeated in the two lineages and thus to attempt to establish what is necessary and sufficient for adhesively competent digits to be incorporated and integrated into the lacertilian pattern of locomotion.

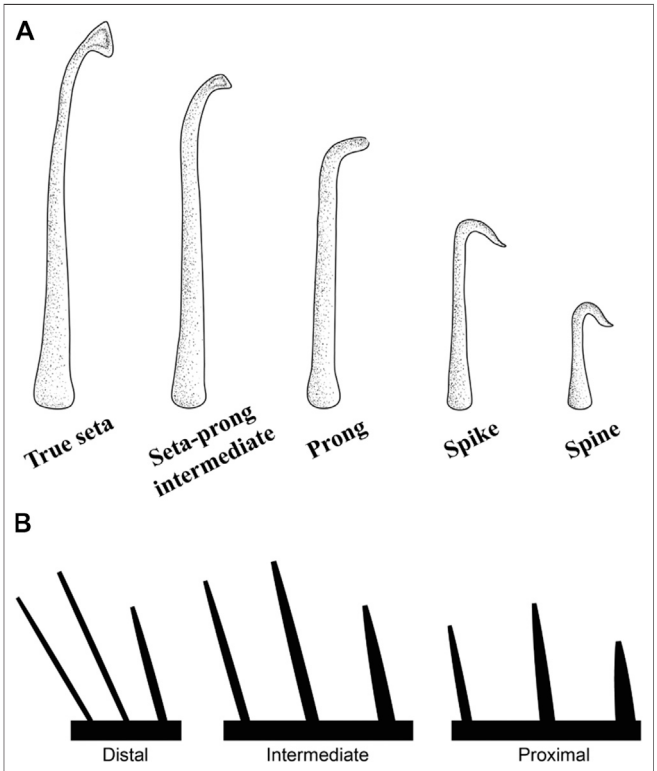

FIGURE 8 | (A) Clinal series of the epidermal outgrowths present on the subdigital pad of anoline lizards (Peterson and Williams, 1981). True setae are outgrowths between 10–30 μm in length that carry a single, expanded spatulate tip. Seta-prong intermediates are outgrowths 5–20 μm in length with flattened tips. Prongs terminate in a blunt tip with a slight taper and are between 5–20 μm in length. Spikes possess straight or recurved, pointed tips and are between 5 and 15 μm in length. Spines are outgrowths up to 5 μm in length with pointed recurved tips. **(B)** Trends of setal morphometrics along subdigital pad regions and lamellar zones of *Anolis equestris* (Garner et al., 2020). Setal length increases and setal base diameter decreases proximodistally along pad regions. Setal length is maximal in the intermediate zones of lamellae. Setal base diameter decreases proximodistally along lamellar zones. Lamella length decreases proximodistally.

Convergence of the Adhesive Fibrils of Geckos and Anoles

As in geckos, the epidermal outgrowths of the subdigital pads of *Anolis* (**Figure 8A**) vary considerably in form along the proximodistal axis of the digit (**Figures 3–5**) and five morphotypes have been recognized (Peterson and Williams, 1981): (1) true setae, outgrowths 10–30 μm in length with expanded, spatulate tips, (2) seta-prong intermediates, 5–20 μm in length with flattened tips, (3) prongs, 5–20 μm in length terminating in blunt tips with a slight taper, (4) spikes, 5–15 μm in length with straight or recurved, pointed tips, and (5) spines, up to 5 μm in length with recurved, pointed tips. All lamellae (scales bearing true setae) of *Anolis* with well-developed subdigital pads are thought to display a proximodistal clinal gradation of all 5 morphotypes (from spines to setae) on each lamella, similar to the clinal variation of epidermal outgrowths on the scales of the incipient toe pads of *Gonatodes humeralis* (Russell et al., 2015). As in gekkotans, it is the true setae and their spatulae that are responsible for the majority of adhesive force capacity in *Anolis*. In *Anolis*, however, the setae are unbranched (Ruibal and Ernst, 1965; Williams and Peterson, 1982; Stork, 1983).

A recent investigation of the morphometrics of the setal arrays of the Cuban knight anole (*Anolis equestris*), a species similar in size to *Gekko gecko*, reveals that its setae increase in length and decrease in basal diameter proximodistally along regions (proximal, intermediate, distal) of the subdigital pad (**Figure 8B**) (Garner et al., 2020). Within a single lamella, however, setal length is greatest in the intermediate region, whereas setal basal diameter decreases proximodistally (**Figure 8B**), a pattern similar to the dimensions observed on the incipient toe pads of *Gonatodes humeralis* (see above). Setal density remains relatively consistent along the entire subdigital pad and along regions (proximal, intermediate, distal) of individual lamellae.

The profuse branching noted for the archetypal gecko seta (Autumn et al., 2000) should result in greater adhesive force production compared to an unbranched seta of similar size, such as those of *Anolis* (Arzt et al., 2003; Peattie and Full, 2007; Murphy et al., 2009; Garner et al., 2020). Thus, if geckos and anoles differed only in the nature of the structural hierarchy of their setae, the setal fields of gekkotans, when scaled against body mass, should be able to induce greater adhesive forces. Gekkotan and anoline setae and setal fields, however, differ not only in setal size and number of spatulae per seta, but also in the number of fibrils present per unit area (Garner et al., 2020). Indeed, when compared to setal density patterns in *Chondrodactylus bibronii*, those of *Anolis equestris* are 33.3–78 times as densely packed. Application of the Johnson-Kendall-Roberts (JKR) theory of elastic contact to the assessment of adhesive performance of gekkotan and anoline setal arrays, in conjunction with the comprehensive morphological data obtained for the setal fields of *Gekko gecko* (Russell et al., 2007) and *Anolis equestris* (Garner et al., 2020), reveal that adhesive performance of gekkotan and anoline setal arrays should theoretically be similar when taking the differences in the morphology and configuration of their setae and setal fields into consideration. Anoles appear to compensate for the lack of structural hierarchy of their setae by possessing greater setal density compared to geckos (Garner et al., 2020), although structural hierarchy of setae may be important in other aspects of the gekkotan adhesive system (Persson, 2003; Yao and Gao, 2007). Peterson et al. (1982) also note that anoles appear to combat increased adhesive demands related to increases in body size by possessing greater setal densities. Not all geckos, however, are characterized by such densities, and the setae of *A. equestris* are only 1.75–2.5 times as densely packed as those of *Naultinus elegans*, the gecko so far examined to exhibit the highest density and shortest setae, and these are also not profusely branched (Bauer, 1998). **Table 2** reveals that many diplodactylid geckos have short, slender, densely packed setae, with values greatly exceeding those for gekkonid geckos (the group to which *Chondrodactylus* and *Gekko* belong). Very little is known about the adhesive capabilities of diplodactylid geckos, although this is now beginning to be explored (Pillai et al., 2020). This again reveals that there is much more to be learned about the variation in structure and function of gekkotan setae, cautioning against making sweeping generalizations that appear to characterize geckos overall.

Theabove-mentioned calculations of adhesive performance of geckos and anoles, based on setal morphometrics (Garner et al., 2020), are supported by whole animal observations. Ruibal and Ernst (1965) qualitatively observed gecko and anole adhesive locomotion on a vertical raceway and noted no obvious differences in performance. More comprehensive work by Irschick et al. (1996) corroborated this finding and found that static clinging performance of geckos and anoles is not markedly different (**Figure 7**). The general similarity of setal form and material properties of anoles and geckos indicate the requirement for similar loading conditions (normal load followed by shear load) because measurements of whole animal adhesive performance indicate that their adhesive systems can be engaged in the same manner (Irschick et al., 1996). The means by which setal loading and unloading occurs in anoles, however, differs from that typically attributed to geckos (Russell and Bels, 2001), but is similar to that employed by *Gonatodes humeralis* (**Figure 6E,F**), with subdigital pad retraction progressing proximodistally (as opposed to the distoproximal pattern thought to be typical of geckos). This pattern of release of the setae is consistent with setal length increasing proximally along the length of each lamella (**Figure 8B**), suggesting that clinal variation in setal length is related to the biomechanics of subdigital pad peeling (Johnson and Russell, 2009; Garner et al., 2020), although further empirical work is needed to validate this.

Convergence of the Digital Anatomy of Geckos and Anoles

The anatomical modifications generally associated with the adhesive system in geckos (Peattie, 2008) are only modestly

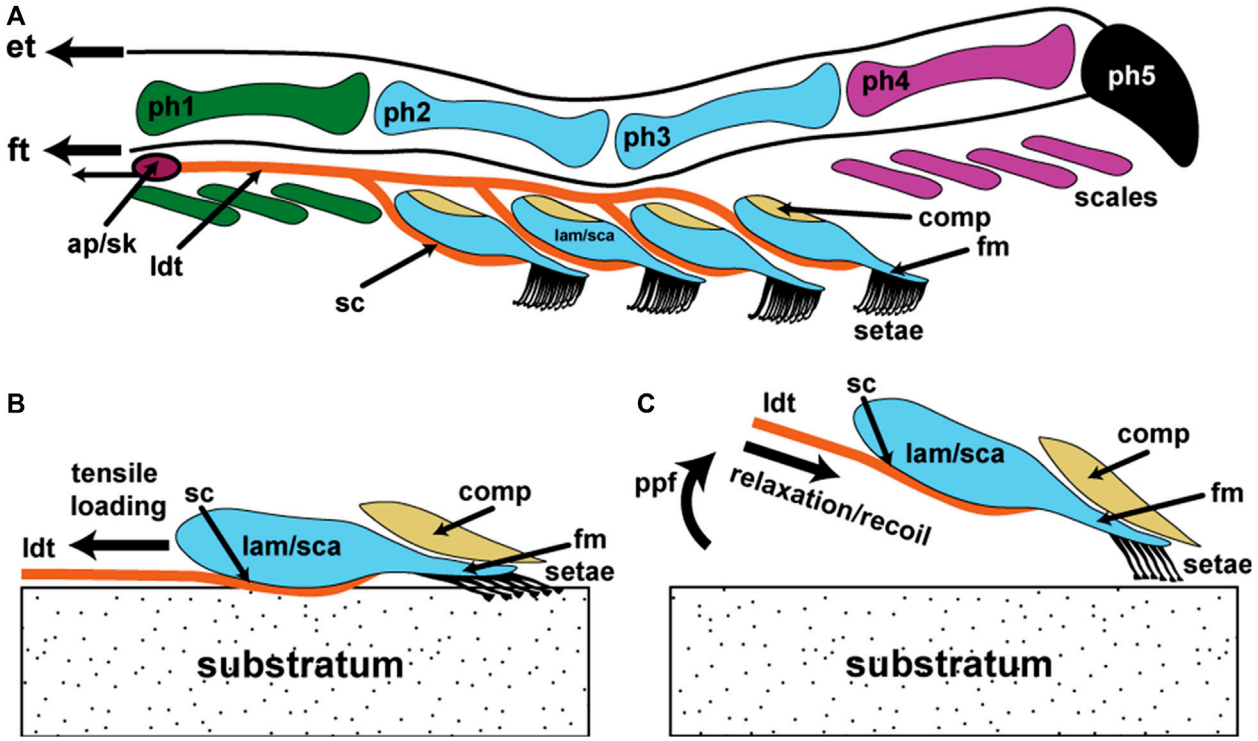

FIGURE 9 | Schematic representation of the basic components of the lacertilian digital adhesive system assembled as a model for the operation of this basic mechanism. Information about structure is derived from a combination of anoles and gekkotan taxa exhibiting incipient toe pads. **(A)** Diagrammatic lateral view of digit IV. Phalanges 1–5 (ph1–ph5) and their associated ventral scales (color coded to match the phalanges) that bear micro-ornamentation that is modified into unbranched setae bearing a single spatulate tip on the free margin of enlarged scales (lamellae/scansors; lam/sca) situated beneath phalanges 2 and 3. The rows of setae on each lamella/scansor increase in length from distal to proximal. Each lamella/scansor has an expanded proximal zone with an extensive dermal and subdermal core. Its ventral integument consists of epidermis and a dermal stratum compactum (sc) dominated by linearly-arranged (parallel with the long axis of the digit) collagen fibers that is continuous with the lateral digital tendons (ldt) lying to either side of the phalanges. This sc/ldt continuum is linked to an aponeurotic network (ap) controlled by muscles in the flexor compartment of the lower limb and anchored onto skeletal elements (sk) that limit the tensile loading placed upon it. Overlying the setal batteries is a flexible compliance system (comp) that, when pressurized during application of the lamellae/scansors to the substratum, assists in aligning the setal batteries into a continuous setal field along the length of the toe pad. Extensor (et) and flexor (ft) tendons, through the actions of their associated muscles, control the claw and flexion and extension of the entire digit. Lamellae/scansors also possess a thin, flexible free margin (fm). **(B)** Diagrammatic lateral view of a single lamella/scansor with the setae applied to the substratum in the adhesion mode. **(C)** Diagrammatic lateral view of a single lamella/scansor in the process of being released from adhesive contact with the substratum as a result of digital hyperextension, driven by pedal plantarflexion (ppf).

represented by *Anolis*, being confined to skeletal (phalangeal) and tendinous features (Russell and Gamble, 2019). The digits of *Anolis* exhibit little in the way of muscular modifications akin to those exhibited by at least some gecko lineages (Russell and Gamble, 2019). *Anolis* does, however, incorporate a compliance-promoting cushioning system (**Figure 9A**) into its toe pads, in the form of hypertrophied lacunar cells of the epidermis (Russell, 2016). This cushioning system is unique to *Anolis* but is analogous and positionally similar to the vascular (Russell, 1981) and adipose tissue (Russell and Bauer, 1988) compliance structures found among geckos.

Modifications of the intermediate phalanges enhance both the pressing of the toe pads onto the substratum during attachment and their hyperextension during release (**Figure 6E,F**). The toe pads of *Anolis* are located basally on the digits, ventral to the location of the digital inflection (between phalanges 2 and 3 of digit IV) of its close relatives, in a similar location to those of *Gonatodes humeralis* (**Figures 5M,N** and **6E,F**). Associated with the toe pads of *Anolis* are lateral digital tendons similar to those of geckos. These course along the lateral and medial borders of the phalanges of the digit and branch to serve each lamella. As in geckos, the dense, collagen rich connective tissue of the lateral digital tendons is continuous with the stratum compactum of the dermis of the lamellae (the lamellar dermis lacking a stratum laxum). Thus, as in geckos (Russell, 1986), the lateral digital tendon/lamellar dermis complex furnishes a tensile skeleton that provides connectivity between the setae and skeleton at the metapodial-phalangeal joint capsules. This chain reinforces the junction between the integument and the underlying tissues (Russell, 1986) and permits the tensile load imposed on the setae (Peterson et al., 1982) to be channeled to points of resistance deep within the manus and pes, and to be regulated in its magnitude.

SYNTHESIS AND THE GENERATION OF A MODEL OF THE FUNDAMENTALS OF FORM AND FUNCTION OF THE DIGITAL ADHESIVE SYSTEM OF LIZARDS

Our examination of transects of setal fields constituting the toe pads of geckos, the evolutionary transition to functionally adhesive digits in the naked-toed gecko genus *Gonatodes*, and the comparison of the structure of gecko and anole adhesive systems has allowed us to deduce what we consider to represent the most basic level of organization and mechanical operation of such a system. Both setal structure, at its most elaborate, and the configuration and operation of the entire adhesive system of the Tokay gecko (*Gekko gecko*) are complex (Russell, 2002). They permit impressive feats of behavior that are assisted by the deployment of the adhesive apparatus (Autumn 2006), but are not typical of all geckos.

Examination of the variability of setal structure exhibited by several species of geckos (and anoles) across the entirety of their setal fields indicates that setae vary considerably in form and dimensions depending on the particular location on the digit (Russell et al., 2007; Johnson and Russell, 2009; Webster et al., 2009; Russell and Johnson, 2014; Garner et al., 2020). Such data indicate that there is no single morphology of setae for the toe pads of lizards bearing adhesive pads and that these parameters vary regionally, presumably reflecting the functional contribution of particular regions of the toe pads to the totality of the adhesive capabilities of the entire setal fields. A common feature, however, regardless of the particular dimensions of setae at different stations on the toe pad, is that the setae on individual scansors show gradation in length (**Figures 1** and **2**). In the case of *Gekko* and *Chondrodactylus*, increase in length of the setae occurs in a proximal to distal direction (**Figures 1** and **2**). This has been suggested to be associated with the achievement of simultaneous release of all setae on a scansor as the digit is hyperextended (Johnson and Russell, 2009). In the case of *Gonatodes humeralis* (Russell et al., 2015) and *Anolis equestris* (Garner et al., 2020), however, setal length decreases proximodistally. Interestingly, the locomotor kinematics of *Gonatodes humeralis* and *Anolis* are essentially unchanged from those typical of lizards in general, the toes being peeled from the substratum proximodistally as the ankle and wrist extend (a motion called plantarflexion) (Russell and Bels, 2001; Higham et al., 2017) (**Figure 6B,D,F**). Thus, a seta-based adhesive mechanism has been co-opted into a pre-existing pattern of foot and digital mechanics in both *G. humeralis* and *Anolis*.

The relatively simple setae, although still branched, at the proximal end of the setal fields of *Gekko gecko* somewhat resemble those of *Gonatodes humeralis* (**Figure 5M,N**). *Gonatodes humeralis* exhibits the early stages of evolutionary acquisition of adhesively-competent digits (Russell et al., 2015) and is capable of adhesively-assisted locomotion on vertical, smooth, low-friction surfaces (Higham et al., 2017). It lacks any of the major skeletal, muscular, tendinous and compliance modifications evident in the digits of the Tokay gecko (Russell, 2002), but is still able to attach and detach its adhesively-competent digits in a controlled fashion (Higham et al., 2017). The morphological modifications that it does show are related to changes of scale size and number on the underside of the digits, alterations of in phalangeal proportions and orientation, and transformation of some of the epidermal outgrowths on the expanded scales of the incipient toe pads into setae with spatulate tips. There are no evident lateral digital tendons associated with the plates of the incipient toe pads, and it appears that tensile loading is placed upon the setae and lamellae by gravitational loading, potentially restricting the circumstances in which this rudimentary adhesive system can be engaged.

It is interesting to note that all geckos capable of supporting static and dynamic adhesion on vertical, low friction substrata, including *Gekko gecko* and *Gonatodes humeralis*, possess setae that exhibit some level of branching. Comparison of both *Gekko gecko* and *Gonatodes humeralis* with *Anolis* reveals a setal structure that is much simpler than that of *Gekko gecko* or *Gonatodes humeralis*. *Anolis* possesses unbranched setae that are relatively short and present in higher density (compared to that of gekkonid geckos–**Table 2**). Its clinging abilities (**Figure 7**) are similar to those of many geckos (Irschick et al., 1996), despite the absence of structural hierarchy that purportedly increases the adhesive capacity of a single fiber (Arzt et al., 2003; Peattie and Full, 2007; Murphy et al., 2009; Garner et al., 2020). The higher setal density of *Anolis* is thought to compensate for the lack of branching in anoline setae (Garner et al., 2020). A number of species of *Anolis* also appear to respond to the increased adhesive demands of increased in body size by increasing setal density (Peterson et al., 1982). Like *G. humeralis*, *Anolis* exhibits proximal to distal hyperextension of its digits (**Figure 6**) and its setae increase in length from distal to proximal on each lamella (**Figure 8B**), consistent with the simultaneous release hypothesis proposed by Johnson and Russell (2009). In terms of digital anatomy, *Anolis* exhibits a simpler manifestation than *Gekko*, but is more fully elaborated than that of *Gonatodes humeralis*. *Anolis* exhibits phalangeal modifications associated with application of the toe pads to the substratum and their hyperextension upon release. Beyond this it also has a lateral digital tendon system and a compliance mechanism associated with enhancing contact of the setae with the substratum.

The foregoing yields information about what is minimally necessary and sufficient for the effective operation of a lacertilian digital filamentous adhesive system. Such information should potentially be useful for simplifying approaches to the development of biomimetic derivatives. From the above-mentioned observations we can conclude that a functional adhesive system, effective at the whole animal level, can exist and operate with relatively short and unbranched or moderately branched setae, and that operational control of such a system requires only minor morphological and behavioral changes compared to lizards in general. Squamate adhesive systems do not need to be morphologically highly divergent from their ancestral non-adhesive precursors. Basic whole animal adhesive competence can be attained with relatively simple morphological and biomechanical underpinnings.

The situation evident in *Anolis* and gekkotans with incipient toe pads provides the best approximation of the necessary and sufficient components. A model for the basic functioning of a digit-based, filamentous adhesive system is presented in **Figure 9**. The presence of spatulate-tipped setae arranged in orderly ranks and rows provide the necessary adhesive interface with the substratum. Such setae do not have to be branched to be effective but must be present in sufficient numbers to enable effective support (of the animal's body mass) when using only a (potentially small) subset of them on surfaces that permit only patchy contact. If a rolling-type pattern of contact and detachment (as embodied in hyperextension of digits, whether proximodistal or distoproximal) is involved, with the filaments carried on a series of plates, then a staggering of filament length, row by row, that is geometrically integrated with the mechanics (angulation) of plate release, is needed to promote simultaneous release and attachment of the fibrils (**Figure 9**).

Digits are inherently directional devices when used to interact with the substratum during locomotion. As such they undergo tensile loading. Setae are inherently tensile (Williams and Peterson, 1982) and directional (Autumn et al., 2000) structures that require a mechanism of controllable application (**Figure 9B**) and release (**Figure 9C**) of tensile loading to exploit available attachment forces. The lateral digital tendon system of anole and gecko digits facilitates this load-bearing function (**Figure 9**). The lamellae (and scansors) bear setae that are intimately connected to such a mechanism through firm interdigitation of the epidermis with a richly collagenous, longitudinally-oriented fibrous sheet that invests the inner face of the lamella/scansor and that is continuous with the lateral digital tendons (Russell, 1986). The collagen fibers, at rest, exhibit crimp and upon loading it is likely that the crimp is straightened (**Figure 9B**), the collagenous bundles thereby shifting into their high modulus phase, preventing further extension. We suggest that the magnitude of extension allowed is tuned to the parallel preload required for the setae to be effectively adhesively engaged with the substratum (Autumn et al., 2000) and that this tensile loading is maintained until detachment is initiated. In lizards, we propose that this is accomplished by the lateral digital tendon/stratum compactum mechanism being connected deep in the foot such that constant tension can be maintained by internally regulated locking devices. We suggest that the perpendicular preload (Autumn et al., 2000) required to establish initial setal tip contact is provided by the unfurling of the hyperextended digit (**Figure 6B,D,F**), and that tension imposed through the lateral digital tendon/stratum compactum system (**Figure 9A**) places tension on the lamella/scansor and its setae, resulting in the lowering the setal angle and the bringing of the broad face of the spatulate tip(s) into contact with the substratum (**Figure 9B**). The small amount of movement required for the application of the parallel preload (Autumn et al., 2000) is likely controlled by the very limited extensibility of the lateral digital tendons/stratum compactum. When this tension is released, the lateral digital tendons and the collagenous networks in the lamellae recoil and the crimp in the collagen fibers is restored (**Figure 9C**). This results in the setae being relieved of their tensile loading, permitting their shafts to increase their angle relative to the surface of the lamella (**Figure 9C**) and allowing them to approach their critical release angle (**Figure 9C**). This process occurs as the digit is hyperextended through actions of the extensor muscles and angular changes between the phalanges driven by pedal plantarflexion (**Figure 6B,D,F**).

Both pad-bearing anoles and geckos exhibit some sort of compliance mechanism to assist with enhancing contact with the substratum (Russell, 1981, 2002, 2017). This may chiefly assist in aligning the setal arrays on individual lamellae/scansors so that the setal field essentially forms one unified structure, with the junctions between the plates being overlain by a continuous cushioning mechanism (**Figure 9A**,**B**). It may also assist the setal fields to match more closely with irregularities in the substratum (Russell and Johnson, 2007). Such a compliance mechanism (differently constructed in different lineages) is a common feature of lizards with adhesive toe pads. Compliance of the setal fields with the substratum may also be assisted by the setae being carried on a relatively slender, free distal component of the lamellae/scansors (**Figure 9**). Indeed, in *Anolis*, the setae are borne on a very thin free margin that is comprised solely of epidermal tissue. The free margin of geckos is slightly more robust. In both cases, the free margin is overlain by the compliance mechanism.

CONCLUSION

The last two decades have witnessed a flood of investigations examining the form, function, and properties of the gecko adhesive system, many of them aiming, directly or indirectly, to inform the design and fabrication of the next generation of smart, reversible, fibrillar synthetic adhesives. Most of such applied research, however, has focused on relatively few species of gecko that exhibit complex manifestations of the entire adhesive apparatus, perhaps unnecessarily complicating the biomimetic process. Here we contend that studies examining setal transects of adhesive pad-bearing lizards, evolutionary transitions from non-adhesive to adhesively competent digits, and the convergent evolution of the adhesive apparatuses of geckos and anoles provide a wealth of information from which researchers may gain engineering inspiration. Specifically, these biologically focused studies collectively demonstrate what is minimally structurally necessary for an effective and functional fibrillar adhesive system that is capable of reversibly attaching to vertical, low friction substrata. We urge researchers focused on bio-inspired adhesives to consider the natural variation in both structure and function of the adhesive fibrils and their associated higher order digital anatomy exhibited by lizards with subdigital adhesive pads. Such information is likely to not only increase the available information for successful

biomimicry, but also decrease functional disparities between synthetic simulacra and their natural counterparts.

DATA AVAILABILITY STATEMENT

The original contributions presented in the study are included in the article. Further inquiries should be directed to the corresponding author.

ETHICS STATEMENT

The animal studies were reviewed and approved by the University of Calgary Animal Research and Education Executive Committee under Protocol Numbers BI2002-013, BI2008-24 for those studies completed by AR and the University of Akron Institutional Animal Care and Use Committee Protocol Number 19-07-13 NGC for those studies completed by AG.

AUTHOR CONTRIBUTIONS

AR conceived of the approach and wrote the first draft of the paper. AR and AG developed the ideas further and contributed equally to subsequent drafts. AR developed the ideas for the figures and these were refined by AG. AR employed various aspects of his previous research on geckos and anoles to develop the synthesis of ideas and AG provided new insights into anole and gecko adhesion based upon his ongoing research.

ACKNOWLEDGMENTS

We thank Stas Gorb and Ken Nakano for inviting us to contribute to this Research Topic collection of papers. AR acknowledges financial support from a Natural Science and Engineering Research Council of Canada Discovery Grant (9745–2008).

REFERENCES

Alexander, R. M. (2006). Introduction to biotribology: animal locomotion. *Proc. Inst. Mech. Eng. Part J J. Eng. Tribol.* 220, 649–656. doi:10.1243/13506501jet157

Alibardi, L., and Toni, M. (2005). Distribution and characterization of proteins associated with cornification in the epidermis of gecko lizard. *Tissue Cell* 37, 423–433. doi:10.1016/j.tice.2005.05.005

Arzt, E., Gorb, S., and Spolenak, R. (2003). From micro to nano contacts in biological attachment devices. *Proc. Natl. Acad. Sci.* U.S.A. 100, 10603–10606. doi:10.1073/pnas.1534701100

Autumn, K. (2006). How gecko toes stick. Am. Sci. 94, 124–132. doi:10.1511/2006.58.124

Autumn, K., and Gravish, N. (2008). Gecko adhesion: evolutionary nanotechnology. *Philos. Trans. R. Soc. Math. Phys. Eng. Sci.* 366, 1575–1590. doi:10.1098/rsta.2007.2173

Autumn, K., and Hansen, W. (2006). Ultrahydrophobicity indicates a non-adhesive default state in gecko setae. *J. Comp. Physiol.* 192, 1205–1212. doi:10.1007/s00359-006-0149-y

Autumn, K., and Peattie, A. M (2002). Mechanisms of adhesion in geckos. Integr. Comp. Biol. 42, 1081–1090. doi:10.1093/icb/42.6.1081

Autumn, K., Liang, Y. A., Hsieh, S. T., Zesch, W., Chan, W. P., Kenny, T. W., et al. (2000). Adhesive force of a single gecko foot-hair. *Nature* 405, 681–685. doi:10.1038/35015073

Autumn, K., Majidi, C., Groff, R. E., Dittmore, A., and Fearing, R. (2006). Effective elastic modulus of isolated gecko setal arrays. *J. Exp. Biol.* 209, 3558–3568. doi:10.1242/jeb.02469

Autumn, K., Sitti, M., Liang, Y. A., Peattie, A. M., Hansen, W. R., Sponberg, S., et al. (2002). Evidence for van der Waals adhesion in gecko setae. *Proc. Natl. Acad. Sci. U. S. A.* 99, 12252–12256. doi:10.1073/pnas.192252799

Bauer, A. M. (1998). Morphology of the adhesive tail tips of carphodactyline geckos (Reptilia: Diplodactylidae). *J. Morphol.* 235, 41–58.

Bhushan, B. (2007). Adhesion of multi-level hierarchical attachment systems in gecko feet. *J. Adhes. Sci. Technol.* 21, 1213–1258.

Bhushan, B., and Sayer, R. A. (2007). *Gecko feet: natural attachment systems for smart adhesion in applied scanning probe methods VII*. Berlin: Springer, 41–76.

Brinkman, D. (1980). Structural correlates of tarsal and metatarsal functioning in Iguana (Lacertilia; Iguanidae) and other lizards. *Can. J. Zool.* 58, 277–289.

Chen, B., Wu, P. D., and Gao, H. (2008). Hierarchical modelling of attachment and detachment mechanisms of gecko toe adhesion. *Proc. R. Soc. -Math. Phys. Eng. Sci.* 464, 1639–1652. doi:10.1098/rspa.2007.0350

Dalla Valle, L., Nardi, A., Toffolo, V., Niero, C., Toni, M., and Alibardi, L. (2007). Cloning and characterization of scale beta-keratins in the differentiating epidermis of geckoes show they are glycine-proline-serine-rich proteins with a central motif homologous to avian beta-keratins. *Dev. Dynam.* 236, 374–388. doi:10.1002/dvdy.21022

Del Campo, A., and Arzt, E. (2007). Design parameters and current fabrication approaches for developing bioinspired dry adhesives. *Macromol. Biosci.* 7, 118–127. doi:10.1002/mabi.200600214

Dellit, W. (1934). Zur anatomie und physiologie der geckozehe. *Jenaische Z. Für Naturwissenschaft.* 68, 613–656.

Filippov, A. E., and Popov, V. (2006). To optimal elasticity of adhesives mimicking gecko foot-hairs. *Phys. Lett.* 358, 309–312. doi:10.1016/j.physleta.2006.05.034

Frazzetta, T. H. (1975). *Complex adaptations in evolving populations*. Sunderland, MA: Sinauer Associates.

Gamble, T. (2019). Duplications in corneous beta protein genes and the evolution of gecko adhesion. *Integr. Comp. Biol.* 59, 193–202. doi:10.1093/icb/icz010

Gamble, T., Greenbaum, E., Jackman, T. R., Russell, A. P., and Bauer, A. M. (2012). Repeated origin and loss of adhesive toepads in geckos. *PLoS One* 7, e39429. doi:10.1371/journal.pone.0039429

Gao, H., Wang, X., Yao, H., Gorb, S., and Arzt, E. (2005). Mechanics of hierarchical adhesion structures of geckos. *Mech. Mater.* 37, 275–285. doi:10.1016/j.mechmat.2004.03.008

Garner, A. M., and Russell, A. P. (In review). Revisiting the classification of squamate adhesive setae: historical, morphological, and functional perspectives.

Garner, A. M., Wilson, M. C., Wright, C., Russell, A. P., Niewiarowski, P. H., and Dhinojwala, A. (2020). The same but different: the setal arrays of anoles and geckos indicate alternative approaches to achieving similar adhesive effectiveness. *J. Anat.* doi:10.1111/joa.13377

Gravish, N., Wilkinson, M., and Autumn, K. (2008). Frictional and elastic energy in gecko adhesive detachment. *J. R. Soc. Interface* 5, 339–348. doi:10.1098/rsif.2007.1077

Hallahan, D. L., Keiper-Hrynko, N. M., Ganzke, T. S., Toni, M., Dalla Valle, L., and Alibardi, L. (2008). Gene expression in analysis of adhesive pads of gecko digits shows they mainly code for significant production of cysteine-rich and glycine-rich beta-keratins. *J. Exp. Zool. B.* 312, 58–73. doi:10.1098/rsif.2007.1077

Hansen, W. R., and Autumn, K. (2005). Evidence for self-cleaning in gecko setae. *Proc. Natl. Acad. Sci. U.S.A.* 102, 385–389. doi:10.1073/pnas.0408304102

Higham, T. E., Gamble, T., and Russell, A. P. (2017). On the origin of frictional adhesion in geckos: small morphological changes lead to a major biomechanical transition in the genus *Gonatodes*. *Biol. J. Linn. Soc.* 120, 503–517. doi:10.1111/bij.12897

Hiller, U. (1968). Untersuchungen zum Feinbau und zur Funktion der Haftborsten von Reptilien. *Z. Morphol. Tiere.* 62, 307–362.

Huber, G., Gorb, S. N., Spolenak, R., and Arzt, E. (2005). Resolving the nanoscale adhesion of individual gecko spatulae by atomic force microscopy. *Biol. Lett.* 1, 2–4. doi:10.1098/rsbl.2004.0254

Hui, C.-Y., Jagota, A., Shen, L., Rajan, A., Glassmaker, N., and Tang, T. (2007). Design of bio-inspired fibrillar interfaces for contact and adhesion—theory and experiments. *J. Adhes. Sci. Technol.* 21, 1259–1280. doi:10.1163/156856107782328362

Irschick, D. J., Austin, C. C., Petren, K., Fisher, R. N., Losos, J. B., and Ellers, O. (1996). A comparative analysis of clinging ability among pad-bearing lizards. *Biol. J. Linn. Soc.* 59, 21–35.

Johnson, M. K., and Russell, A. P. (2009). Configuration of the setal fields of *Rhoptropus* (Gekkota: gekkonidae): functional, evolutionary, ecological and phylogenetic implications of observed pattern. *J. Anat.* 214, 937–955. doi:10.1111/j.1469-7580.2009.01075.x

Kellar, E., and Bogue, R. (2008). Biomimetic adhesives: a review of recent developments. *Assemb. Autom.* 28, 282–288. doi:10.1108/01445150810904422

Kuhn, A., Skipwith, P., and Overcast, I. (2020). Digest: an emerging model system for understanding ecomorphological convergence. *Evolution*. 74, 696–697. doi:10.1111/evo.13935

Lange, B. (1931). "Integument der Sauropsiden," in *Hanbuch der vergleichenden Anatomie der Wirbeltiere*. Editors L. Bolk, E. Göppert, E. Kallius, and W. Lubosch (Berlin: Urban and Schwarzenberg).

Lee, H., Lee, B. P., and Messersmith, P. B. (2007). A reversible wet/dry adhesive inspired by mussels and geckos. *Nature* 448, 338–341. doi:10.1038/nature05968

Maderson, P. F. A. (1964). Keratinized epidermal derivatives as an aid to climbing in gekkonid lizards. *Nature* 203, 780–781.

Müller, R., and Hildenhagen, T. (2009). Untersuchungen zu Subdigital-und Subkaudalstrukturen bei Chamäleons (Sauria: chamaeleonidae). *Sauria*. 31, 41–54. doi:10.1515/9783110928242.11

Murphy, M. P., Kim, S., and Sitti, M. (2009). Enhanced adhesion by gecko-inspired hierarchical fibrillar adhesives. *ACS Appl. Mater. Interfaces* 1, 849–855. doi:10.1021/am8002439

Niewiarowski, P. H., Stark, A. Y., and Dhinojwala, A. (2016). Sticking to the story: outstanding challenges in gecko-inspired adhesives. *J. Exp. Biol.* 219, 912–919. doi:10.1242/jeb.080085

Northen, M. T., Greiner, C., Arzt, E., and Turner, K. L. (2008). A Gecko-inspired reversible adhesive. *Adv. Mater.* 20, 3905–3909. doi:10.1063/pt.5.028438

Padian, K., and Olsen, P. E. (1984). Footprints of the Komodo monitor and the trackways of fossil reptiles. *Copeia*. 14, 662–671.

Peattie, A. M., and Full, R. J. (2007). Phylogenetic analysis of the scaling of wet and dry biological fibrillar adhesives. *Proc. Natl. Acad. Sci. Unit. States Am.* 104, 18595–18600. doi:10.1002/ar.20706

Peattie, A. M. (2008). Subdigital setae of narrow-toed geckos, including a Eublepharid (*Aeluroscalabotes felinus*). *Anat. Rec.* 291, 869–875. doi:10.1073/pnas.0707591104

Peattie, A. M. (2007). *The function and evolution of gekkotan adhesive feet*. Berlin: Springer.

Persson, B. N. J. (2003). On the mechanism of adhesion in biological systems. *J. Chem. Phys.* 118, 7614–7621. doi:10.1063/1.1562192

Peterson, J. A., Benson, J. A., Ngai, M., Morin, J., and Ow, C. (1982). Scaling in tensile "skeletons": structures with scale-independent length dimensions. *Science* 217, 1267–1270.

Peterson, J. A., and Williams, E. E. (1981). A case history in retrograde evolution: the *onca* lineage in anoline lizards: II. Subdigital fine structure. *Bull. Mus. Comp. Zool.* 149, 215–268.

Pillai, R., Nordberg, E., Reidel, J., and Schwarzkopf, L. (2020). Nonlinear variation in clinging performance with surface roughness in geckos. *Ecol. Evol.* 10, 2597–2607. doi:10.1002/ece3.6090

Poe, S., Nieto-Montes de Oca, A., Torres-Carvajal, O., De Queiroz, K., Velasco, J. A., Truett, B., et al. (2017). A phylogenetic, biogeographic, and taxonomic study of all extant species of *Anolis* (Squamata; Iguanidae). *Syst. Biol.* 66, 663–697. doi:10.1093/sysbio/syx02

Pugno, N. M., and Lepore, E. (2008). Observation of optimal gecko's adhesion on nanorough surfaces. *Biosystems* 94, 218–222. doi:10.5353/th_b4552928

Rizzo, N. W., Gardner, K. H., Walls, D. J., Keiper-Hrynko, N. M., Ganzke, T. S., and Hallahan, D. L. (2006). Characterization of the structure and composition of gecko adhesive setae. *J. R. Soc. Interface* 3, 441–451. doi:10.1154/1.2754446

Ruibal, R., and Ernst, V. (1965). The structure of the digital setae of lizards. *J. Morphol.* 117, 271–293. doi:10.1002/jmor.1051170302

Russell, A. P., Baskerville, J., Gamble, T., and Higham, T. E. (2015). The evolution of digit form in *Gonatodes* (Gekkota: sphaerodactylidae) and its bearing on the transition from frictional to adhesive contact in gekkotans. *J. Morphol.* 276, 1311–1332. doi:10.1002/jmor.20420

Russell, A. P., and Bauer, A. M. (1990). Digit I in pad-bearing gekkonine geckos: alternate designs and the potential constraints of phalangeal number. *Mem. Qld. Mus.* 29, 453–472.

Russell, A. P., and Bauer, A. M. (1988). Paraphalangeal elements of gekkonid lizards - a comparative survey. *J. Morphol.* 197, 221–240. doi:10.1002/jmor.1051970208

Russell, A. P., and Bauer, A. M. (2008). "The appendicular locomotor apparatus of *Sphenodon* and normal-limbed Squamates," in *Biology of the Reptilia*. Editors C. Gans, A. S. Gaunt, and K. Adler (Ithaca, New York: Society for the Study of Amphibians and Reptiles), 1–466.

Russell, A. P., and Bels, V. (2001). Digital hyperextension in *Anolis sagrei*. *Herpetologica*. 57, 58–65. doi:10.7717/peerj.1874/fig-1

Russell, A. P. (1981). Descriptive and functional anatomy of the digital vascular system of the tokay, *Gekko gecko*. *J. Morphol.* 169, 293–323.

Russell, A. P., and Gamble, T. (2019). Evolution of the gekkotan adhesive system: does digit anatomy point to one or more origins?. *Integr. Comp. Biol.* 59, 131–147. doi:10.1093/icb/icz006

Russell, A. P., and Garner, A. M. (In review). "Solutions to a Sticky Problem: convergence of the adhesive systems of geckos and anoles (Reptilia: Squamata)," in *Convergent Evolution*. Editors V. Bels and P. Legreneur. (New York, NY: ISTE).

Russell, A. P. (2002). Integrative functional morphology of the gekkotan adhesive system (Reptilia: Gekkota). *Integr. Comp. Biol.* 42, 1154–1163. doi:10.1093/icb/42.6.1154

Russell, A. P., and Johnson, M. K. (2014). Between a rock and a soft place: microtopography of the locomotor substrate and the morphology of the setal fields of Namibian day geckos (Gekkota: gekkonidae: *Rhoptropus*). *Acta Zool.* 95, 299–318. doi:10.1111/azo.12028

Russell, A. P., Johnson, M. K., and Delannoy, S. M. (2007). Insights from studies of gecko-inspired adhesion and their impact on our understanding of the evolution of the gekkotan adhesive system. *J. Adhes. Sci. Technol.* 21, 1119–1143. doi:10.1163/156856107782328371

Russell, A. P., and Johnson, M. K. (2007). Real-world challenges to, and capabilities of, the gekkotan adhesive system: contrasting the rough and the smooth. *Can. J. Zool.* 85, 1228–1238. doi:10.1139/Z07-103

Russell, A. P., Stark, A. Y., and Higham, T. E. (2019). The integrative biology of gecko adhesion: historical review, current understanding, and grand challenges. *Integr. Comp. Biol.* 59, 101–116. doi:10.1093/icb/icz032

Russell, A. P. (1986). The morphological basis of weight-bearing in the scansors of the tokay gecko (Reptilia: sauria). *Can. J. Zool.* 64, 948–955.

Russell, A. P. (2016). The structure of anoline (Reptilia: Dactyloidae: *Anolis*) toe pads in relation to substratum conformity. *Acta Zool.* 14, 2–10. doi:10.1111/azo.12180

Russell, A. P. (2017). The structure of anoline (Reptilia: Dactyloidae: *Anolis*) toe pads in relation to substratum conformity. *Acta Zool.* 98, 300–309. doi:10.1111/azo.12180

Schleich, H. H., and Kästle, W. (1979). Hautstrukturen als kletteranpassungen bei *Chamaeleo* and *Cophotis* (Reptilia: sauria: Chamaeleonidae, Agamidae). *Salamandra* 16, 95–100.

Schleich, H. H., and Kästle, W. (1986). Ultrastrukturen an Gecko-Zehen (reptilia: sauria: gekkonidae). *Amphib.-Reptil.* 7, 141–166.

Spinner, M., Westhoff, G., and Gorb, S. N. (2013). Subdigital and subcaudal microornamentation in chamaeleonidae: a comparative study. *J. Morphol.* 274, 713–723. doi:10.1002/jmor.20137

Stork, N. E. (1983). A comparison of the adhesive setae on the feet of lizards and arthropods. *J. Nat. Hist.* 17, 829–835.

Sun, W., Neuzil, P., Kustandi, T. S., Oh, S., and Samper, V. D. (2005). The nature of the gecko lizard adhesive force. *Biophys. J.* 89, L14–L17. doi:10.1529/biophysj.105.065268

Tian, Y., Pesika, N., Zeng, H., Rosenberg, K., Zhao, B., McGuiggan, P., et al. (2006). Adhesion and friction in gecko toe attachment and detachment. *Proc. Natl. Acad. Sci. U. S. A.* 103, 19320–19325. doi:10.1073/pnas.0608841103

Toni, M., Dalla Valle, L., and Alibardi, L. (2007). The epidermis of scales in gecko lizards contains multiple forms of beta-keratins including basic glycine-proline-serine-rich proteins. *J. Proteome Res.* 6, 1792–1805. doi:10.1021/pr060626+

Uetz, P., Slavenko, A., Meiri, S., and Heinicke, M. (2020). Gecko diversity: a history of global discovery. *Isr. J. Ecol. Evol.* 1, 1–9. doi:10.1163/22244662-bja10003

Webster, N. B., Johnson, M. K., and Russell, A. P. (2009). Ontogenetic scaling of scansorial surface area and setal dimensions of *Chondrodactylus bibronii* (Gekkota: gekkonidae): testing predictions derived from cross-species comparisons of gekkotans. *Acta Zool.* 90, 18–29. doi:10.1111/j.1463-6395.2008.00324.x

Williams, E. E., and Peterson, J. A. (1982). Convergent and alternative designs in the digital adhesive pads of scincid lizards. *Science* 215, 1509–1511.

Xu, Q., Wan, Y., Hu, T. S., Liu, T. X., Tao, D., Niewiarowski, P. H., et al. (2015). Robust self-cleaning and micromanipulation capabilities of gecko spatulae and their bio-mimics. *Nat. Commun.* 6, 8949. doi:10.1038/ncomms9949

Yao, H., and Gao, H. (2007). Bio-inspired mechanics of bottom-up designed hierarchical materials: robust and releasable adhesion systems of gecko. *Bull. Pol. Acad. Sci. Tech. Sci.* 55, 141–150. doi:10.1163/156856107782328326

Yao, H., and Gao, H. (2006). Mechanics of robust and releasable adhesion in biology: bottom–up designed hierarchical structures of gecko. *J. Mech. Phys. Solid.* 54, 1120–1146. doi:10.1016/j.jmps.2006.01.002

Yu, M., Ji, A., and Dai, Z. (2006). Effect of microscale contact state of polyurethane surface on adhesion and friction. *J. Bionic Eng.* 3, 87–91. doi:10.1016/s1672-6529(06)60012-7

Conflict of Interest: The authors declare that the research was conducted in the absence of any commercial or financial relationships that could be construed as a potential conflict of interest.

frontiers in Mechanical Engineering

ORIGINAL RESEARCH
published: 28 April 2021
doi: 10.3389/fmech.2021.661422

Adhesive Droplets of Glowworm Snares (Keroplatidae: *Arachnocampa* spp.) Are a Complex Mix of Organic Compounds

Jonas O. Wolff[1]*, *Janek von Byern*[2], *Dakota Piorkowski*[3], *Jian Fang*[4], *Xungai Wang*[5], *Lewis Adler*[6], *Donald S. Thomas*[7], *James M. Hook*[7,8] and *Sean J. Blamires*[9]*

[1] Department of Biological Sciences, Macquarie University, Sydney, NSW, Australia, [2] Ludwig Boltzmann Institute, Vienna, Austria, [3] Department of Life Science, Tunghai University, Taichung, Taiwan, [4] College of Textile and Clothing Engineering, Soochow University, Suzhou, China, [5] Institute for Frontier Materials, Deakin University, Waurn Ponds Campus, Geelong, VIC, Australia, [6] Bioanalytical Mass Spectrometry Facility, Mark Wainwright Analytical Centre, University of New South Wales, Sydney, NSW, Australia, [7] NMR Facility, Mark Wainwright Analytical Centre, University of New South Wales, Sydney, NSW, Australia, [8] School of Chemistry, University of New South Wales, Sydney, NSW, Australia, [9] School of Biological, Earth and Environmental Science, University of New South Wales, Sydney, NSW, Australia

Adhesive snares built from silks are fascinating adaptations that have rarely evolved outside spiders. Glowworms (*Arachnocampa* spp.) are an iconic part of the fauna of Australia and New Zealand that combine the construction of a sticky snare with a bioluminescent lure. Recently, the structure and biomechanical properties of glowworm silk have been studied in detail, but the chemical composition of its adhesive coating, and how it varies between species of *Arachnocampa* remained unclear, limiting an understanding of the glue function. Here, we studied the chemical composition of the water-soluble fraction of the adhesive droplets from the snares in cave and epigaeic populations of three species of *Arachnocampa* from mainland Australia, Tasmania, and New Zealand, using a combination of nuclear magnetic resonance and mass spectrometry. We found that glowworm glues comprise a large variety of small organic compounds, with organic acids, amino acids, amino acid derivates, alcohols, urea, and urea derivates being the major fraction, supplemented by small amounts of sugars, fatty acids, and other organic compounds. While there was a general overlap in the compounds detected in the adhesives of all tested *Arachnocampa* species and populations, the relative amounts differed considerably. We expect that these differences are a product of diet rather than an adaptive response to different environments, but experiments are needed for clarification. The high amount of polar substances and compounds that are hygroscopic at high humidity explains the adhesive properties of the viscous solution and its stability in damp environments. These results contribute to our understanding of the unique prey capture strategy of glowworms. Further, the comparison with convergent spider webs highlights the use of small polar compounds as plasticizers of macro-molecular bioadhesives as a general principle. This may inspire the biomimetic design of novel pressure sensitive adhesives with high performance under high humidity conditions.

Keywords: biological adhesive, adhesive secretion, chemical ecology, silk, water-based adhesive

OPEN ACCESS

Edited by:
Ken Nakano,
Yokohama National University, Japan

Reviewed by:
Pierangiola Bracco,
University of Turin, Italy
Yoshitaka Nakanishi,
Kumamoto University, Japan

***Correspondence:**
Jonas O. Wolff
jonas.wolff@mq.edu.au
Sean J. Blamires
sean.blamires@unsw.edu.au

Specialty section:
This article was submitted to Tribology, a section of the journal Frontiers in Mechanical Engineering

Received: *30 January 2021*
Accepted: *26 March 2021*
Published: *28 April 2021*

Citation:
Wolff JO, von Byern J, Piorkowski D, Fang J, Wang X, Adler L, Thomas DS, Hook JM and Blamires SJ (2021) Adhesive Droplets of Glowworm Snares (Keroplatidae: Arachnocampa spp.) Are a Complex Mix of Organic Compounds. Front. Mech. Eng. 7:661422. doi: 10.3389/fmech.2021.661422

INTRODUCTION

Many invertebrates use viscous fluids or soft solids as reversible adhesives to capture prey, such as in spider capture silk, velvetworm slime, and harvestmen glue (Betz and Kölsch, 2004; Suter and Stratton, 2009; Haritos et al., 2010; Sahni et al., 2010; Wolff et al., 2014; Wolff and Gorb, 2016). Such adhesives have recently come into focus in ecological and biodiversity research (Agnarsson and Blackledge, 2009; Zhang and Weirauch, 2013; Blamires et al., 2014; Wolff et al., 2016; Opell et al., 2018; Diaz et al., 2020). Biological adhesives are often adapted toward special requirements, such as generating adhesion to contaminated substrates or at variable humidity, and show a remarkable performance under conditions that are challenging for artificial adhesives (Wolff et al., 2014; Opell et al., 2018; Diaz et al., 2020). Therefore, they have also been proposed as promising biomimetic models for the design of novel artificial adhesives (von Byern and Grunwald, 2010; Sahni et al., 2011).

Glowworms (Nematocera: *Arachnocampa* spp.) are the larvae of the fungus gnat, small dipterans that live in the temperate rain forests of Australia and New Zealand. These animals are remarkable in their ability to spin adhesive capture threads and lure prey insects with a bioluminescent organ (Broadley and Stringer, 2001; Meyer-Rochow, 2007). The "web" consists of a horizontal mucous tube that functions as a retreat, and from which a curtain of capture threads hangs (Gatenby and Cotton, 1960). These capture threads bear elliptical mucous droplets that are regularly arranged like beads on a string (Meyer-Rochow, 2007; von Byern et al., 2016). Glowworms spin their snares only in cool, moist, and dark microhabitats, such as caves, the banks of creeks, or shaded canyon walls. Their adhesiveness requires the high humidity to stay hydrated and remain sticky (von Byern et al., 2016; Piorkowski et al., 2018). Under these humid conditions the threads perform remarkably well (Piorkowski et al., 2018; von Byern et al., 2019), where artificial adhesives fail due to water disturbing either the adhesive bonding (Tan et al., 2008) or cohesive strength of the adhesive material itself (Musto et al., 2002).

In a previous study, it was found that adhesion is produced by the salivary gland of the glowworm and is predominantly comprised of water and urea or uric acid, with the addition of trace elements (von Byern et al., 2016), and amino acids (Walker et al., 2015). However, both the exact identity of compounds in the mucous and their variation between species and populations has remained unclear. These aspects are important for advancing our comprehension of the adhesive and hygroscopic functions of this material, to ascertain the relationship between ecological factors and mucous production. Integrating previous results on the function of the glowworm adhesive with a better understanding of the chemical identity and variation of the material could also reveal the principles by which adhesion is enhanced under high humidity, which could help to improve the performance of artificial adhesives and surface coatings.

Here, we comparatively studied the water-soluble fraction of the capture threads of three species and multiple populations of Australian and New Zealand *Arachnocampa*. We expected the adhesive material to contain salts, which have previously been shown to play an important role in adhesion generation by controlling material hydration in the viscid silk of orb web spiders (Sahni et al., 2014). Further, we expected, the chemical profiles show a high variability and differ between populations and species, either due to diet effects, as observed for spider glues (Blamires et al., 2014, 2017), or as an adaptive response to different habitats, as shown for bioluminescent regulation in glowworms (Sharpe et al., 2015).

METHODS

Collection of Wild Glowworm Threads

Arachnocampa tasmaniensis

We collected adhesive capture silk threads from 10 *A. tasmaniensis* nests from the ceilings of Mystery Creek and Bradley Chesterman caves, in Southwest National Park, Tasmania, Australia, in October 2017 (see Piorkowski et al., 2017, 2018 for details about the sites). Collection was permitted by the Tasmanian Department of Primary Industries, Parks, Water, and the Environment (permit No. FA15189 and FA17188). We spooled the capture threads around plastic 500 μL pipette tips, which were immediately placed into 3 mL sterile fluid collection tubes for transportation to the Mark Wainwright Analytical centre at the University of New South Wales, Sydney, Australia,. The 3 mL tubes holding the samples wound around pipette tips were all sealed air tight and transported under identical conditions, i.e., taped together and wrapped in foam to prevent temperature variability. All samples were brought to the laboratory at the Mark Wainwright Analytical Centre, UNSW, Sydney, in tact within 2 days of collection, whereupon they were refrigerated at ∼4°C.

Arachnocampa richardsae

Samples of *A. richardsae* capture threads were collected from the Glow Worm Tunnel on the Newnes Plateau, NSW, under the license SL102029 granted by the NSW National Parks and Wildlife Service. The collection method was the same as for *A. tasmaniensis*.

Arachnocampa luminosa

Samples of *A. luminosa* capture threads were collected with the same method as above, from populations in Spellbound and Hollow Hill Caves (North Island). Samples were transported on dry ice. Five additional samples were collected in biosilicate glass micro-tubes from a population at the river banks and slopes along the Tatare Tunnels Walk in Franz Josef, Westland (South Island). New Zealand samples were collected under the research permit 39535-RES granted by the Department of Conservation of New Zealand.

Sampling Quantities

The number of threads collected per sample varied for each of the species sampled and from sample to sample as the length of the thread and size of the glue droplets showed immense variation between and among species. In general, between 10 and 20 *A. tasmaniensis* threads were wound around one pipette tip, between 20 and 30 *A. richardsi* threads were wound around

one pipette tip, and between 10 and 29 *A. luminosa* threads were wound around a single pipette tip. Ten tips per species and location were collected. However, because the total amount of material extracted per tip was insufficient of itself for the NMR procedures (see below) several (∼2–5) tips were pooled prior to processing. The amount of material collected in the field was not weighed. However, the pooled samples were weighed and diluted to standardize their concentrations prior to being prepared for NMR and MS.

Sample Preparation for NMR Spectroscopy

All of the glowworm glue samples were washed off the sampling tips with a 150 mM potassium phosphate buffer, pH 6.95, containing an internal reference (deuterated trimethylsilyl propanoate, TMSP), a pH indicator (difluorotrimethylsilanylphosphonic acid, DFTMP), and 99.96% D_2O (Cambridge Isotope Laboratories). Single samples were washed with multiple aliquots of buffer adding up to a total volume of 180 μL. Combined samples were prepared from a single aliquot added sequentially to 3 mm NMR tubes (Norell) from the first to last sample in a volume of 180 μL.

Nuclear Magnetic Resonance (NMR) Spectroscopy

Proton (^{1}H) NMR spectroscopy was performed using a Bruker Avance III HD 600 MHz spectrometer (600.13 MHz, ^{1}H; 150.9 MHz ^{13}C) fitted with a 5 mm cryoprobe. Samples were stored in a refrigerated Sample Jet autosampler on the magnet. NMR spectra were acquired using the program TOPSPIN 3.6.0 (Bruker, Preston, Australia). Proton solvent suppression was performed using 1D NOESY pre-saturation (*noesy1dpr*) and the HOD solvent residual chemical shift. ^{1}H-^{13}C HSQC spectra were acquired using an optimized pulse program in the Bruker library (*hsqcedetgpsisp2.4*) (Palmer et al., 1991; Kay et al., 1992; Willker et al., 1993; Schleucher et al., 1994; Zwahlen et al., 1997). A sweep width (time domain) of 12 ppm (2k) in the ^{1}H and 240 ppm (512) in the ^{13}C dimension was used over 16 scans. ^{1}H-^{13}C HMBC spectra were acquired using the Bruker pulse program *hmbcgplpndqf* (Cicero et al., 2001). A sweep width (time domain) of 12 ppm (2k) in the ^{1}H and 195 ppm (512) in the ^{13}C dimension was used over 16 scans. Fourier transformation, phasing, solvent filtering, chemical shift referencing, baseline correction, and reference line shape convolution were performed in TOPSPIN. We compared the relative peak positions of our deconvoluted spectra with a spectral reference database for biological metabolites using BAYESIL (Bovey and Mirau, 1996) to identify the individual organic and inorganic hygroscopic salts, and any other small and large molecular weight compounds, within each species' glues. The relative concentration of each of the compounds identified was calculated upon baseline correction and integration of the peaks using TOPSPIN.

Mass Spectrometry

We used mass spectrometry (MS) to verify the presence of compounds identified in the NMR study as follows.

Individual pipette tips containing glowworm glue were washed with 300 uL methanol (HPC grade, Merk, USA) into a 1.5 mL Eppendorf tube. A 7 uL aliquot of each sample was taken for analysis on an Orbitrap LTQ XL (Thermo Fisher Scientific, San Jose Ca, USA) ion trap mass spectrometer using a nanospray (nano-electrospray) ionization source to generate ions from the analytes in solution.

The instrument was calibrated with a standard calibration solution (as outlined in the instrument manual) on each of the analyses. All analyses were carried out in positive ion mode using the orbitrap Fourier Transform MS analyser at a resolution of 100,000. Sample aliquots were injected into a glass needle and inserted onto the nanospray source. Ions generated were measured over the molecular mass range 100–2,000 m/z. Data was acquired in full scan mode over 60 s. The data generated were analyzed using the Qual Browser feature in Xcaliber 2.1 (Thermo Fisher Scientific, San Jose, Ca, USA) and with searches against the ChemSpider (Royal Society of Chemistry) database.

RESULTS

Compounds Found in the Adhesives of Glowworms

NMR spectra showed peaks that could be assigned to a range of organic molecules, allowing an estimate of the composition of the low mass (i.e., molecules <300 Da) fraction of the glowworm mucous (**Table 1**, **Supplementary Material 1** and **2**). The majority of this fraction comprised alcohols (mainly ethanol and methanol), organic acids (e.g., lactic acid, acetic acid, hydroxyisovaleric acid, hydroxybutyric acid), amino acids (dominantly tyrosine, but also glutamine, threonine, alanine, leucine, and others), and amino acid derivates (e.g., betaine and putative methylhistidines). Urea was consistently found across samples, albeit with varying concentration: In the adhesive of *A. tasmaniensis* urea was the most abundant compound, whereas in the adhesive of *A. richardsae* it made only a small fraction (**Figure 1**), with a concentration of only 2.6% of that in *A. tasmaniensis* (**Table 1**). Further fractions comprised monosaccharides (predominantly glucose) and other organic compounds such as amines and acetates. Trace amounts of acetate and acetone may be contaminants from glassware that was used for sample processing. NMR showed signs of lipids, which, however, could not be further identified with our NMR approach, as it is limited to smaller weight compounds. However, the MS spectra showed several high abundance peaks that indicate the presence of fatty acids, e.g., at 309 and 360 m/z in South Island *A. luminosa*, 244 m/z in *A. richardsae*, and 282, 304, and 585 m/z in *A. tasmaniensis* (**Figure 2**). Further peaks at >500 m/z cannot be unequivocally identified, due to the sheer number of possible isomers, and the additional information from NMR is lacking. The MS spectra revealed that, in contrast to the other two species, the adhesive of *A. richardsae* contained numerous higher mass compounds at higher concentrations. MS also confirmed the presence of urea and urea derivates (see below).

TABLE 1 | Summary of compounds identified from the water soluble fraction of glowworm glue droplets with solution state ^{1}H NMR spectroscopy.

Compound	Confidence score	*A. tasmaniensis*	*A. richardsae*	*A. luminosa* (North Isl.)	*A. luminosa* (South Isl.)
Urea	8	**260.4** (150.9)	**7.2** (47.6)	**21.5** (77.8)	**124.9** (128)
Ethanol	9	**83.9** (3.0)	3.1 (1.0)	2.0 (1.6)	**148.4** (2.6)
1-Methylhistidine	5	**71.3** (3.0)	0.0 (1.0)	**26.1** (1.6)	**97.7** (2.6)
Tyrosine	10	**45.0** (3.0)	0.1 (1.0)	**9.9** (1.6)	**42.3** (2.6)
Formate	9	**31.4** (2.4)	0.6 (0.8)	1.4 (1.2)	36.1 (2.0)
Glycerol	9	30.2 (3.0)	0.1 (1.0)	3.1 (1.6)	**69.7** (2.6)
L-Lactic acid	10	24.2 (6.0)	2.9 (1.9)	6.7 (3.1)	4.0 (5.1)
D-Glucose	10	21.7 (15.1)	3.2 (4.8)	9.2 (7.8)	25.5 (12.8)
L-Glutamine	10	19.7 (3.0)	1.8 (1.0)	**9.3** (1.6)	6.8 (2.6)
L-Threonine	9	15.2 (3.0)	1.7 (1.0)	6.5 (1.6)	10.7 (2.6)
L-Alanine	10	15.0 (6.0)	0.0 (1.9)	0.5 (3.1)	1.1 (5.1)
L-Leucine	10	14.6 (3.0)	3.1 (1.0)	2.0 (1.6)	6.2 (2.6)
Valine	10	14.3 (6.0)	**5.8** (1.9)	0.9 (3.1)	4.7 (5.1)
L-Proline	10	11.8 (3.0)	0.0 (1.0)	2.3 (1.6)	7.9 (2.6)
Isoleucine	7	11.6 (3.0)	**66.3** (1.0)	2.7 (1.6)	4.5 (2.6)
L-Ornithine	6	9.8 (9.1)	1.5 (2.9)	3.3 (4.7)	0.0 (7.7)
Tryptophan	5	9.4 (9.1)	0.3 (2.9)	2.3 (4.7)	2.1 (7.7)
3-Hydroxybutyric acid	10	9.1 (3.0)	1.0 (1.0)	5.5 (1.6)	5.6 (2.6)
Xanthine	7	9.0 (3.0)	0.3 (1.0)	0.6 (1.6)	0.6 (2.6)
Glycine	10	7.5 (3.0)	0.6 (1.0)	1.3 (1.6)	0.0 (2.6)
Acetic acid	10	6.1 (2.1)	0.2 (0.7)	0.0 (1.1)	39.9 (1.8)
L-Lysine	9	5.3 (3.0)	1.6 (1.0)	2.6 (1.6)	2.9 (2.6)
L-Glutamic acid	10	5.1 (3.0)	**8.5** (1.0)	0.0 (1.6)	16.3 (2.6)
L-Phenylalanine	10	4.8 (3.0)	0.6 (1.0)	5.0 (1.6)	5.1 (2.6)
Citric acid	10	4.7 (3.0)	1.3 (1.0)	5.4 (1.6)	1.3 (2.6)
Aspartate	9	4.6 (7.5)	2.9 (2.4)	5.1 (3.9)	3.2 (6.4)
Myo-inositol	9	4.3 (3.0)	0.5 (1.0)	0.0 (1.6)	4.5 (2.6)
2-Hydroxybutyric acid	9	4.1 (3.0)	0.0 (1.0)	3.5 (1.6)	7.8 (2.6)
Methionine	10	3.4 (3.0)	0.7 (1.0)	1.1 (1.6)	3.7 (2.6)
Methanol	10	2.9 (6.0)	**76.8** (1.9)	7.8 (3.1)	12.3 (5.1)
Acetone	10	2.2 (3.0)	0.1 (1.0)	0.8 (1.6)	6.9 (2.6)
Malonate	7	2.0 (6.0)	0.0 (1.9)	0.0 (3.1)	20.6 (5.1)
Isobutyric acid	10	1.8 (2.4)	3.5 (0.8)	0.6 (1.2)	3.4 (2.0)
Succinate	8	1.6 (3.0)	0.5 (1.0)	6.7 (1.6)	0.1 (2.6)
Creatinine	10	1.3 (3.0)	0.2 (1.0)	0.1 (1.6)	0.0 (2.6)
3-Hydroxyisovaleric acid	6	1.1 (3.0)	0.1 (1.0)	**86.0** (1.6)	0.5 (2.6)
Creatine	7	1.0 (3.0)	0.2 (1.0)	1.1 (1.6)	0.3 (2.6)
Propylene glycol	10	0.9 (3.0)	0.1 (1.0)	0.3 (1.6)	1.8 (2.6)
2-Hydroxyisovalerate	10	0.7 (3.0)	2.0 (1.0)	0.3 (1.6)	2.7 (2.6)
L-Arginine	6	0.3 (3.0)	2.4 (1.0)	0.0 (1.6)	0.0 (2.6)
Betaine	10	0.3 (3.0)	0.0 (1.0)	0.0 (1.6)	20.7 (2.6)
Acetoacetate	8	0.0 (3.0)	0.0 (1.0)	0.3 (1.6)	4.5 (2.6)
Isopropyl alcohol	10	0.0 (3.0)	1.3 (1.0)	1.2 (1.6)	4.0 (2.6)
Pyroglutamic acid	10	0.0 (3.6)	1.5 (1.0)	1.4 (1.6)	2.3 (2.6)
3-Hydroxyisobutyrate	9	0.0 (3.0)	1.6 (1.0)	1.7 (1.6)	0.3 (2.6)
Choline	10	0.0 (0.9)	1.4 (0.3)	0.0 (0.5)	0.0 (0.8)
L-Histidine	7	0.0 (3.0)	0.0 (1.0)	4.1 (1.6)	6.5 (2.6)
Dimethyl sulfone	10	-	0.0 (1.0)	5.3 (1.6)	12.7 (2.6)
Pyruvic acid	8	-	0.1 (1.0)	1.0 (1.6)	9.7 (2.6)

Numbers give the concentration (μM) and in brackets the detection threshold used by BAYESIL. Only compounds with a confidence score of at least 5 and a concentration >1 μM in at least one species are given. Please be aware that due to different amounts of sample used in the analysis only the ratios and not the absolute numbers of concentrations are comparable between species. The full data can be found in the ***Supplemental Material****. "-"means not detected. Concentration values of five most abundant compounds are printed in bold.*

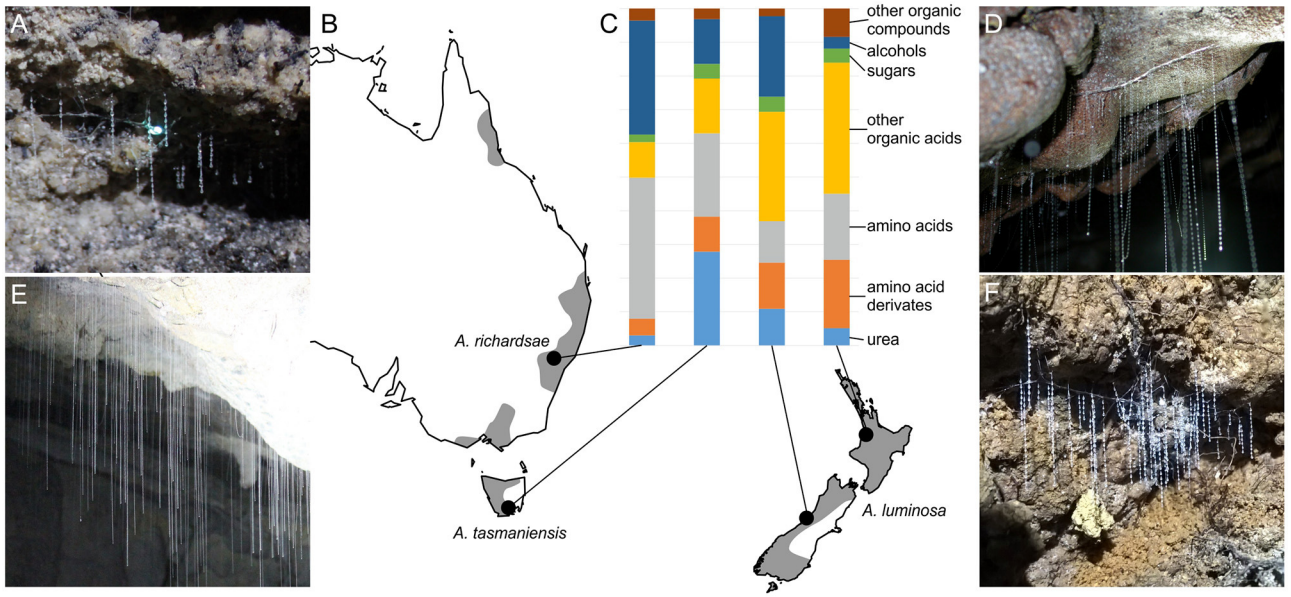

FIGURE 1 | *Arachnocampa* species and composition of their prey capture adhesive. **(A,D,E,F)** Morphology of snares of sampled glowworm species. **(A)** *A. richardsae*. **(D)** *A. luminosa*, North Island. **(E)** *A. tasmaniensis*. **(F)** *A. luminosa*, South Island. **(B)** Map with gray shade indicating the known distribution range of the genus (modified from records in the Atlas of Living Australia, https://www.ala.org.au/), map created using the R package *maps* (Brownrigg, 2013). **(C)** Bar plot showing the relative abundance of compounds identified in the glowworm adhesive wash with NMR. Note that compounds with unspecific identity, such as fatty acids, or that are not captured by solution state NMR (e.g., peptides) are not shown here.

Differences Between Glowworm Species and Population

Although there was a high overlap in the compounds detected in the adhesives of all *Arachnocampa* species the relative amounts of these compounds largely differed (**Table 1**; **Figure 1**). The adhesive of *A. luminosa* contained higher concentrations of organic acids and amino acid derivates, but lower concentrations of amino acids than the other two species. In the adhesive of *A. richardsae* the organic acid fraction was comparatively small, and instead it contained relatively more alcohols and amino acids. Notably, here the alcohol fraction was comprised almost entirely of methanol, and the most abundant amino acid was isoleucine, whereas in both other species it was ethanol and tyrosine, respectively (**Table 1**).

Furthermore, some compounds tended to appear in different forms in the different species. For instance, the high peak at 155 m/z in the mass spectrum of *A. luminosa* is indicative of methylenediurea and 187 m/z a form with additional side branches. *A. richardsae* showed low amounts of pure urea, but instead the peaks in the MS spectrum at 404, 409, 425, and 637 m/z are indicative of molecules comprised of two to four urea units, possibly with side chains (see **Supplementary Material 1** for details). In contrast, these peaks are absent in *A. tasmaniensis*, which instead showed high peaks indicative of pure urea in the NMR spectrum (**Figure 3**).

Glue droplets from South Island *A. luminosa*, i.e., an epigaeic population, generally showed a more balanced composition and higher concentrations of diverse compounds than those of the other species and populations that all originated from cave or cave like habitats. Comparing the composition of the adhesive wash between the cave and epigaeic populations of *A. luminosa*, the most prominent difference is the much higher abundance of alcohols (ethanol and glycerol) in the adhesive of the epigaeic (South Island) population. The adhesive of the South Island population also showed significant amounts of acetic acid, whereas in the North Island populations, as in the other two species, this compound was almost absent and instead showed lactic acid as the most abundant acid.

DISCUSSION

Glowworm Adhesives Are Composed of a Diverse Mix of Organic Compounds

Our results revealed that the adhesive produced by *Arachnocampa* glowworms for prey capture is composed of a much higher diversity of organic compounds than previously thought (von Byern et al., 2016). It confirmed the previous finding that urea is a major compound in *Arachnocampa* adhesives (von Byern et al., 2016), but only in *A. tasmaniensis* was pure, unbound, urea the most abundant compound. However, our MS data indicated that urea frequently occurred as part of macromolecules, that might have evaded detection with ^{1}H NMR. Urea, as well as other compounds that were found at high concentrations, such as methylhistidines, are excretory products. It has been assumed that the adhesive secretion originates from the insect's excretory system (von Byern et al., 2016), but confirmatory experiments are needed.

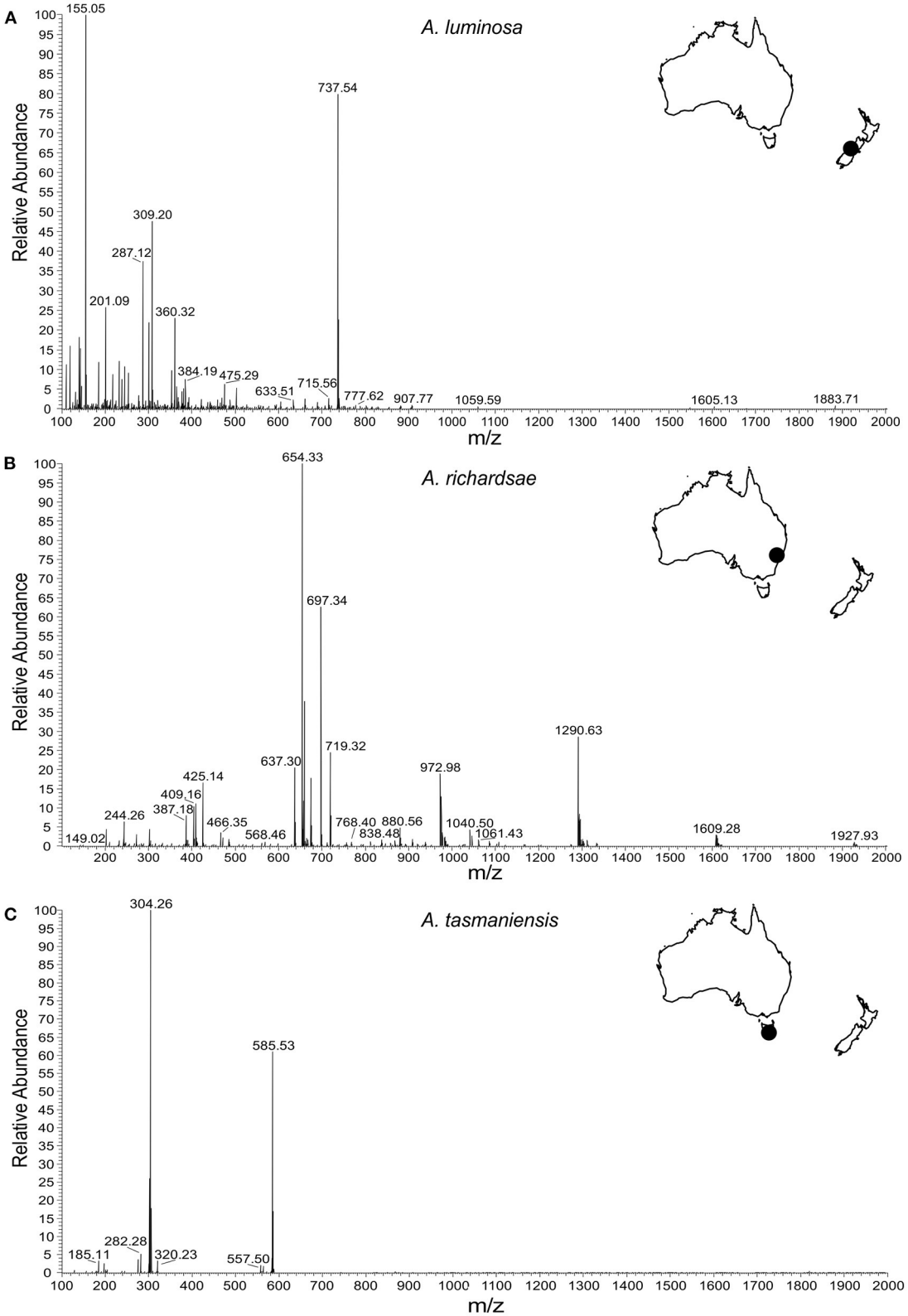

FIGURE 2 | Positive ion nanospray (ESI) high resolution mass spectrometry analysis of glowworm adhesives. **(A)** Spectrum of isolate from New Zealand glowworms (*A. luminosa*, South Island). **(B)** Spectrum of isolate from Australian glowworms (*A. richardsae* from Newnes, NSW). **(C)** Spectrum of isolate from Tasmanian glowworms (*A. tasmaniensis*).

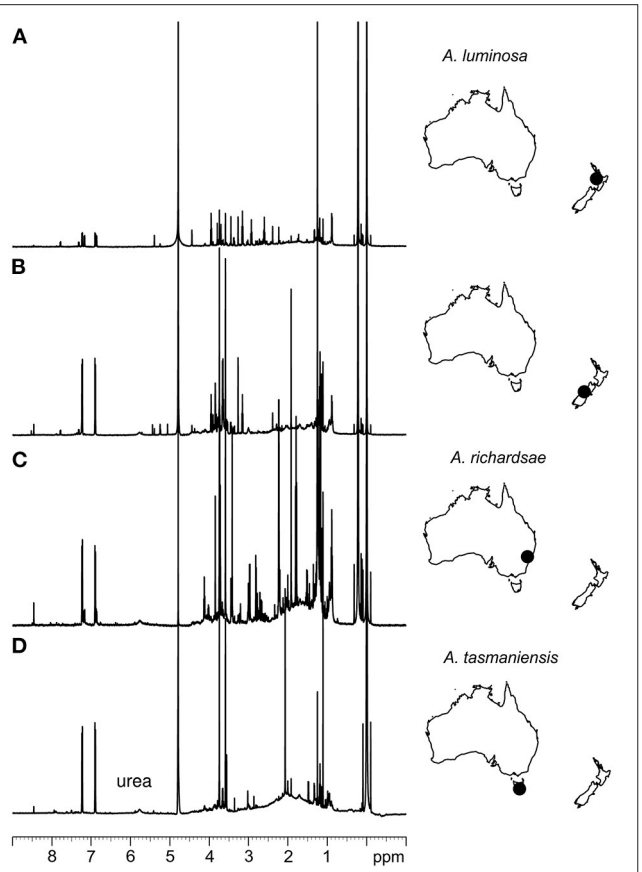

FIGURE 3 | ^{1}H NMR spectroscopic analysis of glowworm adhesives. **(A)** Spectrum of isolate from New Zealand glowworms (*A. luminosa*, North Island). **(B)** Spectrum of isolate from New Zealand glowworms (*A. luminosa*, South Island). **(C)** Spectrum of isolate from Australian glowworms (*A. richardsae* from Newnes, NSW). **(D)** Spectrum of isolate from Tasmanian glowworms (*A. tasmaniensis*).

Previous studies suggested that the glowworm adhesive contains acids, with the proposal of oxalic acid (Fulton, 1941) or uric acid (von Byern et al., 2016) as the predominant acidic compound. This was not confirmed by our results. Instead, we found a diversity of acids that may result from excretion processes or anaerobic metabolism. von Byern et al. (2016) found no evidence of the presence of carbohydrates and proteins in the glue droplets of *Arachnocampa* spp., but found indications of small peptides. Our results showed an abundance of different amino acids, which agrees with Walker et al. (2015). These amino acids could form peptides. Some of the higher range peaks in the MS spectra, such as at 1,290 m/z in the *A. richardsae* adhesive, and any peaks at >700 m/z across all species may be represented by medium to large peptides (∼C30). However, it was difficult to make definitive identifications at this range because there are a wide range of candidate organic compounds and 1H NMR cannot detect many compounds with a molecular weight >300 Da. Additionally - in contrast to von Byern et al. (2016) - we found signals of monosaccharide sugars in the NMR spectra of all three species, albeit at low concentrations.

Relationship Between Composition and Function of Glowworm Adhesives

The capture threads of glowworms can generate high adhesive strength comparable to that of commercial glues on both artificial hydrophilic and hydrophobic surfaces, and on insect surfaces (Piorkowski et al., 2018; von Byern et al., 2019). High adhesion, however, is only observed at high humidity (i.e., close to atmospheric saturation) and at a relative humidity of 60% the adhesive is dry and brittle, and the adhesive properties are lost (Piorkowski et al., 2018; von Byern et al., 2019). This is in stark contrast to artificial adhesives that typically exhibit a loss of adhesion at high humidity, and to the capture threads of some spiders that retain water and stay adhesive across a broad humidity range (∼30–100% R.H.) (Opell et al., 2018).

Capture threads act like pressure sensitive adhesives (PSA): these are soft materials that generate adhesive forces by building a high surface area with the substrate, so that short ranging intermolecular attractive forces are active (Creton, 2003). As no covalent bonds are formed, the adhesion of the PSA is reversible and remains efficient over various attachment-detachment cycles. This function requires a high softness of the material (i.e., Young's modulus <100 kPa; Dahlquist, 1969), and a molecular backbone that enables the cohesion (i.e., inner strength) of the adhesive. In the adhesive of spider capture threads, so-called viscid silk, the backbone is formed by large glycoproteins, which are plasticised by water that is retained and dispersed by hygroscopic compounds (Amarpuri et al., 2015). As different compounds differ in their humidity-dependent hygroscopic properties their specific mix determines an optimal environmental humidity at which the adhesive is hydrated to provide optimal softness, while not being too fluid to lose its cohesive strength (Opell et al., 2018). In spiders, this optimum corresponds to the microhabitat conditions that are preferred by the species (Opell et al., 2018).

In the adhesive coating of glowworm capture threads there is, thus far, no evidence for the presence of (glyco-)proteins (von Byern et al., 2016), however, our mass spectrometry results indicate that the abundant urea could serve as a cohesive by forming poly-urea chains and bonds with other compounds, such as carbohydrates. In addition, von Byern et al. (2016) found that the adhesive may contain peptides bound to urea. Such poly-urea based molecules could interact with substrate surfaces via van der Waals forces, or form hydrogen or even covalent bonds with substrate surfaces due to their polar and reactive groups. Pure urea, along with an abundance of other polar compounds, such as tyrosine and glucose, may aid the hydration of the adhesive. Under natural conditions, the glue droplets are comprised mainly of water and other volatile substances (von Byern et al., 2016). Notably, urea exhibits high hygroscopic properties only at high humidity (Werner, 1937). This may explain, why the capture threads of *A. tasmaniensis* rapidly dry and lose their adhesive properties when removed from their damp cave environments (Piorkowski et al., 2018). However, this was also observed for the capture threads of *A. luminosa* (von Byern et al., 2019), which did not show a similarly high fraction of pure urea in our analysis, so other compounds of the glowworm adhesives may have similar properties.

In contrast to the viscid silk of spiders we found that the glowworm adhesive contained significant amounts of alcohols, predominantly ethanol (in *A. luminosa* and *A. tasmaniensis*) and methanol (*A. richardsae*). These compounds may act as solvents and aid in plasticizing the adhesive. The mechanism with which a volatile compound such as methanol or ethanol is retained in the glue droplet remains unclear.

The abundance of acids in the glowworm droplet, especially those of *A. luminosa*, could have a function in prey ingestion. This was previously speculated (Fulton, 1941), but has not yet been experimentally tested.

Does Plasticity Explain the Differences in Chemical Profiles?

Our analysis uncovered remarkable differences in the composition of adhesives both between species, as well as between cave and epigaeic populations of *A. luminosa*. *A. tasmaniensis* and North Island *A. luminosa* were collected from true cave environments, *A. richardsae* were collected from a cave-like environment (abandoned railway tunnel) in an otherwise dry area and the South Island *A. luminosa* were collected from the creek banks in a temperate rain forest. None of the three species are troglobiont and epigaeic populations exist in suitable, damp microhabitats. It could be expected that epigaeic populations are exposed to a higher variation in humidity, and accordingly show enhanced hygroscopic properties. This supposition nevertheless remains to be experimentally tested. However, the chemical profiles of adhesives of South Island *A. luminosa* or *A. richardsae* did not show a higher abundance of hygroscopic compounds (in *A. richardsae* the adhesive even exhibited a high concentration the non-polar isoleucine).

Different chemical profiles could result from diet influencing the chemical mix within the adhesive secretion. From spider capture threads it is known that the relative abundance of small mass molecular compounds, such as choline and potassium and phosphate salts, varies with spider diet (Higgins et al., 2001; Blamires et al., 2017). As different compounds may fulfill the same function within the adhesives (e.g., different types of hygroscopic substances, different types of solvents, or different forms of urea forming the adhesive backbone, such plastic effects might not necessarily reflect an adaptive function). Furthermore, the threads may also be prone to contamination with foreign substances (e.g., by aerosols), which may also affect their composition after secretion.

Capture Threads as Biomimetic Models for the Design of Tailored Adhesives

More and more materials designers are looking to biological materials for inspiration for new products. This is because biological materials often show a high performance, are synthetized under environmentally benign conditions, and are biodegradable. Moreover, some materials, such as spider silks exhibit a high biocompatibility, which renders them excellent candidates for the design of biomaterials for biomedical applications (Vepari and Kaplan, 2007; Widhe et al., 2012).

A range of bioadhesives have received high attention due to their specific properties that remain challenging to achieve for artificial adhesives, such as the generation of adhesive bonds in marine environments (Bandara et al., 2013) or the reversibility of strong adhesive bonds (Cho et al., 2019). Glowworm glues are different from other bioadhesives in being adapted to work best under extremely humid conditions. Therefore, they have the potential to serve as models for specialized moisture activated adhesives such as tissue adhesives (Mehdizadeh and Yang, 2013).

At the same time, our study has shown some similarities to spider adhesives. The study of such convergent adhesive systems can be a powerful way to separate functional principles from the effects of evolutionary history in biological systems (Wolff et al., 2017). The function of common artificial adhesives is severely affected by water. This is especially true for pressure sensitive adhesives, which lose their stickiness at high humidity. In contrast, the adhesives produced by glowworms and many spiders retain their stickiness at high humidity. In both cases this seems to be based on a on similar principle: the plasticising of an otherwise dry and stiff material with water by the ubiquitous distribution of small organic compounds with hygroscopic properties. An experimental investigation of the functional chemistry in glowworm capture thread adhesives will help us to identify compounds that may be useful for designing specialized adhesives for applications in humidity environments.

CONCLUSION

In summary, here we showed for the first time that the adhesive droplets of *Arachnocampa* glowworms are composed of a complex mix of organic compounds. Our analyses were qualitative and revealed the presence of many of the same compounds or classes of substances between different species and populations of glowworms, albeit with different relative abundance. We assume that such differences rather reflect differences in the diet and remnants of different preys than adaptations to different habitats and functions. Similar to the adhesive coatings of spider capture threads, glowworm glues are characterized by an abundance of low molecular weight organic compounds with hygroscopic properties, which could act as plasticizers and transform the stiff and brittle silk thread into a soft and tacky contact adhesive. More research is required to understand the functional significance of the different compounds, in order to extract design principles for specialized moisture activated adhesives for biomedical and other applications.

DATA AVAILABILITY STATEMENT

The original contributions presented in the study are included in the article/**Supplementary Material**, further inquiries can be directed to the corresponding authors.

AUTHOR CONTRIBUTIONS

SB and JW conceived the study. SB, JH, DT, and LA designed the chemical analysis. JW, DP, JB, and SB organized the logistics of sample collection, including the applications for research permits. SB, JW, JB, DP, JF, and XW collected the samples. DT processed the samples and performed the NMR analysis. LA performed the MS analysis. DT, LA, SB, and JH interpreted the spectroscopy data. JW and SB drafted the manuscript, and all authors contributed in its revisions.

FUNDING

JW was supported by a Macquarie University Research Fellowship of Macquarie University and a Discovery Early Career Researcher Award of the Australian Research Council (DE190101338). JB was supported by COST Action CA15216 (European Network of Bioadhesion Expertise). XW acknowledges the Australian Research Council (ARC) for support through an Industry Transformation Research Hub (IH140100018). SB was supported by a Hermon Slade Foundation grant (HSF 17/6). DP was supported by a grant from the Ministry of Science and Technology, Taiwan (MOST 108-2811-B-029-500). SB was funded by a Hermon Slade Foundation grant (HSF/16).

ACKNOWLEDGMENTS

We thank Niall Doran and Hamish Craig for assistance collecting *A. tasmaniensis* threads and Deb Kane for discussions on *A. richardsae*. Thanks to Dr. Chowdhury Sarowar for his assistance in preparing and running MS samples. Access to instrumentation in the BMSF and NMR Facilities of the Mark Wainwright Analytical Centre, UNSW, is gratefully appreciated.

SUPPLEMENTARY MATERIAL

The Supplementary Material for this article can be found online at: https://www.frontiersin.org/articles/10.3389/fmech.2021.661422/full#supplementary-material

REFERENCES

Agnarsson, I., and Blackledge, T. A. (2009). Can a spider web be too sticky? Tensile mechanics constrains the evolution of capture spiral stickiness in orb-weaving spiders. *J. Zool.* 278, 134–140. doi: 10.1111/j.1469-7998.2009.00558.x

Amarpuri, G., Chaurasia, V., Jain, D., Blackledge, T. A., and Dhinojwala, A. (2015). Ubiquitous distribution of salts and proteins in spider glue enhances spider silk adhesion. *Sci. Rep*. 5:9030. doi: 10.1038/srep09030

Bandara, N., Zeng, H., and Wu, J. (2013). Marine mussel adhesion: biochemistry, mechanisms, and biomimetics. *J. Adh. Sci. Technol.* 27, 2139–2162. doi: 10.1080/01694243.2012.697703

Betz, O., and Kölsch, G. (2004). The role of adhesion in prey capture and predator defence in arthropods. *Arthropod. Struct. Devel.* 33, 3–30. doi: 10.1016/j.asd.2003.10.002

Blamires, S. J., Hasemore, M., Martens, P. J., and Kasumovic, M. M. (2017). Diet-induced co-variation between architectural and physicochemical plasticity in an extended phenotype. *J. Exp. Biol.* 220, 876–884. doi: 10.1242/jeb.150029

Blamires, S. J., Sahni, V., Dhinojwala, A., Blackledge, T. A., and Tso, I. M. (2014). Nutrient deprivation induces property variations in spider gluey silk. *PLoS ONE* 9:e88487. doi: 10.1371/journal.pone.0088487

Bovey, F. A., and Mirau, P. A. (1996). *NMR of Polymers*. San Diego: Academic Press.

Broadley, R. A., and Stringer, I. A. (2001). Prey attraction by larvae of the New Zealand glowworm, *Arachnocampa luminosa* (Diptera: Mycetophilidae). *Inv. Biol.* 120, 170–177. doi: 10.1111/j.1744-7410.2001.tb00121.x

Brownrigg, M. R. (2013). *Package 'maps'*. Available online at: https://cran.r-project.org/web/packages/maps/ (accessed January 13, 2021).

Cho, H., Wu, G., Jolly, J. C., Fortoul, N., He, Z., Gao, Y., et al. (2019). Intrinsically reversible superglues via shape adaptation inspired by snail epiphragm. *Proc. Natl. Acad. Sci. U. S.A.* 116, 13774–13779. doi: 10.1073/pnas.1818534116

Cicero, D. O., Barbato, G., and Bazzo, R. (2001). Sensitivity enhancement of a two-dimensional experiment for the measurement of heteronuclear long-range coupling constants, by a new scheme of coherence selection by gradients. *J. Magn. Reson*. 148, 209–213. doi: 10.1006/jmre.2000.2234

Creton, C. (2003). Pressure-sensitive adhesives: an introductory course. *MRS Bull.* 28, 434–439. doi: 10.1557/mrs2003.124

Dahlquist, C. A. (1969). "Pressure-sensitive adhesives," in *Treatise on Adhesion and Adhesives, Vol. 2*, ed R. L. Patrick (New York, NY: Marcel Dekker), 219–260.

Diaz, C., Maksuta, D., Amarpuri, G., Tanikawa, A., Miyashita, T., Dhinojwala, A., et al. (2020). The moth specialist spider *Cyrtarachne akirai* uses prey scales to increase adhesion. *J. R. Soc. Interface* 17:20190792. doi: 10.1098/rsif.2019.0792

Fulton, B. B. (1941). A luminous fly larva with spider traits (Diptera, Mycetophilidae). *Ann. Entomol. Soc. Am.* 34, 289–302. doi: 10.1093/aesa/34.2.289

Gatenby, J. B., and Cotton, S. (1960). Snare building and pupation in *Bolitophila luminosa*. *Transact. R. Soc. New Zealand* 88, 149–156.

Haritos, V. S., Niranjane, A., Weisman, S., Trueman, H. E., Sriskantha, A., and Sutherland, T. D. (2010). Harnessing disorder: onychophorans use highly unstructured proteins, not silks, for prey capture. *Proc. R. Soc. B Biol. Sci*. 277, 3255–3263. doi: 10.1098/rspb.2010.0604

Higgins, L. E., Townley, M. A., Tillinghast, E. K., and Rankin, M. A. (2001). Variation in the chemical composition of orb webs built by the spider *Nephila clavipes* (Araneae, Tetragnathidae). *J. Arachnol.* 29, 82–94. doi: 10.1636/0161-8202(2001)029[0082:VITCCO]2.0.CO;2

Kay, L., Keifer, P., and Saarinen, T. (1992). Pure absorption gradient enhanced heteronuclear single quantum correlation spectroscopy with improved sensitivity. *J. Amer. Chem. Soc*. 114, 10663–10665. doi: 10.1021/ja00052a088

Mehdizadeh, M., and Yang, J. (2013). Design strategies and applications of tissue bioadhesives. *Macromol. Biosci*. 13, 271–288. doi: 10.1002/mabi.201200332

Meyer-Rochow, V. B. (2007). Glowworms: a review of Arachnocampa spp. and kin. *Luminescence* 22, 251–265. doi: 10.1002/bio.955

Musto, P., Ragosta, G., Scarinzi, G., and Mascia, L. (2002). Probing the molecular interactions in the diffusion of water through epoxy and epoxy–bismaleimide networks. *J. Polym. Sci. B* 40, 922–938. doi: 10.1002/polb.10147

Opell, B. D., Jain, D., Dhinojwala, A., and Blackledge, T. A. (2018). Tuning orb spider glycoprotein glue performance to habitat humidity. *J. Exp. Biol.* 221:jeb161539. doi: 10.1242/jeb.161539

Palmer, A. G., Cavanagh, J., Wright, P. E., and Rance, M. (1991). Sensitivity improvement in proton-detected two-dimensional heteronuclear correlation NMR spectroscopy. *J. Magnet. Res*. 93, 151–170. doi: 10.1016/0022-2364(91)90036-S

Piorkowski, D., Blackledge, T. A., Liao, C. P., Doran, N. E., Wu, C. L., Blamires, S. J., et al. (2018). Humidity-dependent mechanical and adhesive properties of *Arachnocampa tasmaniensis* capture threads. *J. Zool.* 305, 256–266. doi: 10.1111/jzo.12562

Piorkowski, D., Blamires, S. J., Doran, N., Liao, C. P., Wu, C. L., and Tso, I. M. (2017). Ontogenetic shift towards stronger, tougher silk in a web building cave spider. *J. Zool.* 304, 81–89. doi: 10.1111/jzo.12507

Sahni, V., Blackledge, T. A., and Dhinojwala, A. (2010). Viscoelastic solids explain spider web stickiness. *Nature Comm.* 1, 1–4. doi: 10.1038/ncomms1019

Sahni, V., Blackledge, T. A., and Dhinojwala, A. (2011). A review on spider silk adhesion. *J. Adhes.* 87, 595–614. doi: 10.1080/00218464.2011.583588

Sahni, V., Miyoshi, T., Chen, K., Jain, D., Blamires, S. J., Blackledge, T. A., et al. (2014). Direct solvation of glycoproteins by salts in spider silk glues enhances adhesion and helps to explain the evolution of modern spider orb webs. *Biomacromolecules* 15, 1225–1232. doi: 10.1021/bm401800y

Schleucher, J., Schwendinger, M., Sattler, M., Schmidt, P., Schedletzky, O., Glaser, S. J., et al. (1994). A general enhancement scheme in heteronuclear multidimensional NMR employing pulsed field gradients. *J. Biomol. NMR* 4, 301–306. doi: 10.1007/BF00175254

Sharpe, M. L., Dearden, P. K., Gimenez, G., and Krause, K. L. (2015). Comparative RNA seq analysis of the New Zealand glowworm *Arachnocampa luminosa* reveals bioluminescence-related genes. *BMC Genomics* 16, 1–15. doi: 10.1186/s12864-015-2006-2

Suter, R. B., and Stratton, G. E. (2009). Spitting performance parameters and their biomechanical implications in the spitting spider, *Scytodes thoracica*. *J. Insect Sci.* 9:62. doi: 10.1673/031.009.6201

Tan, K. T., Vogt, B. D., White, C. C., Steffens, K. L., Goldman, J., Satija, S. K., et al. (2008). On the origins of sudden adhesion loss at a critical relative humidity: examination of bulk and interfacial contributions. *Langmuir* 24, 9189–9193. doi: 10.1021/la800632r

Vepari, C., and Kaplan, D. L. (2007). Silk as a biomaterial. *Progr. Polymer Sci.* 32, 991–1007. doi: 10.1016/j.progpolymsci.2007.05.013

von Byern, J., Chandler, P., Merritt, D., Adlassnig, W., Stringer, I., Meyer-Rochow, V. B., et al. (2019). Biomechanical properties of fishing lines of the glowworm *Arachnocampa luminosa* (Diptera; Keroplatidae). *Sci. Rep.* 9, 1–14. doi: 10.1038/s41598-019-39098-1

von Byern, J., Dorrer, V., Merritt, D. J., Chandler, P., Stringer, I., Marchetti-Deschmann, M., et al. (2016). Characterization of the fishing lines in Titiwai (=*Arachnocampa luminosa* Skuse, 1890) from New Zealand and Australia. *PLoS ONE* 11:e0162687. doi: 10.1371/journal.pone.0162687

von Byern, J., and Grunwald, I. (2010). *Biological Adhesive Systems. From Nature to Technical and Medical Application*. Wien, New York: Springer, 305. doi: 10.1007/978-3-7091-0286-2

Walker, A. A., Weisman, S., Trueman, H. E., Merritt, D. J., and Sutherland, T. D. (2015). The other prey-capture silk: fibres made by glow-worms (Diptera: Keroplatidae) comprise cross-β-sheet crystallites in an abundant amorphous fraction. *Comp. Biochem. Physiol. B Biochem. Mol. Biol.* 187, 78–84. doi: 10.1016/j.cbpb.2015.05.008

Werner, E. A. (1937). Urea as a hygroscopic substance. *Nature* 139:512. doi: 10.1038/139512a0

Widhe, M., Johansson, J., Hedhammar, M., and Rising, A. (2012). Current progress and limitations of spider silk for biomedical applications. *Biopolymers* 97, 468–478. doi: 10.1002/bip.21715

Willker, W., Leibfritz, D., Kerssebaum, R., and Bermel, W. (1993). Gradient selection in inverse heteronuclear correlation spectroscopy. *Magnet. Res. Chem.* 31, 287–292. doi: 10.1002/mrc.1260310315

Wolff, J., and Gorb, S. N. (2016). "Attachment structures and adhesive secretions in arachnids," in *Biologically Inspired Systems*, *Vol. 7*, ed S. N. Gorb (Cham: Springer), 1–184. doi: 10.1007/978-3-319-45713-0_8

Wolff, J. O., Schönhofer, A. L., Martens, J., Wijnhoven, H., Taylor, C. K., and Gorb, S. N. (2016). The evolution of pedipalps and glandular hairs as predatory devices in harvestmen (Arachnida, Opiliones). *Zool. J. Linn. Soc.* 177, 558–601. doi: 10.1111/zoj.12375

Wolff, J. O., Schönhofer, A. L., Schaber, C. F., and Gorb, S. N. (2014). Gluing the 'unwettable': soil-dwelling harvestmen use viscoelastic fluids for capturing springtails. *J. Exp. Biol.* 217, 3535–3544. doi: 10.1242/jeb.108852

Wolff, J. O., Wells, D., Reid, C. R., and Blamires, S. J. (2017). Clarity of objectives and working principles enhances the success of biomimetic programs. *Bioinspir. Biomimet.* 12:051001. doi: 10.1088/1748-3190/aa86ff

Zhang, G., and Weirauch, C. (2013). Sticky predators: a comparative study of sticky glands in harpactorine assassin bugs (Insecta: Hemiptera: Reduviidae). *Acta Zoologica* 94, 1–10. doi: 10.1111/j.1463-6395.2011.00522.x

Zwahlen, C., Legault, P., Vincent, S. J. F., Greenblatt, J., Konrat, R., and Kay, L. E. (1997). Methods for measurement of intermolecular NOEs by multinuclear NMR spectroscopy: application to a bacteriophage λ N-peptide/boxBRNA complex. *J. Amer. Chem. Soc.* 119, 6711–6721. doi: 10.1021/ja970224q

Conflict of Interest: The authors declare that the research was conducted in the absence of any commercial or financial relationships that could be construed as a potential conflict of interest.

frontiers in Mechanical Engineering

ORIGINAL RESEARCH
published: 07 May 2021
doi: 10.3389/fmech.2021.660517

Adhesive Behavior of Propolis on Different Substrates

Leonie Saccardi[1,2], *Jonas Schiebl*[2], *Katharina Weber*[3], *Oliver Schwarz*[2]*, *Stanislav Gorb*[4] *and Alexander Kovalev*[4]

[1] University of Stuttgart, Stuttgart, Germany, [2] Department of Biomechatronic Systems, Fraunhofer-Institute for Manufacturing Engineering and Automation (IPA), Stuttgart, Germany, [3] Hochschule Aalen, Faculty Mechanical Engineering & Materials Science, Aalen, Germany, [4] Department Functional Morphology and Biomechanics, Zoological Institute, Kiel University, Kiel, Germany

Propolis is a sticky substance used by bees to seal their hive and protect the colony against pathogens. Its main components are plant resins, beeswax, essential oils, pollen, and other organic substances. The chemical and medicinal properties of propolis have been extensively studied, but little is known about its physical and especially adhesive properties. To gain a better understanding of propolis and its potential for adhesive applications, we performed several experiments, including adhesion tests with propolis in different conditions and on various substrates, differential scanning calorimetry analysis, and compression tests. Propolis shows clear viscoelastic behavior and temperature-dependent mechanical properties. Our results demonstrate that propolis adheres well to a wide range of substrates from glass to PTFE, but also enables stronger adhesion at higher temperatures and longer contact times. Even underwater, in wet conditions, quite a substantial adhesion was measured. The data are interpreted from a biomechanical point of view, and the significance of the obtained results for bee biology is discussed.

Keywords: propolis, honeybees, adhesion, surface energy, van der Waals interactions, viscoelasticity, plasticity

OPEN ACCESS

Edited by:
Hongyu Zhang,
Tsinghua University, China

Reviewed by:
Yoshitaka Nakanishi,
Kumamoto University, Japan
Shanhua Qian,
Jiangnan University, China

***Correspondence:**
Oliver Schwarz
oliver.schwarz@ipa.fraunhofer.de

Specialty section:
This article was submitted to Tribology, a section of the journal Frontiers in Mechanical Engineering

Received: *29 January 2021*
Accepted: *06 April 2021*
Published: *07 May 2021*

Citation:
Saccardi L, Schiebl J, Weber K, Schwarz O, Gorb S and Kovalev A (2021) Adhesive Behavior of Propolis on Different Substrates. Front. Mech. Eng. 7:660517. doi: 10.3389/fmech.2021.660517

INTRODUCTION

Propolis is a sticky and ductile material that is produced by honeybees (*Apis mellifera*), mixing plant resins, wax, and other substances. Because of its strong adhesive nature, propolis is sometimes referred to as bee glue (Bankova et al., 2000; Bankova, 2005). Honeybees mainly forage resins from plant buds, but also have been reported to collect resin from tree barks and fruit surfaces (Alfonsus, 1933; Kumazawa et al., 2008; Simone-Finstrom and Spivak, 2010). Bees selectively choose what plants to acquire resin from (Isidorov et al., 2016). In Europe and North America poplars are believed to be the main source of resin for propolis (Greenaway et al., 1990; Bankova et al., 2000; Isidorov et al., 2016). Other plant sources for propolis production in temperate regions are aspen and birch (Isidorov et al., 2016). Since the contents of bud resins differ immensely between different plant species (Bankova, 2005), propolis contents and therefore properties are highly variable. In general, propolis consists of about 50% resin, 30% wax, 10% essential and aromatic oils, 5% pollen, and 5% of various other organic substances (Monti et al., 1983; Cirasino et al., 1987; Burdock, 1998). Meanwhile, more than 300 chemical components have been identified in propolis (Huang et al., 2014). The main constituents are phenolic compounds, such as flavonoids, aromatic acids and their esters (Bankova et al., 2000). Additionally, propolis contains phenolic aldehydes, ketones, terpenes, sugars, hydrocarbons, mineral elements, and enzymes (Bankova et al., 2000; Anjum et al., 2018).

Bees use propolis as a building material, for example to seal cracks and smooth out the internal walls of the hive (Burdock, 1998; Bankova et al., 2000). In addition to its mechanical functions, propolis has important chemical and bio-medical properties that protect the colony and contribute to social immunity (Simone-Finstrom and Spivak, 2010). Propolis possesses antibacterial, antifungal, antiviral, anti-inflammatory and hepatoprotective, antioxidant and antitumor properties (Anjum et al., 2018). Due to its pharmacological properties, propolis has been used by humans for multiple purposes (e.g., treating wounds or preserving corpses) throughout history (Ghisalberti, 1979; Anjum et al., 2018), and it still has manifold applications in medicine and cosmetics today (Burdock, 1998; Huang et al., 2014; Anjum et al., 2018).

Chemical and especially bio-medical properties of propolis have been studied extensively (Burdock, 1998; Cornara et al., 2017; Anjum et al., 2018), but little research has been done to understand its physico-chemical properties. A better understanding of the material properties of propolis could help biologists to understand how bees maintain such a sticky material. Beyond that, there is a strong potential for propolis applications in adhesive technology, as modern adhesive bonding technology is continuously searching for optimized environment-friendly adhesive solutions (Popov et al., 2017). Because of its pharmacological properties in addition to its stickiness, propolis might even be useful as a medical adhesive. Furthermore, knowledge about adhesive behavior of propolis on various surfaces could be used for developing anti-adhesive coatings.

The objective of this work was to characterize propolis mechanics, adhesion and other physico-chemical properties in order to ascertain whether the material might have other areas of application apart from its known medical uses.

MATERIALS AND METHODS

Propolis Material

The raw propolis was provided by private beekeeper Dr. Oliver Schwarz (Stuttgart, Germany) (**Figure 1A**). Samples were harvested from beehives in autumn 2017 and spring 2018 by scraping the inside of hives, frames, and lids. Harvested propolis was stored outside in an unsealed container until summer 2018. To get consistent samples, the propolis chunks were frozen to −20°C, finely ground using a pre-cooled mortar and pestle, mixed, and subsequently stored at −20°C (**Figure 1B**). The pulverizing procedure was based on the method that was previously used to produce propolis extract (Bankova et al., 2016). To prevent contamination, propolis was only handled wearing gloves cleaned with ethanol (Rotipuran® ≥ 99.8%, p.a., Carl Roth GmbH & Co. KG, Karlsruhe, Germany).

Density

Homogenized and kneaded propolis samples were weighed with a balance (AG204 DeltaRange®, Mettler-Toledo, Columbus, USA). The volume of the propolis sample was determined by measuring the volume of water it displaced in a 50 ml measuring cylinder. The samples density was then calculated by dividing the weight by the volume. Three samples were tested independently.

Differential Scanning Calorimetry

The thermal properties of propolis were studied using differential scanning calorimetry (DSC) (DSC 8500, Perkin Elmer, Waltham, USA). Aluminum pans and covers were used for sample preparation and closed manually bending the edges with tweezers. Raw propolis pieces of two harvests (Spring: 5.7 mg and Autumn: 6.8 mg) were analyzed separately. During the first heating cycle, propolis was heated from −50 to 60°C at 20 K/min. The temperature in the chamber was held for 1 min, then rapidly cooled down to −50°C at 200 K/min and held there for 4 min before continuing. For the second cycle, the sample was heated to 70°C at 20 K/min. Homogenized and kneaded propolis samples was also heated in a water bath, in order to observe melting behavior. Three samples were tested independently.

Compression Tests

Stress-strain curves were recorded during compression tests with propolis using a universal testing machine (Autograph AG-X plus, Shimadzu, Kyoto, Japan). Homogenized propolis was kneaded and subsequently filled into a flexible mold to be formed into propolis disks (6.5 mm high, 12.5 mm diameter). To ensure parallel and even surfaces on top and at the bottom of the disc, the discwas pressed between two smooth glass slides held apart by 6.5 mm high spacers on each side. In order to prevent the sample sticking to the compression plates, a piece of cling film was layered underneath and on top of the propolis disc. The sample was continuously loaded to a compression of 1% (engineering strain) and then unloaded. This process was repeated on the same sample for compressions of 5, 10, 20, and 30%, in order to see what degree of compression leads to elastic and which to plastic deformation. Measurements were carried out at different temperatures (4, 23, and 40°C), while applying and removing the load with a constant velocity of 4 mm/min, to examine the effect of temperature on elastic properties of propolis. The temperature was varied by cooling the sample and compression plate in the fridge, or heating it in an oven. Additional measurements were performed at different velocities (1, 2, and 4 mm/min) at a constant temperature of 23°C, in order to analyze the viscous behavior of propolis. Three samples were tested for each combination of temperatures and velocities. Stress-strain curves were generated to obtain information about the mechanical properties of propolis.

Weighing Experiments

Homogenized and manually formed propolis samples were weighed continuously over a period of 7 h using an ultra-microbalance (Sartorius® Cubis MSE2.7S, Sartorius AG, Göttingen, Germany). The lid of a reaction tube was cut off and weighed empty. For each measurement, there were three small propolis spheres, each weighing 40–50 mg, placed on the lid. These samples were weighed at intervals of 10 s for 7 h at 24°C and 45 % relative humidity (RH) (P330 temperature-humidity

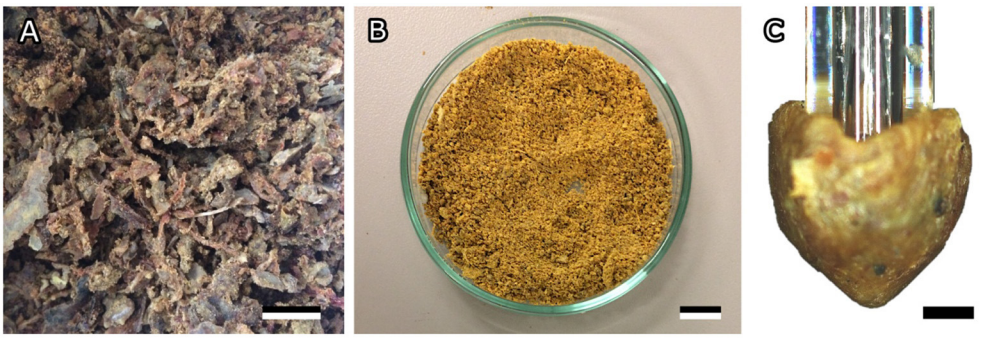

FIGURE 1 | Bee propolis. **(A)** Raw propolis as collected from the hive. **(B)** Homogenized propolis powder. **(C)** Cone-shaped propolis sample used for adhesion tests. Scale bar: 1 cm **(A,B)**, 500 μm **(C)**.

measuring instrument, Dostmann electronic GmbH, Wertheim-Reicholzheim, Germany). Three samples, each consisting of three propolis spheres, were weighed separately.

Adhesion of Propolis

Adhesion of propolis was tested on a clean, smooth glass surface. Just before each adhesion experiment, a small amount of homogenized propolis powder was defrosted and kneaded into a homogeneous mass. Cone-shaped propolis samples with a spherical tip were subsequently formed by hand wearing ethanol-cleaned gloves (**Figure 1C** and **Supplementary Figure 2A**). The topography of the sample was analyzed using a fast scanning 3D measurement microscope (Keyence VR 3100; Keyence Corporation, Osaka, Japan). The profile of the sample was measured in five positions arranged in a star shape through the highest point of the tip. To estimate the radius at the sample tip, a circle was fitted to the sample's profiles in five different orientations (**Figure 2C**). The circle's radii were measured and then averaged.

The effective elastic modulus and the pull-off force of propolis were measured with a microforce measurement device [Basalt-BT01; Tetra GmbH, Ilmenau, Germany (Gorb and Scherge, 2000; Jiao et al., 2000; Gorb et al., 2004)]. The device consists of micromanipulators as a platform holding the substrate material, a metal spring (springs with spring constants of 618 and 539 N/m were used) and a fiber-optical sensor (**Figure 2A**). The piezo-drive moves the sensor with the spring down for loading and up for unloading the sample. A shortened glass capillary (5 μl micropipette Blaubrand® Intra END, BRAND GMBH + CO KG, Wertheim, Germany) was attached to the metal spring with cyanoacrylate glue.

The freshly formed, cone-shaped sample of propolis was then mounted on the tip of the capillary without any additional glue. A glass slide (Standard microscopy slides (soda lime glass); Carl Roth GmbH + Co. KG, Karlsruhe, Germany) was cleaned with ethanol and distilled water. After drying out, the glass slide was fixed to the micromanipulator platform with double-sided adhesive tape to be used as substrate for subsequent adhesion tests (Article number 05338-00000-01, Tesa®, Norderstedt, Germany). The propolis sample was brought into contact with the substrate and retracted from the surface as soon as the load force reached 5 mN. The load was chosen to resemble the load applied by bees when handling propolis. As no studies exist on mandibular forces and pressures of honeybees, pressures previously measured at the tip of mandibles of predacious Coleoptera (Wheater and Evans, 1989) were used as a reference for the load applied to the propolis sample. Tip pressures were calculated as suggested by Wheater and Evans (1989):

$$P = \frac{F_a}{A} \tag{1}$$

where F_a is the applied force and A is the contact area obtained from the contact radius.

Reference Measurements on Glass

On each propolis sample a set of 11 single measurements was performed, each on a different spot of the reference glass surface ($N = 8$ propolis samples, $n = 11$ measurements per sample). The last measurement of each set was carried out with a 60 s contact delay after loading and before unloading the sample to test the viscous properties of propolis. Experiments were carried out at room temperature (24.00 ± 0.53°C) and a relative humidity of 36.80 ± 9.01%. After the adhesion experiments, the substrate material was examined under a binocular microscope (Leica M205 A) in order to find possible propolis residues/prints in the contact area. Additional abbreviated reference measurements on glass (five repetitions) were performed with propolis samples used for tests on various other substrates described below.

Adhesion Under Different Tests Conditions

Some of the test conditions, described above for the reference measurements, were varied to prove whether they have an effect on propolis adhesion. First, repeated measurements were performed on the same spot. Second, measurements without prolonged contact time were performed to estimate the deformation of the sample tip after short contact measurements. Third, several measurements were carried out in fluid conditions, with a drop of distilled water (H_2O) or oil (Mineral oil, light, Sigma-Aldrich, St. Louis, USA) being placed on the substrate (**Figure 2B**). Fourth, to study the influence of temperature on

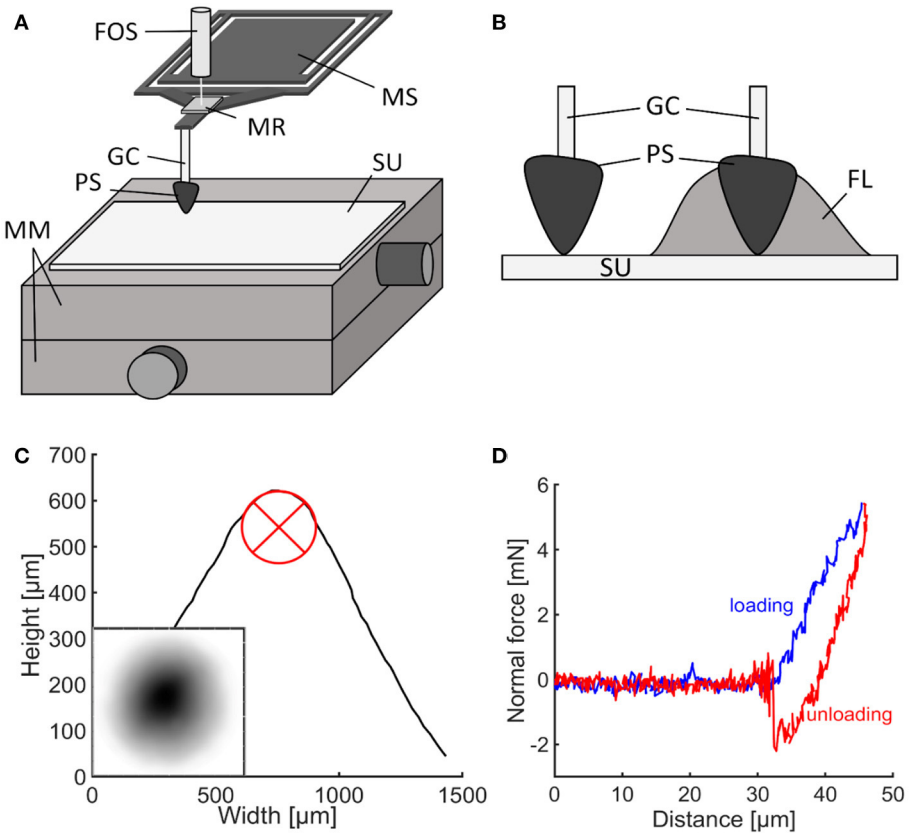

FIGURE 2 | Adhesion experiments. **(A)** Experimental set-up for adhesion testing with Basalt-01 mechanical tester (Tetra GmbH). **(B)** Propolis contact in presence of fluid and without fluid. **(C)** 3D-profile of the propolis sample. The circle was used to measure the tip radius. The small subimage depicts the sample's topography, with darker areas depicted higher than lighter areas. **(D)** Typical force-distance curve obtained from adhesion experiments. FL, fluid droplet; FOS, fiber optical sensor; GC, glass capillary; MM, 2D-micro-manipulators; MR, mirror; MS, metal spring; PS, propolis sample; SU, substrate.

propolis adhesion, measurements were conducted at a higher room temperature, i.e., of 26°C. For each condition, 50–60 single measurements were performed (N = 5–6 propolis samples, n = 10 measurements per sample). Last, the experiments with an extended contact time of 60 s were performed to study the effect of contact time on adhesion. These experiments were performed in the last step of reference measurements on glass (N = 50 propolis samples, n = 1 measurement per sample).

Adhesion on Different Substrates

Various technical materials were used as substrates for subsequent adhesion experiments. A polytetrafluoroethylene (PTFE) plate (Technische Materialien Katarzyna Kowalewska, Görlitz, Germany) and a steel plate (EN 1.4016, Abrams Premium Stahl®, Osnabrück, Germany) were polished using a polishing machine (Minitech 233; Presi, Eybens, France) with alumina oxide suspensions using polishing papers with descending particle sizes (12, 3, 1, and 0.3 µm) to achieve similar and minimal surface roughness for all substrates (**Supplementary Figure 1**). They were cleaned with ethanol and distilled water and dried prior to usage in the experiments. A resin replica of a smooth, clean glass surface was prepared by a two-step molding method (Gorb, 2007; Koch et al., 2008). The negative template of the glass slide was produced using a two-component dental wax (Affinis light body, ISO 4823, polyvinylsiloxane, Coltène Whaledent AG, Altstätten, Switzerland) and filled with resin (Spurr's low viscosity kit, Plano, Wetzlar, Germany) that was subsequently polymerized at 70°C for 48 h. This resin substrate will be further referred to as "Spurr."

Tests on these technical substrate materials were performed as described for the reference glass substrate. After 10 measurements on the substrate material, five additional reference measurements were carried out on glass. For each technical substrate material, 50–60 single measurements on different sites were performed (N = 5–6 propolis samples, n = 10 measurements on substrate per sample).

Examination of Surfaces

The contact angles of water, diiodomethane, and ethylene glycol on the reference glass surface, as well as of the PTFE, steel and Spurr substrates were measured according to the sessile drop method (2 µl drop volume) using an optical contact angle measuring system (OCAH200, DataPhysics Instruments GmbH,

Filderstadt, Germany). For each substrate, 5–10 contact angle measurements were conducted for each liquid. The substrate's surface free energy and its dispersive and polar components were calculated according to the method by Owens and Wendt (1969).

The substrate's surface roughness was measured by a confocal 3D laser scanning microscope (Keyence VK-X250; Keyence Corporation, Osaka, Japan). The corresponding Multi File Analyzer software (Version 1.2.6.106, Keyence Corporation, Osaka, Japan) was used to obtain the following roughness parameters: arithmetical mean height of the surface (S_a), maximum height of the surface (S_z), texture aspect ratio of the surface (S_{tr}), arithmetic mean peak curvature (S_{pc}), and developed area ratio (S_{dr}).

Additionally, for surface examination, standard light microscopy (Leica M205 A, Leica Microsystems Inc., Wetzlar, Germany) and 3D surface profilometry (Keyence VR 3100, Neu-Isenburg, Germany) were used.

Data Analysis

Adhesion experiments were evaluated using Matlab (version R2015b, The MathWorks, Inc., Natick, USA). The unloading part of force-distance curves (**Figure 2D**) acquired from adhesion experiments was fitted according to the JKR theory (Johnson et al., 1971) (**Supplementary Figure 2B**).

$$a^3 = \frac{3R}{4E}\left[F_a + 3\pi R\gamma + \sqrt{6\pi R F_a \gamma + (3\pi R\gamma)^2}\right] \quad (2)$$

where a is the contact radius, F_a is the applied load, R is the tip radius, E and $\Delta\gamma$ are the effective elastic modulus and the work of adhesion, respectively.

The work of adhesion $\Delta\gamma$ is the energy per unit of area needed to separate two bodies in contact. It was chosen as a measure of adhesion, because it is independent of the contact area. Work of adhesion ($\Delta\gamma$) was estimated from the unloading curve:

$$\Delta\gamma = \frac{-2F}{3\pi R} \quad (3)$$

where F is the pull-off force and R is the tip radius.

To characterize viscoelastic properties of propolis, a generalized Maxwell model was used (Christensen, 1982). The sample's viscosity was estimated from experimental force curves using the following equation (Cheng et al., 2005; Kovalev et al., 2018):

$$F_a = \frac{4\sqrt{R}d^{1.5}}{3\left(1-\nu^2\right)}\left(E_\infty + E_1 e^{-\frac{E_1 t}{\eta_1}} + E_2 e^{-\frac{E_2 t}{\eta_2}}\right) \quad (4)$$

where d is the displacement, t is the time under load, $E_\infty/E_1/E_2$ and η_1/η_2 are the Young's moduli and viscosities of the static and two dynamic components, correspondingly ν is the Poisson ratio assumed to be equal to 0.49 (Kovalev et al., 2018).

Statistics

The data were statistically analyzed using the software R, version 3.6.1 (The R Foundation for Statistical Computing, 2019). Data was tested for normal distribution and variance homogeneity using Kolmogorov-Smirnov and Levene's tests, respectively. The comparison of propolis adhesion under different conditions and on different substrates was performed with a one-way ANOVA and a pairwise multiple comparison procedure (Tukey test). An unpaired two-sample t-test was performed to compare the mean Young's modulus of propolis at 24 and 26°C. Correlation analysis of Young's modulus and work of adhesion obtained from adhesion experiments was performed by calculating the Pearson's correlation coefficient.

RESULTS

Density of Propolis

Homogenized and kneaded pieces of propolis were weighed. Subsequently, the volume of weighed pieces was determined by measuring the volume of water it displaced. The propolis sample did not dissolve or absorb water during the experiment. The density of propolis was calculated to be 0.953 ± 0.001 g/cm^3 ($N = 3$).

Thermal Behavior of Propolis

Melting of Propolis

When heating propolis in a water bath to 60–70°C, its separation into two phases was observed ($N = 3$). A phase resembling beeswax melted and turned into a transparent fluid with a yellow tint, while the other phase remained more viscous and dark brown. After once being heated to between 50 and 60°C, cooled down propolis components turned hard at room temperature and did not return to their original malleable state.

Differential Scanning Calorimetry

A DSC analysis of raw, unhomogenized propolis harvested in spring and autumn was performed to further investigate thermal properties of propolis. During the heating cycles, the variation of the heat flow as a function of the temperature revealed endothermic phase transitions at 54–55°C and 64°C (**Figure 3A**). No distinct differences between the samples from different harvests were found.

Compression Tests at Different Temperatures

The hardness of propolis changed depending on temperature. It is hard and brittle at temperatures below 10°C, allowing it to be broken or ground to a fine powder. At room temperature, propolisis is malleable and tacky. When the temperature rises above room temperature, propolis becomes increasingly softer and tackier. These changes were reflected in stress-strain curves obtained from compression tests (**Figure 3B**, $N = 3$). Compared to tests performed at 23°C, ∼4 times higher stresses were necessary at 4°C to achieve the same strain. Furthermore, at 40°C for the same strain the stresses were roughly 10 times lower than that at 23°C. In compression tests, performed at 20–800 kPa stress and temperature 4–40°C, visco-plastic deformation of propolis was observed.

Weighing Experiment

A hardened outer layer formed on propolis samples stored at room temperature for several hours, though the inside of the propolis samples remained softer. To characterize the process

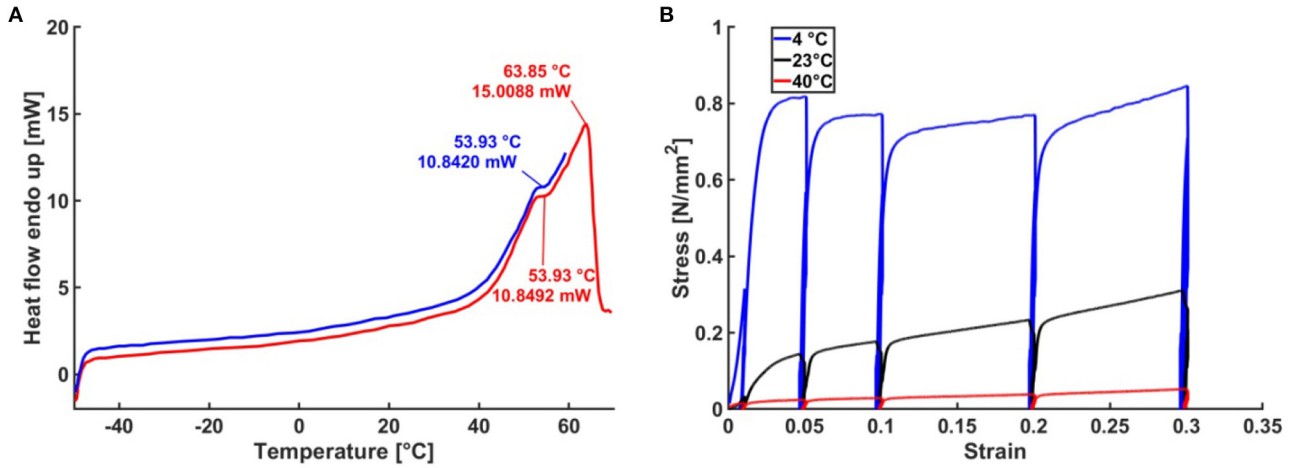

FIGURE 3 | Thermal properties of propolis. **(A)** DSC analysis of propolis. **(B)** Stress-strain curves obtained from compression tests with propolis at different temperatures.

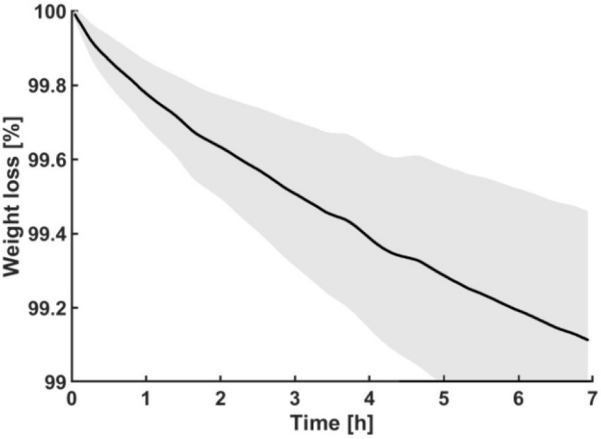

FIGURE 4 | Display of weighing experiments performed on propolis. The curve shows the mean weight of the samples ($N = 3$) over time. The gray area represents standard deviations at corresponding time points of measurement.

of volatile components evaporations, the weight of the propolis samples was measured over time. On average, the samples lost $0.9 \pm 0.3\%$ ($N = 3$) in mass over a period of seven hours at room temperature of 24°C (**Figure 4**).

Adhesion of Propolis

Cone-shaped propolis samples that were used for adhesion experiments had a mean tip radius of $182.08 \pm 55.18\,\mu m$ ($N = 135$) (**Figure 2C**). The samples were brought into contact with different substrates at a mean applied normal force of 5.2 ± 0.7 mN. The contact radius at maximum load was calculated to be $36.06 \pm 17.14\,\mu m$, using **Equation (3)**. Mean pressure at the propolis sample was calculated to be 1.85 MPa. At a room temperature of 24°C, propolis samples had a mean Young's modulus of 11.23 ± 6.77 MPa ($N = 45$). Compared to measurements at 24°C, a 2°C increase in temperature resulted in a significantly lower elastic modulus of 6.55 ± 4.89 MPa ($N = 10$, $P = 0.044$). In adhesion experiments, performed with propolis on a glass surface, the mean pull-off force was 2.12 ± 0.77 mN and the mean work of adhesion was calculated to be 2.96 ± 1.27 J/m^2 using **Equation (3)**. According to Pearson's correlation test, Young's modulus and work of adhesion of propolis are anti-correlated ($r = -0.999$, $p < 0.01$). The mode of failure during experiments was adhesive, since examination of the substrate surfaces after adhesion experiments using light microscope showed no propolis residues in the contact area. 3D surface profilometry of the sample's tip before and after the experiment also showed no shape change and therefore no plastic deformation occurred during testing at short contact times. However, at a contact time of 60 s, samples clearly exhibited viscoplastic deformation, since the tip area was considerably flattened.

Propolis Adhesion Under Different Conditions

Propolis adhesion was subsequently measured on a glass surface under different conditions and compared by performing a one-way ANOVA (**Figure 5A**, **Table 1**). The *P*-value was found to be smaller than the significance level of 0.01. Therefore, a *post-hoc* Tukey test was conducted to find pairwise differences. *P*-values smaller than 0.05 were considered significant. The work of adhesion of propolis did not depend (1) on the contact area and (2) on whether the measurements were repeatedly done at the same location or each measurement was done at new location (3.08 ± 0.79 J/m2, $P = 0.9998$).

Propolis adhesion in oil and water was measured. Propolis adhered to glass, even underwater and in oil, however, the work of adhesion measured (0.86 ± 0.47 J/m^2) was significantly lower than that in the dry condition ($P < 0.0001$). No significant difference between the work of adhesion in water and in oil was found ($P = 1.0$). Raising the temperature from 24 to 26°C, the work of adhesion of propolis increased significantly to 4.67 ±

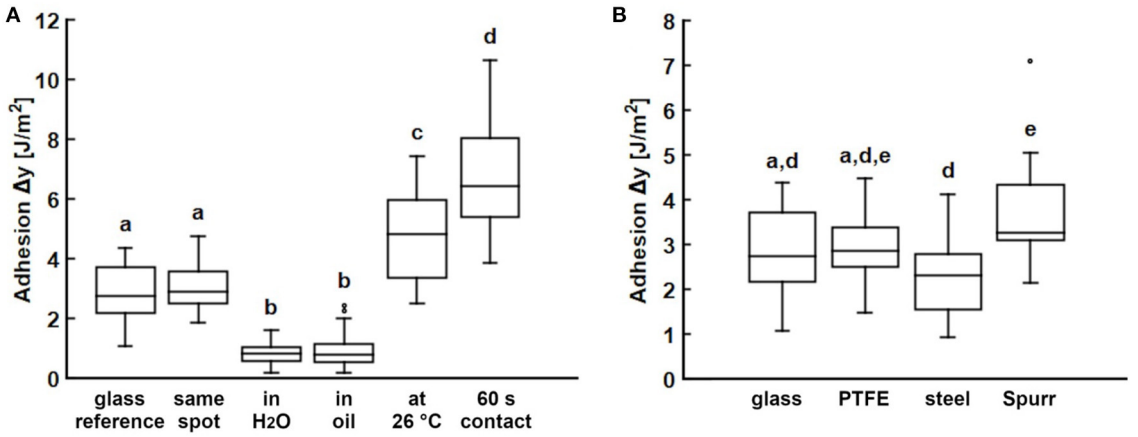

FIGURE 5 | Propolis adhesion. **(A)** Adhesion of propolis on glass under various conditions. **(B)** Adhesion of propolis on different substrates. Experiments were conducted using Basalt-1 mechanical tester (Tetra GmbH, Ilmenau, Germany). If not stated differently, tests were carried out at room temperature (24°C) with a set loading force of 5 mN and with every individual measurement performed on a different location on the substrate ($N = 5$–6 propolis samples per condition or substrate, $n = 10$ individual measurements per sample). Box plots show the median value (line), the ends of the boxes define the 25 and 75th percentiles, and the error bars the 10 and 90th percentiles. The outliers are shown as black dots. Conditions and substrates marked with different letters differ significantly from each other (one-way ANOVA, $P < 0.001$ and Tukey test, $P < 0.05$).

TABLE 1 | Propolis adhesion in different conditions.

Condition	N*n	Work of adhesion [J/m²]		Pull-off force [mN]	
		Mean	s.d.	Mean	s.d.
Reference	80	2.96	1.27	2.12	0.77
Same spot	50	3.08	0,79	2.79	0.39
Water	50	0.80	0.36	0.51	0.13
Oil	60	0.90	0.55	0.74	0.36
26°C	60	4.67	1.36	3.78	1.17
60 s	60	6.72	1.75	5.95	1.55

Work of adhesion and pull-off forces obtained from adhesion experiments conducted using Basalt-01 mechanical tester (Tetra GmbH, Ilmenau, Germany). If not stated differently, tests were carried out at room temperature (24°C) with a loading force of 5 mN and no delay between loading and unloading (N = 5–8 propolis samples per condition or substrate, n = 10 individual measurements per sample). Mean values and standard deviations (s.d.) are given.

1.36 J/m^2 ($P < 0.0001$). Some experiments performed at 26°C were abandoned due to cohesive failure and plastic deformation of the propolis sample after a few single measurements. Significantly higher work of adhesion of 6.72 ± 1.75 J/m^2 also occurred, when increasing the contact time at maximum load to 60 s ($P < 0.0001$).

Viscoelastic Behavior

As stated above, elongated contact times led to plastic deformation of the propolis samples and to a decrease of the load force overtime due to material relaxation ($N = 50$). The force-time curve was fitted with the exponential function (Bankova et al., 2000) with either one or two exponents in the 60 s contact regime (**Figure 6A**). **Table 2** shows the fit parameters for one representative force-time curve. For all measurements a better fit was achieved with two exponents. In compression tests, propolis behaved differently depending on the velocity the load was applied with. At higher velocities, higher stresses had to be applied to achieve the same strain (**Figure 6B**). No elastic deformation occurred in compression tests performed using a universal testing machine.

Adhesion to Different Substrates

To test the effect of substrate materials on propolis adhesion, adhesion tests were performed with several substrates: PTFE, steel, and Spurr's resin with different surface free energies. All tested substrates were smooth with an arithmetical mean height of the surface (Sa) between 0.034 and 0.042 µm (**Supplementary Table 1**), though their surface energies differed (**Supplementary Table 2**). PTFE had the lowest surface energy of 16.7 mJ/m², then Spurr with 28.08 mJ/m², and steel with 37.92 mJ/m², while glass had the highest surface energy of 58.25 mJ/m² among the tested materials. Despite the different surface energies, the work of adhesion obtained from adhesion experiments with propolis was similar for all tested substrate materials and ranged between 2.29 and 3.61 J/m2 (**Figure 5B**, **Table 3**). The highest work of adhesion was measured for Spurr epoxy resin, the lowest on steel. Statistically significant differences were only revealed for

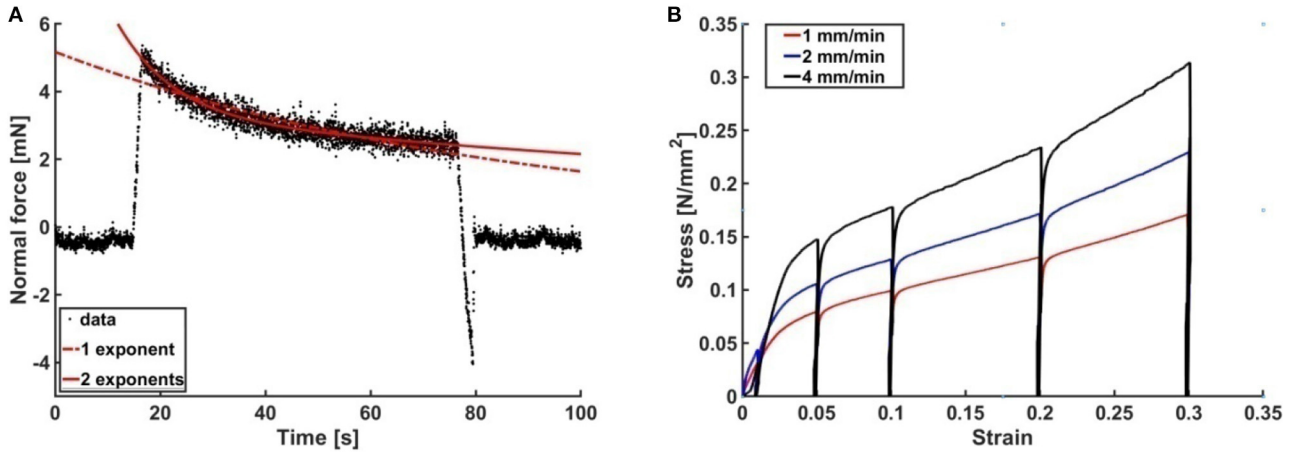

FIGURE 6 | Viscoelasticity of propolis. **(A)** Typical force-time curve obtained from adhesion tests with propolis on glass with a 60 s delay between loading and unloading. **(B)** Stress-strain curves obtained from compression tests with propolis at different velocities (1, 2, and 4 mm/min).

TABLE 2 | Fit parameters to estimate the viscoelasticity of a representative propolis sample using the **Equation (4)**.

	E_∞ [MPa]	E_1 [MPa]	η_1 [MPa*s]	E_2 [MPa]	η_2 [MPa*s]
1 exponent	8.860642	7.139358	292.319869		
2 exponents	6.662493	3.208526	68.960462	6.128982	709.443329

The force-time curve in the 60 s contact period was fitted with one and two exponents. $E_\infty/E_1/E_2$ and η_1/η_2 are the Young's moduli and viscosities of the static and two dynamic components.

work of adhesion between glass and Spurr ($P = 0.0049$), as well as between steel and Spurr ($P = 0.0004$).

DISCUSSION

Chemical composition and medicinal use of propolis have previously been studied (Burdock, 1998; Anjum et al., 2018), but no in-depth analysis of adhesive and other physical material properties of propolis have been conducted so far. To be able to better understand how bees handle this sticky material, propolis was characterized as a biological adhesive in this paper. Accordingly, thermal properties, viscosity, elastic modulus and density mattered as important parameters in this study in addition to propolis adhesion itself (Kellar, 2011). From the density measurements, we can conclude that the density of propolis (0.953 g/cm^3) is very close to the density of beeswax 0.957 g/cm^3 reported in (Bernal et al., 2005). Such a density match might simplify the manufacture and handling of propolis by honeybees.

Thermal Properties of Propolis

Propolis has previously been described to melt at temperatures between 60 and 70°C (Krell, 1996; Wagh, 2013). When heated in a water bath in our experiments, the beeswax component of propolis melted at 60–70°C. The resin component of propolis only softened, but did not become fluid. In our DSC analysis, propolis demonstrated a phase transition at 63°C. This corresponds to the melting temperature of beeswax at 62–66°C depending on its origin (Morgan et al., 2002; Gaillard et al., 2011). During the heating process, another phase transition occurred at about 55°C. Three polymorphic transitions during the heating of beeswax have previously been identified, one corresponding to the peak at 55°C (Gaillard et al., 2011). The other two transitions were not visible in our DSC results, probably due to a higher heating speed of 20 K/min compared to 1 K/min used by Gaillard et al. (2011). Previous DSC studies performed on beeswax/rosin mixtures also showed that a higher resin content leads to a decrease in the total heat flow and less pronounced or lacking secondary peaks corresponding to phase transitions (Gaillard et al., 2011). Amorphous resins, like rosin gum, often do not exhibit a clear melting point, but soften over a wide temperature range until they become liquid (Gaillard et al., 2011), while volatile essential oils usually have low melting points (−0.79°C for essential oil of cassia) (Ghodki and Goswami, 2016). This could explain why no additional peaks are present in the DSC thermograms apart from those corresponding to the beeswax component of propolis. Propolis has been reported to be hard and brittle when cold (under 15°C) (Krell, 1996; Wagh, 2013) and increasingly soft and sticky, when heated above 45°C (Krell, 1996; Wagh, 2013). This was confirmed by our adhesion and compression tests. Propolis behaved distinctly different in compression tests conducted at 0, 23, and 40°C and with 67 μm/s compression speed. Compared to tests performed at lower temperatures, a considerably lower force was needed at 40°C, to achieve the same level of compression. Both propolis elasticity modulus and viscosity decrease with an increasing temperature. Compression tests with beeswax at 3, 24, and 34°C revealed similar behavior (Morgan et al., 2002).

Young's Modulus of Propolis

At 24°C, propolis has an elastic modulus of 11.2 MPa, which resembles elastic modulus of rubber (Smith, 2016). The Young's modulus, however, was very variable between samples, although all were formed from the same batch of homogenized

TABLE 3 | Propolis adhesion on different substrates.

Substrate	N*n	Work of adhesion [J/m²]		Pull-off force [mN]	
		Mean	s.d.	Mean	s.d.
Glass	80	2.96	1.28	2.12	0.77
PTFE	50	2.91	0.71	1.43	0.72
Steel	50	2.29	0.82	1.98	0.51
Spurr	50	3.61	0.95	3.35	0.87

Work of adhesion and pull-off forces obtained from adhesion experiments conducted using Basalt-01 mechanical tester (Tetra GmbH, Ilmenau, Germany). Tests were carried out at room temperature (24°C) with a set loading force of 5 mN and no delay between loading and unloading (N = 5–8 propolis samples per substrate, n = 10 individual measurements per sample). Mean values and standard deviations (s.d.) are given.

propolis. Presumably, small changes in temperature, humidity, or/and kneading procedure had an influence on the modulus. Additionally, local inhomogeneities within the material might influence the modulus, since homogenized propolis consists of many heterogeneous microparticles, the size of which is comparable to the size of the tip (contact area). A small increase in temperature of 2°C decreased the Young's modulus of propolis significantly from 11.2 to 6.6 MPa. This also supports the observation made during compression tests at 40°C and when handling propolis that propolis becomes softer at higher temperatures. The elastic modulus of beeswax at room temperature was reported to be 39 MPa (Hossain et al., 2009). The addition of plant bud resins, oils, and other components, thus results in a softer and more pliable material compared to the pure beeswax (at room temperature).

Viscoelastic Behavior of Propolis

Viscoelastic materials show combined elastic and viscous responses under mechanical stress (Ferry, 1980). We found that propolis exhibited viscoelastic behavior. Deformation and relaxation of viscoelastic materials is time-dependent (Kellar, 2011). This became clear, as propolis deformed elastically during adhesion experiments with short contact times, but viscoelastically, when contact times were extended to 60 s. Elastic contact could be distinguished from plastic contact, as the distance of the sample tip to the substrate and the tip profile did not change between single measurements. The multiple components of propolis also affect its viscoelastic behavior. During extended contact time, the measured loading force gradually decreased over time as the material relaxed. The relaxation curve of propolis was best fitted with an exponential function with two exponents, which is indicative of a composite material with at least two components (Xie et al., 2011). This result is not surprising, since propolis mainly composed of resin (50%) and wax (30%) (Burdock, 1998).

Compression tests at different velocities showed that the material behaved stiffer at higher velocities and more force had to be applied in order to deform it. This rate dependence due to non-Newtonian properties is typical for viscoelastic materials (Smith, 2016).

Hardening of Propolis

After heating propolis over 50–60°C and cooling down, it hardened considerably, and when exposed to the room temperature a hardened layer formed on the outside of the sample over the course of a day. It has previously been reported that propolis hardens over time, becoming brittle and darker in color (Teslenko et al., 2014). A possible reason for hardening could be the evaporation of water or/and volatile components (Kellar, 2011), as weighing propolis over 7 h showed that samples lost ∼0.9% in weight over that period of time. Volatile propolis components, such as mono- and sesquiterpenoids, represent about 10% of propolis constituents and their loss could be responsible for propolis hardening (Bankova et al., 2000; Huang et al., 2014). Some resins also harden over time due to polymerization of diterpenoids initiated by light and oxidation (Langenheim, 1990). While beeswax has not been reported to harden, it is therefore likely that the resin component is responsible for the hardening of propolis.

Adhesion of Propolis

The work of adhesion calculated from the pull-off force was chosen as the measure for propolis adhesion, as it provides comparable values that do not depend on the sample radius. This made it possible to compare the results of adhesion tests conducted with propolis at different conditions and on various substrates. Propolis adhesion on glass served as a reference and was measured to be ∼3 J/m^2. In a previous study, work of adhesion of 3.56 J/m^2 was reported for a blend of 75% rosin and 25% beeswax (Girard et al., 2014). This material resembles propolis, as it is also a mixture of beeswax and resinous substances in a comparable ratio, and it exhibits similar work of adhesion. The mode of failure of propolis during adhesion experiments was rather adhesive than cohesive, as no visible propolis residues were found in the contact area with the substrate.

Adhesion at Various Conditions

Experiments that were conducted repeatedly on the same spot of the substrate further confirmed the assumption that adhesive failure occurs. There was no difference in adhesion between reference measurements and measurements on the same spot, as could be expected if cohesive failure occurs and material residues accumulate in the contact area and tip geometry changes.

Furthermore, propolis also adhered to a glass surface in presence of fluid (oil or water), although here adhesion was significantly lower than that in dry conditions. Most industrial adhesives are not able to adhere in flooded conditions (von Byern and Grunwald, 2010). However, biocompatible glues able to adhere in wet conditions are needed for many biomedical applications (von Byern and Grunwald, 2010). The ability of

propolis to adhere under water could therefore be an interesting property worth investigating further.

Significantly higher propolis adhesion was observed when the temperature was increased by only 2°C from to 24 to 26°C. It has been previously described that propolis becomes increasingly soft and sticky, when heated above 45°C (Krell, 1996; Wagh, 2013), but it seems that this process starts at even lower temperatures. At higher temperatures, the Young's modulus of propolis decreased and the material became softer. Adhesion energy is theoretically independent on Youngs' modulus. However, an elastically soft material can adapt to the substrate surface and thereby increase the real contact area and adhesion (Lorenz et al., 2013). Further experiments are necessary to study propolis adhesion at even higher temperatures and further extend our knowledge about this material, since bees handle propolis in the hive at temperatures usually ranging between 32 and 36°C (Jones, 2004). Higher adhesion of propolis was also measured in experiments with longer contact times, because this viscoelastic material had time to flow and adapt to the substrate surface profile, increasing therefore both the contact area and work of adhesion. This effect of time-dependent deformations has previously been reported (Reitsma et al., 2000). The viscoelastic deformation was also visible in the profile of propolis samples after experiments with prolonged contact times.

Adhesion on Various Substrates

Substrate surface energy usually has a strong effect on adhesion (Gorb and Heepe, 2017). In our adhesion experiments, conducted on various smooth substrates with different surface energies [glass: 64 mJ/m^2 (Weng et al., 2016), PTFE: 19 mJ/m^2 (Kinloch, 1987), steel: 40 mJ/m^2 (Mantel and Wightman, 1994)], the differences in adhesion forces were lower as expected. Substrates with low surface energy, such as PTFE, have low Hamaker constant and polarizability, and affect the strength of van der Waals interactions, which is why lower adhesion would usually be expected on these surfaces (Gorb and Heepe, 2017). However, propolis adhered more or less similarly to all tested substrates. There was no significant difference between adhesion on a polar glass surface and an unpolar PTFE substrate. Low dependence on substrate chemistry is often a characteristic of biological adhesives (Richter et al., 2018). We assume that some fluid components (e.g., mono- and sesquiterpenoids) of propolis may alter the interface between propolis sample and substrate and make adhesion almost independent of the substrate. These fluids might also be responsible for enlarged real contact area. Chemical characteristics of propolis should be further investigated to better understand their influence on propolis adhesion.

GENERAL CONCLUSIONS AND OUTLOOK

Exact composition of propolis can vary immensely depending on environmental conditions, resin sources, bee colony, season, etc. (Bankova, 2005; Mello and Hubinger, 2012). One can expect that the variability of propolis also extends to its physical and adhesive properties. The presented results are therefore a starting point for further experiments with different propolis types, as well as on propolis components, such as bud resins and different bee waxes.

The results of this work show that the composite nature of propolis is reflected in many of its physical properties, such as viscoelasticity, Young's modulus, and adhesion. Different components of propolis, mainly plant resins and beeswax, have long been used in various adhesives due to their characteristic properties. Resin is a good adhesive that can be added to adhesive mixtures, to provide tack and peel (Richter et al., 2018). In contrast, beeswax does not have initial tack, but it can act as a softener for adhesive formulations (Richter et al., 2018). Combinations of a resin (rosin) and beeswax have been used as adhesives since the Mesolithic period and have also previously been studied for their thermal and mechanical properties (Gaillard et al., 2011; Girard et al., 2014).

As propolis was found to adhere to a wide range of substrates and even in underwater and flooded oil conditions, it might be interesting for numerous adhesive applications in the future. Recently, the interest in bio-inspired adhesives has strongly increased due to the growing need for sustainable or environment-friendly adhesive solutions (Richter et al., 2018). For example, adhesives used for medical applications often have to serve different purposes, such as high tack, moisture resistance, durability, biocompatibility, and removability (von Byern and Grunwald, 2010), which all could at least partly be fulfilled by propolis. The antimicrobial effect of propolis might also be an advantageous additional property for future medical adhesives.

DATA AVAILABILITY STATEMENT

The raw data supporting the conclusions of this article will be made available by the authors, without undue reservation.

AUTHOR CONTRIBUTIONS

LS, JS, OS, SG, and AK contributed to conception and design of the study. LS conducted and evaluated the experiments and wrote the first draft of the manuscript. KW performed and evaluated the DSC analysis. All authors contributed to manuscript revision, read, and approved the submitted version.

SUPPLEMENTARY MATERIAL

The Supplementary Material for this article can be found online at: https://www.frontiersin.org/articles/10.3389/fmech.2021.660517/full#supplementary-material

REFERENCES

Alfonsus, E. C. (1933). Some sources of propolis. *Glean Bee Cult*. 61, 92–93.

Anjum, S. I., Ullah, A., Khan, K. A., Attaullah, M., Khan, H., Ali, H., et al. (2018). Composition and functional properties of propolis (bee glue): a review. *Saudi J. Biol. Sci*. 26, 1695–1703. doi: 10.1016/j.sjbs.2018.08.013

Bankova, V. (2005). Chemical diversity of propolis and the problem of standardization. *J. Ethnopharmacol.* 100, 114–117. doi: 10.1016/j.jep.2005.05.004

Bankova, V., Bertelli, D., Borba, R., Conti, B. J., da Silva Cunha, I. B., Danert, C., et al. (2016). Standard methods for *Apis mellifera* propolis research. *J. Apic Res.* 58, 1–49. doi: 10.1080/00218839.2016.1222661

Bankova, V., de Castro, S., and Marcucci, M. (2000). Propolis: recent advances in chemistry and plant origin. *Apidologie* 31, 3–15. doi: 10.1051/apido:2000102

Bernal, J. L., Jiménez, J. J., del Nozal, M. J., Toribio, L., and Martin, M. T. (2005). Physico-chemical parameters for the characterization of pure beeswax and detection of adulterations. *Eur. J. Lipid Sci. Technol.* 107, 158–166. doi: 10.1002/ejlt.200401105

Burdock, G. A. (1998). Review of the biological properties and toxicity of bee propolis (propolis). *Food Chem. Toxicol.* 36, 347–363. doi: 10.1016/S0278-6915(97)00145-2

Cheng, L., Xia, X., Scriven, L. E., and Gerberich, W. W. (2005). Spherical-tip indentation of viscoelastic material. *Mech. Mater.* 37, 213–226. doi: 10.1016/j.mechmat.2004.03.002

Christensen, R. (1982). *Theory of Viscoelasticity, 2nd Edn*. London: Academic Press; doi: 10.1016/B978-0-12-174252-2.50012-0

Cirasino, L., Pisati, A., and Fasani, F. (1987). Contact dermatitis from propolis. *Contact Dermatitis* 16, 110–111. doi: 10.1111/j.1600-0536.1987.tb01394.x

Cornara, L., Biagi, M., Xiao, J., and Burlando, B. (2017). Therapeutic properties of bioactive compounds from different honeybee products. *Front. Pharmacol.* 8:412. doi: 10.3389/fphar.2017.00412

Ferry, J. D. (1980). *Viscoelastic Properties of Polymers*. New York, NY: Wiley-Blackwell.

Gaillard, Y., Mija, A., Burr, A., Darque-Ceretti, E., Felder, E., and Sbirrazzuoli, N. (2011). Green material composites from renewable resources: polymorphic transitions and phase diagram of beeswax rosin resin. *Thermochim. Acta* 521, 90–97. doi: 10.1016/j.tca.2011.04.010

Ghisalberti, E. L. (1979). Propolis: a review. *Bee World* 60, 59–84. doi: 10.1080/0005772X.1979.11097738

Ghodki, B. M., and Goswami, T. K. (2016). Physico-thermal and flavoring characteristics of essential oil of cassia. *J. Essent. Oil Bear Plants* 19, 854–862. doi: 10.1080/0972060X.2016.1187091

Girard, M., Gaillard, Y., Burr, A., Darque-Ceretti, E., and Felder, E. (2014). Nanoindentation of bio-sourced adhesive 75% rosin/25% beeswax: experimental results and modelisation. *Mech. Mater.* 69, 185–194. doi: 10.1016/j.mechmat.2013.10.005

Gorb, E., Kastner, V., Peressadko, A., Arzt, E., Gaume, L., Rowe, N., et al. (2004). Structure and properties of the glandular surface in the digestive zone of the pitcher in the carnivorous plant *Nepenthes ventrata* and its role in insect trapping and retention. *J. Exp. Biol.* 207, 2947–2963. doi: 10.1242/jeb.01128

Gorb, S. N. (2007). Visualisation of native surfaces by two-step moldings. *Microscopy Today* 15, 44–47. doi: 10.1017/S1551929500051038

Gorb, S. N., and Heepe, L. (2017). "Biological fibrillar adhesives: functional principles and biomimetic applications," in *Handbook of Adhesion Technology*, eds L. F. M. da Silva, A. Ochsner, and R. D. Adam (Cham: Springer International Publishing), 1−37. doi: 10.1007/978-3-319-42087-5_54-2

Gorb, S. N., and Scherge, M. (2000). Biological microtribology: anisotropy in frictional forces of orthopteran attachment pads reflects the ultrastructure of a highly deformable material. *Proc. R Soc. London Ser. B Biol. Sci.* 267, 1239–1244. doi: 10.1098/rspb.2000.1133

Greenaway, W., Scaysbrook, T., and Whatley, F. R. (1990). The composition and plant origins of propolis: a report of work at Oxford. *Bee World* 71, 107–118. doi: 10.1080/0005772X.1990.11099047

Hossain, M., Ketata, C., and Islam, M. R. (2009). "Experimental study of physical and mechanical properties of natural and synthetic waxes using uniaxial compressive strength test," in *Proceeding of Third International Conference on Modeling, Simulations and Applied Optimization, Sharjah, United Arab Emirates*, 1–5.

Huang, S., Zhang, C.-P., Wang, K., Li, G. Q., and Hu, F.-L. (2014). Recent advances in the chemical composition of propolis. *Molecules* 19, 19610–19632. doi: 10.3390/molecules191219610

Isidorov, V. A., Bakier, S., Piroznikow, E., Zambrzycka, M., and Swiecicka, I. (2016). Selective behaviour of honeybees in acquiring European propolis plant precursors. *J. Chem. Ecol.* 42, 475–485. doi: 10.1007/s10886-016-0708-9

Jiao, Y., Gorb, S., and Scherge, M. (2000). Adhesion measured on the attachment pads of *Tettigonia viridissima* (Orthoptera, Insecta). *J Exp Biol* 203, 1887–1895. doi: 10.1242/jeb.203.12.1887

Johnson, K. L., Kendall, K., and Roberts, A. D. (1971). Surface energy and the contact of elastic solids. *Proc. R Soc. A Math. Phys. Eng. Sci.* 324, 301–313. doi: 10.1098/rspa.1971.0141

Jones, J. C. (2004). Honey bee nest thermoregulation: diversity promotes stability. *Science* 305, 402–404. doi: 10.1126/science.1096340

Kellar, E. J. C. (2011). "Selection of adhesives, "in *Handbook of Adhesion Technology*, eds L. F. M. da Silva, A. Ochsner, and R. D. Adam (Berlin: Springer Berlin Heidelberg), 373–389. doi: 10.1007/978-3-642-01169-6_16

Kinloch, A. J. (1987). *Adhesion and Adhesives: A Science and Technology*. Dordrecht: Springer Netherlands. doi: 10.1007/978-94-015-7764-9

Koch, K., Schulte, A. J., Fischer, A., Gorb, S. N., and Barthlott, W. (2008). A fast, precise and low-cost replication technique for nano- and high-aspect-ratio structures of biological and artificial surfaces. *Bioinspir. Biomim.* 3:46002. doi: 10.1088/1748-3182/3/4/046002

Kovalev, A., Filippov, A., and Gorb, S. N. (2018). Slow viscoelastic response of resilin. *J. Comp. Physiol. A* 204, 409–417. doi: 10.1007/s00359-018-1248-2

Krell, R. (1996). *Value-Added Products From Beekeeping*. Rome: Food and Agriculture Organization of the United Nations; (FAOAgricul-tural Services Bulletin).

Kumazawa, S., Nakamura, J., Murase, M., Miyagawa, M., Ahn, M.-R., and Fukumoto, S. (2008). Plant origin of Okinawan propolis: honeybee behavior observation and phytochemical analysis. *Naturwissenschaften* 95, 781–786. doi: 10.1007/s00114-008-0383-y

Langenheim, J. H. (1990). Plant resins. *Am. Sci.* 78, 16–24.

Lorenz, B., Krick, B. A., Mulakaluri, N., Smolyakova, M., Dieluweit, S., Sawyer, W. G., et al. (2013). Adhesion: role of bulk viscoelasticity and surface roughness. *J. Phys. Condens. Matter*. 25, 1–16. doi: 10.1088/0953-8984/25/22/225004

Mantel, M., and Wightman, J. P. (1994). Influence of the surface chemistry on the wettability of stainless steel. *Surf. Interface Anal.* 21, 595–605. doi: 10.1002/sia.740210902

Mello, B. C. B. S., and Hubinger, M. D. (2012). Antioxidant activity and polyphenol contents in Brazilian green propolis extracts prepared with the use of ethanol and water as solvents in different {pH} values. *Int. J. Food Sci. Technol.* 47, 2510–2518. doi: 10.1111/j.1365-2621.2012.03129.x

Monti, M., Bertt, E., Carminati, G., and Cusini, M. (1983). Occupational and cosmetic dermatitis from propolis. *Contact Dermatitis* 9:163. doi: 10.1111/j.1600-0536.1983.tb04341.x

Morgan, J., Townley, S., Kemble, G., and Smith, R. (2002). Measurement of physical and mechanical properties of beeswax. *Mater. Sci. Technol.* 18, 463–467. doi: 10.1179/026708302225001714

Owens, D. K., and Wendt, R. C. (1969). Estimation of the surface free energy of polymers. *J. Appl. Polym. Sci.* 13, 1741–1747. doi: 10.1002/app.1969.070130815

Popov, V. L., Pohrt, R., and Li, Q. (2017). Strength of adhesive contacts: influence of contact geometry and material gradients. *Friction* 5, 308–325. doi: 10.1007/s40544-017-0177-3

Reitsma, M., Craig, V. S. J., and Biggs, S. (2000). Measurement of the adhesion of a viscoelastic sphere to a flat non-compliant substrate. *J. Adhes.* 74, 125–142. doi: 10.1080/00218460008034527

Richter, K., Grunwald, I., and von Byern, J. (2018). "Bioadhesives, "in *Handbook of Adhesion Technology*, eds L. F. M. da Silva, A. Ochsner, and R. D. Adam (Cham: Springer International Publishing), p. 1–45. doi: 10.1007/978-3-319-42087-5_53-2

Simone-Finstrom, M., and Spivak, M. (2010). Propolis and bee health: the natural history and significance of resin use by honey bees. *Apidologie* 41, 295–311. doi: 10.1051/apido/2010016

Smith, A. M. (2016). *Biological Adhesives*. Cham: Springer International Publishing. doi: 10.1007/978-3-319-46082-6

Teslenko, I. A., Bobro, S. G., and Tikhonov, A. I. (2014). "Development cosmetics based propolis," in *Actual questions of development of new drugs : Abstracts of XX international scientific and practical conference of young scientists and student*. Available online at: http://dspace.nuph.edu.ua/handle/123456789/5977 (accessed April 20, 2021).

von Byern, J. G., and Grunwald, I. (2010). *Biological Adhesive Systems.* Vienna: Springer-Verlag KG. doi: 10.1007/978-3-7091-0286-2

Wagh, V. D. (2013). Propolis: a wonder bees product and its pharmacological potentials. *Adv. Pharmacol. Sci*. 2013, 1–11. doi: 10.1155/2013/308249

Weng, S-C., Fuh, A., Tang, F-C., and Cheng, K-T. (2016). Effect of surface condition on liquid crystal photoalignment by light induced azo dye adsorption phenomena. *Liq. Cryst.* 43, 1221–1229. doi: 10.1080/02678292.2016.1163740

Wheater, C. P., and Evans, M. E. G. (1989). The mandibular forces and pressures of some predacious Coleoptera. *J. Insect. Physiol.* 35, 815–820. doi: 10.1016/0022-1910(89)90096-6

Xie, Y., Hill, C. A. S., Jalaludin, Z., and Sun, D. (2011). The water vapour sorption behaviour of three celluloses: analysis using parallel exponential kinetics and interpretation using the Kelvin-Voigt viscoelastic model. *Cellulose* 18, 517–530. doi: 10.1007/s10570-011-9512-4

Conflict of Interest: The authors declare that the research was conducted in the absence of any commercial or financial relationships that could be construed as a potential conflict of interest.

frontiers in Mechanical Engineering

REVIEW
published: 07 May 2021
doi: 10.3389/fmech.2021.668262

Applications of Bioinspired Reversible Dry and Wet Adhesives: A Review

*Minsu Kang†, Kahyun Sun†, Minho Seong†, Insol Hwang, Hyejin Jang, Seongjin Park, Geonjun Choi, Sang-Hyeon Lee, Jaeil Kim and Hoon Eui Jeong**

Department of Mechanical Engineering, Ulsan National Institute of Science and Technology, Ulsan, South Korea

Bioinspired adhesives that emulate the unique dry and wet adhesion mechanisms of living systems have been actively explored over the past two decades. Synthetic bioinspired adhesives that have recently been developed exhibit versatile smart adhesion capabilities, including controllable adhesion strength, active adhesion control, no residue remaining on the surface, and robust and reversible adhesion to diverse dry and wet surfaces. Owing to these advantages, bioinspired adhesives have been applied to various engineering domains. This review summarizes recent efforts that have been undertaken in the application of synthetic dry and wet adhesives, mainly focusing on grippers, robots, and wearable sensors. Moreover, future directions and challenges toward the next generation of bioinspired adhesives for advanced industrial applications are described.

Keywords: bioinspired adhesive, dry adhesion, wet adhesion, gripper, robot, attachable sensor, skin patch

OPEN ACCESS

Edited by:
Stanislav N. Gorb,
University of Kiel, Germany

Reviewed by:
Dan Sameoto,
University of Alberta, Canada
Linmao Qian,
Southwest Jiaotong University, China

****Correspondence:***
Hoon Eui Jeong
hoonejeong@unist.ac.kr

†These authors have contributed equally to this work and share first authorship

Specialty section:
This article was submitted to Tribology, a section of the journal Frontiers in Mechanical Engineering

Received: *15 February 2021*
Accepted: *31 March 2021*
Published: *07 May 2021*

Citation:
Kang M, Sun K, Seong M, Hwang I, Jang H, Park S, Choi G, Lee S-H, Kim J and Jeong HE (2021) Applications of Bioinspired Reversible Dry and Wet Adhesives: A Review. Front. Mech. Eng. 7:668262. doi: 10.3389/fmech.2021.668262

INTRODUCTION

Numerous living organisms have evolved various adhesion systems. Robust and repeatable adhesion that has been adapted to various environments is a key factor for survival as it enables efficient activities, including climbing, clinging, and catching prey. Among the various species, gecko lizards, beetles, octopuses, and remoras have attracted substantial attention owing to their excellent adhesion properties, such as high adhesion to curved or rough target surfaces, functionality in wet environments, reusability, and biocompatibility (**Figure 1A**) (Autumn et al., 2000; Dirks and Federle, 2011; Baik et al., 2017; Wang et al., 2017). Extensive studies over the past two decades have revealed that their superior adhesion properties originate from their unique terminal structures (Wang L. et al., 2020). For example, gecko lizards and beetles can walk freely on walls or ceilings with strong adhesion based on numerous pillar structures with spatulated or mushroom-shaped tips on their toes (Autumn et al., 2000; Arzt et al., 2003; Jeong et al., 2009b). Furthermore, they have an efficient self-cleaning property in both dry and wet conditions so that contaminants rarely attach to or are maintained on the adhesive surface (Hansen and Autumn, 2005; Lee and Fearing, 2008; Sethi et al., 2008; Spinner et al., 2013). The self-cleaning capability enables easy removal of the contaminants from the adhesive surfaces, i.e., the dry adhesive can quickly and fully recover a clean adhesion that does not transfer contaminants to the substrate (Bhushan and Sayer, 2007; Sethi et al., 2008). Moreover, underwater organisms, such as octopuses, remoras, and clingfishes, use a

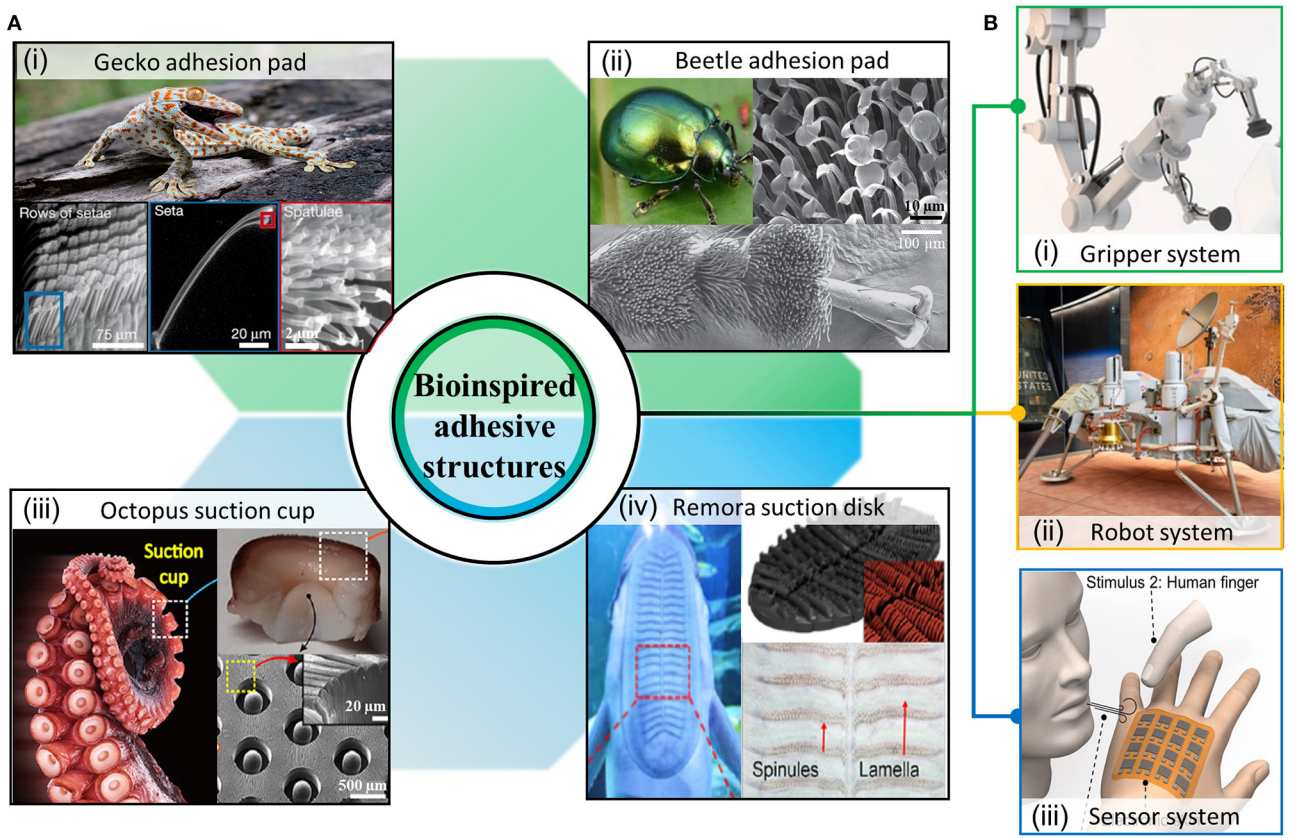

FIGURE 1 | Research schematic of bioinspired adhesive structures for reversible dry and wet adhesion. **(A)** Representative examples of adhesive structures in nature: (i) gecko's toes [reprinted with permission from ref Zhao et al. (2008)] (ii) beetle's pads [reprinted with permission from ref Amador et al. (2017)]. (iii) octopus suction cup [reprinted with permission from ref Baik et al. (2019)]. (iv) remora suction disk [reprinted with permission from ref Lee et al. (2019)]. **(B)** Application field of adhesion structure (i) gripper (top), (ii) robot system (middle), (iii) wearable sensor system (bottom) [reprinted with permission from ref An et al. (2017)].

unique sucker structure to stably adhere to various wet surfaces (Lee et al., 2016, 2019). Strong wet adhesion allows them to grasp objects or to firmly adhere to slippery surfaces with ease.

The unique adhesion systems that exist in nature offer high potential in various advanced industries, such as grippers, robots, and wearable sensors (**Figure 1B**) (Drotlef et al., 2017; Shahsavan et al., 2017). These application fields require strong and repeatable adhesion, particularly under harsh conditions, such as rough surfaces, high humidity, or even underwater environments. However, conventional contact methods, including mechanical fixation and chemical adhesion, are limited by their inferior adhesion performance. Mechanical fixations, whereby friction or an interlocking force are primarily applied, cause surface damage (Fuentes et al., 2015; O'Brien et al., 2019; Ozaki et al., 2020). Chemical adhesives have limitations such as low repeatability, surface contamination by residue, and vulnerability to moisture (Yuk et al., 2016; Pan et al., 2020). As a novel solution to these problems, bioinspired synthetic dry and wet adhesives have been applied to adhesion systems in advanced industries. For example, grippers integrated with bioinspired adhesives have been used for the precise and safe transportation of thin and fragile wafers (Zhou et al., 2013). Similarly, bioinspired adhesive-based mobile robots that can climb vertical walls, hang from the ceiling, or cling to underwater surfaces have been presented (Seo and Sitti, 2013; Yu et al., 2018). Moreover, adhesive microstructures enable wearable sensors that strongly adhere to skin, where continuous deformation and sweat may occur (Drotlef et al., 2017; Wi et al., 2017; Chun et al., 2019). In recent years, bioinspired adhesives with functional materials, such as conductive, biocompatible, and stimuli-responsive polymers or nanocomposites, have been proposed for advanced applications (Gu et al., 2018; Hwang et al., 2020; Tian et al., 2020).

In this review, we provide an overview of the use of bioinspired dry and wet adhesives in advanced applications. The remainder of this paper is organized as follows. In the first section, we briefly introduce the fundamental adhesion mechanisms that can be classified as dry and wet adhesion. In the second section, we describe how these novel adhesion systems are currently applied in three specific applications: grippers, robots, and wearable sensors. Finally, recent challenges and future directions for bioinspired adhesives and their applications are discussed.

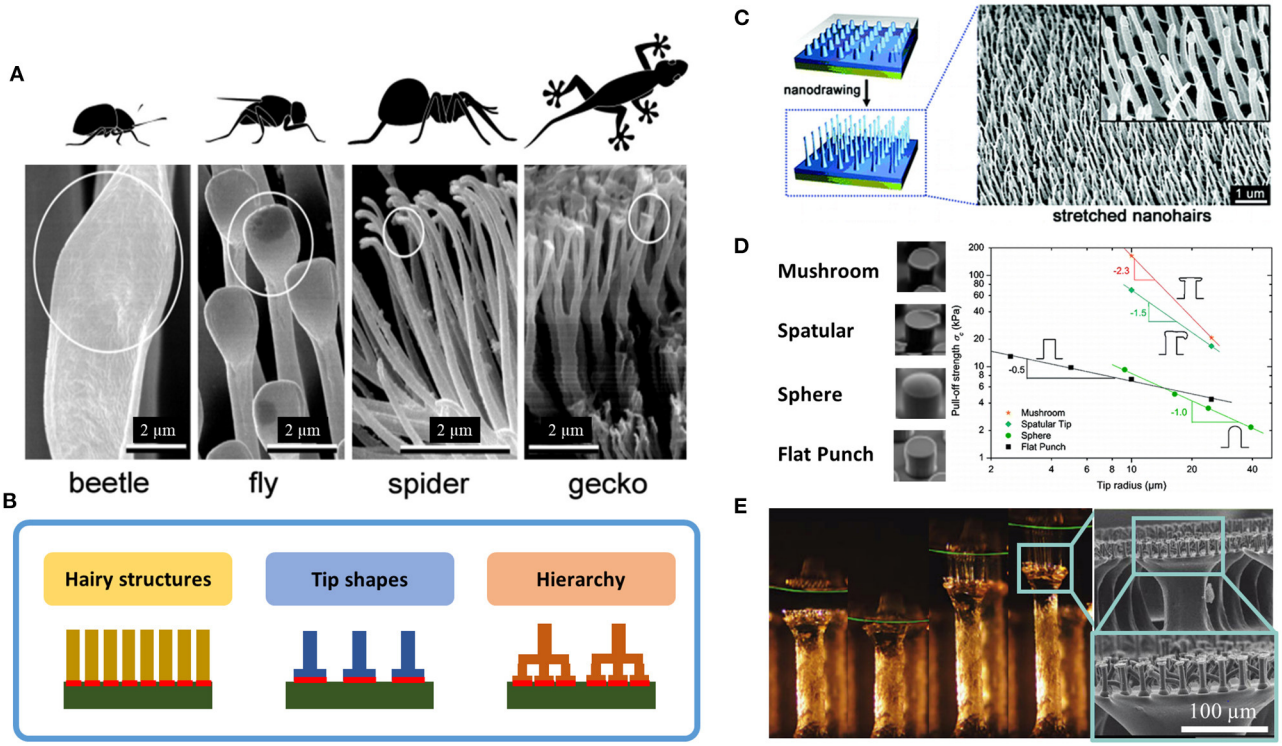

FIGURE 2 | Bioinspired dry adhesive structures. **(A)** Various animals' tips and their properties [reprinted with permission from ref Arzt et al. (2003)]. **(B)** Schematic in hairy structures, tip shapes, and hierarchy of dry adhesive. **(C)** Fabricated high aspect ratio nano hairs [reprinted with permission from ref Jeong et al. (2006)]. **(D)** Experimental results in pull-off test of dry adhesive with different tips [reprinted with permission from ref Del Campo et al. (2007b)]. **(E)** Hierarchical pillar for high efficiency of adhesion [reprinted with permission from ref Murphy et al. (2009)].

REVERSIBLE ADHESION MECHANISMS OF LIVING SYSTEMS

Bioinspired Dry Adhesive Structures

Among the living organisms that exist in nature, beetles, flies, spiders, and geckos have versatile adhesion mechanisms that enable robust, reversible, repeatable, and clean adhesion on various rough surfaces (**Figure 2A**) (Autumn et al., 2000, 2002; Arzt et al., 2003; Geim et al., 2003). Many studies have revealed that their superior adhesion originates from their nano- or micrometer-scale hairy structures (Autumn et al., 2000, 2002; Arzt et al., 2003; Varenberg et al., 2010). For example, the gecko lizard has arrays of millions of microscale foot hairs, containing hundreds of nanoscale projections terminating in spatula-shaped tip structures (Niewiarowski et al., 2016). Similarly, beetles have hierarchical hairy structures on their legs, which are composed of numerous tiny setae with flattened and widened mushroom-shaped plates (Gorb et al., 2010; Bullock and Federle, 2011). These structures maximize the van der Waals interactions based on the three common structural features, grouped as hairy structures, extruded tips, and hierarchical structures (**Figure 2B**).

Hairy structures are one of the most important features of dry adhesive systems. Numerous high-aspect-ratio hair structures enable effective adaptation to rough surfaces, resulting in a maximized contact area. Arzt et al. theoretically suggested that the adhesion of the pillar structure is based on Hertzian theory (Arzt et al., 2003). According to this study, when a single pillar structure with a hemispherical tip contacts the target surface, a finite pull-off force (F_C) occurs, which is expressed as:

$$F_C = \frac{3}{2}\pi R\gamma \tag{1}$$

where γ is the adhesion energy per area and R is the hemisphere radius. Assuming that the entire contact surface consists of n pillars, each with a radius $R/n^{0.5}$, the total adhesion force (F'_C) can be increased to:

$$F'_C = F_C\, n^{0.5} \tag{2}$$

According to Equations (1) and (2), the adhesion resulting from the pillar structure becomes stronger as the number of pillars per unit area increases. Additionally, submicron- or nano-scale structures significantly reduce the effective modulus of the adhesives, enhancing the surface adaptability. The effective modulus (E_{eff}) of the pillar structures is given by (Autumn et al., 2006):

$$E_{eff} = \frac{3EID\sin(\theta)}{L^2\cos^2(\theta)[1\pm\mu\tan(\theta)]} \tag{3}$$

where E is the elastic modulus of the material, I is the moment of inertia, D is the pillar density, L is the pillar length, μ is the friction coefficient, and θ is the slanted angle of the pillar. The effective modulus can describe how relatively hard materials (Young's modulus higher than 100 kPa) function as a pressure-sensitive adhesive, emphasizing the need for high-aspect-ratio hairy structures. However, the effective modulus needs to be incorporated with proper contact geometry because the shape of the tips (or caps) dominates the stress distribution on the contact interfaces (Kroner and Arzt, 2012).

The extruding tip structure, such as spatula and mushroom (symmetric spatulae), which can be observed at the end of the pillar structure, has a significant effect on the adhesion of the dry adhesive structure (Kim and Sitti, 2006; Del Campo et al., 2007b; Bullock and Federle, 2011; Kwak et al., 2011a; Heepe et al., 2012; Kroner and Arzt, 2012; Oh et al., 2019). The extruding tip structures not only increase the contact area of the hairy structures but also uniformly distribute the stress at the contact interface until they are separated from the target substrate (Carbone et al., 2011). As a result, the adhesives can be strongly attached to the substrate with high stability, even over millions of cycles of repeated attachment and detachment.

The hierarchical arrangement of gecko foot hair is also a key element that can maximize adhesion performance (Murphy et al., 2009; Bae et al., 2014). Various studies have revealed that the hierarchy improves adaptability to surfaces with roughness at different length scales (macro – nano). Furthermore, they significantly improved the structural stability by effectively distributing the stress between hierarchies during repeated loading cycles.

Based on these mechanisms, many studies have been conducted to mimic the superior adhesion performance of dry adhesives in nature. Studies have been proposed that maximize the van der Waals interactions of micro-and nanoscale hairy structures by increasing the aspect ratio and reducing the diameter (Geim et al., 2003; Mahdavi et al., 2008). Greiner et al. developed microscale vertical pillars with high aspect ratios using a soft molding method (Greiner et al., 2007). The pull-off strength was measured up to 20 kPa in pillars with aspect ratios above 5. Nanoscale hairy structures with a high aspect ratio of over 20 and a small radius (∼80 nm) were proposed based on the nanodrawing method (**Figure 2C**) (Jeong et al., 2006). Qu et al. presented a carbon nanotube (CNT)-based dry adhesive to achieve an extremely small radius (∼15 nm) and high aspect ratio of the nanoscale hair array (Qu et al., 2008).

On the other hand, to realize adhesion enhancement, many researchers have focused on controlling 3D tip geometries (Del Campo et al., 2007a; Carbone et al., 2011; Kwak et al., 2011b). For example, artificial dry adhesives with various 3D tip structures, including spatulae, mushroom (symmetric spatulae), and triangular shapes have been developed (Del Campo et al., 2007b; Kwak et al., 2011a). Among them, mushroom-shaped tip structures were reported to exhibit outstanding adhesion performance (**Figure 2D**) (Del Campo et al., 2007b; Yi et al., 2016). The diameter and thickness of the mushroom-shaped tip structures are key factors in determining adhesion strength and structural stability. Yi et al. demonstrated that the adhesion of optimized tip structures was ∼10 times stronger than that of non-optimized tips (Yi et al., 2016). Several studies have presented finite element analyses (FEA) incorporating contact geometry optimization of dry adhesives for uniform stress distribution within the tips (Zhang X. et al., 2021). Recently, Kim et al. reported deep learning-based optimization of mushroom-shaped structures composed of smoothly mixed convex and concave parts and demonstrated improved uniformity in the interfacial stress distribution (Kim et al., 2020).

Furthermore, various studies have reported improved adhesion performance based on hierarchical structures. For example, aligned CNT forests integrated with micro-sized pillars were utilized as hierarchical adhesives exhibiting 9 times stronger shear adhesion than that of a micropillar uncovered with CNT forests (Rong et al., 2014). Jeong et al. developed monolithic micro-and nanoscale hierarchical hairs using a 2-step UV-assisted molding technique, which has a robust shear adhesion force even on a rough surface (Jeong et al., 2009b). In addition, Murphy et al. proposed a novel adhesive structure that integrates the structural advantages of hierarchical and extruding tip structures (**Figure 2E**) (Murphy et al., 2009). Hierarchical structures with mushroom-shaped tips fabricated through the multilevel molding technique exhibited 5.3 times higher adhesion than unstructured surfaces.

Bioinspired Wet Adhesive Structures

Organisms that live in wet and underwater environments have different adhesive mechanisms than those living in dry conditions. In particular, the octopus, tree frog, and clingfish can achieve reversible adhesion with a strong attachment to surfaces under wet conditions (Drotlef et al., 2013; Zou et al., 2016; Wang et al., 2017; Zhao et al., 2017; Zhang et al., 2019; Chen et al., 2020). These strong wet adhesions are derived from special micro/nanostructures on the surface of organisms, such as suction cups and polygonal patterns. Their unique structures enable them to maintain strong wet adhesion to various curved and rough surfaces through suction, which is driven by a pressure difference and capillary adhesion. In recent years, extensive research has been conducted to determine the principles of wet adhesion and to emulate the adhesion mechanism (O'Brien et al., 2019; Chen et al., 2020).

An octopus achieves adhesion using a mechanism that causes a pressure difference through a suction cup in a wet environment (**Figure 3A**) (Tramacere et al., 2014, 2015; Oh et al., 2018). A hollowed space, known as the sucker cavity, exists inside the suction cup. With an applied preload, a pressure drop in the suction cup occurs with a volumetric change, where the dome-like structure inside the cavity maximizes the pressure difference between the inside and outside (**Figure 3B**) (Tramacere et al., 2013). The pressure difference can serve as a major mechanism underwater because of the higher external pressure. The governing equation for the adhesion force (F_{normal}) that can be induced through the suction cup structure is expressed as follows (Chen and Yang, 2017):

$$F_{normal} = \Delta P \times A_{total} \tag{4}$$

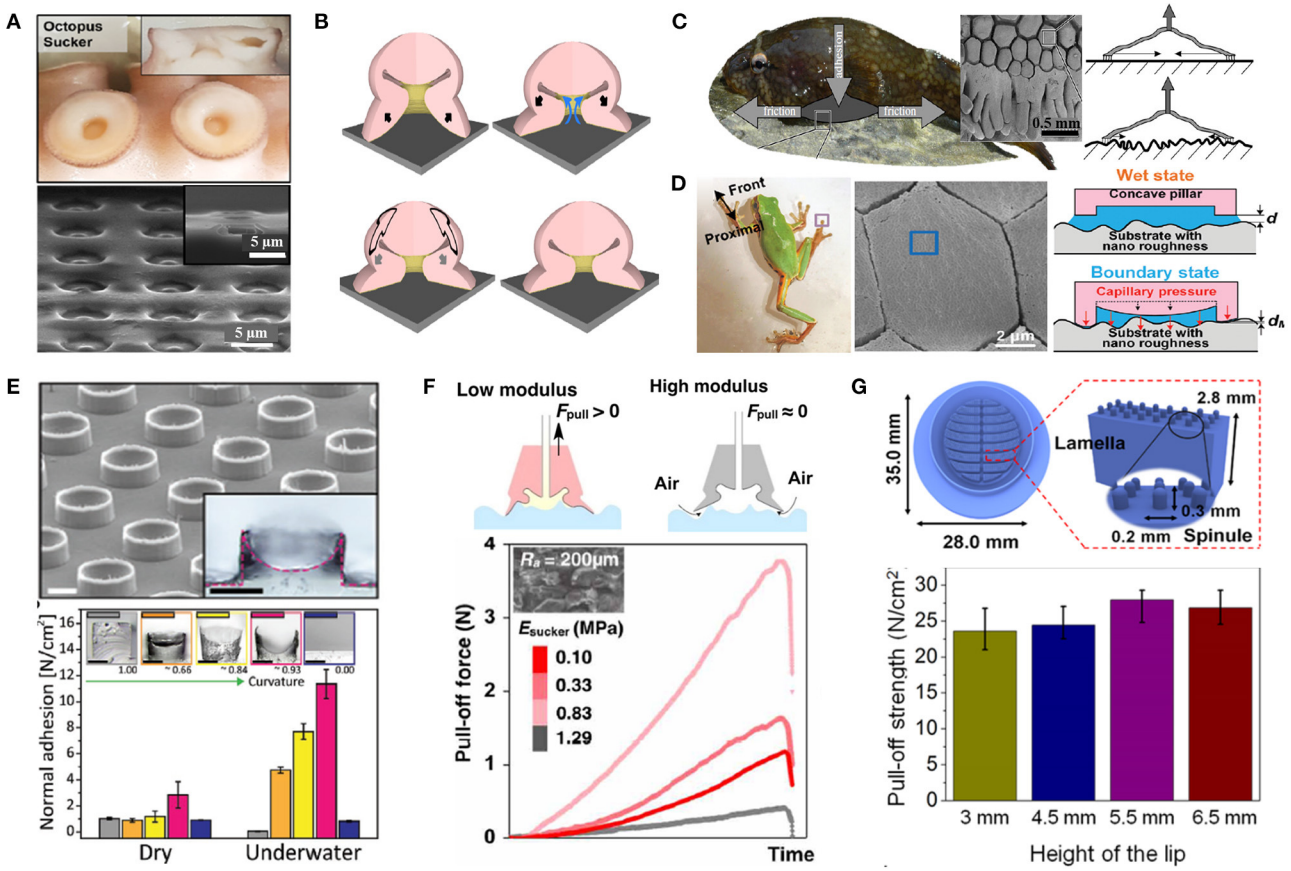

FIGURE 3 | Bioinspired wet adhesive structures. **(A)** Octopus-inspired suction cup [reprinted with permission from ref Oh et al. (2018)]. **(B)** Adhesion mechanism of suction cup under wet conditions [reprinted with permission from ref Tramacere et al. (2013)]. **(C)** Clingfish-inspired sucker and hexagonal microstructure mechanism under wet conditions [reprinted with permission from ref Wainwright et al. (2013)]. **(D)** Tree frog-inspired regular hexagonal microstructure and adhesion mechanism under wet conditions [reprinted with permission from ref Zhang et al. (2020)]. **(E)** Section of sucker cavity and adhesion strength under dry/underwater conditions [reprinted with permission from ref Baik et al. (2018)]. **(F)** Organohydrogel-based sucker and adhesion strength under wet conditions [reprinted with permission from ref Zhuo et al. (2020)]. **(G)** Lamella and spinule structure of suction and varying adhesion strength with lip height under wet conditions [reprinted with permission from ref Lee et al. (2019)].

where ΔP is the pressure difference between the inside and outside of the suction cup, and A_{total} is the total adhesion area of the suction structure. According to this equation, the pressure difference plays a significant role in adjusting the suction cup adhesion.

Clingfish can strongly attach themselves to various wet surfaces because of their hierarchical adhesion mechanism, which consists of suction and friction (Wainwright et al., 2013). The adhesive disc of the clingfish is composed of a suction chamber and rows of papillae structures around the chamber. The papillae structures divided into a polygonal shape increases the friction, regardless of the roughness of the target surface. When the suction chamber fails, the edges slide toward the center of the chamber. However, the increase in friction at the edges significantly improves the adhesion by resisting sliding. Due to this hierarchical structure of the adhesive disc, clingfish adhere well to surfaces of different roughness, developing pull-off forces that are 80 to 230 times the bodyweight of the clingfish (**Figure 3C**) (Wainwright et al., 2013; Sandoval et al., 2019, 2020).

Tree frogs exhibit different types of wet adhesive mechanisms (Iturri et al., 2015; Langowski et al., 2018). Polygonal patterns on the toe pads of the tree frog can strongly adhere to the liquid-vapor interface. The wet adhesion principle originates from the capillary force, whereby the attraction between the surface and structure is transformed into an adhesion force (F_{normal}) (**Figure 3D**) (Zhang et al., 2020). According to this principle, organisms can adhere to surfaces by obtaining high adhesion/friction, even under wet conditions. The capillary-force-based adhesion force is expressed as follows (Chen et al., 2020):

$$F_{normal} = -\pi {R_l}^2 \eta \frac{\cos\theta_1 + \cos\theta_2}{h} - \pi R_l \eta \tag{5}$$

where R_l is the liquid film radius, h is the liquid film thickness, θ_1 and θ_2 are the contact angles, and η is the viscosity coefficient of the liquid.

Research on the superior adhesion mechanism of suction cups and polygonal patterns has promoted the development of

artificial wet adhesives. In particular, several strategies have been reported to construct more complex 3D configurations and scale down to submicron/nano. Nano-or microsuckers with cavity structures were presented based on hole-patterned mold-assisted soft lithography (Chen and Yang, 2017; Oh et al., 2018). In addition, complex configurations of the suction cup components, such as the orifice and protuberance, were successfully mimicked for wet adhesives by controlling the meniscus of a liquid precursor (Baik et al., 2017). They revealed that the combination of the complex structures helps the adhesive to exert a strong adhesion of up to 110 kPa under wet conditions (Baik et al., 2018) (**Figure 3E**). Lee et al. developed a suction cup composed of thermoresponsive polymers exhibiting enhanced adhesion of up to 94 kPa (Lee et al., 2016). Zhou et al. also presented a pneumatic sucker exhibiting excellent adaptable adhesion up to 3.75 N on a rough surface (with surface roughness $R_a = 200\,\mu m$) under a sucker's modulus of 1.29 MPa (**Figure 3F**) (Zhuo et al., 2020). Recently, a 3D Printing based bottom-up approach was applied to a micro-suction disk, which exerts high friction of up to 266.8 kPa (**Figure 3G**) (Lee et al., 2019). Furthermore, hexagonal-shaped micropatterns were presented as strong wet adhesives, where the synergistic effects of the low bending stiffness of the pillars and a high number density of the pattern in the sliding direction exhibit a robust friction force, even underwater (Chen et al., 2015; Iturri et al., 2015; Ko et al., 2017a).

The gecko-inspired nano/microstructure can be utilized as wet adhesives, where the surface wettability of both the gecko adhesives and target substrates can also play a significant role in wet conditions (Stark et al., 2014; Stark and Mitchell, 2019; Mitchell et al., 2020). When the micropillars and wet substrate come into contact, the interfacial water layer reduces adhesion by causing van der Waals interference and the lubrication effect. In the case of a hydrophilic substrate, the surface does not effectively prevent or repel interfacial water, which significantly reduces adhesion compared to dry conditions (Stark et al., 2014). However, on a hydrophobic substrate, the interface between the adhesive and substrate can repel water and maintain dry adhesion based on van der Waals interactions. Based on this principle, Soltannia et al. presented mushroom-shaped microfibers with strong and reversible underwater adhesion (Soltannia and Sameoto, 2014), which can be applied to attachable gaskets in microfluidic devices and microstrips (Wasay and Sameoto, 2015; Zandvakili et al., 2017).

Research on the integration of dry and wet adhesives has also been actively conducted. Representatively, Lee et al. presented a dry-wet hybrid mechanism in which gecko-inspired dry adhesives were integrated with mussel-inspired wet adhesives of 3,4-dihydroxy-L-phenylalanine (DOPA) proteins (Lee et al., 2007) that form non-covalent interactions (hydrogen bonding, cation-pi interaction, metal coordination, hydrophobic interaction) on diverse organic and inorganic substrates, both in air and underwater (Hofman et al., 2018). Furthermore, the hydrogel was combined with gecko adhesives for the synergistic effect of mushroom-shaped micropillars and water-absorbing properties with the hydrophilic nature of the hydrogel (Yi et al., 2018). The combination enables strong van der Waals adhesion under dry conditions and capillary adhesion under wet conditions. Recently, Wang et al. proposed fibrillar adhesives with angled tip structures (cupped microstructures), exhibiting strong and reversible adhesion properties under both dry and wet conditions (Wang et al., 2019b; Wang Y. et al., 2020). The cup-shaped contact geometry enables strong adhesion mechanisms attributed to van der Waals interactions under dry conditions, while suction under wet conditions. Because the wet adhesion of existing flat mushroom structures is feasible under limited conditions (e.g., hydrophobic mating surfaces), the hybrid approach is expected to be an effective solution for robust adhesion in both dry and wet environments.

APPLICATIONS OF BIOINSPIRED DRY AND WET ADHESIVES

Robust adhesion systems have been actively explored in advanced industries. In particular, grippers, robots, and sensors require reversible and versatile adhesion to dry/wet conditions. Accordingly, many researchers have introduced bioinspired dry/wet adhesive structures for advanced applications. In this section, we discuss how dry/wet adhesives are applied to these application fields in detail.

Bioinspired Adhesives on Advanced Grippers

In recent years, gripper systems have been used in various industrial fields to improve the efficiency of manufacturing processes by transporting objects or assisting repetitive work (Tai et al., 2016). With the development of various manufacturing industries, industrial grippers with the ability to grasp fragile or rough objects and to hold and release an object repeatedly without residue or damage are highly required (Sinatra et al., 2019). Wet adhesion capability is also required to allow grippers to easily transport objects in wet or underwater environments (Nishimura et al., 2017).

Bioinspired dry adhesives help grippers improve grasping capability with excellent adhesion properties. Furthermore, the switchable adhesion properties provide simple and efficient grip control (Lee et al., 2008; Zhou et al., 2013; Seo et al., 2014). For example, mushroom-shaped pillar arrays were integrated into a transportation system for fragile wafers (Zhou et al., 2013) (**Figure 4A**). The transportation system exhibited strong adhesion to the objects without a high preloading force, as well as controllable switchable adhesion properties by applying a small shear force without the consumption of external energy. Jiang et al. developed a gripper system with multiple patches and angled microwedges (Jiang et al., 2017). The discrete patches allow the gripper system to hold the curved objects by allowing the patches to form conformal contact from micro- to macroscale on the target surface. A gripper system with an elastic microfibrillar membrane was presented, which could be deformable under pneumatic control to exhibit robust adhesion to curved or irregular objects (**Figure 4B**) (Song and Sitti, 2014; Song et al., 2017).

Moreover, a gripper system with wet adhesives, such as suction cup structures, is capable of grasping wet objects in

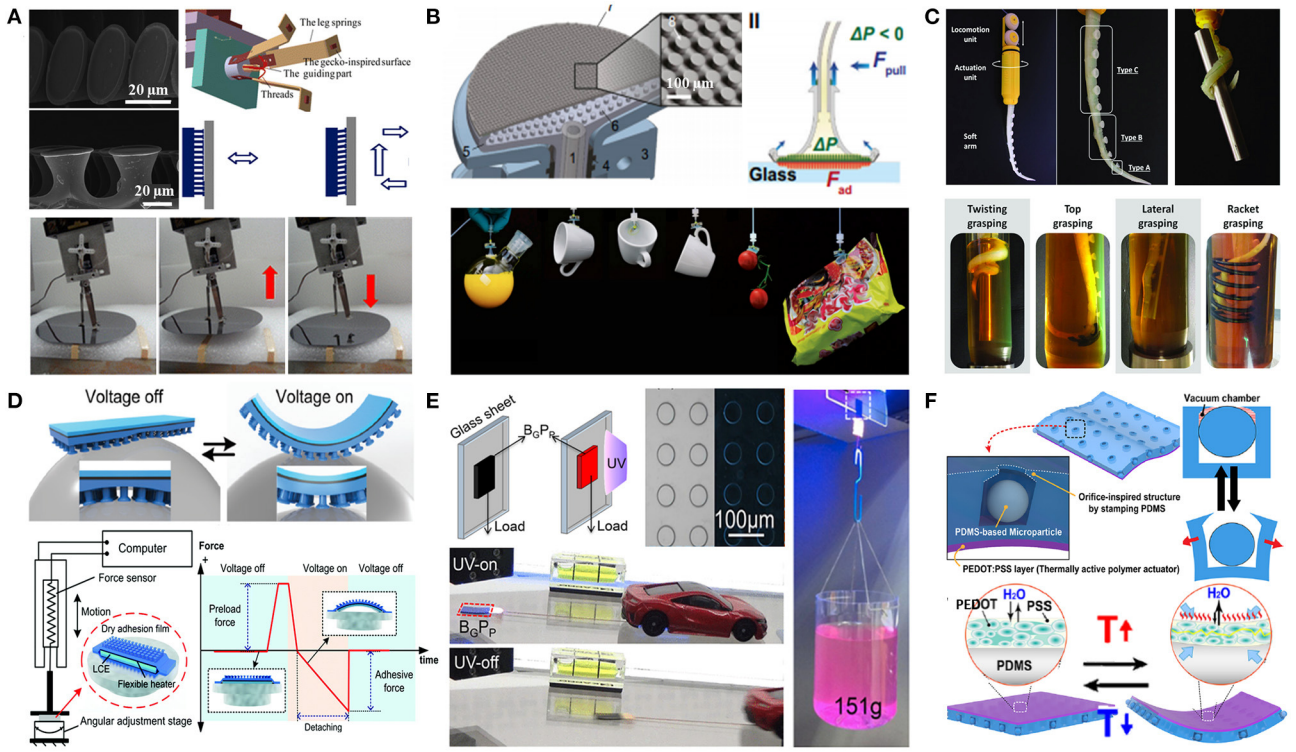

FIGURE 4 | Dry and wet adhesion structure application in gripper system. **(A)** Gecko dry adhesive structure to obtain strong adhesion [reprinted with permission from ref Zhou et al. (2013)]. **(B)** Dry adhesive structure applied to sucker structure [reprinted with permission from ref Song et al. (2017)]. **(C)** Wet adhesive structure applied to gripper system [reprinted with permission from ref Mazzolai et al. (2019)]. **(D)** Control of gripper adhesion with dry adhesion structure at low voltage [reprinted with permission from ref Tian et al. (2020)]. **(E)** Light-responsive adhesion control of dry adhesion structure [reprinted with permission from ref Wang X. et al. (2019)]. **(F)** Electrothermal-based adhesion control of wet adhesion structure [reprinted with permission from ref Baik et al. (2021)].

various morphologies without slipping under wet environments. Mazzolai et al. presented a soft arm with suction cups to retrieve non-standard objects under various dry/wet conditions, including the medium of air, water, and oil (**Figure 4C**) (Mazzolai et al., 2019). Furthermore, the combined pneumatic-controllable suckers enable the soft gripper to grasp objects with various configurations (i.e., flat, spherical, and hexagonal shapes in wet conditions) (Zhuo et al., 2020).

Dry/wet adhesive structures based on stimuli-responsive materials have been applied to gripper systems to achieve controllable adhesion strength. Tian et al. presented a gripper that could control adhesion using a dry adhesive with an electrically responsive characteristic (**Figure 4D**) (Tian et al., 2020). In addition, photothermal polymers were adapted to micropatterned soft grippers for a fast switchable dry adhesive, where the adhesion strength could increase up to a maximum of 2.5 times after exposure to UV light (**Figure 4E**) (Wang X. et al., 2019). A gripper system with an electrothermally controllable sucker was presented, which was capable of fast underwater adhesion control (**Figure 4F**) (Baik et al., 2021).

Bioinspired Adhesives on Advanced Robots

In recent years, various robotic systems have been utilized to perform tasks in extreme situations that are inaccessible to humans, such as confined spaces or underwater (Jiang et al., 2017; Ma et al., 2018). The adhesion system is considered an important technical component: it enables the robotics to be highly mobile, settle down safely, and sense the object through conformal contact, even on a ceiling, steep slope, or underwater (Kwak et al., 2011c). However, conventional adhesive methods, such as vacuum or electrostatic adsorption, are not suitable for tuning the adhesion of remote-controllable robots owing to the connection of the pneumatic or electrical control system. Furthermore, adhesion switching systems are quite energy-consuming because they require a continuous supply of external energy to maintain adhesion (Gu et al., 2018). As a solution to existing problems, various approaches utilizing bioinspired adhesives have been actively conducted.

The nano/micro-scale hairy structures of the gecko and beetle have been applied to dry adhesive systems in robots. A four-legged climbing robot with a bioinspired multi-toe with a dry adhesive exhibited strong adhesion without high pressure during attachment (**Figure 5A**) (Kim et al., 2008; Wang et al., 2018). Furthermore, the adhesive structure enhanced the stability and adaptability to a rough surface. The dry adhesive structure was also integrated into a controllable locomotion wheel (**Figure 5B**) (Liu J. F. et al., 2020). Depending on the rotational direction of the wheel and belt, the anisotropic dry adhesive on the belt can control the adhesion for continuous attachment and

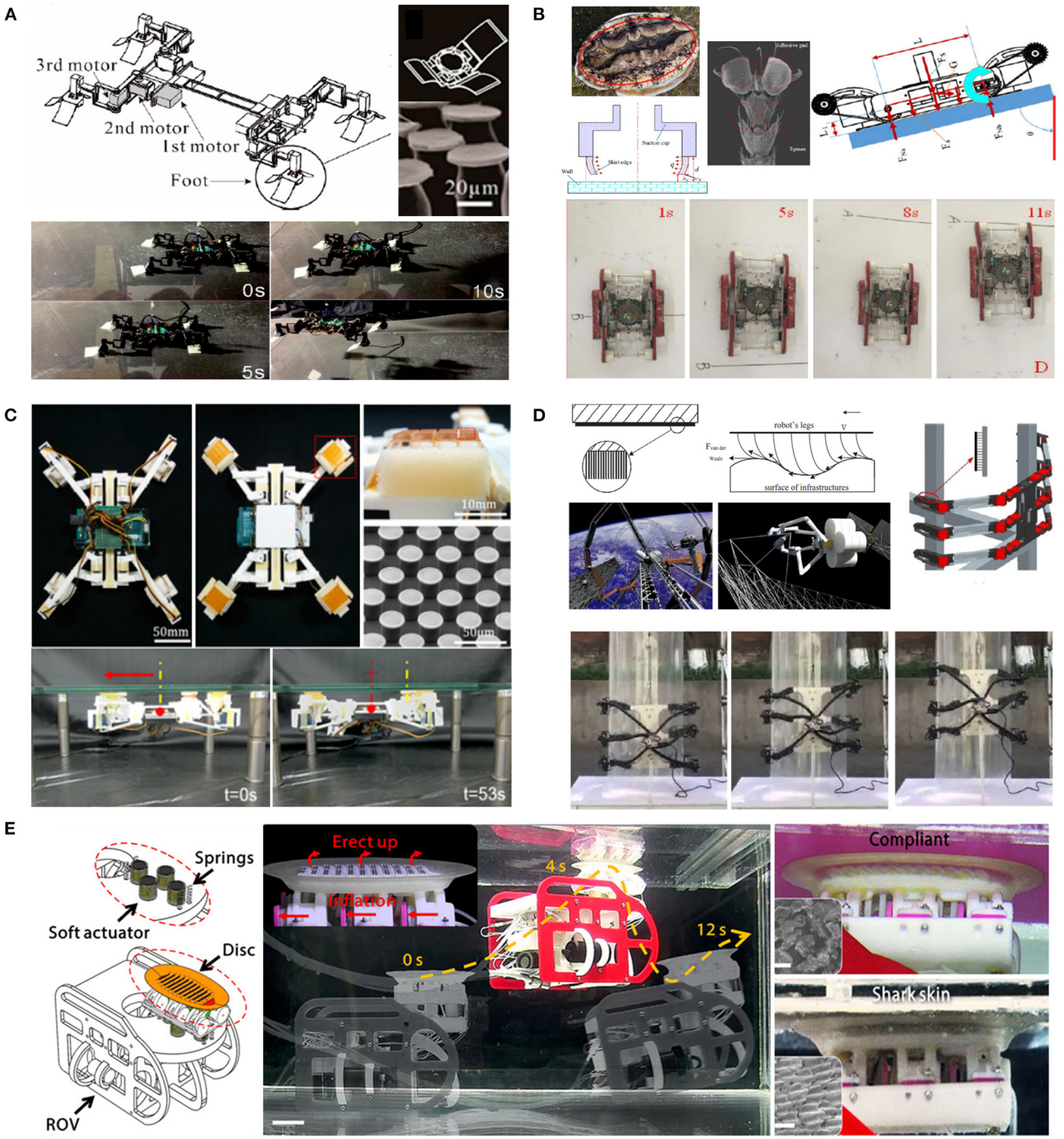

FIGURE 5 | Dry and wet adhesive applied to mobile robots. **(A)** Robot system with mushroom-shaped dry adhesive and locomotion by controlling adhesion strength [reprinted with permission from ref Wang et al. (2018)]. **(B)** Wall-climbing robot with an adhesive belt and four-wheeled system [reprinted with permission from ref Liu J. F. et al. (2020)]. **(C)** Wall and ceiling climbing quadruped robot with mushroom-shaped dry adhesive pads [reprinted with permission from ref Ko et al. (2017b)]. **(D)** Space truss-crawling robot with multi-joint leg and dry adhesive [reprinted with permission from ref Tang et al. (2019)]. **(E)** Remora-inspired biorobot with suction disc and locomotion under wet conditions [reprinted with permission from ref Wang et al. (2017)].

detachment. In numerous studies, a dry adhesive capable of maintaining robust contact under peeling conditions has been applied to robots for high mobility on ceilings, steep slopes, and curved surfaces. Ko et al. presented a wall-and-ceiling-climbing quadruped robot with mushroom-shaped dry adhesive pads positioned on the foot (**Figure 5C**) (Ko et al., 2017b). This design allowed the robot system to adhere firmly to the ceiling or wall against its weight and reduce the peeling stress. In addition,

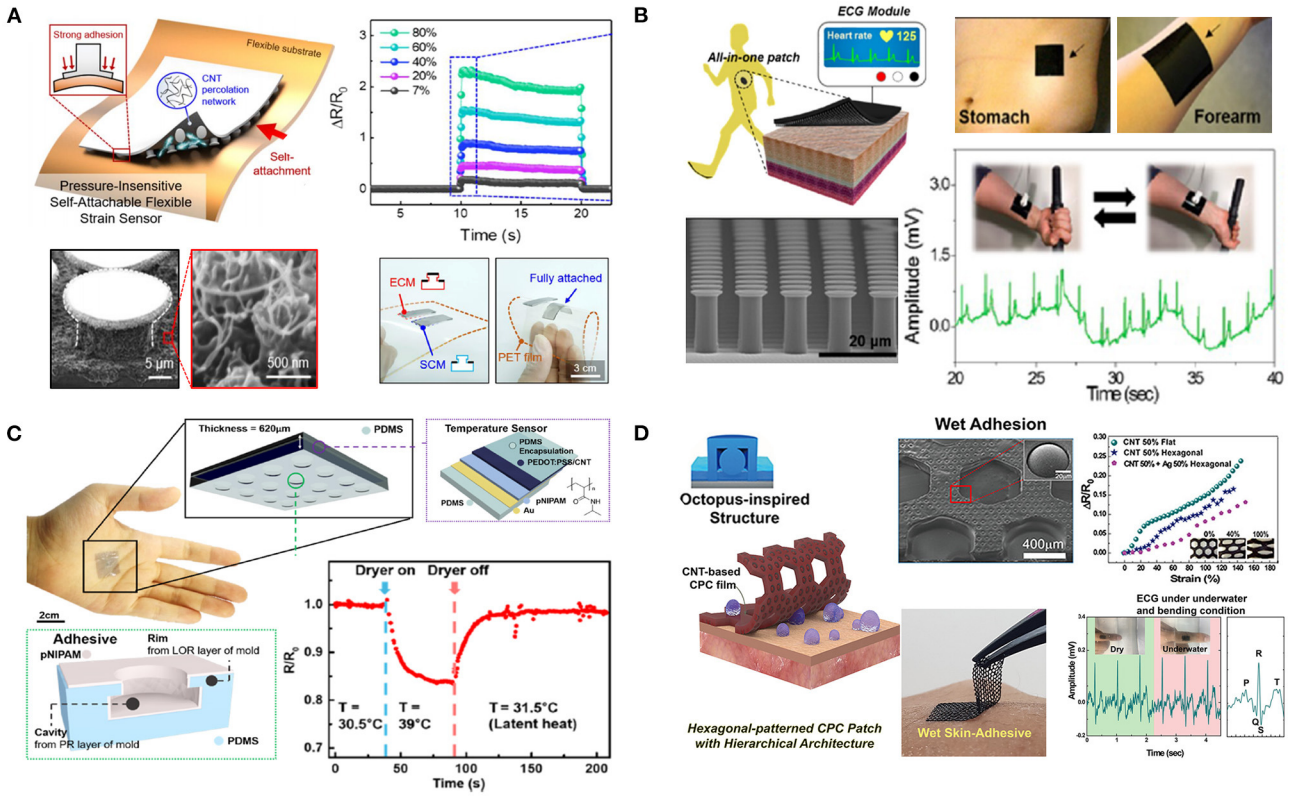

FIGURE 6 | Bioinspired adhesive applied sensors. **(A)** Gecko-inspired dry adhesive applied to strain sensor exhibiting conformal contact on a flexible curved surface [reprinted with permission from ref Seong et al. (2020)]. **(B)** Gecko-inspired dry adhesive applied to a wearable sensor with conductive nanocomposite for ECG signal and motion detection [reprinted with permission from ref Kim et al. (2016)]. **(C)** Octopus-inspired microstructure adhesive applied to temperature sensor exhibiting relative resistance changes according to skin temperature [reprinted with permission from ref Oh et al. (2018)]. **(D)** Octopus-inspired wet adhesive applied to a sensor with conductive polymer composite for bio-signal detection under underwater conditions [reprinted with permission from ref Min et al. (2020)].

a bioinspired robot that mimicked the multi-joint leg and dry adhesive footpad of a gecko has been reported (**Figure 5D**) (Tang et al., 2019). The multi-joint leg with attachable and deformable dry adhesive microstructures enabled the robots to move vertically without slipping.

Moreover, numerous bioinspired wet adhesives have been applied to robots to ensure stable contact with the target object and settle down exactly on the target point in a wet environment. The anatomical properties of suction disks in the clingfish were applied to the marine robot (**Figure 5E**) (Wang et al., 2017). Suction disks allowed clingfish robots to exhibit wet adhesion of up to 436.6 N, which is capable of adhering to biological and non-biological target objects, such as fishes and hulls. Iwasaki et al. presented a medical soft robot with a millimeter-scale suction cup array integrated with a neodymium magnet that could control the adhesion and locomotion via external magnetic fields, enabling strong adhesion to the wet surfaces of an internal organ (Iwasaki et al., 2020). Ma et al. presented a robot system that can climb to a steep slope under dry and wet conditions using a gecko dry adhesive coated poly(dopamine methacrylate-co-2-methoxyethyl acrylate-co-isopropyl acrylamide)(p(DMA-co-MEA-co-NIAAM))/iron oxide (Fe_3O_4) composite (Ma et al., 2018). The superior and reversible adhesion performance enables the robot to move swiftly and adhere firmly on the slippery surface in wet conditions.

Bioinspired Adhesives on Advanced Sensors

Conformal contact without slip or peeling is fundamental for the stable detection of advanced sensors (Wang C. H. et al., 2019; Zhang C. et al., 2021). Conventional approaches, such as a pressure-sensitive adhesive (PSA) and an ionic gel, can adhere to the substrate with a tacky surface. However, these methods not only cause damage or injury to a substrate but also delaminate the sensors from the substrate under wet conditions (Ameri et al., 2017; Park et al., 2020). The application of bio-inspired dry/wet adhesives to sensors has superior advantages compared to previous methods: (1) reversible and restorable adhesion, (2) enhanced conformality to the rough surface, and (3) versatility to diverse substrates with different surface properties (Hwang et al., 2020).

In particular, it is challenging for sensors to adhere to the skin because it is rough and deforms as the body moves (Hwang et al., 2018). To enhance the adhesion of the sensor to the skin, a high-aspect-ratio micro hair electrocardiogram (ECG) sensor was developed, in which conformally adapted microstructures can reduce the noise of the generated pulse signals from the body

(Pang et al., 2015). Furthermore, several microfibrillar adhesives have been applied to wearable sensors that allow conformal contact with the microgroove of the skin and achieve stable detection with a low signal-to-noise ratio even on deformed skin (Drotlef et al., 2017; Liu X. J. et al., 2020).

In addition, various studies have been conducted on smart devices for sensing human motion to maintain high adhesion despite dynamic movements. Seong et al. showed a self-attachable and flexible strain sensor with CNT-coated, mushroom-shaped microstructures (**Figure 6A**) (Seong et al., 2020). The protruding tips of the mushroom structures exhibited robust adhesion to the target surface while the conductive CNT layer was highly sensitive to strain, even for repeatable detection cycles. Furthermore, a mushroom-shaped dry adhesive based on a graphene/CNT/PDMS nanocomposite was utilized as an attachable ECG sensor that sensed a fine electrical signal and precisely distinguished various types of human movements without detachment (**Figure 6B**) (Kim et al., 2016).

Furthermore, wet adhesives have been applied to sensors to maintain strong adhesion and sensing performance on sweaty skin or underwater (Wu et al., 2021). Many studies have integrated octopus-inspired suckers into sensors. Octopus-inspired suction cups have been demonstrated for medical sensor applications to improve wet adhesion by inducing negative pressure within the cavity under wet conditions, where various vital signals — including body temperature, respiration, electrocardiogram (ECG), pulse, and blood pressure — can be detected stably (Choi et al., 2016). Furthermore, wet adhesive microstructures mimicking octopus sucker rims were presented as skin-attachable temperature sensors (**Figure 6C**) (Oh et al., 2018). The octopus-inspired structures enhanced the sensing accuracy of body temperature, even when sweating. Min et al. developed a skin-attachable sensor with a dome-shaped sucker that was drainable owing to mesh patterns, where the skin patch showed high normal adhesion strength under wet and underwater conditions (**Figure 6D**) (Min et al., 2020).

CONCLUSIONS

With the development of advanced industrial applications, such as grippers, robots, and sensors, bioinspired adhesives have become a promising solution to the low adhesion functionality of existing adhesion systems. Accordingly, bioinspired adhesive structures represented by pillar and sucker structures are being actively studied owing to their extraordinary adhesion with conformal, controllable, damage- and contamination-free properties, even in wet environments. In this review, we investigated the application of these adhesive structures in the field. Bioinspired adhesives enable robotic systems to perform efficient locomotion, such as climbing, clinging, and gripping. In addition, they improve the sensing performance of attachable sensors by allowing them to make close contact with the target surfaces, even in wet environments. However, despite these advances, certain problems remain to be solved.

First, although various studies have been conducted on dry and wet adhesives for strong skin adhesion, it is still challenging to adhere to skin that has various surface contaminants, such as dead cells, hair, secreted oil, and sweat (Bae et al., 2013; Choi et al., 2016; Kim et al., 2016; Baik et al., 2017; Stauffer et al., 2018). In particular, repeated deformations, such as bending or stretching of the joints (e.g., elbows and knees), hinder stable and long-term attachment (Liu et al., 2017; Stauffer et al., 2018).

Second, bioinspired adhesives with actively and rapidly switchable adhesion require further development. Controllable adhesives that are responsive to external stimuli enable the rapid transportation of industrial gripper systems, swift climbing of robots, and easy detachment of skin patches. Although various stimuli-responsive materials, such as heat, light, and electricity have been suggested, several limitations restrict their practical application to real industries. For example, thermo-responsive polymers have been integrated into mushroom-shaped adhesives for electrothermally controllable soft grippers, which have a relatively slow response time of ∼10 min per pick and place cycle (Li et al., 2020). An electro-responsive adhesive based on a dielectric elastomer was developed for the feet of soft wall-climbing robots (Gu et al., 2018). Even though they respond quickly (within a second per gait cycle), for adhesion control they require an operating voltage of at least 6,000 V for fast movement, which is quite energy-consuming in terms of industrial application.

Third, the hierarchy structure is an important factor because it improves structural stability and adaptability to surfaces with various roughnesses. However, most studies that mimic the hierarchy of the adhesives tend to produce no net benefit because of manufacturing defects. Various molding techniques, including soft lithography (Jeong et al., 2009a), porous membrane base molding (Kustandi et al., 2007; Bhushan and Lee, 2012), and dip transfer (Murphy et al., 2009), have been applied to hierarchical structures, whereas the dramatic change in geometries between micro-and nanostructures produces concentrated stress in the joints and impedes demolding with reduced yields (Chan-Park et al., 2005). Rohrig et al. introduced a laser printing-based bottom-up approach to fabricate hierarchical structures, whereas the low resolution of laser printing resulted in insufficient adhesion performance (Rohrig et al., 2012). To solve manufacturing problems, various approaches, such as geometrical optimizations (Chan-Park et al., 2005), chemical modifications (Otto et al., 2004; Cortese et al., 2008), and advanced manufacturing methods with high precision (Zhang et al., 2010; Park et al., 2014; Wang et al., 2019a), are required.

Several efforts have been made to commercialize bioinspired dry adhesives (Nanogriptech®, Geckskin®, and Gecko® Nanoplast®). In particular, continuous fabrication techniques based on a roll-to-roll process have been successfully applied to the large-scale fabrication of bioinspired dry adhesives (Sameoto and Ferguson, 2014; Yi et al., 2014; Lee et al., 2018; Yu et al., 2019). Despite these efforts, the complex microstructural features (e.g., suction cups, mushrooms with angled tips) (Wang et al., 2019b) or additional chemical treatments (Lee et al., 2007; Zhao et al., 2017) impede the fabrication process and lower yields in continuous manufacturing, which need to be overcome for the widespread use of bioinspired adhesives. We expect that these limitations can be overcome in the near future through multidisciplinary studies on functional materials, optimal structural design, and precise manufacturing techniques, enabling more versatile uses of bioinspired adhesives in various

industries, including precision manufacturing, biomedical devices, and flexible electronics.

AUTHOR CONTRIBUTIONS

All authors participated fully to the data acquisition, analysis, manuscript writing, and contributed to preparing the manuscript.

FUNDING

This work was supported by the National Research Foundation of Korea (NRF) (2021R1A2C3006297) and Korea Electric Power Corporation (R19XO01-26). The authors declare that the funder Korea Electric Power Corporation was not involved in the study design, collection, analysis, interpretation of data, the writing of this article or the decision to submit it for publication.

REFERENCES

Amador, G. J., Endlein, T., and Sitti, M. (2017). Soiled adhesive pads shear clean by slipping: a robust self-cleaning mechanism in climbing beetles. *J. R. Soc. Interface* 14:20170134. doi: 10.1098/rsif.2017.0134

Ameri, S. K., Ho, R., Jang, H. W., Tao, L., Wang, Y. H., Wang, L., et al. (2017). Graphene electronic tattoo sensors. *ACS Nano* 11, 7634–7641. doi: 10.1021/acsnano.7b02182

An, J. N., Le, T. S. D., Huang, Y., Zhan, Z. Y., Li, Y., Zheng, L. X., et al. (2017). All-graphene-based highly flexible noncontact electronic skin. *ACS Appl. Mater. Interfaces* 9, 44593–44601. doi: 10.1021/acsami.7b13701

Arzt, E., Gorb, S., and Spolenak, R. (2003). From micro to nano contacts in biological attachment devices. *Proc. Natl. Acad. Sci. U. S. A.* 100, 10603–10606. doi: 10.1073/pnas.1534701100

Autumn, K., Liang, Y. A., Hsieh, S. T., Zesch, W., Chan, W. P., Kenny, T. W., et al. (2000). Adhesive force of a single gecko foot-hair. *Nature* 405, 681–685. doi: 10.1038/35015073

Autumn, K., Majidi, C., Groff, R. E., Dittmore, A., and Fearing, R. (2006). Effective elastic modulus of isolated gecko setal arrays. *J. Exp. Biol.* 209, 3558–3568. doi: 10.1242/jeb.02469

Autumn, K., Sitti, M., Liang, Y. C. A., Peattie, A. M., Hansen, W. R., Sponberg, S., et al. (2002). Evidence for van der Waals adhesion in gecko setae. *Proc. Natl. Acad. Sci. U. S. A.* 99, 12252–12256. doi: 10.1073/pnas.192252799

Bae, W. G., Kim, D., Kwak, M. K., Ha, L., Kang, S. M., and Suh, K. Y. (2013). Enhanced skin adhesive patch with modulus-tunable composite micropillars. *Adv. Healthc. Mater.* 2, 109–113. doi: 10.1002/adhm.201200098

Bae, W. G., Kim, H. N., Kim, D., Park, S. H., Jeong, H. E., and Suh, K. Y. (2014). 25th anniversary article: scalable multiscale patterned structures inspired by nature: the role of hierarchy. *Adv. Mater.* 26, 675–699. doi: 10.1002/adma.201303412

Baik, S., Hwang, G. W., Jang, S., Jeong, S., Kim, K. H., Yang, T. H., et al. (2021). Bioinspired microsphere-embedded adhesive architectures for an electrothermally actuating transport device of dry/wet pliable surfaces. *ACS Appl. Mater. Interfaces* 13, 6930–6940. doi: 10.1021/acsami.0c21847

Baik, S., Kim, D. W., Park, Y., Lee, T. J., Ho Bhang, S., and Pang, C. (2017). A wet-tolerant adhesive patch inspired by protuberances in suction cups of octopi. *Nature* 546, 396–400. doi: 10.1038/nature22382

Baik, S., Kim, J., Lee, H. J., Lee, T. H., and Pang, C. (2018). Highly adaptable and biocompatible octopus-like adhesive patches with meniscus-controlled unfoldable 3D microtips for underwater surface and hairy skin. *Adv. Sci.* 5:1800100. doi: 10.1002/advs.201800100

Baik, S., Lee, H. J., Kim, D. W., Min, H., and Pang, C. (2019). Capillarity-enhanced organ-attachable adhesive with highly drainable wrinkled octopus-inspired architectures. *ACS Appl. Mater. Interfaces* 11, 25674–25681. doi: 10.1021/acsami.9b05511

Bhushan, B., and Lee, H. (2012). Fabrication and characterization of multi-level hierarchical surfaces. *Faraday Discuss* 156, 235–241. doi: 10.1039/c2fd00115b

Bhushan, B., and Sayer, R. A. (2007). Surface characterization and friction of a bio-inspired reversible adhesive tape. *Microsyst. Technol.* 13, 71–78. doi: 10.1007/s00542-006-0256-2

Bullock, J. M. R., and Federle, W. (2011). Beetle adhesive hairs differ in stiffness and stickiness: *in vivo* adhesion measurements on individual setae. *Sci. Nat.* 98, 381–387. doi: 10.1007/s00114-011-0781-4

Carbone, G., Pierro, E., and Gorb, S. N. (2011). Origin of the superior adhesive performance of mushroom-shaped microstructured surfaces. *Soft Matter.* 7, 5545–5552. doi: 10.1039/c0sm01482f

Chan-Park, M. B., Lam, Y. C., Laulia, P., and Joshi, S. C. (2005). Simulation and investigation of factors affecting high aspect ratio UV embossing. *Langmuir* 21, 2000–2007. doi: 10.1021/la035124e

Chen, H. W., Zhang, L. W., Zhang, D. Y., Zhang, P. F., and Han, Z. W. (2015). Bioinspired surface for surgical graspers based on the strong wet friction of tree frog toe pads. *ACS Appl. Mater. Interfaces* 7, 13987–13995. doi: 10.1021/acsami.5b03039

Chen, Y. C., and Yang, H. T. (2017). Octopus-inspired assembly of nanosucker arrays for dry/wet adhesion. *ACS Nano* 11, 5332–5338. doi: 10.1021/acsnano.7b00809

Chen, Y. P., Meng, J. X., Gu, Z., Wan, X. Z., Jiang, L., and Wang, S. T. (2020). Bioinspired multiscale wet adhesive surfaces: structures and controlled adhesion. *Adv. Funct. Mater.* 30:1905287. doi: 10.1002/adfm.201905287

Choi, M. K., Park, O. K., Choi, C., Qiao, S. T., Ghaffari, R., Kim, J., et al. (2016). Cephalopod-inspired miniaturized suction cups for smart medical skin. *Adv. Healthc. Mater.* 5, 80–87. doi: 10.1002/adhm.201500285

Chun, S., Son, W., Kim, D. W., Lee, J., Min, H., Jung, H., et al. (2019). Water-resistant and skin-adhesive wearable electronics using graphene fabric sensor with octopus-inspired microsuckers. *ACS Appl. Mater. Interfaces* 11, 16951–16957. doi: 10.1021/acsami.9b04206

Cortese, B., D'Amone, S., Manca, M., Viola, I., Cingolani, R., and Gigli, G. (2008). Superhydrophobicity due to the hierarchical scale roughness of PDMS surfaces. *Langmuir* 24, 2712–2718. doi: 10.1021/la702764x

Del Campo, A., Greiner, C., Alvarez, I., and Arzt, E. (2007a). Patterned surfaces with pillars with controlled 3D tip geometry mimicking bioattachment devices. *Adv. Mater.* 19, 1973–1977. doi: 10.1002/adma.200602476

Del Campo, A., Greiner, C., and Arzt, E. (2007b). Contact shape controls adhesion of bioinspired fibrillar surfaces. *Langmuir* 23, 10235–10243. doi: 10.1021/la7010502

Dirks, J. H., and Federle, W. (2011). Fluid-based adhesion in insects - principles and challenges. *Soft Matter.* 7, 11047–11053. doi: 10.1039/c1sm06269g

Drotlef, D. M., Amjadi, M., Yunusa, M., and Sitti, M. (2017). Bioinspired composite microfibers for skin adhesion and signal amplification of wearable sensors. *Adv. Mater.* 29:1701353. doi: 10.1002/adma.201701353

Drotlef, D. M., Stepien, L., Kappl, M., Barnes, W. J. P., Butt, H. J., and Del Campo, A. (2013). Insights into the adhesive mechanisms of tree frogs using artificial mimics. *Adv. Funct. Mater.* 23, 1137–1146. doi: 10.1002/adfm.201202024

Fuentes, C. A., Brughmans, G., Tran, L. Q. N., Dupont-Gillain, C., Verpoest, I., and Van Vuure, A. W. (2015). Mechanical behaviour and practical adhesion at a bamboo composite interface: physical adhesion and mechanical interlocking. *Compos. Sci. Technol.* 109, 40–47. doi: 10.1016/j.compscitech.2015.01.013

Geim, A. K., Dubonos, S. V., Grigorieva, I. V., Novoselov, K. S., Zhukov, A. A., and Shapoval, S. Y. (2003). Microfabricated adhesive mimicking gecko foot-hair. *Nat. Mater.* 2, 461–463. doi: 10.1038/nmat917

Gorb, E. V., Hosoda, N., Miksch, C., and Gorb, S. N. (2010). Slippery pores: anti-adhesive effect of nanoporous substrates on the beetle attachment system. *J. R. Soc. Interface* 7, 1571–1579. doi: 10.1098/rsif.2010.0081

Greiner, C., Del Campo, A., and Arzt, E. (2007). Adhesion of bioinspired micropatterned surfaces: effects of pillar radius, aspect ratio, and preload. *Langmuir* 23, 3495–3502. doi: 10.1021/la0633987

Gu, G. Y., Zou, J., Zhao, R. K., Zhao, X. H., and Zhu, X. Y. (2018). Soft wall-climbing robots. *Sci. Robot.* 3:eaat2874. doi: 10.1126/scirobotics.aat2874

Hansen, W. R., and Autumn, K. (2005). Evidence for self-cleaning in gecko setae. *Proc. Natl. Acad. Sci. U. S. A.* 102, 385–389. doi: 10.1073/pnas.0408304102

Heepe, L., Kovalev, A. E., Varenberg, M., Tuma, J., and Gorb, S. N. (2012). First mushroom-shaped adhesive microstructure: a review. *Theor. Appl. Mech. Lett.* 2:014008. doi: 10.1063/2.1201408

Hofman, A. H., van Hees, I. A., Yang, J., and Kamperman, M. (2018). Bioinspired underwater adhesives by using the supramolecular toolbox. *Adv. Mater.* 30:1704640. doi: 10.1002/adma.201704640

Hwang, I., Kim, H. N., Seong, M., Lee, S. H., Kang, M., Yi, H., et al. (2018). Multifunctional smart skin adhesive patches for advanced health care. *Adv. Healthc. Mater.* 7:1800275. doi: 10.1002/adhm.201800275

Hwang, I., Seong, M., Yi, H., Ko, H., Park, H. H., Yeo, J., et al. (2020). Low-resistant electrical and robust mechanical contacts of self-attachable flexible transparent electrodes with patternable circuits. *Adv. Funct. Mater.* 30:2000458. doi: 10.1002/adfm.202000458

Iturri, J., Xue, L. J., Kappl, M., Garcia-Fernandez, L., Barnes, W. J. P., Butt, H. J., et al. (2015). Torrent frog-inspired adhesives: attachment to flooded surfaces. *Adv. Funct. Mater.* 25, 1499–1505. doi: 10.1002/adfm.201403751

Iwasaki, H., Lefevre, F., Damian, D. D., Iwase, E., and Miyashita, S. (2020). Autonomous and reversible adhesion using elastomeric suction cups for *in-vivo* medical treatments. *IEEE Robot. Autom. Lett.* 5, 2015–2022. doi: 10.1109/LRA.2020.2970633

Jeong, H. E., Kwak, R., Khademhosseini, A., and Suh, K. Y. (2009a). UV-assisted capillary force lithography for engineering biomimetic multiscale hierarchical structures: from lotus leaf to gecko foot hairs. *Nanoscale* 1, 331–338. doi: 10.1039/b9nr00106a

Jeong, H. E., Lee, J. K., Kim, H. N., Moon, S. H., and Suh, K. Y. (2009b). A nontransferring dry adhesive with hierarchical polymer nanohairs. *Proc. Natl. Acad. Sci. U. S. A.* 106, 5639–5644. doi: 10.1073/pnas.0900323106

Jeong, H. E., Lee, S. H., Kim, P., and Suh, K. Y. (2006). Stretched polymer nanohairs by nanodrawing. *Nano Lett.* 6, 1508–1513. doi: 10.1021/nl061045m

Jiang, H., Hawkes, E. W., Fuller, C., Estrada, M. A., Suresh, S. A., Abcouwer, N., et al. (2017). A robotic device using gecko-inspired adhesives can grasp and manipulate large objects in microgravity. *Sci. Robot.* 2:eaan4545. doi: 10.1126/scirobotics.aan4545

Kim, S., and Sitti, M. (2006). Biologically inspired polymer microfibers with spatulate tips as repeatable fibrillar adhesives. *Appl. Phys. Lett.* 89:261911. doi: 10.1063/1.2424442

Kim, S., Spenko, M., Trujillo, S., Heyneman, B., Santos, D., and Cutkosky, M. R. (2008). Smooth vertical surface climbing with directional adhesion. *IEEE Trans. Robot.* 24, 65–74. doi: 10.1109/TRO.2007.909786

Kim, T., Park, J., Sohn, J., Cho, D., and Jeon, S. (2016). Bioinspired, highly stretchable, and conductive dry adhesives based on 1D−2D hybrid carbon nanocomposites for all-in-one ECG electrodes. *ACS Nano* 10, 4770–4778. doi: 10.1021/acsnano.6b01355

Kim, Y., Yang, C., Kim, Y., Gu, G. X., and Ryu, S. (2020). Designing an adhesive pillar shape with deep learning-based optimization. *ACS Appl. Mater. Interfaces* 12, 24458–24465. doi: 10.1021/acsami.0c04123

Ko, H., Seong, M., and Jeong, H. E. (2017a). A micropatterned elastomeric surface with enhanced frictional properties under wet conditions and its application. *Soft Matter* 13, 8419–8425. doi: 10.1039/C7SM01493G

Ko, H., Yi, H., and Jeong, H. E. (2017b). Wall and ceiling climbing quadruped robot with superior water repellency manufactured using 3D printing (UNIclimb). *Int. J. Precis. Eng. Manuf.* 4, 273–280. doi: 10.1007/s40684-017-0033-y

Kroner, E., and Arzt, E. (2012). Single macropillars as model systems for tilt angle dependent adhesion measurements. *Int. J. Adhes. Adhes.* 36, 32–38. doi: 10.1016/j.ijadhadh.2012.03.008

Kustandi, T. S., Samper, V. D., Ng, W. S., Chong, A. S., and Gao, H. (2007). Fabrication of a gecko-like hierarchical fibril array using a bonded porous alumina template. *J. Micromech. Microeng.* 17:N75. doi: 10.1088/0960-1317/17/10/N02

Kwak, M. K., Jeong, H. E., Bae, W. G., Jung, H. S., and Suh, K. Y. (2011a). Anisotropic adhesion properties of triangular-tip-shaped micropillars. *Small* 7, 2296–2300. doi: 10.1002/smll.201100455

Kwak, M. K., Jeong, H. E., and Suh, K. Y. (2011b). Rational design and enhanced biocompatibility of a dry adhesive medical skin patch. *Adv. Mater.* 23, 3949–3953. doi: 10.1002/adma.201101694

Kwak, M. K., Pang, C., Jeong, H. E., Kim, H. N., Yoon, H., Jung, H. S., et al. (2011c). Towards the next level of bioinspired dry adhesives: new designs and applications. *Adv. Funct. Mater.* 21, 3606–3616. doi: 10.1002/adfm.201100982

Langowski, J. K. A., Dodou, D., Kamperman, M., and van Leeuwen, J. L. (2018). Tree frog attachment: mechanisms, challenges, and perspectives. *Front. Zool.* 15:32. doi: 10.1186/s12983-018-0273-x

Lee, H., Lee, B. P., and Messersmith, P. B. (2007). A reversible wet/dry adhesive inspired by mussels and geckos. *Nature* 448, 338–341. doi: 10.1038/nature05968

Lee, H., Um, D. S., Lee, Y., Lim, S., Kim, H. J., and Ko, H. (2016). Octopus-inspired smart adhesive pads for transfer printing of semiconducting nanomembranes. *Adv. Mater.* 28, 7457–7465. doi: 10.1002/adma.201601407

Lee, J., and Fearing, R. S. (2008). Contact self-cleaning of synthetic gecko adhesive from polymer microfibers. *Langmuir* 24, 10587–10591. doi: 10.1021/la80 21485

Lee, J. H., Fearing, R. S., and Komvopoulos, K. (2008). Directional adhesion of gecko-inspired angled microfiber arrays. *Appl. Phys. Lett.* 93:191910. doi: 10.1063/1.3006334

Lee, S. H., Song, H. W., Kang, B. S., and Kwak, M. K. (2019). Remora-inspired reversible adhesive for underwater applications. *ACS Appl. Mater. Interfaces* 11, 47571–47576. doi: 10.1021/acsami.9b16350

Lee, S. H., Yi, H., Park, C. W., Jeong, H. E., and Kwak, M. (2018). Continuous tip widening technique for roll-to-roll fabrication of dry adhesives. *Coatings* 8:349. doi: 10.3390/coatings8100349

Li, S., Tian, H. M., Shao, J. Y., Liu, H. R., Wang, D. R., and Zhang, W. T. (2020). Switchable adhesion for nonflat surfaces mimicking geckos' adhesive structures and toe muscles. *ACS Appl. Mater. Interfaces* 12, 39745–39755. doi: 10.1021/acsami.0c08686

Liu, J. F., Xu, L. S., Xu, J. J., Liu, L., Cheng, G. X., Chen, S. Q., et al. (2020). Analysis and optimization of the wall-climbing robot with an adsorption system and adhesive belts. *Int. J. Adv. Robot. Syst.* 17:1729881420926409. doi: 10.1177/1729881420926409

Liu, X. J., Liu, J., Wang, J. L., Wang, T., Jiang, Y., Hu, J. Q., et al. (2020). Bioinspired, microstructured silk fibroin adhesives for flexible skin sensors. *ACS Appl. Mater. Interfaces* 12, 5601–5609. doi: 10.1021/acsami. 9b21197

Liu, Z. Y., Wang, X. T., Qi, D. P., Xu, C., Yu, J. C., Liu, Y. Q., et al. (2017). High-adhesion stretchable electrodes based on nanopile interlocking. *Adv. Mater.* 29:1603382. doi: 10.1002/adma.201603382

Ma, Y. F., Ma, S. H., Wu, Y., Pei, X. W., Gorb, S. N., Wang, Z. K., et al. (2018). Remote control over underwater dynamic attachment/detachment and locomotion. *Adv. Mater.* 30:1801595. doi: 10.1002/adma.201801595

Mahdavi, A., Ferreira, L., Sundback, C., Nichol, J. W., Chan, E. P., Carter, D. J. D., et al. (2008). A biodegradable and biocompatible gecko-inspired tissue adhesive. *Proc. Natl. Acad. Sci. U. S. A.* 105, 2307–2312. doi: 10.1073/pnas.0712117105

Mazzolai, B., Mondini, A., Tramacere, F., Riccomi, G., Sadeghi, A., Giordano, G., et al. (2019). Octopus-inspired soft arm with suction cups for enhanced grasping tasks in confined environments. *Adv. Intell. Syst.* 1:1900041. doi: 10.1002/aisy.201900041

Min, H., Jang, S., Kim, D., Kim, J., Baik, S., Chun, S., et al. (2020). Highly air/water-permeable hierarchical mesh architectures for stretchable underwater electronic skin patches. *ACS Appl. Mater. Interfaces* 12, 14425–14432. doi: 10.1021/acsami.9b23400

Mitchell, C. T., Dayan, C. B., Drotlef, D. M., Sitti, M., and Stark, A. Y. (2020). The effect of substrate wettability and modulus on gecko and gecko-inspired synthetic adhesion in variable temperature and humidity. *Sci. Rep.* 10, 1–9. doi: 10.1038/s41598-020-76484-6

Murphy, M. P., Kim, S., and Sitti, M. (2009). Enhanced adhesion by gecko-inspired hierarchical fibrillar adhesives. *ACS Appl. Mater. Interfaces* 1, 849–855. doi: 10.1021/am8002439

Niewiarowski, P. H., Stark, A. Y., and Dhinojwala, A. (2016). Sticking to the story: outstanding challenges in gecko-inspired adhesives. *J. Exp. Biol.* 219, 912–919. doi: 10.1242/jeb.080085

Nishimura, T., Mizushima, K., Suzuki, Y., Tsuji, T., and Watanabe, T. (2017). Variable-grasping-mode underactuated soft gripper with environmental contact-based operation. *IEEE Robot. Autom. Lett.* 2, 1164–1171. doi: 10.1109/LRA.2017.2662086

O'Brien, M., Mortell, D. J., Corbett, M. C., O'Higgins, R. M., and McCarthy, C. T. (2019). Tree frog attachment: mechanisms, challenges, and perspectives. *Int. J. Adhes. Adhes.* 95, 1–21.

Oh, D. K., Lee, S., Lee, S. H., Lee, W., Yeon, G., Lee, N., et al. (2019). Tailored nanopatterning by controlled continuous nanoinscribing with tunable shape, depth, and dimension. *ACS Nano* 13, 11194–11202. doi: 10.1021/acsnano.9b04221

Oh, J. H., Hong, S. Y., Park, H., Jin, S. W., Jeong, Y. R., Oh, S. Y., et al. (2018). Fabrication of high-sensitivity skin-attachable temperature sensors with bioinspired microstructured adhesive. *ACS Appl. Mater. Interfaces* 10, 7263–7270. doi: 10.1021/acsami.7b17727

Otto, M., Bender, M., Richter, F., Hadam, B., Kliem, T., Jede, R., et al. (2004). Reproducibility and homogeneity in step and repeat UV-nanoimprint lithography. *Microelectron. Eng.* 73, 152–156. doi: 10.1016/S0167-9317(04)00090-5

Ozaki, S., Mieda, K., Maegawa, S., and Nakano, K. (2020). Meso–macro coupled analysis of pressure-dependent friction of rubber. *Front. Mech. Eng.* 6:24. doi: 10.3389/fmech.2020.00024

Pan, F., Ye, S. X., Wang, R. X., She, W., Liu, J. P., Sun, Z. M., et al. (2020). Hydrogel networks as underwater contact adhesives for different surfaces. *Mater. Horiz.* 7, 2063–2070. doi: 10.1039/D0MH00176G

Pang, C., Koo, J. H., Nguyen, A., Caves, J. M., Kim, M. G., Chortos, A., et al. (2015). Highly skin-conformal microhairy sensor for pulse signal amplification. *Adv. Mater.* 27, 634–640. doi: 10.1002/adma.201403807

Park, H. W., Seo, H. S., Lee, J. H., and Shin, S. (2020). Adhesion improvement of the acrylic pressure-sensitive adhesive to low-surface-energy substrates using silicone urethane dimethacrylates. *Eur. Polym. J.* 137:109949. doi: 10.1016/j.eurpolymj.2020.109949

Park, J., Tahk, D., Ahn, C., Im, S. G., Choi, S. J., Suh, K. Y., et al. (2014). Conformal phase masks made of polyurethane acrylate with optimized elastic modulus for 3D nanopatterning. *J. Mater. Chem. C* 2, 2316–2322. doi: 10.1039/c3tc32194k

Qu, L. T., Dai, L. M., Stone, M., Xia, Z. H., and Wang, Z. L. (2008). Carbon nanotube arrays with strong shear binding-on and easy normal lifting-off. *Science* 322, 238–242. doi: 10.1126/science.1159503

Rohrig, M., Thiel, M., Worgull, M., and Holscher, H. (2012). 3D direct laser writing of nano-and microstructured hierarchical gecko-mimicking surfaces. *Small* 8, 3009–3015. doi: 10.1002/smll.201200308

Rong, Z. X., Zhou, Y. M., Chen, B. A., Robertson, J., Federle, W., Hofmann, S., et al. (2014). Bio-inspired hierarchical polymer fiber-carbon nanotube adhesives. *Adv. Mater.* 26, 1456–1461. doi: 10.1002/adma.201304601

Sameoto, D., and Ferguson, B. (2014). Robust large-area synthetic dry adhesives. *J. Adhes. Sci. Technol.* 28, 337–353. doi: 10.1080/01694243.2012.693802

Sandoval, J. A., Jadhav, S., Quan, H. C., Deheyn, D. D., and Tolley, M. T. (2019). Reversible adhesion to rough surfaces both in and out of water, inspired by the clingfish suction disc. *Bioinspir. Biomim.* 14:066016. doi: 10.1088/1748-3190/ab47d1

Sandoval, J. A., Sommers, J., Peddireddy, K. R., Robertson-Anderson, R. M., Tolley, M. T., and Deheyn, D. D. (2020). Toward bioinspired wet adhesives: lessons from assessing surface structures of the suction disc of intertidal clingfish. *ACS Appl. Mater. Interfaces* 12, 45460–45475. doi: 10.1021/acsami.0c10749

Seo, S., Lee, J., Kim, K. S., Ko, K. H., Lee, J. H., and Lee, J. (2014). Anisotropic adhesion of micropillars with spatula pads. *ACS Appl. Mater. Interfaces* 6, 1345–1350. doi: 10.1021/am4044135

Seo, T., and Sitti, M. (2013). Tank-like module-based climbing robot using passive compliant joints. *IEEE ASME Trans. Mechatron.* 18, 397–408. doi: 10.1109/TMECH.2011.2182617

Seong, M. H., Hwang, I., Lee, J., and Jeong, H. E. (2020). A pressure-insensitive self-attachable flexible strain sensor with bioinspired adhesive and active CNT layers. *Sensors* 20:6965. doi: 10.3390/s20236965

Sethi, S., Ge, L., Ci, L., Ajayan, P. M., and Dhinojwala, A. (2008). Gecko-inspired carbon nanotube-based self-cleaning adhesives. *Nano Lett.* 8, 822–825. doi: 10.1021/nl0727765

Shahsavan, H., Salili, S. M., Jakli, A., and Zhao, B. X. (2017). Thermally active liquid crystal network gripper mimicking the self-peeling of gecko toe pads. *Adv. Mater.* 29:1604021. doi: 10.1002/adma.201604021

Sinatra, N. R., Teeple, C. B., Vogt, D. M., Parker, K. K., Gruber, D. F., and Wood, R. J. (2019). Ultragentle manipulation of delicate structures using a soft robotic gripper. *Sci. Robot.* 4:eaax5425. doi: 10.1126/scirobotics.aax5425

Soltannia, B., and Sameoto, D. (2014). Strong, reversible underwater adhesion via gecko-inspired hydrophobic fibers. *ACS Appl. Mater. Interfaces* 6, 21995–22003. doi: 10.1021/am5075375

Song, S., Drotlef, D. M., Majidi, C., and Sitti, M. (2017). Controllable load sharing for soft adhesive interfaces on three-dimensional surfaces. *Proc. Natl. Acad. Sci. U. S. A.* 114, E4344–E4353. doi: 10.1073/pnas.1620344114

Song, S., and Sitti, M. (2014). Soft grippers using micro-fibrillar adhesives for transfer printing. *Adv. Mater.* 26, 4901–4906. doi: 10.1002/adma.201400630

Spinner, M., Gorb, S. N., and Westhoff, G. (2013). Diversity of functional microornamentation in slithering geckos Lialis (*Pygopodidae*). *Proc. R. Soc. B* 280:20132160. doi: 10.1098/rspb.2013.2160

Stark, A. Y., McClung, B., Niewiarowski, P. H., and Dhinojwala, A. (2014). Reduction of water surface tension significantly impacts gecko adhesion underwater. *Integr. Comp. Biol.* 54, 1026–1033. doi: 10.1093/icb/icu066

Stark, A. Y., and Mitchell, C. T. (2019). Stick or slip: adhesive performance of geckos and gecko-inspired synthetics in wet environments. *Integr. Comp. Biol.* 59, 214–226. doi: 10.1093/icb/icz008

Stauffer, F., Thielen, M., Sauter, C., Chardonnens, S., Bachmann, S., Tybrandt, K., et al. (2018). Skin conformal polymer electrodes for clinical ECG and EEG recordings. *Adv. Healthc. Mater.* 7:1700994. doi: 10.1002/adhm.201700994

Tai, K., El-Sayed, A.-R., Shahriari, M., Biglarbegian, M., and Mahmud, S. (2016). State of the art robotic grippers and applications. *Robotics* 5, 11. doi: 10.3390/robotics5020011

Tang, T. F., Hou, X. Y., Xiao, Y. N., Su, Y. L., Shi, Y. T., and Rao, X. S. (2019). Research on motion characteristics of space truss-crawling robot. *Int. J. Adv. Robot. Syst.* 16:1729881418821578. doi: 10.1177/1729881418821578

Tian, H. M., Liu, H. R., Shao, J. Y., Li, S., Li, X. M., and Chen, X. M. (2020). An electrically active gecko-effect soft gripper under a low voltage by mimicking gecko's adhesive structures and toe muscles. *Soft Matter* 16, 5599–5608. doi: 10.1039/D0SM00787K

Tramacere, F., Appel, E., Mazzolai, B., and Gorb, S. N. (2014). Hairy suckers: the surface microstructure and its possible functional significance in the octopus vulgaris sucker. *Beilstein J. Nanotechnol.* 5, 561–565. doi: 10.3762/bjnano.5.66

Tramacere, F., Beccai, L., Kuba, M., Gozzi, A., Bifone, A., and Mazzolai, B. (2013). The morphology and adhesion mechanism of octopus vulgaris suckers. *PLoS ONE* 8:e65074. doi: 10.1371/journal.pone.0065074

Tramacere, F., Pugno, N. M., Kuba, M. J., and Mazzolai, B. (2015). Unveiling the morphology of the acetabulum in octopus suckers and its role in attachment. *Interface Focus* 5:20140050. doi: 10.1098/rsfs.2014.0050

Varenberg, M., Pugno, N. M., and Gorb, S. N. (2010). Spatulate structures in biological fibrillar adhesion. *Soft Matter* 6, 3269–3272. doi: 10.1039/c003207g

Wainwright, D. K., Kleinteich, T., Kleinteich, A., Gorb, S. N., and Summers, A. P. (2013). Stick tight: suction adhesion on irregular surfaces in the northern clingfish. *Biol. Lett.* 9:20130234. doi: 10.1098/rsbl.2013.0234

Wang, C. H., Shao, J. Y., Lai, D. S., Tian, H. M., and Li, X. M. (2019). Suspended-template electric-assisted nanoimprinting for hierarchical micro-nanostructures on a fragile substrate. *ACS Nano* 13, 10333–10342. doi: 10.1021/acsnano.9b04031

Wang, L., Ha, K.-H., Rodin, G. J., Liechti, K. M., and Lu, N. (2020). Mechanics of crater-enabled soft dry adhesives: a review. *Front. Mech. Eng.* 6:601510. doi: 10.3389/fmech.2020.601510

Wang, X., Tan, D., Hu, S. Q., Li, Q., Yang, B. S., Shi, Z. K., et al. (2019). Reversible adhesion via light-regulated conformations of rubber chains. *ACS Appl. Mater. Interfaces* 11, 46337–46343. doi: 10.1021/acsami.9b14940

Wang, Y., Kang, V., Federle, W., Arzt, E., and Hensel, R. (2020). Switchable underwater adhesion by deformable cupped microstructures. *Adv. Mater. Interfaces* 7:2001269. doi: 10.1002/admi.202001269

Wang, Y., Kim, J. C., Wu, R. J., Martinez, J., Song, X. J., Yang, J., et al. (2019a). Van der Waals contacts between three-dimensional metals and two-dimensional semiconductors. *Nature* 568, 70–74. doi: 10.1038/s41586-019-1052-3

Wang, Y., Rang, V., Arzt, E., Federle, W., and Hensel, R. (2019b). Strong wet and dry adhesion by cupped microstructures. *ACS Appl. Mater. Interfaces* 11, 26483–26490. doi: 10.1021/acsami.9b07969

Wang, Y. P., Yang, X. B., Chen, Y. F., Wainwright, D. K., Kenaley, C. P., Gong, Z. Y., et al. (2017). A biorobotic adhesive disc for underwater hitchhiking inspired by the remora suckerfish. *Sci. Robot.* 2:eaan8072. doi: 10.1126/scirobotics.aan8072

Wang, Z. Y., Wang, Z. Y., Dai, Z. D., and Gorb, S. N. (2018). Bio-inspired adhesive footpad for legged robot climbing under reduced gravity: multiple toes facilitate stable attachment. *Appl. Sci.* 8:114. doi: 10.3390/app8010114

Wasay, A., and Sameoto, D. (2015). Gecko gaskets for self-sealing and high-strength reversible bonding of microfluidics. *Lab Chip* 15, 2749–2753. doi: 10.1039/C5LC00342C

Wi, J. S., Lee, S., Lee, S. H., Oh, D. K., Lee, K. T., Park, I., et al. (2017). Facile three-dimensional nanoarchitecturing of double-bent gold strips on roll-to-roll nanoimprinted transparent nanogratings for flexible and scalable plasmonic sensors. *Nanoscale* 9, 1398–1402. doi: 10.1039/C6NR08387K

Wu, H., Yang, G. G., Zhu, K. H., Liu, S. Y., Guo, W., Jiang, Z., et al. (2021). Materials, devices, and systems of on-skin electrodes for electrophysiological monitoring and human-machine interfaces. *Adv. Sci.* 8:2001938. doi: 10.1002/advs.202001938

Yi, H., Hwang, I., Lee, J. H., Lee, D., Lim, H., Tahk, D., et al. (2014). Continuous and scalable fabrication of bioinspired dry adhesives via a roll-to-roll process with modulated ultraviolet-curable resin. *ACS Appl. Mater. Interfaces* 6, 14590–14599. doi: 10.1021/am503901f

Yi, H., Kang, M., Kwak, M. K., and Jeong, H. E. (2016). Simple and reliable fabrication of bioinspired mushroom-shaped micropillars with precisely controlled tip geometries. *ACS Appl. Mater. Interfaces* 8, 22671–22678. doi: 10.1021/acsami.6b07337

Yi, H., Lee, S. H., Seong, M., Kwak, M. K., and Jeong, H. E. (2018). Bioinspired reversible hydrogel adhesives for wet and underwater surfaces. *J. Mater. Chem. B* 6, 8064–8070. doi: 10.1039/C8TB02598C

Yu, D., Beckelmann, D., Opsolder, M., Schafer, B., Moh, K., Hensel, R., et al. (2019). Roll-to-roll manufacturing of micropatterned adhesives by template compression. *Materials* 12:97. doi: 10.3390/ma12010097

Yu, Z. W., Shi, Y., Xie, J. X., Yang, S. X., and Dai, Z. D. (2018). Design and analysis of a bionic adhesive foot for gecko robot climbing the ceiling. *Int. J. Robot. Autom.* 33, 445–454. doi: 10.2316/Journal.206.2018.4.206-5412

Yuk, H., Zhang, T., Lin, S. T., Parada, G. A., and Zhao, X. H. (2016). Tough bonding of hydrogels to diverse non-porous surfaces. *Nat. Mater.* 15, 190–196. doi: 10.1038/nmat4463

Zandvakili, M., Honari, M. M., Mousavi, P., and Sameoto, D. (2017). Gecko-gaskets for multilayer, complex, and stretchable liquid metal microwave circuits and antennas. *Adv. Mater. Technol.* 2:1700144. doi: 10.1002/admt.201700144

Zhang, C., Zhou, Y., Han, H., Zheng, H., Xu, W., and Wang, Z. (2021). Dopamine-triggered hydrogels with high transparency, self-adhesion, and thermoresponse as skinlike sensors. *ACS Nano* 15, 1785–1794. doi: 10.1021/acsnano.0c09577

Zhang, L. W., Chen, H. W., Guo, Y. R., Wang, Y., Jiang, Y. G., Zhang, D. Y., et al. (2020). Micro-nano hierarchical structure enhanced strong wet friction surface inspired by tree frogs. *Adv. Sci.* 7:2001125. doi: 10.1002/advs.202001125

Zhang, P. C., Zhao, C. Q., Zhao, T. Y., Liu, M. J., and Jiang, L. (2019). Recent advances in bioinspired gel surfaces with superwettability and special adhesion. *Adv. Sci.* 6:1900996. doi: 10.1002/advs.201900996

Zhang, X., Wang, Y., Hensel, R., and Arzt, E. (2021). A design strategy for mushroom-shaped microfibrils with optimized dry adhesion: experiments and finite element analyses. *J. Appl. Mech.* 88:031015. doi: 10.1115/1.4049183

Zhang, Y., Lin, C. T., and Yang, S. (2010). Fabrication of hierarchical pillar arrays from thermoplastic and photosensitive SU-8. *Small* 6, 768–775. doi: 10.1002/smll.200901843

Zhao, B. X., Pesika, N., Rosenberg, K., Tian, Y., Zeng, H. B., McGuiggan, P., et al. (2008). Adhesion and friction force coupling of gecko setal arrays: implications for structured adhesive surfaces. *Langmuir* 24, 1517–1524. doi: 10.1021/la702126k

Zhao, Y. H., Wu, Y., Wang, L., Zhang, M. M., Chen, X., Liu, M. J., et al. (2017). Bio-inspired reversible underwater adhesive. *Nat. Commun.* 8, 1–8. doi: 10.1038/s41467-017-02387-2

Zhou, M., Tian, Y., Sameoto, D., Zhang, X., Meng, Y., and Wen, S. (2013). Controllable interfacial adhesion applied to transfer light and fragile objects by using gecko inspired mushroom-shaped pillar surface. *ACS Appl. Mater. Interfaces* 5, 10137–10144. doi: 10.1021/am402815x

Zhuo, S., Zhao, Z. G., Xie, Z. X., Hao, Y. F., Xu, Y. C., Zhao, T. Y., et al. (2020). Complex multiphase organohydrogels with programmable mechanics toward adaptive soft-matter machines. *Sci. Adv.* 6:eaax1464. doi: 10.1126/sciadv.aax1464

Zou, J., Wang, J. R., and Ji, C. (2016). The adhesive system and anisotropic shear force of Guizhou gastromyzontidae. *Sci. Rep.* 6:37221. doi: 10.1038/srep37221

Conflict of Interest: The authors declare that the research was conducted in the absence of any commercial or financial relationships or otherwise that could be perceived as a potential conflict of interest.

frontiers in Mechanical Engineering

MINI REVIEW
published: 13 May 2021
doi: 10.3389/fmech.2021.661370

Modeling Bacterial Adhesion to Unconditioned Abiotic Surfaces

Christian Spengler[1†], *Erik Maikranz*[2†], *Ludger Santen*[2*] *and Karin Jacobs*[1,3*]

[1] *Experimental Physics, Center for Biophysics, Saarland University, Saarbrücken, Germany,* [2] *Theoretical Physics, Center for Biophysics, Saarland University, Saarbrücken, Germany,* [3] *Max Planck School Matter to Life, Heidelberg, Germany*

Understanding bacterial adhesion as a first step toward biofilm formation is of fundamental interests in many applications. While adhesion to abiotic surfaces is directly relevant for some applications, it also provides a controlled reference setting to study details of the adhesion process in general. This review describes the traditional approaches from contact mechanics and colloidal science, which treat the bacterium–substratum interaction in a continuous manner. We will discuss its shortcomings and provide an introduction to different approaches, which understand the adhesion process as a result of individual stochastic interactions of many macromolecules with the substratum.

Keywords: bacterial adhesion, living colloids, (x)DLVO, tethering cell wall molecules, single-cell force spectroscopy, Monte Carlo simulation, *Staphylococcus aureus*

OPEN ACCESS

Edited by:
Stanislav N. Gorb,
University of Kiel, Germany

Reviewed by:
Yulia Makhovskaya,
Institute for Problems in Mechanics (RAS), Russia
Rene M. Rossi,
Swiss Federal Laboratories for Materials Science and Technology, Switzerland

***Correspondence:**
Ludger Santen
l.santen@mx.uni-saarland.de
Karin Jacobs
k.jacobs@physik.uni-saarland.de

[†]These authors have contributed equally to this work and share first authorship

Specialty section:
This article was submitted to Tribology, a section of the journal Frontiers in Mechanical Engineering

Received: *30 January 2021*
Accepted: *10 March 2021*
Published: *13 May 2021*

Citation:
Spengler C, Maikranz E, Santen L and Jacobs K (2021) Modeling Bacterial Adhesion to Unconditioned Abiotic Surfaces. Front. Mech. Eng. 7:661370. doi: 10.3389/fmech.2021.661370

1. INTRODUCTION

Bacterial biofilms are complex consortia of bacterial cells and extracellular substances that can form on various interfaces (Dunne, 2002). The presence of such biofilms on solid, abiotic surfaces can cause problems in many applications: Formed on ship hulls, they increase hydrodynamic friction and therewith fuel consumption (De Carvalho, 2007), biofilms formed inside pipes reduce the pipes' diameter and therewith flow rates of fluids (Schwermer et al., 2008), biocorrosion caused by biofilms reduces efficiency of cooling water systems in the processing industry (Narenkumar et al., 2019). On medical equipment, such as catheters, implants, protheses, and pacemakers, biofilms are responsible for device-related infections, which can lead to severe diseases and hence are an important health care problem (Magill et al., 2014; Römling et al., 2014; Jamal et al., 2018).

One of the first steps in biofilm formation is the adhesion of single cells to a surface. Therefore, to manage or prevent biofilm formation, a profound understanding of bacterial adhesion to solid surfaces is necessary. In order to gain experimental access to the basic mechanisms of adhesion, the parameters of the system must be kept as controlled as possible. Hence, the presented studies explore bacterial adhesion to abiotic, unconditioned surfaces, i.e., surfaces that are not covered by other biomacromolecules.

First, the approaches of understanding bacterial adhesion on the whole cell level, namely in the framework of colloidal science, i.e., surface thermodynamics and DLVO[1] theory, and contact mechanics are briefly presented. We discuss the prospects and limitations of those models and describe the efforts made outside these frameworks in describing bacterial adhesion mediated by cell wall macromolecules.

[1]Named after B. Derjaguin, L. D. Landau, E. Verwey, T. Overbeek (Derjaguin and Landau, 1941; Verwey, 1947).

2. EXPERIMENTAL SETUPS

To understand how experimental results led to the creation of different models for bacterial adhesion, the principle experimental approaches that have been used are briefly explained (see also, e.g., Tandogan et al., 2017). There are predominately two principle types of experimental setups: On the one hand, experiments with a rather high number of planktonic cells that freely adsorb to an interface and eventually desorb again; on the other hand, experiments with single cells that are actively manipulated by external forces to precisely measure their behavior during adhesion and detachment.

For the first setup type, flow chambers are commonly used in which a bacterial solution is flushed over a surface of interest by a laminar flow profile that allows to estimate the forces parallel to the surfaces. Using optical microscopy, quartz crystal microbalance, or surface plasmon resonance, the number of attached cells in a certain area can be recorded over time (Filion-Côté et al., 2017; Keskin et al., 2018; Alexander et al., 2019). With the help of high-resolution optical techniques, not only the number of cells but also their motion at or above the surface can be quantified (van der Westen et al., 2018; Vissers et al., 2018). These methods can collect data of large numbers of cells simultaneously under controlled (with or without shear flow) conditions tangential to the surface. However, the forces acting during approach of the cells normal to the surface cannot be controlled. In addition, repeating the experiment and the cellular response for one individual cell is hardly possible.

To repeatedly probe single cells and achieve a high force control, optical tweezers (Fällman et al., 2004; Zhang and Liu, 2008) or atomic force microscopy (AFM) (Hinterdorfer and Dufrêne, 2006; Dufrêne and Pelling, 2013; Thewes et al., 2015a; Krieg et al., 2019) are used. While both methods have essentially the same advantages in terms of precise force and position control, the latter places fewer demands on the system itself. Therefore, AFM-based force spectroscopy with individual bacterial probes, termed single cell force spectroscopy (SCFS), is the method of choice for many researchers investigating adhesion properties of bacteria (Berne et al., 2018; Alam et al., 2019). The cells are immobilized at an AFM cantilever and moved toward and then away from a surface. By measuring the deflection of the cantilever as a function of its motion, force-separation curves, such as one schematically shown in **Figure 1A** can be recorded. SCFS allows to study the adhesion process almost natively by using very small force triggers, i.e., the force threshold at which the cantilever retraction starts[2]. From these curves, many quantities, such as the adhesion force can be determined. Of note, many experimental force-separation curves recorded with bacterial cells show a very characteristic feature: Before the cells reaches the substratum, a sudden change in the cantilever's deflection and a decrease in the distance between cell and substratum is observed, which is referred to as "snap-in" (Bhushan, 2017). In addition, approach and retraction curves do not necessarily overlap; this is sometimes termed hysteresis. While investigating a significant number of individual cells requires a lot of time, the nature of these experiments allows the repetition of approach and retraction curves with one and the same bacterial cell. This allows to study the role of stochasticity in the adhesion process and to distinguish it from population heterogeneity.

[2]Even experiments with minimal force triggers do not fully mimic flow chamber experiments since the bacterium is pushed through eventual energy barriers a planktonic bacterium would encounter.

3. BACTERIAL ADHESION ON A WHOLE-CELL LEVEL

In contact mechanics exist many models, which extend the Hertz model to include the coupling of adhesion and deformation forces: Very simplified cases that included adhesion are the JKR and DMT model (Johnson et al., 1971; Derjaguin et al., 1975), based on which more accurate models were constructed that account for deformations and longer ranging adhesion forces (Muller et al., 1980; Maugis, 1992; Greenwood, 1997; Ciavarella et al., 2019). The models have also been extended to describe interactions of inhomogeneous objects (Barthel and Perriot, 2007; Stan and Adams, 2016), making them suitable candidates for modeling the adhesion of bacterial cells that have an inhomogeneous surface structure with a lipid bilayer, cross-linked peptidoglycan layer, and eventual cellular appendages (Chen et al., 2014; Loskill et al., 2014). A model including these heterogeneities has been constructed by Chen et al. (2012), who considered a layered structure with different elastic properties along the radial direction. It turns out that this already reduces the extracted Young's modulus to 8–50 kPa, which is about a hundred times smaller than what would be extracted from the Hertz model.

Note that the heterogeneity is limited to the radial direction of the spherical cell. Inhomogeneities within the cell surface, such as clusters of adhesins, and different mechanical properties or lengths of single molecules in the cell wall are not considered. One reason for the fact that Chen et al. (2014) did not experimentally observe effects of these properties can be attributed to their way of preparing bacterial probes: The bacteria, already immobilized on the cantilever, were dried for 2 min, which is likely to alter the proteinaceous cell wall layer and change its original properties, such as heterogeneity (Chen et al., 2012, 2014). This might also explain why no cell-individual adhesion behavior was observed.

Colloidal approaches phrase the problem of bacterial adhesion as minimization of thermodynamic potentials, such as the Gibbs free energy. Thus, the theory does not take into account eventual strengthening of adhesive bonds. In the review article by Perni et al. (2014), it is shown that the simple surface thermodynamics approach of considering only interfacial energies to minimize the Gibbs free energy works only in a few cases and is generally considered too simplistic. A different approach applies the DLVO theory to the bacterium-plane geometry considering electrostatic double layer and van der Waals forces that have shown to influence bacterial adhesion (Van Oss et al., 1990; Boks et al., 2008; Loskill et al., 2012). Various publications use different approximations for these forces that can be quite

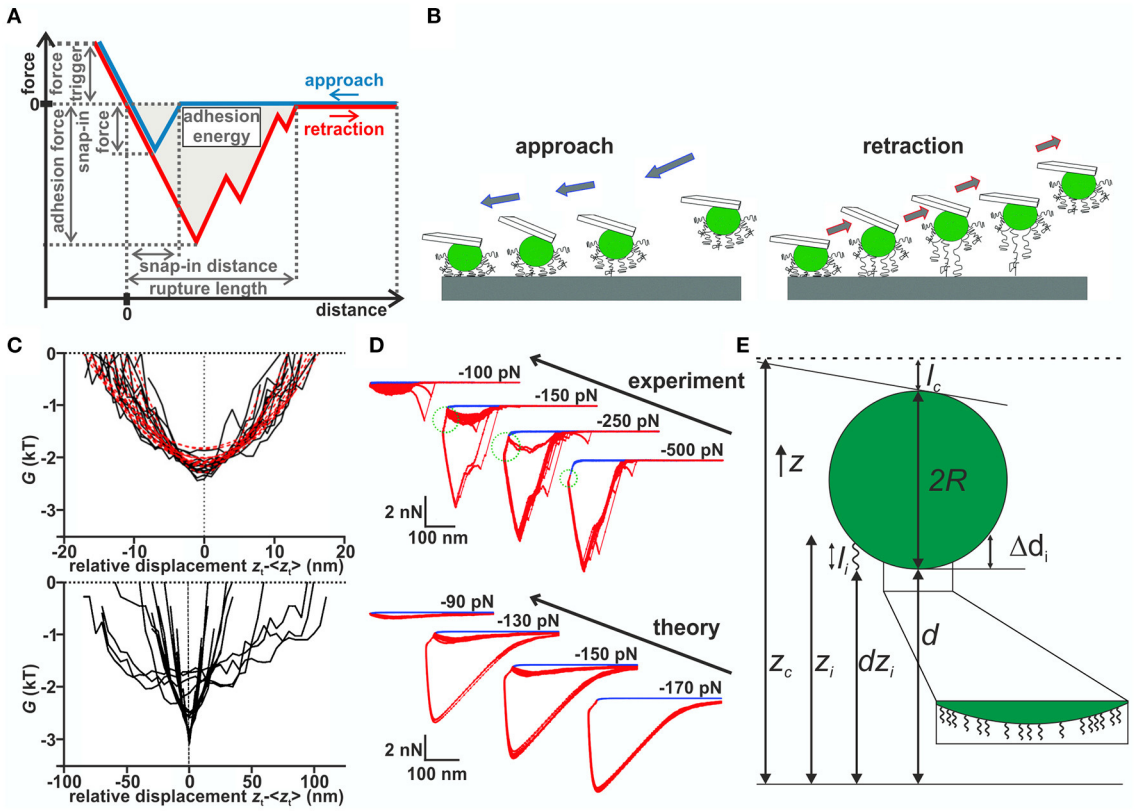

FIGURE 1 | (A) Schematic force–distance curve. **(B)** Sketch of the model: During approach (upper row), the most extend macromolecules start interacting with the surface and pull the bacterium closer to it, which allows more and more molecules to bind. Upon further approach, some molecules may be compressed. During retraction (lower row), the molecules are decompressed and then stretched before the detaching individually. **(C)** Gibb's free energy in dependence of the relative displacement of *Streptococcus salivarius* cells with (top) and without (bottom) fibrillar surface tethers (van der Westen et al., 2018). Image taken from https://pubs.acs.org/doi/10.1021/acs.langmuir.7b04331. For futher information and permissions refer to ACS. **(D)** Partitioned force–distance curves (from experiment and simulations) with varying force trigger. A smaller negative (larger absolute value) force trigger means that the retraction starts later (Thewes et al., 2015b). Blue curves are individual approach curves, while red curves are individual retraction curves with the same cell. Note the bistable behavior of the retraction curves for intermediate force triggers, where either one or the other type of curve is observed for the same cell. The pulling regime is indicated by the green dotted circle. **(E)** Model details for Monte Carlo simulations by Thewes et al. (2015b): Sphere of radius R decorated with springs of length li connected at fixed height Δd_i from bottom of the sphere. The other end is dz_i above the surface and interacts with the potential. In each step, the cantilever's height z_c is changed and a new equilibrium position d for the sphere computed.

evolved and in many instances not analytically solvable. However, qualitatively there are only few scenarios possible: If either of the interactions is attractive and the other repulsive, the free energy landscape displays a minimum close to the surface and eventually—depending on the exact relation between attractive and repulsive potentials—also a secondary minimum. Strong adhesion is achieved when the bacterium can overcome the barrier and weak adhesion is achieved inside the secondary minimum. On experimental time scales, weak adhesion manifests itself as reversibility of the adhesion process, not predicted by the surface thermodynamic approach. In DLVO theory, neglected interactions, such as acid–base interactions and steric effects due to the presence of polymers on the bacterium surface, have been incorporated in the so-called xDLVO theory (Van Oss, 1995). These extensions, however, change the interaction potential quantitatively but do not alter the qualitative picture. The failure of these approaches has, according to Perni et al. (2014), been attributed due to neglecting shear forces and the underlying assumption of a homogeneous bacterial surface composition. However, these models do not aim at describing a full approach and retraction cycle. If the derivative of the potential is considered as the force experience by a bacterium, no hysteresis can be observed since the derivative is unique.

To address these limitations, Jasevičius et al. (2015) extended the DMT model of classical adhesion: The snap-in is incorporated by the van der Waals force of sphere-plane geometry acting from the snap-in distance until direct contact of the surfaces. The magnitude, i.e., the snap-in force, as well as the snap-in distance are fitted from experimental data and are not obtained from the constitute equations of DLVO theory. Once the bacterium is in contact, the usual DMT forces in addition to repulsive electrostatic double layer forces and steric

repulsion forces of polymer brushes are considered. This is complemented by an energy dissipation mechanism including plastic deformation to produce the adhesion hysteresis.[3] Phrased loosely, this model combines xDLVO theory with the Hertzian contact model, while also including an *ad hoc* snap-in mechanism and energy dissipation. Recently, this model has been extended to mimic flow chamber experiments and determine if a given bacterial strain will adhere to a given surface (Jasevičius and Kruggel-Emden, 2017). Therefore, an initial velocity and viscous drag was included into the model and it was demonstrated that *Staphylococcus aureus* cells stick to a glass surface.

We point out that all three models assume continuous interactions of the entire bacterium with the surface while neglecting stochasticity and the responses of individual macromolecules in the adhesion process. However, the next section will show that non-continuous interactions are needed to describe certain aspects of bacterial adhesion.

4. UNDERSTANDING ADHESION THROUGH INDIVIDUAL MACROMOLECULES

In a different set of studies, the displacement of different bacteria after settling in a flow chamber has been monitored by optical microscopy (Sjollema et al., 2017). These experiments, combined with SCFS, demonstrated that the movement of the cells parallel to the surface decreases with increasing adhesion force. These experimental results combined with an *in silico* model led to the conclusion that the bacteria adhere via multiple reversibly binding tethers, which repeatedly detach from and attach to the surface without detaching all at the same time (see **Figure 1B**). An extension of this study has determined if adhering bacteria also exhibit vibrations perpendicular to the surface using internal reflection microscopy (van der Westen et al., 2018). For bacteria without cellular appendages, a comparison of the results with predictions from DLVO theory showed that the surface potential displays two minima with a potential barrier in between that was considered to be too high to be overcome by Brownian motion. The researchers observed on the hydrophobic substrata asymmetric fluctuations inside the secondary minimum with amplitudes fitting to the width of the minimum, independent of ionic strength of the solution.[4] In contrast, cells with fibrils showed symmetric fluctuations with five times smaller vibrational amplitudes, regardless of surface hydrophobicity and ionic strength of the solution (see **Figure 1C**). This lead the authors to distinguish "tether-coupled" and "floating" adhesion where in the latter case adhesion is dominated by the thermal motion inside the secondary minimum predicted by DLVO theory, whereas in the first case the bacterium is bound to the surface by tethers, which penetrate through the potential barrier predicted from DLVO theory.

A different approach toward understanding the adhesion process was taken by analyzing approach curves of *S. aureus* on hydrophobic surfaces (Thewes et al., 2015b). It has been observed that bacterial contact begins at about 50 nm above the substratum (Thewes et al., 2015b), with the aforementioned snap-in. In buffer solution, attractive forces over such large distances cannot be explained by DLVO forces between the bacterium and the substratum. The snap-in was more detailed by analyzing approach and retraction curves with varying negative force triggers, i.e., retraction starts at a certain distance above the substratum before the cell is in direct contact, in experiment and simulation (see **Figure 1D**). While for low and high absolute values of the force trigger the same rupture lengths were observed, the adhesion forces were larger for lower absolute values. In between, an unstable behavior with two types of retraction curves was observed. This stochasticity is not caused by difference of individual cells but—since the same cell is repeatedly used—reflects the internal stochasticity of the adhesion process. In particular, the curves with small force triggers displayed an initial attraction to the surface termed "pulling regime" even though the retraction already started.

To explain these observations, Thewes et al. (2015b) built a stochastic model that treats the bacterium as a hard, incompressible sphere decorated with elastic springs representing the cell wall macromolecules (see **Figure 1E**). One end of the springs is fixed to the bacterium, while the other end fluctuates thermally and interacts with the surface via an interaction potential. In order to mimic SCFS experiments, this sphere is connected to a cantilever, modeled as a spring, which moves toward/away from the surface. After each cantilever step, determined from the step size of the experimental piezo motor, a prescribed number of Monte Carlo (MC) steps is performed in order to incorporate thermal fluctuations. Afterward, the acting force, computed from the length of the connected springs and the deflection of the cantilever, is computed. The separation d of the sphere to the surface is then moved into the mechanical equilibrium position, such that the restoring force of the cantilever F_C and the pulling force of the macromolecules F_M cancel. The pulling force is generated only by macromolecules, which are in range of the interaction potential. That way the binding of individual macromolecules and the macroscopic movement of the cell are combined in a single model, which reproduces the experimentally observed behavior, namely the adhesion hysteresis, the snap-in event, and the behavior of retraction curves with varying negative force trigger. The model shows that for generating a snap-in, the distribution of spring constants is important, while the form of the interaction potential is not (Thewes et al., 2015b).

The model was extended by replacing the Hookean response of cell wall macromolecules to stretching by the more realistic worm-like chains (WLC) response and by reproducing a high number of experimental force–distance curves from many cells on hydrophilic and hydrophobic surfaces by MC simulations, the adhesion process to abiotic surfaces could be understood in more detail (Maikranz et al., 2020): On hydrophilic surfaces, cell wall macromolecules bind to the substratum (most likely by hydrogen bonds) after overcoming a potential barrier while

[3]Different deformation models from contact mechanics display hysteresis even without energy dissipation or plastic deformation (Goryacheva and Makhovskaya, 2001).

[4]On hydrophilic surfaces, adhesion was too low to determine amplitudes.

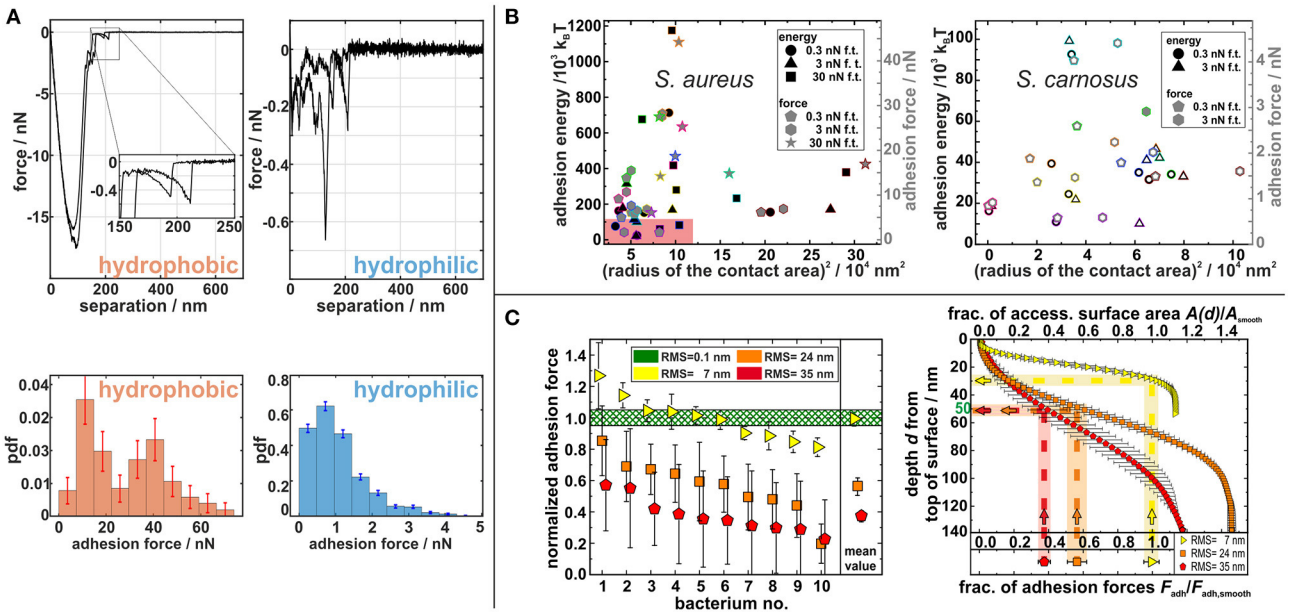

FIGURE 2 | (A) Exemplary force–distance curves (upper row) and probability density function of adhesion forces (lower row) from SCFS with *S. aureus* cells (Maikranz et al., 2020). **(B)** Adhesion energy (black symbols) and adhesion force (gray symbols) of *S. aureus* (left) and *S. carnosus* (right) in dependence of their contact radius squared. The reddish rectangle displays the size of the complete right graph (Spengler et al., 2017). **(C)** (Left) Experimentally determined adhesion forces for 10 individual cells each on different rough substrata. (Right) Correlation of adhesion force and accessible surface area in dependence of the depth from the top of the rough surface (Spengler et al., 2019).

on hydrophobic surfaces, the molecules tether via hydrophobic interactions without an energy barrier. This leads to rather strong adhesion via many molecules on hydrophobic surfaces and hence rather smooth force–distance curves (where WLC like signatures of single molecules detaching events define the rupture length as shown in the inset in **Figure 2A**), and to very "spiky," stochastically varying force–distance curves and rather low adhesion force on hydrophilic surfaces (see **Figure 2A**) (Thewes et al., 2014; Maikranz et al., 2020).

Ostvar and Wood (2016) introduced a similar model with individual macromolecules and heterogeneous mechanical responses, but without thermal fluctuations. The flexibility of the cantilever was not considered, and a plane–plane geometry was used: The bacterial cell wall is considered to have a certain roughness (approximately determined by AFM to be about 10–20 nm) that accounts for differing lengths of surface molecules. In the model, the surface molecules are represented by polymers that can either behave like Hookean springs or WLCs. At the end of each polymer, a bead is located that can directly bind to the surface via a Lennard–Jones potential. Upon retraction, every single polymer can either unbind by the bead escaping the potential. Using this model, retraction parts of experimental force–distance curves obtained with *Staphylococcus epidermidis* cells on glass substrata could be reproduced (Chen et al., 2011; Ostvar and Wood, 2016). In general, the model cannot produce a snap-in event due to the lack of a cantilever that allows the cell to suddenly approach the surface. Both models demonstrate that the adhesion process can be understood as the multi-scale interactions of heterogeneous macromolecules tethering to a surface.

For these models, the number of cell wall macromolecules that are able to bind to the substratum and also the exact knowledge of the cell wall area size that comes in contact with the surface is important. Spengler et al. (2017) investigated the size of this area, i.e., the area of the bacterial cell wall that contributes to the adhesion for *S. aureus* and *S. carnosus* cells: both strains have approximately the same (assumed to be circular) interaction area with radii of about 150–300 nm, although *S. aureus* cells adhere almost one order of magnitude stronger than *S. carnosus* cells. Even on the single species level, no correlation between the adhesion force and interaction area could be measured (see **Figure 2B**). In addition, the study demonstrated that the increase of the contact area with the applied force differs for different individual cells proving that the adhesion cannot be described by the Hertzian contact model.

As mentioned before, the knowledge about the interaction area and the thermal fluctuations can be used to describe bacterial adhesion to non-ideal surfaces (Spengler et al., 2019). It has been found that on nano-rough substrata, the adhesion force of *S. aureus* cells decreases with increasing roughness. The reduced adhesion forces can be directly linked to the decrease in accessible binding area for macromolecules that undergo thermal fluctuations of about 50 nm (see **Figure 2C**). The study also shows that the thermal fluctuation and hence adhesion can be

understood mostly as a passive process: Although cells were killed during SCFS on these spiky surfaces, their adhesion force was not affected (Spengler et al., 2019).

5. CONCLUSION

Several approaches to describe and understand bacterial adhesion on unconditioned abiotic surfaces have been reviewed. Many studies demonstrate that traditional approaches to bacterial adhesion from colloid science and contact mechanics have limitations because adhesion, without external load, is primary mediated by the interaction of cell wall macromolecules with the substratum. The force response and stochastic length fluctuations of individual molecules determine the adhesive behavior. This leads to huge differences in adhesion forces of individual cells even within the same population. This mechanical heterogeneity inside a population can be important on the biofilm level, determining the colonization of small cavities, e.g., catheters.

A recent study has also shown that external factors, such as shear stresses, can change the molecules' force response and even "activate" adhesion (Dufrêne and Viljoen, 2020). The complexity caused by these divers mechanical responses is enhanced through the organization of adhesive molecules into patches, which were needed to interpret our own results (Spengler et al., 2021). These patches lead to a strong variation of the adhesion forces, depending on the contact area between patches and the substrate. In SCFS experiments, rotation of the bacteria is excluded, but typically not in the native setting. Reorientation of the bacteria could lead to more adherent areas coming into contact with the surface, which in principle could lead to stronger adhesion, especially on rough surfaces. Incorporating this and more detailed information, such as experimentally determined mechanical properties of cell wall macromolecules, their density and inhomogeneity (for example, in the division plane) are interesting directions for future research.

AUTHOR CONTRIBUTIONS

CS and EM reviewed and selected the content of the paper and wrote the manuscript. LS and KJ supervised the process, discussed the drafts, and helped in writing the manuscript. All authors contributed to the article and approved the submitted version.

FUNDING

This work was supported by the German Research Foundation (DFG) within the collaborative research center SFB 1027 (Projects B1 and B2). CS and KJ were supported by the DFG-project number JA 905/6. KJ was also supported by the Max Planck School Matter to Life in Heidelberg, Germany.

ACKNOWLEDGMENTS

The authors gratefully acknowledge funding from the above sources. The authors would also like to thank one of the reviewers for his or her detailed comments on contact mechanics, which helped to improve the manuscript.

REFERENCES

Alam, F., Kumar, S., and Varadarajan, K. M. (2019). Quantification of adhesion force of bacteria on the surface of biomaterials: techniques and assays. *ACS Biomater. Sci. Eng.* 5, 2093–2110. doi: 10.1021/acsbiomaterials.9b00213

Alexander, T. E., Lozeau, L. D., and Camesano, T. A. (2019). QCM-D characterization of time-dependence of bacterial adhesion. *Cell Surface* 5:100024. doi: 10.1016/j.tcsw.2019.100024

Barthel, E., and Perriot, A. (2007). Adhesive contact to a coated elastic substrate. *J. Phys. D Appl. Phys.* 40:1059. doi: 10.1088/0022-3727/40/4/021

Berne, C., Ellison, C. K., Ducret, A., and Brun, Y. V. (2018). Bacterial adhesion at the single-cell level. *Nat. Rev. Microbiol.* 16, 616–627. doi: 10.1038/s41579-018-0057-5

Bhushan, B. (2017). *Springer Handbook of Nanotechnology*. Berlin; Heidelberg: Springer. doi: 10.1007/978-3-662-54357-3

Boks, N. P., Norde, W., van der Mei, H. C., and Busscher, H. J. (2008). Forces involved in bacterial adhesion to hydrophilic and hydrophobic surfaces. *Microbiology* 154, 3122–3133. doi: 10.1099/mic.0.2008/018622-0

Chen, Y., Busscher, H. J., van der Mei, H. C., and Norde, W. (2011). Statistical analysis of long- and short-range forces involved in bacterial adhesion to substratum surfaces as measured using atomic force microscopy. *Appl. Environ. Microbiol.* 77, 5065–5070. doi: 10.1128/AEM.00502-11

Chen, Y., Harapanahalli, A. K., Busscher, H. J., Norde, W., and van der Mei, H. C. (2014). Nanoscale cell wall deformation impacts long-range bacterial adhesion forces on surfaces. *Appl. Environ. Microbiol.* 80, 637–643. doi: 10.1128/AEM.02745-13

Chen, Y., Norde, W., van der Mei, H. C., and Busscher, H. J. (2012). Bacterial cell surface deformation under external loading. *mBio* 3:e00378-12. doi: 10.1128/mBio.00378-12

Ciavarella, M., Joe, J., Papangelo, A., and Barber, J. R. (2019). The role of adhesion in contact mechanics. *J. R. Soc. Interface* 16:20180738. doi: 10.1098/rsif.2018.0738

De Carvalho, C. C. (2007). Biofilms: recent developments on an old battle. *Recent Pat. Biotechnol.* 1, 49–57. doi: 10.2174/187220807779813965

Derjaguin, B., Muller, V., and Toporov, Y. (1975). Effect of contact deformations on the adhesion of particles. *J. Colloid Interface Sci.* 53, 314–326. doi: 10.1016/0021-9797(75)90018-1

Derjaguin, B. V., and Landau, L. (1941). Theory of the stability of strongly charged lyophobic sols and of the adhesion of strongly charged particles in solutions of electrolytes. *Acta Physicochim. URSS* 14, 633–662.

Dufrêne, Y. F., and Pelling, A. E. (2013). Force nanoscopy of cell mechanics and cell adhesion. *Nanoscale* 5, 4094–4104. doi: 10.1039/c3nr00340j

Dufrêne, Y. F., and Viljoen, A. (2020). Binding strength of gram-positive bacterial adhesins. *Front. Microbiol.* 11:1457. doi: 10.3389/fmicb.2020.01457

Dunne, W. M. (2002). Bacterial adhesion: seen any good biofilms lately? *Clin. Microbiol. Rev.* 15, 155–166. doi: 10.1128/CMR.15.2.155-166.2002

Fällman, E., Schedin, S., Jass, J., Andersson, M., Uhlin, B. E., and Axner, O. (2004). Optical tweezers based force measurement system for quantitating binding interactions: system design and application for the study of bacterial adhesion. *Biosens. Bioelectron.* 19, 1429–1437. doi: 10.1016/j.bios.2003.12.029

Filion-Côté, S., Melaine, F., Kirk, A. G., and Tabrizian, M. (2017). Monitoring of bacterial film formation and its breakdown with an angular-based surface plasmon resonance biosensor. *Analyst* 142, 2386–2394. doi: 10.1039/C7AN00068E

Goryacheva, I., and Makhovskaya, Y. Y. (2001). Adhesive interaction of elastic bodies. *J. Appl. Math. Mech.* 65, 273–282. doi: 10.1016/S0021-8928(01)00031-4

Greenwood, J. (1997). Adhesion of elastic spheres. *Proc. R. Soc. Lond. A Math. Phys. Eng. Sci.* 453, 1277–1297. doi: 10.1098/rspa.1997.0070

Hinterdorfer, P., and Dufrêne, Y. F. (2006). Detection and localization of single molecular recognition events using atomic force microscopy. *Nat. Methods* 3, 347–355. doi: 10.1038/nmeth871

Jamal, M., Ahmad, W., Andleeb, S., Jalil, F., Imran, M., Nawaz, M. A., et al. (2018). Bacterial biofilm and associated infections. *J. Chin. Med. Assoc*. 81, 7–11. doi: 10.1016/j.jcma.2017.07.012

Jasevičius, R., Baronas, R., and Kruggel-Emden, H. (2015). Numerical modelling of the normal adhesive elastic-plastic interaction of a bacterium. *Adv. Powder Technol*. 26, 742–752. doi: 10.1016/j.apt.2015.04.010

Jasevičius, R., and Kruggel-Emden, H. (2017). Numerical modelling of the sticking process of a *S. aureus* bacterium. *Int. J. Adhes. Adhesiv*. 77, 15–28. doi: 10.1016/j.ijadhadh.2017.03.015

Johnson, K. L., Kendall, K., and Roberts, A. (1971). Surface energy and the contact of elastic solids. *Proc. R. Soc. Lond. A Math. Phys. Sci*. 324, 301–313. doi: 10.1098/rspa.1971.0141

Keskin, D., Mergel, O., van der Mei, H. C., Busscher, H. J., and van Rijn, P. (2018). Inhibiting bacterial adhesion by mechanically modulated microgel coatings. *Biomacromolecules* 20, 243–253. doi: 10.1021/acs.biomac.8b01378

Krieg, M., Fläschner, G., Alsteens, D., Gaub, B. M., Roos, W. H., Wuite, G. J., et al. (2019). Atomic force microscopy-based mechanobiology. *Nat. Rev. Phys*. 1, 41–57. doi: 10.1038/s42254-018-0001-7

Loskill, P., Hähl, H., Thewes, N., Kreis, C. T., Bischoff, M., Herrmann, M., et al. (2012). Influence of the subsurface composition of a material on the adhesion of staphylococci. *Langmuir* 28, 7242–7248. doi: 10.1021/la3004323

Loskill, P., Pereira, P. M., Jung, P., Bischoff, M., Herrmann, M., Pinho, M. G., et al. (2014). Reduction of the peptidoglycan crosslinking causes a decrease in stiffness of the staphylococcus aureus cell envelope. *Biophys. J*. 107, 1082–1089. doi: 10.1016/j.bpj.2014.07.029

Magill, S. S., Edwards, J. R., Bamberg, W., Beldavs, Z. G., Dumyati, G., Kainer, M. A., et al. (2014). Multistate point-prevalence survey of health care-associated infections. *N. Engl. J. Med*. 370, 1198–1208. doi: 10.1056/NEJMoa1306801

Maikranz, E., Spengler, C., Thewes, N., Thewes, A., Nolle, F., Jung, P., et al. (2020). Different binding mechanisms of staphylococcus aureus to hydrophobic and hydrophilic surfaces. *Nanoscale* 12, 19267–19275. doi: 10.1039/D0NR03134H

Maugis, D. (1992). Adhesion of spheres: the JKR-DMT transition using a dugdale model. *J. Colloid Interface Sci*. 150, 243–269. doi: 10.1016/0021-9797(92)90285-T

Muller, V., Yushchenko, V., and Derjaguin, B. (1980). On the influence of molecular forces on the deformation of an elastic sphere and its sticking to a rigid plane. *J. Colloid Interface Sci*. 77, 91–101. doi: 10.1016/0021-9797(80)90419-1

Narenkumar, J., AlSalhi, M. S., Arul Prakash, A., Abilaji, S., Devanesan, S., Rajasekar, A., et al. (2019). Impact and role of bacterial communities on biocorrosion of metals used in the processing industry. *ACS Omega* 4, 21353–21360. doi: 10.1021/acsomega.9b02954

Ostvar, S., and Wood, B. D. (2016). Multiscale model describing bacterial adhesion and detachment. *Langmuir* 32, 5213–5222. doi: 10.1021/acs.langmuir.6b00882

Perni, S., Preedy, E. C., and Prokopovich, P. (2014). Success and failure of colloidal approaches in adhesion of microorganisms to surfaces. *Adv. Colloid Interface Sci*. 206, 265–274. Manuel G. Velarde. doi: 10.1016/j.cis.2013.11.008

Römling, U., Kjelleberg, S., Normark, S., Nyman, L., Uhlin, B. E., and Åkerlund, B. (2014). Microbial biofilm formation: a need to act. *J. Intern. Med*. 276, 98–110. doi: 10.1111/joim.12242

Schwermer, C. U., Lavik, G., Abed, R. M., Dunsmore, B., Ferdelman, T. G., Stoodley, P., et al. (2008). Impact of nitrate on the structure and function of bacterial biofilm communities in pipelines used for injection of seawater into oil fields. *Appl. Environ. Microbiol*. 74, 2841–2851. doi: 10.1128/AEM.02027-07

Sjollema, J., van der Mei, H. C., Hall, C. L., Peterson, B. W., de Vries, J., Song, L., et al. (2017). Detachment and successive re-attachment of multiple, reversibly-binding tethers result in irreversible bacterial adhesion to surfaces. *Sci. Rep*. 7:4369. doi: 10.1038/s41598-017-04703-8

Spengler, C., Glatz, B. A., Maikranz, E., Bischoff, M., Klatt, M. A., Santen, L., et al. (2021). The adhesion capability of *S. aureus* cells is heterogeneously distributed over the cell envelope. *bioRxiv*. doi: 10.1101/2021.01.05.425282

Spengler, C., Nolle, F., Mischo, J., Faidt, T., Grandthyll, S., Thewes, N., et al. (2019). Strength of bacterial adhesion on nanostructured surfaces quantified by substrate morphometry. *Nanoscale* 11, 19713–19722. doi: 10.1039/C9NR04375F

Spengler, C., Thewes, N., Jung, P., Bischoff, M., and Jacobs, K. (2017). Determination of the nano-scaled contact area of staphylococcal cells. *Nanoscale* 9, 10084–10093. doi: 10.1039/C7NR02297B

Stan, G., and Adams, G. G. (2016). Adhesive contact between a rigid spherical indenter and an elastic multi-layer coated substrate. *Int. J. Solids Struct*. 87, 1–10. doi: 10.1016/j.ijsolstr.2016.02.043

Tandogan, N., Abadian, P. N., Huo, B., and Goluch, E. D. (2017). "Characterization of bacterial adhesion and biofilm formation," in *Antimicrobial Coatings and Modifications on Medical Devices*, eds Z. Zhang and V. E. Wagner (Cham: Springer), 67–95. doi: 10.1007/978-3-319-57494-3_3

Thewes, N., Loskill, P., Jung, P., Peisker, H., Bischoff, M., Herrmann, M., et al. (2014). Hydrophobic interaction governs unspecific adhesion of staphylococci: a single cell force spectroscopy study. *Beilstein J. Nanotechnol*. 5, 1501–1512. doi: 10.3762/bjnano.5.163

Thewes, N., Loskill, P., Spengler, C., Hümbert, S., Bischoff, M., and Jacobs, K. (2015a). A detailed guideline for the fabrication of single bacterial probes used for atomic force spectroscopy. *Eur. Phys. J. E* 38:140. doi: 10.1140/epje/i2015-15140-2

Thewes, N., Thewes, A., Loskill, P., Peisker, H., Bischoff, M., Herrmann, M., et al. (2015b). Stochastic binding of *Staphylococcus aureus* to hydrophobic surfaces. *Soft Matter* 11, 8913–9046. doi: 10.1039/C5SM00963D

van der Westen, R., Sjollema, J., Molenaar, R., Sharma, P. K., van der Mei, H. C., and Busscher, H. J. (2018). Floating and tether-coupled adhesion of bacteria to hydrophobic and hydrophilic surfaces. *Langmuir* 34, 4937–4944. doi: 10.1021/acs.langmuir.7b04331

Van Oss, C. (1995). Hydrophobicity of biosurfaces—origin, quantitative determination and interaction energies. *Colloids Surf. B Biointerfaces* 5, 91–110. doi: 10.1016/0927-7765(95)01217-7

Van Oss, C. J., Giese, R. F., and Costanzo, P. M. (1990). DLVO and non-DLVO interactions in hectorite. *Clays Clay Miner*. 38, 151–159. doi: 10.1346/CCMN.1990.0380206

Verwey, E. J. W. (1947). Theory of the Stability of Lyophobic Colloids. *J. Phys. Chem*. 51, 631–636.

Vissers, T., Brown, A. T., Koumakis, N., Dawson, A., Hermes, M., Schwarz-Linek, J., et al. (2018). Bacteria as living patchy colloids: phenotypic heterogeneity in surface adhesion. *Sci. Adv*. 4:eaao1170. doi: 10.1126/sciadv.aao1170

Zhang, H., and Liu, K. K. (2008). Optical tweezers for single cells. *J. R. Soc. Interface* 5, 671–690. doi: 10.1098/rsif.2008.0052

Conflict of Interest: The authors declare that the research was conducted in the absence of any commercial or financial relationships that could be construed as a potential conflict of interest.

frontiers in Mechanical Engineering

ORIGINAL RESEARCH
published: 24 May 2021
doi: 10.3389/fmech.2021.667491

On the Nanomechanical and Viscoelastic Properties of Coatings Made of Recombinant Sea Star Adhesive Proteins

Mathilde Lefevre[1,2], *Thi Quynh Tran*[1], *Thomas De Muijlder*[1], *Bede Pittenger*[3], *Patrick Flammang*[4], *Elise Hennebert*[2] *and Philippe Leclère*[1]*

[1] *Laboratory for Chemistry of Novel Materials, Research Institute for Materials, Department of Chemistry, University of Mons, Mons, Belgium,* [2] *Laboratory of Cell Biology, Research Institute for Biosciences, Department of Biology, University of Mons, Mons, Belgium,* [3] *Bruker Nano Surfaces, Atomic Force Microscopy Unit, Santa Barbara, CA, United States,* [4] *Biology of Marine Organisms and Biomimetics Unit, Research Institute for Biosciences, University of Mons, Mons, Belgium*

To attach to surfaces in the sea, sea stars produce proteinaceous adhesive secretions. Sfp1 is a major constituent of this adhesive, where it is present in the form of four subunits (named Sfp1α to δ) displaying specific protein-, carbohydrate- and metal-binding domains. Recently, two recombinant proteins inspired from Sfp1 have been produced: one corresponding to the C-terminal part of Sfp1β and the other to the full-length Sfp1δ. Adsorption ability tests showed that both recombinant proteins were able to adsorb and to form coatings on different surfaces in artificial seawater as well as in Tris buffer supplemented with NaCl or $CaCl_2$. In this study, we used Atomic Force Microscopy (AFM) to characterize the nanomechanical properties of these coatings with an emphasis on functional characteristics such as adhesive properties and modulus of elasticity. We used AFM techniques which are the most appropriate to characterize the coating microstructure combined with the mapping of its nanomechanical properties.

Keywords: atomic force microscopy, adhesive proteins, nanomechanical AFM modes, viscoelastic properties, peakforce and quantitive imaging modes

OPEN ACCESS

Edited by:
Ken Nakano,
Yokohama National University, Japan

Reviewed by:
Massimiliano Galluzzi,
Shenzhen Institutes of Advanced Technology (CAS), China
Ken Nakajima,
Tokyo Institute of Technology, Japan

***Correspondence:**
Philippe Leclère
philippe.leclere@umons.ac.be

Specialty section:
This article was submitted to Tribology, a section of the journal Frontiers in Mechanical Engineering

Received: *13 February 2021*
Accepted: *27 April 2021*
Published: *24 May 2021*

Citation:
Lefevre M, Tran TQ, De Muijlder T, Pittenger B, Flammang P, Hennebert E and Leclère P (2021) On the Nanomechanical and Viscoelastic Properties of Coatings Made of Recombinant Sea Star Adhesive Proteins. Front. Mech. Eng. 7:667491. doi: 10.3389/fmech.2021.667491

INTRODUCTION

Nowadays, adhesion in wet environments is a crucial economic and medical concern (Almeida et al., 2020). In this context, glues inspired by adhesive secretions produced by marine organisms are increasingly being studied to replace currently available surgical adhesives and sealants which pose toxicity issues (e.g., cyanoacrylate or formaldehyde-based glues), or which cannot be used in areas continuously bathed with body fluids (e.g., fibrin) (Duarte et al., 2012; Annabi et al., 2014). The prerequisite of such applications is the complete molecular and functional characterization of these protein-based marine glues. To date, the best-characterized marine bioadhesive is that from the mussel and it has inspired most of the biomimetic adhesives currently available (see Waite, 2017 for review). DOPA (3,4-dihydroxy-L-phenylalanine), which is formed by the post-translational modification of tyrosine, is the key component of mussel glue, by displaying important interfacial adhesive and bulk cohesive roles (Heinzmann et al., 2016). A number of DOPA-based

inspired bioadhesives have therefore been developed, either in the form of recombinant preparations of mussel adhesive proteins or in the form of chemically synthesized polymers incorporating catechol groups (Kord Forooshani and Lee, 2017). The proteins constituting the adhesive secretions from other species like tubeworms, barnacles, echinoderms and flatworms are also being increasingly characterized and are considered as a source of inspiration for the development of new adhesives (e.g., Becker et al., 2012; Hennebert et al., 2014, Liang et al., 2019; Wunderer et al., 2019). For instance, Sfp1, a major sea star adhesive protein, presents a multimodular structure (i.e., four subunits, each comprising several protein-, carbohydrate- and metal-binding domains) which provides a relatively unexplored design paradigm for potential applications as adhesives and sealants (Hennebert et al., 2014).

The adhesion ability of biomimetic adhesives can be analyzed at the macro-scale by different methods such as tensile or lap-shear tests (e.g., Cha et al., 2009; Choi et al., 2012; Liang et al., 2015). Regarding the nano- and micro-scale, a powerful tool can be used, Atomic Force Microscopy (AFM). Different AFM modes widely described in literature have been developed to study biomolecules. For example, some mussel and barnacle recombinant proteins have been investigated using this technique to understand the topography of dried protein layers (e.g., Hwang et al., 2007; Liang et al., 2018). Chemical Force Microscopy (CFM) has also been used to characterize the adhesion of such proteins (Noy, 2006). This technique uses a modified cantilever presenting at its end a glass bead coated with the proteins of interest. For instance, the interaction between recombinant mussel proteins Mgfp-3A, Mgfp-5 and fp151 and clean glass surface was investigated by recording force-distance curves and showed that these proteins presented a higher adhesion force compared to the Cell-Tak® control (Hwang et al., 2004, 2005, 2007). The characterization of microscale adhesion of the recombinant barnacle protein Balcp19k was also performed using protein modified colloidal probes and AFM-based force spectroscopy (Liang et al., 2018).

Two recombinant sea star adhesive proteins, rSfp1 Beta C-term and rSfp1 Delta (Lefevre et al., 2020) are the focus of the present study. These two multimodular recombinant proteins adsorb on surfaces upon addition of Na^+ and/or Ca^{2+} ions. In artificial seawater (ASW), rSfp1 Beta C-term forms a meshwork (with component walls around 600 nm in height) made up of globular nanostructures about 160–200 nm in diameter, while in Tris buffer supplemented with 450 mM NaCl it forms a very dense homogeneous layer on the surface with smaller globular structures of 80–120 nm. As for rSfp1 Delta, it forms a very thin layer composed of very small globular nanostructures scattered homogeneously on the surface in Tris buffer supplemented with 150 mM $CaCl_2$ (Lefevre et al., 2020). These coatings were imaged in air using AFM in Tapping mode in our previous study (Lefevre et al., 2020). In the present study, we used AFM to image rSfp1 Beta C-term and rSfp1 Delta coatings and measure their mechanical properties at the nanoscale. All coatings were investigated using Peak Force Quantitative Nanomechanical Property Mapping (PF-QNM) both in air and in water. In addition, nanoscale dynamic mechanical analysis (nDMA), a new technique based on AFM, was implemented to investigate the visco-elastic properties of rSfp1 Beta C-term coatings in fluid conditions. This technique is a new mode for quantitative viscoelastic analysis of heterogeneous polymer materials at the nanoscale. AFM-nDMA takes advantage of the exquisite force sensitivity, small contact radius, and nanoscale indentation depth of the AFM to provide dynamic mechanical analysis with 10 nm spatial resolution at rheologically relevant frequencies and variable temperature (Pittenger et al., 2019).

MATERIALS AND METHODS

Production of Recombinant Proteins rSfp1

The coding sequences for two parts of Sfp1 (rSfp1 Beta C-term and rSfp1 Delta) were inserted in a pET-28a (+) protein expression vector (Novagen) in frame with C-terminal 6 × His-tag coding sequence. The recombinant proteins were expressed in the *Escherichia Coli* C2566 strain (New England Biolabs) and purified using a HisTrap HP column (GE Healthcare) connected to an Akta Start system (GE Healthcare) under denaturing conditions as described in Lefevre et al. (2020). After a direct dialysis against 25 mM Tris to remove denaturing compounds, both proteins were stored at 4°C in 25 mM Tris buffer, pH 8 (Lefevre et al., 2020).

Preparation of Samples

The proteins were deposited on glass surfaces pre-cleaned with 5% HCl as described in Lefevre et al. (2020). Briefly, a 40 µl drop of a 0.2 mg/mL stock protein solution in 25 mM Tris buffer was deposited on glass and mixed with 40 µL of different buffers to generate the following conditions: (1) artificial sea water (ASW, 445 mM NaCl, 60 mM MgCl2, 10 mM KCl, 10 mM CaCl2, 2.4 mM NaHCO3, 10 mM Hepes, pH 8.0; Szulgit and Shadwick, 2000) in which rSfp1 Beta C-term forms a meshwork, (2) 25 mM Tris, 450 mM NaCl in which rSfp1 Beta C-term forms a homogeneous coating, and (3) 25 mM Tris, 150 mM $CaCl_2$ in which rSfp1 Delta (monomeric form) forms a homogeneous coating. These conditions were selected based on preliminary adsorption tests on glass coverslips (Lefevre et al., 2020). Bovine serum albumin (BSA) was used as a reference protein and the mix of rSfp1 Beta C-term and rSfp1 Delta was also characterized. In this case, a 20 µL drop of 0.2 mg/mL of each rSfp1 proteins in Tris buffer was mixed with 40 µL of buffers. The surfaces were incubated in a humid environment for 16 h at 25°C and then were washed thoroughly with deionized water for 2 h with shaking. For observations made in air, samples were prepared on microscope coverslips and air dried before measurements. For observations made in fluid, samples were prepared on microscope slides into a Gene Frame seal (ThermoFisher, **Supplementary Figure 1C**) and kept in a humid environment until the measurements.

Peak Force Quantitative Nanomechanical Property Mapping (PF-QNM)

Images were obtained by scanning the protein layer on glass surface in air under ambient conditions using AFM (Bruker, Icon Dimension + NanoScope V controller, Santa Barbara, CA, USA; Bruker NanoScope Software v9.7) operated using

the Peak Force QNM mode (Pittenger et al., 2010) at 25°C. To obtain topography profiles of samples, RTESPA 300-30 probes were used (Bruker AFM Probes, Camarillo, CA, USA; **Supplementary Figure 1A**). Theses silicon probes are pre-calibrated with rounded, well-defined tips, have a spring constant of ∼40 N/m and a tip radius of 30 nm (± 15%). The fluid experiments were performed in deionized water using a specific pre-calibrated probe, the so-called PFQNM-LC-A-CAL (Bruker AFM Probes, Camarillo, CA, USA), particularly suited for biological samples (**Supplementary Figure 1C**). This short paddle-shaped cantilever has a pre-calibrated spring of ∼0.1 N/m, a resonance frequency of ∼45 kHz and a 70 nm radius (**Supplementary Figure 1B**). This tip is particularly useful for imaging soft materials like cells (e.g., Berquand et al., 2019, Efremov et al., 2020). The deflection sensitivity has also been calibrated using ramping on sapphire substrate and was ∼38 nm/V. The peak force amplitude was 300 nm, the scan rate was 0.1 Hz at a peak force frequency of 0.5 kHz. All the captured images were recorded with a resolution of 256 × 256 data points. For each pixel of the image, a force curve was also recorded. Adhesion was measured during pull-off force-distance curve and corresponds to the minimum of the curve. The other quantitative mechanical properties (i.e., rigidity modulus, deformation, …) were obtained using Bruker software applying the Johnson-Kendall-Roberts (JKR) model (Johnson et al., 1971; NanoScope Analysis v2.0). This model is a contact mechanics model which adapted Hertz theory by adding adhesion forces. JKR is known to be be the most appropriate for soft and sticky materials. In that case, the adhesion effect on the contact region shape cannot be neglected. So, unlike the DMT model, it takes into account only the adhesion forces that come inside the contact region (Johnson and Greenwood, 1997).

Nanoscale Dynamic Mechanical Analysis (nDMA)

AFM images were also obtained for the coating formed by rSfp1 Beta C-term in artificial seawater on glass surface, rinsed, and scanned in deionized water using AFM operated using the nDMA mode, and fast force volume measurement. For these fluid measurement, a PFQNM-LC-A-CAL probe was also used. The ramp size was 300 nm and the ramp rate was 5 Hz. The modulate amplitude was 1 mV and the hold time 500 ms. The drive frequency used was 80 Hz and the same drive frequency was applied during the calibration on glass experiment. The calibration allows compensation for the phase shift between Z and deflection ($\phi - \psi$) that occurs in both air and liquid. It is expected that there is an additional drag force on the cantilever in liquid that will influence the measurement slightly. For this work, we do not attempt to compensate for this, but instead assume that the drag force at 80 Hz is small compared to the oscillatory force from the cantilever spring. This technique is able to provide the storage modulus (E'), the loss modulus (E"), and the ratio E"/E' corresponding to loss tangent or tan δ (Pittenger et al., 2019). Because the measurement takes place during the "hold segment" of the force-distance curve (i.e; when the tip is located and stay at the vertical of one pixel), these properties are largely decoupled from the tip-sample adhesion—an important consideration when studying adhesives (Pittenger et al., 2019). The model of AFM-nDMA are described in Pittenger et al. (2019). This mode operates through application of sinusoidal motion to a Z piezo and measurement of resulting low-amplitude oscillating motion of the tip in contact with the sample. Viscoelastic properties are determined through the resulting amplitude and phase shift of the cantilever oscillation. The Z piezo motion as a function of time is described by

$$z(t) = Z_1 \sin(\omega t + \psi)$$

Where Z_1 is the amplitude of Z motion, ω is the measurement frequency, and ψ is its phase. Likewise, the cantilever deflection as a function of time is described by

$$d(t) = D_1 \sin(\omega t + \varphi)$$

Where D_1 is the cantilever deflection amplitude, and φ is the deflection phase. The amplitude ratio (D_1/Z_1) and phase shift ($\varphi - \psi$) are extracted to yield the complex "dynamic stiffness," S*:

$$S^* = S' + iS'' = \frac{force}{deformation} = \frac{K_c D_1 e^{i\varphi}}{(Z_1 e^{i\psi} - D_1 e^{i\varphi})}$$

Where K_c is the cantilever spring constant. The real and imaginary parts of S∗ can then be separated into storage stiffness (S') and loss stiffness (S"), respectively, while the loss tangent (also known as tan δ) is simply the ratio of the two:

$$S' = \frac{K_c D_1}{Z_1} \frac{\cos(\varphi - \psi) - D_1/Z_1}{[\cos(\varphi - \psi) - D_1/Z_1]^2 + [\sin(\varphi - \psi)]^2}$$

$$S'' = \frac{K_c D_1}{Z_1} \frac{\sin(\varphi - \psi)}{[\cos(\varphi - \psi) - D_1/Z_1]^2 + [\sin(\varphi - \psi)]^2}$$

$$\tan\delta = \frac{S'}{S''} = \frac{\sin(\varphi - \psi)}{\cos(\varphi - \psi) - (D_1/Z_1)}$$

Unsupervised Clustering Data

To analyze AFM data, a multi-dimensional data analysis based on KMeans (MacQueen, 1967), a unsupervised clustering algorithm, was performed. KMeans is aimed to sort pixels in k clusters by using the measured properties of the sample. These properties are normalized by min-max normalization to give them an equal weight for the clustering. If the sample can be described in terms of different populations, each one will correspond to a different cluster. After the clustering, populations can be characterized separately by histograms, boxplots, and so on. It is also possible to map the different clusters to highlights the presence of nanostructures in the sample.

The properties used for the clustering were chosen thanks to a Spearman correlation test. When two properties are strongly correlated (i.e., $|rs| > 0.7$), it is often better to only use one of them to avoid the use of redundant information during the clustering.

RESULTS

Topography of rSfp1 Coatings

First, AFM was used to provide topographic images and roughness measurements for each Peak Force Quantitative

Nanomechanical Property Mapping (PF-QNM) image of the rSfp1 coatings both in air and underwater (**Table 1**). As expected, in air, the roughness of Sfp1 Beta C-term coatings were higher than those of rSfp1 Delta (Lefevre et al., 2020), while the roughness of the coatings made up by the mix of the two recombinant proteins was intermediate. Excepted for rSfp1 Delta, the roughness of all the coatings was lower in deionized water than in air. This could be explained by the fact that the globular nanostructures composing these coatings swell in deionized water, thereby limiting the roughness at the nanometer scale (**Supplementary Figure 2**).

In air, the coating made up of rSfp1 Beta C-term ASW was composed of nanoglobular structures of 80–200 nm while coatings prepared in Tris buffer supplemented with 450 mM NaCl (rSfp1 Beta C-term 450 mM NaCl) possessed smaller globular structures (90–150 nm) with some bigger at 400 nm (**Figures 1A,B**). When observed in deionized water, rSfp1 Beta C-term ASW formed a thin layer (few hundreds of nm) with smaller nanostructures then in air (around 30 to 70 nm, **Figures 2A,D**, **Supplementary Figure 2**) while the topography of rSfp1 Beta C-term 450 mM NaCl did not change much, with a large number of globular structures at 80–120 nm, the biggest ones being around 250 nm (**Figure 3A**). Regarding rSfp1 Delta prepared in ASW (rSp1 Delta ASW), in air, it formed a homogenous layer with aggregates of 60–100 nm, while in deionized water, globular nanostrutures were around 75–130 nm with bigger ones of 180 nm (**Figures 1C**, **3D**). When rSfp1 Delta was prepared in Tris buffer supplemented with 150 mM $CaCl_2$ (rSfp1 Delta 150 mM $CaCl_2$), the proteins formed small nanoglobular structures of 50–90 nm in air and of 80–140 nm in deionized water (**Figures 1D**, **3G**). Finally, for the mix of both recombinant proteins prepared in ASW (mix of rSfp1 Beta C-term and rSfp1 Delta ASW), globular structures around 80–130 nm were observed in air (**Figure 1E**) which were sligthy smaller than in rSfp1 Beta C-term ASW and rSfp1 Delta ASW coatings. In deionized water, the mix of rSfp1 Beta C-term and rSfp1 Delta ASW showed a flatter layer compared to air, with globular structures of 100–140 nm (**Figure 3J**). As control, Bovine Serum Albumine prepared in ASW (BSA ASW) was also analyzed using Peak Force QNM mode and showed a very smooth layer (with a roughness of 2.5 nm) in air and in dionized water without any distinguishable structure (**Figures 1F**, **3M**).

TABLE 1 | Roughness (Rq) calculated from height images obtained using PF-QNM measurement of rSfp1 coatings.

	Rq (nm)	
	Air	**Deionized water**
rSfp1 Beta C-term ASW	129	8.48
rSfp1 Beta C-term 450 mM NaCl	66.9	23.2
rSfp1 Delta ASW	3.11	1.8
rSfp1 Delta 150 mM $CaCl_2$	1.71	8.84
Mix of rSfp1 Beta C-term and rSfp1 Delta ASW	31.2	16.7

Nanomechanical Properties of Proteins Layers

The nanomechanical properties of the rSfp1 coatings were investigated using PF-QNM and nanoscale Dynamic Mechanical Analysis (nDMA) in deionized water (**Table 2**). For these experiments, BSA was used as a reference protein as its molecular

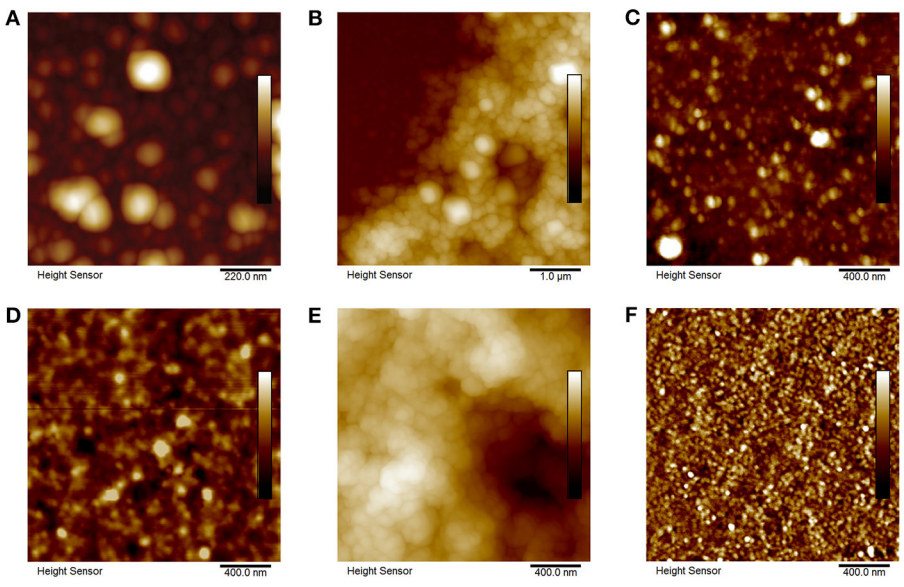

FIGURE 1 | Topography in air of coating formed by rSfp1 Beta C-term, rSfp1 Delta and Bovine Serum Albumin previously prepared in different buffers, rinsed in dionized water and air dried. **(A)** rSfp1 Beta C-term ASW (Scale: 50 nm), **(B)** rSfp1 Beta C-term 450 mM NaCl (scale: 600 nm), **(C)** rSfp1 Delta ASW (Scale: 40 nm), **(D)** rSfp1 Delta 150 mM $CaCl_2$ (Scale: 15 nm), **(E)** mix of rSfp1 Beta C-term and rSfp1 Delta ASW, **(F)** Bovine serum albumine ASW (Scale: 2.5 nm).

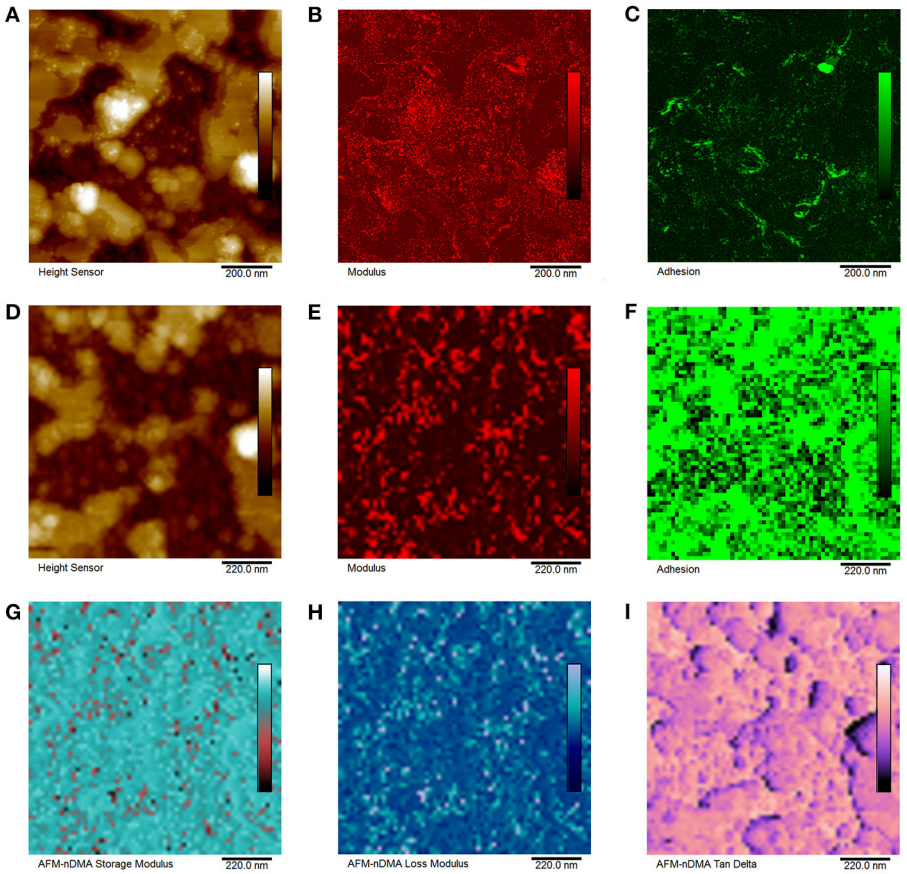

FIGURE 2 | Nanomechanical mapping of rSfp1 Beta C-term coating prepared in artificial sea water and observed in deionized water using **(A,C)** Peak Force QNM mode, **(D–I)** nDMA mode in fluid. **(A)** Height, scale: 50 nm, **(B)** Modulus, scale: 10 MPa, **(C)** Adhesion, scale: 500 pN, **(D)** Height in nDMA mode, scale: 50 nm, **(E)** Modulus, scale: 10 MPa, **(F)** Adhesion, scale: 500 pN, **(G)** Storage modulus, scale: 17.5 MPa, **(H)** Loss modulus, scale: 15 MPa, and **(I)** Tan Delta, scale: 0.400.

weight and isoelectric point are close to those of rSfp1s. Random spots were analyzed on areas without large structures but close to these.

The measured moduli were 300 MPa for rSfp1 Beta C-term ASW for both modes used, and 500 MPa for rSfp1 Beta C-term NaCl (**Figures 2B,E**, **3B**). These values are close to those expected for biological samples (Lakes, 2009). The adhesion was comprised between 90 and 300 pN for rSfp1 Beta C-term ASW and was 200 pN for rSfp1 Beta C-term 450 mM NaCl (**Figures 2C,F**, **3C**). The coating formed in ASW is homogeneous at nanomechanical level and no cluster was observable. The visco-elastic properties of rSfp1 Beta C-term ASW were also analyzed. The storage modulus and loss modulus were 40 and 20 MPa, respectively, and the tan δ was 0.2 (**Figures 2G–I**).

rSfp1 Delta ASW and rSfp1 Delta 150 mM $CaCl_2$ presented a modulus of 5 MPa and 500 kPa, respectively (**Figures 3E,H**). Regarding the adhesion, values were also higher with 150 pN for rSfp1 Delta ASW and lower with 80 pN for rSfp1 Delta 150 mM $CaCl_2$ (**Figures 3F,I**).

The coating made up of the two recombinant proteins and prepared in ASW presented a homogeneous mapping of the nanomechanical properties, with an adhesion force (70 pN) in the same range as that of rSfp1 Beta C-term ASW and rSfp1 Delta ASW. The modulus (10 MPa), on the other hand, was similar to that of rSfp1 Delta ASW but much lower than that of rSfp1 Beta C-term ASW (**Figures 3K,L**).

As control, BSA ASW was also analyzed using Peak Force QNM mode and showed an adhesion of 100 pN and a modulus of 5 MPa (**Figures 3N,O**).

DISCUSSION

Adhesion in fluid and saline environments is an interesting and promising field as much for industry as for the medical and dental fields. Nowadays, biomimetic strategies are often employed to develop new adhesive materials (Almeida et al., 2020). Up to now, most studies have investigated the permanent adhesive mechanism of mussels and barnacles, but the temporary adhesion of sea stars has gained interest in recent years (Hennebert et al., 2014; Lengerer et al., 2019; Lefevre et al., 2020). In the study of biological adhesives, AFM was already used to determine the adhesion ability of natural glues but also of recombinant adhesive proteins. To the best of our knowledge,

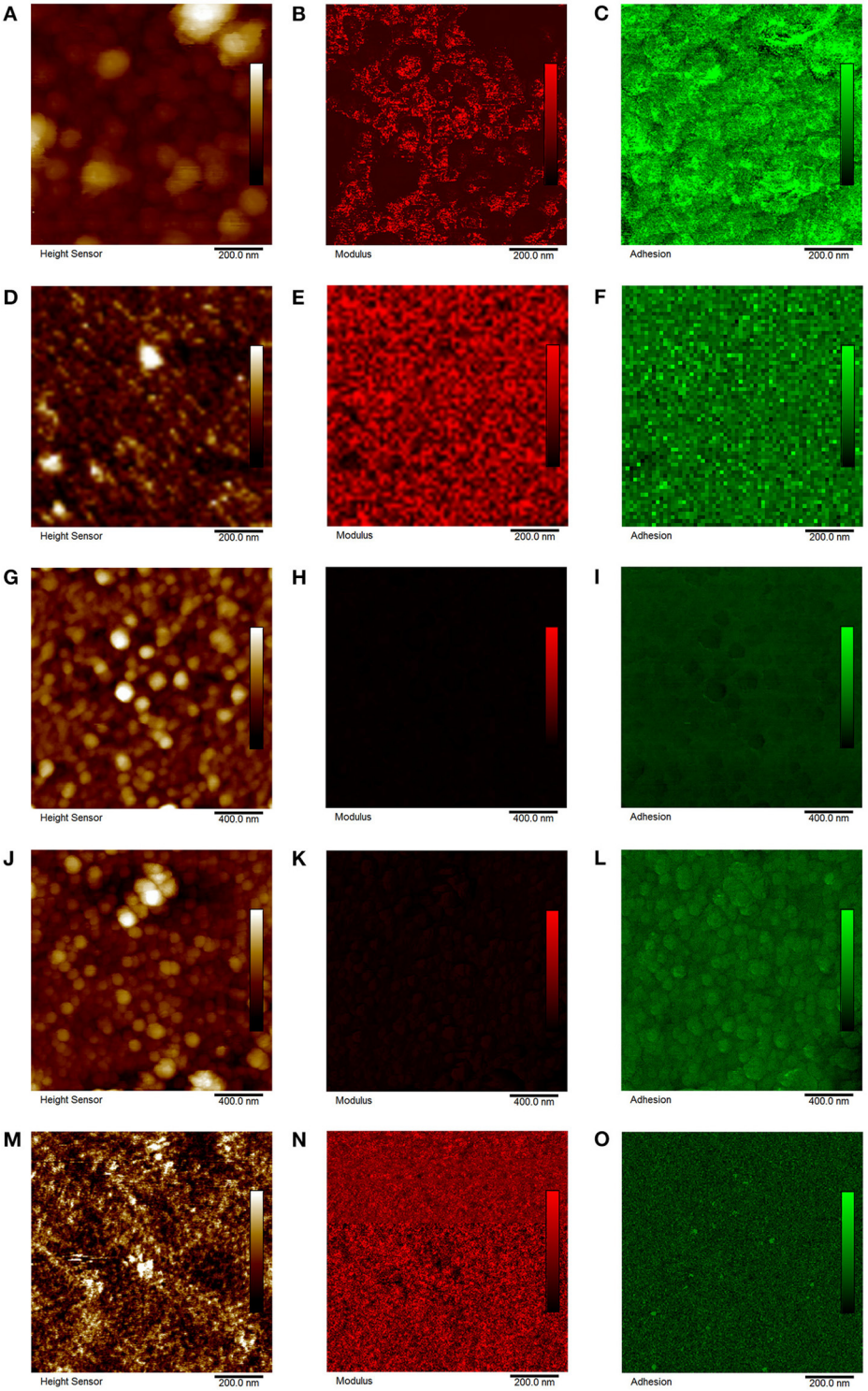

FIGURE 3 | Nanomechanical mapping of **(A–C)** rSfp1 Beta C-term 450 mM NaCl, **(D–F)** rSfp1 Delta ASW, **(G–I)** rSfp1 Delta 150 mM $CaCl_2$, **(J–L)** mix of rSfp1 Beta C-term and rSfp1 Delta ASW, **(N–P)** Bovine serum albumin ASW using Peak Force QNM mode in fluid (observations made in deionized water). **(A)** Height, scale: 200 nm, **(B)** Modulus, scale: 10 MPa, **(C)** Adhesion, scale: 500 pN, **(D)** Height, scale: 15 nm, **(E)** Modulus, scale: 10 MPa, **(F)** Adhesion, scale: 500 pN, **(G)** Height, scale: 70 nm, **(H)** Modulus, scale: 10 MPa, **(I)** Adhesion, scale: 500 pN, **(J)** Height, scale: 115 nm, **(K)** Modulus, scale: 10 MPa, **(L)** Adhesion, scale: 500 pN, **(M)** Height, scale: 2.5 nm, **(N)** Modulus, scale: 10 MPa, and **(O)** Adhesion, scale: 500 pN.

TABLE 2 | Peak Force Quantitative Nanomechanical Property Mapping (PF-QNM) and nanoscale dynamic mechanical analysis (nDMA) of rSfp1 coatings.

	PF-QNM		nDMA				
	Adhesion (pN)	JKR modulus (MPa)	Adhesion (pN)	JKR modulus (MPa)	Storage modulus (MPa)	Loss modulus (MPa)	Tan δ (mU)
rSfp1 Beta C-term ASW	90 ± 20	300 ± 50	300 ± 100	300 ± 45	40 ± 10	20 ± 7.5	500 ± 50
rSfp1 Beta C-term 450 mM NaCl	200 ± 75	500 ± 100	–	–	–	–	–
rSfp1 Delta ASW	150 ± 50	5 ± 1	–	–	–	–	–
rSfp1 Delta 150 mM $CaCl_2$	80 ± 20	0.5 ± 0.05	–	–	–	–	–
Mix of rSfp1 Beta C-term and rSfp1 Delta ASW	70 ± 20	10 ± 2	–	–	–	–	–
BSA ASW	100 ± 25	5 ± 1	–	–	–	–	–

the combination of PF-QNM and AFM-nDMA modes has never been applied before to investigate the nanomechanical properties of coatings composed of recombinant adhesives proteins.

In this study, coatings formed by recombinant proteins based on the sequence of the adhesive protein Sfp1 from the sea star *Asterias rubens* were investigated. The nanomechanical properties of films made up of rSfp1 proteins were previously unknown. Two proteins (rSfp1 Beta C-term and rSfp1 delta) were used separately or in combination, and coatings were made in different solutions (ASW, NaCl, and $CaCl_2$). Using PF-QNM, the adhesion of the coatings measured in deionized water ranged from 70 to 200 pN and their modulus from 0.5 to 300 MPa. Coatings consisting of rSfp1 Beta C-term were stiffer and more adhesive than those made up of rSfp1 Delta. When the two proteins were mixed, the properties of the resulting coatings were closer to those of films made of rSfp1 Delta alone. For the control protein, BSA, these values were 100 pN and 5 MPa, respectively. The moduli of some protein-based materials are know, such as elastin in which the Young's modulus is about 0.6 MPa (Fung and Sobin, 1981), or collagen fibers for which it is 1 GPa (Hiltner et al., 1985). rSfp1 proteins are certainly on the soft side of this range. Their adhesivity, on the other hand, is in the same order of magnitude than that of the negative control BSA. These results could be explained by the cohesive function of Sfp1 in the native adhesive. Indeed, Sfp1 is located in the meshwork of the adhesive footprint and not in direct contact with the surface (Hennebert et al., 2014).

The effect of hydration of human serum abumin (HSA) proteins layer have been studied in Lubarsky et al. (2007). They showed that the thickness and layer density of HSA layer increased when water is adsorbed but also that the viscosity and the modulus were higher for the dry layer. These values were similar to those obtained for rSfp1, with a range of 500 kPa to 2.5 GPa in dry conditions.

To quantify the adhesion ability of mussel recombinant proteins, Hwang et al. used another method. Indeed, the analysis of the adhesion force of recombinant Mgfp-5, Mgfp-3A and a recombinant hybrid mussel bioadhesive fp-151 was performed via force-distance curves using a modified AFM cantilever (Hwang et al., 2004, 2005, 2007). A glass sphere with a radius of 20 μm was fixed to the cantilever tip with epoxy resin and this modified tip was placed in contact with sample solutions for a determined time. The force-distance curve was obtained by separation of the coated cantilever from the glass surface. BSA was also used as a negative control, and commercial Cell-Tak was used as a positive control. These AFM measurements showed that the average adhesion force of tyrosine modified Mgfp-3A (∼230 nN) was much higher that that of modified BSA (∼30 nN), similar to that of modified Cell-Tak (∼240 nN), and lower than that of modified recombinant Mgfp-5 (∼550 nN) and hybrid fp-151 (∼500 nN). All of these values are significantly higher than those obtained in the present study for recombinant Sfp1 proteins. This difference could be explained by the much larger contact area used in the case of recombinant mussel proteins. The advantage of using PeakForce QNM, in our case, is the ability to measure variations in adhesion and elasticity on a same protein coating at a smaller scale based on controled contact geometry. Indeed, both PeakForce QNM and the more general "force-volume" imaging involve acquiring topographic images and nanomechanical mapping simultaneously, allowing identification of elastic properties and pull-off force values with specific regions of a sample (Grierson et al., 2005).

For a soft protein coating, it is also important to measure visco-elastic properties. The visco-elastic behavior of reversible adhesives was particulary studied for the fracture or peeling of soft materials to understand how these soft materials and their visco-elastic properties affected their breakage and detachment from solid surfaces (Creton and Ciccotti, 2016; Perrin et al., 2019). In addition to the mapping of nanomechical properties by PF-QNM, the analysis of one sample by fast force volume in AFM-nDMA mode allowed to measure the visco-elastic properties determined by storage modulus, loss modulus and tan δ. The values of adhesion and JKR modulus obtained for the rSfp1 Beta C-term coating preparted in ASW were similar to those obtained with PF-QNM though slightly higher. The value measured for tan δ was 0.2, corresponding to a soft and visco-elastic material. As described in Lakes (2009), tan δ values between 10^{-1} and 10^{0} correspond to rubber, foam rubber, gels but also polymers.

In conclusion, we were able to successfully characterize the mechanical properties as well as the visco-elastic properties of soft coatings formed by recombinant adhesives proteins from marine organisms. The combination of PF-QNM and

AFM-nDMA techniques should be used for other marine adhesive systems or polymers to understand the impact of visco-elasticity in the adhesive abilities of bio-inspired materials. Futhermore, in next step, the analysis of visco-elastic properties should be performed, for each recombinant proteins, at different drive frequencies. Indeed, the elastic properties are expected to depend on frequency and temperature (Pittenger et al., 2019). The measurement of these properties at lower frequency could improve our knowledge about the mechanical properties of rSfp1.

DATA AVAILABILITY STATEMENT

The raw data supporting the conclusions of this article will be made available by the authors, without undue reservation.

AUTHOR CONTRIBUTIONS

ML, EH, PF, and PL designed the study and wrote the paper. ML and TQT performed the experiments. TD designed the Python code for the unsupervised clustering analysis. BP provided advice regarding AFM nanomechanics and suggestions regarding strategy for analysis. All authors revised and approved the final manuscript.

FUNDING

This research was supported by the ARC project PROTEST (Production and testing of recombinant sea star adhesive proteins; Communauté française de Belgique—Actions de Recherche Concertées, ARC-17/21 UMONS 3), by the ARC project MecaRiboSynth (ARC N° ARC-19/23 UMONS4), by the Fund for Scientific Research of Belgium (F.R.S.-FNRS) under grant Projet de Recherche n °T.0088.20, and by the European Cooperation in Science and Technology (COST) Action CA15216 (STSM n°36,087 and 41,592). PF and PL are Research Directors of the F.R.S.- FNRS (Belgium).

SUPPLEMENTARY MATERIAL

The Supplementary Material for this article can be found online at: https://www.frontiersin.org/articles/10.3389/fmech.2021.667491/full#supplementary-material

REFERENCES

Almeida, M., Reis, R. L., and Silva, T. H. (2020). Marine invertebrates are a source of bioadhesives with biomimetic interest. *Mater. Sci. Eng. C. Mater. Biol. Appl.* 108:110467. doi: 10.1016/j.msec.2019.110467

Annabi, N., Tamayol, A., Shin, S. R., Ghaemmaghami, A. M., Peppas, N. A., and Khademhosseini, A. (2014). Surgical materials: current challenges and nano-enabled solutions. *Nano Today* 9, 574–589. doi: 10.1016/j.nantod.2014.09.006

Becker, P. T., Lambert, A., Lejeune, A., Lanterbecq, D., and Flammang, P. (2012). Identification, characterization, and expression levels of putative adhesive proteins from the tube-dwelling polychaete *Sabellaria alveolata*. *Biol. Bull.* 223, 217–225. doi: 10.1086/BBLv223n2p217

Berquand, A., Meunier, M., Thevenard-Devy, J., Ivaldi, C., Campion, O., Dedieu, S., et al. (2019). A gentle approach to investigate the influence of LRP-1 silencing on the migratory behavior of breast cancer cells by atomic force microscopy and dynamic cell studies. *Nanomed. Nanotechnol. Biol. Med.* 18, 359–370.

Cha, H. J., Hwang, D. S., Lim, S., White, J. D., Matos-Perez, C. R., and Wilker, J. J. (2009). Bulk adhesive strength of recombinant hybrid mussel adhesive protein. *Biofouling* 25, 99–107. doi: 10.1080/08927010802563108

Choi, Y. S., Yang, Y. J., Yang, B., and Cha, H. J. (2012). *In vivo* modification of tyrosine residues in recombinant mussel adhesive protein by tyrosinase co-expression in Escherichia coli. *Microb. Cell Fact* 11:139. doi: 10.1186/1475-2859-11-139

Creton, C., and Ciccotti, M. (2016). Fracture and adhesion of soft materials: a review. *Rep. Prog. Phys.* 79:046601. doi: 10.1088/0034-4885/79/4/046601

Duarte, A. P., Coelho, J. F., Bordado, J. C., Cidade, M. T., and Gil, M. H. (2012). Surgical adhesives: systematic review of the main types and development forecast. *Prog. Polym. Sci.* 37, 1031–1050. doi: 10.1016/j.progpolymsci.2011.12.003

Efremov, Y. M., Kotova, S. L., Akovantseva, A. A., and Timashev, P. S. (2020). Nanomechanical properties of enucleated cells: contribution of the nucleus to the passive cell mechanics. *J. Nanobiotechnol.* 18:134. doi: 10.1186/s12951-020-00696-1

Fung, Y. C., and Sobin, S. S. (1981). The retained elasticity of elastin under fixation agents. *J. Biomech. Eng.* 103, 121–122. doi: 10.1115/1.3138255

Grierson, D. S., Flater, E. E., and Carpick, R. W. (2005). Accounting for the JKR–DMT transition in adhesion and friction measurements with atomic force microscopy. *J. Adhes. Sci. Technol.* 19, 291–311. doi: 10.1163/1568561054352685

Heinzmann, C., Weder, C., and de Espinosa, L. M. (2016). Supramolecular polymer adhesives: advanced materials inspired by nature. *Chem. Soc. Rev.* 45, 342–358. doi: 10.1039/C5CS00477B

Hennebert, E., Wattiez, R., Demeuldre, M., Ladurner, P., Hwang, D. S., Waite, J. H., et al. (2014). Sea star tenacity mediated by a protein that fragments, then aggregates. *Proc. Natl. Acad. Sci. U.S.A.* 111, 6317–6322. doi: 10.1073/pnas.1400089111

Hiltner, A., Cassidy, J. J., and Baer, E. (1985). Mechanical properties of biological polymers. *Annu. Rev. Mater. Sci.* 15, 455–482. doi: 10.1146/annurev.ms.15.080185.002323

Hwang, D. S., Gim, Y., and Cha, H. J. (2005). Expression of functional recombinant mussel adhesive protein type 3A in *Escherichia coli*. *Biotechnol Progress* 21, 965–970. doi: 10.1021/bp050014e

Hwang, D. S., Gim, Y., Yoo, H. J., and Cha, H. J. (2007). Practical recombinant hybrid mussel bioadhesive fp-151. *Biomaterials* 28, 3560–3568. doi: 10.1016/j.biomaterials.2007.04.039

Hwang, D. S., Yoo, H. J., Jun, J. H., Moon, W. K., and Cha, H. J. (2004). Expression of functional recombinant mussel adhesive protein Mgfp-5 in *Escherichia coli*. *Appl. Environ. Microbiol.* 70, 3352–3359. doi: 10.1128/AEM.70.6.3352-3359.2004

Johnson, K. L., and Greenwood, J. A. (1997). An adhesion map for the contact of elastic spheres. *J. Colloid. Interface Sci.* 192, 326–333. doi: 10.1006/jcis.1997.4984

Johnson, K. L., Kendall, K., Roberts, A. D., and Tabor, D. (1971). Surface energy and the contact of elastic solids. *Proc. R. Soc. Lond. A. Math. Phys. Sci.* 324, 301–313. doi: 10.1098/rspa.1971.0141

Kord Forooshani, P., and Lee, B. P. (2017). Recent approaches in designing bioadhesive materials inspired by mussel adhesive protein. *J. Polym. Sci. Part A: Polym. Chem.* 55, 9–33. doi: 10.1002/pola.28368

Lakes, R. (2009). *Viscoelastic Materials*. Cambridge: Cambridge University Press.

Lefevre, M., Flammang, P., Aranko, A. S., Linder, M. B., Scheibel, T., Humenik, M., et al. (2020). Sea star-inspired recombinant adhesive proteins self-assemble and adsorb on surfaces in aqueous environments to form cytocompatible coatings. *Acta Biomater.* 112, 62–74. doi: 10.1016/j.actbio.2020.05.036

Lengerer, B., Algrain, M., Lefevre, M., Delroisse, J., Hennebert, E., and Flammang, P. (2019). Interspecies comparison of sea star adhesive proteins. *Phil. Trans. R. Soc. B.* 374:20190195. doi: 10.1098/rstb.2019.0195

Liang, C., Li, Y., Liu, Z., Wu, W., and Hu, B. (2015). Protein aggregation formed by recombinant cp19k homologue of balanus albicostatus combined with

an 18 kDa N-terminus encoded by pET-32a(+) plasmid having adhesion strength comparable to several commercial glues. *PLoS ONE* 10:e0136493. doi: 10.1371/journal.pone.0136493

Liang, C., Strickland, J., Ye, Z., Wu, W., Hu, B., and Rittschof, D. (2019). Biochemistry of barnacle adhesion: an updated review. *Front. Mar. Sci.* 6:565. doi: 10.3389/fmars.2019.00565

Liang, C., Ye, Z., Xue, B., Zeng, L., Wu, W., Zhong, C., et al. (2018). Self-assembled nanofibers for strong underwater adhesion: the trick of barnacles. *ACS Appl. Mater. Interfaces* 10, 25017–25025. doi: 10.1021/acsami.8b04752

Lubarsky, G. V., Davidson, M. R., and Bradley, R. H. (2007). Hydration–dehydration of adsorbed protein films studied by AFM and QCM-D. *Biosens Bioelectron* 22, 1275–1281. doi: 10.1016/j.bios.2006.05.024

MacQueen, J. (1967). "Some methods for classification and analysis of multivariate observations." in *Fifth Berkeley Symposium on Mathematical Statistics and Probability* (Berkeley, CA: University of California Press), 281–297.

Noy, A. (2006). Chemical force microscopy of chemical and biological interactions. *Surf. Interface Anal.* 38, 1429–1441. doi: 10.1002/sia.2374

Perrin, H., Eddi, A., Karpitschka, S., Snoeijer, J. H., and Andreotti, B. (2019). Peeling an elastic film from a soft viscoelastic adhesive: experiments and scaling laws. *Soft Matter.* 15, 770–778. doi: 10.1039/C8SM01946K

Pittenger, B., Erina, N., and Su, C. (2010). *Quantitative Mechanical Property Mapping at the Nanoscale with PeakForce QNM*. Santa Barbara, CA: Bruker Application Note.

Pittenger, B., Osechinskiy, S., Yablon, D., and Mueller, T. (2019). Nanoscale DMA with the atomic force microscope: a new method for measuring viscoelastic properties of nanostructured polymer materials. *JOM* 71, 3390–3398. doi: 10.1007/s11837-019-03698-z

Szulgit, G. K., and Shadwick, R. E. (2000). Dynamic mechanical characterization of a mutable collagenous tissue: response of sea cucumber dermis to cell lysis and dermal extracts. *J. Exp. Biol.* 203:1539.

Waite, J. H. (2017). Mussel adhesion – essential footwork. *J. Exp. Biol.* 220, 517–530. doi: 10.1242/jeb.134056

Wunderer, J., Lengerer, B., Pjeta, R., Bertemes, P., Kremser, L., Lindner, H., et al. (2019). A mechanism for temporary bioadhesion. *Proc. Natl. Acad. Sci. U.S.A.* 116, 4297–4306. doi: 10.1073/pnas.1814230116

Conflict of Interest: BP was employed by Bruker, a supplier of atomic force microscopes and probes, and developer of AFM-nDMA and PeakForce QNM.

The remaining authors declare that the research was conducted in the absence of any commercial or financial relationships that could be construed as a potential conflict of interest.

frontiers in Mechanical Engineering

ORIGINAL RESEARCH
published: 24 May 2021
doi: 10.3389/fmech.2021.681120

Multi-Technique Investigation of a Biomimetic Insect Tarsal Adhesive Fluid

J. Elliott Fowler[1], *Stanislav Gorb*[2] *and Joe E. Baio*[1]*

[1] The School of Chemical, Biological and Environmental Engineering Department, Oregon State University, Corvallis, OR, United States, [2] Department of Functional Morphology and Biomechanics, Zoological Institute of the University of Kiel, Kiel, Germany

There is substantial motivation to develop novel adhesives which take advantage of the superior adhesive strength and adaptability of many natural animal adhesives; however, the tools typically used to study these mechanisms are incapable of determining the precise interactions of molecules at an adhesive interface. In this study, a surface specific, order sensitive vibrational spectroscopy called sum frequency generation (SFG) is, for the first time, combined with multiple bulk characterization techniques to examine a novel, simple biomimetic adhesive fluid inspired by tarsal fluid of insects. Insects perform complex adhesive demands, including sticking, climbing vertically and running upside-down with little difficulty. Thus, we hypothesize that both bulk and surface specific properties of the fluid contribute to the success of this wet adhesive mechanism. SFG spectra of biomimetic emulsion exhibited similar hydrocarbon organization on hydrophobic and hydrophilic substrates to natural beetle fluid previously studied with the same method. Bulk characterization techniques indicated that the emulsion had a shear-thinning profile with the ability to enhance traction forces during climbing and low surface tension ideal for surface wetting on the majority of natural surfaces. Multi-technique comparisons between emulsion and pure squalane revealed that a hydrocarbon only based fluid could not replicate the traction promoting properties of the emulsion. We conclude that the insect tarsal fluid adhesive mechanism relies upon contributions from both surface-specific properties optimizing traction force and bulk properties promoting rapid surface wetting and maintaining pull-off force for fast detachment.

Keywords: bioadhesion, biomimetic, surface analysis, vibrational spectroscopy, insect adhesion

OPEN ACCESS

Edited by:
Yu Tian,
Tsinghua University, China

Reviewed by:
Ivan Argatov,
Technical University of Berlin, Germany
Feodor M. Borodich,
Cardiff University, United Kingdom

***Correspondence:**
Joe E. Baio
joe.baio@oregonstate.edu

Specialty section:
This article was submitted to Tribology, a section of the journal Frontiers in Mechanical Engineering

Received: *15 March 2021*
Accepted: *27 April 2021*
Published: *24 May 2021*

Citation:
Fowler JE, Gorb S and Baio JE (2021) Multi-Technique Investigation of a Biomimetic Insect Tarsal Adhesive Fluid. Front. Mech. Eng. 7:681120. doi: 10.3389/fmech.2021.681120

INTRODUCTION

Within biological evolution, numerous adhesive systems developed for millions of years. The inspiration from studies of one type of such systems, insect tarsal adhesion, has led to improvements in materials design, such as reversibly-adhering sticky tapes and climbing robots (Gorb et al., 2007; Daltorio et al., 2009). These improvements have been mainly focused on mimicry of the details of the physical structure of insect feet. However, this system additionally contains a fluid secreted from insect pads which mediates contact between foot and surface (Walker, 1993; Dirks and Federle, 2011). Many previous studies have shown that this fluid is vital to the ability of insects to walk and

climb without slipping and sliding on various natural and artificial surfaces (Gorb, 2001; Gorb and Gorb, 2002, 2009; Langer et al., 2004; Gorb et al., 2008, 2010; Busshardt et al., 2012; Hosoda and Gorb, 2012; England et al., 2016). However, a consensus explanation for precisely how this fluid aids both strong adhesion and rapid release does not currently exist (Gilet et al., 2018).

The composition of the tarsal fluid in various insect species has been analyzed directly, using techniques, such as mass spectrometry, and indirectly by assessing its interaction with various chemicals and surfaces (Geiselhardt et al., 2009, 2010, 2011; Gorb et al., 2010; Peisker and Gorb, 2012; Heepe et al., 2016). Mass spectrometry results have concluded that insect adhesive fluid consists of a mixture of branched and unbranched, long and short chain hydrocarbons, fatty acids, sugars, and alcohols (Vötsch et al., 2002; Geiselhardt et al., 2011). Microscopy data suggests insect adhesive fluids to be oil-in-water emulsions. Indeed, this would be an ideal contacting fluid for its ability to spread easily on a wide range of substrates (Peisker et al., 2014). Manipulations of the tarsal fluid of the Colorado Potato Beetle (*Leptinotarsa decemlineata)*, as well as traction force experiments of Seven-Spotted Ladybird Beetles (*Coccinella septempunctata*) on nanoporous substrates, showed that removal of just part of the fluid significantly diminished their adhesive forces (Geiselhardt et al., 2010; Gorb et al., 2010). Additionally, studies have consistently demonstrated that there was a complex relationship between the chemistry of insect adhesive fluid and the chemistry of the contacting surface (Federle et al., 2002; Dirks and Federle, 2011; England et al., 2016).

Recently, natural *C. septempunctata* fluid was studied with sum frequency generation (SFG) spectroscopy—a surface specific, order sensitive vibrational spectroscopy—on surfaces with a range of wettabilities, to determine what molecular groups were surface active and ordered at the interface. It was hypothesized that interfacial chemistry and molecular order were dynamic; however, it was instead found that interfacial fluid consisted of ordered hydrocarbons regardless of substrate hydrophilicity. It was concluded that the hydrocarbons were a mixture of branched and unbranched alkanes which were more highly ordered at hydrophobic interfaces, decreasing traction force of the beetles, thus enhancing lubrication. Nevertheless, this study did not reveal a clear mechanism that solely explained the functional mechanism of the beetle tarsal fluid adhesion.

Therefore, in this study we designed a biomimetic insect adhesive fluid with the distinct aim of deducing the mechanism that enabled natural insect tarsal fluid to generate necessary adhesive forces. We hypothesized that the fluid must take advantage of both surface and bulk properties to maximize traction force while generating appropriate pull-off force. Thus, we believed that both the surface active and surface-inactive components of the emulsion played an important role in the insect tarsal adhesive mechanism.

A simple, three-component biomimetic adhesive emulsion was formulated from squalane, deuterated stearic acid and D_2O, chosen such that each component contained distinct chemical bonds which could be probed at the fluid-substrate interface. This emulsion was initially characterized with dynamic light scattering, surface tensiometry and rheology. SFG spectroscopy was then used to probe C-H, O-D, C-D and C=O vibrations at the interface between the biomimetic fluid and two surfaces—hydrophobic polystyrene and hydrophilic polyethylene oxide—to determine the effect of substrate chemistry on organization of surface active fluid molecules. The fluid was then iteratively deconstructed to determine the influence of the surface-inactive components on the organization of the surface-active layers of the fluid.

MATERIALS AND METHODS

Emulsion Formulation

Ten mL of squalane (96% purity, Sigma Aldrich, St. Louis, MO) was added to a scintillation vial cleaned by rinsing with ethanol and heated to 70°C. A 1 mM deuterated stearic acid in squalane solution was made by adding 3.2 mg of stearic-d_{35} acid (98 atom% d, Sigma Aldrich) and mixing with a magnetic stir-bar at 1,000 rpm. Finally, 0.5 mL of D_2O was added dropwise and allowed to mix for 3 min. Emulsions were formed by ultrasonication at 60°C for 2 min. All experiments were performed with freshly made emulsion.

Rheological and Tribological Characterization of Fluids

The rheological behavior of the formulated emulsion, as well as pure squalane, was determined using a DHR3 Rheometer (TA Instruments, New Castle, DE) in cone-and-plate geometry with a 60 mm, 1.01°, titanium Peltier plate. Flow sweeps were performed at 25°C by measuring the viscosity and shear stress of the fluids while varying the shear rate from 1×10^{-3} to 1,000 s^{-1}. Pull-off force measurements were performed in plate-plate geometry with a 20 mm, titanium plate and an initial gap size of 300 μm. The gap was filled with either emulsion or squalane and the axial force was zeroed. The top plate was lifted at a rate of 300 μm/s and the minimum axial force measured was reported as the pull-off force.

Surface Tensiometry

The surface tension of the emulsion and precursor fluids was measured with an FTA-T10 tensiometer (First Ten Angstroms, Portsmouth, VA) using a Du Nouy Ring. The reported surface tension was the average of ten consecutive dipping cycles. Measurements began only after a consistent force per wetted length peak was achieved.

Substrate Preparation

Fifteen millimeter diameter CaF_2 optics (International Crystal Laboratories, Garfield, NJ) were cleaned via successive ultrasonication in dichloromethane, acetone and ethanol and spun-coat (Laurell Technologies, North Wales, PA) at 2,000 rpm for 60 s with 3 wt% solutions of one of the following: polyethylene oxide (PEO, MW = 100,000 Da) (Sigma Aldrich), polystyrene (PS, MW = 35,000 Da) (Sigma Aldrich), deuterated poly-ethylene oxide (dPEO, MW = 8,960 Da) (Polymer Source Inc., Montreal, CA) or deuterated polystyrene (dPS, MW = 7,420 Da) (Polymer Source Inc.) in toluene. Films were

then baked at 80°C for 20 h at 500 mtorr to remove excess solvent. We have previously shown that this produced optically transparent polymer films of ∼100 nm in thickness. Substrates were stored under N_2 atmosphere in sealed Petri dishes until use to prevent contamination.

Sum Frequency Generation Spectroscopy

An EKSPLA Nd:YAG laser, operating at 50 Hz, was used to generate both a fixed visible (532 nm^{-1}) and tunable IR beam (1,000–4,000 cm^{-1}) via sequential pumping through an EKSPLA optical parametric generation/amplification and difference frequency unit, which utilized barium borate and AgGaS2 crystals, respectively. The visible and IR beams (∼150 μJ/pulse) were overlapped spatially and temporally at the desired interface to generate SFG photons, which were spectrally filtered, dispersed by a monochromator and detected with a gated photomultiplier tube. Both beams were focused to a ∼1 mm diameter at the interface. Spectra were collected in 4 cm^{-1} steps with 400 acquisitions per step.

SFG spectra were generated at two different polarization combinations – ssp (s-polarized SFG, s-polarized visible, p-polarized IR) and ppp (p-polarized SFG, p-polarized visible, p-polarized IR) in four different vibrational regions (C-H – 2,800–3,100 cm^{-1}; D-O – 2,450–2,650 cm^{-1}; C=O – 1,600–1,800 cm^{-1}; C-D – 2,000–2,300 cm^{-1}) through the backside of a CaF2 window which rests on a Teflon o-ring (ID – 7.9 mm) attached to a flat, cylindrical Teflon platform. The void volume of the o-ring was filled with the sample fluid such that the fluid was in full contact with the top window surface at all times during the experiment. SFG signal is optimized in each wavenumber region using an Au-coated CaF_2 window in the same set-up. The fitting routine for SFG spectra is previously detailed elsewhere (Weidner et al., 2010; Baio et al., 2012, 2015; Weidner and Castner, 2013). Briefly, spectra were iteratively fit to the equation below (Equation 1) to determine non-resonant phase, non-resonant background (χ_{nr}), frequency (ω_q), individual peak full width half maximum (FWHM; Γ_q) and individual peak amplitude (A_q).

$$\chi_{eff}^{(2)} = \chi_{nr} + \sum_{q} \frac{A_q}{\omega_2 - \omega_q + i\Gamma_q} \quad (1)$$

RESULTS

Emulsion Characterization

From visual observation, the emulsion was stable over short periods of time (hours) but was susceptible to aggregation of the particle phase overnight. Particle aggregation was supported by dynamic light scattering measurements, which determined the mean particle size of the emulsion to be 8.0 μm with a polydispersity index of 0.4. This indicated a suspension on the borderline between a medium and broad distribution of particle sizes (Aragon and Pecora, 1976). Additionally, particles of various sizes were clearly visible in light microscope images of fresh emulsion (**Figure 1**).

Next, the surface tensions of emulsion as well as two control fluids, pure squalane and a 1 mM d-stearic acid in squalane solution, were determined (**Supplementary Table 1**). The surface tension of pure squalane was measured at 28.4 ± 0.1 mN/m, which was consistent with the reported literature value of 28 mN/m (Korosi and Kovats, 1981). The surface tension of the 1 mM d-stearic acid in squalane solution was lower at 27.1 ± 0.1 mM/m, which was expected due to the amphiphilic nature of stearic acid (Cho et al., 2018). Finally, the emulsion had a surface tension of 27.5 ± 0.1 mN/m. Overall, the surface tensions of all three fluids were consistent with the estimated surface tension of a hydrophobic secretion (∼30 mN/m) (Federle et al., 2004).

Rheometry experiments of both the emulsion and pure squalane revealed distinctly different viscosity profiles. Unsurprisingly, the viscosity of a film of pure squalane was constant (29 mPa*s) across a wide range of shear rates, which was consistent with the many previous analyses of the hydrocarbon as a low viscosity Newtonian fluid (Gupta et al., 1998). However, viscosity measurements taken from a film of emulsion provided a shear-thinning profile, with a very small yield stress of ∼0.01 Pa. Additionally, a plate-plate geometry was used to determine the pull-off adhesive strength of the two fluids. There was no difference in the tackiness of the emulsion compared to the hydrocarbon, with forces of 0.533 ± 0.009 and 0.527 ± 0.007, respectively (**Supplementary Table 2**).

SFG Spectroscopy

As previously mentioned, the composition of the emulsion was carefully selected to allow for isolation of representative molecular bonds from each component in separate vibrational regions, which were measured with SFG spectroscopy. This allowed for the determination of which components in the fluid were surface active. For example, the C-H stretching region (2,800–3,000 cm^{-1}) was used to measure ordered modes at the interface corresponding to squalane as the only source of methyl and methylene modes was that component of the emulsion. Likewise, the O-D stretching region (2,450–2,650 cm^{-1}) was used to observe D_2O at the interface, while the C-D (2,000–2,350 cm^{-1}) and C=O (1,650–1,800 cm^{-1}) regions were for observing d-stearic acid vibrational modes.

SFG spectra of emulsion at dPEO and dPS surfaces in SSP polarization combination at the C-H stretching region are shown in **Figure 2B**. Four vibrational modes were observed in both spectra: near 2,855, 2,880, 2,914, and 2,935 cm^{-1}, corresponding to CH_2 symmetric, CH_3 symmetric, CH_2 asymmetric, and CH_3 Fermi modes, respectively (Himmelhaus et al., 2000; Chen et al., 2003; Ma and Allen, 2006; Baio et al., 2015; Adams et al., 2017). All of these modes were also observed in SSP, C-H region spectra of the natural *C. septempunctata* fluid on the same substrates, except for the CH_2 asymmetric mode (**Figure 2A**). Spectra of the emulsion at the same surfaces in PPP polarization combination produced substantially different spectral profiles. Five total modes were observed in PPP spectra: near 2,864, 2,884, 2,900, 2,925, and 2,962 cm^{-1} corresponding to CH_2 symmetric, CH_3 symmetric, CH (tertiary), CH_2 asymmetric, and CH_3 asymmetric vibrational modes, respectively (**Supplementary Figure 1**). However, unlike in SSP combination, the same set of modes was not present across spectra of fluid on both surfaces, with the CH_2 and CH_3

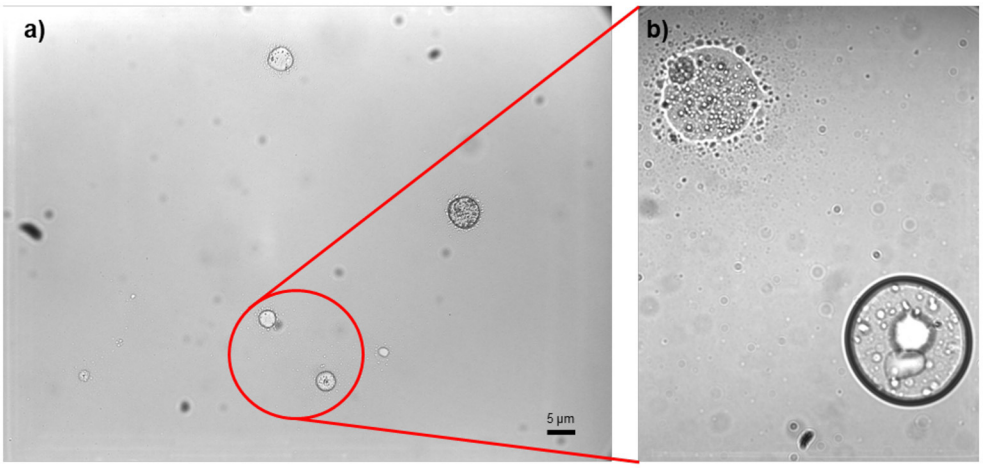

FIGURE 1 | Phase contrast light microscope image of the biomimetic emulsion at 10× **(a)** and 50× **(b)** magnifications. Insect feet fluids are usually emulsions at the nanoscale: one cannot see the second phase in optical microscope, only in an electron microscope (SEM, TEM) or in an atomic force microscope (AFM).

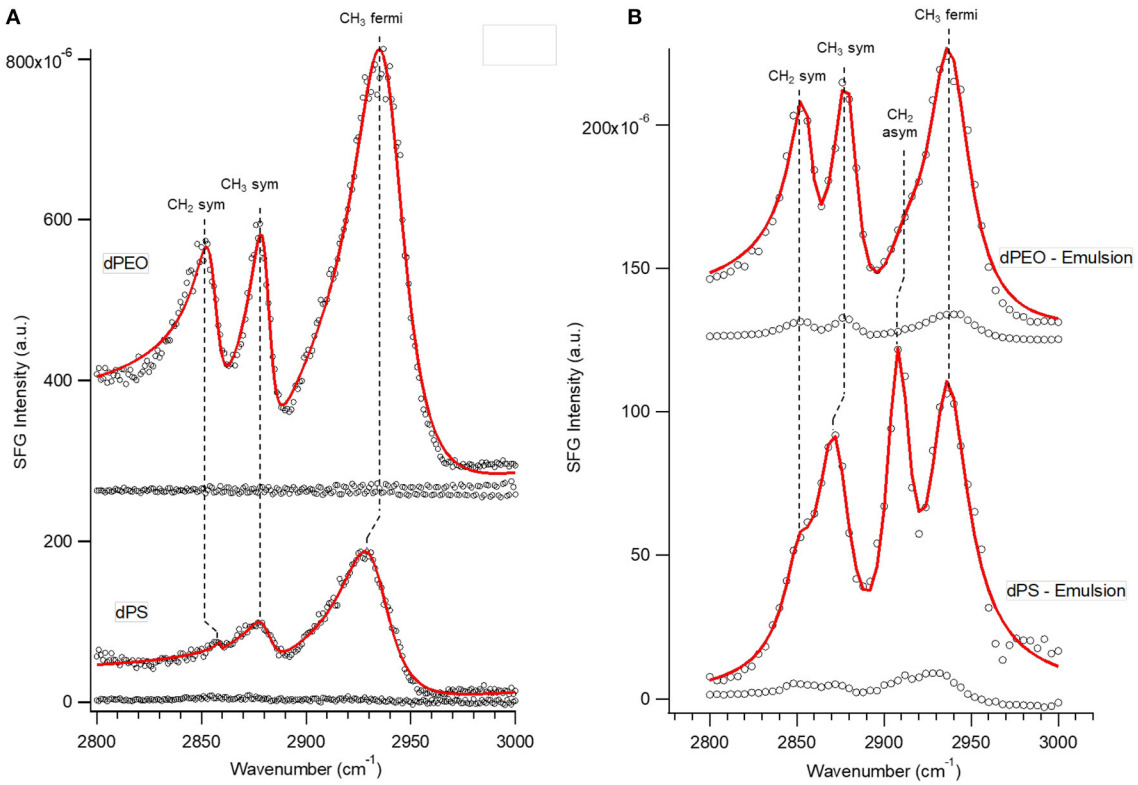

FIGURE 2 | SFG spectra in the C-H stretching region and SSP polarization combination of **(A)** natural beetle *Coccinella septempunctata* tarsal fluid on PEO and PS substrates and **(B)** biomimetic emulsion on PEO and PS substrates. Three vibrational modes were observed in all four spectra: near 2,855, 2,880, and 2,935 cm^{-1} corresponding to CH_2 symmetric, CH_3 symmetric, and CH_3 Fermi vibrational modes, respectively. One mode is unique to the biomimetic emulsion/substrate interfaces, the CH_2 asymmetric stretch near 2,914 cm^{-1}, likely due to different orientation of surface hydrocarbons between natural and biomimetic fluids. Relative SFG intensity of CH_3 and CH_2 symmetric modes and the change in this intensity as hydrophobicity is increased is similar between natural and biomimetic fluid interfaces.

symmetric and CH_2 asymmetric modes absent in the emulsion – dPS spectrum.

The relative ratio of CH_3 symmetric to CH_2 symmetric stretch amplitudes has been shown to be indicative of the relative organization of a layer of hydrocarbons, with larger values indicating a more uniform angle in relation to the surface (Casford et al., 2014; Adams et al., 2017). These values, and the trend between substrates, were similar for the same substrates in the natural and biomimetic fluid spectra, with values of 3.46 ± 0.40 and 1.03 ± 0.07 for the dPS and dPEO spectra of the natural fluid and 4.47 ± and 1.70 ± for spectra of the same surfaces with biomimetic fluid. However, there was one major difference between the C-H SSP spectra of the natural and biomimetic fluids – the presence of a peak corresponding to CH_2 asymmetric stretching near 2,914 cm^{-1} in the latter (**Figure 2B**). Previous SFG studies of alkane chains oriented toward the surface normal at solid/air and liquid/air interfaces have shown that the CH_2 asymmetric stretch has a substantially lower intensity in SSP compared to PPP or SPS polarization combinations. In this study, this trend was reversed, with stronger peak amplitude in SSP than PPP spectra. The mode amplitude was particularly strong at the hydrophobic surface – at which squalane would interact with more favorably. One explanation for this result is that squalane has been shown, via molecular dynamics (MD) simulations for squalane on hydrophilic silicon, to prefer a chain orientation parallel to solid surfaces with its methyl side chains arranged perpendicular from the chain (**Figure 3**) (Mo et al., 2005; Tsige and Patnaik, 2008). As mode amplitudes are sensitive to beam polarization as well as molecular bond orientation and order, it follows that a substantial rotation in chain angle could have led to the observed shifting in preference for the CH_2 asymmetric stretch from PPP to SSP polarization combination (Hirose et al., 1993). Thus, although organization of squalane chains at the emulsion interface was consistent with organization of hydrocarbons in natural adhesive fluid, the squalane layers were rotated perpendicularly from the natural fluid hydrocarbons. Lastly, spectra of the emulsion at non-deuterated substrates collected in the other three (O-D, C-D, C=O) stretching regions did not produce any SFG signal originating from either the D_2O or d-stearic acid molecules at either substrate (**Supplementary Figures 2**, **3**). This was consistent with characterizations of natural *C. septempunctata* fluid, in which hydrocarbons were shown to be the only surface-active component.

Next, spectra of pure squalane and a 1 mM d-stearic acid in squalane solution at PEO and PS surfaces were compared to emulsion spectra to determine whether surface-inactive components of the emulsion (d-stearic acid, D_2O) influenced the organization of the interfacially-active squalane molecules. While spectra were collected in all four regions (C-H, O-D, C-D, C=O), we only observed signal in C-H region spectra for each of the control fluids. The four modes previously identified in C-H SSP spectra were present in both control fluids spectra; however, an additional mode was observed near 2,868 cm^{-1} (**Figure 4**). Due to the wave number proximity of this mode to the CH_3 symmetric mode near 2,880 cm^{-1}, we attributed this mode to the resonance created by the dimethyl branching at either end of squalane molecules. Interestingly, it was only clearly observed in pure squalane spectra for both surfaces (Bellany, 1975). There were distinctly different trends in amplitude for the CH_2 symmetric, CH_3 symmetric and CH_2 asymmetric modes observed between the hydrophobic and hydrophilic surfaces and across the set of fluids. For example, the CH_2 asymmetric stretch amplitude decreased from emulsion to squalane/d-stearic acid to squalane only spectra at the PS surface (**Figure 3B**); however, at the PEO surface, the amplitude was initially negligible, increased for the squalane/d-stearic acid solution and was then negligible again for squalane (**Figure 3A**). Similarly, on the PS surface the CH_2 symmetric stretch was greater for the control fluids compared to the emulsion, but on the PEO surface the amplitude initially decreased for the squalane/d-stearic acid solution and then increased substantially for squalane only. Overall, the mode amplitude trends in this experiment showed that the removal of an amphiphilic molecule and D_2O led to apparent changes in the organization of interfacial squalane, although the specific changes were unique to the wettability of the contacting surface. However, on both surfaces the emulsion spectra exhibited greater organization of interfacial squalane layers than pure squalane.

DISCUSSION

To evaluate the role of secreted tarsal fluid in the adhesion of insects, several factors must be taken into account. For instance, an insect standing upright and still on a flat vertical substrate must generate sufficient contact with the surface, to prevent sliding down, but must not generate sufficiently strong adhesive force that can hamper its detachment from the surface to proceed with the locomotion. This compromise is solved by the specific geometry of the setae (Niederegger and Gorb, 2003; Gorb, 2011), but the corresponding contribution from the molecular organization of the fluid can be additionally expected. An optimal adhesive fluid must be able to handle transitioning from wet to dry, smooth to rough, hydrophobic to hydrophilic or upright to inclined or inverted without failure. Thus, an ideal insect tarsal adhesive fluid would utilize a mechanism which was inherently complex – no single characteristic of the fluid responsible for mitigating all of the aforementioned challenges singularly.

While there have been many attempts to ascertain this mechanism using biomechanical experiments, surface analytical approaches have been underutilized. Thus, this study used SFG showing the organization of molecules within the biomimetic emulsion at the surface of hydrophobic and hydrophilic substrates. As previously introduced, this technique was also recently used to probe natural *C. septempunctata* tarsal adhesive fluid and it was found that a layer of branched and unbranched hydrocarbons organized at all substrate surfaces with organization dependent upon substrate wettability. It has been shown that beetles exhibited significantly different traction forces depending upon the wettability of the contacting surface (Gorb et al., 2008; Gorb and Gorb, 2009). An inverse relationship existed between the ordering of a layer of hydrocarbons at the interface and the magnitude of traction force measured on similar surfaces. Thus, it was concluded that the fluid enhanced traction force on

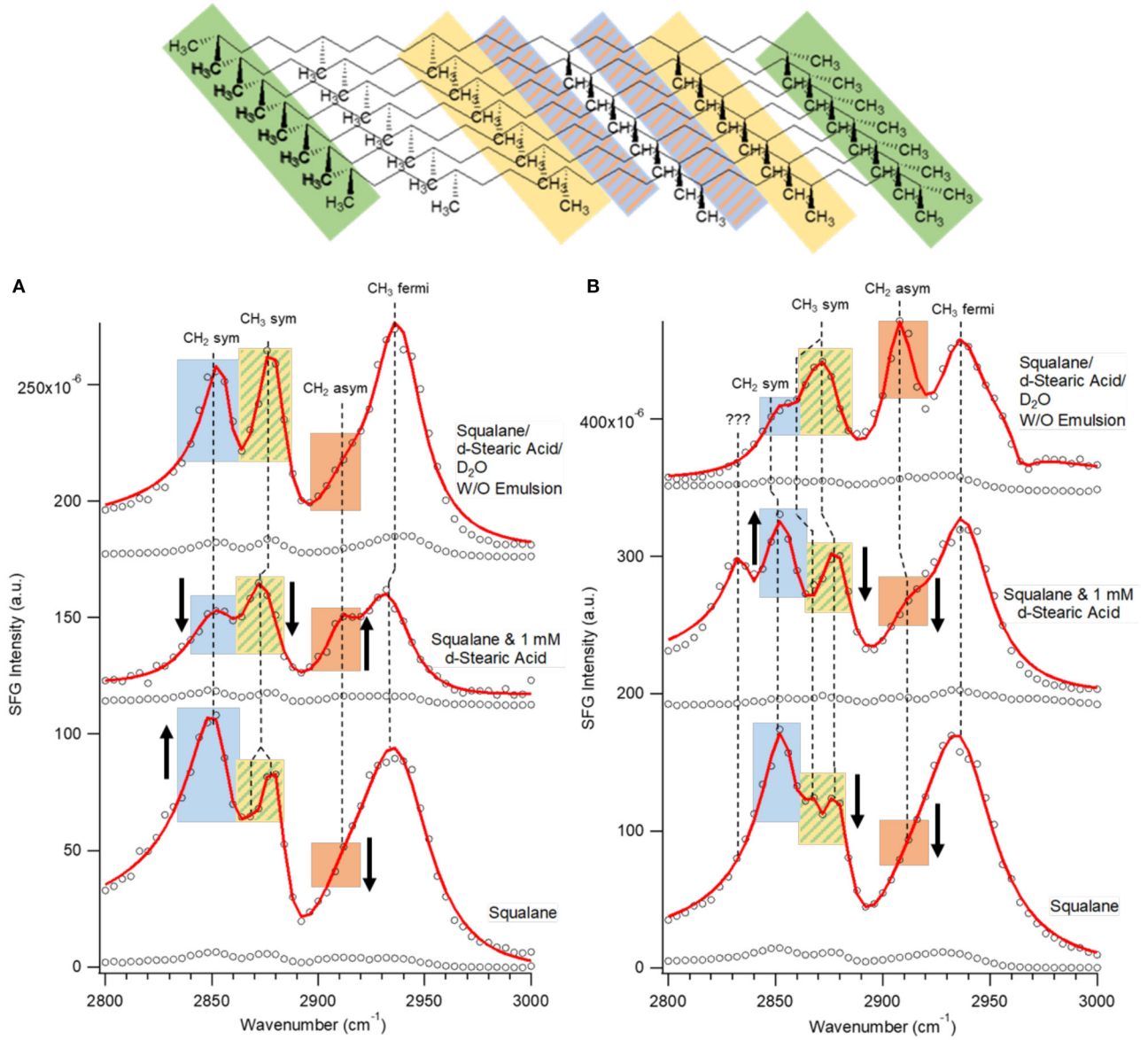

FIGURE 3 | SFG spectra of biomimetic emulsion and control fluids at PEO **(A)** and PS **(B)** surfaces in the C-H vibrational region and SSP polarization combination. Spectra and fits are represented by black circles and red dots, respectively. Five vibrational modes were observed in all of the spectra: near 2,855, 2,868, 2,880, 2,914, and 2,935 cm^{-1} corresponding to CH_2 symmetric, CH_3 symmetric, CH_2 asymmetric, and CH_3 Fermi vibrations, respectively. Colored bars indicate vibrational mode locations on a layer of squalane molecules present at the interface. Black arrows indicate relative change in mode amplitude from the same mode in the spectrum above it.

hydrophilic substrates, where an oily fluid would interact less strongly, and increased lubrication of hydrophobic substrates, where interactions would naturally be stronger.

Yet, limiting factors, such as the very small volume (pL) of fluid droplets and the certain volatility of some components of the fluid limited the ability to definitively conclude, whether chemical surface analytical results were representative of the complete mechanism (Peisker and Gorb, 2012). In this study, a biomimetic emulsion was created in quantities with which fluid volume and chemistry could be carefully controlled during SFG experiments. Resultant SFG spectra provided clear evidence that the hydrocarbon component, squalane, was the only substrate-active chemical in the emulsion. Additionally, the emulsion displayed very similar hydrocarbon chain organization (CH_3/CH_2 stretching ratios) to the natural *C. septempunctata* fluid (**Figure 2**). Both results supported the previous conclusion that a surface-active hydrocarbon component in beetle tarsal fluid was responsible for moderating traction and lubrication in response to changing environmental surface chemistry.

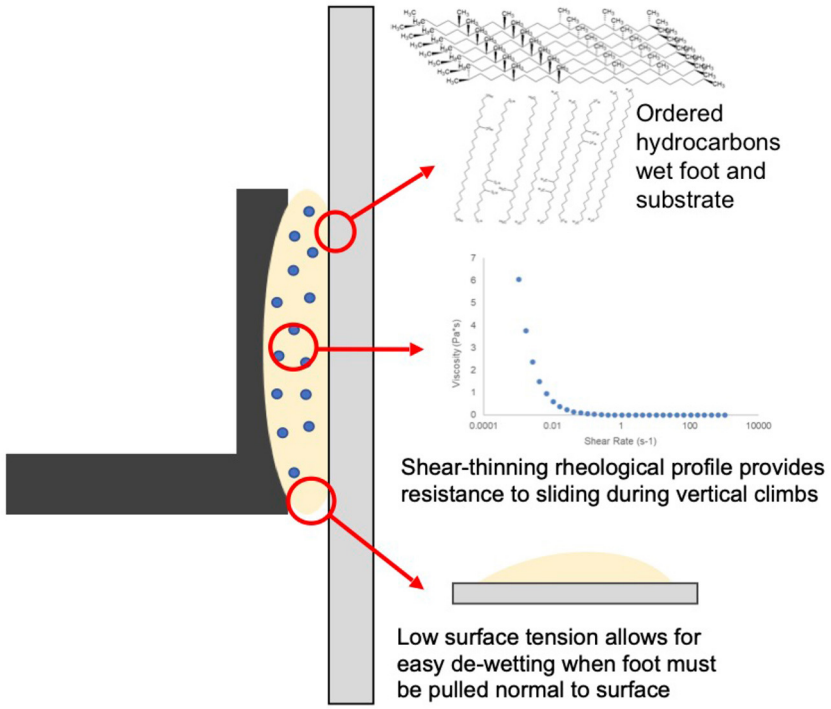

FIGURE 4 | The corresponding properties of natural and biomimetic insect tarsal adhesive fluid allowing fast attachment and detachment both essential for performing rapid locomotion.

However, rheological testing of the biomimetic fluid revealed an additional benefit of an emulsion in generation of traction force. The resistance of the vesicle phase against the bulk phase, when shear was applied, led to a shear-thinning non-Newtonian fluid with a small yield stress (**Supplementary Figure 4**) (Dirks et al., 2010). The higher viscosity exhibited by a fluid with this profile during events with very low or no shear rate, such as clinging on inclined surfaces or ceilings, would be ideal for slip prevention (Bullock et al., 2008; Dirks et al., 2010; Dirks and Federle, 2011). However, the shear rate applied by this system at average beetle walking speed (∼5 mm/s) and with a biomimetic fluid layer 100 nm thick (a conservative estimate of natural fluid thickness) (Gorb et al., 2012; Gilet et al., 2018) would be well above the rate necessary for the fluid to exhibit a constant, low viscosity like that of pure squalane (**Supplementary Figure 4**) (Thornham et al., 2008; Dirks and Federle, 2011). Thus, this fluid would provide a resistance to sliding without increasing the effort required to resume movement. Combined, a slip-resistant bulk structure and a lubricating surface layer sensitive to substrate chemistry indicated that the tarsal adhesive fluid mechanism is adapted to support the dynamic adhesion during locomotion (quick attachment and detachment).

It has been previously shown that some insect fluids may consist only of hydrocarbons (Gorb, 2001; Geiselhardt et al., 2010, 2011). Thus, it was necessary to determine whether a fluid consisting of only hydrocarbon molecules reasonably replicated the complete composition and adhesive properties of the biomimetic emulsion. Squalane, a low viscosity, low surface tension fluid has been shown to have low cohesive forces, which can be correlated to both easier filling of small asperities and faster de-wetting from a surface (Ludviksson and Lightfoot, 1971; Moore et al., 2000; Peisker et al., 2014). These properties would be desired for maximizing contact area and pull-off adhesive force. In fact, if the only consideration for adhesion was pull-off force and surface wetting, pure squalane may be considered an ideal mimic for beetle adhesive fluid. It generated the same pull-off force as the emulsion in this study while having a comparable surface tension (**Supplementary Figure 5** and **Supplementary Tables 1**, **2**).

However, we hypothesized that the shear force (often called traction or friction force in experimental studies on insects) is at least as important as these factors, if not more so (Labonte and Federle, 2015; Amador et al., 2017). Our comparison of the SFG spectra of emulsion vs. pure squalane on hydrophobic and hydrophilic substrates revealed clear differences in the organization of squalane layers between the two fluids on each substrate (**Figure 3**). Most importantly, the contrast in ordering ratio observed in both the emulsion and natural *C. septempunctata* fluid spectra were not present between the squalane spectra on each substrate. This should lead to the absence of the difference in traction force between the hydrophobic and hydrophilic substrates. However, this is inconsistent with biomechanical results obtained with living beetles. Thus, the emulsion was the only fluid which combined the low surface tension spreading advantages to control pull off force and the dynamic organizational response to substrate

hydrophobicity to optimize traction force. Furthermore, we have demonstrated that the surface inactive components of the biomimetic tarsal adhesive fluid—the water and stearic acid emulsion phase—clearly influence the organization of the surface active squalane layers and by extension the adhesive properties of the fluid.

CONCLUSIONS

Our previous experiments on natural beetle adhesive fluid (Fowler et al., 2021) and on the biomimetic fluid presented in this paper have shown that the interfacial interactions between the fluid and substrate are an important component of the foot adhesive mechanism, ensuring wetting during movement across the substrate surface as well as maintaining sufficient surface contact via low surface tension. However, chemistry of the bulk, surface-inactive fluid played an equally important role by bestowing a shear-thinning profile to the fluid and regulating the magnitude of traction forces generated by influencing order of the interfacial components.

An immediate application of biomimetic beetle tarsal adhesive is in the development of climbing robots, as the fluid resists shear well while generating relatively small pull-off forces. This would minimize the necessary energy input for successive climbs. However, additional work is still needed to improve the stability the oil-in-water emulsion. In this study, composition was limited to naturally occurring chemicals with very specific molecular bonds so that each chemical could be tracked. Future formulations may explore surfactants which have stronger affinities for water to prevent aggregation of vesicles above micron sizes. Regardless, herein we have shown that a combination of surface specific and bulk analytical techniques as well as work on artificial fluid systems inspired by biological ones can be used to understand details of a complex adhesive mechanisms developed by nature.

DATA AVAILABILITY STATEMENT

The raw data supporting the conclusions of this article will be made available by the authors, without undue reservation.

AUTHOR CONTRIBUTIONS

JEF, JEB, and SG: conceptualization. JEB and SG: supervision. JEF: investigation and writing—original draft preparation. JEF and JEB: methodology. JEB and SG: writing—review and editing.

FUNDING

This work was partially supported by German Science Foundation (DFG Grant GO 995/34-1 to SG) within Special Priority Program Soft Material Robotic Systems.

SUPPLEMENTARY MATERIAL

The Supplementary Material for this article can be found online at: https://www.frontiersin.org/articles/10.3389/fmech.2021.681120/full#supplementary-material

REFERENCES

Adams, E. M., Champagne, A. M., Williams, J. B., and Allen, H. C. (2017). Interfacial properties of avian stratum corneum monolayers investigated by Brewster angle microscopy and vibrational sum frequency generation. *Chem. Phys. Lipids* 208, 1–9. doi: 10.1016/j.chemphyslip.2017.08.002

Amador, G. J., Endlein, T., and Sitti, M. (2017). Soiled adhesive pads shear clean by slipping: a robust self-cleaning mechanism in climbing beetles. *J. R. Soc. Interface* 14:20170134. doi: 10.1098/rsif.2017.0134

Aragon, S., and Pecora, R. (1976). Theory of dynamic light scattering from polydisperse systems. *J. Chem. Phys.* 64, 2395–2404. doi: 10.1063/1.432528

Baio, J. E., Spinner, M., Jaye, C., Fischer, D. A., Gorb, S. N., and Weidner, T. (2015). Evidence of a molecular boundary lubricant at snakeskin surfaces. *J. R. Soc. Interface* 12, 1–8. doi: 10.1098/rsif.2015.0817

Baio, J. E., Weidner, T., Baugh, L., Gamble, L. J., Stayton, P. S., and Castner, D. G. (2012). Probing the orientation of electrostatically immobilized Protein G B1 by time-of-flight secondary ion spectrometry, sum frequency generation, and near-edge X-ray adsorption fine structure spectroscopy. *Langmuir* 28, 2107–2112. doi: 10.1021/la203907t

Bellany, L. (1975). The infrared spectra of complex molecules. London: *Chapman Hall,* 1p.

Bullock, J. M., Drechsler, P., and Federle, W. (2008). Comparison of smooth and hairy attachment pads in insects: friction, adhesion and mechanisms for direction-dependence. *J. Exp. Biol.* 211, 3333–3343. doi: 10.1242/jeb.020941

Busshardt, P., Wolf, H., and Gorb, S. N. (2012). Adhesive and frictional properties of tarsal attachment pads in two species of stick insects (Phasmatodea) with smooth and nubby euplantulae. *Zoology* 115, 135–141. doi: 10.1016/j.zool.2011.11.002

Casford, M. T. L., Ge, A., Kett, P. J. N., Ye, S., and Davies, P. B. (2014). The structure of lipid bilayers adsorbed on activated carboxy-terminated monolayers investigated by sum frequency generation spectroscopy. *J. Phys. Chem. B* 118, 3335–3345. doi: 10.1021/jp410401z

Chen, C., Loch, C. L., Wang, J., and Chen, Z. (2003). Different molecular structures at polymer/silane interfaces detected by SFG. *J. Phys. Chem. B* 107, 10440–10445. doi: 10.1021/jp035211f

Cho, H.-J. J., Sresht, V., and Wang, E. N. (2018). Predicting surface tensions of surfactant solutions from statistical mechanics. *Langmuir* 34, 2386–2395. doi: 10.1021/acs.langmuir.7b03749

Daltorio, K. A., Wei, T. E., Horchler, A. D., Southard, L., Wile, G. D., Quinn, R. D., et al. (2009). Mini-Whegs TM climbs steep surfaces using insect-inspired attachment mechanisms. *Int. J. Robot. Res.* 28, 285–302. doi: 10.1177/0278364908095334

Dirks, J.-H., Clemente, C. J., and Federle, W. (2010). Insect tricks: two-phasic foot pad secretion prevents slipping. *J. R. Soc. Interface* 7, 587–593. doi: 10.1098/rsif.2009.0308

Dirks, J.-H., and Federle, W. (2011). Fluid-based adhesion in insects - principles and challenges. *Soft Matter* 7, 11047–11053. doi: 10.1039/c1sm06269g

England, M. W., Sato, T., Yagihashi, M., Hozumi, A., Gorb, S. N., and Gorb, E. V. (2016). Surface roughness rather than surface chemistry essentially affects insect adhesion. *Beilstein J. Nanotechnol.* 7, 1471–1479. doi: 10.3762/bjnano.7.139

Federle, W., Baumgartner, W., and Hölldobler, B. (2004). Biomechanics of ant adhesive pads: frictional forces are rate- and temperature-dependent. *J. Exp. Biol.* 207, 67–74. doi: 10.1242/jeb.00716

Federle, W., Riehle, M., Curtis, A. S. G., and Full, R. J. (2002). An integrative study of insect adhesion: mechanics and wet adhesion of pretarsal pads in ants. *Integrat. Compar. Biol.* 42, 1100–1106. doi: 10.1093/icb/42.6.1100

Fowler, J. E., Franz, J., Golbek, T. W., Weidner, T., Gorb, E. V., Gorb, S. N., and Baio, J. E. (2021). Surface chemistry of the ladybird beetle adhesive foot fluid across various substrates. *Biointerphases.* [Epub ahead of print].

Geiselhardt, S. F., Federle, W., Prüm, B., Geiselhardt, S., Lamm, S., and Peschke, K. (2010). Impact of chemical manipulation of tarsal liquids on attachment in the Colorado potato beetle, *Leptinotarsa decemlineata*. *J. Insect Physiol.* 56, 398–404. doi: 10.1016/j.jinsphys.2009.11.016

Geiselhardt, S. F., Geiselhardt, S., and Peschke, K. (2009). Comparison of tarsal and cuticular chemistry in the leaf beetle *Gastrophysa viridula* (Coleoptera: Chrysomelidae) and an evaluation of solid-phase microextraction and solvent extraction techniques. *Chemoecology* 19:185. doi: 10.1007/s00049-009-0021-y

Geiselhardt, S. F., Geiselhardt, S., and Peschke, K. (2011). Congruence of epicuticular hydrocarbons and tarsal secretions as a principle in beetles. *Chemoecology* 21:181. doi: 10.1007/s00049-011-0077-3

Gilet, T., Heepe, L., Lambert, P., Compere, P., and Gorb, S. N. (2018). Liquid secretion and setal compliance: the beetle's winning combination for a robust and reversible adhesion. *Curr. Opin. Insect Sci.* 30, 19–25. doi: 10.1016/j.cois.2018.08.002

Gorb, E., and Gorb, S. (2002). Attachment ability of the beetle *Chrysolina fastuosa* on various plant surfaces. *Entomol. Exp. Appl.* 105, 13–28. doi: 10.1046/j.1570-7458.2002.01028.x

Gorb, E., and Gorb, S. (2009). Effects of surface topography and chemistry of *Rumex obtusifolius* leaves on the attachment of the beetle *Gastrophysa viridula*. *Entomol. Exp. Appl.* 130, 222–228. doi: 10.1111/j.1570-7458.2008.00806.x

Gorb, E., Voigt, D., Eigenbrode, S. D., and Gorb, S. (2008). Attachment force of the beetle *Cryptolaemus montrouzieri* (Coleoptera, Coccinellidae) on leaflet surfaces of mutants of the pea *Pisum sativum* (Fabaceae) with regular and reduced wax coverage. *Arthropod Plant Interact.* 2, 247–259. doi: 10.1007/s11829-008-9049-0

Gorb, E. V., Hosoda, N., Miksch, C., and Gorb, S. N. (2010). Slippery pores: anti-adhesive effect of nanoporous substrates on the beetle attachment system. *J. R. Soc. Interface R. Soc.* 7, 1571–1579. doi: 10.1098/rsif.2010.0081

Gorb, S. N. (2001). *Attachment Devices of Insect Cuticle*. Dordrecht, The Netherlands: Kluwer Academic Publishers.

Gorb, S. N. (2011). "Biological fibrillar adhesives: functional principles and biomimetic applications," in *Handbook of Adhesion, Technology*, eds L. F. M. da Silva, A. Öchsner and R. D. Adams (Berlin, Heidelberg: Springer), 1410–1436.

Gorb, S. N., Schuppert, J., Walther, P., and Schwarz, H. (2012). Contact behaviour of setal tips in the hairy attachment system of the fly *Calliphora vicina* (Diptera, Calliphoridae): a cryo-SEM approach. *Zoology* 115, 142–150. doi: 10.1016/j.zool.2011.10.006

Gorb, S. N., Sinha, M., Peressadko, A., Daltorio, K. A., and Quinn, R. D. (2007). Insects did it first: a micropatterned adhesive tape for robotic applications. *Bioinspir. Biomim.* 2:S117. doi: 10.1088/1748-3182/2/4/S01

Gupta, S., Cochran, H., and Cummings, P. (1998). Nanorheology of liquid alkanes. *Fluid Phase Equilibr.* 150, 125–131. doi: 10.1016/S0378-3812(98)00283-0

Heepe, L., Wolff, J. O., and Gorb, S. N. (2016). Influence of ambient humidity on the attachment ability of ladybird beetles (*Coccinella septempunctata*). *Beilstein J. Nanotechnol.* 7, 1322–1329. doi: 10.3762/bjnano.7.123

Himmelhaus, M., Eisert, F., Buck, M., and Grunze, M. (2000). Self-assembly of n-alkanethiol monolayers. A study by IR-visible sum frequency spectroscopy (SFG). *J. Phys. Chem. B* 104, 576–584. doi: 10.1021/jp992073e

Hirose, C., Yamamoto, H., Akamatsu, N., and Domen, K. (1993). Orientation analysis by simulation of vibrational sum frequency generation spectrum: CH stretching bands of the methyl group. *J. Phys. Chem.* 97, 10064–10069. doi: 10.1021/j100141a028

Hosoda, N., and Gorb, S. N. (2012). Underwater locomotion in a terrestrial beetle: combination of surface de-wetting and capillary forces. *Proc. R. Soc. London B Biol. Sci.* 279, 4236–4242. doi: 10.1098/rspb.2012.1297

Korosi, G., and Kovats, E. S. (1981). Density and surface tension of 83 organic liquids. *J. Chem. Eng. Data* 26, 323–332. doi: 10.1021/je00025a032

Labonte, D., and Federle, W. (2015). Scaling and biomechanics of surface attachment in climbing animals. *Philos. Trans. R. Soc. B Biol. Sci.* 370:20140027. doi: 10.1098/rstb.2014.0027

Langer, M. G., Ruppersberg, J. P., and Gorb, S. (2004). Adhesion forces measured at the level of a terminal plate of the fly's seta. *Proc. R. Soc. London B Biol. Sci.* 271, 2209–2215. doi: 10.1098/rspb.2004.2850

Ludviksson, V., and Lightfoot, E. (1971). The dynamics of thin liquid films in the presence of surface-tension gradients. *AIChE J.* 17, 1166–1173. doi: 10.1002/aic.690170523

Ma, G., and Allen, H. C. (2006). DPPC Langmuir monolayer at the air-water interface: probing the tail and head groups by vibrational sum frequency generation spectroscopy. *Langmuir* 22, 5341–5349. doi: 10.1021/la0535227

Mo, H., Evmenenko, G., and Dutta, P. (2005). Ordering of liquid squalane near a solid surface. *Chem. Phys. Lett.* 415, 106–109. doi: 10.1016/j.cplett.2005.08.142

Moore, J., Cui, S., Cochran, H., and Cummings, P. (2000). Rheology of lubricant basestocks: a molecular dynamics study of C 30 isomers. *J. Chem. Phys.* 113, 8833–8840. doi: 10.1063/1.1318768

Niederegger, S., and Gorb, S. N. (2003). Tarsal movements in flies during leg attachment and detachment on a smoothe substrate. *J. Insect Physiol.* 49, 611–620. doi: 10.1016/S0022-1910(03)00048-9

Peisker, H., and Gorb, S. N. (2012). Evaporation dynamics of tarsal liquid footprints in flies (*Calliphora vicina*)and beetles (*Coccinella septempunctata*). *J. Exp. Biol.* 215 (Pt 8), 1266–1271. doi: 10.1242/jeb.065722

Peisker, H., Heepe, L., Kovalev, A. E., and Gorb, S. N. (2014). Comparative study of the fluid viscosity in tarsal hairy attachment systems of flies and beetles. *J. R. Soc. Interface* 11, 1–7. doi: 10.1098/rsif.2014.0752

Thornham, D. G., Blackwell, A., Evans, K. A., Wakefield, M., and Walters, K. F. A. (2008). Locomotory behaviour of the seven-spotted ladybird, *Coccinella septempunctata*, in response to five commonly used insecticides. *Ann. Appl. Biol.* 152, 349–359. doi: 10.1111/j.1744-7348.2008.00224.x

Tsige, M., and Patnaik, S. S. (2008). An all-atom simulation study of the ordering of liquid squalane near a solid surface. *Chem. Phys. Lett.* 457, 357–361. doi: 10.1016/j.cplett.2008.04.026

Vötsch, W., Nicholson, G., Müller, R., Stierhof, Y. D., Gorb, S., and Schwarz, U. (2002). Chemical composition of the attachment pad secretion of the locust *Locusta migratoria*. *Insect Biochem. Mol. Biol.* 32, 1605–1613. doi: 10.1016/S0965-1748(02)00098-X

Walker, G. (1993). Adhesion to smooth surfaces by insects—a review. *Int. J. Adhesion Adhesives* 13, 6–10. doi: 10.1016/0143-7496(93)90002-Q

Weidner, T., Apte, J. S., Gamble, L. J., and Castner, D. G. (2010). Probing the orientation and conformation of alpha-Helix and beta-strand model peptides on self-assembled monolayers using sum frequency generation and NEXAFS spectroscopy. *Langmuir* 26, 3433–3440. doi: 10.1021/la903267x

Weidner, T., and Castner, D. G. (2013). SFG analysis of surface bound proteins: a route towards structure determination. *Phys. Chem. Chem. Phys.* 15, 12516–12524. doi: 10.1039/c3cp50880c

Conflict of Interest: The authors declare that the research was conducted in the absence of any commercial or financial relationships that could be construed as a potential conflict of interest.

frontiers in Mechanical Engineering

ORIGINAL RESEARCH
published: 26 May 2021
doi: 10.3389/fmech.2021.659468

Adhesion Behaviors of Abalone Under the Action of Water Flow

*Yun Zhang[1], Shanpeng Li[2], Pingcheng Zuo[1], Xiangling Xu[1], Jing Li[3] and Jianlin Liu[1]**

[1]College of Pipeline and Civil Engineering, China University of Petroleum (East China), Qingdao, China, [2]College of Engineering, Lishui University, Lishui, China, [3]College of Mechanical and Electrical Engineering, China University of Petroleum (East China), Qingdao, China

The abalone is well known as a non-permanent adhesive organism, and its adhesion mechanism is beneficial to such areas as underwater robotics, high precision sensors, and intelligent devices. Firstly, we observe the posture response of an abalone under the action of different water flow conditions. The result shows that under a high velocity of water, it tends to make its tail comply with the water flow, and vice versa, under a low speed, its head tends to comply with the water flow. The finite element method (FEM) simulation is performed to display the stress field, which can reasonably explain this phenomenon, and the strength check is also made on the pedal and shell. Next, the critical velocity of water flow when the abalone is peeled from the substrate is calculated, where the CEL (Coupled Eulerian-Lagrangian) method is used in simulation. At last, the adhesion behaviors of an abalone located in a trough or when it is behind an obstacle are explored. Most of these findings can be supported by the experimental results. This analysis is helpful to make a deep understanding on the adhesion behaviors of marine creatures.

Keywords: abalone, adhesion, water flow, stress field, critical flow velocity

OPEN ACCESS

Edited by:
Ken Nakano,
Yokohama National University, Japan

Reviewed by:
Qunyang Li,
Tsinghua University, China
Clemens F. Schaber,
University of Kiel, Germany

****Correspondence:***
Jianlin Liu
liujianlin@upc.edu.cn

Specialty section:
This article was submitted to Tribology, a section of the journal Frontiers in Mechanical Engineering

Received: *27 January 2021*
Accepted: *03 May 2021*
Published: *26 May 2021*

Citation:
Zhang Y, Li S, Zuo P, Xu X, Li J and Liu J (2021) Adhesion Behaviors of Abalone Under the Action of Water Flow. Front. Mech. Eng 7:659468. doi: 10.3389/fmech.2021.659468

INTRODUCTION

In nature, being faced with the threat from predators, all kinds of marine organisms are challenged with wild environments all the time. In the process of adapting to nature, many marine organisms have mastered various and unique materials, structures and behaviors to meet the need of survival and reproduction (Ortiz and Boyce, 2008; Vincent, 2009; Wan et al., 2019). Among these, one interesting issue is the adhesion of marine creatures. For instance, mussels, barnacles and oysters have evolved to possess the ability of attachment, and actually the organic glue secreted from glands plays a key role during adhesion (Waite, 1987; Khandeparker and Anil, 2007; Burkett et al., 2010; Alberts et al., 2015; Wilker, 2015). On one hand, the adhesion phenomenon brings numerous inspirations for scientists and engineers to develop new typed materials and devices, such as adhesive robotics and underwater adhesion suckers (Autumn et al., 2006; Wang et al., 2017). On the other hand, the attachment of these adhesive animals on the surfaces of ships and other underwater devices will increase the drag and accelerate the corrosion of the surface (Eashwar et al., 1992; Coutts et al., 2007). Much effort has been made to focus on the removal of such fouling organisms, including biological, chemical, and physical methods (Clare et al., 1992; Flemming et al., 1996; Cho et al., 2001; Holm et al., 2003). One typical method is the water sweeping, which has proved to be an effective approach to removing juvenile barnacles on the ship surface (Denny et al., 1985; Larsson et al., 2010).

Another fouling organism is abalone, which has been less cared in the past decades. Although being classified as a kind of non-permanent adhesion animal, abalones seem normally very "lazy", and they tend to stay at one place all days (Momma and Sato, 1969; Momma and Ryuhei, 1970;

Nakamura and Soh, 1997). Recently, extensive studies have been performed about the adhesion behaviors of abalones from various perspectives. Firstly, it has been disclosed that the adhesion mechanism of abalone is mainly due to the van der Waals force between the substrate and the setae on the surface of abalone pedal (Li et al., 2018a). During moving in water, the abalone receives information through its eyes and cephalic tentacle (Wanichanon et al., 2004; Li et al., 2006), and once detecting potential threats it would cling tightly on the surface (Ahmed et al., 2005). In this situation the foot of abalone would generate a huge adhesion force, which is higher than many creatures, such as leech, clingfish and tree frog (Federle et al., 2006; Wainwright et al., 2013; Li et al., 2018b). It was declared that the adhesion strength of the abalone is greatly affected by the wettability and roughness of the substrate (Li et al., 2018a). The result shows that an abalone with the length of 7 cm, can generate an adhesive strength with the value of 0.5 Pa $\times 10^5$ Pa, even on the PTFE (Poly tetra fluoroethylene) plane whose surface energy is very low (Li et al., 2018b). Not limited to the case of adhesion on smooth surfaces, such as the smooth plane made of glass, steel and PTFE, the abalone could crawl and even attach on the surfaces with very sharp elements, e.g., knifes and nails. The most surprising fact is that the abalone foot has no injury when it quickly climbs on these sharp surfaces (Zhang et al., 2019). Moreover, the abalone foot can not only generate a large adhesive strength, but also can perform large strain (approximately 0.65) in its self-righting process. A recent study shows that, the abalone can produce enough adhesive strength, and the muscle can generate large strain to ensure that it could correct its posture after being flipped (Zhang et al., 2020).

Although the abalone can have a very strong adhesion capability on all kinds of surfaces, the underwater environment is very complicated and the water flow may cause a serious effect on its adhesion state. Obviously, the problem is intractable and challengeable, as it deals with many difficult issues, such as interfacial adhesion, fluid-structure coupling, and flow field demonstration. Thus the current study is directed towards a comprehensive exploration on the adhesion behaviors of abalone under different conditions of water flow.

The outline of this article is organized as follows. In *Materials and Methods*, we conduct the experiments to observe the response of abalone under different water flows. In *Smooth Substrate*, the maximum stress of the foot and shell of the abalone is computed by FEM simulation, and it is compared with the tolerant strength which we have measured in our previous study (Zhang et al., 2019). The critical flow speed when the abalone is swept away from the substrate is also figured out by simulation, which is compared with the result obtained by energy analysis. In *Substrate With Trough or Obstacle*, the adhesion behaviors of an abalone located in a trough or an obstacle are thoroughly explored.

MATERIALS AND METHODS

Materials

All of the abalones *Haliotis discus hannai* in the experiment are artificially cultured and bought from a marine aquaculture plant located at the coastal region in Qingdao of China. These alive abalones are selected with the length approximately 5 cm. The abalones are fed in a 480 l tank which is equipped with a thermostat to form a filtering and water circulating system. The temperature of water in the tank is 19 ± 0.5°C. The sea water is made of fresh water and sea salt. The rectangular glasses with the size of 200 mm^3 × 200 mm^3 × 8 mm^3 are used as substrates on which the abalones are raised. All of the substrates are placed in cages which are suspended in the tank. To make sure that each abalone could adapt to the new environment, all the individuals are held in the tank for seven days at least. The abalone is fed with kelp every other three days before the experiment to ensure that all the abalones are healthy (Li et al., 2018a; Zhang et al., 2019; Zhang et al., 2020).

Adhesive Strength Measurement

The adhesive strength measurement of abalone is conducted on the universal testing machine (UTM–1432, Cheng De Jin Jian Testing Instrument Co. Ltd.). Firstly, a self-developed three-pronged steel jaw, which is designed to hold the abalone shell, is clamped by the upper fixture of the machine. And the substrate on which the abalone adheres is fixed on the sample stage. The pulling force is applied to pull the animal from the substrate with the velocity of 20 mm/min, which can be seen as a quasi-static load (Li et al., 2018b; Zhang et al., 2019). And the value of adhesion strength could be recorded by the machine.

Flow Experiment

The experiment conducted in a self-assembled circulatory system consists of a transparent cuboid aquarium with the volume of 0.8 × 0.6 × 0.5 m^3, submersible pumps with various displacements and water channels with the size of 0.1 × 0.1 × 1 m^3. Flowing in the water channel, the sea water with the salinity of 1.024 is pumped from the aquarium and flows back to the aquarium. In order to reduce turbulence, a rectifying net is installed near the entrance of the channel.

The number of abalone is 43, all samples are divided into three groups. Before being scoured, three groups of abalone are put in the channel with three different initial postures, i.e. facing water with tail, head and the side of the body, shown in **Figure 1A**. And the water velocity gradually increases to the target to guarantee that each abalone could stretch its foot and generate adhesion on the channel surface. The scouring process under the same target velocity is repeated five times. And each process is kept for at least 30 min. The number of abalones of each posture is recorded after each test. Then the probability p of these three postures is the mean value of five repeated experiments. Then we change the target velocity of water flow and repeat the same procedure.

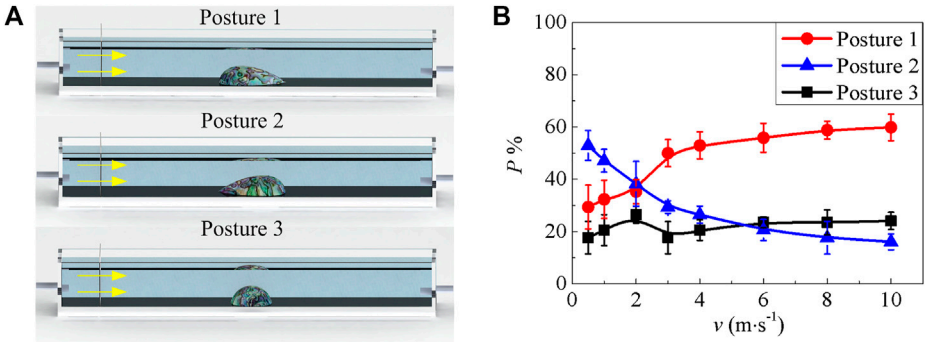

FIGURE 1 | Abalone postures in the flowing experiment **(A)** Abalone with three postures, i.e. it uses the tail, head and side to comply with water (the yellow arrow is the direction of the water flow) **(B)** Probabilities of three postures under various flow velocities. Error bar is the standard error of five repeated scouring experiments.

Finite Element Method Simulation

We use the commercial software ABAQUS to simulate the pulling off process of abalone from the substrate. Both of the substrate and the abalone are considered as isotropic materials. The Young's modulus of the abalone foot and shell are 1 MPa and 20 GPa respectively (Menig et al., 2000; Zhang et al., 2019). The Poisson's ratios of the foot and the shell are 0.16 and 0.3 respectively. For convenience of calculation, the substrate, includes the trough and obstacle, could be treated as a rigid body in simulation. All the substrates are set as the fixed boundary in simulation. The density of water, the abalone foot and the shell are 1,024, 1,500, and 2,700 kg/m^3 (Zhang et al., 2020). The foot and shell of abalone is tied *via* a small area (about 36 mm^2) on the top surface of the foot.

The Eulerian and Lagrangian grids are used in liquid and solid parts respectively. The velocities of liquid area walls are set as that the vertical component is zero to avoid the penetration from the walls. The entrance boundary is set as the velocity condition, and the exit boundary is set as the Eulerian boundary with "nonreflecting" to avoid liquid reflection. In order to reduce the calculation, the adhesion between the abalone foot and the substrate is set as the "cohesive behavior", as the mucus layer is very thin. The contact between solid and liquid is set as the "general contact". The number of element is 17,839, which consists of 1671 C3D4 elements (abalone foot and shell), 168 C3D8R elements (substrate) and 16,000 EC3D8R elements (liquid).

SMOOTH SUBSTRATE

Experimental Result

In water, three potential postures of the abalone might occur to deal with the water flow. When the abalone faces water with its tail, head and side body, the postures are named as posture 1, posture 2 and posture 3 respectively, which are shown in **Figure 1A**. The probability for these three postures p with respect to the water velocity v is demonstrated in **Figure 1B**. It can be observed that, if the velocity is in the range from 0.5 to 2 m/s, the probability of posture 2 is the biggest, and that of posture 3 is the smallest. This indicates that the creature tends to face the water current with its head when the water is in a low velocity. However, with the increase of the velocity, the probability of posture 2 becomes the smallest, especially after $v = 6$ m/s. On the contrary, the probability of posture 1 increases and it is bigger than that of posture 2 after $v = 2$ m/s. It is guessed that, under the condition of low speed of water, the abalone can capture necessary information about the water under posture 2. However, when the water has a big velocity it may produce an impact on the abalone, and the abalone will modulate the posture to avoid the impact of water. In addition, the probability of posture 3 fluctuates with the increase of flow velocity, and its values are maintained at about 21%, which are smaller than those of posture 1 throughout the whole process. This is the reason that we have seldom observed posture 3 of abalone during water flow.

Stress Field on the Abalone Pedal

We then use the finite software ABAQUS to simulate the stress field of abalone and the flow field of water. Firstly, at three typical velocities, i.e. the submarine flow velocity ($v = 0.5$ m/s), the speed of ship ($v = 15.43$ m/s) and the speed of speedboat ($v = 22$ m/s), the stress cloud diagrams of abalone pedal are shown in **Figure 2**. The von Mizes stress of the pedal is defined as

$$\sigma_p = \frac{\sqrt{(\sigma_x - \sigma_y)^2 + (\sigma_y - \sigma_z)^2 + (\sigma_z - \sigma_x)^2 + 6\tau_{xy}^2 + 6\tau_{yz}^2 + 6\tau_{zx}^2}}{2}, \quad (1)$$

where σ_x, σ_x, σ_x, τ_{xy}, τ_{xy}, and τ_{xy} are the stress components. Generally, the maximum stress of the pedal σ_{pmax} increases by 2.59–3.29 times when the velocity increases from 0.5 to 22 m/s for all of the three postures.

When the fluid velocity $v = 0.5$ m/s, the maximum stress of posture 2 is the biggest in comparison with the two other postures, as shown in **Figures 2A,D,G**. This stress distribution is not beneficial for the abalone keeping posture 2, but in the experiment we observe that this posture has the highest probability. This phenomenon could be explained from the perspective of the physiological structure of the abalone. Indeed, the animal can capture various information through

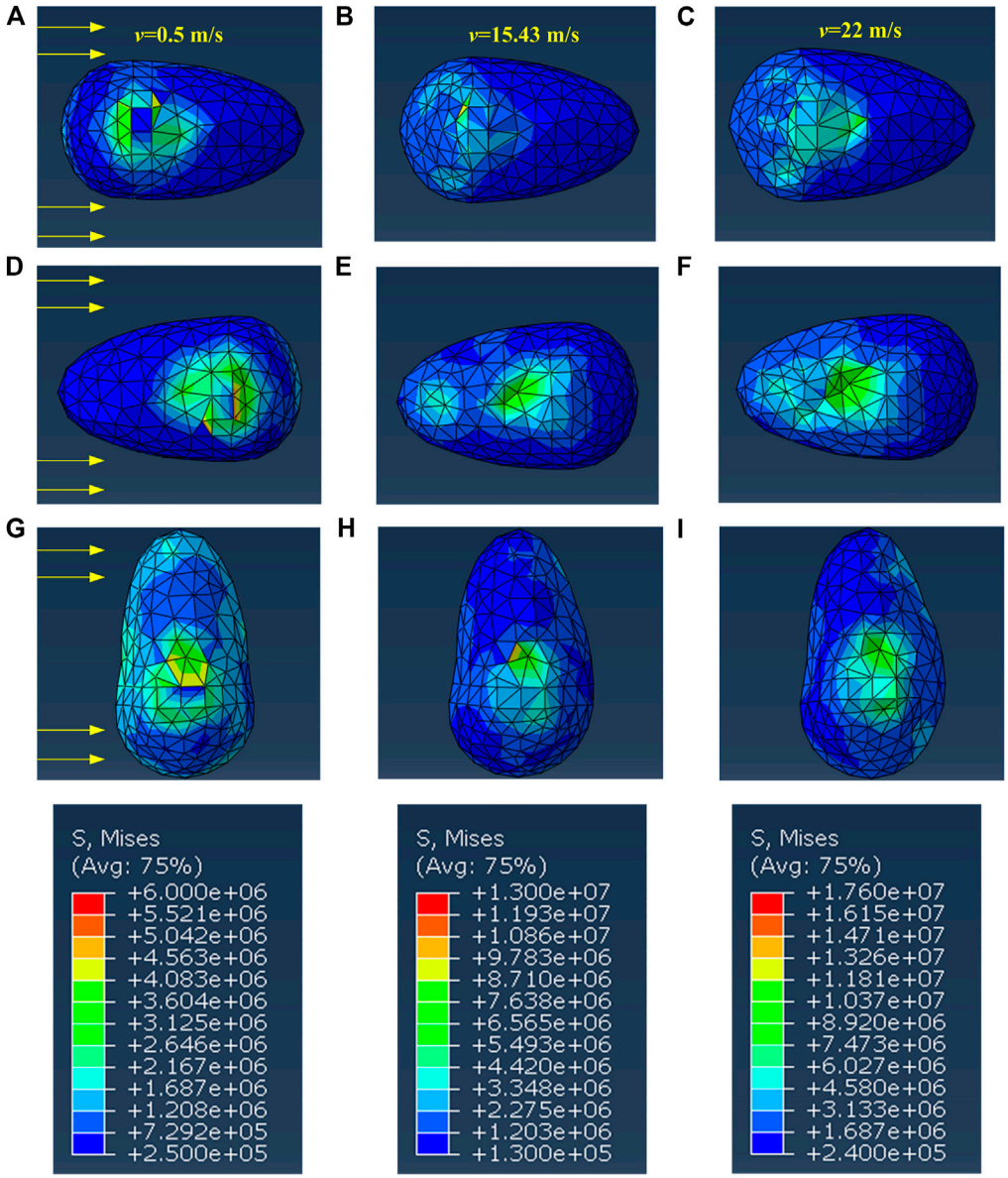

FIGURE 2 | The cloud diagram of the pedal's stress with **(A–C)** posture 1 **(D–F)** posture 2 **(G–I)** posture 3.

the antennae and eyes on its head (Wanichanon et al., 2004; Li et al., 2006), and its mouth can also filter algal debris from the current. Although the maximum stress is bigger than those of the other postures, posture 2 is used to deal with water flow, indicating that the abalone can adapt to this stress field conveniently.

Moreover, the locations of the pedal maximum stress for the three postures all change with the increase of the fluid velocity. In detail, when v = 0.5 m/s, the maximum stress appears at the junction between the shell and the foot, see **Figures 2A,D,G**. With the increase of the current speed, the maximum stress location has transferred to the surface impacted by water, as shown in **Figures 2C,F,I**. This means that, under the low velocity condition, it is the abalone shell that bears the water impact. However, when the flow velocity further increases, the abalone shell is lifted slightly by water, and thus the abalone pedal is impacted directly by water.

In addition, more cases of the abalone under different fluid velocities are also simulated *via* FEM. For convenience, the Reynold number is defined as

$$\mathrm{Re} = \frac{\rho v L}{\mu}, \tag{2}$$

where ρ is the water density, L is the characteristic length of the abalone, and μ is the kinematic viscosity of water (with the value of 0.001 Pa herein). Then the dependence relationship between the maximum stress of the pedal and the Reynold number is demonstrated in **Figure 3**. Based on the stress field we can judge

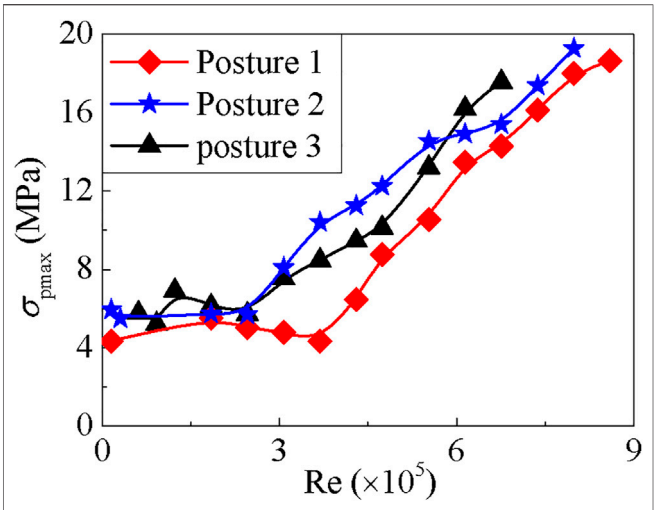

FIGURE 3 | The relationship between the maximum pedal's stress and the Reynold number Re.

that, roughly the posture 1 is the best strategy in which the maximum stress of abalone foot is the smallest with the whole variation process of the Reynold number.

However, when the velocity is in the low range, such as when $0 < Re < 3 \times 10^5$, the curves for the three postures are not monotonic. In order to explain this phenomenon, we give the velocity field distributed around the abalone. It can be noticed that there is a vortex for each case, as shown in **Figures 4A,D,G**, respectively. The vortex is associated with very complicated fluid dynamics, and it will cause the fluctuation of the curves on the pedal stress. The vortex gradually fades and even disappears with the increase of the flow velocity, as shown in **Figures 4B,C,E,F,H,I**. As a consequence, there are disturbances in the initial stage of the pedal stress curves and then the curves become monotonic at high Reynold number values.

As shown in **Figure 3**, the maximum stress of abalone pedal is $\sigma_{pmax} = 19.28$ MPa, which occurs in case of posture 2 when $v = 26$ m/s. The tolerant strength of the abalone pedal has already been measured as $[\sigma_p] = 31.82$ MPa (Zhang et al., 2019). Evidently, one has $\sigma_{pmax} < [\sigma_p]$. This means that although the fluid flow can bring impact on the abalone, its muscle cannot be broken and the abalone is still safe under the high speed flow.

Stress Field on the Abalone Shell

Under the action of water flow, the impact is directly applied on the abalone shell. Although the shell looks much stiffer than the muscle, its experimental value was measured as $[\sigma_s] = 700$ MP

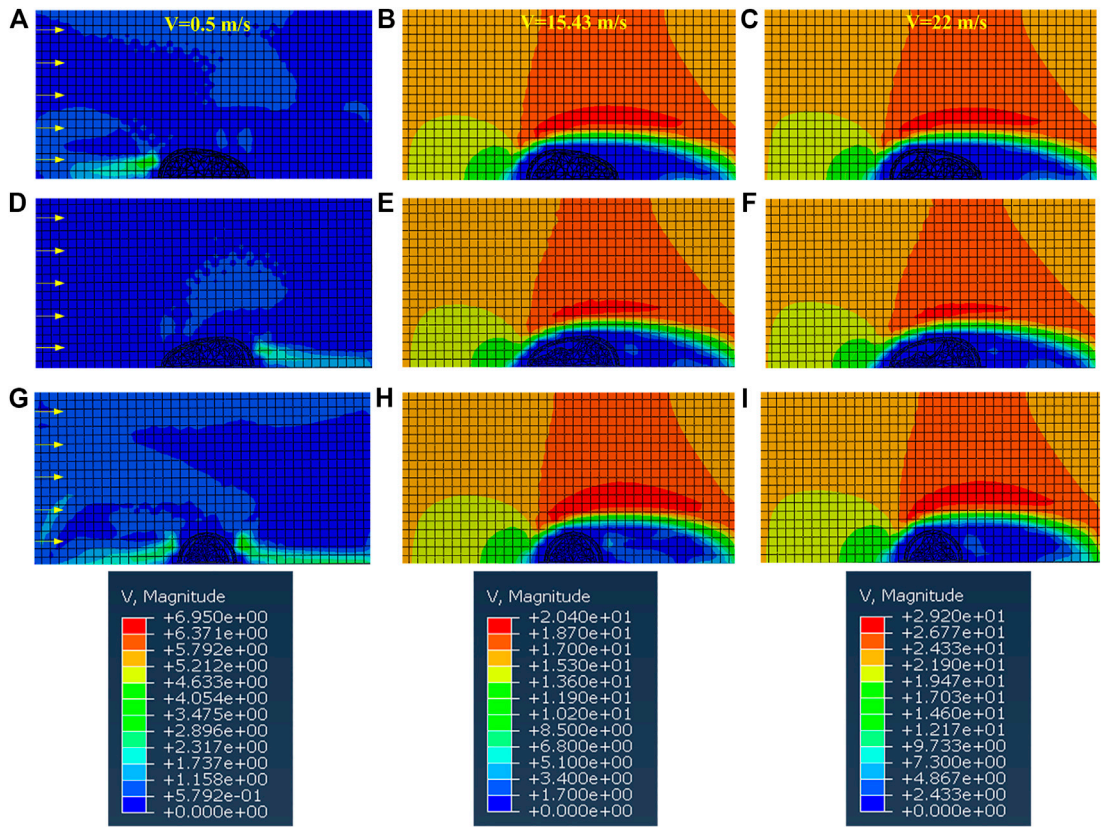

FIGURE 4 | The cloud diagram of the velocity field when the abalone faces the water flow with **(A–C)** posture 1 **(D–F)** posture 2 **(G–I)** posture 3.

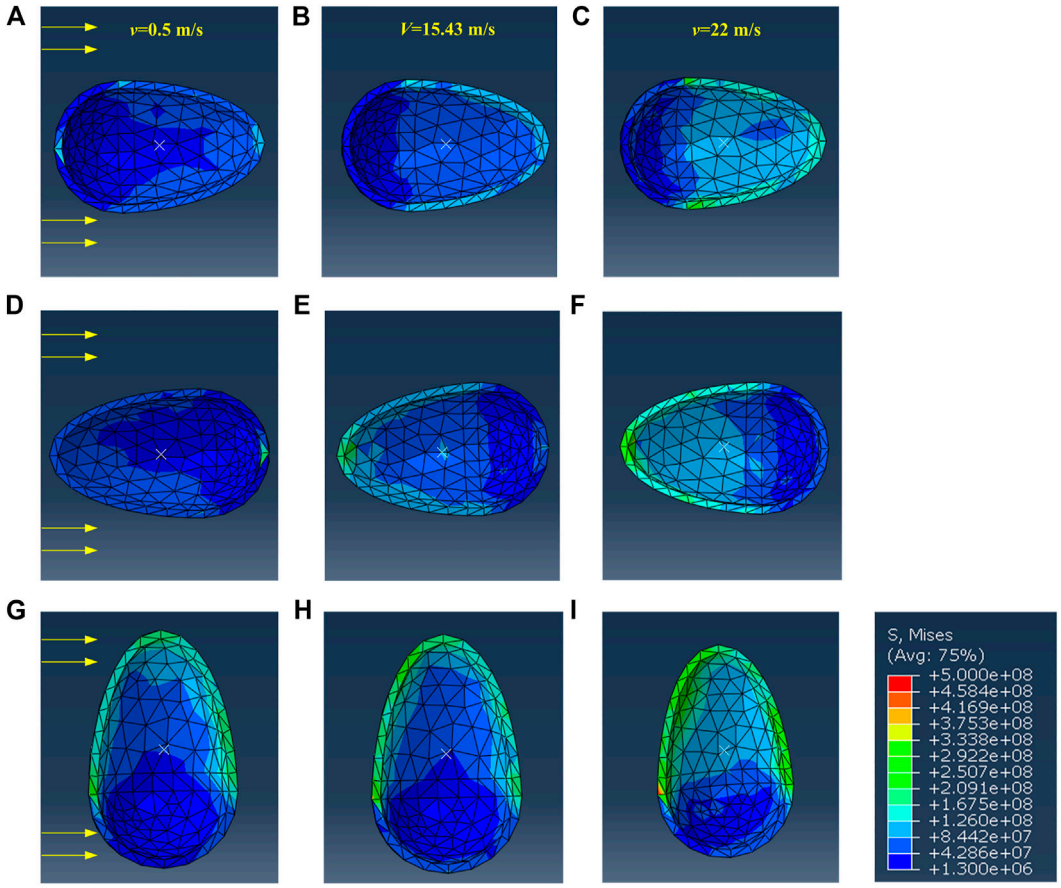

FIGURE 5 | The cloud diagram of the shell's stress when the abalone faces the water flow with **(A–C)** posture 1 **(D–F)** posture 2 **(G–I)** posture 3.

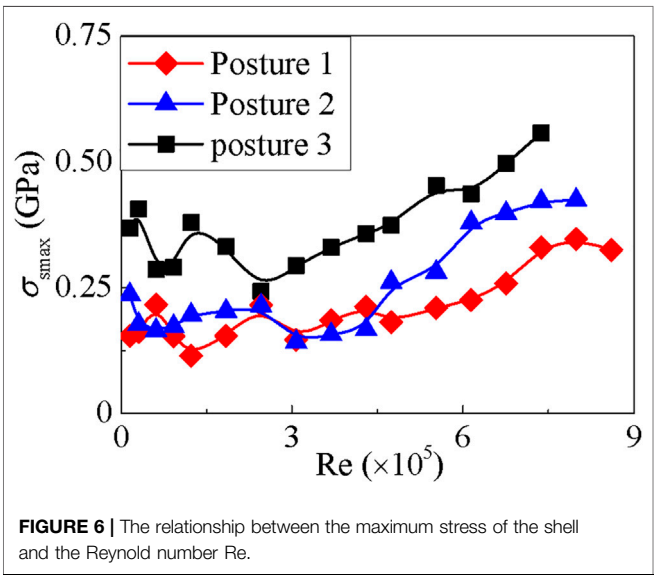

FIGURE 6 | The relationship between the maximum stress of the shell and the Reynold number Re.

(Menig et al., 2000), the velocity and pressure fields are different from those of the pedal. Therefore a similar strength check must be performed to ensure the reliability of analysis.

Based on the FEM simulation, the stress field of the shell for the above three postures is given in **Figure 5**. It can be seen that the maximum stress increases by 1.38–1.67 times when the velocity changes from v = 0.5 m/s to v = 22 m/s. Moreover, the maximum stress on the shell for posture 1 is the smallest, and that for posture 3 is the biggest when v = 0.5 m/s, v = 15.43 m/s, and v = 22 m/s. This again stresses that posture 3 is seldom observed in experiments.

The maximum stress of the shell is located at the side impacted by the water flow, except the case of posture 2 at v = 0.5 m/s. When v = 0.5 m/s, the maximum stress appears at the contralateral side of the impacted aspect of the shell, as during this situation one vortex appears at the tail of the shell. Furthermore, the curves on the maximum stress always fluctuate at low Re values (see **Figure 6**), and this phenomenon may be due to the appearance of vortex, as shown in **Figures 4A,D,G**. The curves grow monotonically with the increase of Re, which is the result of the reduction of the vortex, as shown in **Figures 4C,F,I**.

For the strength check, we select the maximum stress value of the shell shown in **Figure 6** as σ_{smax} = 500 MPa, which is much higher than that of the pedal. This value corresponds to the small area under fluid impact in conjunction with the pedal, and the stress concentration must happen. Although this value is

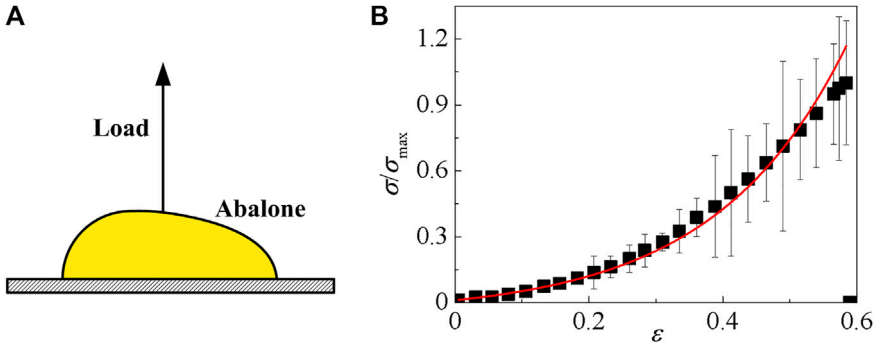

FIGURE 7 | Strength measurement experiment on the abalone **(A)** Schematic of the Experiment **(B)** The relationship between the dimensionless pulling stress and the strain.

sufficiently huge, its value is smaller than the tolerant strength of the shell, i.e. $\sigma_{smax} < [\sigma_s]$. This condition ensures the safety of the shell under the action of fluid dynamics. We also find that the maximum stress value in posture 1 under high Re values, is actually the smallest among the three curves, see the red one in **Figure 6**. This may be one of the reasons that the abalone tends to face the high velocity fluid with its tail.

Calculation of Critical Water Velocity

It can be easily imagined that, when the flow velocity increases continuously, the adhesion of the abalone on the substrate would fail. The critical cases that the abalone is detached from the substrate in these three postures, are thus investigated. Generally speaking, the energy required for detachment of the abalone pedal comes from the water current. For convenience of simplification, the kinetic energy of the muscle is ignored. As the resistance of the abalone, the kinetic energy varies not much even at the critical case.

According to the balance of energy, all the work W done by the current as well as the work W_1 done by normal force in normal detachment experiment are converted into the strain energy U and used to overcome the interfacial energy E of the pedal-substrate interface, which can be expressed as

$$W = W1 = U + E, \tag{3}$$

The uniaxial tension experiment on the peeling process of the abalone is schematized in **Figure 7A**, and then the stress-strain curve is given in **Figure 7B**. The dimensionless stress is defined as σ/σ_{max} in which σ and σ_{max} are the normal stress and maximum stress of the abalone (along the pulling direction) in the stress-strain curve. According to the stress-strain curve, one exponential function can be fitted as

$$\frac{\sigma}{\sigma_{max}}(\varepsilon) = 0.062\exp(5\varepsilon) - 0.05162,\ R^2 = 0.99, \tag{4}$$

Thus, $W1$ can be deduced as

$$W_1 = \sigma_{max} A_F h \int_0^{\varepsilon_F} \frac{\sigma}{\sigma_{max}}(\varepsilon)d\varepsilon, \tag{5}$$

where h is the initial maximum height of the abalone, ε_F is the strain when the abalone is pulled off from the substrate, and A_F is the initial adhesive area.

The abalone is subjected to the effect of the flow, which consists of the lift force F_L and the drag force F_D:

$$F_L = 0.5 C_L \rho A_F v^2, \tag{6}$$

$$F_D = 0.5 C_D \rho A_D v^2, \tag{7}$$

where C_L and C_D are the lift coefficient and drag coefficient respectively, and A_D is the frontal area which is measured as 3.5 cm^2 for posture 1, 2, and 5.5 cm^2 for posture 3. The work of water applied to the abalone can be written as

$$W = F_L U_L + F_D U_D, \tag{8}$$

where U_L and U_D are the displacements of the abalone when it is peeled, which are obtained *via* simulation. The symbols C_L and C_D are affected by the characteristic length L of the abalone and the flow velocity. The values of C_L and C_D used in this study are obtained at Re $\approx 10^5$, and all of our experimental parameters fall in this range. Since the shape and size of abalone are similar to that of limpet, C_L and C_D are selected as 0.35 and 0.45 respectively (Denny et al., 1985).

As a consequence, the critical velocities of three postures are theoretically computed as v_c = 26.2 m/s for posture 1, v_c = 25.8 m/s for posture 2 and v_c = 23.02 m/s for posture 3. The results obtained *via* FEM simulation are v_c = 32 m/s for posture 1, v_c = 28 m/s for posture 2 and v_c = 26 m/s for posture 3 respectively. It can be seen that the errors between two results are 18.12% for posture 1, 7.86% for posture 2 and 11.46% for posture 3. These discrepancies mainly come from the simplification process and energy loss of the water flow, but the theoretical computation and the simulation results are on the same order. According to these results, posture 1 is the best strategy to avoid detachment from the substrate, which agrees with our experimental results.

SUBSTRATE WITH TROUGH OR OBSTACLE

Another issue is the protective strategy of the abalone, i.e. they can select proper areas to face with the water flows. In the daily life, it is found that many abalones tend to live in narrow crevices whose sizes are similar to abalones, in order to avoid high velocity

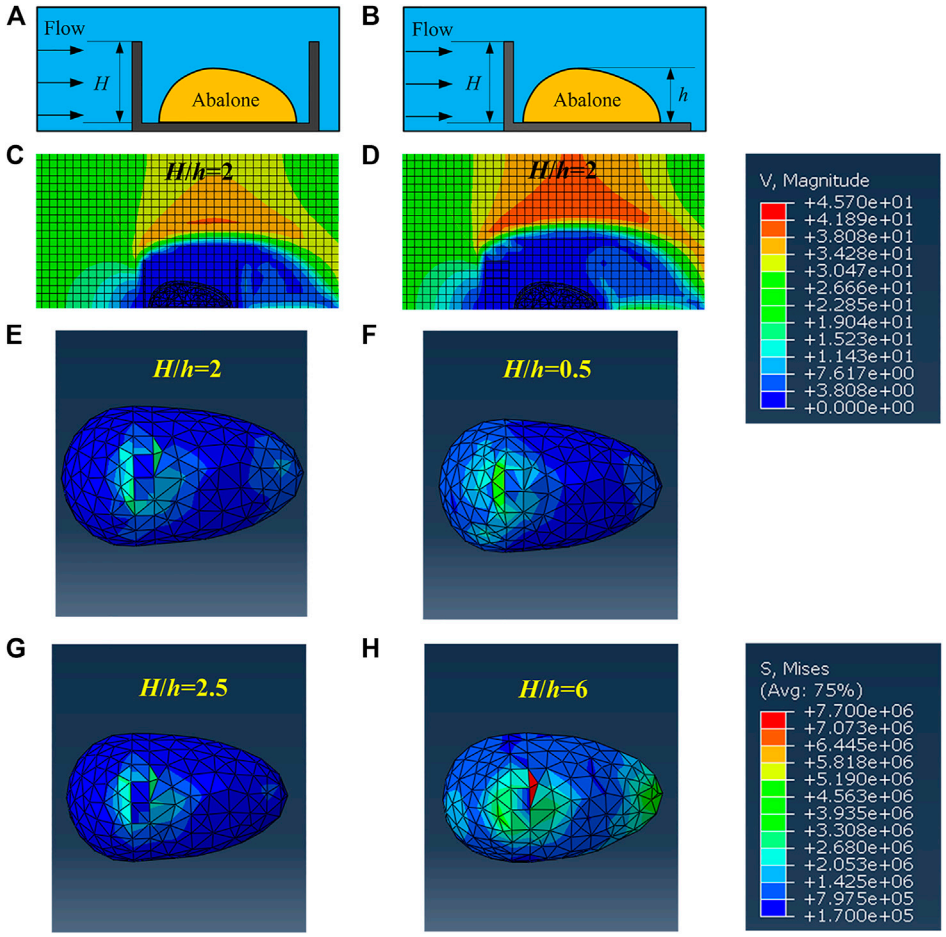

FIGURE 8 | Two models including the trough and the obstacle related with the abalone and the cloud diagram of the velocity field and the pedal's stress **(A)** and **(B)** are schematics of the models of trough and obstacle **(C)** and **(D)** are the cloud diagrams of the velocity field in the trough and behind the obstacle **(E)** and **(F)** are the cloud diagrams of the pedal's stress in the trough **(G)** and **(H)** are the cloud diagrams of the pedal's stress behind the obstacle.

flows and predators (Shepherd, 1973). Thus, in this section, we discuss the influence of the trough with different heights H on the abalone foot stress field under $v = 22$ m/s. For convenience, the dimensionless height H/h is used as below. As the trough is narrow and the gap between the abalone and the trough wall is very small, the length between the abalone and the wall is set as 2 mm in the model. This is in agreement with the observations on living abalones. As a contrast, we also conduct the simulation that the abalone hides behind an obstacle. The gap between the obstacle and the abalone is also set as 2 mm. Two terrain models of trough and obstacle are shown in **Figures 8A,B** respectively, and the parameter H/h ranges from 0 to 6.

Compared with **Figure 4C**, water field has been changed by the trough and obstacle (**Figures 8C,D**). Thus, the stress state of abalone pedal must be different. Shown in **Figure 8**, the minimum stress of the foot appears at $H/h = 2$ for trough (**Figure 8E**) and $H/h = 2.5$ for obstacle (**Figure 8G**). Moreover, the locations of the pedal's maximum stress appears at the junction between the shell and the foot, even when the pedal's maximum stress meets its biggest value, i.e. $H/h = 0.5$ for the trough and $H/h = 6$ for the obstacle (**Figures 8F,H**). The similar phenomenon only appears when the abalone adheres on the planar substrate, i.e., $H/h = 0$ under the low water flow. It implies that two terrains, i.e. trough and obstacle, can significantly reduce the effect of water impact. In particular, the pedal's maximum stress under the two terrains decreases by 65.89–77.58% for the trough, and 46.2–78.51% for the obstacle respectively, as shown in **Figure 9**.

Additionally, when the abalone hides behind the obstacle, the curve of the foot's maximum stress reduces to the smallest value of 3.071 MPa when $H/h = 2.5$, then increases and stabilizes at the value of 7 MPa around. When the abalone is in the trough, the curve decreases firstly and attains to the minimum value of 3.2 MPa when $H/h = 2$, then increases and stabilizes near the value of 4.8 MPa.

It is obvious that the two minimum values are very close, and the foot's maximum stress is maintained a smaller value when the abalone is located inside the trough. Therefore, the trough is more suitable for the abalone to stay than the obstacle, and this phenomenon has already been observed in previous study (Shepherd, 1973).

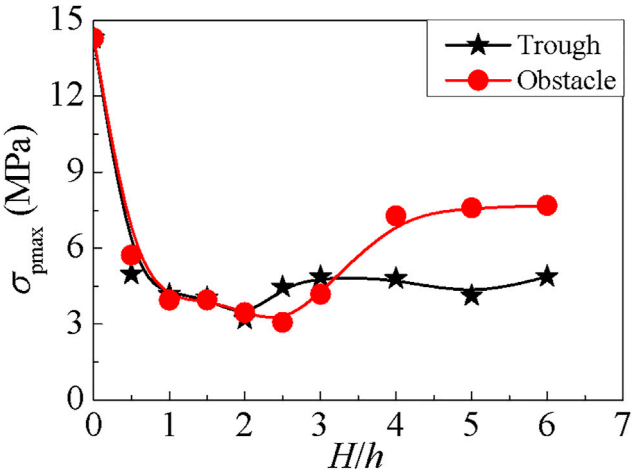

FIGURE 9 | The maximum stress of the abalone foot in the trough or behind the obstacle with various values of *H*//*h*, where the red curve represents obstacle and the black curve represents trough.

CONCLUSIONS

In conclusion, the adhesion behaviors of abalone under the action of fluid dynamics is comprehensively studied in this work. We observe that the abalone can adjust its posture in different water flows, and its tail tends to comply with the water flow. We performed the FEM simulation to demonstrate the stress field, and the strength check shows that the shell and pedal are tough enough not to be damaged. The behavior that abalone tends to face water with its tail under high velocity flows as its maximum stress has a small value. Next, the critical water flow velocities of these three postures when the abalone is peeled off from the substrate are calculated *via* energy analysis and FEM simulation. The results show that the critical velocity obtains the biggest and smallest values when the abalone faces water with tail and head respectively. And this again stresses that the abalone tends to use its tail to deal with water flow. Moreover, the trough and obstacle have both proved to be effective in reducing the pedal's stress, and the trough may be the better one.

Although more detailed experiments and simulation can be done in future, it is expected that these findings can provide some inspirations to engineer new-typed sensors and devices under water. Indeed, trough-shaped shell could be utilized to protect the core components from the water flow, during the sensor developing.

DATA AVAILABILITY STATEMENT

The original contributions presented in the study are included in the article/Supplementary Material, further inquiries can be directed to the corresponding author.

ETHICS STATEMENT

Ethical review and approval was not required for the animal study because The experiments in this study cause no harm to the animal.

AUTHOR CONTRIBUTIONS

JL (6th author), YZ and SL proposed the theoretical and experimental strategy. YZ, PZ, XX, and JL (5th author) performed the experiment, and YZ carried out the FEM simulation. JL (6th author) wrote the paper. All authors discussed the results and commented on the manuscript.

FUNDING

This project was supported by the National Natural Science Foundation of China (11972375, 11911530691), and Key R & D Program in Shandong Province (ZR202011050038, 2017GGX20117).

REFERENCES

Ahmed, F., Yokota, M., Watanabe, S., Koike, Y., Segawa, S., and Strüssmann, C. A. (2005). Time to Recover the Upright Posture in Juvenile Abalones (Haliotis Discus Discus Reeve, H. Gigantea Gmelin and H. Madaka Habe). *Aquac. Res.* 36, 799–802. doi:10.1111/j.1365-2109.2005.01289.x

Alberts, E. M., Taylor, S. D., Edwards, S. L., Sherman, D. M., Huang, C.-P., Kenny, P., et al. (2015). Structural and Compositional Characterization of the Adhesive Produced by Reef Building Oysters. *ACS Appl. Mater. Inter.* 7, 8533–8538. doi:10.1021/acsami.5b00287

Autumn, K., Dittmore, A., Santos, D., Spenko, M., and Cutkosky, M. (2006). Frictional Adhesion: a New Angle on Gecko Attachment. *J. Exp. Biol.* 209, 3569–3579. doi:10.1242/jeb.02486

Burkett, J. R., Hight, L. M., Kenny, P., and Wilker, J. J. (2010). Oysters Produce an Organic–Inorganic Adhesive for Intertidal Reef Construction. *J. Am. Chem. Soc.* 132, 12531–12533. doi:10.1021/ja104996y

Cho, J. Y., Kwon, E. H., Choi, J. S., Hong, S. Y., Shin, H. W., and Hong, Y. K. (2001). Antifouling Activity of Seaweed Extracts on the Green Alga *Enteromorpha* and the Mussel *Mytilus edulis*. *J. Appl. Phycol.* 13, 117–125. doi:10.1023/A:1011139910212

Clare, A. S., Rittschof, D., Gerhart, D. J., and Maki, J. S. (1992). Molecular Approaches to Nontoxic Antifouling. *Invertebrate Reprod. Dev.* 22, 67–76. doi:10.1080/07924259.1992.9672258

Coutts, A. D. M., Taylor, M. D., and Hewitt, C. L. (2007). Novel method for assessing the en route survivorship of biofouling organisms on various vessel types. *Mar. Pollut. Bull.* 54, 97–100. doi:10.1016/j.marpolbul.2006.09.014

Denny, M. W., Daniel, T. L., and Koehl, M. A. R. (1985). Mechanical Limits to Size in Wave-Swept Organisms. *Ecol. Monogr.* 55, 69–102. doi:10.2307/1942526

Eashwar, M., Subramanian, G., Chandrasekaran, P., and Balakrishnan, K. (1992). Mechanism for Barnacle-Induced Crevice Corrosion in Stainless Steel. *Corrosion* 48, 608–612. doi:10.5006/1.3315979

Federle, W., Barnes, W. J. P., Baumgartner, W., Drechsler, P., and Smith, J. M. (2006). Wet but Not Slippery: Boundary Friction in Tree Frog Adhesive Toe Pads. *J. R. Soc. Interf.* 3, 689–697. doi:10.1098/rsif.2006.0135

Flemming, H.-C., Griebe, T., and Schaule, G. (1996). Antifouling Strategies in Technical Systems - a Short Review. *Water Sci. Technol.* 34, 517–524. doi:10.1016/0273-1223(96)00687-710.2166/wst.1996.0591

Holm, E. R., Haslbeck, E. G., and Horinek, A. A. (2003). Evaluation of Brushes for Removal of Fouling from Fouling-Release Surfaces, Using a Hydraulic Cleaning Device. *Biofouling* 19, 297–305. doi:10.1080/0892701031000137512

Khandeparker, L., and Anil, A. C. (2007). Underwater Adhesion: the Barnacle Way. *Int. J. Adhes. Adhesives* 27, 165–172. doi:10.1016/j.ijadhadh.2006.03.004

Larsson, A. I., Mattsson-Thorngren, L., Granhag, L. M., and Berglin, M. (2010). Fouling-release of Barnacles from a Boat Hull with Comparison to Laboratory Data of Attachment Strength. *J. Exp. Mar. Biol. Ecol.* 392, 107–114. doi:10.1016/j.jembe.2010.04.014

Li, J., Zhang, Y., Liu, S., and Liu, J. (2018a). Insights into Adhesion of Abalone: A Mechanical Approach. *J. Mech. Behav. Biomed. Mater.* 77, 331–336. doi:10.1016/j.jmbbm.2017.09.030

Li, N., He, S., Li, H., and Ke, H. (2006). Microstructure and Ultrastructure of the Cephalic Tentacle of *Haliotis Diversicolor*. *Acta Zool. Sin.* 52, 755–764. doi:10.1016/S1004-4132(06)60023-6

Li, S., Zhang, Y., Dou, X., Zuo, P., and Liu, J. (2018b). Hard to Be Killed: Load-Bearing Capacity of the Leech Hirudo Nipponia. *J. Mech. Behav. Biomed. Mater.* 86, 345–351. doi:10.1016/j.jmbbm.2018.07.001

Menig, R., Meyers, M. H., Meyers, M. A., and Vecchio, K. S. (2000). Quasi-static and Dynamic Mechanical Response of *Haliotis rufescens* (Abalone) Shells. *Acta Materialia* 48, 2383–2398. doi:10.1016/S1359-6454(99)00443-7

Momma, H., and Ryuhei, S. (1970). The Locomotion Behavior of the Disc Abalone, *Haliotis Discus Hannai* Ino, in a Tank. *Tohoku J. Agr. Res.* 21, 20–25.

Momma, H., and Sato, R. (1969). The Locomotion Behavior of the Disc Abalone, *Haliotis Discus Hannai* Ino, and the Siebold's Abalone, *Haliotis Sieboldi* Reeve, in the Fishing Grounds. *Tohoku J. Agr. Res.* 20, 150–157. doi:10.1016/j.ijpara.2006.09.009

Nakamura, K., and Soh, T. (1997). Mechanical Memory Hypothesized in the Homing Abalone *Haliotis Diversicolor Supertexta* under Experimental Conditions. *Fish. Sci.* 63, 854–861. doi:10.2331/fishsci.63.854

Ortiz, C., and Boyce, M. C. (2008). MATERIALS SCIENCE: Bioinspired Structural Materials. *Science* 319, 1053–1054. doi:10.1126/science.1154295

Shepherd, S. (1973). Studies on Southern Australian Abalone (Genus *Haliotis*). I. Ecology of Five Sympatric Species. *Mar. Freshw. Res.* 24, 217–258. doi:10.1071/MF9730217

Vincent, J. F. V. (2009). Biomimetics - a Review. *Proc. Inst. Mech. Eng. H* 223, 919–939. doi:10.1243/09544119JEIM561

Wainwright, D. K., Kleinteich, T., Kleinteich, A., Gorb, S. N., and Summers, A. P. (2013). Stick Tight: Suction Adhesion on Irregular Surfaces in the Northern Clingfish. *Biol. Lett.* 9, 20130234. doi:10.1098/rsbl.2013.0234

Waite, J. H. (1987). Nature's Underwater Adhesive Specialist. *Int. J. Adhes. Adhesives* 7, 9–14. doi:10.1016/0143-7496(87)90048-0

Wan, C., Ma, Y., and Gorb, S. N. (2019). Compromise between Mechanical and Chemical Protection Mechanisms in the *Mytilus edulis* Shell. *J. Exp. Biol.* 222, jeb201103. doi:10.1242/jeb.201103

Wang, Y., Yang, X., Chen, Y., Wainwright, D. K., Kenaley, C. P., Gong, Z., et al. (2017). A Biorobotic Adhesive Disc for Underwater Hitchhiking Inspired by the Remora Suckerfish. *Sci. Robot.* 2, eaan8072. doi:10.1126/scirobotics.aan8072

Wanichanon, C., Laimek, P., Chitchulanon, N., Suphamungmee, W., Apisawetakan, S., and Linthong, V. (2004). Sensory Receptors on Cephalic and Epipodial Tentacles of *Haliotis Asinina Linnaeus*. *J. Shellfish Res.* 23, 1097–1107.

Wilker, J. J. (2015). Positive Charges and Underwater Adhesion. *Science* 349, 582–583. doi:10.1126/science.aac8174

Zhang, Y., Li, S., Zuo, P., Ji, J., and Liu, J. (2019). The Mechanics of Abalone Crawling on Sharp Objects without Injury. *Sci. Rep.* 9, 1–7. doi:10.1038/s41598-019-40505-w

Zhang, Y., Li, S., Zuo, P., Li, J., and Liu, J. (2020). A Mechanics Study on the Self-Righting of Abalone from the Substrate. *Appl. Bionics Biomech.* 2020, 1–9. doi:10.1155/2020/8825451

Conflict of Interest: The authors declare that the research was conducted in the absence of any commercial or financial relationships that could be construed as a potential conflict of interest.

frontiers in Mechanical Engineering

ORIGINAL RESEARCH
published: 11 June 2021
doi: 10.3389/fmech.2021.702297

Adhesion of Individual Attachment Setae of the Spider *Cupiennius salei* to Substrates With Different Roughness and Surface Energy

*Bastian Poerschke, Stanislav N. Gorb and Clemens F. Schaber**

Functional Morphology and Biomechanics, Zoological Institute, Kiel University, Kiel, Germany

Dynamic adhesion is a key ability for animals to climb smooth surfaces. Spiders evolved, convergent to geckos, a dry adhesive system made of setae branching into smaller microtrichia ending as spatulae. Several previous studies concentrated either on the whole adhesive claw tuft on the spider´s foot that consists of attachment setae or on the single adhesive contact elements, the microtrichia with spatula-shaped tips. Here, the adhesion of single setae of the spider *Cupiennius salei* was examined and the morphology of the pretarsus and the fine structure of the setae were studied in further detail. Using individual setae fixed to force sensing cantilevers, their adhesion at different contact angles with a glass substrate was measured as well as their adhesive performance on substrates with different roughness and on smooth surfaces with different surface energies. The results show an individual variability of the adhesive forces corresponding to the seta morphology and especially to the seta tip shape. The tip shapes of the setae vary largely even in neighboring setae of the pretarsal claw tuft that comprises approximately 2,400 setae. Regarding surface energy of the substrate, the adhesion force on hydrophobic polytetrafluoroethylene was 30% of that on a hydrophilic glass substrate, which points to the importance of both van der Waals interactions and hydrogen bonds in spider adhesion.

Keywords: adhesion, claw tuft, locomotion, pretarsus, scopula, spider hair, surface properties

OPEN ACCESS

Edited by:
Yonggang Meng,
Tsinghua University, China

Reviewed by:
Antonio Papangelo,
Politecnico di Bari, Italy
Feodor M Borodich,
Cardiff University, United Kingdom

****Correspondence:***
Clemens F. Schaber
cschaber@zoologie.uni-kiel.de

Specialty section:
This article was submitted to Tribology, a section of the journal Frontiers in Mechanical Engineering

Received: *29 April 2021*
Accepted: *25 May 2021*
Published: *11 June 2021*

Citation:
Poerschke B, Gorb SN and Schaber CF (2021) Adhesion of Individual Attachment Setae of the Spider Cupiennius salei *to Substrates With Different Roughness and Surface Energy. Front. Mech. Eng 7:702297. doi: 10.3389/fmech.2021.702297*

INTRODUCTION

The ability to climb almost every surface is a big advantage for animals. Therefore, many species convergently evolved different types of adhesive footpads to perform locomotion even on smooth vertical surfaces. One of these types is a soft bubble based smooth adhesive system that has been discovered for example in *Orthoptera, Hymenoptera, Solifugae and Scincidae*. The second type are fibrillary/hairy, seta based adhesive pads found for example in *Dipterans, Coleopterans, Araneae, Gekkonidae and Anolinae* (Gorb and Heepe, 2017). Among the animal groups using fibrillary pads, the geckos (*Gekkonidae*) and spiders (*Araneae*) developed an exceptionally effective reversible adhesive system for so called "dry adhesion" that works without any sticky fluid involved. In geckos, the dry adhesive system consists of a multitude of keratinous setae that branch at the tips and are arranged in lamella on the toes (Rizzo et al., 2006). In spiders, the dry adhesive system for locomotion is located on the most distal leg parts (pretarsi) and made up of chitinous setae bundled in the so-called scopula claw tuft. From each of these setae, a multitude of microtrichia branch off, which are

arranged densely close to the seta tips and face the substrate (Niederegger and Gorb, 2006; Schaber et al., 2019). As in geckos, the terminal contact elements of the setae are flat and thin platelet-shaped spatulae.

Adhesion of the dry attachment systems is enhanced by shearing, which promotes alignment of the spatulae with the substrate surface and increases the contact area for attractive van der Waals forces (Wolff and Gorb, 2013; Flenner et al., 2020). In the gecko, the adhesive force of a single seta strongly depended on its sliding in contact with a substrate. The adhesion force ranged from 0.6 μN without sliding, to 13.6 μN with sliding, and 194 μN at 5 μm sliding and a preload of 15 μN. Assuming that all setae were simultaneously and maximally attached, these data indicated an adhesive force of 100 N of the single gecko foot (Autumn et al., 2000). In the jumping spider *Evarcha arcuata*, the adhesive force of a single spatula was measured to be 38 nN. The assumption that all spatulae were in contact resulted in an adhesive force that could support 173 times the body weight of the animal (Kesel et al., 2003; Kesel et al., 2004). In the Central American wandering spider species *Cupiennius salei*, which was also used in the present study, the adhesion of a single leg scopula on glass when shear force was applied was found to be 35 mN, which would suffice to hold an adult female animal on a vertical surface. However, the vertical pull-off force without shear preload was zero (Wohlfart et al., 2014). The arrangement of the spatulae on the setae was previously explained to be most important for the spider's traction forces on different micro-rough substrates in the species *Philodromus dispar* (Wolff and Gorb, 2012a).

Up to now, the adhesive forces of the single spider setae that make up the adhesive scopula on the claw tufts of the spider remained unknown. To find out more on the interplay of the adhesive setae with different kinds of substrates, here we examined the morphology of the claw tuft and the setae and measured adhesion forces of individual setae on various characterized substrates with different surface energies and roughness and at different setal contact angles on glass.

MATERIALS AND METHODS

Animal Sample Preparation

Air-dried exuviae of the last molt of female wandering spiders of the species *Cupiennius salei* (Barth, 2002) were used for reflected light microscopy and scanning electron microscopy. Individual setae were plucked in the center of the pretarsal scopulae from autotomized legs of adult female specimen that were bred and raised in the Department of Functional Morphology and Biomechanics at Kiel University and kept at temperatures between 20 and 25°C and relative humidity of 70–100%. For *in vivo* examination of adhesion, spiders were anesthetized and fixed upside-down to a sample holder using adhesive tape.

Surface Samples

Different rough surfaces with the same surface chemistry were fabricated in a two-step casting technique. First, casts were taken from glass slides, polishing papers with different defined roughness (P0.05, P1, P3, P9, and P12; Buehler Ltd., Lake Bluff, IL, United States) and sand papers (P800, P1500, P2500; Bauhaus GmbH, Mannheim Germany) using polyvinyl siloxane (Coltène President light body; Coltène Whaledent AG, Altstätten, Switzerland). In the second step, these negative impressions were cast using epoxy resin (low viscosity kit; Electron Microscopy Sciences, Hatfield, PA, United States). The smooth surfaces for testing adhesion at different surface energies were uncoated glass slides, silicon wafers, polytetrafluoroethylene (PTFE; Goodfellow Ltd. Huntingdon, United Kingdom), and epoxy resin casts of glass slides.

Microscopy

Reflected light microscopy was performed using a Leica M205A microscope equipped with a Leica DFC420 camera (Leica Microsystems GmbH, Wetzlar, Germany) in multifocus imaging mode. For scanning electron microscopy, single setae were fixed to the sample holders using conductive carbon adhesive tape. Whole pretarsi were additionally mounted using conductive carbon cement (LEIT-C; Plano GmbH, Wetzlar, Germany). The samples were examined without sputter coating using a Hitachi S-4800 (Hitachi Ltd., Tokyo, Japan) scanning electron microscope at an acceleration voltage of 3 kV or sputter coated with 10 nm gold-palladium using a Hitachi TM3000 at 15 kV. Plucked single setae were inspected in 70% ethanol cover slipped on glass slides using a transmitted light microscope (Axioplan; Carl Zeiss Microscopy GmbH, Jena, Germany) equipped with a digital camera (AxioCam MRc).

Surface Characterization

The surface energy and its polar and disperse shares were characterized on the four different smooth substrates using a contact angle measurement system (OCA20; DataPhysics Instruments, Filderstadt, Germany). The contact angle of three different liquids (double distilled water, diiodomethane, ethylene glycol) was measured on ten random spots of each substrate. The polar and disperse shares of the surface energy were calculated using the software of the instrument, and the mean values determined for each substrate.

For roughness characterization, 3D surface measurements were performed using a white light interferometer (NewView 6k; Zygo Corporation, Middlefield, Connecticut, United States). Using the software MetroPro (version 8.1.5) of the instrument, height maps were plotted and their surface roughness determined in μm as the root mean square deviation of the roughness profile (*rms* roughness).

Adhesion Force Measurements

Piezo-electric force sensing cantilevers (FMT-120b; Kleindiek Nanotechnik, Reutlingen, Germany) mounted on a micromanipulator (MM3A; Kleindiek Nanotechnik, Reutlingen, Germany) were calibrated by pushing the tip against a calibrated spring. Calibration curves were plotted from the cantilever deflection measured using white light interferometry and recordings of the corresponding voltage signal from the force measurement amplifier (FMS-01; Kleindiek Nanotechnik, Reutlingen, Germany). The sensitivities of the cantilevers were in the range between

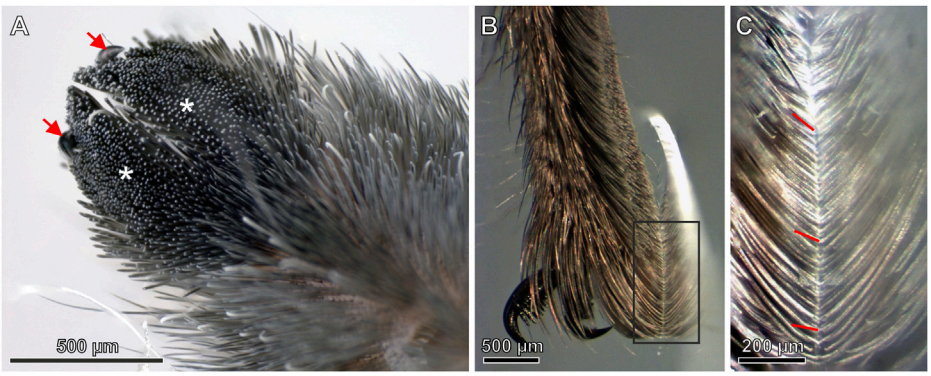

FIGURE 1 | (A) Ventral surface of the two-lobed pretarsal scopula claw tuft (blackish; asterisks) comprising the tips of thousands of densely arranged setae. Arrows mark the claws **(B)** Side view of the pretarsal scopula in contact with a glass slide **(C)** Magnified view of the rectangle marked in **(B)**. There is a notable increase of the angles of the seta tips with the glass surface from top (proximal) toward the bottom (distal) of the image caused by the increased curvature of the setae. Exemplarily, the lines indicate the angles of individual seta tips with the substrate.

2.7 µN V^{-1} and 6.5 µN V^{-1} (linear regression coefficients $R^2 \geq 0.995$).

The adhesion force measurements were performed under a reflected light microscope (LMS310; Carl Zeiss Microscopy GmbH, Jena, Germany) equipped with a digital camera (BLS 5 MP; BMS microscopes b.v., Capelle aan den IJssel, Netherlands). The cantilevers with single setae glued to their tips using polyvinyl siloxane as well as the substrates were arranged in side view. For the tests, the cantilevers were pushed vertically onto the substrate up to a force of 0.5 µN using the software NanoControl 3.1 (Kleindiek Nanotechnik, Reutlingen, Germany) and immediately pulled off. The sampling rate of the analogue/digital converter was set to 10 kHz and the data smoothened by a moving average calculation of 100 data points. The adhesion peaks just before the loss of contact between the setae and the substrates were used for further analysis. All measurements were performed at temperatures between 22.8°C and 26.1°C and at relative humidity between 31 and 58.7%. For statistical analysis the software SigmaPlot (12.5; Systat Software, Inc. San Jose, CA, United States) and R Studio (R Studio Inc. Boston, United States) were used.

RESULTS

Morphology of the Pretarsus

Besides the adhesive setae of the scopula, on the pretarsus there are two claws for clamping on compliant and rough substrates. Additionally, in between of the claws there is a much shorter middle hook. The ventral side of the pretarsus is two-lobed and densely covered by the adhesive setae (**Figure 1A**). The seta tips of the pad form a rather flat sole-like surface that well gains contact with a substrate surface (**Figure 1B**). The setae show an increased curvature in their distal parts so that the angles at which their tips approach a substrate increase from approximately 45° in the proximal part of the scopula up to approximately 90° in the most distal part (**Figure 1C**).

Morphology of the Adhesive Setae

Using SEM on partly shaved pretarsi showed highly ordered regular arrangement of the setae of the scopulae. The single setae are densely covered with branching microtrichia. In the uppermost 30 µm of the seta, its shape appears flatter and the density of microtrichia increases, especially on the ventral side facing the substrate upon contact (**Figure 2A**). The distance between the seta tips amounts to 10–15 µm (**Figure 2B**). On the ventral side, the microtrichia of the tip regions consist of less than 1 µm thick narrowing stalks with flattened ends, the spatulae, that are responsible for building up contact with the substrate and generating adhesion force (**Figure 2C**). No spatulae were found on the dorsal sides of the setae. In the SEM, after some exposure to the electron beam, the previously separated spatulae attracted each other and congregated.

Seta Adhesion at Different Contact Angles

The individual setae used for the force measurements were plucked from the mid-region of the scopula. The three randomly selected setae clearly showed different curvatures and tip shapes (**Figures 3A–C**). For the determination of a significant angle for the measurements of adhesion on different substrates, the adhesion forces of the individual setae were measured at different contact angles with smooth glass (**Figures 3D–F**, **4**). Seta 1 showed increasing adhesion with decreasing contact angles. With 412 ± 15 nN (mean ± standard deviation; n = 12 measurements), adhesion was highest at an angle of 38°. However, because of the curvature of the seta, this angle could only be reached at the edge of the glass substrate. Therefore, the naturally more realistic angle of 45° was used for the further measurements. The measurements of adhesion for seta 2 showed a peak force of 277 ± 13 nN at approximately 61°, a smaller peak of 187 ± 16 nN at 72°, and constantly high values between 232 ± 10 nN and 319 ± 7 nN in the range from 83° to 97°. Here, the angle of 85° close to the force maximum was selected for the further measurements. The adhesion values of seta 3 did not vary as much as those of setae 1 and 2 and they were in the range between 120 ± 11 nN and

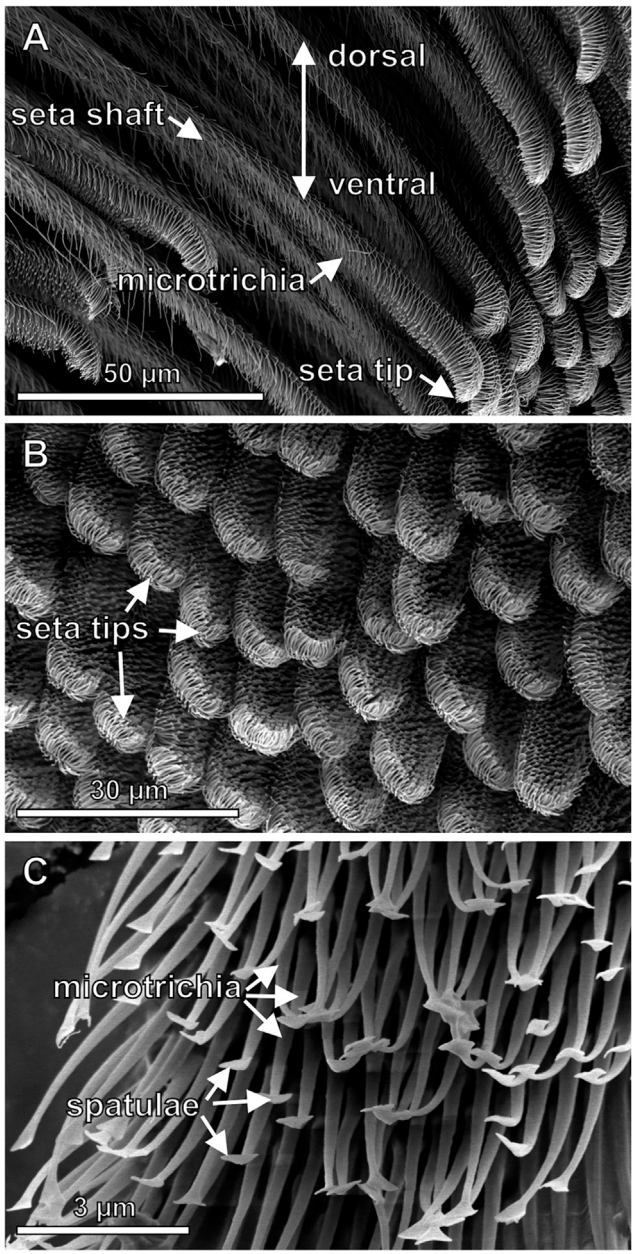

FIGURE 2 | Scanning electron micrographs of the fine structures of the adhesive setae **(A)** Side view of the setae consisting of the up to 1.8 mm long hair shaft (not shown in full length) and the tip region with differently shaped microtrichia. Differences of the shapes of the tips are noticeable **(B)** Top view of the ventral pretarsal scopula surface. At the end of the setae there are densely arranged spatula-shaped microtrichia contacting a substrate surface during locomotion **(C)** Higher magnification image of the spatula-shaped microtrichia in the tip region.

179 ± 6 nN at angles from 49° to 80°. The lowest adhesive force of 99 ± 8 nN was measured at an angle of 85°. At higher angles, adhesion increased again, and 88° was chosen for the measurements on different substrates (**Figure 4**).

Seta Adhesion to Surfaces With Different Surface Energies

Substrate Surface Properties

The *rms* roughness values for the four smooth substrates were 0.006 ± 0.002 µm for the glass, 0.131 ± 0.011 µm for the epoxy resin mold of the glass surface, 0.002 ± 0.001 µm for the silicon, and 0.014 ± 0.001 µm for the PTFE surface (mean values ± standard deviations of measurements on five different areas of the substrates).

The contact angles of water on the different smooth substrates indicated the strongest hydrophilicity for the glass surface with a contact angle of 31.9 ± 11.6° (mean ± standard deviation; $n = 10$). The epoxy resin and silicon surfaces were slightly hydrophilic with contact angles of 85.2 ± 1.6°, and 84.9 ± 4.6°, respectively. The PTFE surface showed hydrophobic properties with a contact angle of water of 103.9 ± 3.8°.

The surface energies calculated from the contact angles of the different liquids showed the highest value for the hydrophilic glass surface with a total of 59.24 J m^{-2} dominated by a polar share of 44.13 J m^{-2} (74.5%), and a disperse share of 15.11 J m^{-2} (25.5%). The total values of the surface energy and the distribution of its shares were similar for the epoxy resin and the silicon surface. The values for the epoxy resin were 30.33 J m^{-2} dominated by a disperse share of 25.26 J m^{-2} (83.3%), and a polar share of 5.07 J m^{-2} (16.7%). The surface energy of the silicon surface was 28.45 J m^{-2} with a disperse share of 22.70 J m^{-2} (79.8%) and a polar share of 5.75 J m^{-2} (20.2%). The lowest value of surface energy was found for the hydrophobic PTFE with 18.07 J m^{-2} as the sum of 16.61 J m^{-2} (91.9%) disperse and 1.46 J m^{-2} (8.1%) polar shares (**Figure 5A**).

Adhesion Forces on Smooth Substrates With Different Surface Energies

The highest adhesive force of the setae was measured on the glass with 263 ± 86 nN (mean ± standard deviation; $N = 3$ setae, $n = 108$ measurements) and a median value of 262 nN. The mean adhesion force on the epoxy resin surface was 156 ± 56 nN and a median of 142 nN; that to the silicon amounted to 174 ± 61 nN and a median of 188 nN. The weakest adhesion was found on the PTFE substrate with 82 ± 53 nN (median 81 nN). A box plot of the results is shown in **Figure 5B**. Kruskal-Wallis one way analysis of variance (ANOVA) on ranks indicated very high statistically significant difference ($p < 0.001$) of the adhesion values between the substrates. An all pairwise multiple comparison procedure (Tukey test) of the data on a significance level of $p < 0.05$ yielded significant differences between all the surfaces except for silicon and the epoxy resin. **Figures 5C,D** clearly show increasing seta adhesion with increasing polarity of the substrates and no or little influence of the disperse shares. Correlation statistics for the influence of relative humidity using the Spearman method gained a not significant p value of 0.0992 for all measurements, which were performed in a humidity range between 31 and 58.7%.

Seta Adhesion on Substrates With Different Roughness

Morphology and Roughness of the Test Substrates

The surface P0 (glass mold) was smooth. The white light interferometric height maps showed increasing grain sizes,

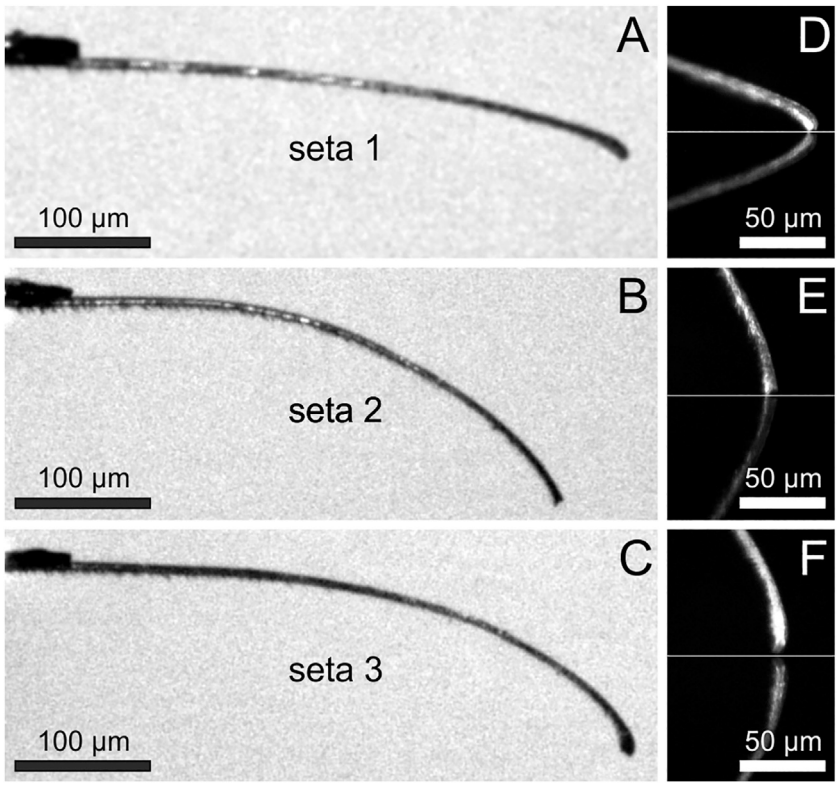

FIGURE 3 | (A–C) Individual adhesive setae in side view fixed to the force sensing cantilevers (top left). Note the different curvatures and tip shapes of the setae taken randomly from the center of the pretarsal scopula **(D–F)** Tip regions of the setae shown in **(A–C)** adhering to a glass surface (marked by the white horizontal lines) at the angles used for the measurements on different substrates. Below the white lines, the mirror images of the setae are visible. The angles of the most distal 20 µm of the setae with the glass surface were measured to be 44.8° for seta 1, 85.1° for seta 2, and 88.4° for seta 3.

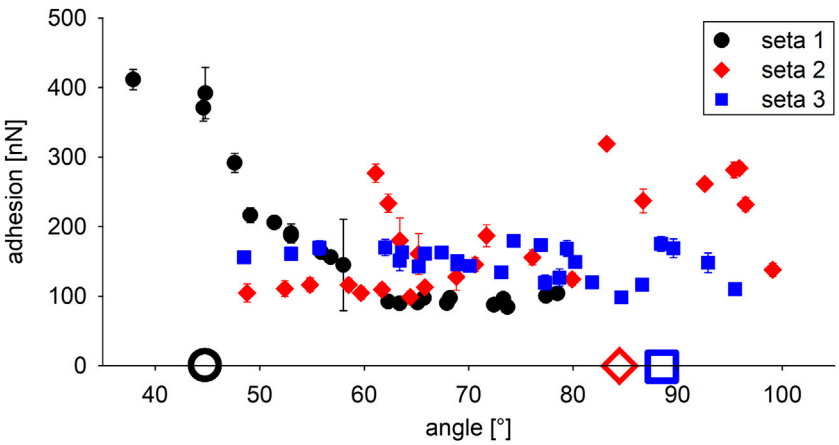

FIGURE 4 | Adhesion of the three different attachment setae at different angles with the glass substrate. The full symbols show mean values ± standard deviation of 12 measurements each. The large open symbols on the *x*-axis indicate the angles of the individual setae shown in **Figures 3D–F** chosen for the further measurements on different substrates.

height differences, and irregularities of the surface structures from P0.05 to P12 (molds of polishing papers). Small granules were visible in the molds of the polishing papers P3, P9, and P12 in addition to the larger asperity structures. The shapes of the grains of the sand paper molds SP1 and SP2 were more distinct. In SP2 the grains were larger compared to those in SP1 and

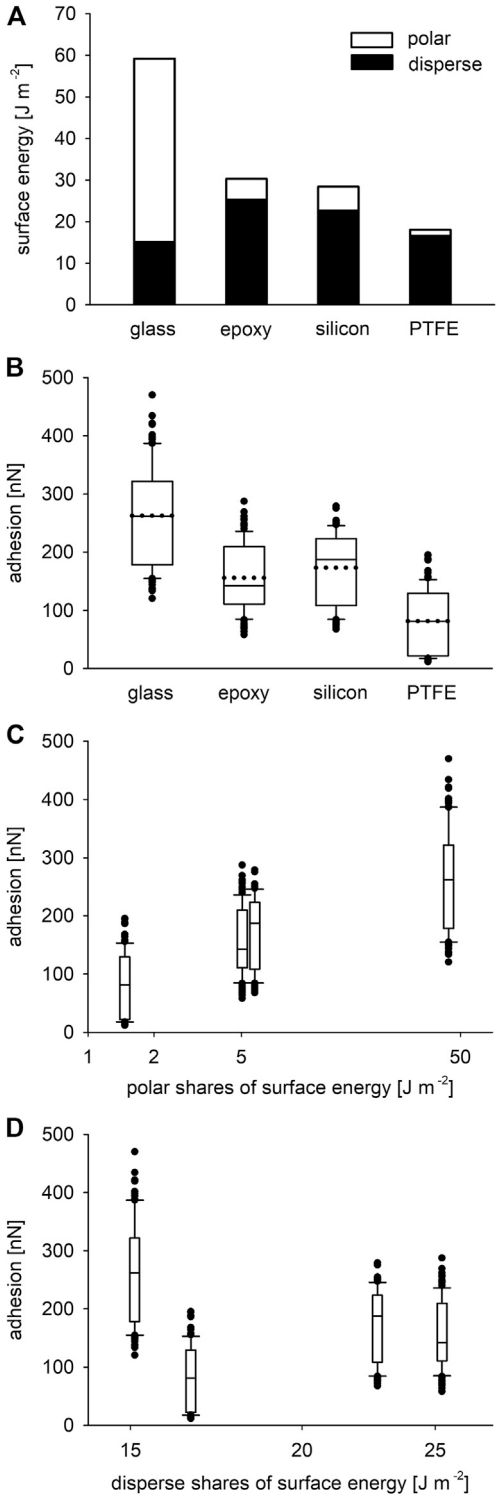

FIGURE 5 | (A) Summed up disperse and polar shares of the surface energies of the four tested smooth substrates (mean values from 10 measurements each). **(B)** Adhesion force of the three adhesive setae on the four smooth substrates after 500 nN loading perpendicular to the surfaces. The boxes show the 25th and 75th, and the whiskers the 10th and the 90th percentiles of the data. The solid horizontal lines inside the boxes indicate the median values, the dotted horizontal lines the mean values of the data. The dots represent outliers (N = 3 setae, n = 108 measurements for each surface). **(C)** Same adhesion force data as in **(B)** plotted over the polar shares of the surface energies of the substrates shown in **(A)**. **(D)** Adhesion force plotted over the disperse shares of the surface energies of the substrates in **(A)**. The x-axes of **(C, D)** are scaled logarithmically.

highest in comparison to all other samples. The sand paper mold SP3 showed the highest degree of irregularity having smaller but more densely arranged grains of different shapes (**Figure 6**). The mean *rms* roughness values of these nine different rough substrate surfaces are plotted in **Figure 7A**.

Adhesion Forces on Different Rough Substrates

Adhesive forces of individual setae considerably differed on all tested surfaces and no general trend is indicated by the data (**Figure 7B**). For seta 1, the mean values of adhesion force were the highest on all substrates except for P3. For seta 1, there was a trend toward stronger adhesion to surfaces with increasing *rms* roughness up to 533 ± 249 nN (n = 36) on substrate SP3. In addition, the standard deviations increased with increasing mean values of adhesion force. Adhesion values obtained for seta 2 were generally lower (<200 nN) than those of seta 1. Seta 2 did not show any trend of adhesion force on the differently rough substrates, with mean values between 67 ± 31 nN on substrate P12 and 160 ± 48 nN on substrate P3. Adhesion forces of seta 3 were the lowest on all substrates with the minimum values of 34 ± 13 nN on the relatively smooth substrate P1 and 34 ± 16 nN on the rough SP2. The maximum value of 100 ± 24 nN was measured on the smooth substrate P0. Without considering the individual setae, a statistical comparison of all pooled values using a pairwise t-test and a Tukey HSD test indicated that the adhesion force on the substrates P0.05 and SP2 was significantly lower than on all other substrates and significantly higher on SP3.

DISCUSSION

The examination of the general morphology of the pretarsus of *Cupiennius salei* in the present study showed the claws and the two lobed claw tufts of scopula setae. This finding confirms those of previous authors (Wolff and Gorb, 2013; Labarque et al., 2017). It enables the spider to use the specific attachment mechanism dependent on the geometry and the mechanical properties of the substrate. The claws are assumed to enable clamping on soft or very rough surfaces, whereas the adhesive setae are used for adhesion to smoother and hard surfaces (**Figures 1B,C**). The setae themselves are covered with differently shaped microtrichia. The microtrichia with pointed tips along the shaft can be interpreted as spacers similar to those of other spider species (Eggs et al., 2015) and avoid that the setae to stick to each other. The increased density of the spatula-shaped microtrichia in the tip region and their arrangement toward the substrate make them well suited to make contact with a surface during locomotion. This hierarchical structure of the pretarsal attachment system of spiders is different from the structure of fibrillary adhesive systems of insects, e.g. in

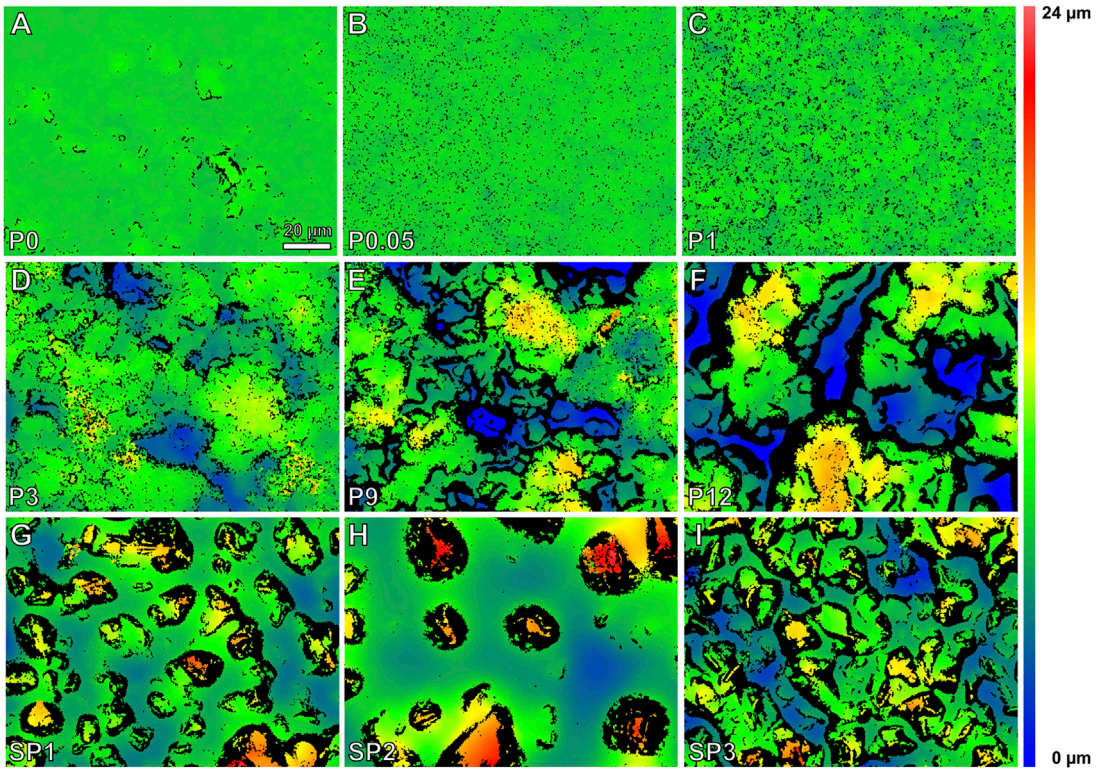

FIGURE 6 | (A–I) White light interferometric height maps of the tested epoxy resin surfaces with increasing *rms* roughness.

beetles and earwigs, which are made up of shorter, unbranched setae on the tarsi (Haas and Gorb, 2004; Gilet et al., 2018).

On the smooth substrates with different surface energy, the setae adhered best to the glass, which also exhibited the highest hydrophilicity and a highest amount the polar shares of surface energy (**Figure 5**). For adhesion, the polar shares are responsible for hydrogen bonds between two materials. The disperse shares result in attractive van der Waals forces (Autumn et al., 2002). On the epoxy resin and the silicon surface that are only slightly hydrophilic and for which the amount of disperse shares of surface energy are similarly high, the adhesive force of the setae dropped down to approximately two thirds of that on glass. On the hydrophobic and non-polarizable PTFE substrate, the adhesive forces of the setae was lowest and approximately 30% of those on glass.

For the gecko seta, it has been shown that its adhesion purely relies on van der Waals forces, because the adhesive forces were the same on polarizable hydrophilic and hydrophobic substrates and confirmed the model prediction (Autumn et al., 2002). For a single Gecko spatula, however, adhesion increased with increasing relative air humidity and substrates with increasing hydrophilicity (Huber et al., 2005), and the authors suggested monolayers of water being adsorbed between the spatulae and the substrate leading to additional capillary forces. For the spider setae, here we show stronger adhesion on the hydrophilic glass surface with a high polar share of surface energy, which makes the influence of thin layers of water on the adhesion strength likely. For different spider species with scopulae, the capillary forces between the thin water layer on a substrate and the scopula hairs were found to be most important for their adhesion (Homann, 1957). On the polarizable epoxy resin and the silicon substrate, which mainly exhibit disperse shares of surface energy, the adhesion of the spider setae is still fair. Together with the presence of adhesive force on the hydrophobic non-polarizable PTFE substrate, these findings lead to the conclusion that a combination of van der Waals forces and hydrogen bonds between polar substrates and the spatulae is responsible for the adhesion of the attachment setae of *Cupiennius salei* on substrates with different surface energies. Capillary forces may also play an important role especially at higher relative humidity, because it has been shown that the shear adhesion of the spider *Philodromus dispar* on an epoxy resin substrate was highest at a relative humidity of 60% (Wolff and Gorb 2012b).

The tests for seta adhesion on differently rough surfaces were performed on the same material of epoxy resin molds to avoid different chemistry of the substrates. The small adhesion forces of the setae to the P0.05 substrate likely result from its *rms* roughness of 396 nm and the size of the spatulae. This roughness may be too small for the single spatulae to form proper contact. For the reduced adhesion to the SP2 surface, the interplay between the substrate morphology and the seta size likely is the limiting factor. The grains on the SP2 substrate appear

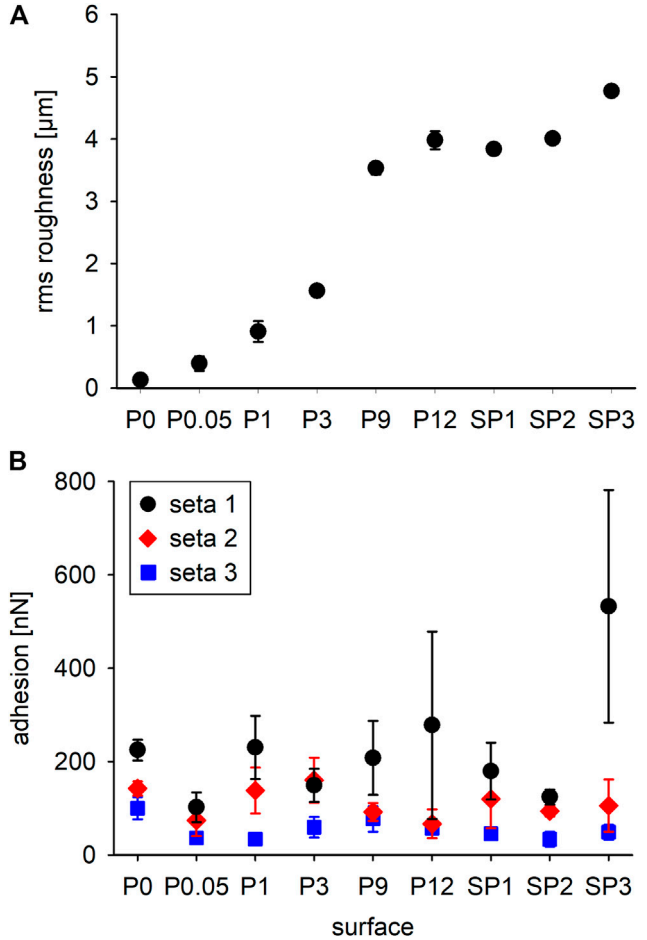

FIGURE 7 | (A) Mean root mean square roughness (± standard deviations; n = 5 measurements on different spots of each sample) of the different tested epoxy resin surfaces shown in **Figure 6**. P0 is the mold of a glass surface, P0.05–P12 are the molds of polishing papers, and SP1–SP3 are the molds of different sand papers. **(B)** Adhesion forces of individual setae (mean values ± standard deviations; 36 measurements each) on different rough surfaces after 500 nN perpendicular loading.

spherically shaped and spread on a rather flat surface. For an approaching seta, it is crucial whether it hits a grain and which aspect of the seta tip – the one with or the one without the spatula – gets in contact on top or at the edges of the grain. If the seta tip makes contact with its spatula-free side at the edges of the grains, adhesion forces will be low. It can be assumed that the surface morphology of the SP2 substrate strongly inhibits proper contact making of the spatulae. The statistically significantly increased adhesion value of the setae on the roughest substrate SP3 results from the high adhesion force of the seta 1. Both seta 2 and seta 3 on SP3 do not show values higher than on other substrates. The obvious different adhesion of different setae to the substrates with different roughness indicates that most likely the tip shape and the distribution of the spatulae plays the key role for the attachment of the individual setae. Neighboring setae plucked from the center of the claw tuft scopula showed four different tip shapes and arrangements of the tip microtrichia in four randomly selected setae (**Figure 8A**).

Shear force applied on an already attached seta, however not sliding the seta, was shown to largely increase the pull-off force from 3.6 µN up to 25 µN by the alignment of a large number of spatulae with a smooth glass surface (Flenner et al., 2020). In the present study, no shear force was applied on the three individual tested setae. Therefore, we measured the result of the arrangement of the spatulae, which spontaneously aligned with the substrate structures upon contact. For such an adhesive behavior, the tip shapes and the arrangement of the microtrichia and spatulae of the seta is crucial for the adhesive force generation. The tip shapes of the three individual tested setae clearly differed (**Figures 8B–D**), as most likely did the arrangement of the spatulae. As can be seen in **Figure 4**, adhesion on glass greatly differed at different contact angles of the setae. The mostly higher adhesion forces of seta 1 at the angle of 45° may be the result of the orientation of the spatula-rich side of the seta toward the structural features of the rough substrates. The higher number of the flexible microtrichia and spatulae are more likely to find proper surface features to attach. For seta 2 and seta 3, the angles of 85°, and 88°, respectively, were also selected within ranges of high adhesion for the respective setae. However, their adhesion on differently rough surfaces was low compared to that of seta 1. For seta 2, at the chosen angle of 85°, likely only the microtrichia next to the tip contacted the substrate with their sides. This lead to alignment and adhesion of a smaller number of spatulae and less adhesive force compared to seta 1. Seta 3 showed the lowest adhesion on the differently rough epoxy resin surfaces. Considering the angle of 88° chosen for the measurements and the rounded shape of the tip, it appears likely that seta 3 contacted the surface with the backbone and not with the ventral side, rich in spatula-shaped microtrichia, which resulted in reduced attachment forces.

Even when taking the highest adhesive value of 830 nN into account and assuming that all 18,800 setae (~2,350 per leg; Wolff and Gorb, 2012c) of the spider were in contact with a substrate, the resulting adhesive force of approximately 16 mN could not support the body weight (~3.6 g) of an adult female spider. Since *Cupiennius salei* easily climbs vertical surfaces and is able to walk upside-down also on smooth surfaces, there must be mechanisms of adhesion other than those examined in the single setae in the present study. Interestingly, the adhesive setae are not rigidly fixed in the pretarsal cuticle. In the natural situation, the movability of the setae toward the substrate is strictly limited by a stopper-like structure of the basal hair shaft directly at the insertion of the seta in its socket (**Figure 9**). This stopper keeps the position of the seta fixed in its position in the socket at dorsad movements of the claw tuft to facilitate pulling-off. On the dorsal (distal) side of the socket, however, there is some space that allows a seta deflection by approximately 6–7° when placed onto a substrate. In our experiments, the setae were well fixed to the stiff silicon cantilevers. In the natural situation, the flexibility of the seta suspension in the pretarsal cuticle may help each individual seta of the claw tuft to find better contact with the structural features of the substrate and consequently a good place to adhere. This movability of the setae also supports their

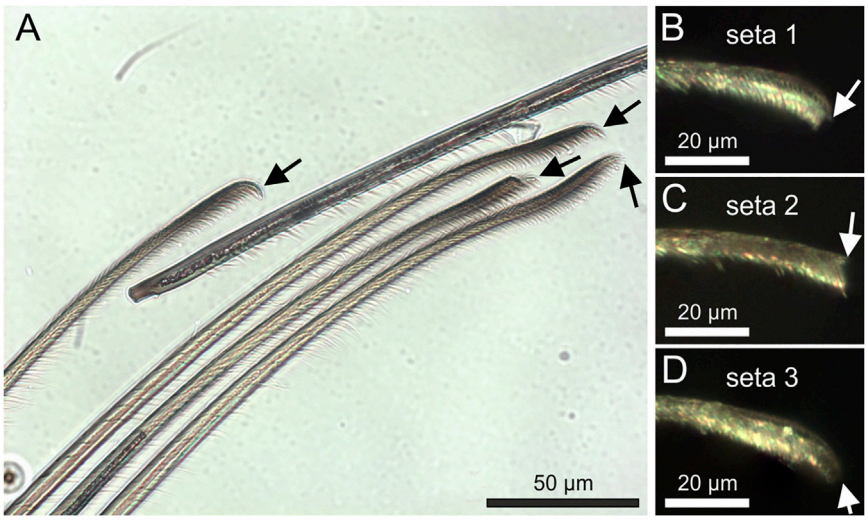

FIGURE 8 | (A) Transmitted light microscopic side view of a bunch of neighboring attachment setae plucked from the center of the pretarsal scopula. Different tip shapes (arrows) are clearly visible **(B–D)** Reflected light microscopic images of the tips of the setae used for the adhesion measurements in the experimental setup. The arrows point to the tips of the seta backbone.

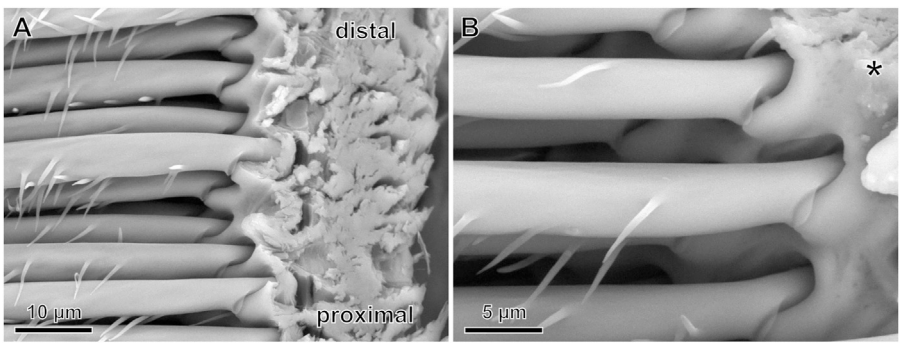

FIGURE 9 | SEM images of the bases of pretarsal adhesive setae and their insertion into the cuticle in a vertically dissected exuvia cuticle. **(A)** On the left are the most proximal parts of the adhesive setae. At their insertion in the cuticle, the hair shaft is narrowed and a stopper-like structure is situated on the ventral (lower) aspect. Distal and proximal refer to the arrangement the claw and the leg. **(B)** Magnified cuticle insertion region of the setae. The asterisk exemplary marks the pivot point of a seta for dorsad (upward) deflections.

shearing in order to bring more adhesive spatulae in contact with the substrate (see Flenner et al., 2020), which likely resulted in the better adhesion of *Cupiennius*, when opposing leg pairs were in contact with the ground at pulling-off the whole spider (Wohlfart et al., 2014). Considering the previously measured 25 µN adhesive force of a single attachment seta preloaded in shear, 1,400 setae in contact (which is less than two thirds of the setae of a single leg) would suffice for an adult female *Cupiennius salei* to adhere on smooth glass. Interestingly, adhesion of the whole scopula claw tuft was zero at vertical pulling-off even after shearing (Wolff and Gorb, 2013; Wohlfart et al., 2014). In the present study the single setae did show adhesive forces at vertical pulling-off on all the different substrates tested. These results indicate that the specific movements of the individual setae of the claw tuft may be most important for making adhesive contact with the substrate.

The results of the present study indicate a distribution of different adhesive tip shapes of the adhesive setae, which likely represents an adaptation of the spider attachment system for efficient interaction with substrates of different roughness. The cuticle of *Cupiennius salei* has been reported to have an effective Young's modulus of 18 GPa (Blickhan and Barth, 1985). For the individual seta, the specific structural arrangement of the mechanically stiffer dorsal seta backbone (Schaber et al., 2019) and the softer ventral "brush" of spatula-shaped microtrichia is crucial for adhesion at certain angles with the substrate. It can be assumed that the individual morphology of each individual seta and its position within the scopula orchestration are optimized for maximal adhesion on natural substrates with many different properties as found in the habitat of the spider.

The individual variability of the morphology of the spider attachment setae, which is strongly interdigitated with their adhesive performance, has been shown here for the first time. Furthermore, we reveal the importance of examining the relevant different length and force scales for understanding the functionality of specific structures in the entire adhesive system of the spider. This knowledge can lead to new bioinspired materials with outstanding properties such as nanostructured reversible residue-free dry adhesives e.g. based on cellulose nanofibers (Schaber et al., 2018), carbon nanotubes (Bhushan et al., 2008; Schaber et al., 2015a; Schaber et al., 2015b; Su et al., 2020; Yang et al., 2020) or other polymeric materials (Xue et al., 2012; Pattantyus-Abraham et al., 2013; Xue et al., 2013; Borodich and Savencu 2017; Di Tan et al., 2020).

DATA AVAILABILITY STATEMENT

The raw data supporting the conclusions of this article will be made available by the authors, without undue reservation.

AUTHOR CONTRIBUTIONS

CS and SG conceived of the research. CS and BP designed the experiments. BP conducted the experiments and analyzed the data. BP, CS, and SG interpreted the data. BP wrote the first draft. CS edited the draft and wrote the manuscript. SG and CS revised the manuscript. All authors read and approved the final manuscript.

FUNDING

Funding was provided by the Deutsche Forschungsgemeinschaft (DFG grant GO 995/38-1).

ACKNOWLEDGMENTS

We thank Lea Schäfer for the preparation of the epoxy resin molds and collection of white light interferometric data and Tobias Bols for help with SEM images.

REFERENCES

Autumn, K., Liang, Y. A., Hsieh, S. T., Zesch, W., Chan, W. P., Kenny, T. W., et al. (2000). Adhesive Force of a Single Gecko Foot-Hair. *Nature* 405, 681–685. doi:10.1038/35015073

Autumn, K., Sitti, M., Liang, Y. A., Peattie, A. M., Hansen, W. R., Sponberg, S., et al. (2002). Evidence for van der Waals adhesion in gecko setae. *Proc. Natl. Acad. Sci.* 99, 12252–12256. doi:10.1073/pnas.192252799

Barth, F. G. (2002). *A Spider´s World: Senses and Behavior*. Berlin: Springer. doi:10.1007/978-3-662-04899-3

Bhushan, B., Galasso, B., Bignardi, C., Nguyen, C. V., Dai, L., and Qu, L. (2008). Adhesion, Friction and Wear on the Nanoscale of MWNT Tips and SWNT and MWNT Arrays. *Nanotechnol.* 19, 125702. doi:10.1088/0957-4484/19/12/125702

Blickhan, R., and Barth, F. G. (1985). Strains in the Exoskeleton of Spiders. *J. Comp. Physiol.* 157, 115–147. doi:10.1007/bf00611101

Borodich, F. M., and Savencu, O. (2017). "Hierarchical Models of Engineering Rough Surfaces and Bio-Inspired Adhesives," in *Bio-inspired Structured Adhesives, 179–219*. Editors L. Heepe and L. Xue (Basel: Springer International).

Eggs, B., Wolff, J. O., Kuhn-Nentwig, L., Gorb, S. N., and Nentwig, W. (2015). Hunting without a Web: How Lycosoid Spiders Subdue Their Prey. *Ethol.* 121, 1166–1177. doi:10.1111/eth.12432

Flenner, S., Schaber, C. F., Krasnov, I., Stieglitz, H., Rosenthal, M., Burghammer, M., et al. (2020). Multiple Mechanical Gradients Are Responsible for the strong Adhesion of Spider Attachment Hair. *Adv. Mater.* 32, 2002758. doi:10.1002/adma.202002758

Gilet, T., Heepe, L., Lambert, P., Compère, P., and Gorb, S. N. (2018). Liquid Secretion and Setal Compliance: the Beetle's Winning Combination for a Robust and Reversible Adhesion. *Curr. Opin. Insect Sci.* 30, 19–25. doi:10.1016/j.cois.2018.08.002

Gorb, S. N., and Heepe, L. (2017). "Biological Fibrillar Adhesives: Functional Principles and Biomimetic Applications," in *Handbook of Adhesion Technology*. Editors L. da Silva, A. Öchsner, and R. Adams (Cham: Springer).

Haas, F., and Gorb, S. (2004). Evolution of Locomotory Attachment Pads in the Dermaptera (Insecta). *Arthropod Struct. Dev.* 33, 45–66. doi:10.1016/j.asd.2003.11.003

Homann, H. (1957). Haften Spinnen an einer Wasserhaut? *Naturwissenschaften* 44, 318–319. doi:10.1007/bf00630926

Huber, G., Mantz, H., Spolenak, R., Mecke, K., Jacobs, K., Gorb, S. N., et al. (2005). Evidence for Capillarity Contributions to Gecko Adhesion from Single Spatula Nanomechanical Measurements. *Proc. Natl. Acad. Sci.* 102, 16293–16296. doi:10.1073/pnas.0506328102

Kesel, A. B., Martin, A., and Seidl, T. (2003). Adhesion Measurements on the Attachment Devices of the Jumping Spider *Evarcha Arcuata*. *J. Exp. Biol.* 206, 2733–2738. doi:10.1242/jeb.00478

Kesel, A. B., Martin, A., and Seidl, T. (2004). Getting a Grip on Spider Attachment: an AFM Approach to Microstructure Adhesion in Arthropods. *Smart Mater. Struct.* 13, 512–518. doi:10.1088/0964-1726/13/3/009

Labarque, F. M., Wolff, J. O., Michalik, P., Grisworld, C. E., and Ramírez, M. J. (2017). The Evolution and Function of Spider Feet (Araneae: Arachnida): Multiple Acquisitions of Distal Articulations. *Zool J. Linn. Soc-lond*, 181, 308–341. doi:10.1093/zoolinnean/zlw030

Niederegger, S., and Gorb, S. N. (2006). Friction and Adhesion in the Tarsal and Metatarsal Scopulae of Spiders. *J. Comp. Physiol. A.* 192, 1223–1232. doi:10.1007/s00359-006-0157-y

Pattantyus-Abraham, A., Krahn, J., and Menon, C. (2013). Recent Advances in Nanostructured Dry Adhesives. *Front. Bioeng. Biotechnol.* 1, 22. doi:10.3389/fbioe.2013.00022

Rizzo, N. W., Gardner, K. H., Walls, D. J., Keiper-Hrynko, N. M., Ganzke, T. S., and Hallahan, D. L. (2006). Characterization of the Structure and Composition of Gecko Adhesive Setae. *J. R. Soc. Interf.* 3, 441–451. doi:10.1098/rsif.2005.0097

Schaber, C. F., Filippov, A. E., Heinlein, T., Schneider, J. J., and Gorb, S. N. (2015b). Modelling Clustering of Vertically Aligned Carbon Nanotube Arrays. *Interf. Focus.* 5, 20150026. doi:10.1098/rsfs.2015.0026

Schaber, C. F., Flenner, S., Glisovic, A., Krasnov, I., Rosenthal, M., Stieglitz, H., et al. (2019). Hierarchical Architecture of Spider Attachment Setae Reconstructed from Scanning Nanofocus X-ray Diffraction Data. *J. R. Soc. Interf.* 16, 20180692. doi:10.1098/rsif.2018.0692

Schaber, C. F., Heinlein, T., Keeley, G., Schneider, J. J., and Gorb, S. N. (2015a). Tribological Properties of Vertically Aligned Carbon Nanotube Arrays. *Carbon* 94, 396–404. doi:10.1016/j.carbon.2015.07.007

Schaber, C. F., Kreitschitz, A., and Gorb, S. N. (2018). Friction-active Surfaces Based on Free-Standing Anchored Cellulose Nanofibrils. *ACS Appl. Mater. Inter.* 10, 37566–37574. doi:10.1021/acsami.8b05972

Su, Y. L., Hou, X. Y., Jiang, S. Y., Li, M., Liu, Y. M., Yang, Z., et al. (2020). Adhesion Properties of Carbon Nanotube Arrays for an Adhesive Foot of a Space Crawling Robot. *Smart Mater. Struct.* 29, 025001. doi:10.1088/1361-665x/ab5ad4

Tan, D., Luo, A., Wang, X., Shi, Z., Lei, Y., Steinhart, M., et al. (2020). Humidity-modulated Core-Shell Nanopillars for Enhancement of Gecko-Inspired Adhesion. *ACS Appl. Nano Mater.* 3, 3596–3603. doi:10.1021/acsanm.0c00314

Wohlfart, E., Wolff, J. O., Arzt, E., and Gorb, S. N. (2014). The Whole Is More Than the Sum of All its Parts: Collective Effect of Spider Attachment Organs. *J. Exp. Biol.* 217, 222–224. doi:10.1242/jeb.093468

Wolff, J. O., and Gorb, S. N. (2013). Radial Arrangement of Janus-like Setae Permits Friction Control in Spiders. *Sci. Rep.* 3, 1101. doi:10.1038/srep01101

Wolff, J. O., and Gorb, S. N. (2012c). Comparative Morphology of Pretarsal Scopulae in Eleven Spider Families. *Arthropod Struct. Dev.* 41, 419–433. doi:10.1016/j.asd.2012.04.004

Wolff, J. O., and Gorb, S. N. (2012a). Surface Roughness Effects on Attachment Ability of the Spider *Philodromus Dispar* (Araneae, Philodromidae). *J. Exp. Biol.* 215, 179–184. doi:10.1242/jeb.061507

Wolff, J. O., and Gorb, S. N. (2012b). The Influence of Humidity on the Attachment Ability of the Spider *Philodromus Dispar* (Araneae, Philodromidae). *Proc. R. Soc. B.* 279, 139–143. doi:10.1098/rspb.2011.0505

Xue, L., Steinhart, M., and Gorb, S. N. (2013). "Biological and Bioinspired Micro- and Nanostructured Adhesives," in *Biomaterials Surface Science, 409–439*. Editors A. Taubert, J. F. Mano, and J. C. Rodriguez-Cabello (Weinheim: Wiley VCH).

Xue, L., Kovalev, A., Thöle, F., Rengarajan, G. T., Steinhart, M., and Gorb, S. N. (2012). Tailoring normal Adhesion of Arrays of Thermoplastic, spring-like Polymer Nanorods by Shaping Nanorod Tips. *Langmuir* 28, 10781–10788. doi:10.1021/la3020354

Yang, X., Chen, L., Zhang, P., Zhong, H., Zhang, Y., Zhang, R., et al. (2020). Investigation of the Relationship between Adhesion Force and Mechanical Behavior of Vertically Aligned Carbon Nanotube Arrays. *Nanotechnol.* 31, 295701. doi:10.1088/1361-6528/ab85ed

Conflict of Interest: The authors declare that the research was conducted in the absence of any commercial or financial relationships that could be construed as a potential conflict of interest.

frontiers in Mechanical Engineering

ORIGINAL RESEARCH
published: 24 June 2021
doi: 10.3389/fmech.2021.667857

Perspective for a New Bioinspired Permanent Adhesive for dry Conditions - Insights in the Glue Producing Japanese art of Defence System of the Oita Salamander *Hynobius dunni*

Janek von Byern [1,2], Robert Farkaš [3], Daniel Steinort [4], Sophie Greistorfer [2], Margret Eckhard [2] and Norbert Cyran [5]*

[1]Austrian Cluster for Tissue Regeneration, Ludwig Boltzmann Institute for Experimental and Clinical Traumatology, Vienna, Austria, [2]Department of Evolutionary Biology, Unit Integrative Zoology, University of Vienna, Vienna, Austria, [3]Laboratory of Developmental Genetics, Biomedical Centre, Institute of Experimental Endocrinology, Slovak Academy of Sciences, Bratislava, Slovakia, [4]Birkhahnweg, Bottrop, Germany, [5]Faculty of Life Science, Core Facility Cell Imaging and Ultrastructure Research, University of Vienna, Vienna, Austria

OPEN ACCESS

Edited by:
Ken Nakano,
Yokohama National University, Japan

Reviewed by:
T V V L N Rao,
Madanapalle Institute of Technology and Science (MITS), India
Yoshitaka Nakanishi,
Kumamoto University, Japan

***Correspondence:**
Janek von Byern
vByern@freenet.de

Specialty section:
This article was submitted to Tribology, a section of the journal Frontiers in Mechanical Engineering

Received: 14 February 2021
Accepted: 09 June 2021
Published: 24 June 2021

Citation:
von Byern J, Farkaš R, Steinort D, Greistorfer S, Eckhard M and Cyran N (2021) Perspective for a New Bioinspired Permanent Adhesive for dry Conditions - Insights in the Glue Producing Japanese art of Defence System of the Oita Salamander Hynobius dunni. Front. Mech. Eng 7:667857. doi: 10.3389/fmech.2021.667857

Novel medical bioadhesives are proposed to fulfil numerous ideals as being biocompatible, non-toxic, include tissue healing and regeneration characteristics, have high mechanical properties onto different surfaces and other important key features. Mussel-inspired adhesives have provided the basis for many new applications under wet conditions. In contrast, the defence secretion system in amphibians may provide potential for novel fast-curing secretion able to adhere to surfaces under dry conditions. With the microanatomical and histochemical characterization of the endemic Japanese Oita salamander *Hynobius dunni* details on its anatomical organization, the nature of the chemical composition of both glue-producing glands and its divergence to the other well-characterized species *Plethodon shermani* are discussed. The study shows that the cutaneous glands of both glue-producing salamanders (*H. dunni* and *P. shermani*) exhibit certain morphological and histochemical similarities. Nevertheless, clear differences exist between the two species, especially with regard to the sugar composition of the mucous glands and the pH level of the granular glands. Moreover, the adhesive secretions of *H. dunni* show a clear reactivity to Arnow staining (indicating the presence of L-DOPA), which is lacking in *P. shermani*. This is the first indication of the presence of L-DOPA in the adhesive secretions of a terrestrial vertebrate, which has thus far only been found for marine invertebrates, such as mussels and polychaetes.

Keywords: adhesive system, bonding, L-dopa (L-3, 4-dihydroxyphenylalanine), defence strategy, amphiba

INTRODUCTION

Amphibians have a simple skin arrangement: a thin epidermis with a superficial stratum corneum epithelium, and a thicker two-layered dermis with two types of cutaneous glands in the superficial stratum spongiosum: the mucous glands and granular glands, also named poison glands (Zug et al., 2001). The mucous gland type is usually smaller and more numerous than the granular gland type. It contains a fine-grained material, has a characteristic lumen, and is proposed to secrete mucus to keep the skin moist and facilitate gas exchange. Meanwhile, the granular gland type is filled with granules of different sizes and secretes toxins (Brodie and Gibson, 1969; Sever, 1989; Fontana et al., 2006; Largen and Woodley, 2008). Both gland types are enclosed by melanocytes, connective tissue, and blood vessels. Below these, the second dermis layer, known as the stratum compactum, comprises connective tissue fibres.

However, the anatomical organization of the cutaneous glands and the nature of their chemical substances vary across salamander species and appear to have different functions (Hecker et al., 2003; Fontana et al., 2006; Heiss et al., 2009). The cutaneous mucus mainly plays a role in the control of body surface pH and the maintenance of skin moisture, lubricating the horny layer (Bueno et al., 1981; Hopkins and Migabo, 2010). However, many species also release toxic, noxious, or adhesive cutaneous secretions for defence (Nowak and Brodie, 1978; Brodie et al., 1979; Arnold, 1982; Brodie, 1983; Brodie and Smatresk, 1990; Duellman and Trueb, 1994; Evans and Brodie, 1994). Studies on these glue synthesis and composition in amphibians are rare (Graham et al., 2005, 2006; Tyler, 2010), although the bonding strength (up to 2.8 MPa for the Australian frog genus *Notaden*) is among the highest in the animal kingdom and is comparable with industrial super glues such as cyanoacrylates (Graham, 2005). This strong bonding frog is currently the best studied example of adhesives in amphibians. When provoked by potential predators, *Notaden* secretes a sticky nontoxic material from its dorsal skin (Graham et al., 2006). The secretions transform rapidly into an elastic solid (hydrogel) and adhere tightly to a wide range of materials including glass, plastic, metal, and even Teflon (Graham, 2005). Studies of its glue nature show that, in a dry state, the secretions contain few carbohydrates and consist mainly of proteins (13–400 kDa) (Graham et al., 2013). Graham et al. (2005) indicate that the *Notaden* glue functions rather as a pressure-sensitive adhesive (PSA) than as a more chemical mechanism such as in mussels and barnacles (Kamino et al., 2000; Sagert et al., 2006).

Up to know less is known on the glue composition and its biomechanical properties in salamanders. As *Notaden* these animals use the glue as defence and within seconds upon exposure to air it hardens (Brodie and Gibson, 1969; Williams and Anthony, 1994; von Byern et al., 2017a) and immobilizes large predators as a snake immediately. The adhesive antipredator strategy has only been reported in Salamandroidea species (*Ambystoma* spp. *Plethodon* spp. *Batrachoseps* spp. and *Bolitoglossa* spp.) (Brodie and Gibson, 1969; Williams and Larsen, 1986; Evans and Brodie, 1994) and characterized in more detail in *Plethodon shermani* (Largen and Woodley, 2008; von Byern et al., 2015). In *P. shermani* both cutaneous glands are involved in glue production, suggesting a two-component system involved in glue synthesis (von Byern et al., 2015; von Byern et al., 2017a). The mucous glands are smaller and contain flocculent to granular material consisting of mostly acidic glycoproteins. Meanwhile, the granular glands synthesize differently sized granules, including basic proteinaceous components (von Byern et al., 2015). The adhesive secretions of *P. shermani* are cytocompatible with different cell lines, indicating that toxins are missing in the glue (von Byern et al., 2017b).

The goal of the present study is to histochemically characterize the cutaneous secretions of Cryptobranchoidea salamanders as the japanese genus *Hynobiidae* and compare the results with the data given for *P. shermani* (von Byern et al., 2015). The Japanese Oita salamander *Hynobius dunni* is known to use noxious skin secretions for defence (Brodie, 1977). Unpublished observations by the Austrian breeder Günther Schultschik further indicate that the cutaneous secretions released by *H. dunni* Tago, 1931 during animal handling appear to be adhesive. This species is endemic to Japan, restricted to the Kyushu region (Sugawara et al., 2018), and listed as vulnerable on the IUCN Red List (Stuart et al., 2008). It reaches a total length of 12–13 cm, is coloured dorsally dark greenish-brown, ventrally bluish grey and lighter on the throat (Sparreboom, 2014). The tail is short, thick at the base, and laterally compressed toward the tip (**Figure 1**). The animals occur in secondary forests and bamboo or paddy fields and breed in pools or ponds (Stuart et al., 2008; Sparreboom, 2014). The adhesive cutaneous secretions are released across all body parts, whereby the collectable amount appears to be greater on the tail than on the trunk or head (unpubl. observation by Günther Schultschik). Within this study special emphasis is placed on the morphology of the two cutaneous glands in *H. dunni* and their granular content at the ultrastructural level.

FIGURE 1 | Overview image of *H. dunni*. The animals have a gray-green background color with black dots dorsally and reach a total length up to 16 cm. In their natural habitat on the Japanese Island groups of Shikoku and Kyushu they are listed as "vulnerable" according to the Japanese Amphibian Red List. Image provided by the co-author D.S.

MATERIALS AND METHODS

Three adult specimens of *H. dunni* ($n = 3$) were offspring raised in Germany by the third co-author, who provided them for this study. In Vienna, the animals were housed communally in terrariums with a substrate of moist soil and mulch at a temperature of 18°C, a humidity of 80%, and a dark-light cycle of 12:12 h. They were maintained on a diet of crickets. During cultivation, one specimen died and was immediately fixed for a morphological characterization of the skin gland system. The other two animals remained healthy and are at the time of writing still kept alive for secretion harvesting.

Secretion Collection

To collect the secretions, the animal's legs were gently twitched with a blunt forceps at 1–2 min intervals for 10–15 min while keeping the animal in a large Petri dish, as done previously with *P. shermani* (von Byern et al., 2015). After 5–10 min, the animals started to exude a visible amount of a milky adhesive secretion which bonded on different surfaces (Petri dish glass, Aclar film, metal forceps, wood, and human skin). Shortly after exposure, the glue hardened strongly. This "milking" approach was repeated monthly, giving the animals a resting and recovery phase in between.

Tissue Fixation

For the histochemical analyses and lectin affinity tests, parts of the dorsal and ventral skin of the trunk, tail, and legs were fixed in an acetic-alcohol-formalin (AAF) mixture (Böck, 1989) or in Carnoy's solution (Kiernan, 1999) for 3 h at 25°C.

For the ultrastructural analyses, tissue samples from the head, trunk and tail were immersed for 6 h at 25°C in 2.5% glutardialdehyde with sodium-cacodylate buffer (0.1 M, pH 7.4) and directly frozen in liquid nitrogen.

For fluorescence labelling and lipid characterization, the tissue was fixed in 4% paraformaldehyde (PFA), dissolved in phosphate-buffered saline (PBS; 0.1 M, pH 7.4) for 2 h at 25°C, and subsequently washed three times in PBS. Further details about the follow-up procedures are presented below.

Histochemistry, Lectin Affinity Tests

In the first approach, the isolated glue secretions were collected on glass slides, dried, and directly used for the histochemical characterization and lectin affinity tests. In the case of a positive outcome (in particular for the lectin tests), a morphological allocation towards the two glands was subsequently done using paraffin tissue samples. For this, the Carnoy and AAF-fixed samples were washed several times in 96% EtOH and immersed in methyl benzoate until they had sunk to the vial bottom (von Byern et al., 2015). Subsequently, the tissue samples were deposited first in 100% benzene (5–10 min) and then in a 50: 50 benzene:paraffin mixture overnight before being infiltrated in 100% paraffin for several hours. From each region of interest (dorsal and ventral skin, tail excluding spine and legs), about 500 sections (each 7 µm thick) were cut using a Reichert-Jung 2030 rotary microtome (Co. Reichert-Jung, Germany), mounted on glass slides with Ruyter's solution (Ruyter, 1931), and dried at 37°C before staining.

In the case of lipid characterization, only the PFA-PBS-fixed and vibratome-cut tissue samples (see below) with a thickness of 100 µm were used as the ethanol-fixed samples were considered inappropriate for this staining.

For a general overview of the dermis and its glands, Azan trichrome as well as hematoxylin and eosin (HE) staining were applied. Histochemical tests included the periodic acid-Schiff (PAS) method (McManus and Mowry, 1960) to detect the presence of hexose-containing mucosubstances. Blocking of PAS was done through acetylation for 12 h (Kiernan, 1999). Alcian Blue 8GX (McManus and Mowry, 1960) was used at pH 1.0 (only sulfated mucosubstances) and pH 2.5 (sulfated and carboxylated mucosubstances) for 1 h at 20°C in addition to Toluidine Blue O (in 0.2 M acetate buffer at pH 4.5 according to Mulisch and Welsch (2010)).

Basic proteins were detected through Biebrich Scarlet (0.04%) for 30 min at 20°C in a phosphate buffer at pH 6.0 (Spicer and Lillie, 1961) and in Laskey's glycine buffer at pH 8.5, 9.5, and 10.5 (McManus and Mowry, 1960) (all chemicals supplied by Co. Sigma–Aldrich, United States).

Calcium was determined by Alizarin Red S (Kiernan, 1999) and von Kossa staining (Sheehan and Hrapchack, 1980).

To verify the presence of L-3,4-dihydroxyphenylalanine (L-DOPA) containing proteins in the *H. dunni* glue, isolated secretions and paraffin sections were stained according to Arnow's (1937) protocol. Samples from the tube-dwelling polychaete *Sabellaria alveolata* were used as positive control (Becker et al., 2012).

Sudan Black B (Böck, 1989) was used to first visualize lipids in the secreted glue before repeating the staining with the vibratome slides.

Sugar moieties were characterized using 24 different lectins (all supplied by Co. Vector Laboratories Inc., United States). A summary of all tested lectins and their sugar moieties affinities can be found in **table 1**. In the present study, dried glue samples of *P. shermani* from a previous study (von Byern et al., 2015) were likewise re-examined for all 24 lectins.

All lectins were diluted to a final concentration of 50 mg/ml in 0.1 M PBS (pH 7.4, mixed with 1% Triton X and 5% bovine serum albumin). Initially, the dried glue samples collected on glass slides were investigated. For this, the samples were rinsed three times (for 20 min each time) in 0.1 M PBS (pH 7.4), three times in 0.1 M PBS with 1% Triton X (20 min each time), and finally in 0.1 M PBS with 1% Triton X and 5% bovine serum albumin again for 20 min. After lectin incubation on the glue samples (in a dark humidity chamber) for 60 min at room temperature, the lectin solution was rinsed first with 0.1 M PBS with 1% Triton (again three times), and then three times in 0.1 M PBS immediately prior embedding in Fluoromount-G (Co. Thermo Fisher Scientific, Austria).

Afterwards, the paraffin-embedded samples were de-paraffined two times in Rotihistol for 5 min each and afterwards hydrated in 100% isopropanol, 100, 95, 70, 50, and 30% ethanol and distilled water for 3 min each. Afterwards, the samples were rinsed in PBS as well as PBS with Triton X, as for the glue samples.

Autofluorescence was controlled by incubating sections in buffer solution without fluorescent-labelled lectin. Specific

TABLE 1 | Overview of the applied histochemical tests and lectin affinity tests for the two cutaneous glands in *P. shermani* (von Byern et al., 2015) and *H. dunni*. In *P. shermani* some stainings and lectins were additionally tested and are highlighted grey in this table.

Staining applied	Specifity	*Plethodon shermani* (von Byern et al., 2015 and present study)		*Hynobius dunni* (present study)		
		Mucous gland	Granular gland	Mucous gland	Granular gland	Epithel/ Dermis
Periodic acid schiff reagent	Hexose mucosubstances	++	++ GGA	++	–	–
Alcian blue pH 1.0	Sulfated mucosubstances	+/–		++	–	+ nuclei
Alcian blue pH 2.5	Sulfated and carboxylated mucosubstances	++	++ GGA	++	–	++ nuclei
Alcian blue pH 1.0 + PAS	Sulfated glycoproteins	++ only for AB 1.0	–	++ combi (AB and PAS)	–	–
Alcian blue pH 2.5 + PAS	Sulfated and carboxylated mucosubstances	++ only for AB 2.5	++ GGA	++ AB+ PAS (local)	–	–
Toluidine blue O pH 4.5	Acidic proteins	++	++ GGA	+ to ++ (dorsal to ventral)	–	++ nuclei
Biebrich scarlet pH 6.0	Basic proteins	–	++	–	++ dorsal and ventral (both granula types)	++ nuclei
Biebrich scarlet pH 8.5			+/–		++ dorsal + ventral (both granula types)	+ nuclei
Biebrich scarlet pH 9.5			–		+ dorsal and ventral	+ nuclei
Biebrich scarlet pH 10.5			–		+/–dorsal and ventral	+ nuclei
Alicerin red S	Calcium	–	–	–	–	–
von Kossa	Calcium	–	–	++	++ GGA	–
Sudan black B	Lipids	+	+/–		+/–	
Arnow Staining	L-DOPA	–	–	–	++	–
Lectin applied	**Specifity**	***Plethodon shermani* (von Byern et al., 2015 and present study)**			***Hynobius dunni* (present study)**	
Concanavalin agglutinin (ConA)	α-linked Mannose	+	+	+	+/–membrane around GGA nuclei	++
Datura stramonium agglutinin (DSA)	N-acetylglucosamine (oligomers)	–	–	–	–	+/–
Maackia amurensis lectin (MAL)	N-acetylneuraminic acid linked to galactose and N-Acetylglucosamine (Neu5Ac (α2–6)gal (β1–4) GlcNAc)	–	–	–	–	+
Galanthus nivalis agglutinin (GNA)	Mannose-linked (Mana (1,3)Man)	++	++ GGA	+ Membrane around nuclei	+ Membrane around GGA nuclei	+/–
Artocarpus integrifolia lectin (JAC)	Galactose-linked to N-acetylgalactosamine (Galβ(1,3)GalNAc)	++	–	++	–	–
Vicia villosa Lectin (VVL)	N-acetylgalactosamine (GalNAca (1,3)Gal)> blood goup A	+	–	++	–	–
Succinylated wheat germ agglutinin (WGAs)	N-acetylglucosamine, no sialic acid residues	–	–	+ Granula membrane	–	–
Wheat germ agglutinin (WGA)	N-acetylglucosamine (oligomer > monomer > NANA)	–	+	–	–	–
Ulex europaeus agglutinin (UEA II)	Oligomers of b (1,4)- linked NAcetylglucosamine	–	++	–	–	–

The following lectins showed no affinity to the glue of Plethodon shermani *and* Hynobius dunni*: EEA, ECA, GSL II, LEL, PNA, SNA, STL, DBA, GSL I, LC.The data indicate that differences are in particular given for the granular glands, which are more alkaline in* H. dunni *and positive for calcium (von Kossa staining) and L-DOPA (Arnow staining). In view of the lectin residuals, a similar affinity could be observed, whereby the glue of* H. dunni *showed a strong positive reaction to N-acetylgalactosamine (lectin JAC and VVL). In* P. shermani *mannose-linked lectins (ConA and GNA) are also found.*

blockage with the inhibitory carbohydrate was not carried out as it could not be done for all the tested lectins.

Ultrastructure

As done earlier (von Byern et al., 2015), the glutardialdehyde-fixed samples were processed for transmission electron microscopy (TEM) as follows: Washing three times for 30 min in the cacodylate buffer (0.1 M, pH 7.4 at room temperature), immersing for 1.5 h in 1% osmium tetroxide (dissolved again in cacodylate buffer), dehydration in an ascending series of ethanol, and finally embedding the tissue sections in Epon resin (Co. Hexion, United States). After polymerization, ultrathin sections (50–70 nm; 200 sections per region in total) were prepared on a Leica UC7 ultra-microtome using ultra diamond knives (Co. Diatome AG, Switzerland). Sections were mounted on copper slot grids coated with formvar in dioxane, stained with 2.5%

gadolinium acetate and 2.5% lead citrate, and examined under a Zeiss Libra 120 electron microscope (Co. Zeiss AG, Germany). Serial semi-thin sections (1 µm) were stained with Toluidine Blue O and observed under a standard light microscope (Co. Olympus, Japan).

For scanning electron microscopy (SEM), the liquid nitrogen fixed samples were cryo-fractured, freeze-dried overnight (Alpha 1–4 LSC, Co. Christ, Germany), and subsequently mounted with conductive double-sided adhesive carbon on aluminum stubs. Element analysis of the gland content was performed via energy-dispersive x-ray spectroscopy (EDAX) in backscatter mode in an SEM JEOL IT 300 (Co. JEOL, Japan) using Ametek x-ray microanalysis and the TEAM Software 4.3 (Co. Ametek GmbH, Germany). The following parameters were used: >20.000 counts per seconds, 4 kV, and dead time >32. Subsequently, the samples were sputtered with gold (instrument JEOL JFC-2300HR, Co. JEOL, Japan) and imaged at high resolution in the same instrument.

Fluorescence Labelling

The PFA–PBS fixed samples were embedded in gelatin, fixed overnight in 4% formalin, and afterwards mounted and cut with a vibratome (Mod. VT 1200S, Co. Leica Germany) into 100 µm thick sections. To visualize the nuclei, muscles, and nerve fibres in the salamander skin, the sections were incubated with 2.5% Alexa Fluor TRITC-conjugated phalloidin (R415; Co. Invitrogen, United States) and DAPI (D21490; Co. Invitrogen, United States) as well as 1:100 diluted acetylated α-tubulin (T-6793; Sigma–Aldrich, United States) with FITC-labelled secondary antibody (M308012; Co. Invitrogen, United States), following the protocols of Wollesen et al. (2009, 2010).

The L-DOPA antibody testing was used as for other glue-producing animals (Zeng et al., 2019) with the following modifications: The paraffin-embedded sections were de-paraffined as previously, washed several times in 0.1 M PBS (pH 7.4), three times in 0.1 M PBS with 1% Triton X (again for 20 min each), and finally in 0.1 M PBS with 1% Triton X and 5% bovine serum albumin, again for 20 min. The sections were then incubated in primary antibody rabbit-anti-DOPA (ab6426, Co. Abcam, United States) diluted 1:500 for 4 h at 4°C. After several washing steps with 0.1 M PBS with 1% Triton X, the samples were incubated in secondary antibody goat anti-rabbit Alexa Fluor 488 (A 11,008 Co. Invitrogen, United States) diluted 1:500 in 0.1 M PBS with 1% Triton X for 1 h at 4°C in the dark. The samples were then washed three times in 0.1 M PBS with 1% Triton X (again 20 min each), three times in 0.1 M PBS, and finally embedded in resin (Fluoromont G, Co. Invitrogen, United States).

Additional Analyses for *Plethodon shermani*

Within the course of this study, paraffin-embedded tissue samples of *P. shermani* from the previous study (von Byern et al., 2015) were additionally stained for calcium (von Kossa and Alizarin Red S) and acidic proteins (Toluidine Blue O pH 4.5). Furthermore, isolated glue samples were used for the lectin affinity tests, parallel to those for *H. dunni*.

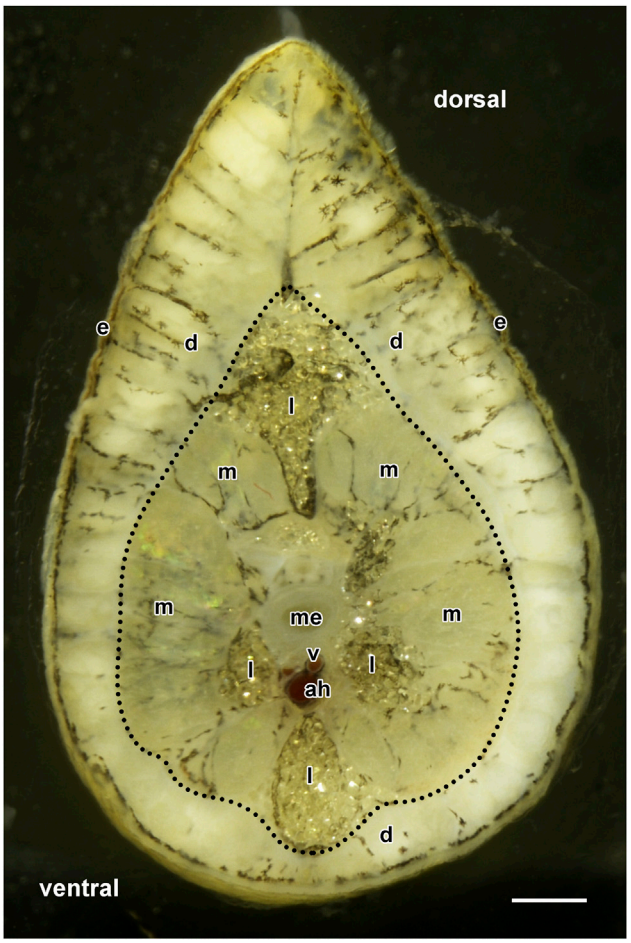

FIGURE 2 | Cross-section image of an *H. dunni* tail with its epidermis (e) and dermis (d, enclosed by red dotted lines) including its two cutaneous glands. The dermis varies considerably and is thicker on the pointed dorsal side than on the ventral side. Below the dermis, the subcutaneous muscles (m), medulla (me), vertebra (v), and arcus haemalis (ah) are visible. The tail contains large accumulations of lipid droplets (l). Scale bar = 1,000 µm.

RESULTS

General Structure of *Hynobius dunni* Skin

The epidermis has a thickness of about 50 µm dorsally and 60 µm ventrally, while the dermis is about 350 µm thick dorsally and 260 µm thick ventrally (data not statistically evaluated) (**Figure 2**). The epidermis contains about four to five layers of epithelial cells, showing a positive reaction for acidic (Toluidine Blue O) and basic proteins (Biebrich Scarlet at all pH values). Its nuclei furthermore reacted positive to Alcian Blue (both pH values), Toluidine Blue O, and Biebrich Scarlet at pH 6.0. PAS and both calcium stains (von Kossa and Alizarin Red S) showed no reaction in the epidermis. Back scattered electron detection from the SEM image (**Figures 3A,D**) confirmed the presence of potassium (**Figure 3B**) in this layer.

The *stratum compactum* of the dermis only stained positive for Biebrich Scarlet at all pH values. Pigment cells were present in

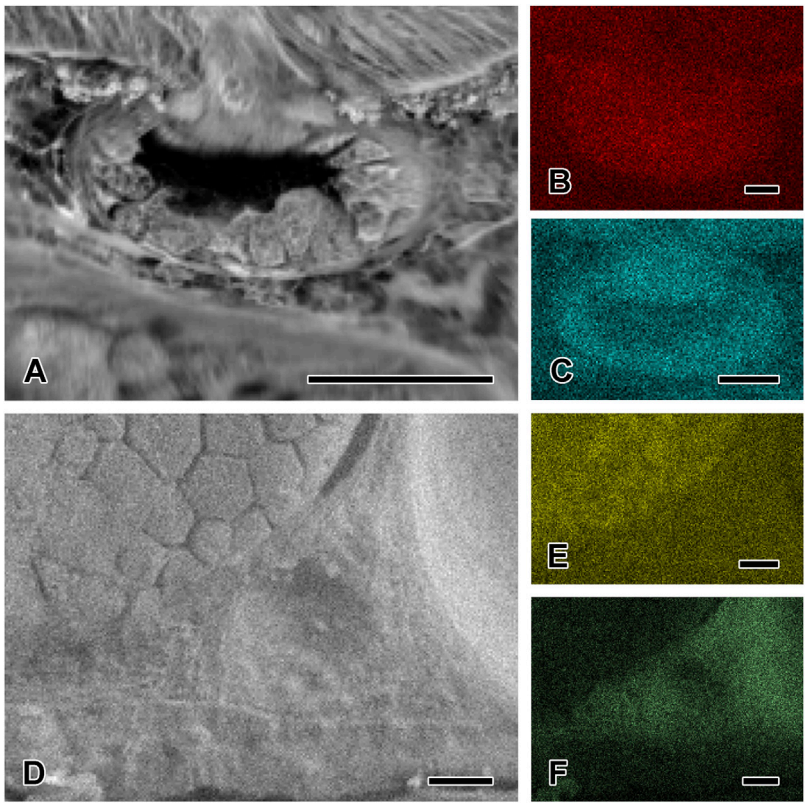

FIGURE 3 | Element distribution in the two cutaneous glands by EDX analysis. **(A)** SEM image of the mucous gland and the contributing dot mapping images confirming the presence of **(B)** potassium and **(C)** phosphorous in this gland type, and for potassium also in the epidermis. **(D)** SEM image of the granular gland and the contributing dot mapping images confirming the presence of **(E)** sulfur in this gland type. The surrounding dermal tissue contains **(F)** sodium and chloride. Scale bar in figures A, D, E, and F = 50 µm, in figures B and C = 25 µm.

between the mucous and granular glands in the *stratum spongiosum*. The EDX analysis revealed the presence of sodium (**Figure 3F**) and chloride (data not shown) in this layer.

The connective tissue in the epidermis and dermis showed strong reactivity to N-acetylneuraminic acid-linked sugars (lectin MAL) (**Figure 4A**) and mannose-linked moieties (lectin ConA and GNA) (**Figures 4C,D**) as well as a weak reaction to N-acetylglucosamine (lectin DSA) (**Table 1**).

Gland Types

As shown in the literature (Duellman and Trueb, 1994) and an earlier study on the glue-producing salamander *P. shermani* (von Byern et al., 2015), the mucous and granular gland types in *H. dunni* are multicellular. Both glands are distributed across the skin and are round to oval in shape.

Each gland type contains several glandular cells that are arranged patchwork-like along the outer periphery of the glands and synthesize secretory content of a different nature (**Figures 4C**, **5A**). Their nuclei are flat in shape, unlike those in the epidermis. Each gland is completely enclosed by a myoepithelial layer. Secretion of the glandular material takes place through a short flask-shaped open duct passing through the epidermis. In both gland types, funnel cells with elongated flat nuclei are present around the duct opening. A certain distribution pattern between the gland types could be observed in the different tissue regions: body regions:

The mucous glands (MG) are roundish and predominantly present in the ventral body and foot epidermis. The ovate granular glands (GG) are present in all skin samples with a high abundance in the dorsal body region and tail. In the tail they are especially concentrated but larger in size than in the dorsal tail region. This gland type is rarely present in the foot skin compared to the mucous gland.

Concerning their morphology and chemical properties, however, no variations between the gland types in the different body regions of. *H. dunni* could be observed in this study.

Mucous Gland

The mucous gland consists of several cells, filled with large roundish to polygonal granules, containing electron-bright and dense material (**Figures 6A,B**), which appear as smooth, homogenous sheet-like material when freeze-dried (**Figures 5A,B**). The nucleus of each cell type is located at its cell periphery; in the cytoplasm, various amounts of rough endoplasmatic reticulum (RER) could be observed. The cell extensions all around the mucus cells (toward the lumen and neighbouring cells) are connected to the adjacent cells only by

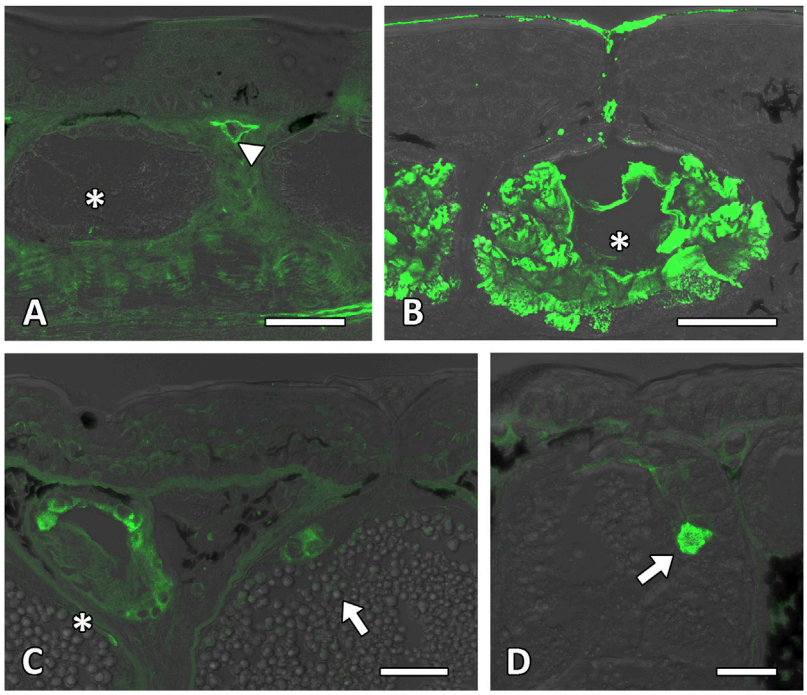

FIGURE 4 | Lectin affinity tests of the cutaneous glands. Lectin affinity tests confirm the presence of mannose-linked lectin. **(A)** The surrounding tissue and blood vessel membrane (white arrowhead) in the *stratum spongiosum* and *stratum compactum* show a light affinity to the lectin MAL. **(B)** The material of the mucous gland (white asterisk) shows a strong affinity to the lectin JAC. As also shown, the external secretion reacts to this applied lectin. **(C)** Positive reactions to the lectin GNL occur around the nuclei in the mucous gland (white asterisk), granular grand area (white arrow), epidermis and dermis. **(D)** The membranes of the granular gland area (white arrow) beside the surrounding tissue in the *stratum spongiosum* react positive to alpha-linked mannose (lectin ConA). Scale bar in all figures = 50 µm.

desmosomes (**Figure 5B**). In the secreted stage, only a thin alignment of secretory cells along the outer periphery of the mucous gland remains present.

The content of the *H. dunni* mucous glands showed a strong positive staining to PAS (**Figure 7A**, **Table 1**), Alcian Blue (both pH values) and Toluidine Blue O (**Figure 7B**) indicating the presence of hexose, sulfated and carboxylated mucosubstances. The combined staining of PAS and Alcian Blue (at pH 2.5), however, indicates that the gland cells produce different contents, whereby a few stained positive for PAS while others showed reactivity to Alcian Blue (**Figure 6C**). Blockage of the PAS staining was negative for the mucous gland. At Alcian Blue pH 1.0 (in combination with PAS), this clear difference could not be observed and here the stainings merged slightly, indicating the presence of sulfated glycoproteins in the gland (data not shown). A detailed characterization of the sugar moieties showed a strong affinity of the glandular content to N-acetylgalactosamines, such as JAC and VVL (**Figure 4B**). Mannose-linked moieties (lectin ConA and GNA) (**Figures 4C,D**) induced a light reactivity to the granular membranes and around the nuclei, as already given for the epidermis. The membranes furthermore showed a light affinity to N-acetylglucosamine (lectin WGAs) (**Table 1**).

Additionally to the mucosubstances, some glands were positive for calcium (von Kossa but negative for Alizarin Red S), and this element was also secreted, as shown in **Figure 7D**. The mucous gland was negative for Biebrich Scarlet at all pH values.

In the mucous gland, potassium (**Figure 3B**), and phosphorous (**Figure 3C**) were detected by EDX analysis from the SEM image (**Figure 3A**).

Granular Gland

The granular gland is ovoid to tubular in shape (**Figure 6D**). As in the mucous cells, the nuclei of the glandular cells are located at the outer periphery (**Figure 5C**). In addition, a significant amount of rough endoplasmatic reticulum surrounds the nuclei. The gland cells produce spherical to ovoid granules (**Figure 5D**), with a two- or three-layered appearance near the apical gland area: an electron-lucent core surrounded by a membrane, an electron-dense middle layer, and small dark spots in the outer margin (**Figure 6C**). Granules located in the basal area of the glands have an electron-light sheath, which is tightly packed and has a polygonal appearance (**Figure 6F**). This sheath is lacking in granules in the apical and central areas.

Hexose-containing mucosubstances (PAS staining) as well as sulfated and carboxylated glycoproteins (Alcian Blue at a pH 1.0 and 2.5 combined staining with PAS) and acidic proteins (Toluidine Blue O pH 4.5) were negative in the *H. dunni* granular gland (**Table 1**). The granular content was also negative for calcium (Alizarin Red and von Kossa staining) and lipids (Sudan Black B staining). Also, no affinity to any tested lectin could be found.

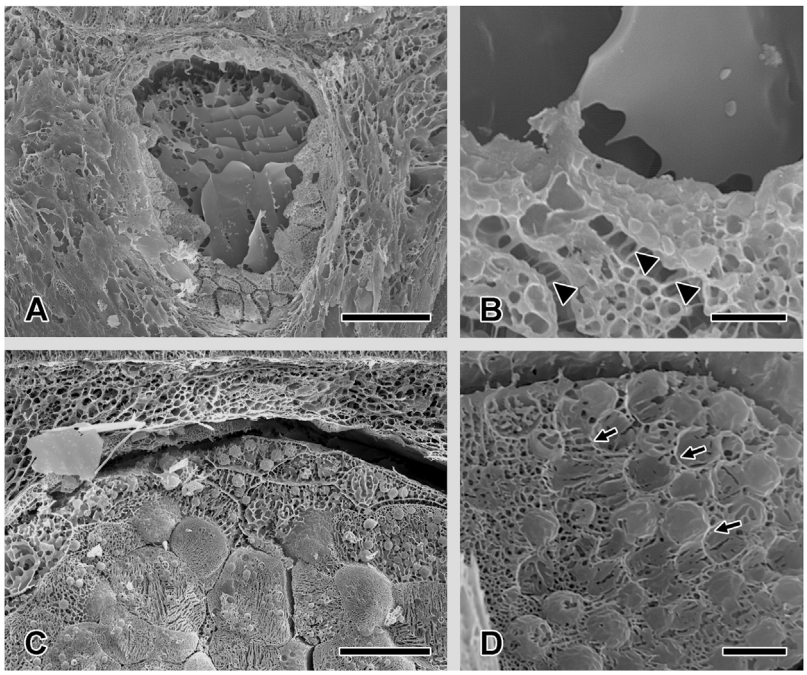

FIGURE 5 | Scanning electron microscopy characterization of the two cutaneous glands after freeze-drying. **(A)** and **(B)** The content of the mucous gland appears centrally as a smooth, homogenous sheet-like material. At the outer gland rim, the single gland cells, interconnected through desmosomes (white arrowhead), can be seen. **(C)** The secretory material of the granular glands appears as packages of different sizes. **(D)** Higher magnification shows that the granules are enclosed by membranes (white arrow). Scale bar in figures A and C = 50 µm, in figures B and D = 5 µm.

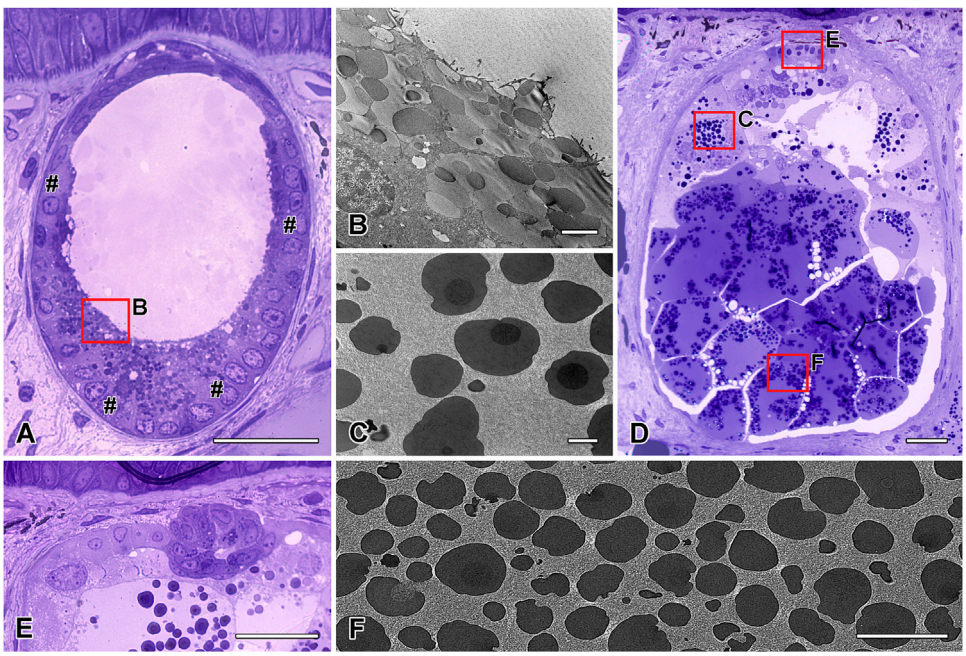

FIGURE 6 | Semithin and transmission electron microscopy characterization of the two cutaneous glands. **(A)** The roundish to oval mucous gland with its multicellular gland cells in the outer periphery (#) and **(B)** its granular content. The content of the **(D)** ovoid granular gland display a **(C)** two- or three-layered appearance near the apical gland area, while those of **(F)** the basal area have an electron-light sheath surround the granules. In the apical area of the granular gland, **(E)** a restricted granular gland area (GGA) is present. Scale bar in figures A and E = 50 µm, in figures B and C = 2.5 µm, in figure D = 100 µm.

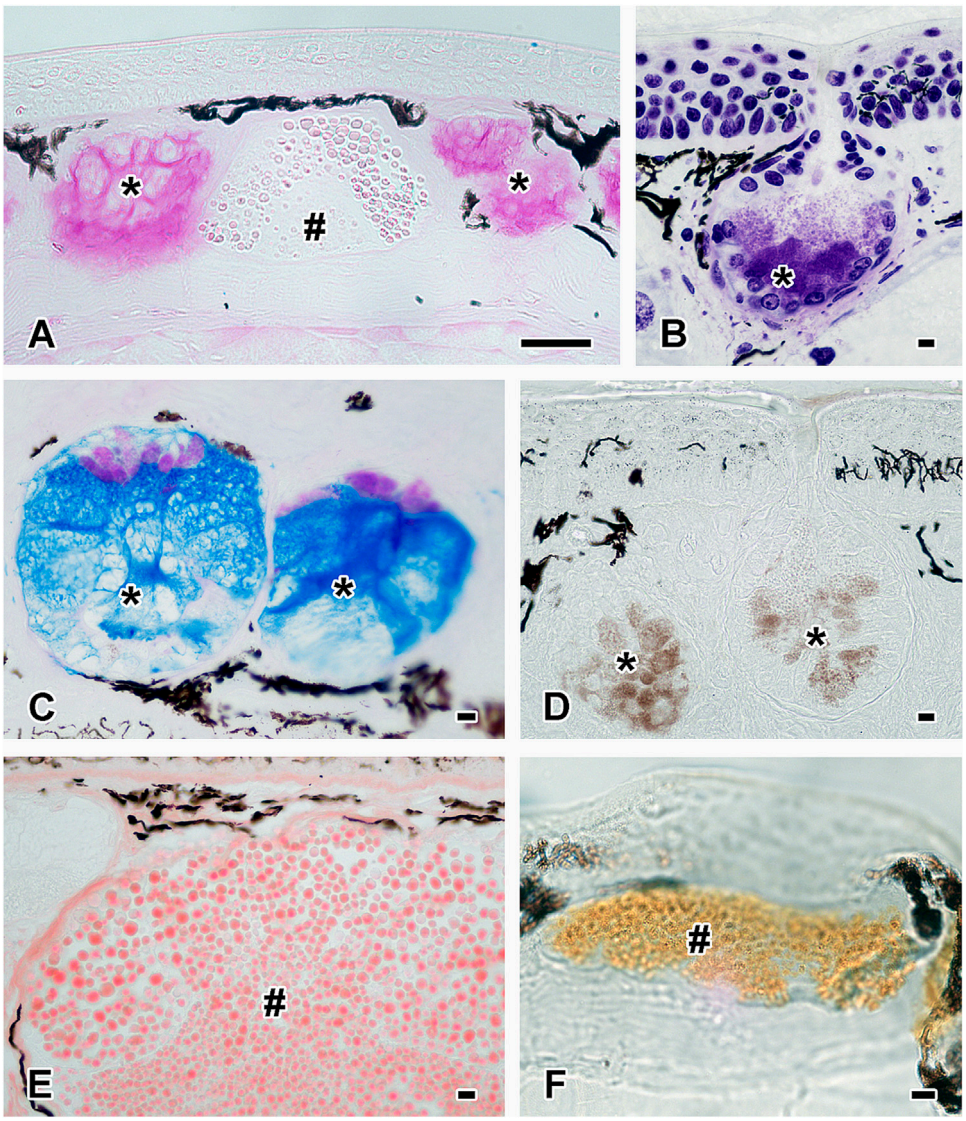

FIGURE 7 | Histochemistry of the two cutaneous glands. Histochemical staining confirms the presence of **(A)** hexose-containing mucosubstances (PAS staining) and **(B)** acidic proteins (Toluidine Blue) in the mucous gland (black asterisks). The content of the granular gland (black hashtag) partly stains positive for PAS in image A. **(C)** The combined staining (Alcian Blue pH 2.5 and PAS) shows that mucous glands (black asterisks) produce different material; pink stains positive for PAS and blue for Alcian Blue. **(D)** The mucous glands (black asterisks) also contain calcium (von Kossa staining). The content of the granular glands (black hashtag) reacts positively to **(E)** basic proteins (shown here Biebrich Scarlet pH 9.5) as well as to **(F)** L-DOPA (Arnow staining). Scale bar in all figures = 50 μm.

Instead, the content of the granular gland reacted strongly to basic proteins at pH 6.0 and 8.5 (Biebrich Scarlet staining), slightly stronger in the dorsal and tail epidermis than in the ventral and foot layers. With increasing pH level (9.5) of the Biebrich Scarlet (**Figure 7E**), the staining ability decreased, becoming barely visible at 10.5 in the epidermis. Also, some granules exhibited a dark red central core, indicating a higher density or stronger staining reaction, than in the granular periphery. Besides Biebrich Scarlet, the granules also reacted positively to Arnow staining, indicating the presence of L-DOPA in this gland type (**Figure 7F**), while tests with the respective anti-conjugated L-DOPA antibody remained negative. In the granular glands, sulfur (**Figure 3E**) could be detected (**Figure 3D**).

Granular Gland Area

Apart from the large GG cells described above, a restricted granular gland area (GGA) is also present in *H. dunni*, as observed previously for *P. shermani* (von Byern et al., 2015). This area is filled with large granules of uniform electron-dense material (**Figure 6E**). The nucleus of each cell, flat in shape, is located in the periphery; RER is barely visible.

The content of the GGA showed only a moderate reactivity to calcium (von Kossa staining), and its nuclei stained positive to

Alcian Blue (both pH values), Toluidine Blue O and Biebrich Scarlet at pH 6.0, as also given for the nuclei of the surrounding tissue. All other applied stainings remained unreactive.

As observed for the mucous gland and the surrounding tissue, the granular membranes in the granular gland also showed a slight positive affinity to mannose-linked residues (lectin ConA and GNA) (**Figures 4C,D**). All other lectin tests were negative.

P. shermani Gland Re-examination

The histochemical re-examination of the *P. shermani* cutaneous glands showed a positive reaction to Toluidine Blue O, but they were negative for both calcium stainings (Alizarin Red and von Kossa). Detailed characterization of the sugar moieties in *P. shermani* showed a strong affinity of the glandular content to N-acetylgalactosamines, such as JAC and weaker to VVL, as confirmed in *H. dunni* (**Table 1**). As for *H. dunni*, the anti-conjugated L-DOPA antibody also remained negative in *P. shermani*.

DISCUSSION

Although amphibian skin has various gland types and specific gland regions, two cutaneous gland types (mucous and granular glands) dominate the integument. The skin secretions have a wide variety of functions as defence, as a protective barrier, and for physiological regulation and respiration (Zug et al., 2001). Detailed morphological and chemical studies on these two cutaneous glands have been given for Ambystomatidae (e.g. *Ambystoma gracile*) (Brodie and Gibson, 1969), Plethodontidae (e.g. *Plethodon cinereus, Eurycea bislineata*) (Sever, 1989; Hecker et al., 2003; Sever and Siegel, 2015) and Salamandridae (e.g. *Pleurodeles waltl*) (Heiss et al., 2009). Histochemical and ultrastructural studies of the gland content of the glue and toxin-releasing species (*Pleurodeles waltl* and *P. shermani*) (Heiss et al., 2009; von Byern et al., 2015) indicate significant differences in view of the granules' appearance and staining reactivity. In the present study, we aim to focus on the Old World salamander *H. dunni* (Sparreboom, 2014) and verify the morphological and chemical differences to the data given for *P. shermani* (von Byern et al., 2015).

Gland Morphology

The results for *H. dunni* agree with the previous literature (Zug et al., 2001), confirming the presence of the mucous and granular gland types in the integument. According to the literature, the mucous glands are primarily dorsally located, while the granular glands are concentrated on the head and shoulders (Zug et al., 2001). In *H. dunni* and *P. shermani* the distribution is the opposite, with the mucous glands being distributed ventrally to a higher extent, and even on the foot (confirmed for *H. dunni*), while the granular glands show a higher density dorsally and in the tail region (von Byern et al., 2015 and present study). Nevertheless, in both species both gland types are involved in glue formation, as indicated by the histochemical results, although the extent to which each gland type contributes remains unclear. Observations (pers. comment first author) show that the adhesive secretions are primarily secreted from the tail and the dorsal side, and they have thus far not been observed through the skin of the foot region.

Ultrastructurally, the secretory droplets of the mucous gland in *H. dunni* somewhat agree with the data given for *P. shermani* (von Byern et al., 2015). While in *P. shermani* three different granule types (electron-dense, electro-bright, and fine-grained) appear, the granules of *H. dunni* partly concentrate and become electron-dense. A certain similarity with the *H. dunni* mucous content is given for the relevant gland type in *P. waltl,* which likewise contains only granules with a few dark spots or an opaque centre (Heiss et al., 2009).

On the other hand, the content of the granular glands in *H. dunni* (present study) exhibits a three-layered appearance as found in *P. shermani* (von Byern et al., 2015). The granular glands in *P. waltl* instead contain homogeneously distributed granules (Heiss et al., 2009). As shown for *P. shermani* (von Byern et al., 2015), also in *H. dunni* "the dark or spotted areas within the granules remain unclear and could not be verified histochemically; either the various granule types represent different stages of maturation or degrees of condensation or artifacts caused by the fixation process."

Gland Chemistry

The mucous glands in *H. dunni* react positively for carboxylated glycoproteins (e.g. Alcian Blue at pH 2.5 as well as strong PAS staining) and weakly for sulfated groups (e.g. Alcian Blue at pH 1.0). This resembles to results for *P. shermani* (von Byern et al., 2015) and most other glue or toxin-producing species (Brodie and Gibson, 1969; Hensel and Brodie, 1976; Sever, 1989; Hecker et al., 2003; Largen and Woodley, 2008; Heiss et al., 2009). However, exceptions exist among amphibians; in *P. waltl*, for example, the content of the mucous gland only stains positive for PAS and it lacks carboxylated mucosubstances (negative Alcian Blue pH 2.5 staining) (Bueno et al., 1981). The present study also confirms similarities in view of one of the major sugar moieties (lectin JAC) to *P. shermani*, indicating the presence of galactose-linked glycoproteins in the mucous gland material. Besides, mannose-linked moieties (lectin ConA and GNA) and the N-acetylglucosamine related sugars (lectin WGAs) are also part of the granules. However, the *P. shermani* lectin affinity tests were performed with 100 µm vibratome sections (von Byern et al., 2015), and not with 7 µm paraffin sections as in the case of *H. dunni*. Therefore, differences in the staining intensity and locality (i.e. granule content, granule membrane, etc.) of the sugar moieties are to be expected. In general a clear histochemical and lectin affinity congruence has been observed for the mucous glands of both glue-producing species.

The secretory material of the granular glands in *H. dunni* is of a proteinaceous nature, as indicated by the positive Biebrich Scarlet staining (present study), with slight staining differences related to the pH value: Those of *P. shermani* decrease with increasing pH value, while the granular gland content in *H. dunni* remains positive at all values (von Byern et al., 2015 and present study). In other salamanders (i.e., *P. waltl*, *Ensatina eschscholtzii oregonensis*), the granular gland reacts positively for basic glycoprotein components (positive PAS and Biebrich Scarlet/Bromphenol Blue/Naphthol Yellow S reaction) (Kuchta et al., 2008; Heiss et al., 2009; Sever and Siegel, 2015) and (at least *P. shermani*) has a certain affinity to N-acetylglucosamine related lectins as WGA and UEA II (von Byern et al., 2015). Such

reactivity could not be observed in *H. dunni*. Its content shows no affinity to sugar at all. Surprisingly, the *H. dunni* granular gland material as well as the secreted glue clearly stained positive for 3,4-dihydroxypheny-L-alanine (L-DOPA) using Arnow staining, confirming this well-known key adhesive molecule for the first time in salamander secretions (see chapter below).

Nevertheless, the here tested anti-conjugated L-DOPA antibodies were negative in relation to the positive results given for tunicates (Zeng et al., 2019). It remains unclear whether the antibodies showed no antigenicity response because paraffin-embedded tissue sections were used in this study. Alternatively, the L-DOPA in *H. dunni* may be linked in the granules and glue, inhibiting a clear reactivity. Further tests with native tissue and glue are planned to morphologically confirm the presence of L-DOPA in the granular glands beyond its chemical confirmation (see below).

The "third gland type" (granular gland area—GGA) adequately addressed in *P. shermani* (von Byern et al., 2015) could also be observed in *H. dunni* (present study). While the GGA in *P. shermani* has a distinct histochemical composition similar to that of the MG (**Table 1**), the GGA in *H. dunni* reacts positive to calcium. Also, consistency with the "modified granular glands" (MGG) (Staub and Paladin, 1997; Largen and Woodley, 2008) or "caudal courtship glands (CCG)" (Sever and Siegel, 2015) could be excluded as both showed a clear reactivity to sugars (PAS staining) and basic proteins (Naphthol Yellow S staining). Therefore, it could be assumed that the GGA in *H. dunni* show a different staining effect than that in *P. shermani* (von Byern et al., 2015). However, its involvement in the granular gland material formation of. *H. dunni* or even secretion remains unclear as the positive calcium staining in the isolated glue could have originated from the mucous gland as well.

Glue Formation

According to the literature, the mucopolysaccharide and proteoglycan secretions from the mucous gland form the slippery and slimy amphibian mucus (Zug et al., 2001). The granular gland, on the other hand, contains various substances, including biogenic amines (catecholamines and indolealkylamines) (Brandon and Huheey, 1981; Habermehl, 1981), toxins (Daly et al., 1994; Mebs and Pogoda, 2005), alkaloids (Brodie and Gibson, 1969; Brodie et al., 1979; Hamning et al., 2000), and different types of proteins (Williams and Larsen, 1986). Meanwhile, studies on the glue-producing salamander *P. shermani* have shown that both cutaneous glands are involved in glue formation (Largen and Woodley, 2008; von Byern et al., 2015). Histochemical and lectin affinity tests confirm that also in *H. dunni*, the content of both gland types and both body regions (dorsal/ventral) seems to be involved in the glue formation. This may also be the consequence that in the foot region less or no glue is released, related to the small number of granular glands present there.

L-DOPA Presence

3,4-dihydroxypheny-L-alanine (L-DOPA) is probably the best-characterized compound in the field of bioadhesion and it is prominent in the literature for its numerous novel biomimetic and adhesive-inspired applications (Hofman et al., 2018; Li et al., 2020; Kang et al., 2021). Thus far, L-DOPA has been confirmed in the glue of a few species, including bacteria (*Alteromonas* spp.) and marine invertebrates such as molluscs (*Mytilus* spp.), annelids (*Phragmatopoma* spp., *Sabella* spp.), and Platyhelminthes (*Entobdella* spp.) (Richter et al., 2018). L-DOPA has been detected in the glue of *P. shermani* by amino acid analyses (von Byern et al., 2017a) but in very low amounts (0.1 residues per hundred) compared the marine annelid *Phragmatopoma* spp (2.1 residues per hundred). The respective Arnow staining (von Byern et al., 2015) and L-DOPA antibody test (present study), however, remain negative in *P. shermani*. Thus far, L-DOPA has not been confirmed in the glue of any terrestrial or vertebrate species, including the glue-producing amphibians *Breviceps* spp. (Evans and Brodie, 1994) or *Notaden* spp. (Graham, 2005; Graham et al., 2006; Tyler, 2010; Graham et al., 2013). Further amino acid analyses are planned to quantify the L-DOPA amount in the *H. dunni* glue and verify its involvement in the glue formation and hardening.

Tribological Properties of Salamander Glues

To date, most bioadhesives from animals are mainly characterized chemically in particular as only a few microgram are necessary to analyse its composition, identify relevant key molecules and design recombinant analogues as the case for L-DOPA.

Characterizations of its tribological properties are rarely and limited to a few species only, mainly because the sample amount is often too low for the demanded measurements, the secretions could hardly being isolated or then show insufficient performance under *in vitro* conditions. Also in the case of amphibian adhesives as *Notaden* glue (Graham, 2005) the given tribological characteristics are insufficient although unpublished observations show remarkable performance concerning its hydrodynamic, wetting and adhesive properties:

Rheological properties of the *P. shermani* glue indicate a high water loss after secretion with a total weight loss of around 70% (von Byern et al., 2017a). While also in other species a water content of 85–90% (in the frog *Notaden*) or even up to 98% in the New Zealand glowworm larvae *Arachnocampa luminosa* could be measured (von Byern et al., 2017a; Wolff et al., 2021) a clear indication for a hydrodynamic performance after secretion is not stated. Up to know, no information is given for *H. dunni*, however a weight loss due to glue curing could likewise be observed. The secretions of *H. dunni* and *P. shermani* transform rapidly into a resin-like solid and adhere tightly to a wide range of materials, including glass, plastic, metal, or human skin (unpub. observation by the first author) as given for *Notaden* (Graham, 2005). Unpublished contact angle measurement for *P. shermani* indicate that the secretion appear hydrophilic after release but transform into a hydrophobic resin-like secretion after water loss and hardening. While marine species as mussels (850 kPA) and barnacles (>2 MPa) show a high bonding strength under wet conditions and after long curing time, amphibian species as the Australian frog *Notaden* reach strength values up to 78 kPA under wet and dry conditions within minutes (Graham, 2005). As hypothesized for *Notaden* (Graham et al., 2005) it remains unclear whether the salamander glue also represents a pressure-sensitive adhesive (PSA). The fact that the secretion of both glands contributes in the glue formation, that a strong loss of water is given after secretion and, in the case of *H. dunni*, L-DOPA may participate in the bonding effect presently favours also a chemical

bonding mechanism as is the case in other glue-producing animals. The question arises whether the presence of L-DOPA in *H. dunni* results in different tribological properties and bonding strength in relation to L-DOPA free adhesives in other glue-producing salamanders or amphibians as *Notaden*. Although most bioadhesives are per se hydrogels as mentioned above (Graham, 2005; Richter et al., 2018; Richter et al., 2019), such a high and fast water loss as observed for the salamander glue are not documented. Further studies are planned to determine the tribological properties of salamander adhesives, to understand its hydrodynamics and use this phenomena to design novel adhesives with improved lubrication features as planned with *ex vivo* models (Pailler-Mattei et al., 2015).

Demand of Bioadhesives in Future

The characterization and use of biological adhesives represent a promising area for the production of smart, biocompatible, and sustainable adhesives and sealants to various engineering domains (Kang et al., 2021). For example, a natural polymer based on mussels' glue components is used as surgical tissue adhesive (Lee et al., 2007; Mahdavi et al., 2008; Haller et al., 2011) while the visco-elastic properties of snail mucus provide new applications as patch for wound healing (Li et al., 2017). With the increasing progress in the tissue engineering and regenerative sector there will be surely much more demand for special adhesives with improved adhesion properties not only to covalently bind biomaterial to tissue but also as site-specific drug delivery (Mehdizadeh and Yang, 2013). Given medical glues base on proteins like fibrin and BSA-glutaraldehyde or synthetic cyanoacrylates, epoxy, or urethanes suffer from weak bonding strengths or negative side effects (toxic reaction products, inflammatory reactions or danger of contamination with viruses) (Rimpler, 1996; Donkerwolcke et al., 1998; Heiss et al., 2006; Blume and Schwotzer, 2010; Richter et al., 2019). This call for efforts is necessary to discover and to develop new biomimetic glue prototypes. The high bonding strength of amphibian glues and their ability to adhere onto dry surfaces makes this biomaterial interesting for practical applications in the industrial (Tyler and Ramshaw, 2002; Tyler, 2010) and medical sector (Millar et al., 2009; Szomor et al., 2009).

CONCLUSION

Although amphibians share the same skin organization, large differences appear in view of the characteristics of the integumentary mucous and granular gland. Their involvement in adhesive secretions has already been demonstrated chemically in North-American salamanders. The present study shows that also Japanese species as *H. dunni* produce adhesives as defence. The presence of L-DOPA in the glue of this terrestrial vertebrate is a novelty as this key molecule has so far only been detected in the adhesives of marine invertebrates. However, its participation in the glue formation and hardening is far from being settled.

DATA AVAILABILITY STATEMENT

The original contributions presented in the study are included in the article/supplementary material, further inquiries can be directed to the corresponding author.

ETHICS STATEMENT

Ethical review and approval was not required for the animal study because during cultivation, one specimen died and was immediately fixed for a morphological characterization of the skin gland system. Written informed consent was obtained from the owner for the participation of his animals in this study.

AUTHOR CONTRIBUTIONS

All authors listed have made a substantial, direct, and intellectual contribution to the work and approved it for publication.

FUNDING

This publication is based upon work from COST Action CA15216, supported by COST (European Cooperation in Science and Technology) and the Austrian Science Fund FWF (Project P31612-21), , APVV-16-0219 and VEGA 2/0103/17. Our particular thanks goes to Patrick Flammang from the Université de Mons, Laboratoire de Biologie Marine, Belgium for providing paraffin samples of *Sabellaria alveolata* as a positive control for the Arnow staining and Ute Rothächer for providing the L-DOPA antibody for this study.

ACKNOWLEDGMENTS

We specially would like to thank Livia Rudoll from the Unit Integrative Zoology, University of Vienna for her help and support during the histochemical studies and analyses.

REFERENCES

Arnold, S. J. (1982). A Quantitative Approach to Antipredator Performance: Salamander Defense against Snake Attack. *Copeia* 1982 (2), 247–253. doi:10.2307/1444602

Arnow, L. E. (1937). Colorimetric Determination of the Components of 3,4-Dihydroxyphenylalaninetyrosine Mixtures. *J. Biol. Chem.* 118, 531–537. doi:10.1016/s0021-9258(18)74509-2

Becker, P. T., Lambert, A., Lejeune, A., Lanterbecq, D., and Flammang, P. (2012). Identification, Characterization, and Expression Levels of Putative Adhesive Proteins from the Tube-Dwelling Polychaete *Sabellaria Alveolata*. *Biol. Bull.* 223 (2), 217–225. doi:10.1086/bblv223n2p217

Blume, J., and Schwotzer, W. (2010). "Medical Products and Their Application Range," in *Biological Adhesive Systems: From Nature to Technical and Medical Application*. Editors J. von Byern and I. Grunwald (WienNewYork: Springer-Verlag), 213–224. doi:10.1007/978-3-7091-0286-2_14

Böck, P. (1989). *Romeis Mikroskopische Technik*, München: Urban und Schwarzberg.

Brandon, R. A., and Huheey, J. E. (1981). Toxicity in the Plethodontid Salamanders *Pseudotriton Ruber* and *Pseudotriton Montanus* (Amphibia, Caudata). *Toxicon* 19 (1), 25–31. doi:10.1016/0041-0101(81)90114-8

Brodie, E. D. (1983). "Antipredator Adaptations of Salamanders: Evolution and Convergence Among Terrestrial Species," in *Plant, Animal and Microbial Adaptations to Terrestrial Environment*. Editors N. S. Margaris, M. Arianoutsou-Faraggitaki, and R. J. Reiter (New York: Plenum Publishing Corporation), 109–133. doi:10.1007/978-1-4615-8345-5_10

Brodie, E. D., and Gibson, L. S. (1969). Defensive Behavior and Skin Glands of the Northwestern Salamander, *Ambystoma gracile*. *Herpetologica* 25, 187–194.

Brodie, E. D., Nowak, R. T., and Harvey, W. R. (1979). The Effectiveness of Antipredator Secretions and Behavior of Selected Salamanders against Shrews. *Copeia* 1979 (2), 270–274. doi:10.2307/1443413

Brodie, E. D. (1977). Salamander Antipredator Postures. *Copeia* 1977, 523–535. doi:10.2307/1443271

Brodie, E. D., and Smatresk, N. J. (1990). The Antipredator Arsenal of Fire Salamanders: Spraying of Secretions from Highly Pressurized Dorsal Skin Glands. *Herpetologica* 46 (1), 1–7.

Bueno, C., Navas, P., Aguirre, J. A., Aijon, J., and Lopez-Campos, J. L. (1981). Skin Mucous Glands of *Pleurodeles Waltii* Mich. Histochemical and Ultrastructural Study. *Arch. de biologie (Bruxelles)* 92, 67–72.

Daly, J. W., Martin Garraffo, H., Spande, T. F., Jaramillo, C., and Stanley Rand, A. (1994). Dietary Source for Skin Alkaloids of Poison Frogs (Dendrobatidae)? *J. Chem. Ecol.* 20, 943–955. doi:10.1007/bf02059589

Donkerwolcke, M., Burny, F., and Muster, D. (1998). Tissues and Bone Adhesives-Historical Aspects. *Biomaterials* 19, 1461–1466. doi:10.1016/s0142-9612(98)00059-3

Duellman, W. E., and Trueb, L. (1994). *Biology of Amphibians*. Baltimore: John Hopkins University Press.

Evans, C. M., and Brodie, E. D. (1994). Adhesive Strength of Amphibian Skin Secretions. *J. Herpetology* 4 (499), 502. doi:10.2307/1564965

Fontana, M. F., Ask, K. A., MacDonald, R. J., Carnes, A. M., and Staub, N. L. (2006). Loss of Traditional Mucous Glands and Presence of a Novel Mucus-Producing Granular Gland in the Plethodontid Salamander *Ensatina eschscholtzii*. *Biol. J. Linn. Soc.* 87, 469–477. doi:10.1111/j.1095-8312.2006.00592.x

Graham, L. D. (2005). "Biological Adhesives from Nature," in *Encyclopedia of Biomaterials and Biomedical Engineering*. Editors G. L. Bowlin and G. Wnek (Oxon: Taylor & Francis), 1–18.

Graham, L. D., Glattauer, V., Huson, M. G., Maxwell, J. M., Knott, R. B., White, J. W., et al. (2005). Characterization of a Protein-Based Adhesive Elastomer Secreted by the Australian FrogNotadenbennetti. *Biomacromolecules* 6 (6), 3300–3312. doi:10.1021/bm050335e

Graham, L. D., Glattauer, V., Li, D., Tyler, M. J., and Ramshaw, J. A. M. (2013). The Adhesive Skin Exudate of Notaden Bennetti Frogs (Anura: Limnodynastidae) Has Similarities to the Prey Capture Glue of Euperipatoides Sp. Velvet Worms (Onychophora: Peripatopsidae). *Comp. Biochem. Physiol. B: Biochem. Mol. Biol.* 165 (4), 250–259. doi:10.1016/j.cbpb.2013.04.008

Graham, L. D., Glattauer, V., Peng, Y. y., Vaughan, P. R., Werkmeister, J. A., Tyler, M. J., et al. (2006). "An Adhesive Secreted by Australian Frogs of the Genus *Notaden*," in *Biological Adhesives*. Editors A. M. Smith and J. A. Callow (Heidelberg: Springer-Verlag), 207–223. doi:10.1007/978-3-540-31049-5_11

Habermehl, G. G. (1981). *Venomous Animals and Their Toxins*. Berlin: Springer-Verlag. doi:10.1007/978-3-642-88605-8

Haller, C. M., Buerzle, W., Brubaker, C. E., Messersmith, P. B., Mazza, E., Ochsenbein-Koelble, N., et al. (2011). Mussel-mimetic Tissue Adhesive for Fetal Membrane Repair: a Standardized *Ex Vivo* Evaluation Using Elastomeric Membranes. *Prenat. Diagn.* 31 (7), 654–660. doi:10.1002/pd.2712

Hamning, V. K., Yanites, H. L., and Peterson, N. L. (2000). Characterization of Adhesive and Neurotoxic Components in Skin Granular Gland Secretions ofAmbystoma Tigrinum. *Copeia* 2000 (3), 856–859. doi:10.1643/0045-8511(2000)000[0856:coaanc]2.0.co;2

Hecker, L., Madison, D. M., Dapson, R. W., and Holzherr, V. (2003). Presence of Modified Serous Glands in the Caudal Integument of the Red-Backed Salamander (*Plethodon Cinereus*). *J. Herpetology* 37 (4), 732–736. doi:10.1670/175-02n

Heiss, C., Kraus, R., Schluckebier, D., Stiller, A.-C., Wenisch, S., and Schnettler, R. (2006). Bone Adhesives in Trauma and Orthopedic Surgery. *Eur. J. Trauma* 32, 141–148. doi:10.1007/s00068-006-6040-2

Heiss, E., Natchev, N., Rabanser, A., Weisgram, J., and Hilgers, H. (2009). Three Types of Cutaneous Glands in the Skin of the salamandridPleurodeles Waltl. A Histological and Ultrastructural Study. *J. Morphol.* 270 (7), 892–902. doi:10.1002/jmor.10728

Hensel, J. L., and Brodie, E. D. (1976). An Experimental Study of Aposematic Coloration in the Salamander *Plethodon jordani*. *Copeia* 1976, 59–65. doi:10.2307/1443772

Hofman, A. H., van Hees, I. A., Yang, J., and Kamperman, M. (2018). Bioinspired Underwater Adhesives by Using the Supramolecular Toolbox. *Adv. Mater.* 30, 1704640–1704641. doi:10.1002/adma.201704640

Hopkins, G. R., and Migabo, S. W. (2010). Antipredator Skin Secretions of the Long-Toed Salamander (*Ambystoma macrodactylum*) in its Northern Range. *J. Herpetology* 44 (4), 627–633. doi:10.1670/09-216.1

Kamino, K., Inoue, K., Maruyama, T., Takamatsu, N., Harayama, S., and Shizuri, Y. (2000). Barnacle Cement Proteins. *J. Biol. Chem.* 275 (35), 27360–27365. doi:10.1016/s0021-9258(19)61519-x

Kang, M., Sun, K., Seong, M., Hwang, I., Jang, H., Park, S., et al. (2021). Applications of Bioinspired Reversible Dry and Wet Adhesives: A Review. *Front. Mech. Eng.* 7, 668262. doi:10.3389/fmech.2021.668262

Kiernan, J. A. (1999). *Histological and Histochemical Methods: Theory & Practice*. Oxford: Butterworth Heinemann.

Kuchta, S. R., Krakauer, A. H., and Sinervo, B. (2008). Why Does the Yellow-Eyed Ensatina Have Yellow Eyes? Batesian Mimicry of Pacific Newts (Genustaricha) by the Salamanderensatina Eschscholtzii Xanthoptica. *Evolution* 62 (4), 984–990. doi:10.1111/j.1558-5646.2008.00338.x

Largen, W., and Woodley, S. K. (2008). Cutaneous Tail Glands, Noxious Skin Secretions, and Scent Marking in a Terrestrial Salamander (*Plethodon shermani*). *Herpetologica* 64 (3), 270–280. doi:10.1655/08-010.1

Lee, H., Lee, B. P., and Messersmith, P. B. (2007). A Reversible Wet/dry Adhesive Inspired by Mussels and Geckos. *Nature* 448, 338–341. doi:10.1038/nature05968

Li, J., Celiz, A. D., Yang, J., Yang, Q., Wamala, I., Whyte, W., et al. (2017). Tough Adhesives for Diverse Wet Surfaces. *Science* 357 (6349), 378–381. doi:10.1126/science.aah6362

Li, Y., Cheng, J., Delparastan, P., Wang, H., Sigg, S. J., DeFrates, K. G., et al. (2020). Molecular Design Principles of Lysone-DOPA Wet Adhesion. *Nat. Commun.* 11 (3895), 1–7. doi:10.1038/s41467-020-17597-4

Mahdavi, A., Ferreira, L., Sundback, C., Nichol, J. W., Chan, E. P., Carter, D. J. D., et al. (2008). A Biodegradable and Biocompatible Gecko-Inspired Tissue Adhesive. *Proc. Natl. Acad. Sci.* 105 (7), 2307–2312. doi:10.1073/pnas.0712117105],

McManus, J. F. A., and Mowry, R. W. (1960). *Staining Methods: Histological and Histochemical*. New York: Paul Hoeber Inc.

Mebs, D., and Pogoda, W. (2005). Variability of Alkaloids in the Skin Secretion of the European Fire Salamander (*Salamandra Salamadra Terrestris*). *Toxicon* 45, 603–606. doi:10.1016/j.toxicon.2005.01.001

Mehdizadeh, M., and Yang, J. (2013). Design Strategies and Applications of Tissue Bioadhesives. *Macromol. Biosci.* 13 (3), 271–288. doi:10.1002/mabi.201200332

Millar, N. L., Bradley, T. A., Walsh, N. A., Appleyard, R. C., Tyler, M. J., and Murrell, G. A. C. (2009). Frog Glue Enhances Rotator Cuff Repair in a Laboratory Cadaveric Model. *J. Shoulder Elbow Surg.* 18 (4), 639–645. doi:10.1016/j.jse.2008.12.007

Mulisch, M., and Welsch, U. (2010). *Romeis Mikroskopische Technik*. Heidelberg: Spektrum Akademischer Verlag.

Nowak, R. T., and Brodie, E. D. (1978). Rib Penetration and Associated Antipredator Adaptations in the Salamander *Pleurodeles waltl* (Salamandridae). *Copeia* 1978, 424–429. doi:10.2307/1443606

Pailler-Mattei, C., Vargiolu, R., Tupin, S., and Zahouani, H. (2015). *Ex Vivo* approach to Studying Bio-Adhesive and Tribological Properties of Artificial Salivas for Oral Dryness (Xerostomia). *Wear* 332-333, 710–714. doi:10.1016/j.wear.2015.02.020

Richter, K., Grunwald, I., and von Byern, J. (2018). "Bioadhesives," in *Handbook of Adhesion Technology*. Editors L. F. M. da Silva, A. Oechsner, and R. Adams (Cham: Springer International Publishing), 1–45. doi:10.1007/978-3-319-42087-5_53-2

Richter, K., Pinheiro, M., Borcherding, K., Hartwig, A., Byern, J. V., and Grunwald, I. (2019). "CHAPTER 6. Adhesives for Medical Applications," in *Green Chemistry for Surface Coatings, Inks and Adhesives: Sustainable Applications*. Editors R. Höfer, A. S. Matharu, and Z. Zhang (Croydon: The Royal Society of Chemistry), 120–144. doi:10.1039/9781788012997-00120

Rimpler, M. (1996). Gluing - a Challange in Surgery. *Int. J. Adhes. Adhesives* 16, 10–20. doi:10.1016/0143-7496(96)88480-6

Ruyter, J. H. C. (1931). Eine einfache Methode für das Aufkleben von Zelloidin-Paraffinschnitten. *Z. für wissenschaftliche Mikroskopie für mikroskopische Technik* 48, 226–227.

Sagert, J., Sun, C., and Waite, J. H. (2006). "Chemical Subtleties of Mussel and Polychaete Holdfasts," in *Biological Adhesives*. Editors A. M. Smith and J. A. Callow (Heidelberg: Springer-Verlag), 125–143. doi:10.1007/978-3-540-31049-5_7

Sever, D. M. (1989). Caudal Hedonic Glands in Salamanders of the *Eurycea bislineata* Complex (Amphibia: Plethodontidae). *Herpetologica* 45 (3), 322–329.

Sever, D. M., and Siegel, D. S. (2015). Histology and Ultrastructure of the Caudal Courtship Glands of the Red-Backed Salamander, *Plethodon cinereus* (Amphibia: Plethodontidae). *J. Morphol.* 276 (3), 319–330. doi:10.1002/jmor.20342

Sheehan, D., and Hrapchack, B. (1980). *Theory and Practice of Histotechnology*. St. Louis USA: Mosby.

Sparreboom, M. (2014). *Salamanders of the Old World - the Salamanders of Europe, Asia and Northern Africa*. Zeist, Netherlands: KNNV Publishing. doi:10.1163/9789004285620

Spicer, S. S., and Lillie, R. D. (1961). Histochemical Identification of Basic Proteins with Biebrich Scarlet at Alkaline pH. *Stain Technology* 36, 365–370. doi:10.3109/10520296109113312

Staub, N. L., and Paladin, J. (1997). The Presence of Modifies Granular Glands in Male and Female *Aneides lugubris* (Amphibia: Plethodontidae). *Herpetologica* 53 (3), 339–344.

Stuart, S. N., Hoffmann, M., Chanson, J. S., Cox, N. A., Berridge, R. J., Ramani, P., et al. (2008). *Threatened Amphibians of the World*. Barcelona, Spain: Lynx Edicions.

Sugawara, H., Watabe, T., Yoshikawa, T., and Nagano, M. (2018). Morphological and Molecular Analyses ofHynobius dunniReveal a New Species from Shikoku, Japan. *Herpetologica* 74 (2), 159–168. doi:10.1655/herpetologica-d-17-00002.1

Szomor, Z. L., Murrell, G. A. C., Appleyard, R. C., and Tyler, M. J. (2009). Meniscal Repair with a New Biological Glue: An *Ex Vivo* Study. *Tech. Knee Surg.* 7, 261–265.

Tyler, M. J. (2010). "Adhesive Dermal Secretions of the Amphibia, with Particular Reference to the Australian Limnodynastid Genus *Notaden*," in *Biological Adhesive Systems: From Nature to Technical and Medical Application*. Editors J. von Byern and I. Grunwald (WienNewYork: Springer-Verlag), 181–186. doi:10.1007/978-3-7091-0286-2_11

Tyler, M. J., and Ramshaw, J. A. (2002). *An Adhesive Derived from Amphibian Skin Secretions*. Australia: PCT/AU2001/001172, 1–29.

von Byern, J., Dicke, U., Heiss, E., Grunwald, I., Gorb, S., Staedler, Y., et al. (2015). Morphological Characterization of the Glandular System in the Salamander *Plethodon shermani* (Caudata, Plethodontidae). *Zoology* 118 (5), 334–347. doi:10.1016/j.zool.2015.04.003

von Byern, J., Grunwald, I., Kosok, M., Saporito, R. A., Dicke, U., Wetjen, O., et al. (2017a). Chemical Characterization of the Adhesive Secretions of the Salamander *Plethodon shermani* (Caudata, Plethodontidae). *Scientific Rep.* 7 (1), 66471–664713. doi:10.1038/s41598-017-05473-z

von Byern, J., Mebs, D., Heiss, E., Dicke, U., Wetjen, O., Bakkegard, K., et al. (2017b). Salamanders on the Bench - A Biocompatibility Study of Salamander Skin Secretions in Cell Cultures. *Toxicon* 135, 24–32. doi:10.1016/j.toxicon.2017.05.021

Williams, T. A., and Anthony, C. D. (1994). Technique to Isolate Salamander Granular Gland Products with a Comment on the Evolution of Adhesiveness. *Copeia* 2 (540), 541.

Williams, T. A., and Larsen, J. H. (1986). New Function for the Granular Skin Glands of the Eastern Long-Toed Salamander, *Ambystoma macrodactylum* Columbianum. *J. Exp. Zool.* 239, 329–333. doi:10.1002/jez.1402390304

Wolff, J. O., von Byern, J., Piorkowski, D., Fang, J., Wang, X., Adler, L., et al. (2021). Adhesive Droplets of Glowworm Snares (Keroplatidae: Arachnocampa spp.) Are a Complex Mix of Organic Compounds. *Front. Mech. Eng.* 7. doi:10.3389/fmech.2021.661422

Wollesen, T., Cummins, S. F., Degnan, B. M., and Wanninger, A. (2010). FMRFamide Gene and Peptide Expression during central Nervous System Development of the Cephalopod Mollusk, Idiosepius Notoides. *Evol. Development*, 12, 113–130. doi:10.1111/j.1525-142x.2010.00398.x

Wollesen, T., Loesel, R., and Wanninger, A. (2009). Pygmy Squids and Giant Brains: Mapping the Complex Cephalopod CNS by Phalloidin Staining of Vibratome Sections and Whole-Mount Preparations. *J. Neurosci. Methods* 179 (1), 63–67. doi:10.1016/j.jneumeth.2009.01.021

Zeng, F., Wunderer, J., Salvenmoser, W., Ederth, T., and Rothbächer, U. (2019). Identifying Adhesive Components in a Model Tunicate. *Philosophical Trans. R. Soc. Ser. B, Biol. Sci.* 374, 1–10. doi:10.1098/rstb.2019.0197

Zug, G. R., Vitt, L. J., and Caldwell, J. P. (2001). "Anatomy of Amphibians and Reptiles," in *Herpetology - an Introductory Biology of Amphibians and Reptiles*. Editors G. R. Zug, L. J. Vitt, and J. P. Caldwell (San Diego: Academic Press), 33–76.

Conflict of Interest: The authors declare that the research was conducted in the absence of any commercial or financial relationships that could be construed as a potential conflict of interest.

Advantages of publishing in Frontiers

OPEN ACCESS
Articles are free to read for greatest visibility and readership

FAST PUBLICATION
Around 90 days from submission to decision

HIGH QUALITY PEER-REVIEW
Rigorous, collaborative, and constructive peer-review

TRANSPARENT PEER-REVIEW
Editors and reviewers acknowledged by name on published articles

Frontiers
Avenue du Tribunal-Fédéral 34
1005 Lausanne | Switzerland

Visit us: www.frontiersin.org
Contact us: frontiersin.org/about/contact

REPRODUCIBILITY OF RESEARCH
Support open data and methods to enhance research reproducibility

DIGITAL PUBLISHING
Articles designed for optimal readership across devices

FOLLOW US
@frontiersin

IMPACT METRICS
Advanced article metrics track visibility across digital media

EXTENSIVE PROMOTION
Marketing and promotion of impactful research

LOOP RESEARCH NETWORK
Our network increases your article's readership